Engineering and optimising a functional *in vitro* model of basal ganglia circuitry

Matthew James Köse-Dunn

PhD

June 2019

Keele University

Abstract

The majority of neurological diseases (such as Parkinson's and Huntington's diseases) are progressive, debilitating and currently incurable. In an ageing population, the prevalence of such diseases will only increase over time, creating a need for better pre-clinical tools that allow for more research into such diseases, as clinical trails are expensive and time-consuming. In this thesis I describe the development and optimisation of a pre-clinical *in vitro* neural model of functional basal ganglia circuitry. When this circuitry in the basal ganglia breaks down or is damaged, it can result in Parkinson's or Huntington's diseases, and by modelling these areas in both a healthy and damaged state *in vitro* we create a powerful platform for pre-clinical research into neurological disease. The model described here is a microfluidic compartmentalised device consisting of five sections linked by micro-scale channels, designed in AutoCAD and fabricatd by soft lithography. The design of this model allows for neural cell populations to be simultaneously isolated and connected, as axons grow through the channels to adjacent sections and create a neural circuit. The design of the device, chemical coating and microchannel width were all optimised in order for the device to better mimic the basal ganglia, culturing primary cells obtained from the cortex, striatum, globus pallidus and substantia nigra of rat embryos within the device. Extracellular recording methods were also introduced, using a multi-electrode array (MEA) in order to record spontaneous electrophysiological activity from the neural cultures (whether seperate or connected) and determine that the cells were functional. The effects of connectivity on functionality was determined across all relevant co-cultures. In order to make the device a mimic of Parkinson's disease, 6-OHDA was used to damage/destroy nigrostriatal dopamine neurons, and the effects of this loss on functionality were also assessed. The device is a powerful pre-clinical platform for research, modelling aspects of a healthy physiological basal ganglia and aspects of a damaged pathological Parkinsonian basal ganglia. The novel findings presented in this thesis show the potential of this microfluidic model to study basal ganglia circuitry and accelerate Parksinon's research.

Table of Contents

List of abbreviations

5PD	Five-port device
6-OHDA	6-hydroxydopamine
AD	Alzheimer's disease
ALS	Amyotrophic lateral sclerosis
AMPAR	α-amino-3-hydroxy-5-methyl-4-isoxazolepropionate receptor
ANOVA	Analysis of variance
AP	Action potential
BG	Basal ganglia
CAD	Computer-aided design
CNS	Central nervous system
CNT	Carbon nanotubes
CTX	Cortex
D1-5	Dopmaine receptor 1-5
DA	Dopamine
DAPI	4',6-diamidino-2-phenylindole
DAT	Dopamine transporter
DIV	Days in vitro
DMEM	Dulbecco's modified Eagle medium
E	Embryonic day
EAP	Extracellular action potential
ECM	Extracellular matrix
FSN	Fast-spiking neuron
GABA	Gamma aminobutyric acid
GDNF	Glial-derived neurotrophic factor
GFAP	Glial fibrillary acidic protein
GPi/e	Globus pallidus internal/external
HD	Huntington's disease
IMS	Industrial methylated spirit
iPSC	Induced pluripotent stem cell
IT	Intratelencepahlic
LAM	Laminin
LGE	Lateral ganglionic eminence
LTD	Long-term depression
LTP	Long-term potentiation
MAP2	Microtubule-associated protein II
MEA	Multi-electrode array
MGE	Medial ganglionic eminence
MPTP	1-methyl-4-phenyl-1,2,3,6-tetrahydropyridine
MSN	Medium spiny neuron
NCM	Neural culture media
NMDAR	N-methyl-D-aspartate receptor
NSC	Neural stem cell
PAN	Phasically activate neuron
PBS	Phosphate-buffered saline
PD	Parkinson's disease
PDL/PLL	Poly-D-lysine/poly-L-lysine
PDMS	Polydimethylsiloxane
PEI	Polyethylenimine
PNS	Peripheral nervous system
PT	Pyramidal type
PY	Phosphotyrosine
RMS	Root mean square
ROS	Reactive oxygen species
SEM	Scanning electron microscopy
SNc/r	Substantia nigra pars compactra/reticulate
STD	Standard deviation
STN	Subthalamic nucleus
STR	Striatum
TAN	Tonically activate neuron
TBS	Tris-buffered saline
TH	Tyrosine hydroxylase
UV	Ultraviolet
VGLUT2	Vesicular glutamine transporter II
VM	Ventral midbrain
VTA	Ventral tegmental area

List of tables

List of figures

Acknowledgements

First and foremost, I'd like to thank my excellent supervisory team in Professor Rosemary Fricker and Dr Paul Roach, along with my gifted senior Dr Munyaradzi Kamudzandu, without them this thesis would not have been possible as they have been supportive and insightful throughout the whole process.

I am also deeply grateful to Keele University, both the staff and students of the Huxley building and everyone at the Guy Hilton Research Centre, who I know will be dear friends for many years to come. Special thanks to Dr Dimitra Blana, whos expertise at writing Python code and handling large data sets saved me many weeks of fumbling around in the dark and generated some very pretty graphs.

Finally, I'd like to thank my wonderful wife Hati Köse-Dunn, we met thanks to this PhD and I would never have completed it without your support, love and warmth at all times.

Disclaimer

I declare that this is an original work and all sources of information are fully acknowledged and cited. Dr Dimitra Blana assisted in data processing by writing Python code to perform the complex analysis.

Chapter One: Introduction

The current development models for drugs designed to counteract or treat neurological and neurodegenerative diseases are insufficient to predict what pharmaceuticals will work on human disease patients. More efficient pre-clinical models are required, particularly at an *in vitro* level where a high level of control can be asserted, using cells in order to mimic specific areas of the brain in both a healthy and diseased state. By combining cell culture and scaffold fabrication, diverse *in vitro* models can be created to mimic *in vivo* systems, organs and disease states. The advancement from simple cell monolayer culture models to complex multilayer organ-on-a-chip models to multiple organ modelling systems shows the great promise of potentially mimicking the brain, the most complex functional organ. Microfluidic models and organ-on-a-chip models represent a multidisciplinary approach to fulfilling these criteria, with the ability to exert control over shape, size, biochemical and physical factors and gradients, the inclusion of 3D elements and flow and the integration with current cell culture systems. These models are far more efficient than current *in vivo* animal models, being high throughput, cheaper, faster and far more customisable. The model described in this thesis is fabricated to a high degree of accuracy and reproducibility, resulting in a device that can model both healthy brain circuitry and the transition that occurs during a disease state, all while retaining a high degree of control over all components within the model that would be lost in *in vivo* research. This chapter focuses on such *in vitro* neural modelling devices and their potential for researching neurological and neurodegenerative diseases. This modelling paradigm is discussed in relation to the brain, with an end goal of being able to create an *in vitro* model of the brain, specifically the basal ganglia, to study neurodegenerative diseases caused by damage to this area such as Parkinson's and Huntington's diseases. Once a functioning basal ganglia can be reproduced *in vitro*, the model can further be used as a platform for disease study.

1.0 Modelling the central nervous system

A detailed and comprehensive understanding of the structure and function of specific cells and tissues is vital for countering disorders and dysfunction within the human body. Gathering data on physiology and pathology *in vivo* is challenging due to issues with observing, accessing and manipulating cells and tissues while still retaining a reliable *in vivo* environment for the specific niche of study. One solution to these issues involves *ex vivo* research, studying biological models such as model organisms and cell/tissue cultures (Martinez-Morales and Liste. 2012, Meyer *et al.* 2013). Whilst animal testing on model organisms such as mice and rats is an established alternative technique to studying the human body itself, it has numerous shortcomings. Despite certain genetic and developmental similarities, rodent models are not sufficient for study of the human body. These

animals can develop artificial diseases and have unacceptably high risks of tumorigenesis and cancer, which means that the use of these animals as models can lead to unrealistic treatments with sub-par results which are often not reproducible, with only 11-25% of academic pre-clinical studies on animal models being reproducible in industry (Begley and Ellis. 2012). In addition, these models can lack heterogeneity compared to humans, especially important when modelling disease (Morgan *et al.* 2013, Simmons *et al.* 2013). For these reasons there are pressures to find alternatives and move away from using animal models. The 3R concept to replace, reduce and refine animal experiments has been established for over 50 years, and alternatives have been in constant development (Russell and Burch. 1959).

Cell and/or tissue models are far easier to access and modulate when compared to animal models, but they can lack the complexity of the *in vivo* environment (Yum *et al.* 2014). Due to this compromise, only the most simple, robust and reproducible models which also accurately mimic the *in vivo* environment can be considered for study. The more factors accounted for and sufficiently mimicked, the closer the model comes to representing the *in vivo* environment and being a suitable replacement for study (Bhatia and Ingber. 2014). Important factors to consider include: recreating the multicellular 3D niche of the tissue of interest (C. P. Huang *et al.* 2009), the interfaces and interactions with other cells and tissues such as cell-cell and tissue-tissue interaction (Strand *et al.* 2010), involving a suitable concentration of chemicals and growth factors (and when necessary, including a physiochemical gradient) (Almodovar *et al.* 2013), the inclusion of a perfusion system (similar to vascular perfusion *in vivo*) (Bergh *et al.* 2005, Kelly *et al.* 2013), using a material of a similar stiffness to that found *in vivo* (Klein *et al.* 2009, Tse and Engler. 2011), and use of micro- and nano-scale physical topographical features to mechanically stimulate and manipulate cells and tissues (Curtis *et al.* 2001), as *in vivo* areas are rarely as uniform and featureless as typical tissue culture surfaces.

Such a wide range of factors are necessary to consider when developing an *in vitro* model due to the inherent complexity and chaos in biology. Biological systems are composed of many proteins and chemical factors supporting millions of cells, which themselves are held in specific biochemical and physical environments, and interact with both neighbouring cells and any new or foreign factors. These systems exhibit a hierarchy ranging from proteins and other biological molecules/biochemical factors to cells which form tissues, to multicellular systems combining several tissues that form organs and organ systems, finally to multi-organ systems and the entire physiological mechanisms that form a complete organism. Organs and bodily systems are composed of not just cells, but cells arranged in a specific 3D manner, with structural scaffolds, blood supply to maintain nutrient levels and deliver signals, and the ability to respond to internal and external cues to modulate the function of the organ. This makes the creation of an accurate *in vitro* mimic of an *in vivo* microenvironment an extremely difficult task (Marx. 2015).

Systematic complexity reaches a peak when considering the nervous system, the most complex system of the body. This system is broadly split into two parts, the central nervous system (CNS, consists of the brain and spinal cord) and the peripheral nervous system (PNS consists of nerves that connect the CNS to the rest of the body, chiefly the limbs and organs). Neurons of the PNS carry information to the CNS, where complex decisions and functional changes are made (Laight. 2013). As a result, the PNS is functionally simplistic while structurally complex as PNS nerves need to innervate to the very peripheries of the body. These PNS neurons can be sensory or motor neurons, with the former carrying information to the CNS while the latter send CNS information to muscles and/or glands where orders are carried out. As PNS neurons often need to travel long distances and are unprotected by bone (unlike the CNS that has the skull for protection), the PNS is not dense and consists of long nerves stretching to peripheries and clusters of nerves in certain locations termed ganglia.

Unlike the PNS, the CNS is both structurally and functionally complex. Briefly, the brain contains both neuronal and non-neuronal cells (collectively referred to as neural cells). The neuronal cells (henceforth referred to as **neurons**) are the functional cells of the brain, carrying information in the form of electrical signals and chemical messengers (termed neurotransmitters) to other neurons, joined by junctions termed synapses to create the many neural networks/circuits within and between different areas of the brain. These neurons are mainly grouped by the kind of neurotransmitter they produce, as signals can be excitatory or inhibitory. Sufficient excitation results in an action potential being sent along the neuron, activating other neurons connected by synapses, whereas inhibition can reduce or halt these signals, making different neuron types vital when modulating signals in the brain. With this in mind, neurons can be classified as GABAergic (main inhibitory type, produce gamma aminobutyric acid (GABA)), glutamatergic, (main excitatory type, produce glutamate), cholinergic (produce acetylcholine), dopaminergic (produce dopamine, which modulates neuron signals) and serotonergic (produce serotonin, which can be excitatory or inhibitory). These neuronal subtypes can be found in different concentrations in different areas of the brain, and carefully modulate the wildly complex signals of the brain.

Non-neuronal cells (henceforth referred to as **glia**) are a family of different cell types, including oligodendrocytes that insulate neurons from misfiring by covering their axons with a myelin sheath; microglia that destroy pathogens and remove dead neurons, and astrocytes (also called astroglia).

Astrocytes are cells with complex structural and functional roles in the brain, despite classical ideas that they were simply structural ‘glue’ (hence glia) that held the brain together. Astrocytes can be morphologically classified as either protoplasmic or fibrous and are typically found in grey and white matter of the brain respectively (Sofroniew and Vinters. 2010). There is no CNS region where astrocytes cannot be found, they occupy non-overlapping domains throughout their anatomical

regions and interact with CNS vasculature to form a complex gliovascular network, defining cortical and subcortical functional regions while also regulating blood flow (Nedergaard *et al.* 2003). Protoplasmic astrocytes extend 5-10 main branches and are shaped like a star (hence astro), with each branch further branching to very fine points, resulting in a single astrocyte in the hippocampus or cortex being in contact with several hundred dendrites from multiple neurons and enveloping more than 100,000 synapses (Halassa *et al.* 2007). Despite this contact with neurons, astrocytes do not fire or propagate action potentials, but feature changes in their intracellular Ca^{2+} concentration, which allows for astrocyte-astrocyte and astrocyte-neuron communication and signalling. These internal Ca^{2+} changes can be intrinsic, triggered by neurotransmitter (especially glutamate) release from either neurons or astrocytes and propagated to nearby astrocytes, allowing for astrocytes to play a direct role in synaptic transmission (with astrocytes forming gap junctions with adjacent astrocytes) (Perea *et al.* 2009).

With astrocytes in contact with and enveloping virtually every synapse in the brain, it is clear that astrocytes play both an important structural and functional role. Other roles of astrocytes include maintaining homeostasis of the interstitial fluid in the brain (regulating fluid, ion, pH and neurotransmitter levels), delivering glucose and other energy metabolites from blood vessels to neurons (to allow sustained high neuronal activity), regulation of the blood brain barrier, and reactive gliosis/glial scar formation. Reactive gliosis is a response of astrocytes to CNS injury, varying with the severity of the injury, where astrocyte function is altered and regulated. Reactive gliosis can range from upregulation of glial proteins such as glial fibrillary acidic protein (GFAP) and reduced proliferation to tissue reorganisation and formation of a glial scar (astrocyte processes overlap across domains and deposit dense ECM to form a dense, narrow scar, which acts as a neuroprotective barrier to inflammatory cells and infectious agents) (Sofroniew and Vinters. 2010). Neurons and glia are maintained in a sensitive ratio, and numerous types of both families of cells exist within the brain.

A generic 1.5 kg human brain contains approximately 90 billion neurons and 90 billion glia (Herculano-Houzel. 2009). In addition, each neuron can connect with other neurons (and astrocytes, forming tripartite synapses (Perea *et al.* 2009, Bernardinelli *et al.* 2014)) via synapses, at an average of 7000 connections per neuron, resulting in approx. 100 trillion connections in the adult human brain (Drachman. 2005, Horn *et al.* 2014). Surely *in vivo* work with a system this complex would bypass the need to recreate this level of complexity in the lab, *in vitro*? Unfortunately, due to the innate complexity, heterogeneity and dense structure of the brain, *in vivo* work on a specific area of the brain is virtually impossible without damaging or influencing other areas of the brain and therefore changing its physiological state (Bilston. 2011). Thorough study of human and animal brains is sometimes only possible after death and dissection but due to a large number of physiological changes in the brain after death, data gleaned from a dead brain cannot be compared to a live brain and is limited (Szabo. 2004, Gordon and McKinlay. 2012). A better approach to take in order to

understand the brain is the 'bottom-up' *in vitro* approach as opposed to the 'top-down' *in vivo* approach. In line with this view, successes with brain study *in vivo* have largely been due to the use of micro-scale neural devices and models fabricated *in vitro* (Takehara *et al.* 2014).

Development of *in vitro* cell therapies and pre-clinical models aiming to better understand the brain are extremely active areas of research, partly in due to the fact that mature neurons in the CNS do not divide and consequently do not regrow functional axons after damage, resulting in degeneration and cell death over time after injury or throughout aging (Horner and Gage. 2000, Shoichet *et al.* 2008). Due to this lack of regeneration, injury in the CNS is a serious issue and the cause of many major neurological diseases.

1.0.1 Neurological diseases and disorders

There are multiple ways to categorise neurological diseases, but the major types of neurological diseases include those caused by:

- **Genetic disorders** such as Huntington's disease (HD) (Pringsheim *et al.* 2012) and muscular dystrophy (Mah *et al.* 2014)
- **Cellular degeneration** such as Parkinson's disease (PD) (Pringsheim *et al.* 2014) and Alzheimer's disease (AD) (Reitz. 2012)
- **Peripheral movement disorders** such as amyotrophic lateral sclerosis (ALS) (Robberecht and Philips. 2013) and multiple sclerosis (Goldenberg. 2012)
- **Damage to CNS blood supply** resulting in stroke (Sahathevan *et al.* 2012)
- **Electrophysiological disorders** such as epilepsy (Acharya *et al.* 2013)
- **Physical injury** resulting in spinal cord injury (Silva *et al.* 2014) and/or traumatic brain injury (Blennow *et al.* 2012)
- **Cancers** including glial and non-glial tumours (Crocetti *et al.* 2012)
- **Infections** such as bacterial meningitis (van de Beek *et al.* 2012).

The vast majority of neurological conditions have unknown causes. This lack of knowledge concerning causative mechanisms of human neurodegenerative disease further outlines the vital importance of developing efficient research methods, especially when taking into account the prevalence and fatality of some of the conditions. More effective pre-clinical assessment is required in order to produce more relevant clinical trials and make further discoveries about these diseases and disorders, so as to further refine the process from the pre-clinical phase.

Of these diseases, Parkinson's disease will be the focus of the work in this thesis.

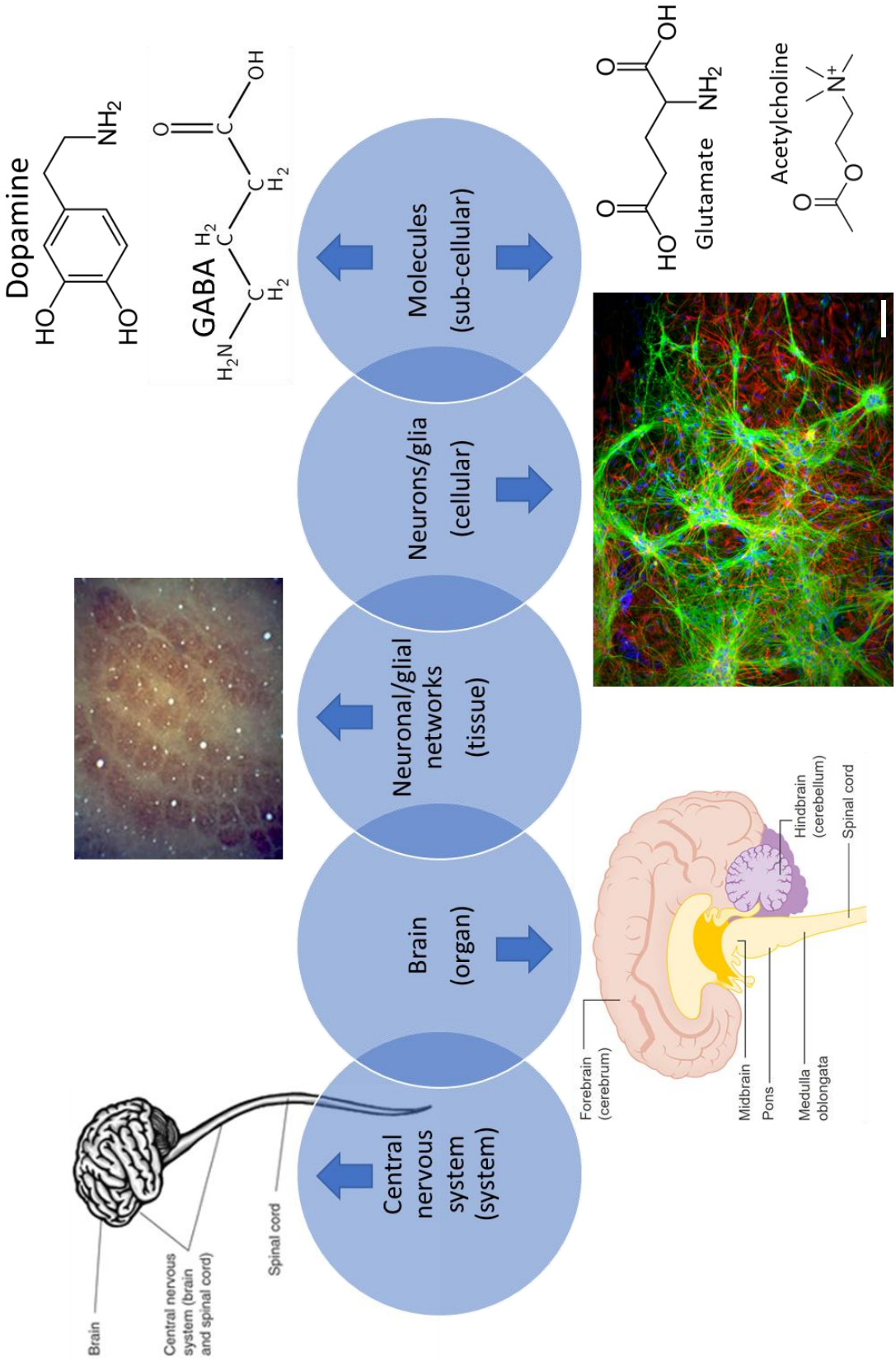

Figure 1.1: Complexity within the central nervous system (CNS). Tissue level: rat barrel corticies, cellular level, image shows neurons in green (β-tubulin stain), astrocytes in red (GFAP stain) and cell nuclei in blue (DAPI stain) (scale bar 100 µm). Images from Wikimedia Commons: central nervous system.svg (by Grm wnr), brain human sagittal section.svg (by Patrick J Lynch), CO40xComplete.jpg (by Imbrickle). Images released into the public domain.

1.1 Parkinson's disease

First described in 1817 by James Parkinson as a shaking palsy, Parkinson's disease (PD) is caused by the loss of nigrostriatal dopamine (DA) neurons in the substantia nigra pars compacta (SNc) resulting in striatum (STR) DA deficiency (Lees. 2007). With DA not identified in the brain until 1958 (Montagu. 1957) and PD still without a reliable cure or treatment today (at time of writing), PD represents the second most common age-related neurodegenerative disease (first being Alzheimer's disease). Accelerated research is sorely needed in order to make some headway towards a solution, now over 200 years after the discovery of PD.

1.1.1 Prevalence

PD is a progressive disease with the mean age of onset being 55, incidence increasing with age from 2/10,000 overall to 12/10,000 by age 70 (Dauer and Przedborski. 2003, Pringsheim *et al.* 2012), in general affecting 1-2% of all individuals above the age of 65 (Van Den Eeden *et al.* 2003). The symptoms of PD worsen from onset over time, with the mortality rate of PD patients up to three times greater than normal subjects of the same age. In a persistently ageing population, the incidence of PD will only increase, leading to exponentially more cases. Approximately 95% of PD cases have an unknown cause, with the remaining 5% having a heritable genetic component (Lazaro *et al.* 2017).

1.1.2 Genetic component

As with other neurological diseases (such as Alzheimer's and Huntington's), PD is a complex disorder involving both genetic, environmental and unknown factors. Numerous genetic mutations are linked to PD and are associated with familial PD susceptibility: dominant mutations in leucine-rich repeat kinase 2 (LRRK2) and α-synuclein, as well as recessive mutations in Parkin, PTEN-induced putative kinase (PINK1), DJ-1 and glucocerebrosidase (Lazaro *et al.* 2017). Alongside these mutations, genome-wide association studies have identified over 25 genetic risk factors associated with PD (Verstraeten *et al.* 2015).

Of all these mutations, there has been a particular focus of study on α-synuclein, due to the fact that a classic pathological hallmark of PD is the accumulation of protein aggregates termed Lewy Bodies (LBs), and these LBs are mainly composed of α-synuclein protein. Notably, α-synuclein protein is highly abundant in both CNS and PNS neurons (up to 1% of the total protein content) (Mizuno *et al.* 2012) and is associated with synaptic vesicles (Nemani *et al.* 2010). In addition, α-synuclein exists in multiple forms and can act in a prion-like manner, spreading from Parkinsonian neurons to healthy neurons and recruiting healthy α-synuclein into aggregates and LBs, propagating throughout cell cultures *in vitro* and CNS tissue *in vivo* (Recasens *et al.* 2014). Despite this wealth of knowledge concerning PD genetic components and α-synuclein mechanisms, there is still a limited

understanding of how these mutations lead to the cytotoxicity seen in PD (Lazaro *et al.* 2017), again highlighting the need for better pre-clinical cell-based models that can mimic aspects of PD for accelerated research.

1.1.3 Symptoms

PD symptoms include but are not limited to (Dauer and Przedborski. 2003, Hague *et al.* 2005, Jankovic. 2008, Benam *et al.* 2015):

- *Tremor at rest* (which decreases with voluntary movement)
- *Rigidity* (an increased resistance to passive movement of limbs)
- *Bradykinesia* (slowness of movement, impairs normal daily activities such as dressing and eating significantly)
- *Hypokinesia* (reduced movement amplitude)
- *Akinesia* (absence of normal unconscious movements such as arm swinging while walking).

These main symptoms lead to a constellation of other symptoms such as *hypomimia* (lack of normal facial expressions), *hypophonia* (decreased voice volume), *drooling* (failure to swallow automatically), *micrographia* (decreased size), decreased stride length while walking and slower handwriting speed. PD patients also exhibit other general motor symptoms such as loss of reflexes, a stooped posture, tendency to fall (resulting in eventual confinement to wheelchairs) and freezing during voluntary movement. In addition, there are numerous non-motor symptoms such as abnormal cognition, lack of initiative (becoming passive and withdrawn), delayed responses to questions, slower cognitive processes, gradual loss of taste, depression and dementia (especially in older patients).

1.1.4 Pathology

PD pathology involves loss of nigrostriatal DA SNc neurons that usually project to the STR and deliver DA, and presence of LB protein aggregates within select neurons (Cronin-Furman *et al.* 2013, Cipriani *et al.* 2014). These LBs are spherical and are composed of numerous proteins including α-synuclein, parkin, ubiquitin and neurofilaments and are found within the cells of all affected areas (Dauer and Przedborski. 2003).

Cell bodies in the SN contain neuromelanin, a complex polymer pigment that gave the SN region its name: substantia nigra, literally black substance. The loss of these neurons during PD results in a depigmented and less black SN, the classical method of diagnosing PD post-mortem. Neuromelanin is also associated with the oxidation of dopamine within the SN and with PD itself, as LBs are found within the boundaries of the pigment (Dauer and Przedborski. 2003). One study on neuromelanin treated cells with both neuromelanin and synthetic dopamine melanin, with the data suggesting a

protective role for neuromelanin under conditions of high oxidative load (J. Li *et al.* 2005). Findings such as this constantly provide new evidence for a physiological role of essential components in the SNc, dopamine or the BG itself both *in vitro* and *in vivo* and highlights the caution with which data based upon model systems should be interpreted.

By the time PD symptoms appear 60% of SNc DA neurons have been lost and levels of DA in the STR have decreased by 80%. This cell loss is distinct to PD and different to age-related cell loss (despite age being a major factor in PD), affecting nigrostriatal terminals in the STR more than cell bodies in the SNc (suggesting that the DA neuron terminals in the STR are dying back) (Dauer and Przedborski. 2003). Destruction of nigrostriatal terminals at the STR occurs first and SNc neuron death occurs later, protecting these STR terminals has been shown to prevent SNc neuron death in mice (Wu *et al.* 2003). Notably, DA neurons in the nearby ventral tegmental area (VTA) are largely unaffected by PD and continue to project to the caudate nucleus. This may be related to the fact that the SNc mainly projects to the STR and the VTA projects mainly to the prefrontal cortex, where synaptic DA uptake in the STR is dependent solely on DAT while the prefrontal cortex has other transporters that take up DA more efficiently (Dauer and Przedborski. 2003).

While PD is mainly focused on the SNc-STR nigrostriatal pathway, the consequence of losing this pathway in PD has major impacts on other nuclei of the basal ganglia (BG). PD can be characterised by hyperactivity and synchronised oscillations in the subthalamic nucleus (STN) and globus pallidus internal/external (GPi/e), with the STN potentially being involved with inhibition, impulsivity and executive control in PD (Jahanshahi *et al.* 2015). Loss of SNc-STR connections also leads to a doubling of the number and strength of synaptic connections between GPe-STN, opposing hyperactivity but contributing to abnormal firing patterns in the STN during PD (Fan *et al.* 2012). These downstream changes are a consequence of the nigrostriatal pathway being an early input to the BG, changes in this pathway result in changes to all downstream nuclei. However, upstream nuclei are also affected, such as the CTX. D1 and D2 receptors are expressed in CTX intratelencepahlic (IT) neurons (but not pyramidal type (PT) neurons) and DA has a huge influence on corticostriatal connectivity and modulation of IT and PT CTX neurons. There are IT/PT-specific changes in response to PD, such as a reduced PT neuron firing rate while IT neurons are largely unaffected, resulting in a reduction of excitatory input to STR medium spiny neurons (MSNs) of the indirect pathway. Reduced PT neuron firing is significant as they are a part of the motor system and project to the STN (which becomes hypersensitive to input during PD). Deep brain stimulation of the STN and optogenetic stimulation of PT neurons have both been used to alleviate PD symptoms (Shepherd. 2013).

1.1.5 Potential causes

While the exact cause and mechanism of action of sporadic PD is still unknown, two centuries of experimentation and speculation have led to several robust theories.

The earliest was the environmental toxin theory, that the neurodegeneration found in PD was due to exposure to an exogenous neurotoxin. This theory was given weight by the existence of several chemicals that caused similar pathologies to PD upon exposure, such as 1-methyl-4-phenyl-1,2,3,6-tetrahydropyridine (MPTP), paraquat (herbicide similar to MPTP's metabolised form, MPP+) and rotenone (insecticide, also similar to MPP+) (Langston *et al.* 1999). These are mitochondrial and cellular toxins found in the environment and were often used as insecticides or to remove unwanted organisms, resulting in human exposure and resultant damage. However, while MPTP can cross the blood brain barrier, the toxic metabolite ionic form MPP+ cannot pass the blood brain barrier due to the charge. In addition, rotenone and paraquat are unstable in solution and chronic environmental exposure has not been linked to causing PD, resulting in a lack of convincing data to support the environmental toxin theory (Dauer and Przedborski. 2003). Despite this, environmental and lifestyle factors are still important considerations, for example cigarette smoking and coffee are associated with decreased PD risk (Hernan *et al.* 2002).

Another theory also relies on toxins, but endogenous rather than exogenous. Metabolic processes can produce harmful waste products in the body, and DA metabolism generates reactive oxygen species (ROS) that can cause mitochondrial damage (Cohen. 1984). Patients who lack enzyme cytochrome P450 (which has a role in in detoxification) have a greater risk of developing early-onset PD (Sandy *et al.* 1996), and Parkinsonian brains have been found to contain substances toxic to DA neurons such as isoquinoline (interestingly, these substances can be derived from exogenous MPTP) (Nagatsu. 1997).

Regardless of initial causative source, studies have suggested two major mechanisms for PD pathogenesis: protein misfolding and aggregatioin, and mitochondrial dysfunction linked to oxidative stress (Dauer and Przedborski. 2003). These theories are not mutually exclusive and may well act in concert, with oxidative damage to α-synuclein shown to result in misfolding and aggregation (Giasson *et al.* 2000). Notably, these potential mechanisms are shared with other neurodegenerative diseases, specifically Alzheimer's disease and Huntington's disease (Rajput *et al.* 1993, Rosen *et al.* 2007), and data from these fields is a useful perspective on age-related neurodengerative diseases.

In sporadic PD, it is uncertain if protein aggregates are neurotoxic (by causing direct damage, deforming cells, interfering with intracellular trafficking, hoarding proteins that are important for neuronal survival, etc) and aggregation formation results in neurodegeneration, or if protein misfolding and subsequent aggregation is not associated with cell death and is a cellular defense mechanism (Cummings *et al.* 2001). Soluble misfolded proteins (such as α-synuclein) have been shown to be neurotoxic, and while protein aggergates and LBs are a classic sign of PD, it is unclear how these aggregates affect sporadic PD (Auluck *et al.* 2002). In heritable PD, mutations either

directly induce abnormal protein conformations, or indirectly interfere with chaperone processes that would normally recognise and process toxic misfolded proteins.

There is abnormal activity in mitochondrial complex I in PD, suggesting that the neurons are subject to oxidative stress and increased production of ROS. These ROS cause cellular damage by reacting with biochemical factors with the cell, resulting in further damage to mitochondria and further production of ROS, a cascade that causes serious oxidative damage to the cell (Cohen. 2000). SNc dopaminergic neurons in PD patients have demonstrated signs of oxidative damage and reduced glutathione, indicating that oxidative stress may also be responsible for PD (Jackson-Lewis *et al.* 2012). In addition, increased ROS also increases the amount of misfolded proteins, and DA neurons inparticular are at greater risk due to DA metabolism also generating ROS (Cohen. 1984, Giasson *et al.* 2000). However, it should be noted that this data was gathered from post-mortem or PD models with extremely low numbers of DA neurons, as these have been destroyed in the disease, and this data was mostly gleaned from glial and non-DA neurons. In addition, diseases where oxidative phosphorylation and mitochondrial function are directly affected are rarely associated with subsequent PD, suggesting that abnormal levels of ROS in PD may be due to the dying cells, and not causative of cell death (Dauer and Przedborski. 2003).

1.2 The basal ganglia

Neurons within the brain are highly organised, both structurally – cells can organise into dense groups termed 'nuclei' or layered sheet structures such as the cortex – and functionally, with both excitatory and inhibitory signals travelling between brain areas in hierarchical or cyclical fashions, controlling and modulating signals from other brain areas, both directly and indirectly. An area that exemplifies this standard of both structural and functional organisation is the basal ganglia (BG), a group of subcortical nuclei. The main nuclei of the BG include the **striatum** (STR), the largest structure of the BG; the **globus pallidus** (GP), consisting of functionally distinct internal (GPi) and external (GPe) sections; the **subthalamic nucleus** (STN), the only excitatory structure of the BG; and the **substantia nigra** (SN), which consists of two functionally distinct parts, namely the pars compacta (SNc) and the pars reticulata (SNr). These BG nuclei receive input from the **cortex** (CTX) and output to the thalamus, the brainstem and the spinal cord, outlining the importance of the BG in movement (Blandini *et al.* 2000, Smeets *et al.* 2000, H. F. Kim and Hikosaka. 2015). The location of the BG within the brain is seen in **Fig.1.2A** while a basic diagram of BG connectivity is reproduced in **Fig.1.2B.**

The importance of carefully regulated signals in the BG is highlighted when the system breaks down. Damage to certain areas of the BG results in a number of infamous neurological diseases: Huntington's disease (HD), caused by a degeneration of GABAergic neurons in the STR (Walker. 2007) and Parkinson's disease (PD), caused by a loss of dopaminergic neurons in the SNc (Blandini *et al.*

2000, Hague *et al.* 2005). Due to the currently incurable, progressive and prevalent nature of these diseases, the BG has received a great deal of scientific attention. Creating an *in vitro* model of this area would result in a pre-clinical model and a powerful platform for study, both of a physiologically healthy and pathologically damaged BG.

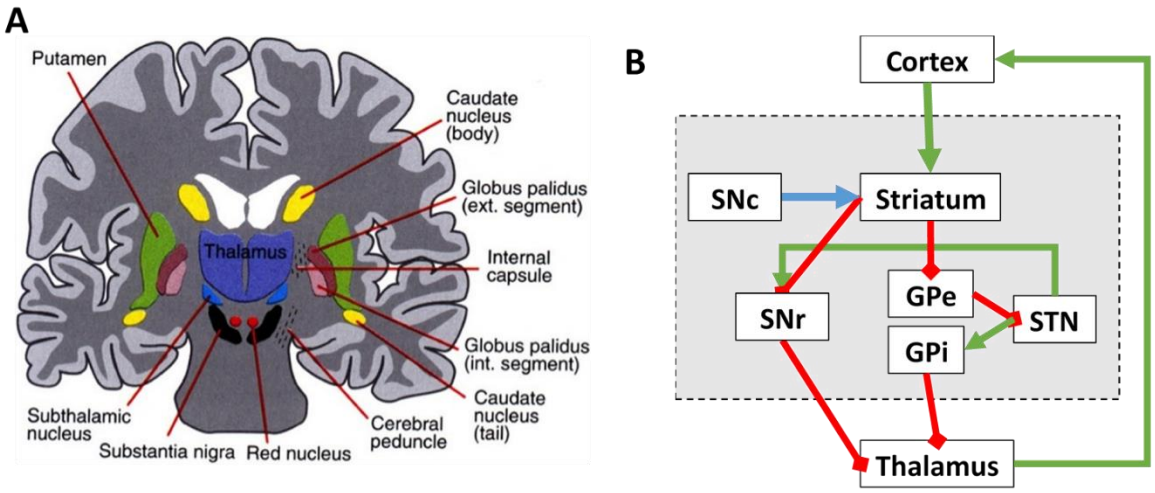

Figure 1.2: On the basal ganglia. A) Location of BG nuclei in the brain. B) Diagram of the connectivity of BG nuclei (the boundaries of the BG indicated by the dashed grey box). Arrows indicating connections are coloured as follows: green for excitatory connections, red for inhibitory connections, and blue for dopaminergic connections. Acronyms are explained in text above. Image A from Wikimedia Commons (user Anaru), under Gnu Free Documentation License.

1.2.1 Anatomy of the basal ganglia

As the BG is a complex circuit of excitation and inhibition, it is necessary to appreciate the neurotransmitters involved in causing each type of specific response from certain BG nuclei. Upon being excited by an AP, neurons release neurotransmitters across synapses to communicate signals to other synapsed neurons. In the BG, there are three main types of neurotransmitter: glutamate, the principal and most abundant excitatory neurotransmitter in vertebrates (Meldrum. 2000); γ-aminobutyric acid (GABA), the principal inhibitory neurotransmitter (K. Li and Xu. 2008); and dopamine, a neuromodulatory chemical that maintains balance across the BG (Bezzi and Volterra. 2001). While dopamine is only found in the SNc within the BG, each of the other nuclei of interest express a majority of either glutamate or GABA neurons and are excitatory or inhibitory respectively.

1.2.1.1 Cortex

The cerebral cortex, or specifically in the case of the basal ganglia, the motor areas of the neocortex, consists of both diverse excitatory glutamatergic pyramidal projection neurons and inhibitory GABAergic interneurons, all separated into well-defined layers (Marin and Muller. 2014). The glutamatergic neurons have dense dendritic trees, with studies showing a single cell in the CTX receives 30,000 excitatory inputs compared to 1700 inhibitory inputs (Megias *et al.* 2001). These glutamatergic neurons project to different areas depending on their layer within the CTX, with some

populations projecting to the STR and others to the STN, forming the two excitatory inputs to the BG. The STR input features projections from pyramidal neurons of layers III and V (the corticostriatal pathway) in a unidirectional manner; while the STN input features projections from CTX layer V (the 'hyperdirect' pathway), which are then relayed to the GPi and SNr (Mathai and Smith. 2011).

1.2.1.2 Striatum

The STR is a major part of the BG, receiving massive inputs from the CTX (glutatmatergic) and SNc (dopaminergic) and as such the STR has a large number of neurotransmitter receptors for dopamine, glutamine and others such as acetylcholine, endocannabinoids and endogenous opiates (Crittenden and Graybiel. 2011). In particular, the STR contains five types of dopamine receptor, with the majority consisting of dopamine receptor 1 (D1) and 2 (D2), which act excitatory and inhibitory in response to dopamine binding respectively (Gerfen and Surmeier. 2011). More information on DA receptor distribution in the forebrain can be found in the following review (Tritsch and Sabatini. 2012).

95% of the STR is made up of GABAergic medium spiny projection neurons (MSNs), with the remainder being smaller cholinergic and/or parvalbumin (PV, a calcium binding protein) -expressing interneurons (Ellens and Leventhal. 2013). The MSNs express either D1, D2 or both (both in 40% of cases), with D1-type promoting movement and being part of the direct pathway (projecting directly to BG output nuclei GPi and SNr) and the D2-type suppressing movement and being part of the indirect pathway (projecting to the intermediate BG nuclei GPe, which then projects to the STN and the output nuclei GPi and SNr), meaning that an influx of dopamine to the STR would excite the D1-type promoting circuits and inhibit the D2-type suppressing circuits, therefore being doubly pro-movement (Yager *et al.* 2015). Reassuringly, MSNs grown in organotypic cultures *in vitro* show morphological and electrophysiological characteristics similar to those seen *in vivo*, reinforcing the idea of an *in vitro* model of the BG (Plenz and Kitai. 1998, Sharott *et al.* 2012).

1.2.1.3 Globus pallidus

The GP is often categorised anatomically into two sections, the internal (GPi) and external (GPe), both mostly consisting of inhibitory GABAergic neurons. The GPi is an output nucleus of the BG that receives GABAergic projections from both the STR direct pathway (D1 MSNs) and the indirect pathway via the GPe (D2 MSNs), as such the GPi is rich in GABA receptors. The GPi also receives glutamatergic projections from the STN and (along with the SNr) projects inhibitory GABAergic neurons out of the BG to the motor relay nuclei of the thalamus and brain stem/spinal cord (Bergman *et al.* 1994, Kliem *et al.* 2007, Nambu. 2007). The GPe is an intermediate nucleus that receives inhibitory GABAergic D1 MSNs from the STR indirect pathway and excitatory glutamatergic neurons from the subthalamic nucleus (STN). The GPe projects inhibitory GABAergic neurons to the GPi, STN, SNr and back to the STR, giving the GPe a considerable co-ordination role in the BG (Kita. 2007).

1.2.1.4 Substantia nigra

The substantia nigra (SN) is often categorised anatomically into two sub-nuclei with markedly different functions and connectivity, namely the pars compacta (SNc) and pars reticulata (SNr). Similarly to the GPi, the SNr consists mostly of GABAergic inhibitory neurons which project to the thalamus and the brainstem/spinal cord, and acts as an output nucleus for the BG. However, unlike the GPi, the SNr is in close proximity to the SNc and as such dendrites from dopaminergic neurons of the SNc supply dopamine to the SNr over several hundred microns distance, directly depolarising SNr GABAergic neurons (Hausser *et al.* 1995, Ford *et al.* 2010, Rommelfanger and Wichmann. 2010) as the neurons in the SNr have mostly D1-like receptors (Kliem *et al.* 2010). Axons from the SNr project to the SNc in return, allowing for the SNr to regulate nigrostriatal DA neurons (Tepper *et al.* 1995, F. M. Zhou and Lee. 2011).

The SNc is a vital and unique structure of the BG in that it is mostly composed of dopaminergic neurons which project to their principal target, the STR (creating the nigrostriatal system), but other projections also exist to the CTX, thalamus and other BG nuclei (Ellens and Leventhal. 2013). These dopaminergic neurons are heavily regulated by upstream processes outside the BG (S. Hong *et al.* 2011, Beeler *et al.* 2012). The importance of these dopaminergic projections from SNc to STR are highlighted in Parkinson's disease, which is caused by the loss of these projections. Inputs to the SNc are mostly inhibitory (70% GABAergic), including afferent projections from the STR (Fujiyama *et al.* 2011) and SNr (Tepper *et al.* 1995), along with some excitatory afferent projections from the STN (Morikawa and Paladini. 2011) and other nuclei as seen in **Fig.1.3**.

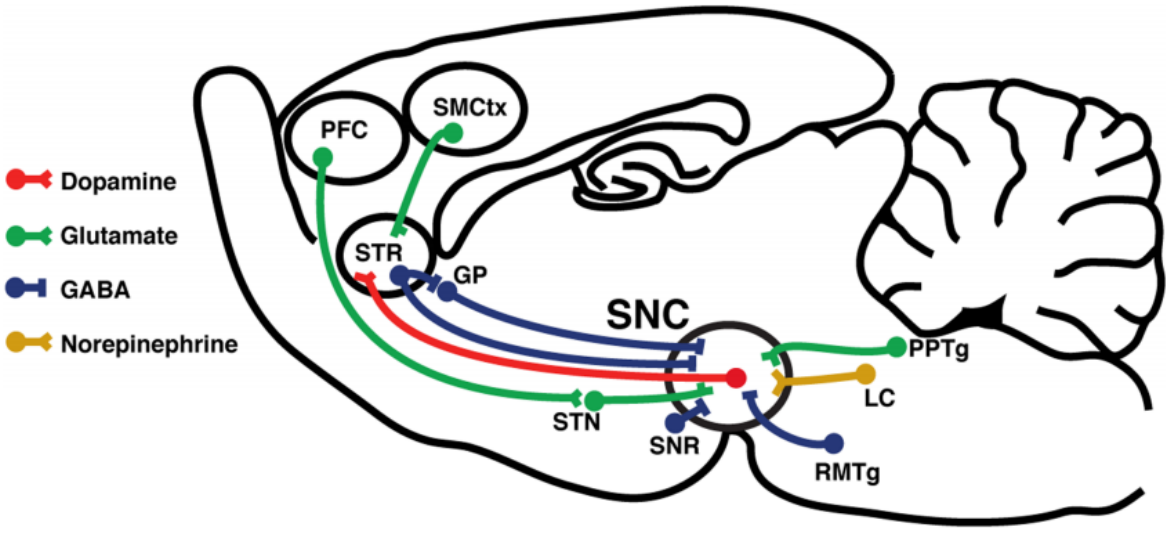

Figure 1.3: Projections to and from the substantia nigra pars compacta (SNC). PFC: prefrontal cortex, SMCtx: sensorimotor cortex, STR: striatum, GP: globus pallidus, STN: subthalamic nucleus, SNR: substantia nigra pars reticulate, PPTg: pedunculopontine tegmental nucleus, LC: locus coeruleus, RMTg: rostromedial tegmental nucleus. Coloured projections shown in key.

1.2.1.5 Subthalamic nucleus

The STN is the only glutamatergic nuclei of the BG, giving it a unique excitatory role in signalling. The STN receives excitatory input directly from the motor CTX via the hyperdirect pathway (cortico-subthalamo-pallidal or CTX-STN-GP), bypassing the STR and working alongside the other major signal pathways of the BG, namely the direct and indirect pathways (Nambu *et al.* 2002), also taking part in the latter. Other inputs to the STN include inhibitory GABAergic neurons from the GPe and a small number of dopaminergic afferents from the SNc (Rommelfanger and Wichmann. 2010, Ellens and Leventhal. 2013). In turn, STN glutamatergic neurons project to the GPe (creating a GPe-STN feedback loop where the two nuclei are reciprocally connected) and the two BG output nuclei, GPi and SNr.

1.2.1.6 Summary

Taking into account this anatomical information, the signal connectivity diagram of the BG seen in **Fig.1.2B** at the beginning of this section can be updated with a more accurate diagram, seen below in **Fig.1.4.**

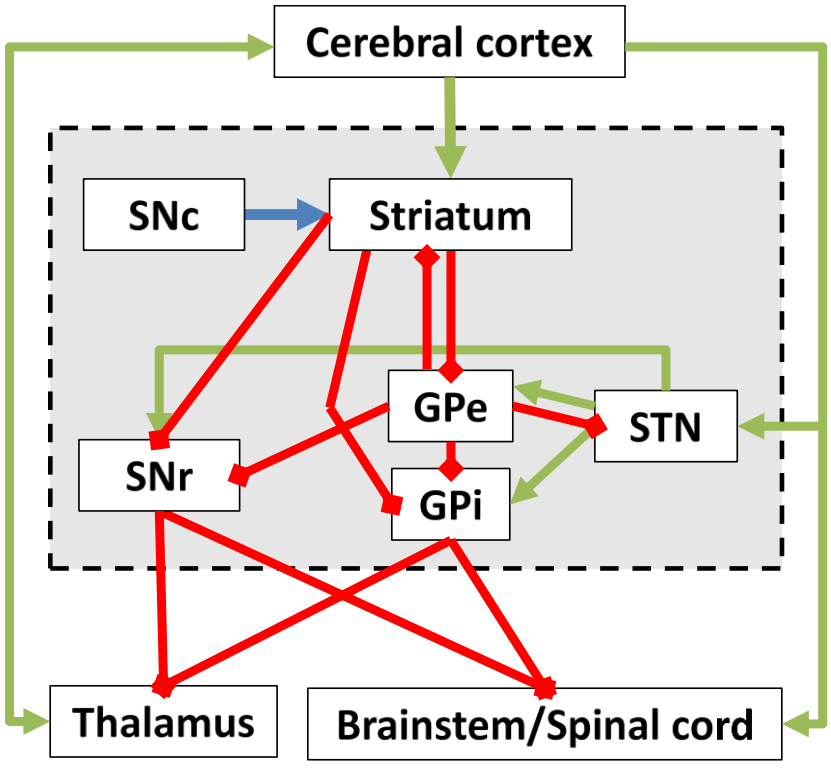

Figure 1.4: Diagram of the connectivity within the basal ganglia as well as immediate inputs and outputs. The basal ganglia is indicated by the dashed grey square. Green, red and blue arrows indicate excitatory glutamatergic, inhibitory GABAergic and modulatory dopaminergic connections respectively. Most connetions are unidirectional but cortex to thalamus is bidirectional. SNc/r: substantia nigra pars compacta/reticulata, GPe/i: globus pallidus external/internal, STN: subthalamic nucleus.

Fig.1.4 highlights the importance of the BG as a functional bridge between the CTX and the thalamus, brainstem and spinal cord. Information is input into the BG via the CTX, where it is then processed by the STR and GPe, then output via the GPi and SNr. The SNc and STN input dopaminergic and glutamatergic signals into this process. For the purpose of studying PD, the vital nuclei are the **CTX** (input), **STR** (intermediate), **GP/SNr** (output) and **SNc**, seeing as the nigrostriatal pathway contains all the dopaminergic neurons lost in PD. Containing these five nuclei within an *in vitro* model would make for a powerful platform for study of PD and the BG.

1.2.2 Development of the basal ganglia

The BG anatomy described above is typical for an adult human or rodent, but how does the BG form and change throughout development? If neural cells for an *in vitro* model are taken prenatally it is vital to ensure that the correct neurons are cultured in the correct place. The early CNS first has the form of a neural plate, containing all neural progenitor cells. This plate forms ridges and grooves and folds inwards, fusing together into a hollow tube termed the neural tube, which then closes at both ends. This forms the three sections of the early CNS, namely the prosencephalon, mesencephalon and rhombencephalon, which develop into the forebrain, midbrain and hindbrain respectively. The prosencephalon and rhombencephalon further subdivide, forming the five areas that make up the primary organisation of the CNS: the telencephalon and diencephalon (from the prosencephalon), the metencephalon and myelencephalon (from the rhombencephalon) and the mesencephalon (Stiles and Jernigan. 2010).

1.2.2.1 Cortical, striatal and pallidal development

The telencephalon divides into dorsal and basal ventricular zones, which develop into the CTX and STR/GP respectively (Medina *et al.* 2014). The basal ventricular zone forms a dome shaped protuberance into the ventricular cavity, termed a ganglionic eminence. This eminence is split into two sections by a sulcus (or groove), the lateral ganglionic eminence (LGE) and the medial ganglionic eminence (MGE) (Lavdas *et al.* 1999), with the LGE developing into the STR, and the MGE developing into the GP. This development has been demonstrated classically (Holmgren. 1925) with autoradiography (Marchand and Lajoie. 1986) and more recently with genetic fate mapping and transcription factors (Medina and Abellán. 2012), with only LGE-derived cells expressing $PAX6^+$ and $ISLET1^+$, and only MGE-derived cells expressing NKX2.1 and LHX6/7/8 (Medina *et al.* 2014).

60% of CTX GABAergic interneurons originate from the MGE but not the LGE, as the neurons cannot migrate across the separating sulcus, while the pyramidal glutamatergic neurons of the CTX develop from local radial glia in the ventricular zone and radially migrate along radial glial fibres to the developing cerebral cortex (Medina and Abellán. 2012, Marin and Muller. 2014, Medina *et al.* 2014).

Five distinct progenitor zones were identified in the MGE, named pMGE1-5. These zones give rise to different classes of neurons, due to the tight spatial control of neurogenesis and migration within the brain (Wonders *et al.* 2008). Not only do the dorsal (1-2) and ventral (3-5) MGE zones give rise to GABAergic interneurons respectively, the extent of migration origin also differs, with pMGE5 being the source of GABAergic neurons in the GP and similar interneurons from pMGE3-4 migrating to the CTX (Gelman and Marin. 2010). As a result, after birth both the GP and CTX contain GABAergic interneurons originally from the MGE. This migration and development is particularly important as GABA receptors are excitatory during development, rather than inhibitory (Sanes *et al.* 2012).

Development of the CTX, STR and GP precursors all occur at well-defined times, following the development of a rat embryo (where E signifies embryonic day and P signifies postnatal day). The MSNs of the STR are generated in the LGE from E12 to P2, peaking at E15, while GP GABAergic neurons are generated in the MGE between E12-15, peaking at E14 (Marchand and Lajoie. 1986).

1.2.2.2 Nigral development

SNc dopaminergic cells develop from an entirely separate area of the early CNS tube, namely the floor plate of the ventral midbrain (or ventral mesencephalon, both VM). This floor plate is the most ventral part of the neural tube and contains radial glia-like cells that develop into postmitotic migratory dopaminergic precursors, which differentiate into dopaminergic neurons (Bonilla *et al.* 2008). This neurogenesis process takes place in the rodent from E10-14, peaking around E12 (Gates *et al.* 2006). Notably, the VM floor plate extends from the mesencephalon to the diencephalon, with the most rostral section of the plate giving rise to glutamatergic STN neurons. Both these glutamatergic neurons and the dopaminergic neurons express transcription factors $FOXA2^{+}$/$LMX1A^{+}$/$OTX2^{+}$, unlike neurons derived from the LGE or MGE (Nelander *et al.* 2009, Nolbrant *et al.* 2017). More information can be seen in **Fig.1.5** below.

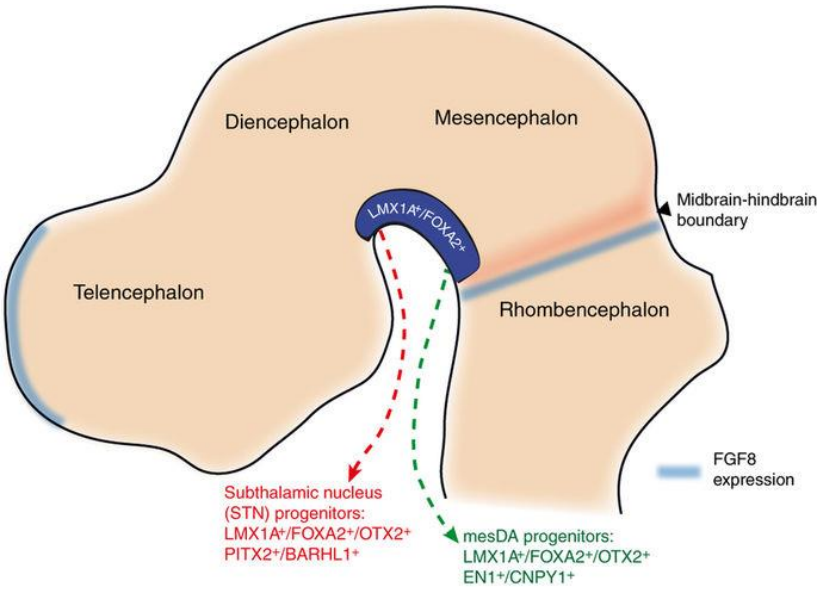

Figure 1.5: Anatomical patterning of the ventral diencephalon/mesencephalon during development. Both STN and SNc progenitors originate from the floor plate of the VM, expressing LMX1A+/FOXA2+/OTX2+. Proximity to FGF8 expression regions appear to cause this change in progenitor, at the midbrain–hindbrain boundary. Image from (Nolbrant *et al.* 2017)**.**

The GABAergic neurons of the SNr are partly generated in the VM and partly from the rhombencephalon. VM-generated SNr GABAergic neurons are generated by unknown mechanisms but express TAL2/GATA2 proteins (Madrigal *et al.* 2016, Nolbrant *et al.* 2017), while rhombencephalon-generated SNr GABAergic neurons are generated in a region named rhombomere 1 (R1) and express TAL1/GATA2 proteins (Achim *et al.* 2012). In this manner, the SNr can be split into anterior and posterior sections based on the distinct development of the GABAergic neurons of each section, but it is unknown how this is related to the functional diversity of the SNr GABAergic neurons of the BG.

The CTX, STR, GP and SN can therefore be obtained by dissecting from the cortex, LGE, MGE and VM, areas anatomically and developmentally distinct (as seen in **Fig.1.6**).

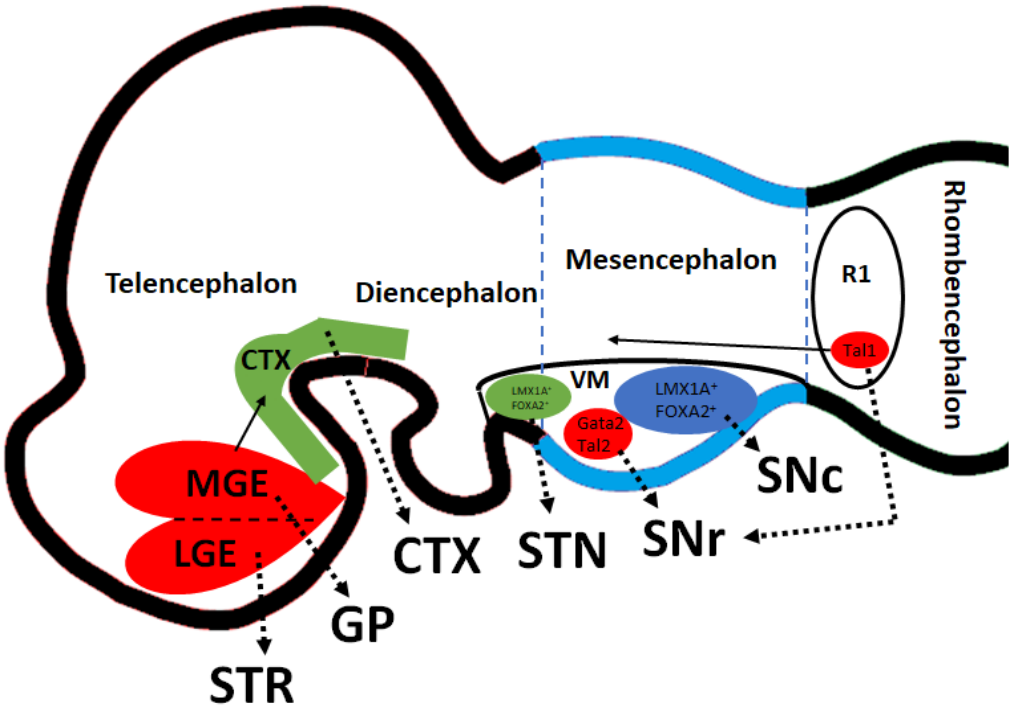

Figure 1.6: The embryonic brain and its development into different nuclei of the BG. Blue for dopaminergic, red for GABAergic, and green for glutamatergic.

1.2.2.3 Development of GABA as a neurotransmitter

There are three other notable facts to consider during brain development, all concerning the neurotransmitter GABA. Firstly, there is an absence of a GABA uptake system in the early stages of development, which causes GABA to accumulate in the extracellular space and reach concentrations sufficient to affect even distal neurons (Ben-Ari. 2014). Secondly, GABAergic synapses form before glutamatergic synapses, a feature that is conserved in multiple species (Tyzio *et al.* 1999) and across different brain regions (Ben-Ari. 2002). Lastly, during development GABA is initially excitatory, able to elevate intracellular Ca^{2+} concentration and trigger action potentials. Later in development, there is a 'GABA switch' where the action of GABA switches from excitatory to the more standard inhibitory, changing electrophysiological action from depolarising to hyperpolarising. The presence of inhibitory signals in the brain is necessary as it allows for more complex and diverse activity within the neural networks (Maric *et al.* 2001, Ben-Ari. 2002).

Initial excitatory action of GABA is as a result of high intracellular concentration of chloride ions (Cl^-) (Ben-Ari *et al.* 2012). The GABA switch to inhibitory action has been observed to occur in two phases, shortly before and shortly after birth. The first phase is temporary, oxytocin-dependent and occurs during labour/delivery (can be blocked with oxytocin antagonists) in a period extending from E20 to P0 (postnatal day zero, the day of birth), peaking at E21, 1-2 hours before delivery (Tyzio *et al.* 2006). The second and permanent phase begins soon after birth and completes by the end of the first

postnatal week (P0-P7) (Valeeva *et al.* 2013) using Cl^- transporters such as GABA receptor A and KCC2 (a K^+-Cl^- cotransporter) to decrease the concentration of intracellular Cl^- and completing the switch to inhibitory action by P7 (Leonzino *et al.* 2016). This change is detectable with both intracellular and extracellular electrophysiological measurements (Khalilov *et al.* 1999). However, while this has been shown to occur *in vivo* and in the presence of oxytocin, does this excitatory/inhibitory switch occur in cells taken at early embryonic age, then grown and matured *in vitro*? Most work on the topic of the GABA switch *in vitro* has taken place using rat hippocampus tissue which, when grown *in vitro,* shows a switch after ~11 DIV (Ganguly *et al.* 2001, Khazipov *et al.* 2004, Mohajerani and Cherubini. 2005). However, work done in other brain areas shows a similar trend, as seen in **Table 1.1** below.

GABA can also regulate the GABA switch itself (Ganguly *et al.* 2001). Significantly, the developmental switch to Ca^{2+} mediated signalling is itself GABA-mediated and triggered by endogenous GABAergic transmission. The increase in GABAergic activity throughout development promotes the switch of GABA signalling. This switch is not dependent on electrophysiological spiking activity from neurons, as it still occurs in the presence of tetrodotoxin (TTX), which blocks Na^+-dependent APs in neurons. GABAergic activity also modulates the mRNA levels of KCC2, expression of which correlates with the GABA switch. In summary, GABA itself can also promote the GABA switch from excitation to inhibition, meaning neuronal cells taken at embryonic ages and grown *in vitro* can undergo a GABA switch, even in just a population of GABAergic neurons.

1.2.2.4 Synapse development

When taking cells at developmental ages (such as E12-16 in the rat), it is possible that synapses have not fully formed or functionally matured. At birth, approx. E22/P0, 80% of interneurons have functional GABAergic and glutamatergic synapses, but less than 20% of pyramidal neurons have formed synapses, which decreases further to almost none at E19/20 (Ben-Ari. 2014). In addition, in the CNS glutamate binds to ionotropic receptor ion channels, such as α-amino-3-hydroxy-5-methyl-4-isoxazolepropionate receptors (AMPARs) and N-methyl-D-aspartate receptors (NMDARs), which are highly expressed and evolutionarily conserved (Lauder. 1993, Gallo *et al.* 1995, Ulrich and Majumder. 2006). However, neonatal rat glutamatergic synapses lack AMPARs, NMDARS are present but remain closed at the resting membrane potential. This leads to 'silent synapses', which do not become fully active until around P3, when glutamate and GABA transporters first appear in the rat (increasing to adult levels over the next two weeks) (Sanes *et al.* 2012).

Therefore, neurons from the developing rat can lack both synapses and the vital transmembrane proteins that support synapses, which would lead to difficulties when constructing a functional neural circuit *in vitro*. In the *in vivo* rodent, these synapses form in the few weeks after birth, so it is vital to ensure that they also form as the cells mature *in vitro*.

Table 1.1: Instances of the GABA switch (excitatory to inhibitory) observed *in vitro.*

CNS structure	Age	Methods	Action	Reference
Spinal cord (dorsal horn L11 slices)	P0-7	Gramicidin perforated patch	Excitatory in 40% of neurons at P0-2, inhibitory in all cells by P6-7	(Baccei and Fitzgerald. 2004)
Spinal cord (dorsal horn L1 slices)	P0-60	Gramicidin perforated patch, whole cell patch, Ca^{2+} imaging	Depolarizing for first week, switched by P7, Cl^- extrusion not complete until P10-11	(Cordero-Erausquin *et al.* 2005)
Brain stem (lateral superior olive slices)	E18-P17	Intracellular recording	Depolarising at E18-P4, hyperpolarizing after P8	(Kandler and Friauf. 1995)
Basal ganglia (SNr slices)	P4-26	Gramicidin perforated patch	Inhibitory at embryonic ages, switch occurred in males at P17 and females at P10	(Kyrozis *et al.* 2006)
Hypothalamus (neuronal culture)	E15-18 (with 2-25 DIV)	Ca^{2+} imaging	Excitatory/inhibitory switch occurs between 8-13 DIV	(Obrietan and van den Pol. 1995)
Neocortex (slices of layer II/III)	P4-41	Intracellular recordings	Excitatory from P4-10, inhibitory from P11-41	(Luhmann and Prince. 1991)
Neocortex (neuronal culture)	E17 (with 11 DIV)	Intracellular ^{36}Cl measurement	Transient decrease in intracellular ^{36}Cl after 11 DIV	(Schomberg *et al.* 2003)
Neocortex (slices of layer II/III)	P1-21	Gramicidin perforated patch, Ca^{2+} imaging, single cell RT-PCR	Depolarising at P1-3, hyperpolarising at P11-20	(Yamada *et al.* 2004)

In the developing rat cerebral cortex *in vivo*, the number of synapses and synapse density is low at birth but increases rapidly to adult levels by P16-21. This is closely followed by the time course of synapse formation in primary rat cortical cultures *in vitro*, shown by experimentation where E18 neurons cultured for up to 35 days *in vitro* (DIV) demonstrated increased synapse: number, density, morphological development, contact zone size and vesicles per terminal (Ichikawa *et al.* 1993), along with more recent studies showing similar results (Ulrich and Majumder. 2006, Goyal and Nam. 2011), concerning *in vitro* maturation of primary neurons from embryonic rodents. This *in vitro* maturation can also be observed with cell lines, such as the P19 embryonic carcinoma cell line. These cells can be differentiated into neuron-like cells which mature *in vitro* once differentiated and are capable of neurotransmitter release and formation of functional synapses. This maturation occurs in a culture density-dependent manner, with more dense cultures demonstrating up-regulation of synaptic

vesicle proteins, enhanced glutamate and H-aspartate release and accelerated neuronal maturation (Parnas and Linial. 1997). In addition, after approx. 10 days of *in vitro* growth, these cells are capable of Ca^{2+} depolarization-dependent acetylcholine release and express all major proteins implicated in synapse functionality at both at RNA and protein levels (including cytoskeletal proteins, synaptic vesicle proteins and terminal specific proteins) (Parnas and Linial. 1995), along with carrying high-affinity uptake sites for GABA (McBurney *et al.* 1988). This type of *in vitro* maturation and differentiation is also seen in embryonic stem and embryonic body stages, with these cell types developing into neurons with functional synapses (Barberi *et al.* 2003) that can integrate into the *in vivo* brain, in this case migrating into the residual cortex (Chiba *et al.* 2003). Finally, this has also been shown with induced pluripotent stem cells (iPSCs), in order to develop *in vivo*-quality dopaminergic neurons *in vitro* (Nolbrant *et al.* 2017). Functional synapses can therefore develop *in vitro* as cell cultures functionally mature.

1.3 Modelling of Parkinson's disease

In order to understand the underlying mechanisms at play in PD and develop more effective drugs, treatments strategies or therapies, it is vital to have the ability to reproduce the disease symptoms and progression in a model for study. However, as the cause of sporadic PD is unknown it is difficult to create models that can entirely model PD, or to create models that can model aspects of PD within an acceptable timeframe, as PD takes years and decades to develop in the human brain *in vivo*. The main materials for accurate study of human PD are post-mortem tissues which only represent the end-stage of the disease and are fundamentally different to live tissue (Martinez-Morales and Liste. 2012).

An important distinction to make at this point is that non-human animals do not naturally develop PD, with the possible exception of mild PD in aged non-human primates in captivity (Terzioglu and Galter. 2008). Due to this limitation, while many different PD models have been developed in many different species, PD cannot be entirely modelled or accurately simulated in current animal, cell or tissue models. The ideal sporadic PD model would be a model of progressive nigrostriatal neurodegeneration, with similar mechanistic changes in the brain and onset of PD symptoms with time, along with the formation of α-synuclein-containing LBs and emergent behavioural changes (Dauer and Przedborski. 2003). Once PD symptoms had manifested sufficiently, drugs or other treatments could be applied to the model and tested for effectiveness. For genetic PD, these drugs or other treatments could be applied before onset to test prevention.

In the search for this ideal PD model many animal species have been utilised, including relatively simple worms (*C. elegans*) (Harrington *et al.* 2010) and flies (*Drosophila*) (Botella *et al.* 2009) that have been modified to express human genes. These models have been used to study aspects of

cellular processes involved in PD, such as apoptosis, oxidative stress, protein misfolding, and protein aggregation. However, while these models are far cheaper and easier to use than more complex animal species, they cannot replicate loss of neurons in the brain, PD disease progression or manifestation of PD symtpoms (Maetzler *et al.* 2009).

Larger animal species such as dogs, cats and non-human primates have also been used to model PD, but are limited by difficult ethical concerns, far higher costs and much greater timescales (Potashkin *et al.* 2010). Non-human primates are of particular interest as they can develop mild PD-like symptoms when aged and have the same bipedal motor organisation as humans, but as they are the most complex they are also the most expensive and ethically unjustifiable in most cases. The most widespread and popular models for PD are rodents (rats and mice), which are readily available, genetically malleable and low cost, and have been used to study PD for over 40 years (Ungerstedt. 1968), despite having different motor system organisation in the brain (Dauer and Przedborski. 2003). As these rodent models will not naturally develop PD symptoms, PD must be induced in these models, with the the two main methods used being neurotoxins and genetics.

1.3.1 Neurotoxin-based animal models

Certain neurotoxins can be applied to models in order to acutely damage the nigrostriatal pathway and mimic PD pathology. Thus, it is necessary to first understand the range of key neurotoxins available to mimic PD in animal models, namely 6-hydroxydopamine (6-OHDA), MPTP, paraquat and rotenone (the latter three were mentioned briefly in the 'potential causes' section as exogenous environmental toxins). These toxins inhibit mitochondrial fuction and create ROS (Terzioglu and Galter. 2008), but feature three major drawbacks. Firstly, none of these toxins reproduce all the symptoms and pathology of human PD in rodent models. Secondly, this toxic effect is very acute and not at all progressive as in PD, where similar changes occur over many years. Lastly, the rodent models are often very young due to the inconvenience and increased cost of using aged animals, despite aged models being a better model for PD which occurs mainly in elderly patients over 60 years of age (Potashkin *et al.* 2010). Structures of the relevant neurotoxins can be seen in **Fig.1.7**.

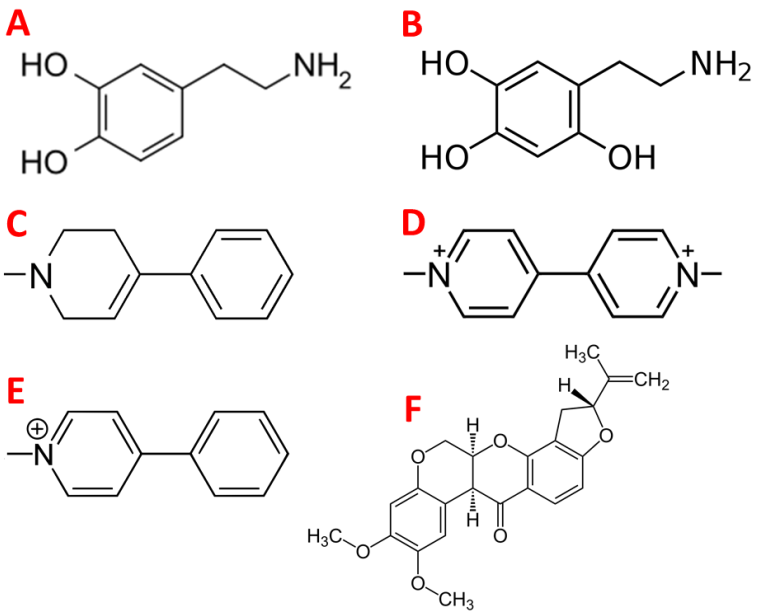

Figure 1.7: Neurotoxins used in PD research. A) Dopamine itself, included by way of comparison as most neurotoxins bear some similarity to dopamine structure in order for dopaminergic neurons to mistake them for dopamine and take them up. B) 6-OHDA, only differs from dopamine due to the extra hydroxyl (OH) group on the 6th carbon of the ring, making it very specific to dopaminergic neurons. C) MPTP, the non-toxic precursor of MPP+. D) MPP+, the metabolised form of MPTP and a neurotoxin that is taken up by dopamingergic neurons. E) Paraquat, a highly toxic pesticide that can lead to Parkinson's-like symptoms, note the similarity to MPP+. F) Rotenone, a more complex pesticide that also leads to Parkinson's-like symptoms developing.

1.3.1.1 MPTP

MPTP, paraquat and rotenone all resemble each other in structure and have all been shown to induce DA neuron degeneration and death. Humans are sensitive to MPTP and MPTP application has been shown to incude PD-like symptoms, in the case where MPTP was mistaken for synthetic heroin and injected by several people (Langston *et al.* 1983). Using MPTP on both cell (SN4741 dopaminergic cell line) and animal models (C57BL/6 mouse models) has resulted in increased ROS activity (including hydrogen peroxides, superoxides and hydroxyl radicals), activation of JNK1/2 MAP kinases, activation of caspases and eventual apoptotic cell death (Brooks *et al.* 1999), along with inhibition of mitochondrial complex I (Betarbet *et al.* 2000). Use of antioxidants and caspase inhibitors exerted a significant neuroprotective effect on ROS-induced DA neuron death (Chun *et al.* 2001).

In animal models, MPTP administered outside the brain can easily cross the blood brain barrier, where astrocytes and serotonergic neurons convert it into the toxic metabolite MPP+ over time via monoamine oxidase-B (MOA-B) (neither MPTP nor MPP+ being neurotoxic to astrocytes) (Marini *et al.* 1992) and release MPP+ into the extracellular space. MPP+ has a high affinity for the dopamine transporter (DAT) along with noradrenaline and serotonin transporters, and can therefore affect serotonergic and catecholaminergic neurons, but has the most pronounced effect in DA neurons. MPP+ itself cannot cross the blood brain barrier, but can be administered directly to the brain, and once in the brain (either by direct administration or by MOA-B metabolism of MPTP) it has a

significant and selective neurotoxic effect on SN DA neurons due to uptake by DATs and movement along a number of possible pathways. Once within DA neurons, MPP+ can be concentrated into mitochondria where it inhibits mitochondrial complex I, translocated into synaptic vesicles (a possible defense mechanism as this protects MPP+ from accessing mitochondria) or remain in the cytosol and interact with enzymes/other biochemical factors (Dauer and Przedborski. 2003).

As a result MPTP/MPP+ have a significant toxic effect on SN DA neurons. For example, pumping MPP+ into the left cerebral ventricle of rats for 28 days caused a selective ipsilateral loss of 35% of SN DA neurons, increasing to 65% after a further 14 days (Yazdani *et al.* 2006). LB-like aggregates were found in STR neurons near the infusion site, and surviving SN DA neurons had swollen and abnormal mitochondria. There was no animal death, meaning that this study modelled a progressive neurodegeneration of SN DA neurons, more similar to PD than other acute toxin models and showing why MPTP is a popular neurotoxin to model PD in animals.

Despite these desired effects of MPTP/MPP+ on animal and cell models, it is only effective in select conditions. If MPTP is administered outside the brain the activity of astrocytic MOA-B is necessary for conversion to the toxic MPP+ (once MPTP crosses the blood brain barrier). However, levels of MOA-B in the brain differ wildly between animal models, even between specific strains of rats and mice. Only specific stains of mice are sensitive to MPTP activity, with all rat strains and some mouse strains being entirely resistant (Sedelis *et al.* 2000), with resistant defined as MPTP resulting in less than 25% SN DA neuron loss (Meredith and Rademacher. 2011) (while humans are very sensitive to MPTP). The reason for these resistances is largely unknown, likely to be differences in MOA-B levels, different tolerances to oxidative changes, differential DAT uptake and kinetics, astrocytic activity and even coat colour (albino strains are more resistant to MPTP). The mouse strain C57BL/6 is most widely used in research as it is the most sensitive to MPTP. In summary, unless specifically using C57BL/6 mice or applying MPP+ directly to the brain or neural cultures, MPTP is unsuitable for use as a neurotoxin in this project, as it also demonstrates non-specific damage once past the blood brain barrier (Meredith and Rademacher. 2011). Similar toxins such as paraquat/rotenone are also unsuitable for modelling as they are not specific to DA neurons and cause high mortality and high experimental variability (Bove *et al.* 2005). These major physiological differences between rodents and humans are always represent a point for caution when interpreting results from rodent models.

1.3.1.2 6-OHDA

6-OHDA has been in use to successfully selectively damage DA neurons for over 40 years (Ungerstedt. 1968, Michel and Hefti. 1990, Jellinger *et al.* 1995, Pietz *et al.* 1996, Kramer *et al.* 1999, von Coelln *et al.* 2001, Barkats *et al.* 2002, Ding *et al.* 2004, Hernandez-Baltazar *et al.* 2015). 6-OHDA is a structural analogue of DA, the only difference being an additional hydroxyl (-OH) group on the sixth carbon (Hanrott *et al.* 2006). Due to 6-OHDA being so similar in structure to DA, 6-OHDA exhibits a high

affinity for DATs (similarly to MPP+) and other catecholaminergic transports, and is taken up selectively via DAT into DA neurons. Once within DA neurons, 6-OHDA has a cytotoxic effect due to a number of possible mechanisms (Hernandez-Baltazar *et al.* 2017). 6-OHDA can rapidly oxidise in solution, producing hydrogen peroxide (H_2O_2), superoxides, hydroxyl radicals, para-quinones and other ROS. This results in oxidative damage to DA neurons either intra- or extracellularly, depending on whether 6-OHDA is taken up by DA neurons before or after auto-oxidation takes place (Blum *et al.* 2001). Alongside auto-oxidation, 6-OHDA can also directly inhibit mitochondrial complex I (Jenner *et al.* 1992), and it is likely that a combination of these two mechanisms result in overall oxidative stress and damage to DA neurons. Further loss of mitochondrial membrane permeability may lead to increased cytoplasmic free calcium, intensifying the oxidative stress and inducing cell death by apoptosis (Singh *et al.* 2010). It should be noted that these mechanisms of 6-OHDA in DA neurons do not involve the generation or presence of LBs

In addition to 6-OHDA being selective for DA neurons, 6-OHDA also is a good mimic for PD as it affects SNc DA neurons more than other DA neuron populations in the brain (such as DA neurons in the ventral tegmental area (VTA)). SNc DA neurons are particularly affected by 6-OHDA-induced oxidative stress as they have higher baseline ROS levels and low levels of glutathione peroxidase, which converts H_2O_2 to H_2O and lessens ROS damage (Hirsch *et al.* 1997, Double. 2012, Surmeier *et al.* 2017). In addition, the SN contains a high concentration of neuromelanin, which can combine with iron and affect the ability of SN DA neurons to remove OH radicals and ROS (Gerlach *et al.* 2008). This specific selectivity of 6-OHDA for SNc DA neurons makes it an ideal neurotoxin for mimicking the effects of PD, depending on dosage concentration and exposure time (Bove *et al.* 2005). 6-OHDA neurotoxicity provokes molecular alterations comparable to those seen in PD, thus supporting the meaningfulness of 6-OHDA when exploring the mechanisms of neurodegeneration in PD. It should be noted, however, that 6-OHDA creates acute models of PD by rapidly damaging and killing only DA neurons, rather than the slow progressive loss of DA neurons and degeneration of other neuron types seen in PD *in vivo* (Ellens and Leventhal. 2013).

In PD animal models, 6-OHDA is typically injected directly into the SN or STR (as it cannot cross the blood brain barrier), where it selectively damages DA neurons in these areas. When 6-OHDA is injected into the SN, DA neurons degenerate within 24 hours, compared to 1-3 weeks of retrograde degeneration of DA neurons when 6-OHDA is injected into the STR. Unilateral injections of 6-OHDA can be used to mimic the early-to-mid-stages of the disease (Mercanti *et al.* 2012) (with the contralateral side serving as an internal control), and can also result in behavioural changes in rodents, such as circling, fine motor tasks and walking across a rotating cylinder (Emborg. 2004).

However, it is unclear if DA neurons are damaged/destroyed in the same way as they are in PD, and these 6-OHDA models also lack the formation of LBs. While limited, 6-OHDA animal models have

been widely used to assess anti-PD pharmaceuticals, neuroprotective agents and therapies (Dauer and Przedborski. 2003).

1.3.2 Gene-based animal models

As mentioned in **1.1.2 Genetic component**, approximately 5-10% of PD cases are caused by hereditary genetic mutations, with over 25 genetic factors associated with risk of PD. Knowing which specific genes have been altered allows for the development of very specific animal models that directly apply to human PD from a genetic point of view, with the potential to apply data generated from these models to sporadic PD. Despite the genotypic differences between sporadic and heritable PD patients, there are many phenotypic similarities which indicate both forms of the disease follow similar mechanisms.

Animal models of heritable PD are typically genetically modified mice, with recessive mutations in *Parkin*, *DJ-1* and *PINK1* made by knockout mice (null mutations), and dominant mutations in *α-synuclein* and *LRRK2* made using transgenic mice (where extra copies of the gene are inserted into the mouse genome, usually by viral vector transfection) (Fleming *et al.* 2005). In general, genetic animal models of PD have demonstrated subtle effects on the DA system but no loss of DA neurons, indicating how these models are useful for study of heritable PD but very different to toxin-based models. When used in combination (administering toxins to genetically modified animal models) there are interesting effects, such as *α-synuclein* knockout mice being less sensitive to MPTP, while *α-synuclein* transgenic and DJ-1 knockout mice being more sensitive (Terzioglu and Galter. 2008). Genes implicated in PD are often associated with mitochondrial function, with *PINK1, DJ-1, Parkin* and *LRRK2* being localised to mitochondria. This interplay between toxin-based models of sporadic PD and gene-based models of heritable PD indicate the value in both types of model being used together.

1.3.2.1 A-synuclein

A-synuclein protein makes up LBs in sporadic PD, with further implications for a role in synaptic vesicle function, particularly significant as this means α-synuclein protein participates in movement of DA at DA neuron terminals in the STR (Kahle *et al.* 2002). As for the *α-synuclein* gene, two different mutations in *α-synuclein* (sometimes called *PARK1*) cause dominantly-inherited PD (A53T and A30P), and both have been recreated in transgenic mice. This resulted in abnormal DA neuron axons/terminals, age-related impairment in motor coordination and age-related reductions in DA (Richfield *et al.* 2002). When observing *α-synuclein* knockout mice, they have decreased DA in the STR, decreased vesicles in the hippocampus and rearing behaviour in open areas (Fleming *et al.* 2005). However, when overexpressing *α-synuclein* in mice, very few models show alternations in the nigrostriatal DA system, instead showing affected spinal cord and neuromuscular junctions

(Giasson *et al.* 2002). But the models that do show alterations are valuable experimental tools for study of PD. Overexpression of wild-type human *α-synuclein* (with Thy1 promoter) in mouse models resulted in a SN that was more vulnerable to MPTP, progressive sensorimotor impairment (measured with behavioural motor tests, worsened with age after 2 months), decreased levels of DAT binding in the STR, abnormal behavioural response to DA agonists, and impairments to smell and gastrointestinal function (both associated with non-motor PD symptoms) (Fleming *et al.* 2004). Models such as these are extremely useful for study of heritable PD as the impairments worsen with age, even the lack of DA nigrostriatal neuron loss is useful as the model simulates the early stages of the disease (Terzioglu and Galter. 2008).

However, despite the numerous *α-synuclein*-based genetic models of PD, very few models show the same *α-synuclein* pathology and progressive neurodegeneration as seen in human PD, with the exception of a mouse prion promoter A53T transgenic mouse (Chesselet. 2008). These models remain speculative but useful platforms for study of heritable PD.

While animal models have been widely used to study both sporadic and heritable PD, they are limited. *In vivo* rodent models (toxin or genetic) still cannot completely reproduce the pathophysiology of PD seen in humans, and there is a lack of control and reproducibility seen in these models. Current pre-clinical assessment is insufficient to predict what pharmaceuticals and treatments will work on human PD patients, potentially due to this lack of *in vivo* animal models that duplicate the causes, symptoms and progression of a human neural disorder (Pinel. 2013). Alternative *in vitro* modelling has the potential to lead to development of less expensive and less time-consuming clinical trials by improving study at a pre-clinical level.

1.3.3 Cell/tissue *in vitro* models

The ability to recreate a disease such as PD in defined cell populations *in vitro* would allow for the creation of models where it is far easier to observe, modify and understand cellular/molecular mechanisms of neurodegeneration and other aspects of PD. While *in vivo* animal models represent a competent experimental platform for study of PD, there is a lack of control. For example, not knowing if sufficient SN DA neurons have been destroyed by neurotoxins and only being able to observe behavioural changes or cell characterisation post-mortem. With an *in vitro* model, some complexity is lost but a great deal of control over the model and experimental design is gained. Other advantages of *in vitro* cell models include: models are cheaper, develop pathologies faster (cutting down on experimental time), less constrained by ethics, can be subject to large-scale and high-throughput testing, are easier to manipulate with genetics or pharmaceuticals and are easier to observe with microscopy (Falkenburger *et al.* 2016).

By using these *in vitro* models it is possible to model specific components of PD, such as SN DA neurodegeneration, LBs, α-synuclein protein aggregates and changes in functional electrophysiological activity. In addition, there are numerous choices for the cell source to use, which are discussed in more detail below. All summarised in **Fig.1.8**.

1.3.3.1 Cell line models

Cell lines are immortalised populations of cells that can proliferate indefinitely (given sufficient growth media and space), due to most lines being derived from mutant or cancerous cells (but still displaying similar genotypic and phenotypic characteristics as normal cells of the same type). Cell lines can be derived from numerous different species, most significantly humans, and have numerous advantages when it comes to *in vitro* study. Cell lines are suitable tools for prolonged periods of research *in vitro*, can be used for high-throughput studies (such as drug screening studies where numerous drugs can be pre-clinically tested before use *in vivo*), are highly reproducible due to being derived from a homogenous population and display features relevant for PD study, such as enzymes for DA metabolism and synapse formation (Lopes *et al.* 2017). However, the fact that cell lines can proliferate (indefinitely) makes them highly different to neurons *in vivo*, which are post-mitotic and do not divide (Luchtman and Song. 2010). Cell lines also differe greatly from *in vivo* neurons in morphology, physiology, protein levels and changes over time in culture. Despite this, cell lines are widely used in research to make *in vitro* models of PD.

The most widely used cell line for *in vitro* modelling of PD is the human neuroblastoma line SH-SY5Y, due to the fact that this cell line can synthesise DA (as they contain tyrosine hydroxylase (TH) and dopamine-β-hydrozylase enzymes), expresses DATs, can grow axons/dendrites and is a human cell line, so a better mimic of a human disease (Alberio *et al.* 2012, Lazaro *et al.* 2017, Xicoy *et al.* 2017). While SH-SY5Ys do not resemble neurons if cultured *in vitro*, they can be differentiated into a DAergic neuronal phenotype that better resembles *in vivo* DAergic neurons and decreases their levels of proliferation (Lopes *et al.* 2017). With the application of retinoic acid and brain-derived neurotrophic factor (BDNF), as well as a reduction in the concentration of serum in cell growth media, SH-SY5Y cells can be differentiated into neuron-like cells with a DAergic phenotype. However, this differentiation procedure is lengthy and challenging, with the majority of cells killed in order to select for a small surviving neuronal minority.

Once differentiated these cells can be subject to toxins or genetic manipulation in order to mimic PD, in a similar manner to previously mentioned animal models. 6-OHDA and MPTP remain the most commonly used toxins to induce PD-like neurodegeneration *in vitro*, but 6-OHDA use is more widespread as SH-SY5Y cells cannot metabolise MPTP into MPP+ themselves (Xicoy *et al.* 2017). The greater levels of DATs on differentiated SH-SY5Ys makes 6-OHDA use very effective in modelling PD neurodegeneration *in vitro*. The majority of genetic manipulation models involved overexpression of

α-synuclein (whether the wildtype form or the A53T/A30P mutant forms) which result in aggregates forming within SH-SY5Y cells and inducing toxicity in some cases (Liangliang *et al.* 2010). Notably, SH-SY5Y cells also demonstrate spontaneous α-synuclein aggregation even after no tranfection (Xin *et al.* 2015). SH-SY5Ys have been used to model abnormal mitochondrial function, oxidative stress, autophagy, protein dysfunction and more, highlighting SH-SY5Y as a popular and attractive tool for *in vitro* study of PD. However, this widespread use of SH-SY5Y as a cell line has highlighted how each study has used different conditons (for cell source, growth, differentiaton, inducing PD-like degeneration, etc) and how results have widly varied between studies with many contradictions, making data produced by these cell lines borderline unreliable unless sufficient characterisation and differentiaton methodologies are in place (Xicoy *et al.* 2017).

While there are many other notable examples of cell lines used to study PD, there are relatively few human-derived lines, the only other commonly used human line being the Lund human mesencephalic (LUHMES) line. Other lines are typically rodent-derived, such as the PC12 rat pheochromocytoma line, the mouse neuronal progenitor (MN9D) line and rat dopaminergic (N27) line, all of which are immortalised (Falkenburger *et al.* 2016). Unlike SH-SY5Y, LUHMES cells need to be differentiated to aquire a DAergic phenotype, with undifferentiated LUHMES cells expressing no DA, TH or DATs (Zhang *et al.* 2014). In addition, LUHMES are slow-growing and need numerous expensive growth media supplements to survive, making LUHMES use more time-consuming and costly than SH-SY5Y. But experimentally, LUHMES cells are not derived from a tumour as SH-SY5Y cells are and are more similar to primary neurons *in vivo*. In essense, there are many types of cell line to choose from when attempting to model PD

1.3.3.2 Stem cell models

Stem cells are cells that have the ability to renew themselves through cell division and differentiate into different cell types. Stem cells vary in potency, namely how many different classes of cell they can differentiate into, but this is of limited usefulness when only the cells of the brain (specifically BG) are needed to best mimic PD. Embryonic stem cells are pluripotent cells can differ into virtually any cell type but require a lengthy and difficult differentiation process in order to develop into functional midbrain DA neurons. These cells also come with a whole host of ethical issues as their isolation involves destruction of the embryo, consequently their use is controversial, especially when human stem cells are desired (Martinez-Morales and Liste. 2012). A better source of human pluripotent stem cells are induced pluripotent stem cells (iPSCs) that have the same potency but can be established from any cell (Takahashi *et al.* 2007). This is especially useful as not only can human iPSCs be obtained, iPSCs can be derived directly from PD patients and compared with healthy iPSCs, studying any changes in biochemical factors or genetic backgrounds. However, in order to obtain glia, neurons and specifically DAergic midbrain neurons, there is still an unavoidably lengthy, expensive

and difficult differentiation procedure. By using stem cells that are less potent and further down a differentiaton path (that can only differentiate into a few cell types), it is easier to obtain neural cells. The specific multipotent cell type is the neural stem cell (NSC) that can be derived from neural tissues and differentiates into neurons, astrocytes or oligodendrocytes. NSC use for PD modelling is less popular as while they can generate DAergic neurons, they grow poorly in culture and their properties change over time (generating neurons becomes more difficult), making them hard to use in large-scale or long-term experiments (Martínez-Serrano and Liste. 2010). Of these potential stem cell sources, the most widely used to model PD are iPSCs.

As iPSCs can be generated from any cell type, usually an easily accessible human source such as skin is used. Fibroblasat from skin biopsies are converted into iPSCs, then differentiated into the relevant type of neural cell. This differentiation process has numerous stages and produces mature neural cells within approximately 4-10 weeks (Lopes *et al.* 2017). iPSC-derived DAergic neurons express high levels of DA, TH and DAT and develop spontaneous functional synaptic activity (Hartfield *et al.* 2014). The human source of the initial skin fibroblasts is significant: by obtaining iPSCs from healthy patients or patients with sporadic or heritable PD, different experiments can be developed to observe changes based on the patient genetic background and PD susceptibility. As age does not seem to interfere with the reprogramming process, primary fibroblasts can be isolated from patients at any stage of the disease, including late-onset PD (Marchetto *et al.* 2010). iPSCs derived from PD patients have demonstrated mitochondria with reduced oxygen consumption, altered mobility and increased vulnerability to neurotoxins. When iPSCs were generated from a heritable PD patient with a mutation in the *LRRK2* gene, the differentiated DA neurons (55 day differentiaton protocol) displayed increased susceptibility to oxidative stress and higher levels of cell death than controls (Nguyen *et al.* 2011). Major drawbacks are due to the relevent recent development of iPSC technology, such as the lengthy differentiation protcols, technical difficulty of differenatiaton (requires experienced researchers) and loss of ageing-related effects due to the introduction of pluripotency (Lopes *et al.* 2017). Despite these drawbacks, iPSCs are a useful model to study PD due to the ability to replicate DA neuron physiology on a patient-specific basis (latter being dependent on patient consent and ethical approval), including effective isolation and modelling of specific mutations in heritable PD, studying the pathogenesis of PD at a cellular level (Martinez-Morales and Liste. 2012).

1.3.3.3 Primary cell models

Primary cells are cells that are directly cultured *in vitro* after isolation from their *in vivo* source organ, in this case the brain. As the brain becomes more complex throughout development, this isolation process is easier in embryonic brain tissue, before specific cell populations have migrated. Due to the ethical issues surrounding human embryonic tissue, most primary cells are extracted from rodent models. In this case, primary DA cultures can be obtained from the embryonic midbrain of rodents.

Precursors of SN DA neurons are found in the ventral midbrain (VM), and are best isolated during peak neurogenesis, which for the VM is embryonic day (E) 14 in rats and E13 in mice (Gates *et al.* 2006). DAergic cells are isolated via dissection and enzymatically digested to dissociate the tissue into individual cells that can be cultured *in vitro* (Schmidt *et al.* 2012). These primary cell cultures differ to cell line and stem cell cultures as they are extracted directly from the embryonic brain, and therefore: differentiate rapidly, do not undergo mitosis (similar proliferation rates to *in vivo*), form developed axons/dendrites (referred to collectively as neurites), contain large numbers of glial cells, and highly express TH and DAT. Due to these characteristics, primary cells most closely resemble DA neuron morphology and physiology *in vivo*, and make for very effective models of PD *in vitro* (Lopes *et al.* 2017).

However, there are several drawbacks to using primary cells. The cell source is rodent-based and lacks similarity to human cells and human PD, preparation of primary cultures is technically challenging as the VM and other brain subregions are very small at E13-14 (even taking less than 1 mm extra tissue during dissection can result in widly different neural cultures), the process is time consuming, the VM is a highly heterogenous environment resulting in experimental variability and lack of reproducibility, and finally DA neurons consist of the minority of *in vitro* cultures of primary cells (5-10%) making it difficult to specifically manipulate a neuronal sub-type (Lopes *et al.* 2017).

Once a primary VM culture is established *in vitro*, in order to model PD pathology the same neurotoxins (6-OHDA or MPTP) or genetic manipulations are used. For neurotoxins, it is important to consider the sensitivity of primary cells to neurotoxins, resulting in the need for low dosages at carefully optimised times and concentrations. Use of MPTP is more viable than other models due to the presence of glial cells, as the MOA-B in astrocytes in culture can metabolise the MPTP into the active metabolite MPP+ (Segura-Aguilar and Kostrzewa. 2015). The use of 6-OHDA can be very effective if optimised correctly, and until 2004, 6-OHDA effects *in vitro* were not restricted to DA neurons or were observed to be non-specific, limiting the effectiveness of *in vitro* models of DA neuron loss. However, Ding *et al.* produced a methodology wherein primary DA neurons from the VM were selectively damaged by 6-OHDA-induced apoptosis, the effect of which could be reversed by use of glial-derived neurotrophic factor (GDNF). 6-OHDA-induced morphological and biochemical signs of cell death in DA neurons after less than 3 hours, followed by loss of tyrosine hydroxylase (TH) immunoreactive neurons within 2 days. In SN cultures, DA neurons were affected and GABA neurons unaffected, showing that 6-OHDA can selectively destroy DA neurons in *in vitro* primary cell cultures of SN, acting at least in part by initiating caspase-dependent apoptosis, and this effect can be attenuated early but not late by GDNF (Y. M. Ding *et al.* 2004). This ability to recapitulate PD-like neurodegeneration in *in vitro* primary cell models highlights their usefulness as tools for *in vitro* research into PD. In addition, observing the effects of neurotoxins and other chemicals/pharmaceuticals on mixed neuronal/glial (and indeed, mixed neuronal as the majority of

neurons are GABAergic with5-10% being DAergic) cultures gives data that is more relevant to the *in vivo* situation (Griggs *et al.* 2014).

As for genetic manipulation in order to mimic PD, lentiviral vectors have been used to manipulate levels of certain genes. Overexpressing *α-synuclein* in primary cultures resulted in a significant decrease in numbers of DA neurons (~50% loss) (Cooper *et al.* 2006), while expression of *DJ-1* rescued primary DA neurons from rotenone and mutant *α-synuclein* toxicity (Liu *et al.* 2008). Primary midbrain cultures from rat embryos have been used as very effective *in vitro* models, as they replicate many of the morphological and physiological features of mature neurons *in vivo*. If animal models cannot be used, primary cells represent the most complex cell model that is the closest to the *in vivo* midbrain.

1.3.3.4 Tissue slice/organotypic models

Despite the direct access and ease of observation offered by *in vitro* cell models, there are also general drawbacks such as the lack of relevant environmental cues and tissue organization (such as input/output connections) which have a role in disease progression. By taking slices of primary tissue (rather than dissociating the tissue into primary cultures) and culturing them, an *in vitro* model is created where there is still direct access and manipulation, but in an organotypically relevant model where 3D structure and cellular interactions are preserved (Kearns *et al.* 2006, Lopes *et al.* 2017).

This technique is typically performed on postnatal rodents, usually from postnatal day (P)2 up to P15, as the brain needs to be of sufficient size to obtain slices (embryonic brains not typically used). By taking slices of the VM the architecture of the BG is preserved, meaning that tissue slice *in vitro* models are often used to study connections between the SN and other areas such as the STR and cortex, including their functional connectivity and electrophysiological activity. However, these slices age rapidly in culture, are very difficult to reliably reproduce due to transverse changes in brain structure, lose the degree of control found in primary cell cultures, and as more mature rodents are necessary, there are increased ethical concerns as large numbers of animals are required for experimental reproducibility (Polikov *et al.* 2008, Lopes *et al.* 2017).

Tissue slice models have shown that DA neurons in VM slices will project axons to an adjacent STR slice (Gates *et al.* 2004) and form functional synapses (Tseng *et al.* 2007). Lyng *et al*. used E14 VM and E21 STR tissue slices from rats to model the nigrostriatal system in development, analysing DA neurochemistry, numbers of DA neurons as well as protein expression of TH, DAT, and glutamic acid decarboxylase (GAD 65/67) over 17 DIV. Experiments showed that DA neurons developed in a similar way as *in vivo*, with the the numbers of VM DA neurons remaining relatively constant while levels of VM DA progressively increased. After 3 DIV, the levels of striatal DA increased substantially, both indicating that release and metabolism of DA are similar to these characteristics observed *in vivo*

(Lyng *et al.* 2007). These studies also demonstrated the disadvantages of using postnatal tissue (tissue slice models) vs embryonic tissue (primary cell models), due to the DA neurons having fully differentiated or fully projected to the STR, limiting the ability to model this development *in vitro* and the ability to better direct neurodegeneration.

In order to incude PD pathology, neurotoxins are the most commonly used method (again MPTP/MPP+ and 6-OHDA preferentially used). Typically, brain slices are incubated in a neurotoxin bath for up to 60 min (acute exposure) or for a few weeks (chronic exposure). These treatments result in degeneration of neurons in both SNpc and striatum, leading to decreased TH expression (Kearns *et al.* 2006, Stahl *et al.* 2009). Alteratively, PD pathology can be induced by mechanical damage of the nigrostriatal pathway. Such lesions have been shown to induce asynuclein aggregation and nigrostriatal neuron degeneration in organotypic slice models (Cavaliere *et al.* 2010, Daviaud *et al.* 2014).

Developing *in vitro* models that include DA neurons allows for the creation of powerful platforms for PD research, both for neurodegeneration and potential therapeutics such as pharmaceuticals and neuroprotective factors. The potential options for such a model (decreasing in biological complexity in order) are as follows: organotypic tissue slices; neural primary cells; neuronal-only primary cells; stem/progenitor cells (including iPSCs and NSCs) and neural cell lines (such as SH-SY5Y, LUHMES etc). While *in vitro* cell culture alone offers great models for PD, combining cell models with bioengineering allows for more efficient and improved *in vitro* models of PD.

1.3.3.5 Organoids and 3D models

Most cell models are 2D cultures that lack cell-cell and cell-matrix interactions, limiting their ability to best mimic cellular functions within tissues *in vivo*. While tissue slices better mimic the structural organisation, they quickly lose their phenotyoe and are difficult to maintain over long periods of time (Yin *et al.* 2016). But by placing stem cells into a scaffold hydrogel in the presence of suitable exogenous factors, the stem cells can form organised and structured clusters of cells, termed ‘organoids’. 3D neural tissues can therefore be generated from stem cells, termed brain/cerebral organoids. Cells in aggregates exhibit an innate self-organising capacity and can be grown into brain organoids with structural features resembling the developing brain *in vivo*, including specific genetic backgrounds (Nakano *et al.* 2012, Muguruma *et al.* 2015). If grown without inductive cues, multiple brain regions can randomly develop, as seen in a model from Lancaster *et al.*, who reported a culture system involving neuroectodermal tissues maintained in 3D Matrigel scaffold, resulting in heterogenous organoids that contained multiple independent brain regions (such as dorsal cortex, ventral telencephalon, choroid plexus, hippocampus and retina) and growing to 4 mm long in 2 months (Lancaster *et al.* 2013). If grown with specific combinations, concentrations and timings of exogenous substances and signalling molecules, the resultant brain organoids can be more directed,

involving multiple brain regions that can be fused into 'assembloids' to model brain region connectivity (Amin and Pasca. 2018).

These brain organoids make effective models of the *in vivo* brain as they contain multiple cell types, heterogenous tissue-specific cells, cell-cell and cell-matrix interactions, as well as functionality, making them better mimics of brain physiology than 2D cultures. In addition, some organoids demonstrate neuronal functionality, development and maturation *in vitro* in a similar manner to the *in vivo* brain (Yin *et al.* 2016). Future work with organoids aims to include vascularisation, presence of an immune system (by inclusion of microglia-like cells in assembloids), circuitry and microenvironments to better mimic the brain (Mansour *et al.* 2018), as well as inclusion of sensory and motor outputs (via functional integration into mouse models) (Amin and Pasca. 2018).

Complex brain architectures have been recreated by organoids *in vitro* using serum-free floating culture of embryoid body-like aggregates, such as cerebral cortex (Kadoshima *et al.* 2013) (exhibited self-organisation along an axis and an inside-out pattern, similarly to the developing human cortex *in vivo*), (Mariani *et al.* 2012) (used iPSCs to generate multi-layered structures that expressed a gene profile typical to that of the embryonic telencephalon) and pitruitary (Suga *et al.* 2011). By including customisable/responsive biomaterials, patterned/gradient signalling and microfluidic networks, brain organoids can future develop spatially, becoming better mimics of the *in vivo* brain (Yin *et al.* 2016).

Despite the fact that most brain organoids are best suited for studying brain development, such as corticogenesis and neurodevelopmental disorders, some directed differentiation can result in organoids that can be used for study of PD. Jo *et al*. developed a brain organoid resembling the midbrain and containing functional DA neurons, making it a relevant model for PD. The group differentiated hPSCs into human midbrain-like organoids (expressed midbrain markers) that recapitulated features of the midbrain. Midbrain DA and TH^+ neurons were electrically active and functionally mature, producing dopamine and neuromelanin-like granules (similar to substantia nigra *in vivo*), resulting in a potentially powerful model of the healthy midbrain for study of PD (Jo *et al.* 2016). These midbrain organoids can be maintained for very long periods of time (months-years), allowing for a potentially better mimic of the slow progression of PD over time.

In addition, these organoids can be assessed functionally, albiet in a destructive manner. Pasca *et al.* generated pyramidal neurons from human iPSCs in a 3D cortex-like structure. These human cortical organoids only generated excitatory glutamatergic neurons of the dorsal telencephalon, but the internal structure was similar to a laminated neocortex with deep- and superficial-layer cortical markers. After two and a half months the organoids resembled the prenatal brain at 19-24 weeks post-conception, with networks of nonreactive astrocytes and spontaneously active neurons that formed functional synapses. These matured organoids were sliced in a similar manner to organotypic

slice cultures, allowing for the recording and electrical stimulation of neurons. Electrophysiological analysis via calcium imaging and patch clamping indicated that the neurons participated in network activity and produced complex synaptic events in the presence and absence of stimulation (Amin and Pasca. 2018).

While brain organoids can model more physiologically relevant cellular interactions and feature structural and organisational features of the brain not present in 2D monolayer cultures, there are some downsides. Organoids are time-consuming, expensive and technically challenging to develop and maintain, lack homogeneity and scalability (less suitable for high-throughput studies and screenings), and have less uniform access to nutrients/biochemical factors than monolayers (the centre of an organoid may be starved of resources) (Amin and Pasca. 2018). In comparison to compartmentalised microfluidic devices functional testing methods are challenging and destructive, making it difficult to assess the functionality of neural cells in organoids over time across the whole population, whereas this is a simple manner with an MEA. Organoids form complex yet isolated structures, unlike the desired networks of different brain subregions needed to model the basal ganglia.

1.4 Bioengineering complexity into *in vitro* models

1.4.1 Modelling with reduced complexity

Current pre-clinical assessment is insufficient to predict what pharmaceuticals and treatments will work on human disease patients, with a lack of *in vivo* animal models that duplicate the causes, symptoms and progression of a human neural disorder (Pinel. 2013). In some cases, the models are non-existent, such as rodents not naturally acquiring PD (Meredith and Rademacher. 2011). Better *in vitro* modelling would lead to less expensive and time-consuming clinical trials by improving study on a pre-clinical level.

In vitro cell or tissue models involve culturing large numbers of cells or an intact slice of tissue and using the resulting cell/tissue culture as a platform for experimental study. With tissue models, the tissue is extracted directly from an animal model and kept alive *ex vivo* for an extended period of time for study by recreating an environment similar to that found *in vivo*, both using specialised biochemical methods such as culturing the tissue in a specific nutrient rich medium and using specialised equipment including a tissue culture incubator to maintain physiological temperature (37°C) and gas concentrations (5% CO_2) and a laminar flow cabinet to maintain sterility and avoid infection (Morrison *et al.* 2011). It should be noted that there is often a considerable lack of diseased neural tissue for study, especially concerning human models, due to biopsies involving limited environmental control, variable sample thickness, and destruction of countless input/output

connections from both neural and non-neural cells upon biopsy (Arbab *et al.* 2014). Therefore, it is preferable to go to the most 'bottom-up' approach available, by working with the neuronal and non-neuronal cells themselves.

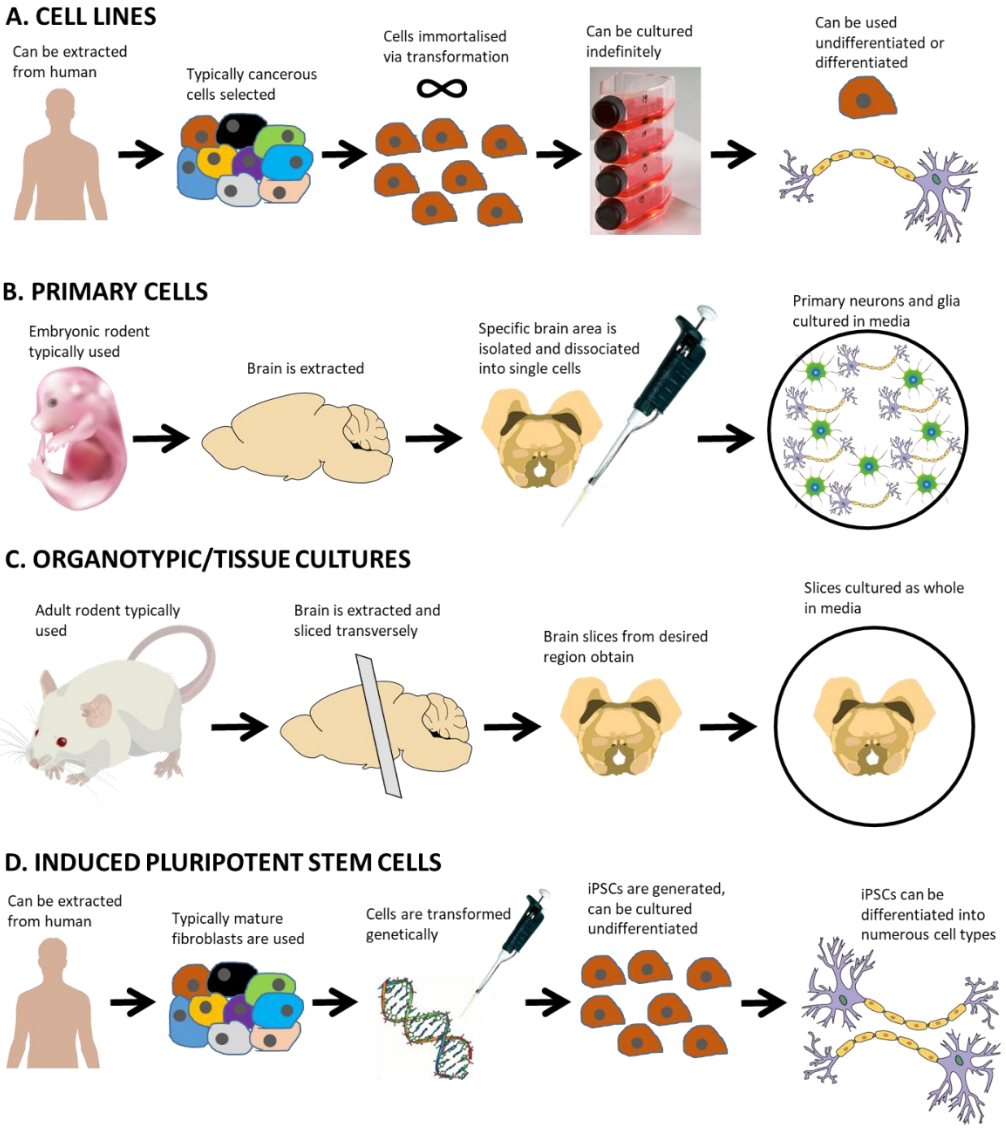

Figure 1.8: Different methods to use in order to generate *in vitro* models of PD (ordered from lowest to highest in terms of cost, technical difficulty and time). A) Cell lines: can be human-based, reproducible, and easily scaled up, but require differentiation and are oncogenic. B) Primary cells: provide accurate neuronal physiology and morphology, also contain glial cells so are more accurate as mimics of *in vivo* brains, but are non-human, time-consuming and unsuitable for genetic manipulation. C) Organotypic cultures: better mimic 3D *in vivo* connectivity, but are non-human, time-consuming, technically challenging to obtain and rapidly degenerate in culture. D) iPSCs: Can be derived from both healthy and PD humans and produce accurate neurons, but is very time-consuming, expensive and carries additional ethical considerations. All images from Wikimedia Creative Commons, based on a figure from (Lopes *et al.* 2017).

With cell models, cells are cultured in the same manner as tissue but there are multiple sources available, namely primary cells, stem cells (Paspala *et al.* 2011), pluripotent cells created in a laboratory setting (Takahashi and Yamanaka. 2006) and cell lines. This results in *in vitro* cell models being very simplistic in comparison to tissue models and *in vivo* animal studies. By using neural tissue engineering, surface modifications, specialised culture conditions and a similar nutrient medium,

in vitro models can be modified and improved so that they may attempt to represent a select area of the brain. It should be noted that while modelling smaller isolated portions of the brain makes for more accurate and focused models, it should take into account that connections with other brain areas are unrepresented and this lack of inter-neural connections may affect the model (Chiappalone *et al.* 2006). With the success of an *in vitro* model hinging on the design process, a summation of considerations for design can be seen in **Table 1.2**.

Neural circuitry is delicate, morphologically and functionally complex and exerts numerous chemical and mechanical forces on other cells and material present in culture. However, the relative impact of these issues is dependent on the design and ingenuity of the model, meaning that good awareness of these issues alongside improvements in design of experimental techniques and relevant technological advances should alleviate these problems. By taking advantage of the *in vitro* model's simplicity and exerting control over neurons and glia, the model can become more flexible and complex as it mimics the *in vivo* environment within the brain.

1.4.2 Surface parameters to control cell responses

In order to develop *in vitro* neural cell models, it is vital to consider the surface that the cells will be in contact with, and how the characteristics of this surface can be used to control cell responses.

Surface characteristics of biomaterials supporting cell culture are a major factor when culturing neurons and glia. These adherent cells anchor to the growth surface, this can be influenced by using certain chemicals to change the characteristics of the surface, such as the hydrophobicity or charge. The latter is important to consider as cells have a negatively charged membrane due to glycoproteins and glycolipids on the surface of the plasma membrane and display enhanced adhesion to positively charged polymers (Lakard *et al.* 2004, B. Liu *et al.* 2008). As a result, most surface coatings have a net positive charge.

Chemical factors are used to modify surfaces to modify cell culture. For instance, proteins in the cell media adsorb to the growth surface within a fraction of a second, creating an intermediary between the cell and the surface (Ma *et al.* 2005), making pre-treatment of a culture surface a viable option for cell culture work as cell-protein interactions can be used to encourage or discourage cell growth (Vroman and Adams. 1969, Roach *et al.* 2010). Chemical factors are used to modify surfaces to modify cell culture. For instance, proteins in the cell media adsorb to the growth surface within a fraction of a second, creating an intermediary between the cell and the surface (Ma *et al.* 2005), making pre-treatment of a culture surface a viable option for cell culture work as cell-protein interactions can be used to encourage or discourage cell growth (Vroman and Adams. 1969, Roach *et al.* 2010).

Table 1.2: What to consider when planning an *in vitro* model of the brain, adapted from (Fedoroff and Richardson. 2001)

Design Consideration	Options
Cell culture class	Primary cells are isolated directly from tissues and therefore best represent the endogenous phenotype but difficult to maintain. Immortalized cell lines can be maintained indefinitely but may have excessive variation.
Cell developmental age	Certain cell types are only available past certain developmental times, but too many days of development leads to a more challenging dissection process. Less developed networks are easier to extract and culture, but are potentially less functionally mature.
Similarities to human brain	Comparison to the *in vivo* system. Can use adult human iPS cells, embryonic/foetal human cells, animal cell lines or primary animal cells.
Culture type	Can culture tissue/organ slices or individual cells.
Preservation of *in vivo* organisation (2D or 3D?)	Neural cells can grow effectively in a 2D planar culture (monolayer) or 3D matrix (neurosphere), but this doesn't represent the anatomy *in vivo*. Cell-cell and cell-matrix interactions are numerous in 3D but limited in 2D. Can disaggregate or re-aggregate cells.
Electrophysiological integrity	Neural cells within the model should have similar electrical activity as the same cell type *in vivo*. Recording devices should discriminate between signals and have a low signal-noise ratio, so as to isolate spikes and other activity (Faisal *et al.* 2008, Avila Akerberg and Chacron. 2009).
Culture environment	Extracellular fluid composition, temperature, pH, gas phase, substrate, dimensions.
Model material	Non-toxic, non-inflammatory, non-allergenic, non-carcinogenic, light, soft, mechanically durable, chemically stable and simple to fabricate.
Model fabrication	What technology will be used to fabricate the model, is it reproducible, high-throughput? Can modifications be easily made, and will any interface will exist between the cultured cells and inorganic devices?

Some biological substances can also be used on surfaces to induce a cell response, usually by presenting cell binding domains that interact with integrin receptors on the cell surface (Cooke *et al.* 2008). An example of this are the positively charged peptide sequences RGD, IKVAV and YIGSR, found in a protein called laminin (LAM) (Freire *et al.* 2002, Durbeej. 2010, Domogatskaya *et al.* 2012). As a result, tissue culture plastic can be pre-treated with LAM (itself a positively charged polymer of amino acids) before cell seeding (Bledi *et al.* 2000), which has been shown to induce axon growth (T. Esch *et al.* 1999). Another popular surface treatment is the positively charged polymer poly-lysine (either optical isomer poly-L-lysine (PLL) or poly-D-lysine (PDL), often used in tandem with LAM) due to its anime group, which have been shown to increase neural cell attachment and growth (Yavin and Yavin. 1974, Kleinfeld *et al.* 1988, B. Liu *et al.* 2008, Roach *et al.* 2010). It should be noted that PDL is

more widely used compared to PLL, with the latter shown to interfere with certain biological functions (Lelong *et al.* 1992), whereas PDL does not occur naturally and interacts with fewer biological systems. However, coating surfaces with PDL and LAM needs be done with great care due to how different factors can influence the effectiveness of the coating, especially when using the surface for culturing neurons and glia. LAM pH influences neurite outgrowth (Freire *et al.* 2002), the presence of LAM and proteoglycans together can suppress neurite outgrowth (Hynds and Snow. 1999), and LAM is dependent on the presence and concentration of serum in cell media (Blau *et al.* 2001, Kam *et al.* 2001), indicating that protein-protein interactions can have just as much effect as protein-surface and subsequent cell-surface interactions.

The range of different chemicals for coating a cell culture surface results in some chemicals/polymers being better for specific situations and models of specific areas than others. For example, while organic polypeptides such as PDL/PLL are very popular and effective as a surface treatment, they feature amide bonds in the backbone and can thus be hydrolyzed and broken down with relative ease (Garza *et al.* 2005). Synthetic polymers present an alternative to organics. One such example is polyethylenimine (PEI), a positively charged synthetic polymer that lacks amide linkages, and has long been shown to support attachment, growth and maturation of neural cells (Lelong *et al.* 1992, Ruegg and Hefti. 1984, Bledi *et al.* 2000, Lakard *et al.* 2004, Vancha *et al.* 2004, B. F. Liu *et al.* 2006, B. Liu *et al.* 2008), in most cases more effectively than PDL/PLL or LAM. In addition, PEI can be either linear or branched, meaning that changing variables during synthesis can modify the positive charge density and molecular weight of PEI (Jeong *et al.* 2001), allowing PEI to be more attractive for neurons by using electrostatic attraction due to the high charge density, making PEI a very effective and powerful chemical for use as a coating for neural cell culture.

Pre-treating surfaces with specific chemicals that mimic the chemical composition of the neural niche within the brain allow for *in vitro* work to more accurately represent the *in vivo* neural environment, and neuron growth can be improved (Roach *et al.* 2010). By using a bioactive polymer based on the neurotransmitter dopamine, neurite outgrowth was significantly improved (comparatively, when dopamine itself was added to culture media, no such effect was seen), compared to a surface treated with tissue culture polystyrene, laminin and PDL (J. Gao *et al.* 2006). A follow-up experiment using a tyrosine-based polymer (dopamine being synthesized from tyrosine *in vivo*) showed no effect, indicating that an *in vitro* model designed to mimic the *in vivo* environment will need to be designed with great precision, due to the preferences of the cells.

1.4.3 Determining electrophysiological functionality

When developing an *in vitro* neural model it is vital to ensure that the cells are electrophysiologically active in a similar manner to *in vivo*. Neural cells must be demonstrably producing their own spontaneous electrical signals and forming synapses in order to be labelled as functional, and to better mimic the behaviour of neural cell *in vivo*. A good *in vitro* neural model therefore needs a method to record and quantify the spontaneous electrical signals spontaneously produced by neural cells to ensure they are functional, without this ability the model will be insufficient no matter how well developed the cells are or how morphologically desirable the network may be.

Electrical activity in the brain is caused by a number of transmembrane proteins that form pores, termed ion channels. These channels are found in the membrane of every cell in the CNS and allow specific ions to travel across the cell membrane in a controlled manner, which establishes a resting membrane potential. These ion channels also create the dynamic voltage changes seen in action potentials (APs), namely the electrical signalling measured in neural electrophysiology.

The resting membrane potential of a neuron is determined by the uneven concentration gradients of sodium (Na^+) and potassium (K^+) ions across the cell membrane, making the membrane polarised. With Na^+ and K^+ ion channels regulating the flow of each respective ion across the membrane, it can become more positively charged (depolarised) or more negatively charged (hyperpolarised). In an AP, the membrane becomes rapidly depolarised upon stimulus (classically from -70 mV to 40 mV), then rapidly hyperpolarises and overshoots the resting potential (classically to -90 mV) and then re-establishes the resting membrane potential, returning to a resting state. Due to the rapid nature of these APs (~3.5 ms) and the sharp increase and decrease of voltage, these signals are often referred to as 'spikes' in activity. The AP travels down the entire axon of a neuron, and then passes across a synapse to connected neurons. Neurons communicate cell-to-cell via APs: receiving signals, integrating them, and passing the signal along to other cells.

The AP signal passes from neuron to neuron via neurotransmitters (more information seen below in **Fig.1.9**). These chemicals are triggered by an AP depolarising the membrane and respond by travelling across the synaptic cleft from the presynaptic membrane to the postsynaptic membrane within a vesicle, where they will bind to receptors and trigger one of two responses: excitatory or inhibitory, increasing or decreasing the chance of a AP in the postsynaptic cell respectively. Within the brain, the main inhibitory and excitatory neurotransmitters are GABA and glutamate respectively. The effects of these neurotransmitters depend on the connectivity of the neuronal network they are based in.

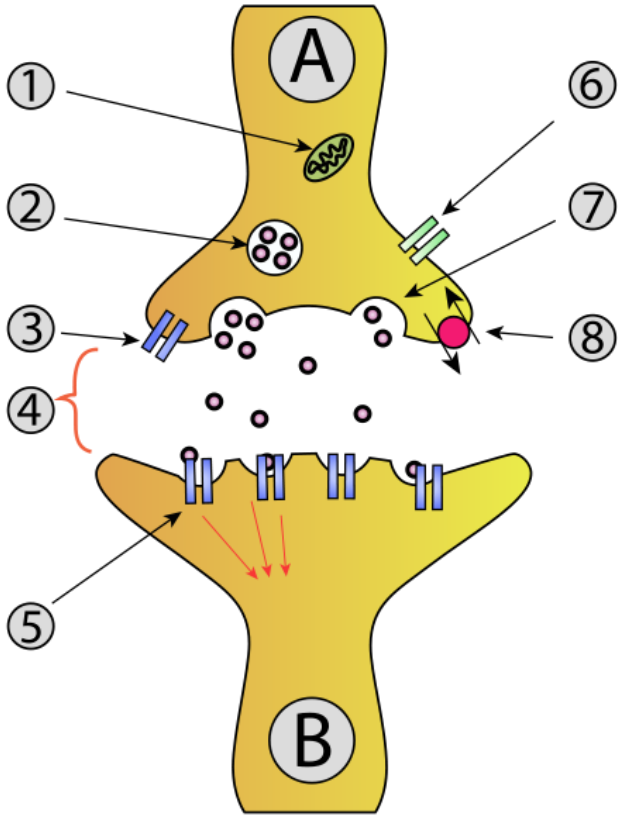

Figure 1.9: A diagram of a synapse between two neurons, A and B. 1: mitochondrion, 2: pre-synaptic vesicle with neurotransmitter, 3: autoreceptor, 4: cleft between the presynaptic and postsynaptic membranes, 5: transmembrane neurotransmitter receivers on the postsynaptic neuron, 6: Ca^{2+} ion channel, 7: a fused vesicle releasing neurotransmitter into the synaptic cleft, 8: neurotransmitter re-uptake pump. Image from Wikimedia Commons (user Mouagip) permission granted under Gnu Free Documentation License.

1.4.4 Measuring electrophysiological activity

There are several established methods for quantifying electrophysiological signals in neuron populations, mostly involving electrodes, either inserted into the cell interior (intercellular recording) or in contact with the exterior of the cell (extracellular recording). Examples include patch-clamping and whole call clamping (intercellular), voltage/ion sensitive dyes, acutely isolated neuron models, and multi-electrode arrays (MEAs) (extracellular) (Aston-Jones and Siggins. 2000).

Inserting electrodes into cells (e.g. patch-clamping) is a classic methodology and therefore well-established technique (Hodgkin and Huxley. 1939) that provides electrical coupling with the cell and very accurate intracellular readouts with little noise, but it should be noted that it is a technically difficult and time-consuming process that usually records electrical activity from a single cell over the short-term while stressing them mechanically (Jokinen *et al.* 2013). While recent advances in patch clamping technology allow for assessment of multiple cells, these processes are expensive and require advanced specialised equipment (Franz *et al.* 2017). Even with these advanced techniques it would be too time-consuming to acquire enough information to determine the functionality of a whole cell population. An alternative is extracellular recording, which in comparison to intracellular recordings cannot provide electrical data from within the cell and therefore lacks signal resolution

and amplitude (see **Fig.1.10**) and often features more noise. On the other hand, extracellular recording can record from large numbers of cells simultaneously over long-term experiments (timescale of months), is non-invasive and causes no damage to the cells, which are usually cultured in a monolayer directly on top of the electrodes (Spira and Hai. 2013).

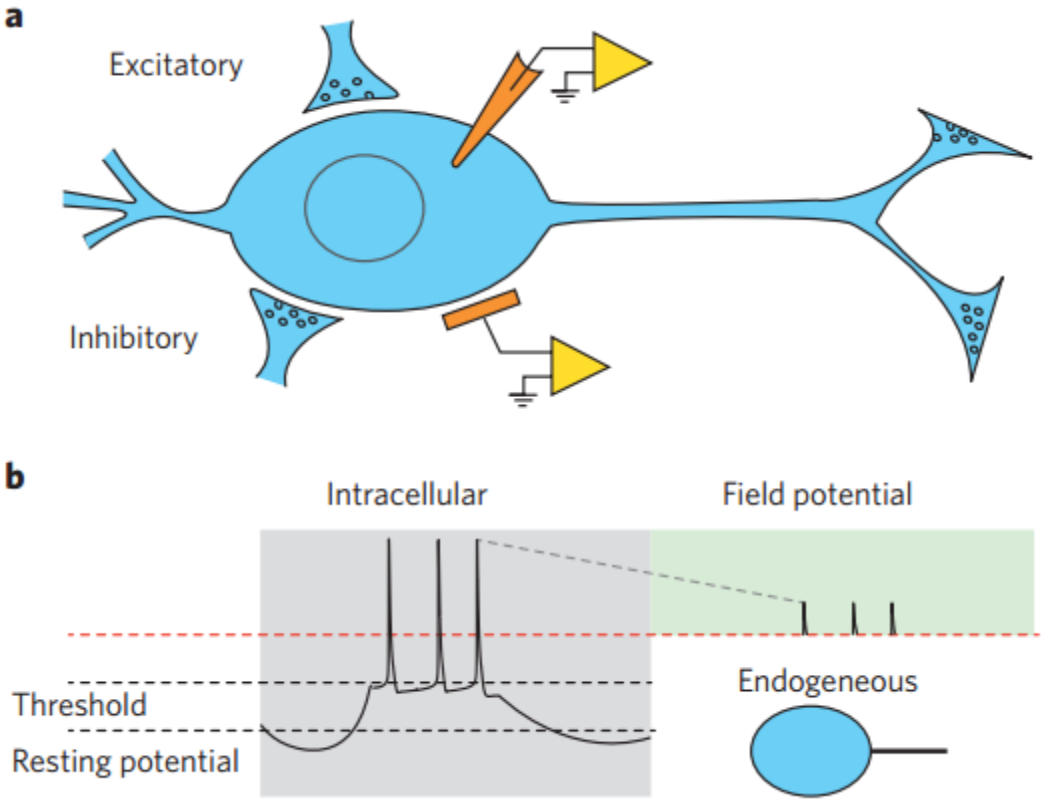

Figure 1.10: Intracellular and extracellular electrical recording. (A) A diagram of a neuron showing intracellular (top orange electrode) and extracellular (bottom orange electrode) with amplifiers in yellow. (B) Action potentials (APs) generated endogenously by a neuron, with the intracellular reading on the left and the extracellular reading on the right. The latter is only sensitive enough to pick up the tips of the peaks of the AP whereas the former can record the entire process. Image adapted from (Spira and Hai. 2013).

If recordings cannot be taken constantly, it is always possible that some neurons may not be active and producing electrical signals during the recording time and may be seen as non-functional, and indeed *in vivo* there are brain areas where neurons do not produce electrophysiological spikes or produce them at such a low rate that they are not recorded and are thus termed 'dark neurons' (Shoham *et al.* 2006). It is therefore important to select electrophysiological recording methods that allow for continuous recording over whole neuronal networks *in vitro*, which would produce the most relevant data for determining the functionality of an *in vitro* neural model, compared to intercellular recording methods.

The most challenging type of recording would be to obtain single cell resolution over a large cell population over the long term, combining the best factors of intra- and extracellular recordings methods. One potential method that can achieve this are Ca^{2+} indicators.

Unlike small molecule fluorescent Ca^{2+} dyes (used to analyse changes in cell Ca^{2+} signalling), which often feature poor loading and poor long-term retention (Perry *et al.* 2015), genetically encoded calcium ion (Ca^{2+}) indicators (GECIs) are optical sensors that are produced by translation of a specific nucleic-acid sequence, comprising of a fluorescent protein and a Ca^{2+}-binding element. When Ca^{2+} binds to a GECI, it changes the optical properties in a detectable manner (Palmer and Tsien. 2006). The appeal of GECIs is twofold, based on their genetic and optical nature. From the genetic side comes the considerations that GECIs can be delivered to target organisms/tissues/cells via minimally invasive methods such as tranfection or trangenesis, and are sensitive enough to detect single APs *in vivo* or *in vitro* over the long-term (months) (Tian *et al.* 2012, Akerboom *et al.* 2013), and as such could be used to track disease progression. In addition, genetic encoding allows for GECIs to be targeted to neuronal subtypes or even neurons with specific anatomical connectivity (via axonal or trans-synaptic labelling) (Lin and Schnitzer. 2016). From the optical side, loading a whole neural population with GECIs and using optical imaging allows for thousands of neurons to be simultaneously observed *in vitro* or *in vivo* in an unbiased manner (Sofroniew *et al.* 2016).

However, both the genetic and optical components of GECIs have associated disadvantages. For long-term expression of GECIs, viral infection or transgenesis are required, both of which are challenging techniques requiring heavy optimisation, appropriate laboratory settings and limited construct size, as GECIs need to be expressed at sufficiently high levels to function (Perez Koldenkova and Nagai. 2013, Lin and Schnitzer. 2016). From the optical side, the fidelity of detecting neural signalling and the accuracy of timing this signalling are both limited by photon emission/detection quantum mechanics. To counteract this, complex calculations and equipment are required, such as two-photon confocal microscopy or laser-scanning. Due to the wide variety of uses for GECIs there are many types available (Akerboom *et al.* 2013), with each requiring re-optimisation, such as different illumination/acquisition parameters and photobleaching, both of which limit the length of time each experiment can run for (photobleaching occurring after ~15 mins for single-cell studies) (St-Pierre *et al.* 2014).

Additional drawbacks to GECIS involve the numerous calibration steps required when using GECIs to measure neural activity, such as attached-cell recording and patch clamping, in order to verify that GECI expression does not alter the physiological properties or network interactions of the neurons (Tian *et al.* 2012). As neuronal signalling and action potentials (APs) involve rapid Ca^{2+} influx, when using GECIs to analyse neural models it is vital to choose a GECI with fast response kinetics. Engineering of GECIs with an improved signal-to-noise ratio (SNR) has been shown to alter the fast kinetics and cytotoxicity of newer GECIs, requiring inducible/reversible expression cassettes (Tian *et al.* 2012). Due to these factors, GECIs may not be suitable for long-term experiments across a whole population.

1.4.5 Multi-electrode arrays (MEAs)

One of the best examples of extracellular recording across a cell culture is the MEA, an ordered array of electrodes typically arranged into grids. Cells can be seeded directly onto MEAs and are cultured in contact with the electrodes, which can record extracellular electrophysiological activity from the cells (see **Fig.1.11A-B**). MEAs record spontaneous activity and activity in response to stimulation, both over a long time-frame and across an entire culture, giving MEAs vast temporal and spatial ability (Gross *et al.* 1977, Pine. 1980, Fejtl *et al.* 2006).

A limitation of MEAs is that they can only stimulate or record from cells that are in physical contact with electrodes or cells that are functionally networked to cells in physical contact with electrodes. Due to the size and position of MEA electrodes, some electrodes may be in contact with no cells, whereas some may be in contact with more than ten neurons, resulting in variable signal quality and amplified noise (Kanagasabapathi *et al.* 2011). However, with dense cultures and the many connections that neurons typically make, very large portions of a neural culture can still be assessed with an MEA, constantly recording electrophysiological signals from the majority of an entire culture. Therefore, MEAs can record and analyse the spatiotemporal distribution of electrical activity across a monolayer of neuronal and glial cells. Changes in morphology in the cell monolayer can be easily monitored with imaging techniques (as the MEA is transparent with the exception of the electrodes), with cells cultured on MEAs surviving for the long term (in some cases over a year) which removes certain time limitations on studies (Hales *et al.* 2010). Due to the numerous advantages of using MEA systems, there are a great deal of studies using MEAs with a variety of different cells from the CNS in order to assess the functionality of neuronal models and cultures (Keefer *et al.* 2001, Gramowski *et al.* 2004, Gramowski *et al.* 2006, van Vliet *et al.* 2007, Heikkilä *et al.* 2009, Yla-Outinen *et al.* 2010, Hogberg *et al.* 2011, Makinen *et al.* 2013). MEAs can also record oscillations in neural activity, most useful in identifying diseases such as schizophrenia which can result in disturbed gamma oscillations (Gonzalez-Burgos and Lewis. 2012).

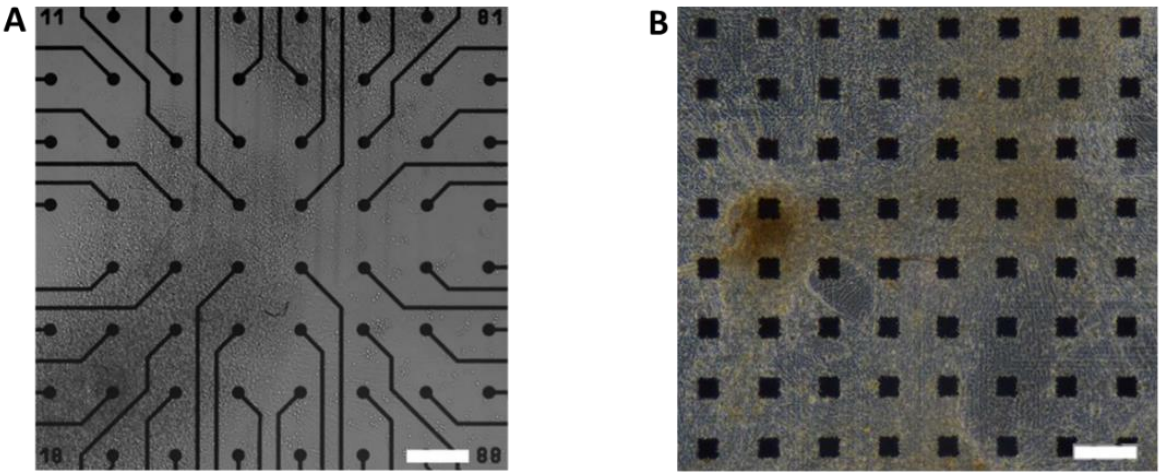

Figure 1.11: Two different MEAs. A) An MEA with 60 circular electrodes (20 µm diameter with 200 µm spacing), scale bar 200 µm, adapted from (Yla-Outinen *et al.* 2010). B) An MEA with 64 square electrodes (50 µm diameter with 200 µm spacing), scale bar 200 µm, from AlphaMED and used in this project.

The ability to record network activity from different neuronal subtypes in different spatiotemporal conditions *in vitro* and to simultaneously qualify the functionality of these neurons as well as the timing of that functionality and any connections between the neural networks demonstrates the huge potential of the MEA. When used as a recording device in *in vitro* neural models, MEAs can characterise and manipulate neural subtypes *in vitro* to form and analyse more complex circuits representing different CNS areas, playing an important role in studying neural networks and their dynamics.

1.4.5.1 Examples of MEAs combined with in vitro *neural models*

Combining an *in vitro* neural model with an MEA allows for functional testing of neural cells cultured in the model, reinforcing the accuracy of the *in vitro* model. Previous studies have shown that neural activity *in vitro* matures over time (Goyal and Nam. 2011), particularly from the first week to the third week, the characteristic timing of synapse maturation and increase in synapse density *in vivo* (Jimbo. 2007). These studies took place in microfluidic devices, allowing for long-term culture of neural cells with MEA readings taken throughout, this long-term culture (multiple weeks) allows for the assessment of functionally mature neural network formation.

MEAs have also been used to determine the differences in spontaneous electrophysiological activity between neural cells cultured in isolation and neural cells cultured together in an *in vitro* model with two compartments (Takayama *et al.* 2012). When grown separately, primary cortex neurons demonstrated periodic bursts of activity with long quiescent periods for the first two weeks and high frequency patterns of activity from three weeks onward (timings were compatible with development changes normally seen in these neurons (van Pelt *et al.* 2005)). When grown together with P19 neurons in a microfluidic device, activity was more widespread across the MEA and spike frequency was significantly increased after three weeks *in vitro*. This means that any functional connections and

interactions between the neurons in the microfluidic device occurred between two and three weeks *in vitro*. This trend was also seen in *in vitro* hippocampal primary networks joined to MEAs (Brewer *et al.* 2013), where the frequency and duration of spiking increased when cell populations were connected This spiking was also directional, with >99% of spikes propagating in one direction only, showing a preference of certain cell types to form functional synapses with other cell types. This experiment indicated that hippocampal sub-regions can self-wire in anatomically appropriate patterns compared to *in vivo* and maintain a distinct phenotype profile *in vitro*.

MEAs can also be chemically coated, with studies coating the surface of MEAs with PEI to promote cell-surface attachment over cell-cell attachment and stop rafts of cells lifting off the surface after long-term culture (Kanagasabapathi *et al.* 2013). This experiment also showed cortical cells in one compartment initiating bursts of electrical activity which then occurred in the other compartment (containing thalamic cells), indicating a functional connection between these neuronal subtypes in a similar manner to their connectivity *in vivo*. The use of PEI with MEAs is established in the literature, as well as increasing cell attachment, depositing PEI on the surface of electrodes can also improve the signal to noise ratio by providing an insulating layer between the sensitive membrane of the neuron and the material of the electrode (Zairi *et al.* 2002, McMahon *et al.* 2007).

One limitation of MEAs is their lack of interaction with 3D cultures. Recent *in vitro* neural models have developed in ways that make it difficult to integrate MEAs or other methods of extracellular electrophysiological recording. While these models have great complexity, they lack the ability to functionally assess the neural cells cultured within. Some examples include networked neurospheres (used to test neurotoxicity of the amyloid beta protein, a causative factor of Alzheimer's disease) by (Choi *et al.* 2013b), a 3D micro-physiological system (or 'mini-brain', that exhibit migration, neuronal differentiation, network elaboration, cell-cell interactions (both neuron-neuron and neuron-glia), myelination and synapse formation) by (Bal-Price *et al.* 2010) and (Pamies *et al.* 2014), as well as an organoid model by (Lancaster *et al.* 2013). All these models involve a 3D aggregate of cells, which may act as a good mimic for the *in vivo* brain but makes it far more challenging to assess the function of all the neural cells within, as MEAs and other extracellular electrode systems work best with 2D cell monolayers. This can result in otherwise impressive 3D *in vitro* models having no functional assessment or method of recording electrical activity throughout the culture, limiting the usefulness as a model of the *in vivo* brain. One solution to this issue would be the use of MEAs compatible with 3D cultures, and indeed 3D MEA systems are in development (Musick *et al.* 2009, Frega *et al.* 2014a), but have not seen much use outside of select cases and mostly consist of stacks of 2D MEAs or glass beads respectively rather than a 'true' 3D MEA. Some MEA manufacturers have developed several MEA types that involve spiked or raised MEAs that protrude up to 50 µm out of the MEA surface and into sample tissues/cells, but these are pseudo-3D at best and unnecessarily damage samples at worst. Examples can be seen in **Fig.1.12**.

A recent *in vitro* study compared a 2D neural culture directly on a MEA with a 3D neural culture within a 3D scaffold (such as collagen), with the base of the 3D structure in contact with the MEA, and noted several differences between 2D and 3D, including that the 3D cultures better mimicked native brain activity. However, note that all cells were in contact with electrodes in 2D, while in 3D only the 'lowest' cells were in contact with electrodes (Bourke *et al.* 2018).

Early 'true' 3D MEAs involved some interesting designs, such as a push-pull actuated capillary-wire mechanism where wires could penetrate into tissue slices at different z-axis points in order to record from different planes. This mechanical actuation appears to have similar drawbacks to intracellular recording, where the cells are physically pierced repeatedly in order to move up and down the z-axis (Zuo *et al.* 2017).

Other examples of 'true' 3D MEAs include those developed via low-temperature co-fired ceramic (LTCC) and miniaturised ceramic circuit boards (MCBB) technologies, allowing for 3D MEAs up to 2 mm in height, as well as flow and control of temperature (typically kept at 37 ^{o}C). This allows for maintenance and investigation of neural tissues hundreds of micrometres in height, and culture of primary neural cells over the long term (over six months). These arrays can also be functionalised with coatings (such as laminin or titanium oxynitride on gold electrodes), making them suitable for signal recording in 3D *in vitro* cultures (Bartsch *et al.* 2018). It should be noted that as the base of this device is co-fired ceramic, it is not transparent and imaging may be challenging. A summary of these designs can be seen in **Fig.1.12**.

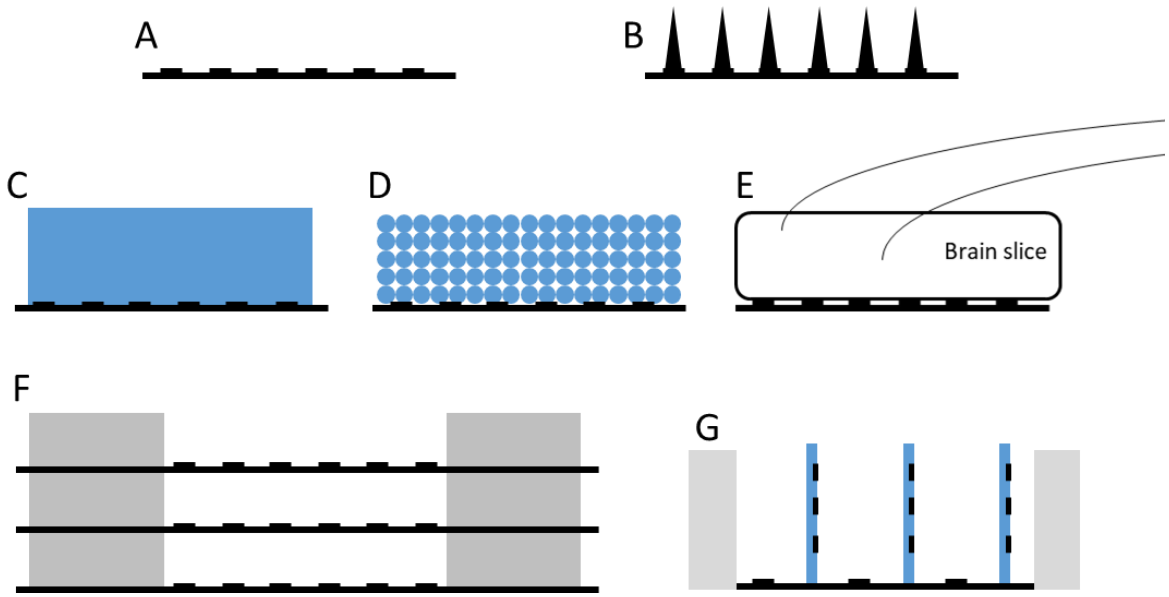

Figure 1.12: Different design approaches to fabricating 3D MEAs. A) a typical 2D MEA. B) MEA with raised or 'spiked' electrodes, these can pierce up to 50 µm into a sample for recording beyond the outer layer of cells, but can do significant damage to the sample. C) Culturing a 3D scaffold of cells (blue, typically a hydrogel scaffold) on a typical MEA, signals received from base layer of cells only (based on work from (Bourke *et al.* 2018)). D) Culturing cells on a 3D array of glass beads (blue), has similar issues to C, where only the base bead layer can be recorded from (based on work from (Frega *et al.* 2014)). E) Capillary-wire mechanism, where two wires can be positioned throughout the z-axis of a tissue slice in order to give recordings from multiple planes (based on work by (Zuo *et al.* 2017)). F) Stacks of 2D MEAs supported by PDMS (grey) and silicon, allow for recording from multiple cell monolayers throughout the z-axis, but not 'true' 3D (based on work from (Musick *et al.* 2009)). G) Recent work involving fabricating ceramic circuits into z-axis extensions, resulting in a 2D MEA with interspersed electrode-studded pillars (blue) that can measure cell activity throughout a 3D area (based on work by (Bartsch *et al.* 2018)).

Rather than increasing complexity of *in vitro* models via a move from 2D to 3D, it may be better to increase the complexity of a 2D monolayer model in order to retain functional assessment.

1.5 Organ-on-a-chip

For *in vitro* 2D cell models to better mimic *in vivo* physiology, one of the most successful approaches is to combine microfabricated devices, cell culture and microfluidics. By utilising techniques from the microchip industry, these devices can be remarkably efficient while still retaining a small size (Huh *et al.* 2011). These devices represent a collaboration between biosciences and engineering, resulting in powerful experimental platforms, and are often referred to as lab-on-a-chip or organ-on-a-chip devices. For this project the model of interest is a brain-on-a-chip, but areas of the body successfully modelled *in vitro* include the heart, cartilage and skin, as well as functional systems such as the vascular, endocrine, musculoskeletal, and nervous systems, as well as models of infectious diseases and cancer, reviewed in (Benam *et al.* 2015).

When designing a model as an organ-on-a-chip, considerations include: the multicellular niche of a relevant tissue (Huh *et al.* 2011, Baker and Chen. 2012a), interfaces and interactions with other cells and tissues, a suitable concentration or gradient of chemicals and growth factors (Almodovar *et al.*

2013), a perfusion/flow system similar to vascular perfusion and interstitial flow *in vivo* (Kelly *et al.* 2013), using a material of a similar stiffness to that found *in vivo* (Tse and Engler. 2011, Sur *et al.* 2013), and use of micro- and nano-scale physical features (topographies) such as channels or pits to mechanically stimulate neural cells and tissues for alignment, elongation or differentiation (Bugnicourt *et al.* 2014). As such, there are numerous ways to fabricate such devices.

1.5.1 Fabrication techniques

Common micro-engineering techniques used to develop organs-on-chip devices include soft photolithography, micro-contact printing (μCP) and injection moulding, all of which are able to create micro-scale structures with specific shapes, which are then used to control cell proliferation, morphology, elongation and interactivity. However, as μCP and replica moulding fall under the category of soft lithography only lithographical techniques will be discussed here.

In general terms, photolithography uses UV to transfer a pattern from a mask to a substrate which has been coated with a photoresist (a substance that becomes soluble or insoluble to developer upon exposure to UV). Different photoresist materials have different viscosities, with more viscous photoresists being able to create thicker layers for larger surface features, and less viscous photoresists being used to create micron-thickness layers and micro-scale surface features. This transfer of patterns from masks to substrates is highly reproducible, reliable and has a very high resolution, creating sub-micron sized features with a lower resolution limit of approx. 0.5 μm (T. Pan and Wang. 2011). However, to achieve this resolution requires expensive machinery, custom-made geometric patterned masks, exposure systems, toxic photo-reactive chemicals, special environments such as dark rooms (to avoid activating the photo-reactive chemicals) and clean rooms (any dust or particulates will interfere with the process), meaning there is a compromise between the high quality of pattern produced by this technique with the cost and difficulty of doing so.

Highly-customised designs from lithography techniques have been used in on-chip cell culture, starting as simple cell arrays and developing into organs-on-chips. Microfluidic devices are created by bonding a polymer (usually polydimethylsiloxane, PDMS) containing micro-channels (created by soft lithography) to glass or plastic. This then creates a semi-closed environment where micro-scale amounts of liquid can flow through the micro-channels by laminar flow/capillary action, and where cells can be cultured (Therriault *et al.* 2003). This kind of *in vitro* cell model is not as limited as previous static 2D cell monolayer *in vitro* models (Pamies *et al.* 2014). Due to the high resolution and customisable nature of these techniques, devices produced in this manner can be specifically designed for mimicking neural *in vivo* microenvironments. Previous success has been had with modelling complex functional organs, such as the intestine (Imura *et al.* 2009), lung (Huh *et al.* 2011, Douville *et al.* 2011) and kidney (Jang and Suh. 2010).

The majority of organ-on-a-chip models are fabricated using soft lithography and PDMS, to create a microfluidic model with a compartmentalised design. The compartments represent different experimental modules for further development (for example, a porous membrane and dynamic fluid flow can be added) and can maintain viable cell populations. These factors make for the design of an efficient organ-on-a-chip model, and have been combined into multiple organs-on-a-chip (Luni *et al.* 2014), with accurate tissue-to-tissue size ratios, extremely useful models for drug development as a physiologically based pharmacokinetic model (M. B. Esch *et al.* 2011).

1.6 Brain-on-a-chip

A brain-on-a-chip model is required to accurately mimic neural conditions such as: neuron plasticity, neuronal development, the presence of glia to guide neuronal growth, the correct ratio of neurons and glia, using typse of neuron with suitable neurotransmitters (excitatory vs inhibitory), precise cell-cell communication both chemical (ions) and electrical (action potentials), synapse morphology, cell migration, accurate ECM composition and neurogenesis, all whilst mimicking the functional neuron processes in the brain (Pamies *et al.* 2014) and recording electrophysiological signals from the neurons to assure functionality.

Neglecting to include certain factors when designing a brain-on-a-chip can result in a model that accurately mimics certain features of the *in vivo* CNS while ignoring other features. A good example is a model that focused on including both 3D cytoarchitecture and interstitial flow (J. Park *et al.* 2014), the former due to the lack of cell-cell contact in 2D monolayer cultures and the subsequent decrease in mechanical cell signalling (Smalley *et al.* 2006, Baker and Chen. 2012b), and the latter due to the interstitial fluid delivering nutrients, removing waste from the brain, and affecting cell-cell communication between neurons that do not form synapses, even at a slow flow rate of 0.1-0.3 μL min^{-1} (Abbott. 2004). Park *et al* have previously used concave microwell arrays to grow size-controllable networked neurospheres (designed to mimic the 3D cytoarchitecture of the cortex) and used this model to test the toxicity of amyloid beta (Choi *et al.* 2013b). By combining this model with other models that could mimic physiological speeds of interstitial flow (Choi *et al.* 2013a, J. Park, Koito, Li and Han. 2009b), Park *et al* developed a brain-on-a-chip. Despite the advantages of including both 3D cell culture and interstitial fluid flow, this brain-on-a-chip model is still limited:

- The model only includes E16 primary cortical neurons that are cultured into neurospheres, no glial cells are included. Without glial cells the model is a less accurate mimic of the *in vivo* brain, as astrocytes, oligodendrocytes and microglia all have vital structural, functional and immune roles in the brain. The same group has stated that inclusion of oligodendrocytes in a model allows for myelin production and a more physiologically relevant model compared to *in vivo* (J. Park, Koito, Li and Han. 2009a).

- The model has no ability to control the direction and length of neurite growth from the neuron cell body. The ability to direct growth of neurites allows for control over which cell populations form synapses and link together, to form a functional and morphological connection between neurons. This kind of control can be achieved by using chemical or physical patterns to guide neurite growth in a specific direction, as seen in work by (Peyrin *et al.* 2011), who used asymmetric tapered micro-scale channels to impose unidirectional neurite growth with 97% selectivity. Without this degree of control, the model is limited by the formation of a stochastic network rather than a specific network in order to better mimic brain subregions.
- The model has no consideration of the extracellular materials. The extracellular matrix (ECM) of the brain is unique compared to other ECM materials and plays a large role in regulating function and growth of cells in the brain *in vivo* (Frischknecht and Gundelfinger. 2012). One study cultured cells with an ECM mimic consisting of a 3D collagen type I-hyaluronan scaffold, which resulted in a 70% increase in the number of neurons generated (Brannvall *et al.* 2007). However, it should be noted that primary neuronal and glial cells can generate ECM components to a limited degree (Dzyubenko *et al.* 2016), but this further highlights the importance of including glial cells in such a model, as with only neurons less ECM is generated.
- The model lacks any method to test the functionality of neurons by measuring their electrophysiological activity. Only the viability, differentiation status and morphology were analysed, excluding a large portion of data and resulting in no firm idea if the neurons in the model are functional. By taking into account functional testing, these models can be improved and be more accurate mimics of the *in vivo* brain. Neurospheres are challenging to fully assess with electrophysiological methods, as most methods could only record from the exterior cells.

Considering these flaws when designing a new model would allow for a model that better mimics the *in vivo* brain. These changes would increase complexity, and it is reasonable to assume that in the future a device can be fabricated with flow, cell culture abilities and an electrophysiological testing device such as an MEA, resulting in a powerful *in vitro* device for pre-clinical research. The ideal *in vitro* model would be able to align neural cells to create unidirectional circuits, test the circuits are functional, and then use this circuit model to mimic existing circuits *in vivo* and therefore study both physiological and pathological brain circuit states.

1.6.1 Compartmentalised microfluidic neural cell models

With a standard monolayer culture of neural cells, it is difficult to isolate data from single cells or groups of cells that have differentiated into a specific subpopulation of neurons (GABAergic vs dopaminergic, or cortical vs hippocampal). A solution was developed in the 1980s by designing compartmentalised cultures (Campenot. 1982) to isolate processes of various types of long-projection neurons (see **Fig.1.13A**). This model was later refined to have smaller chambers to accommodate neurons with shorter processes (see **Fig.1.13B**) (Ivins *et al.* 1998). However, whilst these two models allow for direct study of neurites from various types of neurons, they do not allow study of neurons interacting with each other, they support the growth of only one neuronal subtype, and they do not allow for live cell imaging. By using photolithography fabrication techniques it was possible to make the fabrication process more reproducible and allow for a more flexible structure including micro-scale grooves and wells linked by channels (see **Fig.1.13C**) (Taylor *et al.* 2003). Fabrication involved creating a mould and then casting the device using PDMS (Taylor *et al.* 2003, J. W. Park *et al.* 2006). This type of model was a better mimic of the neural microenvironment that cells face *in vivo* and was further developed to accommodate more than two types of cell (see **Fig.1.13D**), so that astrocytes could also be used in co-culture with neurons (Y. H. Kim *et al.* 2011).

The model in **Fig.1.13C** has become a popular method for culturing two neuronal subtypes together, connecting the cell populations via axons grown through channels while isolating the cell bodies in chambers to prevent contamination. This model has been used in numerous studies of different cell types, with recent examples including: cortical neurons (Kanagasabapathi *et al.* 2009, Kanagasabapathi *et al.* 2011), cortical-cortical and cortical-thalamic co-culture systems (Kanagasabapathi *et al.* 2012, Kanagasabapathi *et al.* 2013), hippocampal-glial co-culture systems (Majumdar *et al.* 2011, Shi *et al.* 2013), cortical neurons co-cultured with genetically modified astrocytes (Kunze *et al.* 2013), embryonic forebrain neurons co-cultured with oligodendrocytes (J. Park, Koito, Li and Han. 2009b), primary CNS neurons co-cultured with oligodendrocytes and astrocytes (J. Park *et al.* 2012), dendrite growth (Taylor *et al.* 2010), hippocampal axon compression injury (Hosmane *et al.* 2011), synapse formation in hippocampal neurons (Y. Gao *et al.* 2011), embryonic neurons (Dworak and Wheeler. 2009) and P19-derived neurons co-cultured with mouse cortical neurons (Takayama *et al.* 2012).

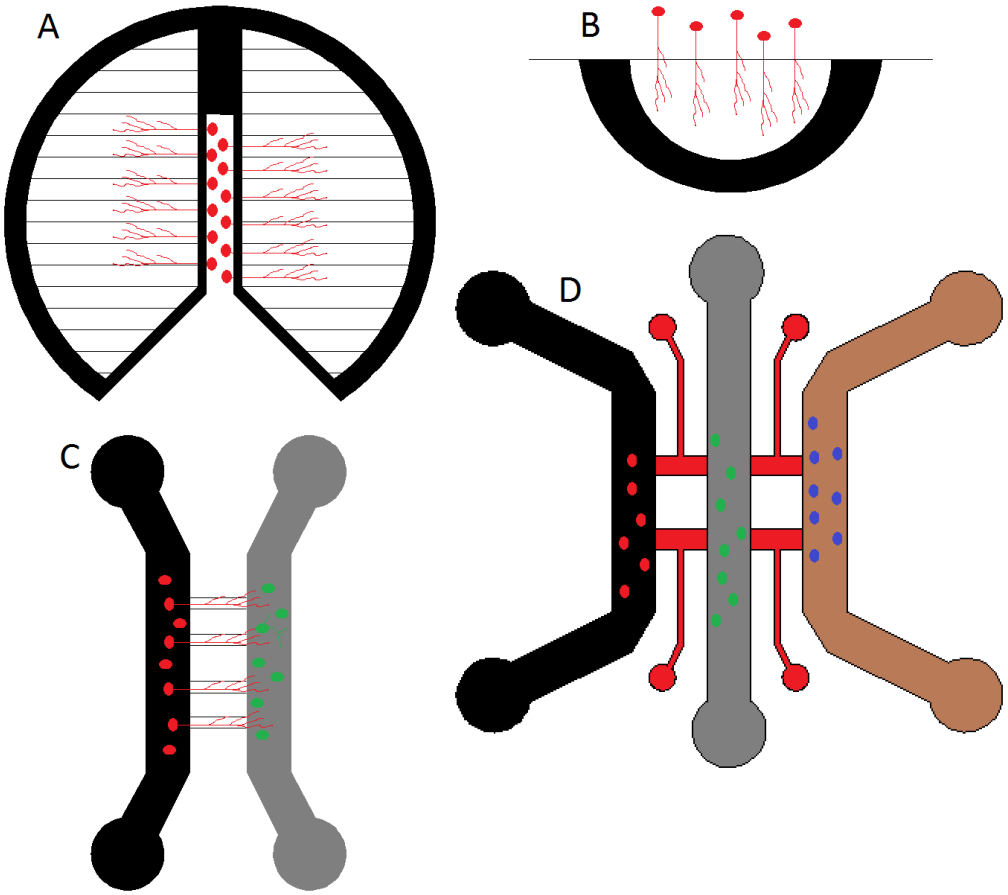

Figure 1.13: Progress of compartmentalised neural models over time. (A) The Campenot chamber, neurons are plated in the centre area and neurites grow and align into the other chambers where they can be studied. (B) The Ivins chamber, neurons are plated outside the ring and grow under the coverslip into the main chamber, where they can be studied. This model is limited to neurons with short neurites. (C) Two chambers connected by 120 micro-scale channels (image not to scale). Neurons can be cultured in either chamber and grow through the channels to the other chamber, creating a rudimentary neural circuit. (D) A more advanced version of the previous model, including a third chamber in the centre, allowing for use of three different neural subtypes at once. The four small red chambers were designed to supply collagen mixed with primary astrocytes to the other chambers, allowing for neuronal-glial co-culture as well as ECM study. From (Kose-Dunn *et al.* 2017).

By modifying the microchannel width it is possible to create unidirectional connections, mimicking certain input-output connections in the brain where there is projection but no return. Unidirectional channels (also referred to as tapered/asymmetrical/diode channels) had modified widths that created a physical pressure for a preferential direction of axonal growth (Peyrin *et al.* 2011), specifically by having channels from 15 µm wide to 3 µm wide at the other (seen in **Fig.1.14**), selecting for axons growing from the larger to smaller ends.

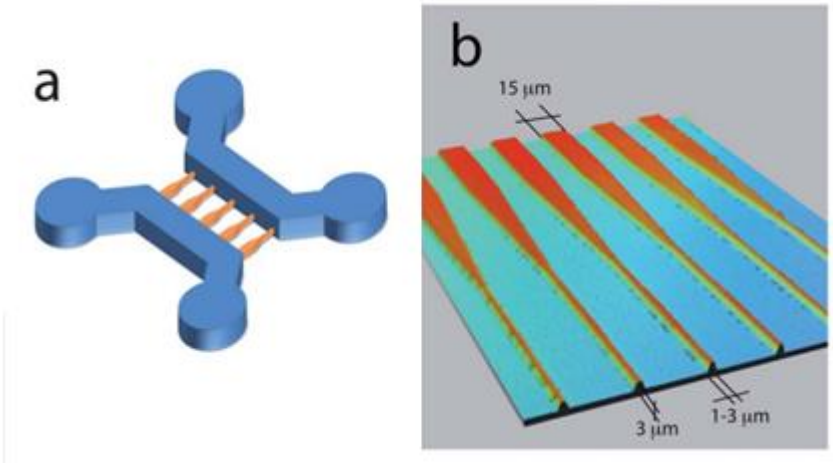

Figure 1.14: Microfluidic device designed by (Peyrin *et al.* 2011) **(A) an overall view of the model, consisting of two chambers linked by channels (channels not to scale), (B) asymmetrical 'diode' channels, starting at 15 µm and terminating at between 1-3 µm, in order to select for axonal growth in one direction.**

Compartmentalised microfluidic models can mimic the *in vivo* brain microenvironment with increased accuracy whilst still being accessible and customisable (Whitesides. 2006). Other advantages of these compartmentalised models include (Harris *et al.* 2007, Robertson *et al.* 2014):

- Specific localisation of cells and/or chemicals
- Potential for high-throughput if scaled up
- Exhibit highly sequential/parallel experimentation
- Involve extremely small volumes of media/chemicals per experiment (reducing cost)
- Fabricated via lithography and can therefore be virtually any shape/size
- Microchannels allow fluidic isolation between compartments, stopping the spread of treatments between chambers
- Greater control over cell patterning/manipulation
- Greater control over extracellular and cellular microenvironments
- Visible to conventional microscopes when made with optically transparent material (e.g. PDMS) and are low-cost disposable devices.

As mentioned in section **1.1.5 Potential causes**, misfolded proteins may be responsible for numerous neurodegenerative diseases, which highlights another advantage for compartmentalised microfluidic devices, namely controlling the flow of misfolded proteins. The compartments are fluidically isolated and consequently any misfolded protein won't spread between compartments, allowing for effective modelling of the effects of misfolded proteins. Altering the channel sizes will allow misfolded protein to spread, further allowing modelling of misfolded protein spread.

Compartmentalised microfluidic models represent a significant platform for studying neurobiology *in vitro*. These *in vitro* models offer a solution for studying specific parts of the brain in a simpler, more versatile and customisable way than current *in vivo* protocols. By combining models with

different surface chemistries and electrophysiological techniques they can be further improved and tailored to neurobiology, a review of microfluidic-based neurobiology can be found in (Wang *et al.* 2009).

With these established and advanced models available, it is necessary to decide which area of the brain should be subject to *in vitro* study. The main motivation for study has always been neurological disease, with the majority of conditions still incurable and mostly misunderstood. Epilepsy, Alzheimer's disease (AD), schizophrenia, Parkinson's disease (PD), amyotrophic lateral sclerosis (ALS), autism, Huntington's disease (HD), stroke and trauma from brain injuries affect up to one billion people worldwide (WHO (World Health Organisation). 2006). Both PD and HD are caused by damage to the same area of the brain, the basal ganglia. Pre-clinical *in vitro* research into these diseases is lacking, and the development of a microfluidic compartmentalised model with functional testing would represent a powerful and accessible platform for study into both PD and HD. This thesis describes the development and optimisation of such a model, and its power as an experimental tool. Aims and objectives are presented in **section 1.8.**

1.7 Concluding Remarks

Neurological and neurodegenerative diseases are incurable and debilitating progressive conditions that currently have no cure, due to the difficulty of researching an organ as complex as the brain, the long timeline of the disease, the lack of fundamental understanding and the lack of clinically translated research. These difficulties can be mostly abated by studying the brain *in vitro* at a pre-clinical level, but current pre-clinical assessment is insufficient to predict which treatments will work on human disease patients. The solution is to develop more efficient *in vitro* models, where there is a high level of control and the complexity can be increased to make the model more relevant as a mimic. These models are low-cost and reproducible, combining cells with biomaterials and microfluidics to make lab-on-a-chip devices, which are the efficient *in vitro* models necessary for progress in research at a pre-clinical level, with the resulting data driving clinical trials in a more relevant direction, and contributing towards potential treatments for neurological or neurodegenerative diseases.

1.8 Aims and objectives

The aim of this project was to engineer a functional *in vitro* model of basal ganglia circuitry. Damage to areas of the basal ganglia can result in Parkinson's or Huntington's disease, and by modelling this area I could create a pre-clinical platform to accelerate research into these diseases. The chapters of this thesis all contribute towards this goal. The working hypothesis of this thesis was that engineering

principles could be applied to fabricate a functional *in vitro* model of basal ganglia neural circuitry, and by extension Parkinson's disease.

Key objectives:

- Design and fabricate a compartmentalised microfluidic device for modelling the basal ganglia
- Isolate cells from specific brain regions specific to the basal ganglia and successfully culture these cells within the device
- Ensure the device can physically isolate cell bodies of separate neural cell populations whilst connecting them in a manner relevant to the *in vivo* brain
- Ensure this connectivity is unidirectional and can be controlled
- Determine the functionality of cells within the model and track this function across the long term
- Track any changes to this functionality upon the introduction of different factors to the device
- Create a living neural *in vitro* model of a healthy physiological basal ganglia
- Create a living neural *in vitro* model of a damaged pathological Parkinsonian basal ganglia

Chapter Two: Materials and Methods

This chapter details the techniques used throughout this project and the protocols followed, detailing reagents and suppliers.

2.0 Device fabrication

2.0.1 Software design

The original five port device (5PD) design was based on previous work by Dr Munyaradzi Kamudzandu (Keele University, 2015), designed to model the *in vivo* circuitry of the basal ganglia and cortex. The 5PD was designed using AutoCAD software [Autodesk 2015]. As indicated in **Fig.2.1A**, in the area between the two input ports (left hand side) and the centre port, as well as between the centre port and the two output ports (right hand side) are micro-scale channels. These were designed to provide directed guidance to orient the outgrowth of axons, encouraging cells to grow axons through the channels in a certain direction, from input, to centre, to output, in an effort to control the direction of axonal elongation to connect cell populations into the desired circuit. These microchannels, based on previous publications (Peyrin *et al.* 2011), were tapered from a larger width – either 15 µm, 25 µm or 50 µm – to a smaller width, 5 µm. The channels were 450 µm long in order to select against dendrites (which range between 100 and 300 µm) and only allow axons through, which can grow up to a few millimetres (Brunello *et al.* 2013, Jokinen *et al.* 2013). More information on the microchannels can be seen in **Fig.2.1C**.

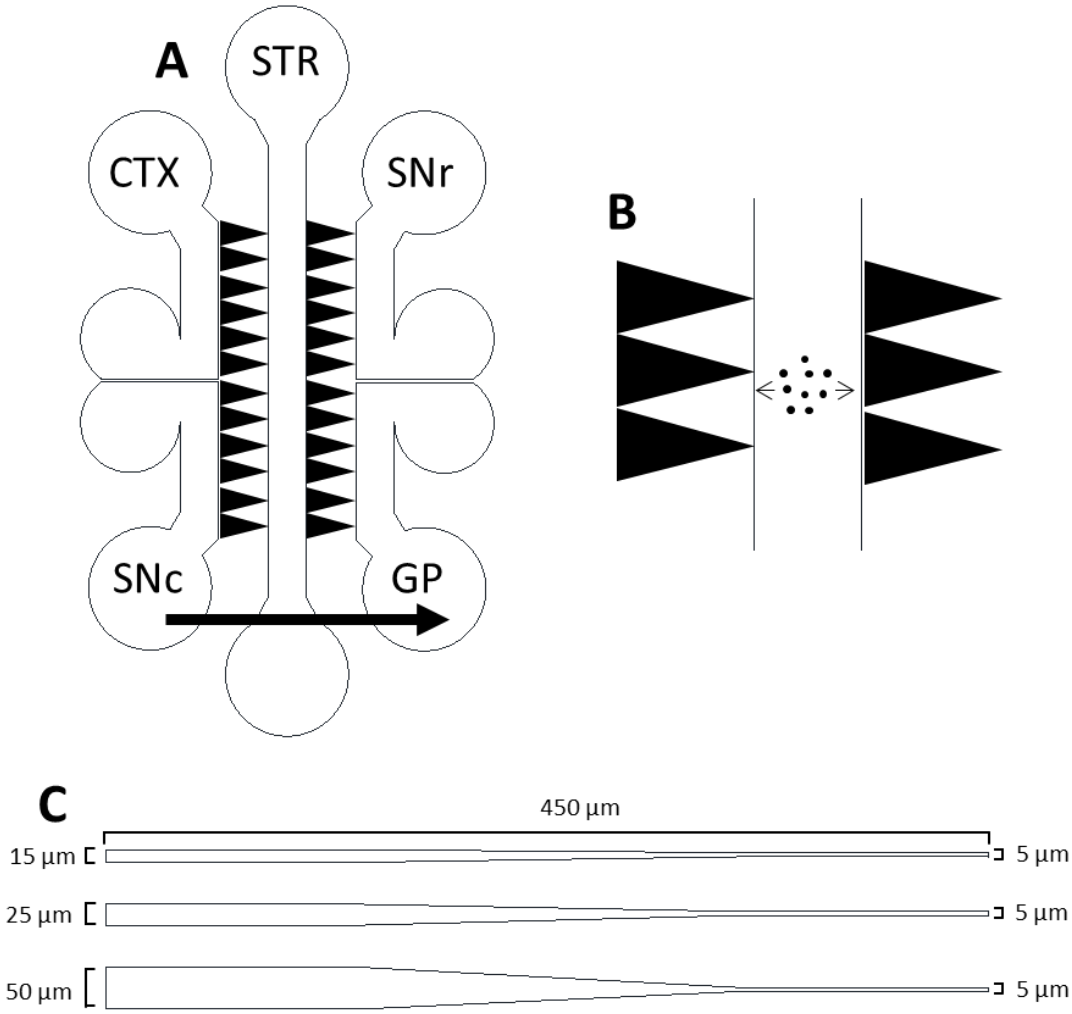

Figure 2.1: The design of a 5PD in schematics (A) the 5PD device as a whole, showing five separate ports linked with tapered channels (channels represented by black triangles, not to scale). Cells in the left-hand input ports and right-hand output ports have only one direction for axonal outgrowth, and cells in the centre port have two possible directions for axonal outgrowth as they are presented with two sets of channels. The arrow shows the desired direction of growth. The labels indicate what cell type is seeded where, CTX: cortex, SNc: substantia nigra pars compacta, STR: striatum, SNr: substantia nigra pars reticulata, GP: globus pallidus (B) Magnified version of the centre port. Cells growing in this port are presented with a larger channel entrance for the 'correct' direction for axonal outgrowth (to the right-hand output ports), and a smaller channel entrance for the opposite, undesired direction. This aims to create a directional pressure, ensuring that the cells connect in the same manner as *in vivo*, with no backtalk. (C) The three types of tapered microchannel available for the 5P device.

The introduction of the multi-electrode array (MEA) to experimentation added a further limitation to the design of the 5PD, as the circular MEA bracket could only accommodate a device that was smaller than 30 mm in diameter. This resulted in a redesign of the original model, as seen in **Fig.2.2**. This smaller device was used for experiments involving MEAs (**Chapters Four, Five and Six)**, whilst the original larger device was used for preliminary cell culture and channel width optimisation (**Chapter Three**).

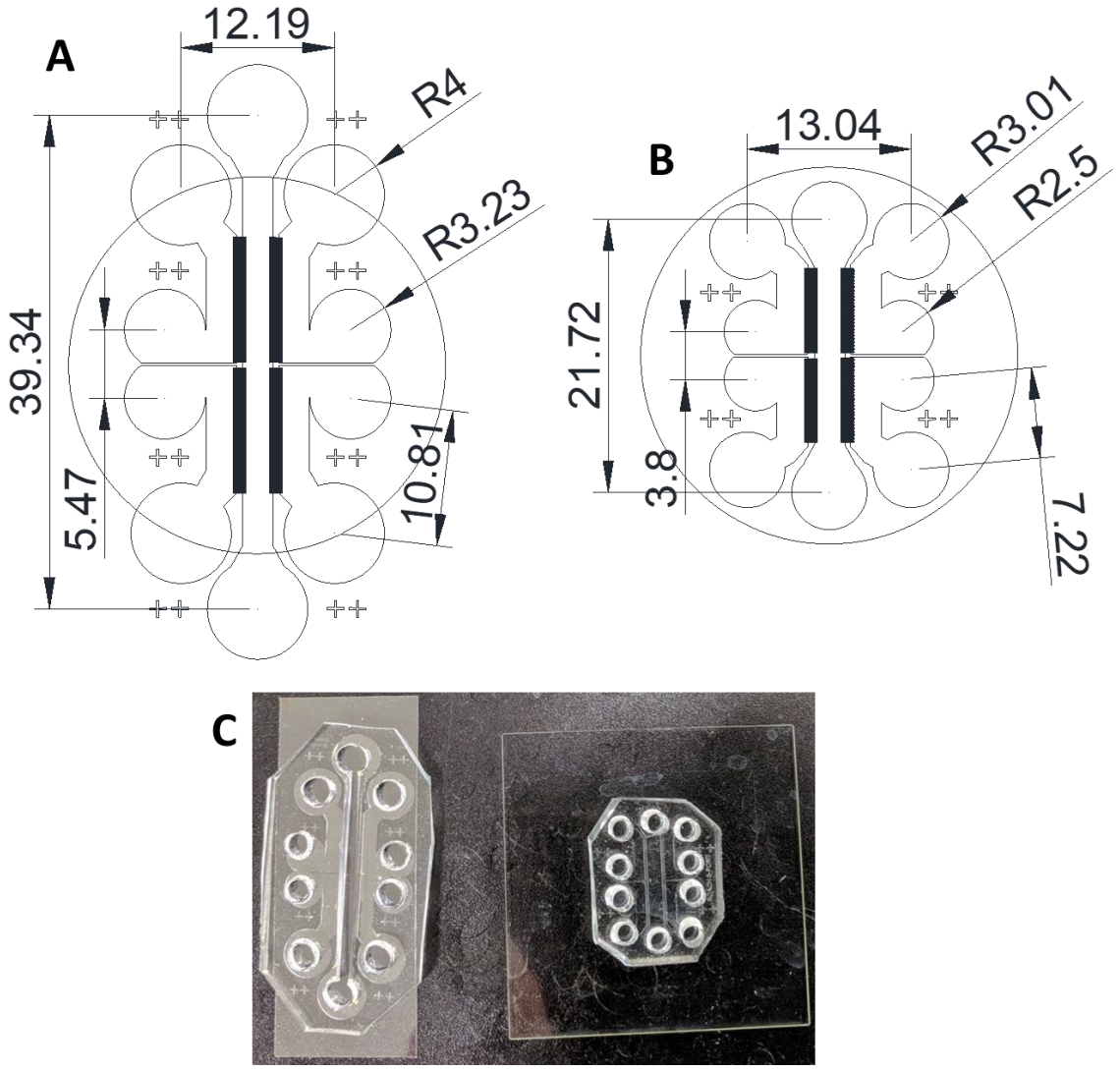

Figure 2.2: 5PD redesign to accommodate MEA hardware. A) The original 5PD design including a scaled 30 mm diameter circle to indicate the maximum size that the MEA bracket can accommodate. This design was too large for the MEA, but better suited for non-MEA cell culture. B) 5PD redesign. This new device easily fits into a 30 mm diameter circle and is suitable for MEA experimentation. C) A photograph of both finished 5PD types, original on the left and redesigned on the right (attached to MEA for scale). For A and B all dimensions are in millimetres, R: radius.

The 5PD designs were arranged into templates, in order to develop photolithographic masks for the next stage of fabrication. The intended design had ~5 µm channel feature height while ports had much larger feature height of ~150 µm. Due to these differences in size between channels and ports two stage lithography was needed (one lithography step each for small scale elements and larger scale elements), therefore two lithography masks were needed. These two masks were designed using AutoCAD: one for microchannels and one for ports, as seen in **Fig.2.3**. Each mask also features alignment crosses at the extremities of each device and set of channels in order to align the ports onto the channels. These mask designs were printed onto chrome/soda lime glass by JD PhotoTools LTD at high resolution.

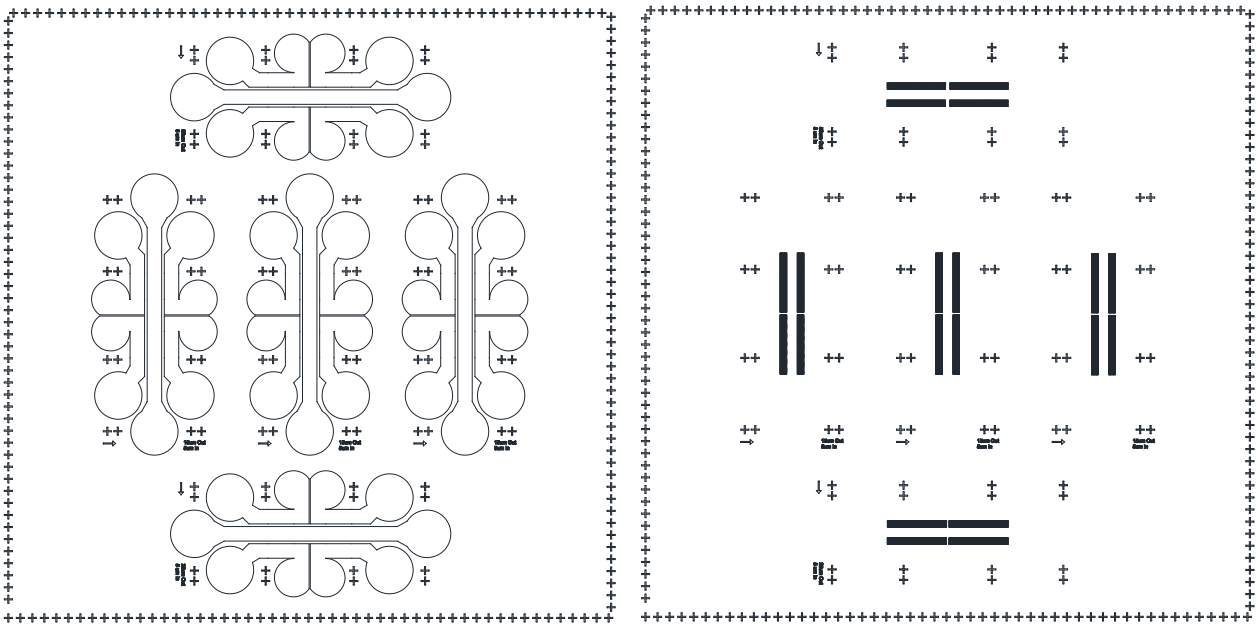

Figure 2.3: Photolithographic mask designs for the larger 5PD, made with AutoCAD software. The left image shows the ports layer, and the right image shows the microchannels layer, with the top set of channels being 50 µm to 5 µm in width, the middle three sets being 15 µm to 5 µm in width, and the bottom set being 25 µm to 5 µm in width. These designs were fabricated into masks for use in lithography.

2.0.2 Two-stage photolithography

Briefly, the two-stage photolithography process involved using i-line (265 nm) UV light to transfer the mask design onto a surface coated with a photo-reactive substance, termed a photoresist. An epoxy-based SU-8 negative resist [A-GAS Electronic Materials, UK] was used so that the resulting patterns could be used as templates for soft lithography. The channels layer (**Fig.2.3** right image) was exposed first with the ports layer (**Fig.2.3** left image) superimposed onto the channels layer, the two layers were aligned using a Canon PLA-500F parallel light mask aligner via the alignment crosses on both masks, creating the master template for the devices. A schematic of the two-stage lithography process can be seen in **Fig.2.4**.

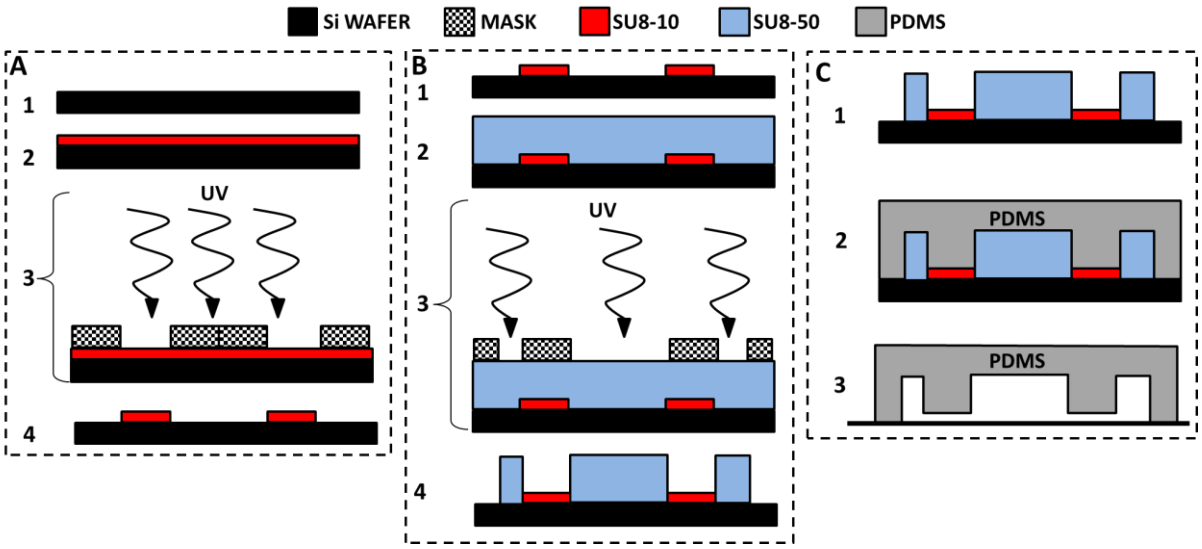

Figure 2.4: The two-step lithography process (legend at top). A) Channels stage. 1) Silicon wafer, 2) wafer coated with SU-8 10, 3) coated wafer exposed to UV through the channel mask, 4) after development, the inverse of the channel pattern remains on the wafer. B) Ports stage. 1) Wafer with channels from A, 2) wafer coated with SU-8 50, 3) coated wafer exposed to UV through ports mask, 4) after development, the inverse of the ports remain, aligned to channels. C) PDMS casting. 1) Wafer with channels and ports from A and B. 2) PDMS is cast onto the patterns, 3) PDMS is removed and sealed to glass to create the microfluidic device.

The chosen substrate surface for the photolithographic process was a circular 100 mm diameter silicon wafer [PI-KEM, UK]. Firstly, the wafer was washed with acetone and then propanol [both Fisher Scientific, UK], removing any dust or particulates, to prepare the wafer for the photoresist. Two types of SU-8 negative epoxy series photoresist were used: SU-8 10 for the tapered microchannels (feature height 5 µm) and SU-8 50 for the ports (feature height 150 µm). These SU-8 photoresists become insoluble in developer upon exposure to UV and formed the features of the master device template.

The photoresist was spread onto the cleaned silicon wafer using a WS-650HZB-23NPP Modular Spin Processor [Laurell Technologies Corporation, USA], spinning the wafer at 500 rpm to spread the photoresist evenly across the surface. The wafer was then spun at high speeds to determine the thickness of the photoresist layer, which would become the feature height. After spinning, the wafer was heated to set the photoresist, and then exposed to UV light through the appropriate photolithographic mask in order to transfer the pattern to the wafer. The wafer was heated again to set the pattern. This whole process differed for SU-8 10 (for channels) and SU-8 50 (for ports) photoresists and is detailed overleaf.

- **Spin stage**
    - SU-8 10: wafer spun at 4400 rpm for 30 seconds (resulting in 5 µm height)
    - SU-8 50: wafer spun at 1000 rpm for 30 seconds (resulting in 150 µm height)
- **Pre-bake**
    - SU-8 10: wafer heated at 95 °C for 60 seconds
    - SU-8 50: wafer heated at 65 °C for 10 minutes, 95 °C for 30 minutes then 110 °C for 10 minutes
- **Exposure**
    - SU-8 10: wafer exposed to UV light for 50 seconds through the channel mask (**Fig.2.3** right image, also see **Fig.2.4A**)
    - SU-8 50: wafer exposed to UV light for 50 seconds through ports mask (**Fig.2.3** left image, also see **Fig.2.4B**)
- **Post-exposure bake**
    - SU-8 10: wafer heated at 65 °C, 95 °C, then 110 °C for one minute each, then slowly cooled to room temperature
    - SU-8 50: wafer heated at 65 °C for one minute and then 95 °C for 10 minutes, then slowly cooled to room temperature

After the post-exposure bake, wafers were immersed in developer solvent [A-GAS Electronic Materials, UK] to remove any unexposed photoresist, leaving only the exposed structures. After this the wafer was washed with propanol and air dried.

For a complete master template, the SU-8 10 process for the microchannels was performed first, and then the SU-8 50 process was performed on the same wafer, aligning and superimposing the ports over the microchannels. This process can be seen in **Fig.2.4A-B** and **Fig.2.5**.

Once the master template was complete, the final devices were fabricated by using the wafer with the SU-8 template features as a mould for polydimethylsiloxane (PDMS), seen in **Fig.2.4C**. Quantum silicone 216 (QSil 216) [ACC Silicones, UK], composed of PDMS (A) and crosslinker (B), was mixed in a 10:1 ratio (A:B). The mixture was poured onto completed master templates and incubated at 50 °C for one hour to set. The cured PDMS was then cut away from the wafer, excess PDMS was shaved off and access holes were punched in each end of each port to form wells. The PDMS casts were then stored in sterile petri dishes, in preparation for sealing to a glass surface. This process can be seen in **Fig.2.5** and **2.6**.

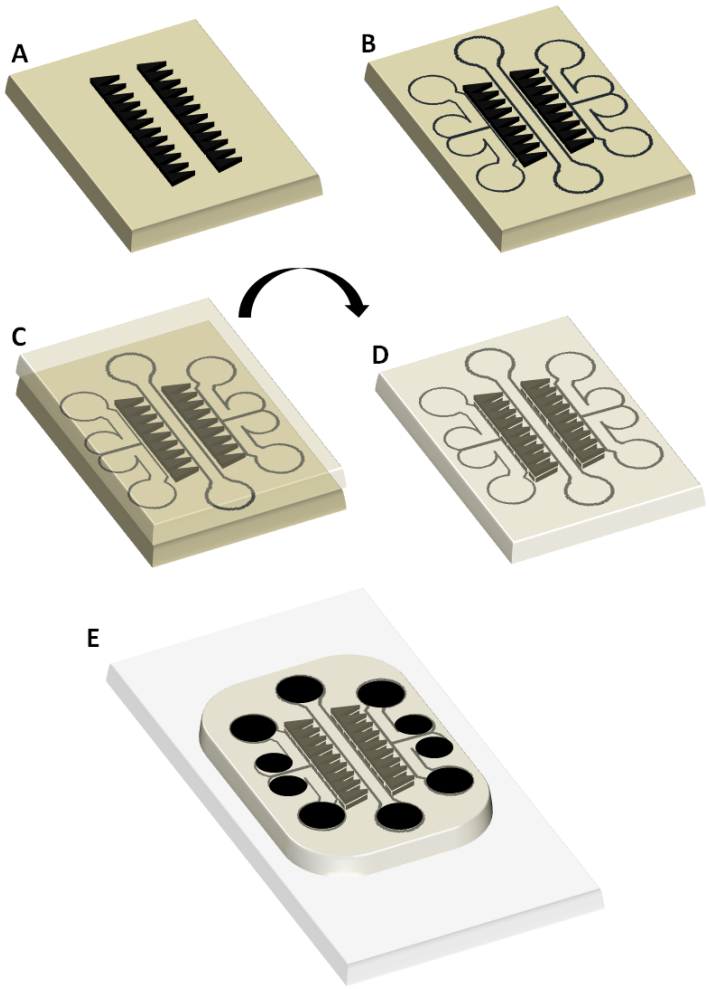

Figure 2.5: 5PD fabrication via soft lithography. A) SU-8 10 channels on wafer after exposure through channels mask, B) SU-8 50 ports superimposed onto channels, aligning the two patterns using alignment crosses and mask aligner, (C) crosslinked PDMS was cast onto the exposed patterns, creating the inverted pattern, D) once set, the PDMS was cut away from the pattern and inverted pattern side up, E) holes were punched in each end of each port and the PDMS cast is inverted again and bonded onto glass, pattern side down, before sterilisation.

2.0.3 Bonding and sealing

Once the PDMS cast was completed, the 5PDs needed to be sealed to a surface, pattern side down, to finish the microfluidic device and allow for cell culture. 5PDs were sealed to either a glass microscope slide or an MEA. For early experiments with microscope slides, 5PDs were permanently bonded via oxygen plasma, and for later experiments with microscope slides and MEAs, 5PDs were semi-permanently bonded via polyethylenimine (PEI).

2.0.3.1 Permanent bonding via exposure to oxygen plasma

Glass slides were cleaned with propanol and air dried. The slides and PDMS casts were exposed to a 13.65 MHz RF oxygen plasma within a Deiner plasma unit [Diener Electronic, Germany] for 30 seconds (oxygen pressure was set to 300 pressure). After exposure, the PDMS was immediately placed onto microscope slides [Fisher Scientific, UK] pattern side down, forming a permanent bond and sealing the two together, forming a microfluidic device. The plasma also sterilised the devices,

which were then flooded with 2% penicillin/streptomycin/fungizone [Fisher Scientific, UK] and kept under UV light for one hour for further sterilisation immediately prior to chemical coating.

2.0.3.2 Semi-permanent bonding via chemical coating with PEI

Glass sides were immersed in 70% ethanol [Fisher Scientific, UK] to sterilise and clean, then air dried. The slides were then immersed in 0.05% polyethylenimine (PEI) [Sigma-Aldrich, UK], diluted using 25 mM borate buffer (sodium tetraborate [Sigma-Aldrich, UK] dissolved in dH_2O and pH set to 8.0), for one hour at room temperature. The slides were then washed four times with distilled water (dH_2O) to clear any excess PEI, and then air dried. Once dry, the PDMS casts were placed onto the slides (pattern side down), forming a seal when slight pressure was applied. The PDMS could be attached and detached as many times as necessary, as the PEI makes the slides very attractive due to the dense positive charges. The sealed devices were then sterilised by flooding with 2% penicillin/streptomycin/fungizone and kept under UV light for one hour immediately prior to chemical coating.

The full device fabrication process is pictured in **Fig.2.6.**

2.1 Device preparation: chemical coating

Prior to cell seeding, the completed devices were chemically treated by incubating with either a combination of poly-d-lysine (PDL) and laminin (LAM), or polyethylenimine (PEI) and PDL [all listed reagents obtained from Sigma-Aldrich, UK].

2.1.1 Chemical coating: PDL/LAM

Devices were flooded with 0.1 mM PDL solution in distilled water and incubated overnight at 37° C, then washed three times with dH_2O and incubated with 0.01 mM laminin solution in distilled water for two hours at 37 °C. After this incubation, the laminin was removed and immediately prior to cell seeding.

2.1.2 Chemical coating: PEI/PDL

Devices were flooded with 0.05% PEI (diluted in solution with 25 mM borate buffer from sodium tetraborate [Sigma-Aldrich, UK] adjusted to pH 8.0) and left for one hour at room temperature, then washed four times in dH_2O and incubated with 0.1 mM PDL in distilled water overnight at 37 °C, again washed three times with dH_2O. After these washes, devices were ready for cell seeding. It should be noted that devices sealed with PEI only needed PDL coating, whereas oxygen plasma sealed devices needed both the PEI and PDL coatings steps.

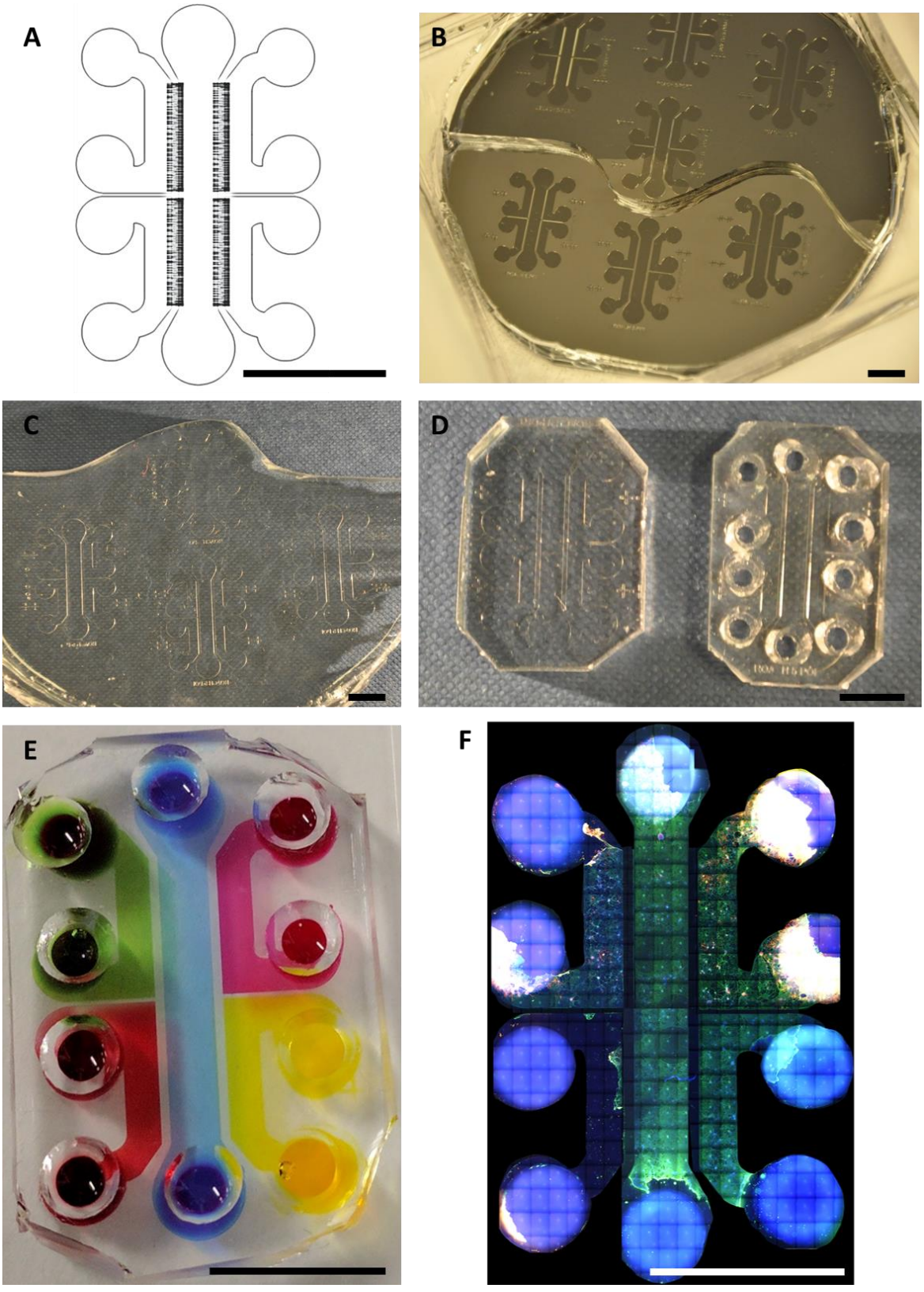

Figure 2.6: The 5PD fabrication process in images. A) The original AutoCAD software design, B) a completed master template wafer after a full photolithography process, featuring seven 5PDs, the top four covered in PDMS, C) PDMS from B, removed from the wafer before individual devices were cut out, D) a single 5PD before and after access holes were punched, E) a 5PD sealed to a glass microscope slide and filled with coloured dye to indicate the five ports and their fluidic isolation, F) a 5PD after 21 days of cell culture, stained and imaged in an XY tile scan on a fluorescent microscope. Blue for DAPI, green for β-tubulin, red for GFAP. All scale bars are 10 mm.

2.2 Primary cell culture

2.2.1 Brain tissue dissection

The cells used throughout this project were primary cells from rat embryos, requiring several stages of dissection. The four areas dissected from the developing brain for experimentation were the cortex (CTX), medial and lateral ganglionic eminences (MGE and LGE) and ventral midbrain (VM). The MGE, LGE and VM develop into the globus pallidus (GP), striatum (STR) and substantia nigra (SN) nuclei respectively and were used in order to mimic the basal ganglia circuitry (with SN containing both SNc and SNr, making five cell types, one for each port of the devices). These brain areas were dissected from rat embryos ranging from 12 to 16 days old (E12-E16) depending on the type of experiment being seeded, with E0 being the date of identifying the vaginal plug.

Dissection tools were first sterilised at 250 °C using a glass bead steriliser [Simon Keller Steri 250, Switzerland]. These tools were as follows: large and small scissors [Fine Science Tools, Cambridge, UK], bracken forceps [Roboz Surgical Instrument Co, Kent, UK] and Dumont forceps [Fine Science Tools, Cambridge, UK]. The tools were cooled in a sterile container and left under a UV light. 50 mL falcon tubes [Greiner Bio-One, UK] were filled with Dulbecco's Modified Eagle's Medium (DMEM) [Sigma-Aldrich, UK] and placed on ice; the number of tubes corresponding to the number of animals. 1.5 mL micro centrifuge tubes [Greiner Bio-One, UK] were also filled with ice cold DMEM, the number of tubes corresponding to the number of types of tissue to be dissected (the maximum number being four).

Pregnant Sprague-Dawley rats, bred in-house at Keele University, were sacrificed by approved Schedule 1 methods, following guidelines from the UK Animals, Scientific procedures Act, 1986 and authorization from Keele University's local ethics committee. The peritoneum was opened using scissors; first horizontally through the skin then vertically to expose the uterine horns containing the embryos. Sterilized forceps were used to lift each uterine horn whilst a pair of small scissors was used to trim off fat and tissue attached to the abdomen. Uterine horns were transferred into a sterile 100 mm diameter petri dish [Greiner Bio-One, UK] containing ice cold DMEM [Sigma Aldrich, UK]. Scissors and forceps were used to remove one embryo at a time, and embryos were decapitated following the Schedule 1 procedure set out in the UK Animals, Scientific procedures Act, 1986 (since embryos were older than E11). Resulting tissues were transferred to pre-prepared 50 mL falcon tubes containing ice cold DMEM and then transported to a dissection hood. Using the previously sterilised tools, the skin and skull of each embryo head were cut open using a horizontal cut slightly above eye level to exposure the brain (as seen in **Fig.2.7A-B**), which was then removed and transferred to a fresh 100 mm petri dish containing ice cold DMEM.

2.2.2 Brain tissue microdissection

As mentioned above, four different tissues were dissected from rat embryo brains, namely the CTX, MGE, LGE and VM. For the CTX, MGE and LGE, a longitudinal cut was made along the medial dorsal cortex, close to the midline. It was opened up to reveal the ganglionic eminence, a heart-shaped structure, medial and lateral portions corresponding to MGE and LGE respectively, as seen in **Fig.2.8C-D**. A vertical cut was made to divide the LGE from MGE, and a horizontal cut was made to detach the tissues. These tissue pieces were transferred into small micro centrifuge tubes containing ice cold DMEM, kept on ice to prevent excess cell death. The tissue surrounding the ganglionic eminence forms the CTX, and pieces of CTX distal from the location of the ganglionic eminences (to avoid any potential cross contamination of cell types) were cut away and separated from the outer layer of meninges, then transferred to a micro centrifuge tube. For the VM, the dissection procedure was as follows: two vertical cuts were made on the mesencephalic flexure. Two further cuts were made, one horizontally across the flexure and another to isolate the VM tissue (a butterfly shaped piece of tissue), as seen in **Fig.2.7E-F**. This tissue was then placed into a micro centrifuge tube.

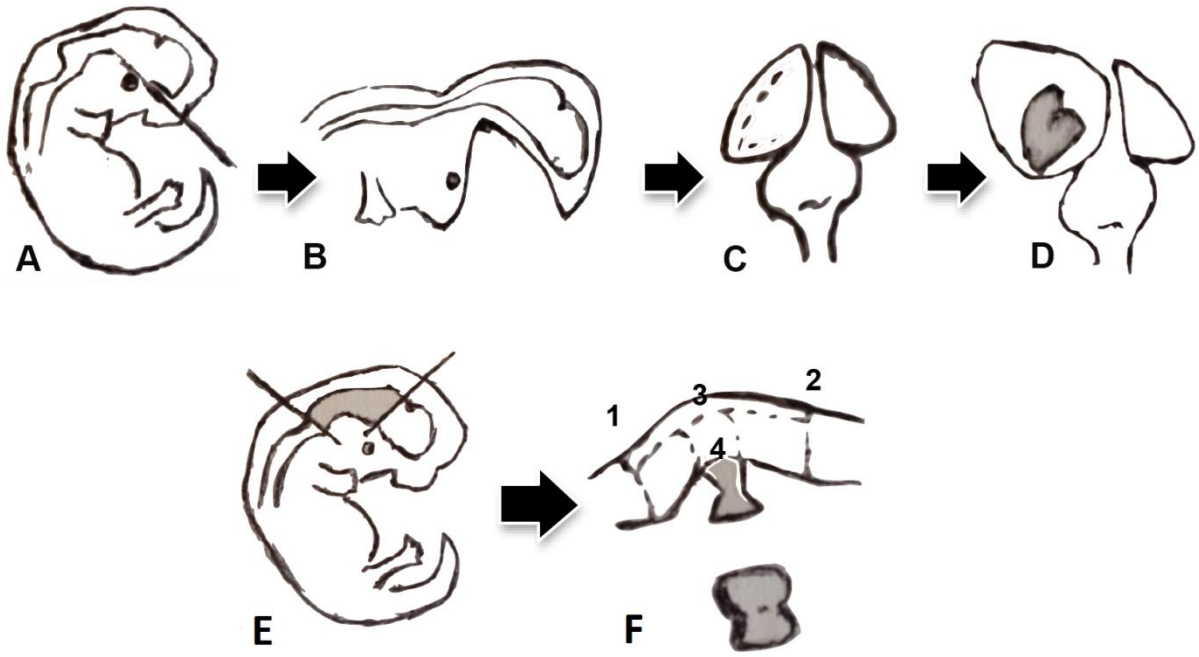

Figure 2.7: Dissecting E15/16 rat embryos. A-B demonstrate the removal of the brain from the skull, C-D shows the CTX, MGE and LGE dissection procedure and E-F shows the VM dissection procedure. Image adapted from (Dunnett and Bjorklund. 1992).

2.2.3 Cell suspension preparation

Micro centrifuge tubes containing dissected tissue pieces were washed twice with ice cold DMEM-F12 [Sigma-Aldrich] to remove any detritus or meninges, and then incubated with 500 µL 0.05% DNase/0.1% trypsin [both from Worthington Biochemical Corp., Reading, UK] in solution with DMEM-F12 at 37 °C for 20 minutes, inverting the tubes at least three times through incubation to ensure good mixing and full tissue exposure. The tissue pieces were then washed three times with

100 µL 0.05% DNAse solution to break down any free DNA. The tissues were then re-suspended in 200 µL of ice-cold DMEM and mechanically dissociated using a Gilson P200 pipette, breaking apart the digested tissues, resulting in individual cells. Excess dissociation was avoided to prevent cell damage. Dissociated cells were counted using a haemocytometer [Fisher Scientific, UK] while stained with trypan blue [Fisher Scientific, UK] to check viability. After counting, the cells were centrifuged at 1200 rpm at 4 °C for three minutes, the supernatant washed out and the pellet re-suspended in 200 µL of neuronal culture media (NCM), consisting of: neurobasal [Fisher Scientific, UK] with 1% foetal calf serum (FCS), 1% B27 supplement, 1% penicillin/streptomycin/fungicide (PSF) [all from Invitrogen, UK], 0.5% L-glutamine [PAA Laboratories, UK] and 0.45% glucose [Sigma-Aldrich, UK] solutions.

When seeding cells onto 13 mm diameter coverslips [Fisher Scientific, UK] within a 24-well plate [Fisher Scientific, UK], cells were plated as a micro-drop culture, with 75,000-100,000 cells suspended in 50 µL of NCM and placed into the centre of the coverslip for two hours before being flooded with 500 µL of NCM after cell attachment. Cells were then incubated at 37 °C in a 5% CO_2 atmosphere, with the NCM media being replaced every two to three days, 500 µL per change.

When seeding cells onto 5PDs, 100,000 cells were suspended in 50 µL NCM and added directly to the port via the access wells, with extra media added after two hours to flood all the ports of the device, at approximately 200 µL NCM for side ports and 500 µL NCM for the centre port. Cells were seeded into specific ports, as shown in **Fig.2.1A**. Cells were then incubated at 37 °C in a 5% CO_2 atmosphere, with the NCM media being replaced every two to three days, 200 µL per side port and 500 µL for the centre port. Cells were cultured until ready for the next stage of experimentation.

2.2.4 6-OHDA treatment

SN cells were treated with the 6-hydroxydopamine (6-OHDA) neurotoxin to selectively damage and/or kill dopamine neurons, in order to mimic Parkinson's disease. 1.6 mg of 6-OHDA powder [Sigma-Aldrich, UK] was dissolved into 8 mL of 0.15% ascorbic acid (antioxidant vehicle) [Sigma-Aldrich, UK], making up a 1 mM 6-OHDA solution. NCM was removed from the cells to be treated and replaced with a 200 µL solution consisting of 180 µL NCM (serum-free) and 20 µL 6-OHDA/ascorbic acid solution (thus diluting to a working concentration of 100 µM). The cells were incubated in this solution for 20 minutes, the solution was removed and the cells washed twice with 300 µL NCM, then 500 µL of NCM was added as a feeding medium. The cells were then subject to a 48 hour post-toxin incubation.

2.2.5 Live/dead staining

The LIVE/DEAD Viability/Cytotoxicity Kit for mammalian cells was used (L3224, ThermoFisher Scientific, UK) for live-dead experimentation. NCM was removed from samples and replaced with

100 µL live-dead solution. Live-dead solution was made up with 10 mL PBS, 20 µL ethidium homodimer-1 (EthD-1, the 'dead' marker) and 5 µL calcein (the 'live' marker). The samples were incubated with the live-dead solution at room temperature for 30 minutes, then washed three times with PBS and immediately imaged via fluorescent microscopy.

2.3 Immunocytochemistry

For fluorescent tagging and imaging, cell cultures first had to be fixed. NCM was removed from the cell culture, and cells were washed three times with phosphate-buffered saline (PBS) [Sigma-Aldrich, UK] before being fixed in 4% polyformaldehyde (PFA) [Sigma-Aldrich, UK] for 20 minutes at 4 °C. Cells were then washed three times with tris-buffered saline (TBS) (12 g trizma base, with 9 g NaCl [both from MERCK, Germany] in 1 L dH_2O), then blocked and permeablised with 5% normal goat serum (NGS) [Vector Laboratories, USA] and triton-X (1:500) [Sigma-Aldrich, UK] in solution with TBS for one hour at 4 °C, without agitation.

The primary antibody solutions consisted of TBS with 1% NGS, 1:500 triton-X and the selected antibody, dilutions and antibody details are described in **Table 2.1**.

Table 2.1: Antibodies used in experimentation for immunocytochemistry and fluorescent imaging

Antibody	Clone	Dilution	Purpose	Identifier
β-tubulin III	Chicken anti-mouse polyclonal	1:1000	Neural cell identification	119-15057 [RayBiotech, USA]
Glial fibrillary acidic protein (GFAP)	Rabbit polyclonal	1:500	Glia cell identification	Z0334 [DAKO, UK]
Microtubule-associated protein 2 (MAP2)	Rabbit polyclonal	1:500	Dendrite identification	ab32454 [abcam, UK]
Tau	Mouse monoclonal	1:500	Axon and dendrite identification	ab80579 [abcam, UK]
Tyrosine hydroxylase (TH)	Rabbit polyclonal	1:300	Dopaminergic neuron identification	ab112 [abcam, UK]
Gamma-aminobutyric acid (GABA)	Rabbit monoclonal EP2411Y	1:500	GABAergic neuron identification	ab75838 [abcam, UK]
Vesicular glutamate transporter II (VGLUT2)	Mouse monoclonal 8G9.2	1:500	Glutamatergic neuron identification	ab79157 [abcam, UK]
Phosphotyrosine (PY)	Mouse monoclonal PY20	1:500	GP cell identification	ab10321 [abcam, UK]

Primary antibodies were prepared in solution, and then added to the cells after the removal of the blocking solution for incubation overnight at 4 °C. The cells were then washed three times with TBS to remove any background staining, and then incubated with fluorescent secondary antibody solutions, made up of TBS with 1% NGS, triton-X (1:500) and the selected secondary antibody, namely FluoProbes 488 (goat anti-mouse, green fluorescence) [FP-SA4000, Interchim, France] or FluoProbes 547H (goat anti-rabbit, red fluorescence) [FP-SB5010, Interchim, France], both at a dilution ratio of 1:300, for two hours at room temperature in the dark. Cultures were then washed three times with TBS.

For cultures on coverslips, the coverslips were removed from the 24-well plates and washed with dH_2O, then dried and mounted onto microscope slides using Vestashield softset mounting medium with 4',6-diamidino-2-phenylindole (DAPI) [Vector Laboratories, UK]. These devices were then sealed with nail polish to ensure liquid retention for long term storage, and stored at 4 °C in the dark overnight, at which point they were ready for imaging. For cultures in 5PDs, all liquid was removed from the ports and enough DAPI hardset mounting medium was added to the cell culture ports to cover the cells. These devices were then sealed with a microscope slide on top of the access wells and stored at 4 °C in the dark until imaging.

2.4 Fluorescent microscopy

A Nikon Eclipse 80i microscope was used to view the fixed and stained cells cultured on either glass coverslips or devices. Images were captured using a Nikon DS-U2/L2 camera and analysed using NIS Elements (BR3.00, SP3) [Nikon, USA] imaging software as well as ImageJ software [NIH Images]. Analysis consisted of counting specific cell types, performed with the MultiPoint tool on ImageJ.

2.5 MEA extracellular electrophysiological recording

2.5.1 MEA: Hardware

Devices and cells were attached to multi-electrode arrays (MEAs) in order to record the spontaneous extracellular electrical activity from the primary neural cultures. MEAs used in this project consisted of 50 x 50 mm square indium tin oxide (ITO) coated glass with an 8 x 8 grid array of square electrodes in the centre, each electrode being 50 µm x 50 µm with 200 µm between each electrode, resulting in an array size of 1.8 x 1.8 mm [MEA model MED-P515A, obtained via Stratton Technologies, UK from AlphaMed Scientific, MED64, Japan], seen in **Fig.2.8C**. Two different types of this model of MEA were used, one type featured platinum black (PtB) electrodes surrounded by a glass ring, and the other type featured carbon nanotube (CNT) electrodes without a ring (the lack of ring allowed attachment of 5PDs to the MEA), seen in **Fig.2.8A-B**.

These MEAs were treated in the same way as glass coverslips, both with chemical coatings (PDL/LAM or PEI/PDL) and primary cell culture. For PtB ringed MEAs, cells were cultured directly in the centre of the ring, on top of the electrode array. For the CNT non-ringed MEAs, these were first coated with PEI as described previously, then PDMS devices were adhered to the MEA, on top of the electrode array (as seen in **Fig.2.8B**). Cells were then cultured within the PDMS device, in contact with the electrodes. As the cultures grew on the MEAs, their spontaneous extracellular electrophysiological activity was recorded using MEA software at select time points over a 0-70 day period.

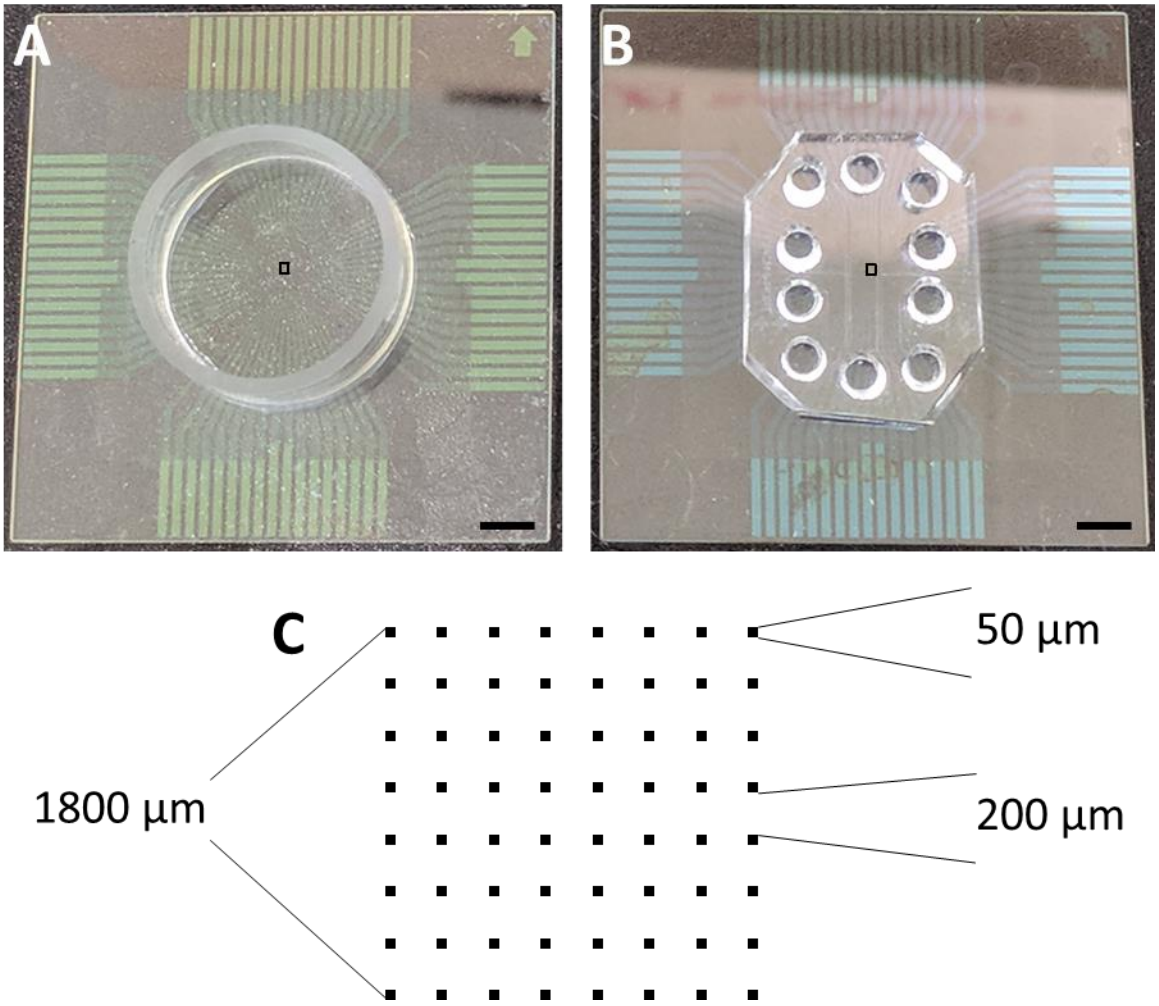

Figure 2.8: Concerning MEA design. A) Photograph of a ringed MEA (used with PtB electrodes), the approximate location of the electrode array itself shown by the black square, scale bar 5 mm. B) Photograph of a flat MEA (used with CNT electrodes) with a PDMS 5PD attached, approximate location of electrode array indicated by black square, scale bar 5 mm. C) Diagram of the electrode array itself, an 8x8 grid of square electrodes, 50 x 50 µm with 200 µm spacing in each direction, resulting in a total array size of 1800 x 1800 µm.

2.5.2 MEA: Recordings

Spontaneous extracellular electrophysiological activity of neural cells cultured on the MEAs was recorded throughout this project over a 70 day culture period at regular intervals. These recording sessions were always taken before a media change, as changing the media affected recording. On days of recording, the MEA bracket was first placed into a sterile flow hood, heated to 37 °C and

sterilised with 70% IMS while the amplifiers were activated and the Mobius MEA software was opened [Alpha MED Scientific, Japan]. MEA devices were removed from cell culture incubators and transported to the MEA bracket in sterile petri dishes wrapped in Parafilm [Sigma-Aldrich, UK] to reduce any potential contamination. The MEA bracket was opened and the MEA placed into the bracket, each conductive strip in contact with its corresponding pin, and the bracket was closed and tightened.

The activity of the cell cultures growing on the MEA was recorded from all 64 electrodes (across the whole array) in a four minute session, for three immediately consecutive sessions, resulting in a total of 12 minutes of recording. This allowed for a window where results were represented in triplicate, and sufficient length so that any outliers, aberrant signals or noise can be represented evenly against the signal data. These recordings were taken via Mobius software, using the modules displayed in **Fig.2.9** from the Spontaneous_recording/Spike_recording predefined workflow. **Fig.2.9A** indicates the MAIN section, including the 'Acquire MED64R2 Data', 'Export Raw Data' (allows for export of raw data as a variety of file types) and 'Display All Channels' (allows for viewing of any recorded activity across 64 channels) modules. The 'Acquire MED64R2 Data' module allows for modificiations to the timing of recording (changing the number and duration of traces), the input range (typically 2.3 mV), and the band-pass filtering thresholds (typically 100 Hz low cut and 10,000 Hz high cut). **Fig.2.9B** indicates the EXTRACTION section, including the 'Extract Spikes Advanced' module. The main purpose of this module is to adjust the threshold at which recorded activity becomes signals rather than noise. A typical threshold of 500% of the root mean square (RMS) was established, and only data exceeding this threshold was considered signal data (data below this threshold was identified as noise and not considered for analysis), these signals being either extracellular action potentials (EAPs) or high-amplitude noise and were subject to further analysis. Signals received from the MEA are referred to as **spikes**, with activity referred to as spiking, spike frequency, etc. **Fig.2.9C** indicates the SPIKE section, including the 'Save Spikes' (saves spike data after extraction), 'Compute Spike Freqs' (calculates spike frequency based on an arbitrary 1 s window), 'Save Spike Freqs' (saves spike feqs once calculated) and 'Display Spike Measures' modules. In 'Display Spike Measures', spikes (signal after extraction) are displayed in a 10 s and 10 ms window, and the spike frequency is also displayed over 10 s. This view is only for one channel at a time, which can be changed at any time. Once 12 minutes of recording was completed, signal data was saved in the form of a .modat data file under 'Save Raw Data' in the 'Acquire MED64R2 Data' module until analysis. These workflows and modules are displayed in full screencapture in **Fig.2.9**.

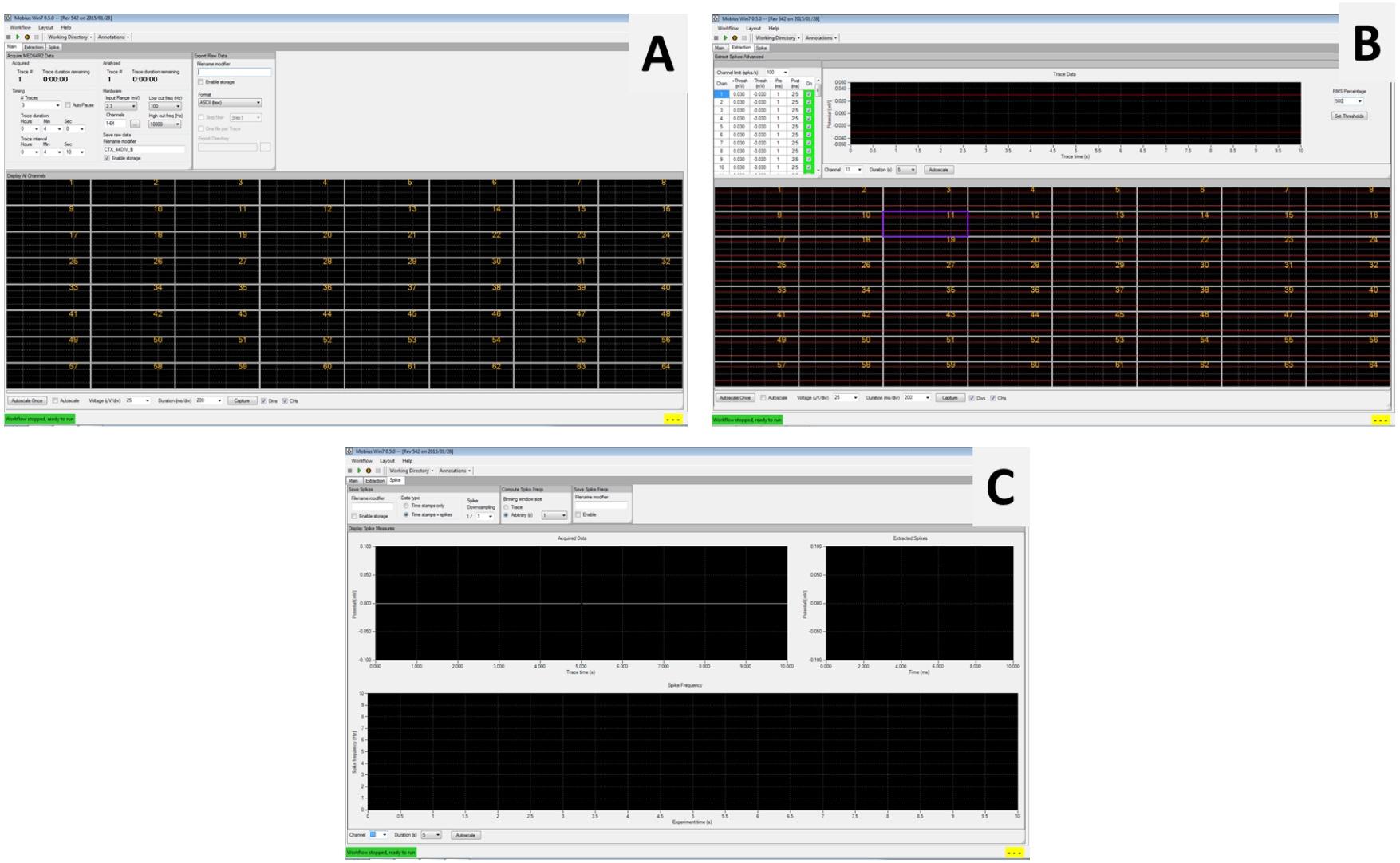

Figure 2.9: MOBIUS modules involved in the recording process. The Spontaneous_recording/spike_recording workflow is split into three main sections, A) MAIN, B) EXTRACTION and C) SPIKE. Each of these sections contains modules involved in the recording of spontaneous extracellular activity from the MEA. Useage is detailed in text body.

2.5.3 MEA: Analysis

Mobius software was used to analyse the raw data exported in a .modat file from the recording process. The Spike_analysis/Spike_sorting predefined analysis workflow was used to analyse activity recorded across the MEA, this workflow is outlined in **Fig.2.10**. **Fig.2.10A** indicates the MAIN section, which contains the 'Display All Channels' (allows for viewing of any recorded activity across 64 channels), 'Export Raw Data' (similarly to Recording workflow, exports raw data file) and 'Replay Raw Data File' modules. The 'Replay Raw Data' module allows for the selection and replay of individual .modat recording files, which can be modified to look at select channels and/or select portions of recording traces. **Fig.2.10B** indicates the EXTRACTION section, which contains the 'Extract Spikes Advanced' module. This is the same as MEA recording, in which the threshold was set to 500% of the RMS, and only data above this threshold is categorised as signal. When replaying .modat files, spike signals above the threshold can be analysed, indepdent of the threshold used during recording. **Fig.2.10C and D** indicate the all-important SPIKE section, where the analysis occurs. This section includes the 'Cluster Spikes', 'Save Spikes' (used to save and export spike data), 'Compute Spike Freqs' and 'Save Spike Freqs' modules (both the last two are the same as they were in recording). The 'Cluster Spikes' module is where spikes were sorted into groups of similarly shaped spikes, termed 'centroids'. The formation of centroids was controlled by two variables: the similarity radius (percentage similarity in shape between spike waveforms) and the minimum number of similar spikes necessary for a centroid to be formed. These variables allowed the thousands of spikes per electrode per recording to be reduced to a handful of centroids, indicative of the activity within the cultures. Throughout this project, centroids were determined by grouping spikes with 80% similarity, and creating a centroid when 50 such similar spikes were accumulated. **Centroid** is henceforth used as the term for raw spiking data that has been analysed and grouped into groups of similar spikes. Mobius software is hard limited to 20 centroids per recording, indicated by the 'Mapping' section where centroids (or 'clusters') are ranked by number of spikes. Each centroid is given a colour, as seen from the single red centroid from **Fig.2.10C** (from CTX cultures after 21 DIV) and the red then blue centroids seen in **Fig.2.10D** (from SN cultures after 44 DIV). The averaged shape of these centroids can be seen in the 'Extracted Spikes' section (also colour coded by centroid) and the frequency can be seen in 'Spike Frequency' section (also colour coded).

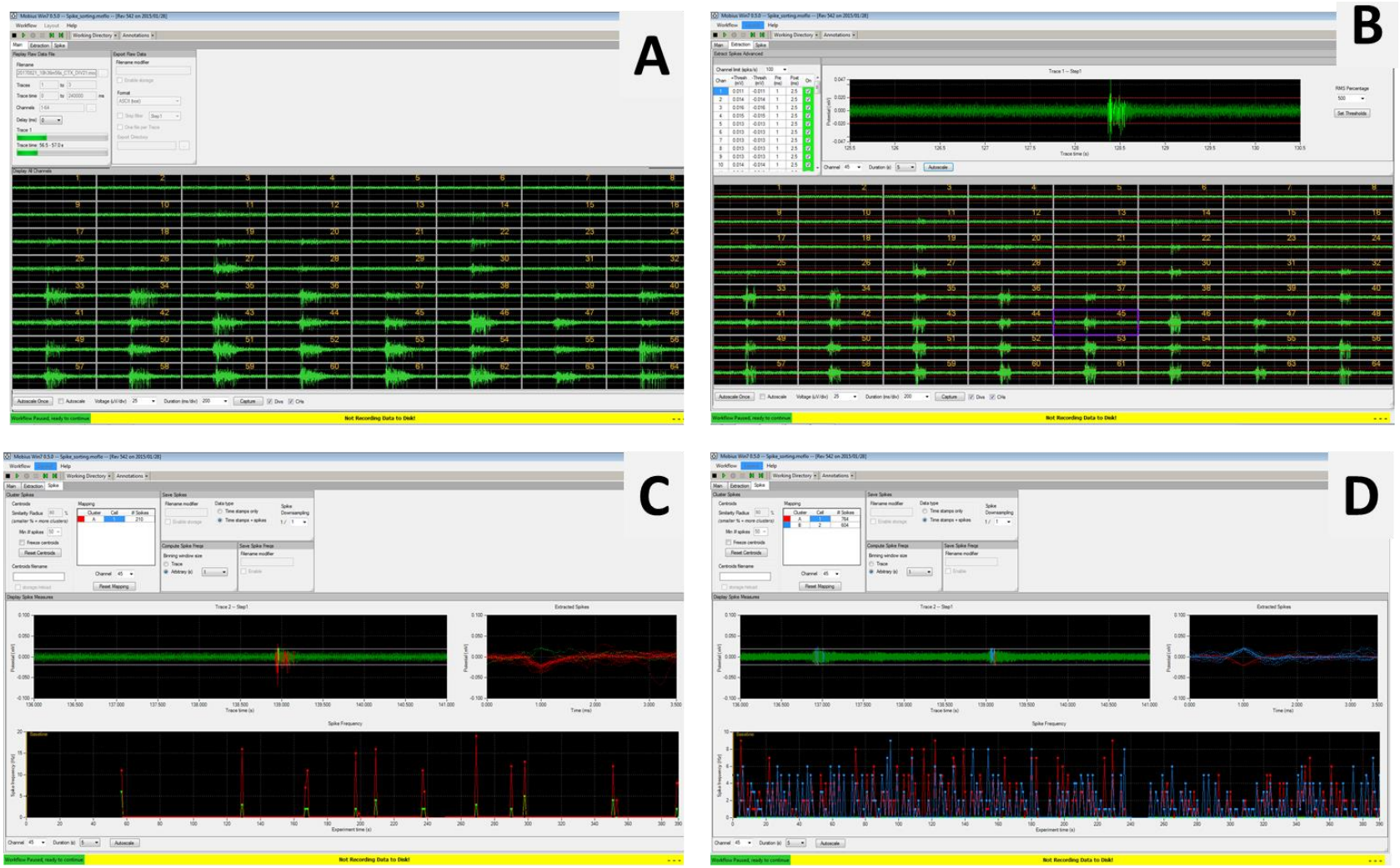

Figure 2.10: MOBIUS modules involved in the analysis process. The Spike_analysis/spike_sorting workflow is split into three main sections, A) MAIN, B) EXTRACTION and C/D) SPIKE. Each of these sections contains modules involved in the analysis of spontaneous extracellular activity from the MEA. Useage is detailed in text body.

These centroid files were exported as comma separated value data sheets that were further analysed using Microsoft Excel [Microsoft, USA] and Matlab [Mathworks, USA]. These data files listed the number of centroids for each of the 64 channels, the number of spikes grouped into each centroid, and the centroid waveform as mV over 3.5 ms. These data were analysed in order to determine the total number of spikes and centroids produced by each electrode over the entirety of the recording session. This data was used to produce the:

- Percentage activity: with 'activity' defined as a custom threshold (number of spikes) for each MEA recording, the percentage of electrodes that were active for a recording session.
- Spatial heatmaps of activity: An 8x8 grid of total spikes recorded per electrode conditionally formatted with a traffic light scale, with red for lowest number of spikes and green for highest. A visual representation of activity across the MEA.
- Mean spike frequency: an average of the spikes recorded by each electrode across all 64 electrodes of the MEA divided by time (720 seconds).
- Maximum spike frequency: spike number from the single electrode that recorded the most spikes across the recording session, divided by time (720 seconds).

This combination of raw spiking data, sorted centroid data and analysed data was gathered across all 64 electrodes for cultures involving one or more of CTX, STR, GP and SN primary neural cell types, from the first day of culture (0 days *in vitro* or DIV) for a ten-week period (final recording on 70 DIV). This extensive recording created the data set analysed in **Chapters 4-6.**

2.6 Statistics

Statistical significance in the data was determined with GraphPad Prism software [GraphPad Software, USA], using two-way analysis of variance (ANOVA) when possible, in order to assess the main effect of each independent variable and the presence of any interaction between them. If significance was found through this test, posthoc Student's t-test was performed to determine significance and assign asterisks to graphs.

Chapter 3: Design and optimisation of a five-port microfluidic neural device

3.0 Introduction

Having outlined the need for an *in vitro* device that can model the *in vivo* basal ganglia (BG) in order to study Parkinson's disease (PD), the first stage was to design such a model, using lithographic and microfluidic techniques.

3.0.1 Designing a basal-ganglia-on-a-chip

Neurons within the brain are highly organised, both structurally – cells can organise into dense groups termed 'nuclei' or layered sheet structures such as the cortex – and functionally, with both excitatory and inhibitory signals travelling between brain areas in hierarchical or cyclical fashions, controlling and modulating signals from other brain areas, both directly and indirectly.

The basal ganglia (BG), a group of subcortical nuclei, features a high standard of both structural and functional organisation. The main nuclei of the BG include the **striatum**, which receives signals from the sensory areas of the cerebral cortex and acts as the primary input for the BG; the **globus pallidus** (GP, consisting of internal (GPi) and external (GPe) sections), composed mostly of GABAergic neurons and therefore inhibitory; the **subthalamic nucleus** (STN), composed mostly of glutamatergic neurons and therefore excitatory; and the **substantia nigra**, which consists of two differently functioning parts, namely the pars compacta (SNc) and the pars reticulata (SNr). The SNr serves as a GABAergic inhibitory output along with the GPi, conveying signals to the thalamus, which influences corticospinal projections and feeds back to the motor areas of the cerebral cortex. The SNc has a more specialised role, being an input that provides the neurotransmitter dopamine to the striatum as a method of indirect regulation, being either excitatory or inhibitory depending on activation of different receptor subtypes on target striatal neurons (Blandini *et al.* 2000, Smeets *et al.* 2000, H. F. Kim and Hikosaka. 2015). This connectivity is reproduced in **Fig.3.1A.**

The importance of the carefully regulated signals in the BG is highlighted when the system breaks down. When certain areas of the BG are damaged, it results in a number of classical neurological diseases: Huntington's disease; caused by a degeneration of GABAergic neurons in the striatum (Walker. 2007) and Parkinson's disease; caused by a loss of dopaminergic neurons in the SNc (Blandini *et al.* 2000, Hague *et al.* 2005). Due to the currently incurable, progressive and prevalent nature of these diseases, the BG has received a great deal of scientific attention. Creating an *in vitro*

model of this area would result in a pre-clinical model and a powerful platform for study, both of a physiologically healthy and pathologically damaged BG.

Due to the sheer complexity of the brain, BG circuitry must first be somewhat simplified in order for a successful model to be produced. This constitutes a '*bottom-up*' approach, rebuilding the BG connectivity using relevant neural cells, and gradually increasing the complexity of the *in vitro* model until it is a relevant mimic of the BG *in vivo*. Part of this simplification design process can be seen in **Fig.3.1A** and **3.1B**.

The *in vitro* model must connect different neural cell populations together via axons, taking into account two major technical issues that arise when studying axonal growth and synapse formation: firstly the cell bodies should be separated from the neuronal endings so they can be studied locally in different compartments to avoid contamination between compartments whilst simultaneously connecting them, and secondly the difficulty involved in creating oriented neuronal networks involving different neuronal subtypes (Peyrin *et al.* 2011). The latter point refers to the directionality of connections in the BG. For example, as seen in **Fig.3.1A**, the cortex inputs to the striatum, but not vice versa, meaning the signals flow in one direction (a unidirectional connection). By isolating the cell bodies, allowing the axonal outgrowths to grow between cell compartments to link them, and encouraging these outgrowths to grow preferentially in one direction, an accurate *in vitro* model of the BG can be produced.

Compartmentalised microfluidic devices have been used to overcome these issues, as discussed previously in **section 1.7.1 Compartmentalised microfluidic models**. These devices culture cells within compartments (**henceforth referred to as 'ports'**) that are linked by micro-scale channels (**henceforth referred to as 'channels'**), where the cell bodies remain in the port and extend axons through the channels into adjacent ports, avoiding contamination of cells between ports and allowing cell populations to connect together via synapses, creating a neural circuit. However, the majority of these models are limited to two ports, connecting two cell populations. For a system as complex as the BG two cell populations are insufficient, requiring the design of a novel five-port microfluidic device with an aim to mimic the connectivity of five main functional nuclei of the BG, as seen in **Fig.3.1C**. This device is designed to support the growth of and isolate different neural cell subtypes while also providing a way for neural cell populations to connect to one another via axons, forming a circuit that mimics brain connectivity *in vivo*.

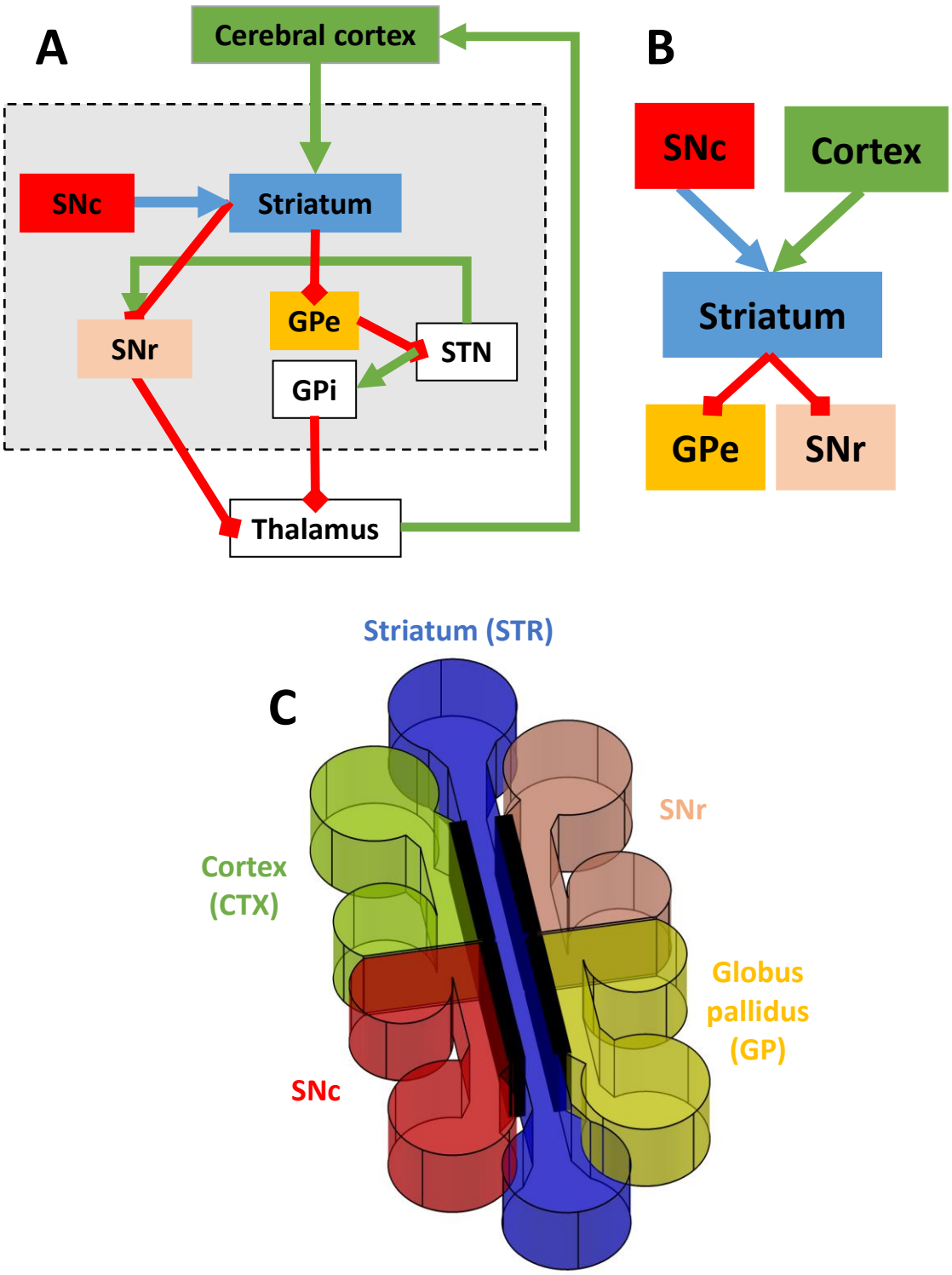

Figure 3.1: From an *in vivo* circuit to an *in vitro* model, the process of designing a device to mimic BG connectivity. (A) A schematic of BG connectivity (BG boundaries indicated by dashed grey box). Arrows indicate directed connetivity: green for excitatory glutamatergic, red for inhibitory GABAergic, and blue for regulatory dopaminergic. SNc: substantia nigra pars compacta, SNr: substantia nigra pars reticulata, GPe/i: globus pallidus exterior/interior, STN: subthalamic nucleus. (B) The connectivity between the five main functional nuclei, highlighting the input, middle and output sections. (C) AutoCAD render of a device with five ports, organised in the same manner as the simplified *in vivo* BG circuitry, as seen in B. The thick black lines between the two input ports, the middle port, and the two output ports indicate the location of micro-channels, which allow for cells to extend axons between ports connected by channels, communicating with cells in the adjacent port. This device allowed for BG connectivity to be reproduced *in vitro*.

The five-port device (5PD) was generated within our research group, based on a previous thesis and project work by Dr Munyaradzi Kamudzandu (**Fabrication of functional basal ganglia circuitry in vitro: from nano- and micro-scale topographies to microfluidic devices,** Keele University).

This model features a compartmentalised design with five ports. As seen in **Fig.3.1C** the two left hand ports represent the main inputs to the BG, the cortex (**CTX**) and the substantia nigra pars compacta (**SNc**, containing dopaminergic neurons). The centre port represents the striatum (**STR**), which receives the inputs and transmits to the outputs. The two right hand ports represent the main outputs of the BG, the substantia nigra pars reticulata (**SNr**) and the globus pallidus (**GP**).

Each port consists of a rectangular section and two circular sections (seen in **Fig.3.1C and 3.2**). The rectangular sections are a set distance from the rectangular sections of parallel adjacent ports, and the channels are positioned within the space between these sections. The circular sections represent locations where access wells will be made in order to add cells, media and other factors to the microfluidic sections of the device. These wells are positioned apart in order to avoid any overlap or contamination, and to maintain an acceptable wall thickness. Apart from the channels between certain ports, each port is isolated from the other ports, resulting in a compartmentalised system.

Between the two input ports and the centre port are sets of channels, as well as between the centre port and the two output ports (as represented by the thick black lines in **Fig.3.1C** and **Fig.3.2B,** in more detail in **Fig.3.2C-D**). In this manner, the cell populations cultured within the ports can extend axons through the channels and communicate in a manner similar to that of the *in vivo* BG. These channels are tapered, having a different width at the beginning and end of the channel, creating a directional pressure intended to mimic the unidirectional connections within the BG, previously seen and described in (Hattori *et al.* 2010, Peyrin *et al.* 2011).

The model features four sets of channels, one for each side port, in order to link them to the centre port. Each set of channels features 200 channels, making 800 channels across the whole device. Each channel is 1.05 mm from end to end, but due to the way that the ports are superimposed onto the channels during the fabrication process, only the section of the channel between the ports will remain, resulting in channels 450 µm long from port to port. Channels are spaced ~40 µm apart, this measurement varying with different experiments using channels of different internal diameters. Channels have an internal width of 5 µm at one end and >5 µm at the other end, in order to create a tapered channel that exerts directional pressure on the axons extending into channels. There are a variety of widths for the larger end of the channels, and part of this experiment was to determine which width is optimal for a directional pressure. The available widths were 15 µm, 25 µm and 50 µm (**Fig.3.2D**).

3.0.2 Five-Port Device Fabrication

Once the 5PD was designed with AutoCAD software, two separate masks were designed for fabrication purposes, as the 5PDs are made through two stage lithography: one mask for the channels (the first stage) and one mask for the ports (the second stage, aligned and superimposed onto the channels), both masks can be seen in **Fig.3.3**. Each mask allows of the fabrication of five 5PDs, three with channel width 5-15 µm and one each of channel width 5-25 µm and 5-50 µm.

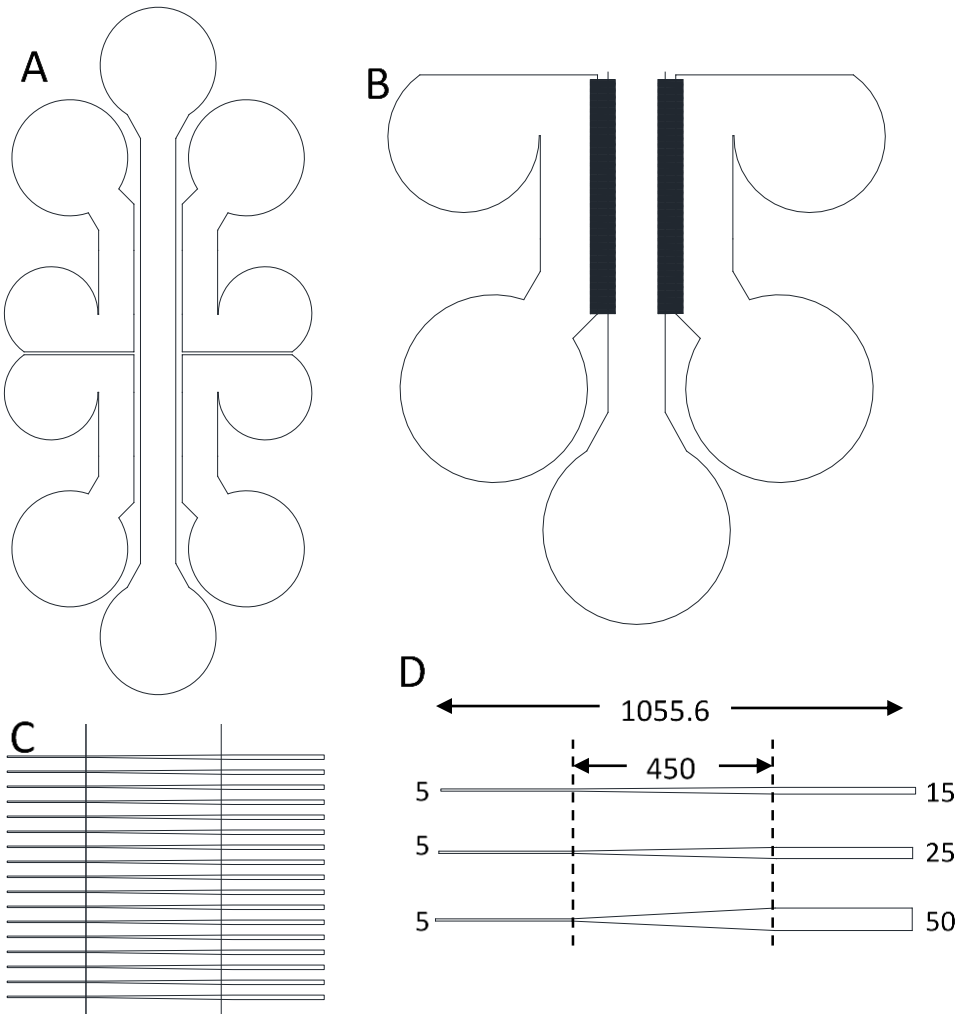

Figure 3.2: Schematics detailing the design of the 5PD. A) The positioning of the five ports in relation to each other. The channels were removed in this image to improve clarity. B) A magnified view of the bottom half of the device, showing the positioning of two sets of channels in relation to the ports. As the channels are so small and densely packed they appear as a single black bar. C) A magnified view of the channels between ports, showing the smaller width end on the left and the larger width end on the right. The two vertical lines indicate the edges of the ports. D) The dimensions of each of the three available channel types used for different experiments (in micrometres). Whilst the channels are over 1 mm in length in the design, only the middle 450 µm remains after the two-stage lithography, making this the final length of the channel. All channels begin 5 µm wide but can end at 15, 25 or 50 µm wide. These widths were tested to determine which exerts the most directional pressure on axon elongation, in order to create a unidirectional network mimicking the *in vivo* basal ganglia circuitry.

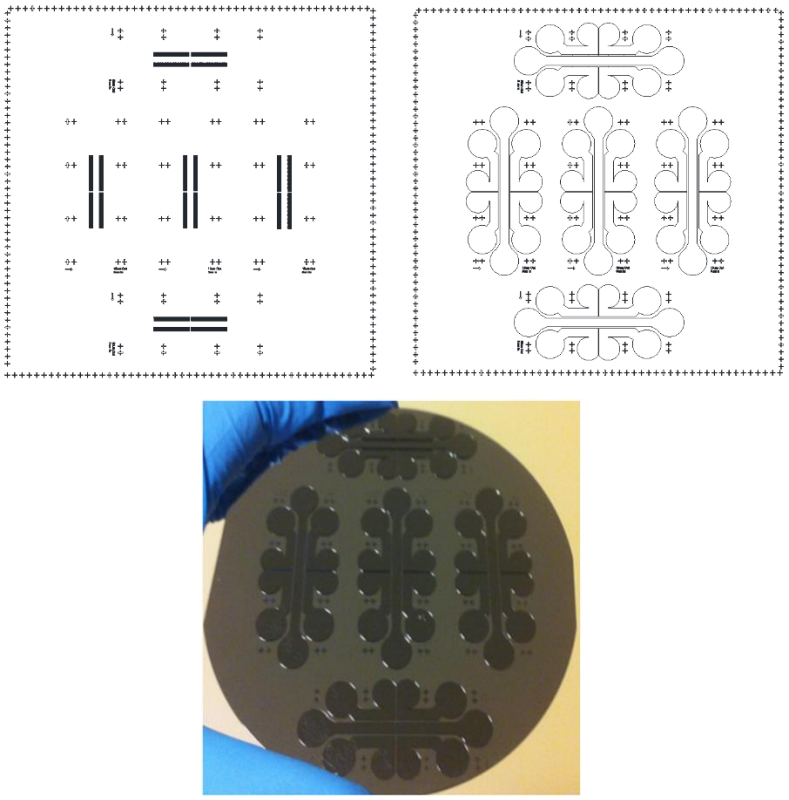

Figure 3.3: Photolithography masks and final result. The top left is the channel mask and the top right is the ports mask. Each set of alignment crosses align the masks, indicating the location of channels and ports in relation to each other, with ports superimposed onto channels. The final result is pictured below, a 100 mm diameter silicon wafer with the designs transferred onto the surface via photolithography.

These masks were involved in the photolithographic fabrication process, detailed previously in **Chapter 2 (section 2.1.2 Device fabrication: two-stage photolithography)**. Briefly, the final product of the photolithography process was a silicon wafer with the ports and channels design transferred onto the surface, ready to be used as a template to mould 5PDs (**Fig.3.3**).

Liquid-state polydimethylsiloxane (PDMS) is poured onto the silicon wafer, creating an inverted pattern that can be cut out and peeled off once set. This PDMS casting process is repeated many times to produce numerous devices. Due to the nature of the photolithographic process, each feature on the silicon wafer has a specific height: the channels are 5 µm high and the ports are 150 µm high (measured by scanning electron microscopy, SEM). These heights are inverted upon casting with PDMS, becoming cavities and airspace when the PDMS is attached to glass. The finished product can be seen in **Fig.3.4**.

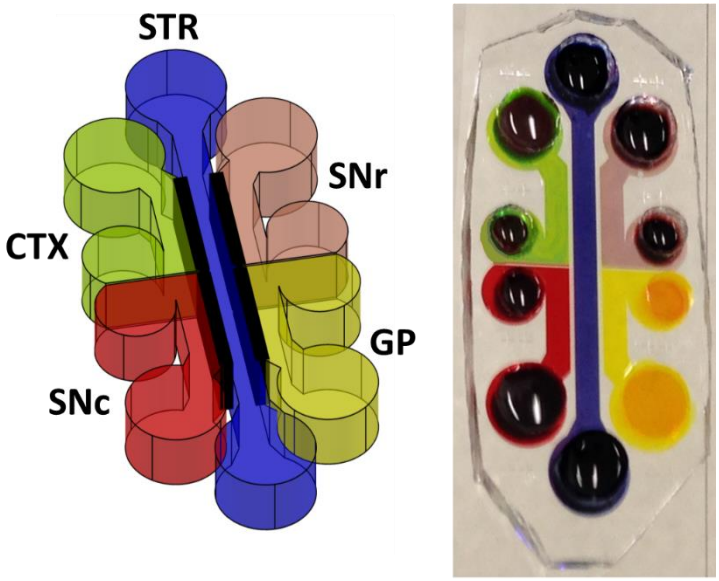

Figure 3.4: The finished 5PD (right hand side) compared to the original 5PD design (left hand side). The finished device is a PDMS mould, inverted and sealed to a glass coverslip. Each port was then filled with dye representing the colour that corresponds to the original design. Note that the ports were all isolated from each other, with no mixing of colours. Channels were present in this device, but they are too small to view.

By culturing cells from the CTX, STR, GP, SNc and SNr in their respective ports (as seen in **Fig.3.1C** and **Fig.3.4),** their axons will extend unidirectionally down the channels to connect to adjacent cell populations and create an *in vitro* model of the BG. The same brain nuclei will connect in the same manner as they do *in vivo*. However, for this model to function as an effective *in vitro* basal ganglia for pre-clinical research into Parkinson's disease, several factors required optimisation.

3.0.3 Device Optimisation

Several factors were optimised before the model could function as intended, to ensure the 5PD was designed efficiently. These factors can be categorised by: chemical coating, physical channel width and ensuring dopaminergic neuron isolation to SNc port.

3.0.3.1 Chemical coating

Two important factors to maintain when culturing cells within the 5PD is that the cell bodies should stay within the ports they were seeded into (in order to avoid contamination between neuronal sub-regions), and that they extend axonal processes through a 450 µm channel into an adjacent port, where they can interact and synapse with a different cell population, in order to make a circuit similar to the *in vivo* basal ganglia. The cell source for the model is primary rat (E12-16), the resultant neural cells are sensitive and less robust than a cell line (Potter and DeMarse. 2001). Due to this sensitivity, these primary cells were rarely seeded onto bare surfaces, requiring a chemically coated surface in order to exhibit proliferation and axonal growth. Therefore, an ideal chemical coating for the five-port device was one that would not cause the primary cells to lose viability upon seeding, promotes axonal outgrowth and proliferation, and reduces cell migration.

As outlined in **Chapter 1 (section 1.1.1 Surface chemical coatings)**, the most frequently used surface chemical coatings are poly-D-lysine (PDL) and laminin (LAM), with other synthetic positively-charged chemicals like polyethylenimine (PEI) also used. All of these chemicals are to be tested in combination to determine which is the most suitable for cell culture within the 5PDs, identifying which combination resulted in the least cell migration and most axonal outgrowth through channels.

3.0.3.2 Physical channel width

Two characteristics of axons are exploitable and should be considered when designing channels: axons can act as guide cues for other axons (with pioneer axons guiding follower axons through fasciculation and axonal bundling) meaning that larger channels accommodate more axons as soon as a pioneer axons finds the channel and enters; and axons react differently when meeting surfaces at different angles, either growing along the surface when aligned in parallel or deviating from their original direction when aligned in perpendicular, meaning sharp angles can be used to dissuade axonal growth whereas planar surfaces support axonal growth (N. Li and Folch. 2005, Francisco *et al.* 2007, Peyrin *et al.* 2011, Renault *et al.* 2015). As such, it was important to optimise the tapered channel width to determine which best selects for unidirectional connections.

Fig.3.2D shows the three channel width types available in fabrication: 5-15 µm, 5-25 µm and 5-50 µm. While these channels needed to be able to direct axonal processes between adjacent ports, it is important to consider the differences between the four side ports (the two input and two output ports) and the centre port. Cells cultured in the side ports were only presented with one row of channels and therefore only had one possible direction for axonal outgrowth. While this is not an issue for the input ports, as they can only grow in their wanted direction (input -> centre), it is an issue for the output ports as the only direction for axonal outgrowth is in the opposite, unwanted direction (output -> centre). In addition, cells in the centre port are presented with two sets of channels, one set coming from the input ports and one set leading to the output ports. The wanted direction of connectivity for the device is as follows: input ports -> centre port -> output ports, and the channels require orientation in order to create pressure in this direction. This concept is further outlined in **Fig.3.5**.

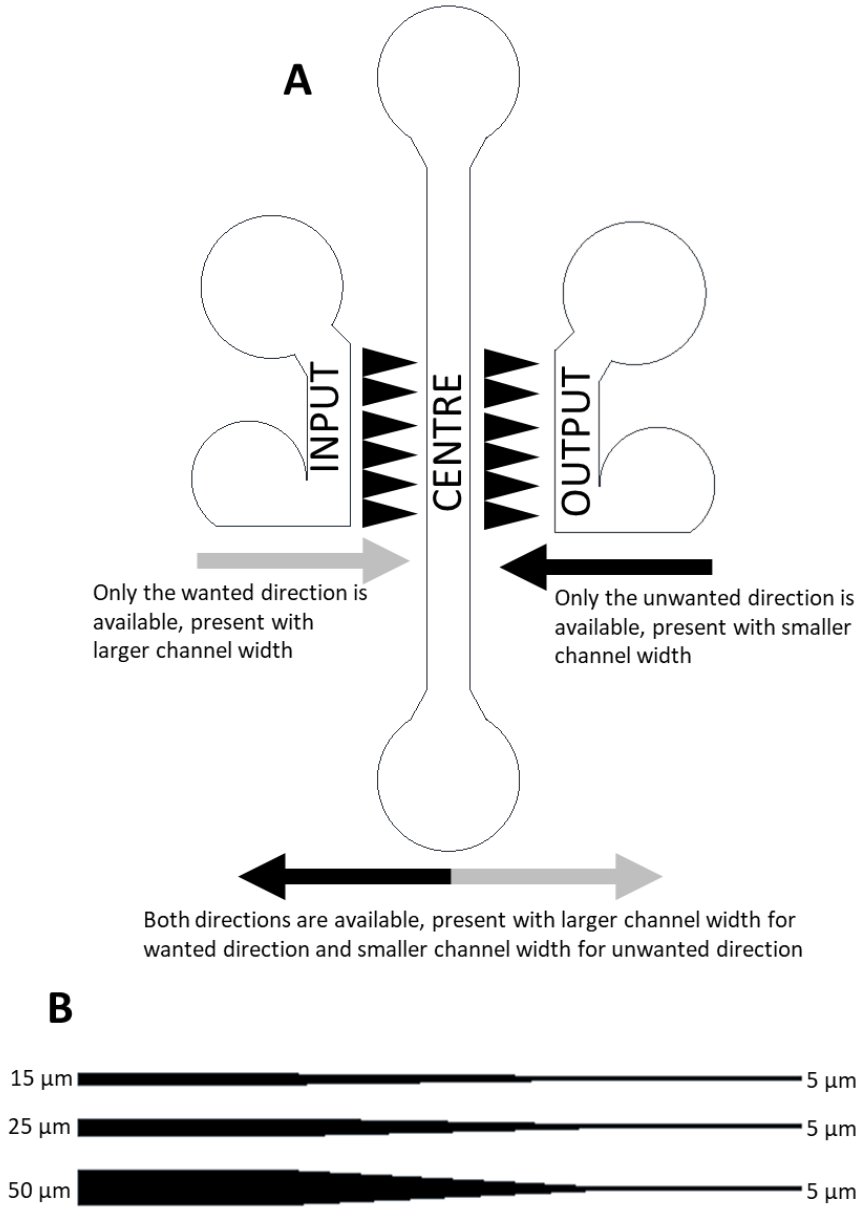

Figure 3.5: Unidirectional connectivity in the 5PD. A) A simplified version of our 5PD, showing the three types of port and the channel orientations (channels represented by black triangles, not to scale). Cells within input ports can only grow in the wanted direction (as indicated by the grey arrow), and cells within output ports can only grow in the unwanted direction (as indicated by the black arrow). Cells within the centre port can grow in either direction, and thus can access both larger widths for the wanted direction and smaller widths for the unwanted direction. B) The three types of tapered channel available.

The orientation and dimensions of the tapered channels is important to maintain the unidirectional connectivity found in the BG *in vivo*, and thus it was necessary to determine what channel widths best select for and against axonal entry into the channel. While all the channels featured a smaller end of 5 µm to select against axonal outgrowth, the choices for the larger end included 15 µm, 25 µm and 50 µm. It may initially seem that the wider the channel, the more axons can enter it and the more efficient it will be as a directional cue, but axons are known to be responsive to local topography and smaller channels may offer increased surface area for axonal guidance (N. Li and Folch. 2005, Francisco *et al.* 2007, Peyrin *et al.* 2011).

3.0.3.3 Presence of dopaminergic neurons in both SNc and SNr ports

Due to the cell source for this project being rat primary cells (embryonic age E12-16), it can be manually challenging to obtain all the necessary tissues. While the CTX, STR and GP can be isolated without issue, the other two ports of our *in vitro* 5PD BG model are the SNc and SNr, both being subdivisions of the SN. It is not possible to reliably separate the SNc and SNr through microdissection as the region is both too small and intermixed throughout development. This results in the SN as a whole being isolated and used in seeding the device, with both the SNc and SNr ports containing a mixture of cells from the SN, including both the SNc and the SNr. While the SNr consists of mostly GABAergic neurons (similarly to the rest of the BG), the SNc contains the all-important population of dopaminergic (DA) neurons, loss of which is a causative factor in Parkinson's disease. Whilst the entirety of the SN contains DA neurons the SNc contains roughly 6-7 times as much as any other subdivision of the SN (Nair-Roberts *et al.* 2008) including the SNr, these DA neurons are essential to create an accurate BG model *in vitro* and for it to function as a disease model. With the SN being dissected as a whole, both the SNc and SNr ports would be seeded with SN as a whole, meaning the SNr port would contain a much greater proportion of DA neurons compared to *in vivo*, potentially making the model inaccurate. As the model is intended to mimic Parkinson's disease, having two populations of DA neurons introduces issues when DA neurons need to be removed or inactivated in order to mimic Parkinson's pathology (Roeper. 2013).

DA neurons in the SNr port would need to be removed, or greatly reduced, in order for the model to function as intended and be as accurate as possible to the *in vivo* basal ganglia. Numerous options exist for selectively removing a neuronal population in an *in vitro* culture, including **physically** (chronically via trauma (Hutson *et al.* 2011) or acutely via scalpels or lasers), **chemically** (with toxins that destroy DA neurons (Bilsland *et al.* 2002, Y. M. Ding *et al.* 2004, Hernandez-Baltazar *et al.* 2015, Filograna *et al.* 2016)) or **electrophysiologically** (by blocking the DA neuron signals, they would become 'dark neurons' that don't signal and therefore aren't sensed by the other neurons in the device, essentially the same as removing the DA neurons entirely (El Ayadi *et al.* 2001, Momiyama. 2002, Guzman *et al.* 2010)). Due to the generalised and severe nature of physical methods, only chemical or electrophysiological methods were considered.

3.0.4 Chapter Three Aims and Objectives

The aim in this chapter is to optimise the 5PD previously designed by our research group, in order to better mimic basal ganglia circuitry. The factors to optimise include chemical coating (to reduce migration and promote axonal outgrowth), physical channel width (to control the directional of axonal outgrowths) and characterising the cells obtained from dissection. All these factors are necessary to optimise in order to generate a device that can model physiologically relevant basal ganglia circuitry.

3.1 Experimental Methods

3.1.1 Device fabrication

The devices were fabricated using two stage lithography (**section 2.0.2 Two-stage photolithography**), by first exposing the channels onto a silicon wafer, and then exposing the ports on top of the channels. These templates were used to cast polydimethylsiloxane (PDMS) devices, which were then sealed to chemically-coated glass microscope slides and sterilised (**section 2.0.3 Bonding and sealing**).

3.1.2 Primary cell culture

Primary neural cells were dissected from rat embryos, ranging from E12-E16 depending on the experiment, and then dissociated and seeded onto 5PDs or coverslips (**section 2.2 Primary cell culture**). The following areas were dissected: cortex (CTX), lateral ganglionic eminence (LGE), medial ganglionic eminence (MGE) and ventral midbrain (VM). These areas develop into the cortex (CTX), striatum (STR), globus pallidus (GP) and substantia nigra (SN) respectively, making up all five ports of the device. The cells were cultured until sufficiently confluent and mature to image or experiment with, at which point they were fixed and stained.

3.1.3 Immunocytochemistry

Cells were fixed, blocked and stained with the relevant antibodies (**section 2.3 Immunocytochemistry**). Cells were stained for DAPI (blue, marks nuclei), β-tubulin (marks neural cells), and GFAP (marks glial cells). During cell characterisation other stains were used, for GABA (GABAergic neurons), TH (DA neurons), VGLUT2 (glutamatergic neurons) and Py (GP cells containing phosphor-tyrosine). Cells were then incubated with secondary antibodies in order to confer red or green fluorescence, and imaged with a fluorescent microscope (**section 2.4 Fluorescent microscopy**).

3.1.4 Statistical analysis

Once data was gathered, Student's t-test was used to compare single pairs of results (e.g. PDL/LAM vs PEI/PDL for the same condition) and two-way analysis of variance (ANOVA) was used to determine significant effects over whole data sets, with ANOVA results displayed as (ANOVA x,y F=Z, p=q) where x is the number of groups, y is the sum of sample sizes, Z is the F statistic and q is the p value, where $p < 0.05$ is significant (**section 2.6 Statistics**).

3.2 Results

3.2.1 Device fabrication

As the dimensions of the 5PD micro-channels approached sub-micron resolution, scanning electron microscopy (SEM) was used to determine if the channels were fabricated with similar dimensions to the original AutoCAD design, as shown in **Fig.3.6**. Five different 5-50 µm devices were imaged with an average width of 4.96 ± 0.02 µm, demonstrating the accuracy and reproducibility of the technique.

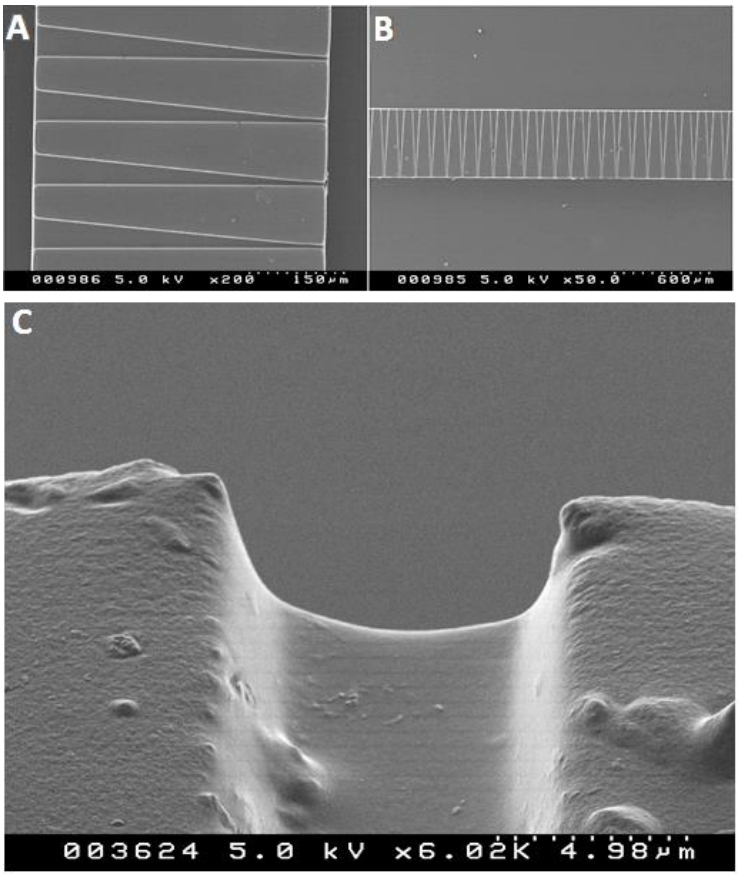

Figure 3.6: SEM images from a 5PD with 5 µm to 50 µm width channels. (A) Top-down view of the channels, indicating the 450 µm channel length between the ports, (B) showing the distribution of channels between ports, (C) the 5 µm width end of a channel, also showing the 5 µm height of the channel (observed at a 45° angle). Magnification and scale observed at the bottom right of each image.

The fabrication process accurately reproduced the 5-50 µm channel widths and 450 µm channel length, as well as the number, shape and distribution of the channels and the ports. The 5-15 and 5-25 µm width channels were also fabricated to the same level of accuracy and reproducibility (images not shown). Throughout experimentation, each end-stage PDMS device was carefully inspected via light microscopy (SEM was not used throughout as it was a destructive technique that rendered the PDMS devices unsuitable for cell culture) for any deviations or imperfections, such as collapsed or incomplete channels, and these devices were disposed. Through the accuracy of the lithography and a stringent quality control process, each device was identical to other devices at a micron level.

The three stages of fabrication (AutoCAD software design, photolithographic transfer of the patterns onto a silicon wafer and PDMS casting of the patterns) can be seen conserved in **Fig.3.7**, via SEM.

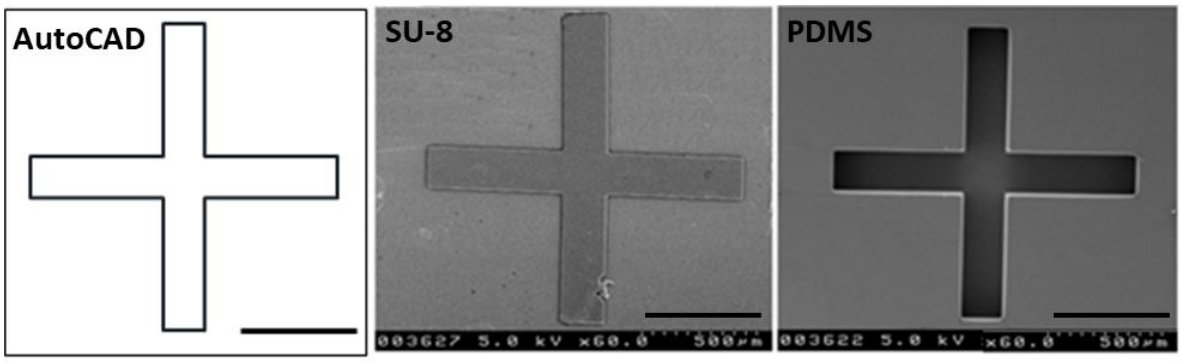

Figure 3.7: The conservation of a pattern throughout the 5PD fabrication process. Alignment crosses were used to align the channels layer to the ports layer during the photolithography process. From left to right, the crosses are: original AutoCAD software design, hardened SU-8 photoresist on silicon wafer, PDMS from mould. In this manner, the design was translated from software, through mould fabrication, and into the final PDMS device form. For the latter two images, magnification and scale can be observed in the bottom right corner.

3.2.2 Cell characterisation

Note: all characterisation cell experiments were seeded onto PEI/PDL coated surfaces.

3.2.2.1 Cell specific markers

To determine the accuracy of dissecting CTX, LGE, MGE and VM tissues from foetal rat brains (E12-16) (the tissues that develop into CTX, STR, GP and SN respectively) the resultant tissues from sample dissections were subject to characterisation via antibody staining. The following antibodies were used for each cell type: vesicular glutamine transporter 2 (VGLUT2) for CTX, phosphotyrosine (PY) for GP, gamma aminobutyric acid (GABA) for STR, and tyrosine hydroxylase (TH) for SN. The results can be seen in **Fig.3.8.** CTX, GP and SN all stained positive for their specific marker (VGLUT2, PY and TH respectively), confirming that they are indeed the correct cell type as intended, with the levels quantified in **Fig.3.8A**. All four cell types stained positive for GABA, but the signal was significantly increased for STR cells. The proportions of GABAergic neurons within each cell type is shown in **Fig.3.8B**. These data indicate that the dissections were accurate and the desired neural subtypes were obtained.

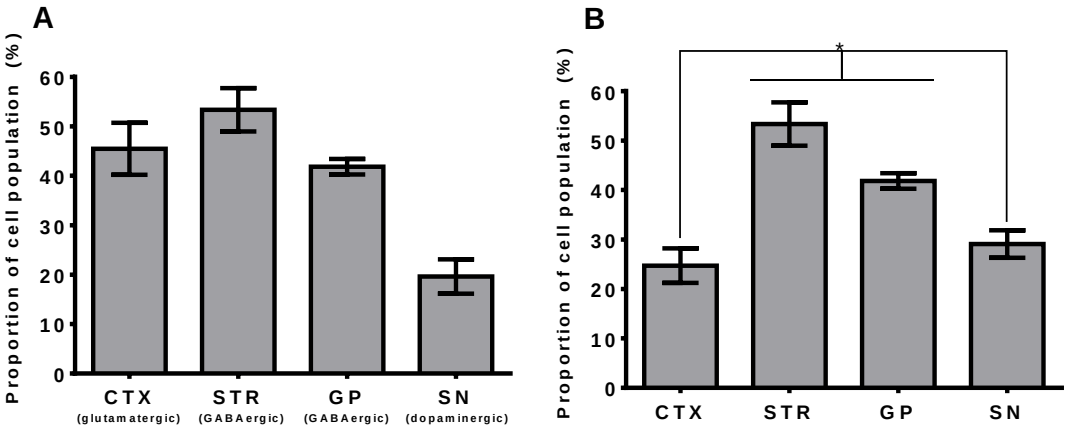

Figure 3.8: Quantified data from cell specific staining experiment (images in Fig.3.9). A) Proportions of each specific neuron type for each area by way of comparison. B) Proportions of GABAergic neurons in each cell type, based off GABA antibody staining (n=4) (*): p<0.05 (compared to CTX and SN).

Despite the importance of DA neurons in the basal ganglia, these neurons only make up a small proportion of the SN (10-20%), while the other three areas have a larger proportion of inhibitory/excitatory neurons. In addition, as all four cell types contained a portion of GABAergic neurons, the levels of these neurons were also compared, as seen in **Fig.3.8B**. STR and GP showed significantly higher levels of GABAergic neurons when compared to CTX and SN, as STR and GP are inhibitory nuclei of the basal ganglia, possessing mostly GABAergic neurons.

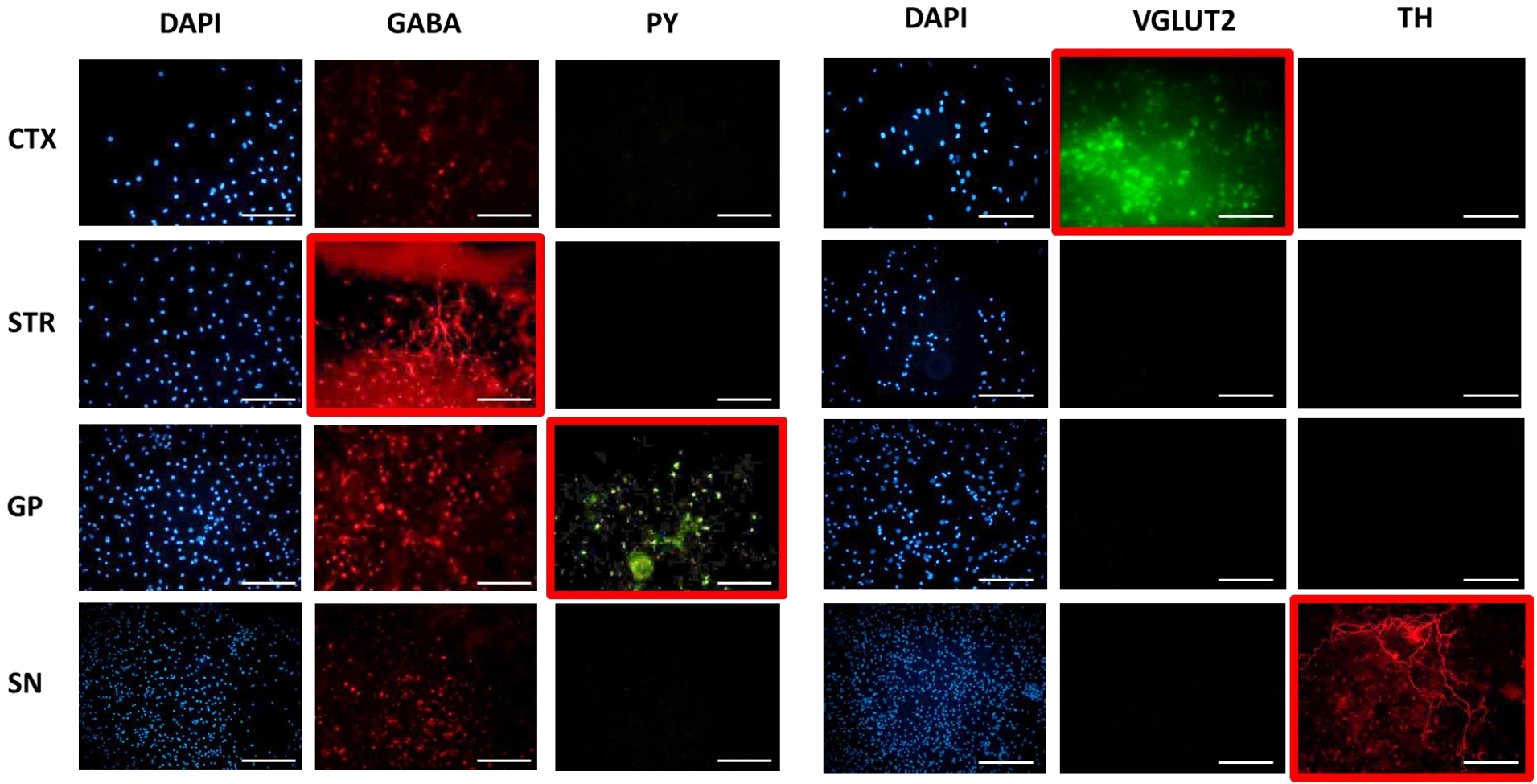

Figure 3.9: Cell specific staining of CTX, STR, GP and SN cells. 100,000 cells were seeded onto 13 mm coverslips and imaged after 8 DIV. Cells were stained two sets of fluorescent markers, first DAPI (blue, marks cell nuclei), GABA (red, GABAergic neuron marker), and PY (green, GP marker), then DAPI (blue, marks cell nuclei), VGLUT2 (green, glutamatergic neuron marker) and TH (red, dopaminergic neuron marker). The red squares indicate which cell type is intended to stain for which marker, scale bars are all 100 µm. Images are representative of n=4.

3.2.2.2 Neuron-astrocyte ratio

The neuron/astrocyte ratio within the cultures was quantified by staining for neurons with β-tubulin III (microtubule component found only in neurons) and for astrocytes with glial fibrillary acidic protein (GFAP, found in astrocyte filaments) as shown by **Fig.3.10**. The effect of cell type on the neuron-glia ratio was not significant (ANOVA (3,16), F=2.99, p=0.06) showing a constant neuron-astrocyte ratio between CTX, STR, GP and SN of approximately a 40:50 astrocytes:neurons on day 8.

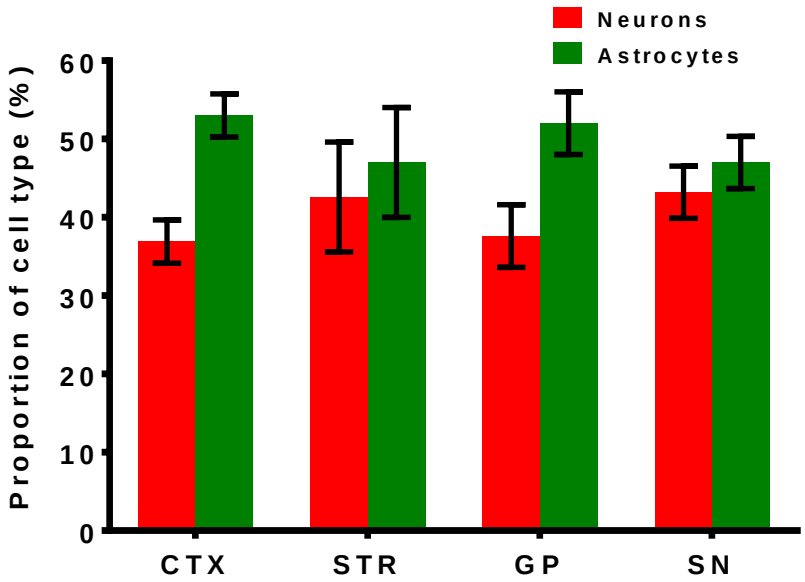

Figure 3.10: The neuron/astrocyte percentage proportion across all four cell types after 8 DIV. 100,000 cells were seeded onto 13 mm coverslips and labelled with β-tub (neuronal marker) and GFAP (astrocyte marker), then counted via fluorescent microscopy (n=4).

3.2.2.3 Dopaminergic neuron analysis

Due to their importance for this project, cells from the SN were subject to additional characterisation in order to determine the proportion of DA neurons obtained from tissues of rats at different developmental ages (E12-16), and the proportion of DA neurons within a culture on a surface over time, both displayed in **Fig.3.11**. The raw images used to generate the data in **Fig.3.11** are shown in **Fig.3.11A-B**.

The effect of time on neural cell proportions was significant (ANOVA 3,24, F=5.83, p=0.004), with significantly more DA neurons at days 3 and 4 vs 1 and 2 (shown by asterisk on **Fig.3.11A**). For the first two days after seeding, SN cultures had high levels of neurons compared to astrocytes, but no visible DA neurons (no neurons that stained positive for TH). Over time, the neuron/astrocyte ratio changed, with astrocytes proliferating in culture, and, DA neurons became visible to TH staining during this time, with approx. 20% of neurons being DA neurons at days 3-4 *in vitro* (DIV). **Fig.3.11B**

shows that there were more DA neurons available at earlier developmental ages (E12-14) when compared to later ages (E16), but it should be noted that this difference was not significant.

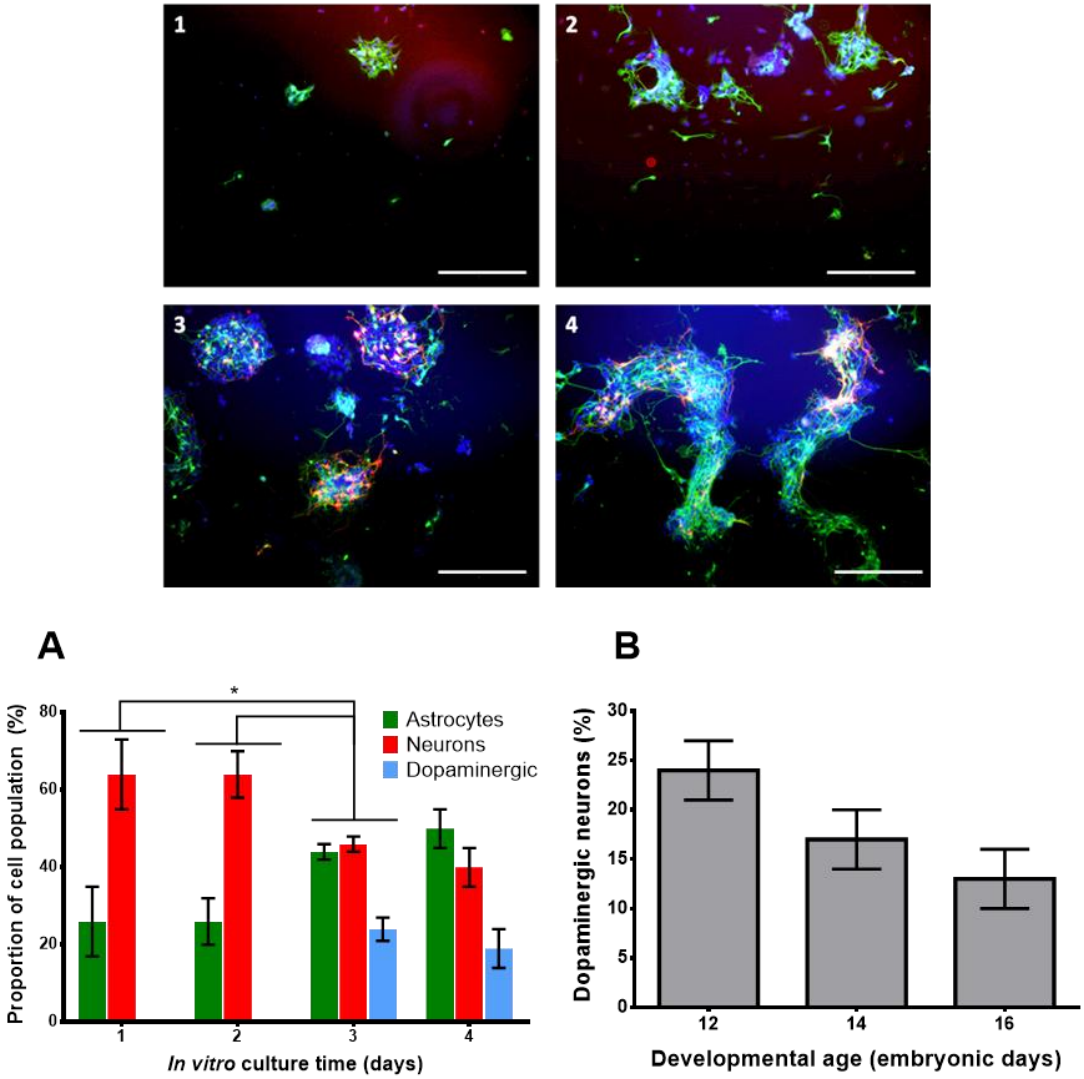

Figure 3.11: Changes in SN neural cultures over time during *in vitro* culture. 100,000 SN cells were seeded onto 13 mm coverslips and imaged after 1, 2, 3 and 4 DIV. Images 1-4 refer to their number of days of growth. Blue is DAPI (cell nuclei stain), green is β-tubulin (neuron stain) and red is TH (dopaminergic neuron stain). Both the number of cells overall and the number of DA neurons increases over time, the scales are 100 µm. A) Quantified proportions of astrocytes, neurons and DA neurons over time, B) quantified proportions of DA neurons after 4 DIV taken from different embryonic ages, namely E12, E14 and E16.

3.2.3 Chemical coating optimisation

A combination chemical coating of PDL and laminin (LAM) was compared to an alternative combination of PEI and PDL.

3.2.3.1 Cell body migration

13 mm coverslips coated with either PDL/LAM, PEI or PEI/PDL were seeded with 100,000 E16 CTX cells to determine the extent of cell migration. The coverslips were stained and imaged after 21 days

of growth, as seen in **Fig.3.12**. While cells migrated across the whole surface of the PDL/LAM coated coverslip, creating a random distribution of neurons and astrocytes, cells seeded onto PEI and PEI/PDL coated coverslips remained where they were seeded (in the centre of the coverslip) and the neurons extended axons out towards the edge of the coverslip. PEI/PDL coated coverslips appeared to feature longer axons than PEI coated coverslips, making PEI/PDL coating the preferential combination out of the three surface coatings, as it limited migration and promoted axonal outgrowth, ideal for circuit formation.

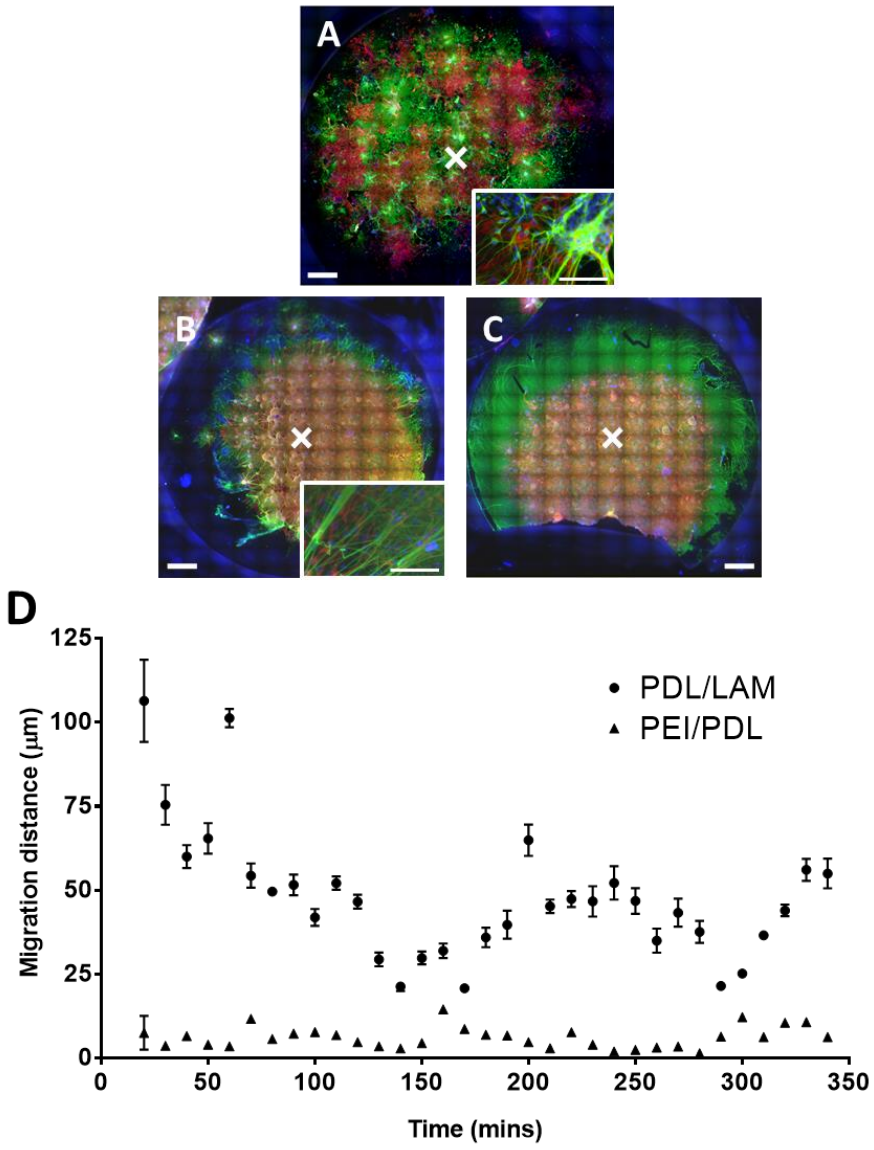

Figure 3.12: Comparing chemical coatings. 100,000 E16 CTX cells were seeded into the centre (marked by white cross) of three different 13 mm coverslips, A) PDL/LAM-coated, B) PEI-coated, C) PEI/PDL-coated, and imaged after 21 DIV: blue for DAPI (nuclei), green for β-tubulin (neurons) and red for GFAP (astrocytes), representative of n=3. A) PDL/LAM-coated, neurons and astrocytes spread across the surface of the coverslip B) PEI-coated surface, majority of cell bodies and astrocytes remained adhered where seeded, neurons extend axons into surroundings, elongated neurites seen in insert. C) PEI/PDL-coated, similar to B except the axonal halo was larger. Main image scale bar is 1 mm, insert scale bar is 100 µm. D) Time lapse imaging of 100,000 E16 CTX cells seeded onto PDL/LAM or PEI/PDL-coated coverslips (n=6). Migration distance from original seeding location of ten cells recorded every ten minutes via light microscopy. Error is standard error, too small to see on PEI/PDL data points (except initial point).

Fig.3.12D shows a quantified experiment where PDL/LAM and PEI/PDL coated coverslips were compared in order to determine the extent of cell migration for each. The position of the cells were tracked over the first 350 minutes immediately after seeding in a time-lapse with brightfield images taken every 10 minutes. Individual cells were tracked in ImageJ software, and the distance that cells moved from their original seeding location over time was recorded. 20 cells over 9 repeats were tracked.

As seen in **Fig.3.12D, t**he effect of chemical coating over time was extremely significant (ANOVA 33,136, $F=91.18$, $p<0.0001$), with each data point from 10 minutes onwards being significantly different ($p < 0.0001$). Both the effects of time and chemical coating alone on migration were extremely significant (ANOVA 33,136, $F=107.8$, $p<0.0001$ for time), (ANOVA 1,136 $F=11278$, $p<0.0001$ for chemical coating). This shows that the migration distance was significantly higher over time for cells seeded onto PDL/LAM coated surfaces compared to cells seeded onto PEI/PDL coated surfaces. Cells on PDL/LAM migrated the furthest in the first hour after seeding, whereas on PEI/PDL the lower levels of migrations were consistent throughout the experiment.

This migration experiment was repeated in 5PDs using all four cell types, namely CTX, STR, GP and SN. The cells were seeded into the centre port of 5PDs, and any cells that travelled through a channel into an adjacent port were determined to be migratory. All three available channel widths were used, namely 5-15 µm, 5-25 µm and 5-50 µm, in order to also determine if channel width had any extra effect (explored in more detail later, in **channel directionality assessment**), and 5PDs were again coated with either PDL/LAM or PEI/PDL. The results of this experiment can be seen in **Fig.3.13**.

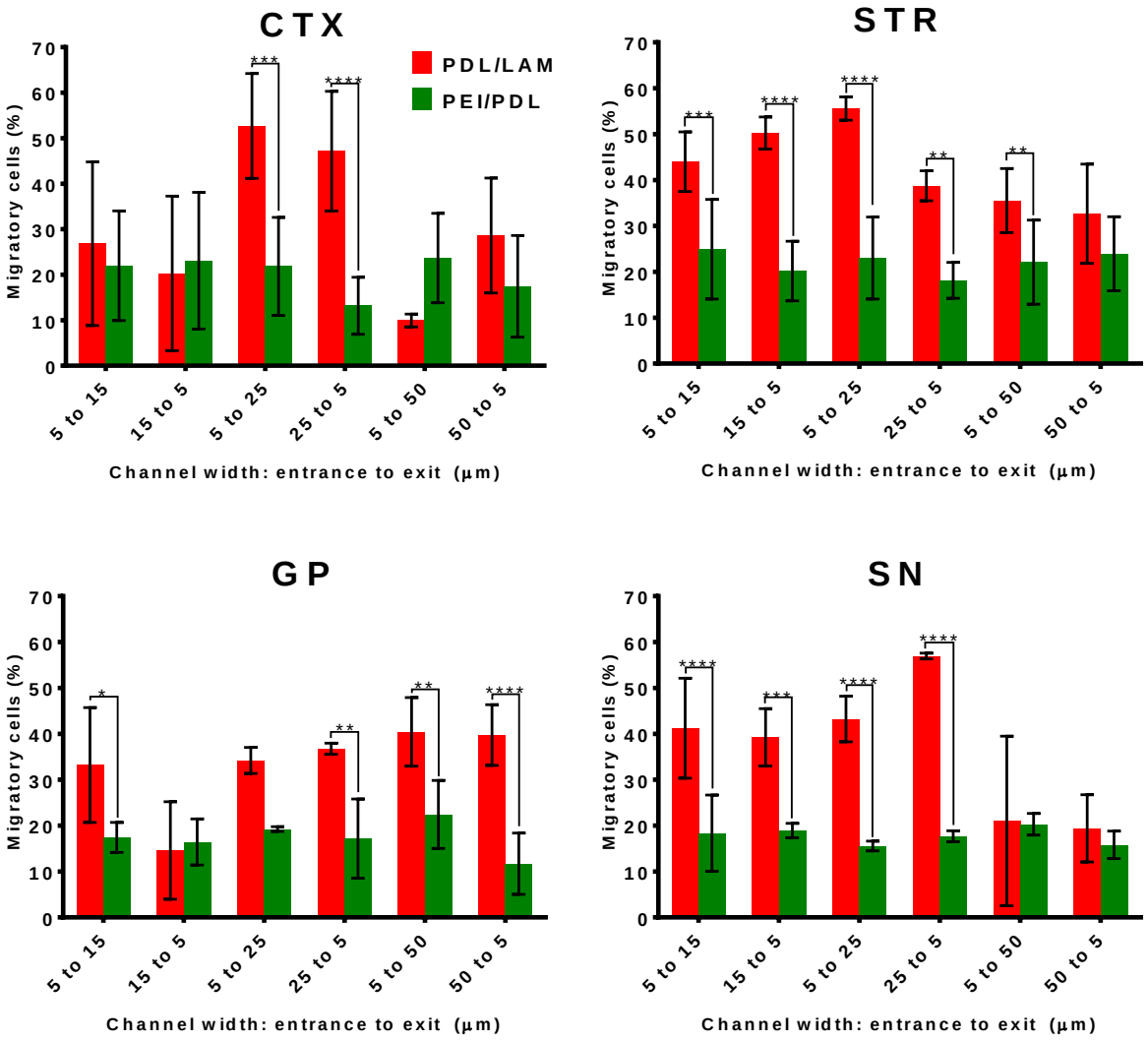

Figure 3.13: Cell migration of all four cell types when seeded into the centre port of 5PDs with different chemical coatings and different width channels. 100,000 cells were seeded into the centre port and those that had migrated into a side port were counted after 8 DIV. '5 to 15' indicates that cells had entered the 15 µm channel opening and exited the 5 µm end, and vice versa. Post hoc t-tests indicated by asterisks, compare PDL/LAM and PEI/PDL for the same width. (*): p<0.05, (**): p<0.01, (***): p<0.001, (****): p<0.0001, (n=6).

PEI/PDL vs PDL/LAM chemical coating across different channel widths had a significant effect on the percentage of cells that migrated to adjacent ports after seeding, for all four cell types (ANOVA (5,79), (CTX F=7.15, p<0.0001), (STR F=3.6, p=0.0068), (GP F=3.23, p=0.0124), (SN F=8.5, p<0.0001)). PEI/PDL coating resulted in a significantly lower percentage of migratory cells when compared to PDL/LAM coating ($p < 0.0001$). In addition, channel width did not affect migration on PEI/PDL coated devices, but smaller channel widths on PDL/LAM coated devices showed significantly more migration compared to larger channel widths, for all cell types ($p < 0.001$).

Cells seeded onto PEI/PDL-coated 5PDs consistently exhibited approx. 20% migratory cells whereas PDL/LAM coatings resulted in much higher levels of migratory cells on all channel widths, as high as 50-60% in some cases. As PEI/PDL migration was independent of channel width, this 20% may represent a baseline of near unavoidable migration regardless of the channels.

3.2.3.2 Cell monolayer morphology

In addition, cell morphology also differed between cells on PDL/LAM or PEI/PDL coated surfaces, as seen in **Fig.3.14**, with images showing cultures on differently chemically coated surfaces. Cells seeded onto PEI/PDL migrated less resulting in an even monolayer of cells, whereas PDL/LAM cells grouped together into large aggregates that extended axons to other aggregates.

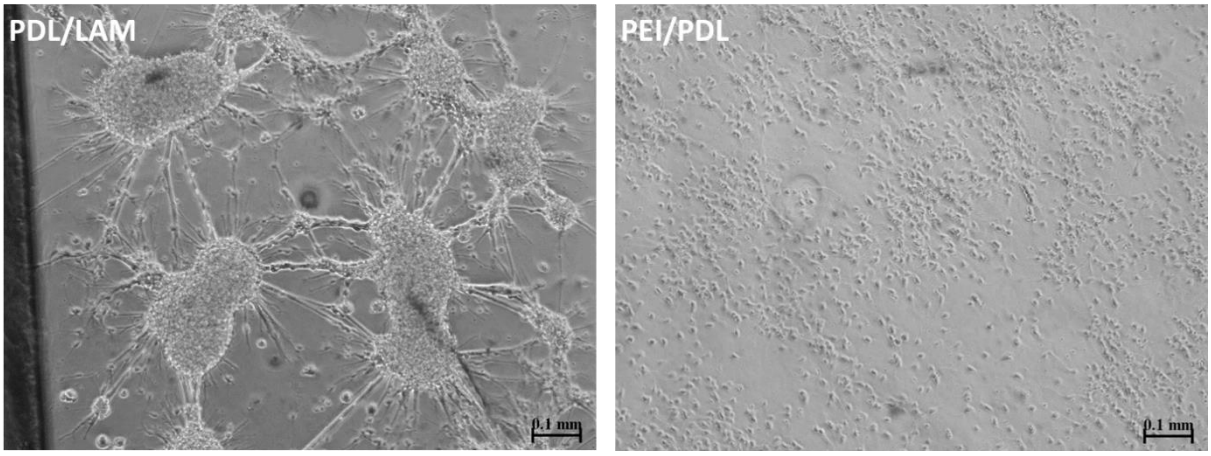

Figure 3.14: 100,000 E16 CTX cells cultured on PDL/LAM (left) or PEI/PDL (right) coated surfaces and brightfield imaged after 8 DIV. Images are representative of n=6, scale is 100 µm.

3.2.3.3 Neuronal process outgrowth

The effect of chemical coating was also tested on neuronal process (axonal) outgrowth from neuronal cells. The average number of processes per channel in 5PDs coated with PDL/LAM or PEI/PDL was calculated from fluorescent imaging from 5PDs with all three available channel widths (see **Fig.3.15**). It should be noted that for this experiment, the SN tissue was dissected at E16, an optimal developmental age for CTX, STR and GP but suboptimal for SN (peak neurogenesis at E12-14 (Gates *et al.* 2006)).

PEI/PDL vs PDL/LAM chemical coating across different channel widths had a significant effect on the number of axons extending through microchannels for CTX, (ANOVA 2,12 $F=4.3$, $p=0.039$), GP, (ANOVA 2,12 $F=13.18$, $p=0.0009$) and SN devices (SN ANOVA 2,12 $F=82.02$, $p<0.016$), not significant for STR devices ($p=0.12$). The effect of chemical coating alone on the number of axons extending through microchannels was only significant for CTX (ANOVA 2,12 $F=21.83$, $p=0.0001$) and GP devices (GP ANOVA 2,12 $F=13.58$, $p=0.0008$), while the effect of channel width alone was significant for all four cell types, an effect that is further investigated in the **Channel Directionality Assessment** section. Conditions where PEI/PDL-coated devices had significantly more processes per channel compared to PDL/LAM-coated devices (t-test, indicated by asterisks on **Fig.3.15**) were as follows: 15, 25, 50 µm channels for CTX and 15, 50 µm channels for GP, with no significant difference seen for STR and SN.

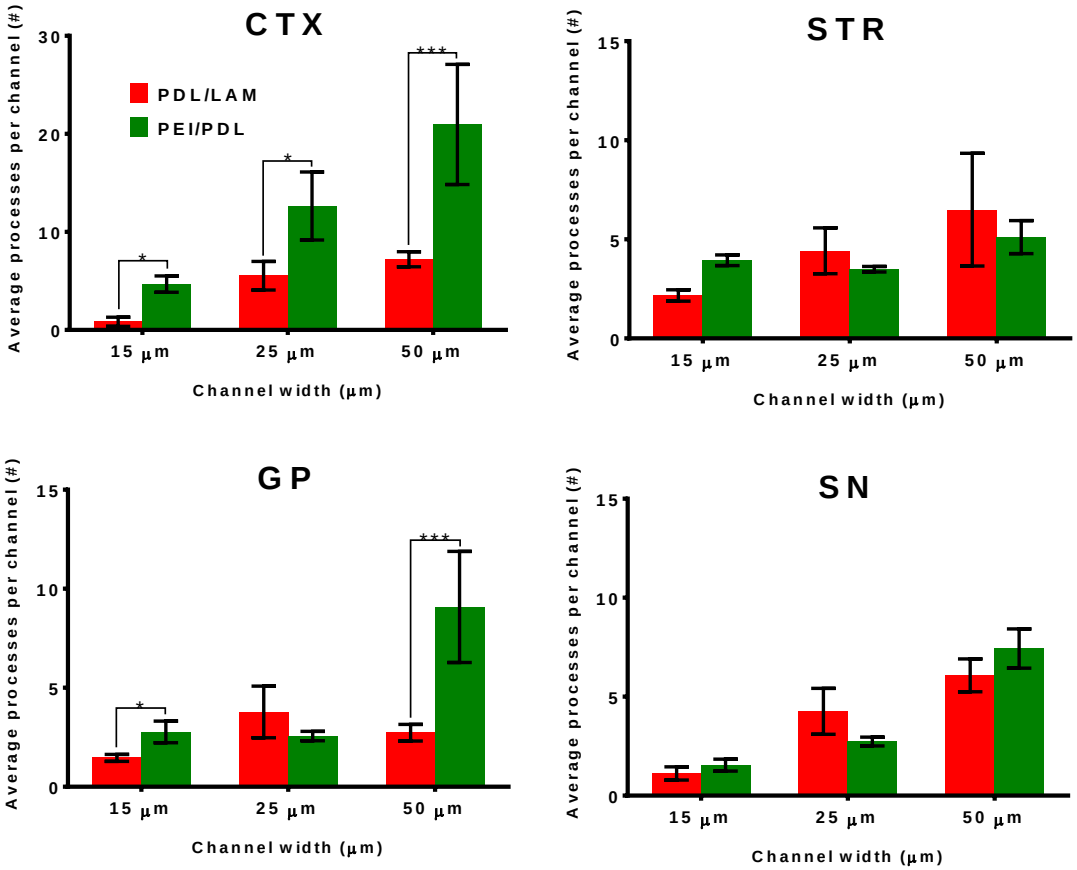

Figure 3.15: Effect of chemical coating and channel width on axonal processes per channel within 5PDs. 100,000 cells were seeded into the centre port and extended axonal processes into the side ports, which were counted and averaged per channel after 21 DIV. Post hoc t-tests indicated by asterisks, (*): p<0.01, (***): p<0.001, comparing PDL/LAM to PEI/PDL in each case, (n=4).

PEI/PDL surfaces therefore had a significant effect on the number of axonal processes produced by cells (particularly CTX and GP cells) irrespective of channel width. This combination of restricting migration while accelerating axonal process growth made PEI/PDL a clear improvement for a chemical coating over PDL/LAM.

3.2.4 Primary cell culture

CTX, STR, GP and SN cells were seeded onto one of three PEI/PDL-coated environments in order to see how the cells grew: flat featureless coverslips (as seen in **Fig.3.16**); the centre ports of 5PDs (as seen in **Fig.3.17**); and all ports of a 5PD (as seen in **Fig.3.18A**) in order to see how the cells interacted with the channels and PDMS walls, along with increased magnification views in **Fig.3.18B-C**.

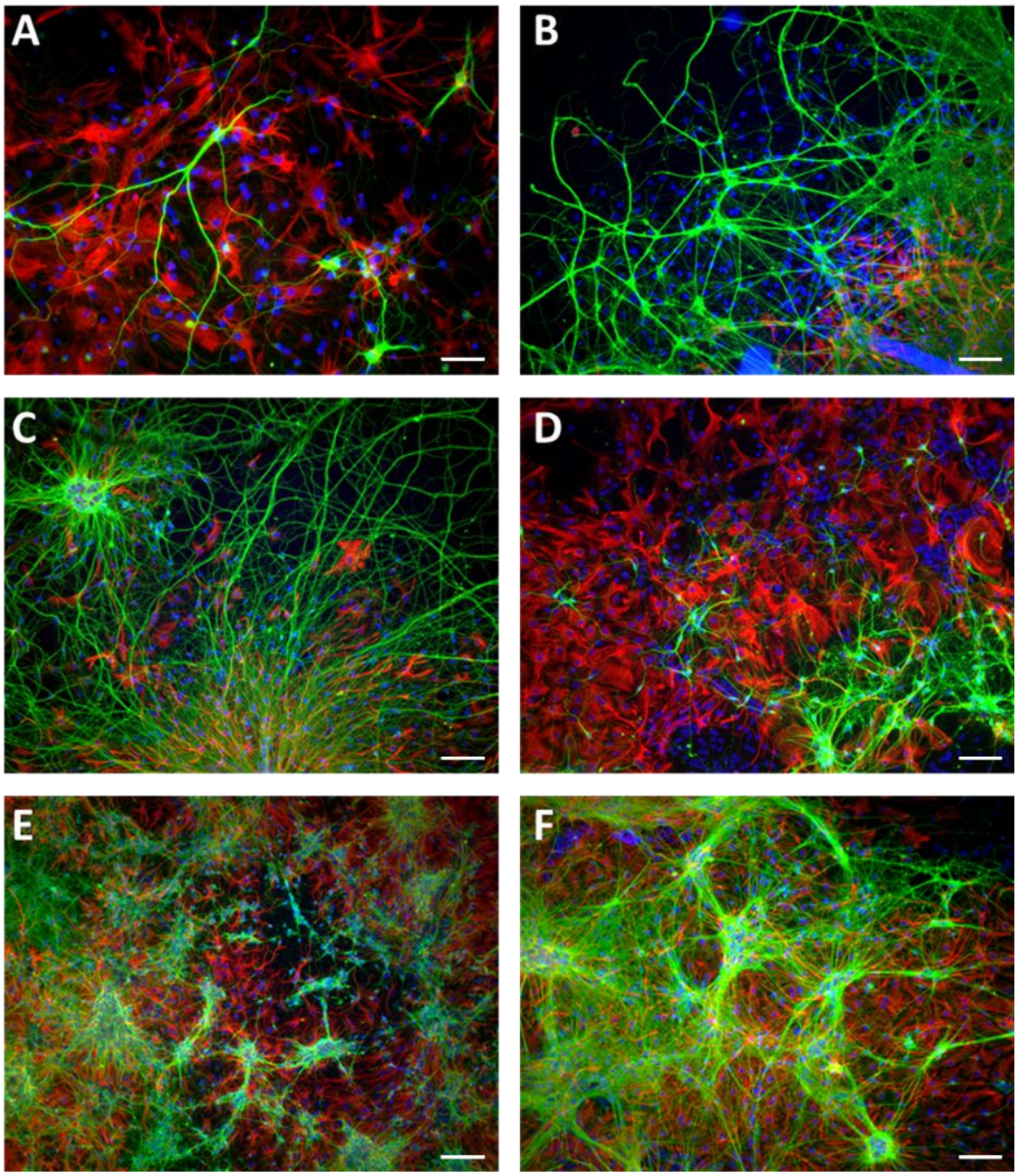

Figure 3.16: Fluorescent images of 100,000 E16 neural cells on PEI/PDL coated coverslips after 21 DIV. Blue: DAPI (marks cell nuclei), Green: β-tubulin III (neuronal marker), Red: GFAP (astrocytic marker). A and B are CTX cells, C and D are SN cells, E and F are STR cells. Scale bars are 100 µm, images representative of (n=6).

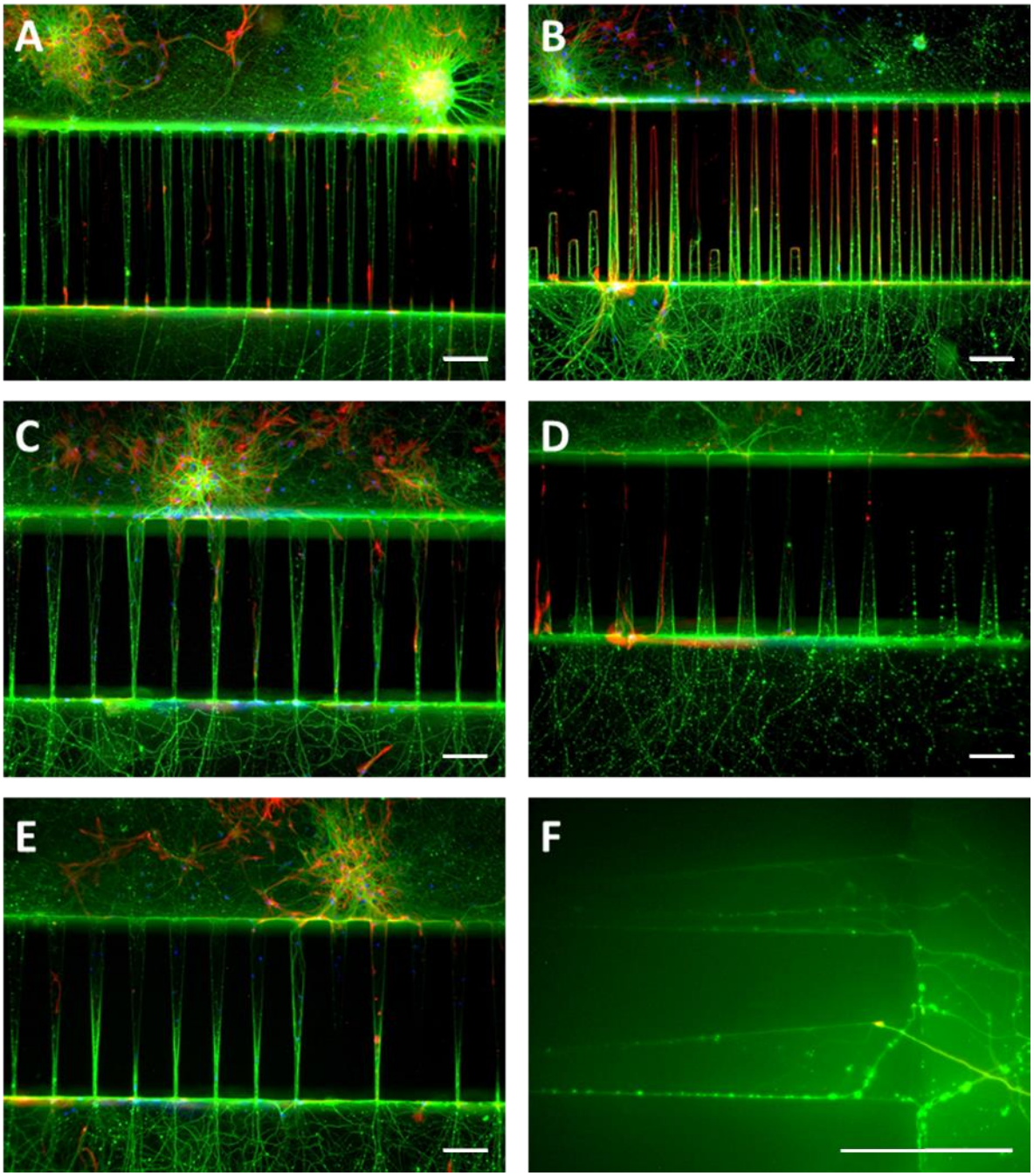

Figure 3.17: Fluorescent images of 100,000 E16 CTX cells seeded into the centre port of PEI/PDL coated 5PDs and imaged after 21 DIV. Blue: DAPI (marks cell nuclei), Green: β-tubulin (neuronal marker), Red: GFAP (astrocytic marker). Cells were seeded onto the top side of the channels in A-E, and to the left of the channels in F. Image F highlights the behaviour of axons in the PDMS channels, following the walls until the channel exit. Images are representative of n=6, scale bars all 100 µm.

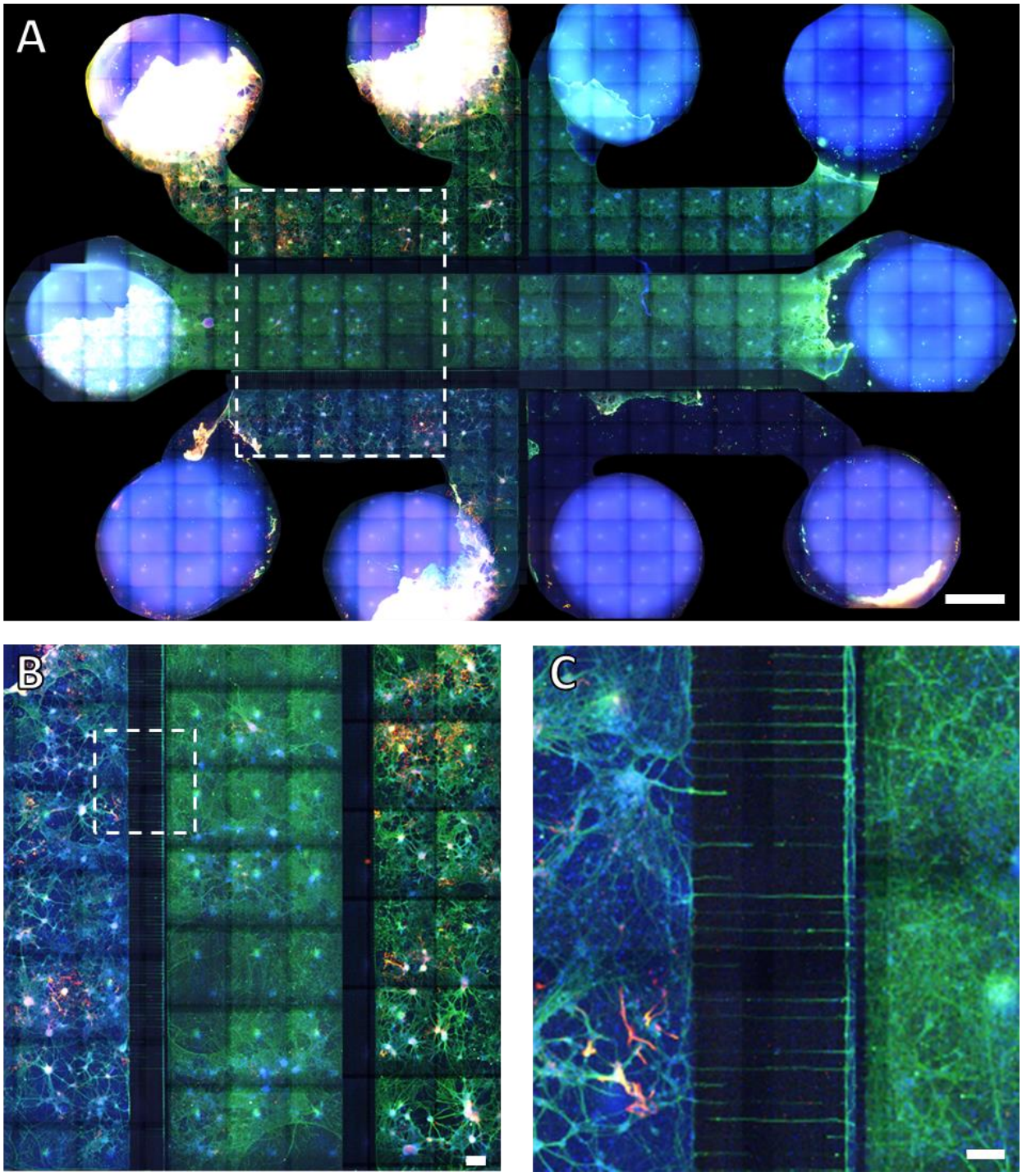

Figure 3.18: Whole 5PD imaging via an XY tile scan across an entire 5PD. A) Fluorescent image of an entire 5PD seeded with E16 CTX cells, 100,000 CTX cells were seeded into each port andimaged after 21 DIV. Image is at 10:1 scale compared to real 5PD, scale bar is 1 mm. B) Magnified view of A indicated by dashed white square on A. Shows interface between input, centre and output ports, scale bar 100 µm. C) Magnified view of B indicated by dashed white dashed square on B. Shows neurons extending into channels, scale bar is 100 µm. For all images blue: DAPI (marks cell nuclei), green: β-tubulin (neuronal marker), red: GFAP (astrocytic marker).

3.2.4.1 Rate of axonal outgrowth

The number of neuronal cell bodies and axons also differed between each cell type when the neurons are proximate to channels, shown in **Fig.3.19**.

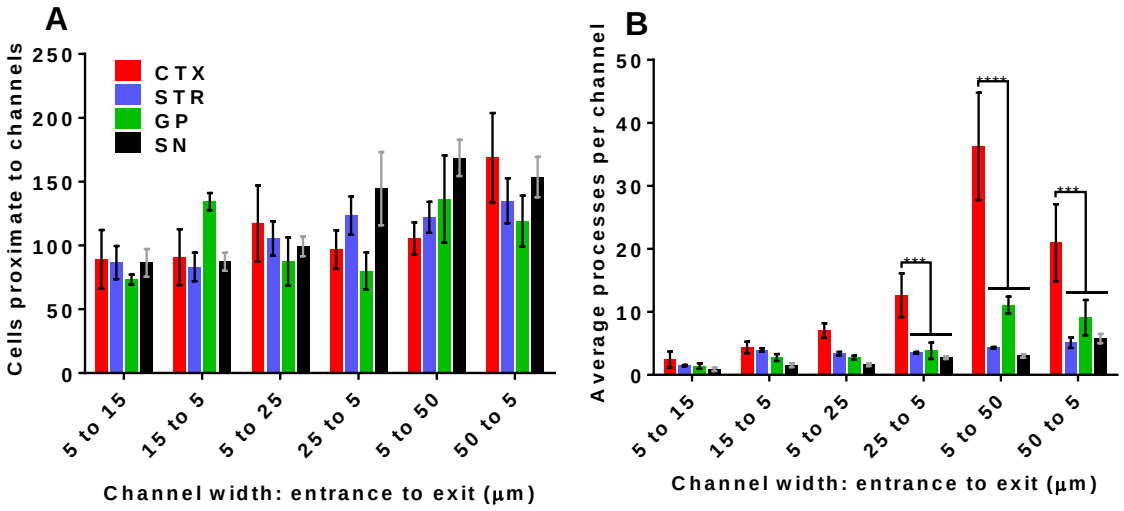

Figure 3.19: Cell number and axonal outgrowth compared between all four cell types, on all available channel widths. 100,000 E16 cells were seeded into the centre port of each device, imaged and counted after 21 DIV. A) Cells within 200 µm of channel entrances were deemed proximate, counted and averaged. B) Axons that extended the length of each channel were counted and averaged. (n=4), (***): p<0.0001, (****): p<0.00001.

Fig.3.19A showed that all four cell types had similar numbers of cell bodies within 200 µm of channel entrances, with a trend showing that more cells were proximal to larger width channels. There was a significant effect of both the channel width and cell type on the average number of cell bodies close to channels (Channel width ANOVA 5,140 $F=27.24$, $p<0.0001$), (Cell type ANOVA 3,140 $F=4.9$, $p=0.003$), showing that wider channels could accommodate more cells. Analysis also showed that there was no significant difference between the cell types on similar channel widths (t-test, no asterisk on graph)

While the number of cells proximate to each channel was the same for each cell type, the number of axons per channel was remarkably different, as seen in **Fig3.19B**. CTX neurons produced a much higher number of axonal outgrowths, with greather numbers of processes per channel compared to STR, GP and SN. There was a significant effect of both the channel width and cell type on the average number of processes per channel (Channel width ANOVA 5,48 $F=45.08$, $p<0.0001$), (Cell type ANOVA 3,48 $F=83.24$, $p<0.0001$), and CTX neurons produced significantly more processes than other cell types on 25 µm and 50 µm channels, indicating that there were more processes present in wider channels.

3.2.5 Channel directionality assessment

As previously outlined, cells seeded into the centre port of the five-port device had two options for growth, a wall of channel openings of either 15, 25 or 50 µm width, or a wall of channel openings of 5 µm width. Cells were seeded into the centre port and imaged after 21 days of growth to determine if there was any directional pressure presented by the tapered channels.

Axons and/or neurites (referred to as 'processes') that entered, travelled the entire length of the channel and exited were counted. Firstly, the number of processes per channel was compared for all three channel widths, in both channel directions, between all four cell types, as seen in **Fig.3.20**.

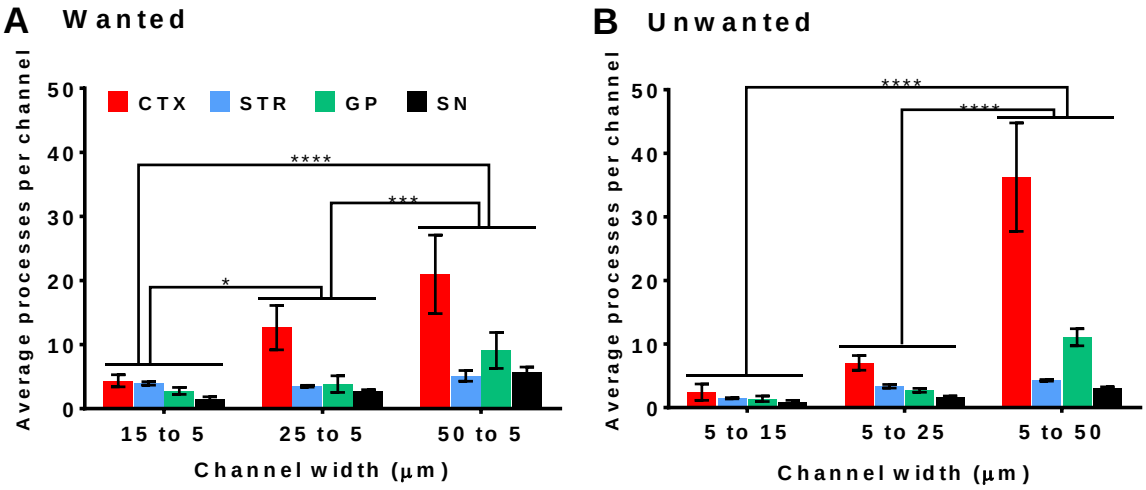

Figure 3.20: Effect of channel width (in both directions) on the number of axonal processes extending the entire length of a channel. 100,000 E16 cells were seeded into the centre port of each device and imaged after 21 DIV.A) Wanted direction of growth, through the larger end to the 5 µm end. B) Unwanted direction of growth, through the 5 µm end to the larger end of a channel, (n=4). (*): p<0.05, (***): p<0.001, (****): p<0.0001.

For the wanted direction (**Fig.3.20A**), both the channel width and cell type had a significant effect on the average number of processes per channel (Channel width ANOVA 2,24 F=30.01, p<0.0001), (Cell type ANOVA 3,24 F=31.88, p<0.0001), with each channel width resulting in significantly different numbers of processes per channel (see asterisks on **Fig.3.20A**).

For the unwanted direction (**Fig.3.20B**), both the channel width and cell type also had a significant effect on the average number of processes per channel (Channel width ANOVA 2,24 F=77.2, p<0.0001), (Cell type ANOVA 3,24 F=51.73, p<0.0001), with 5-50 µm channels containing significantly more processes than 5-15 µm and 5-25 µm channels (see asterisks on **Fig.3.20B**). These data suggested that the only channel dimensions that can control axonal outgrowth are 5-15 µm channels, as in all other channel sizes CTX and GP extend in undesirable directions more, while STR and SN are seemingly unaffected by channel size.

5-15 µm was the only channel width that exerted any directional pressure on axons, by having more axons that extend in the wanted direction (larger to smaller, 15 µm to 5 µm) than the unwanted direction (smaller to larger, 5 µm to 15 µm). The number of axons that travelled in the desirable direction were divided by the number that travelled in the undesirable direction, to generate a directionality ratio (seen in **Fig.3.21)**.

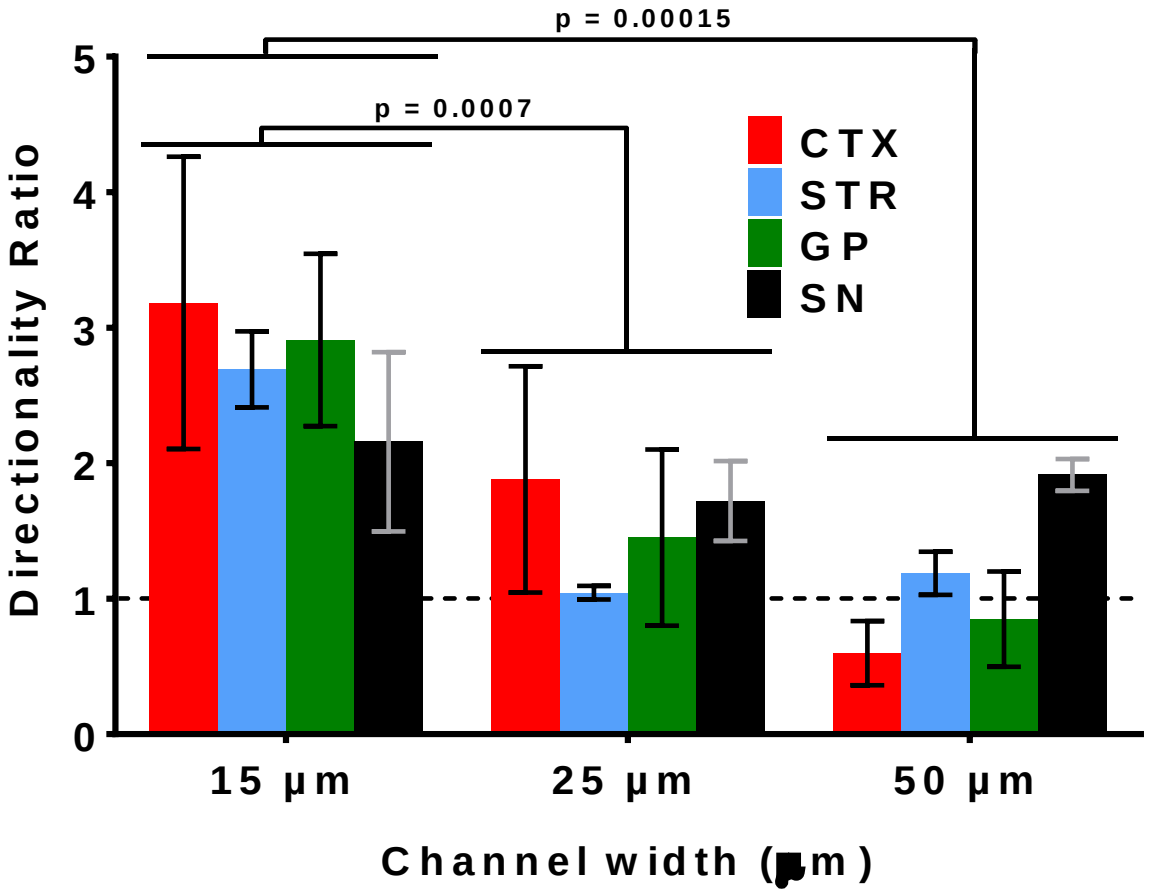

Figure 3.21: The directional pressure exerted by channels of different widths, for all four cell types, based on data from Fig.3.20 (n=4). A directionality ratio of 1 means that a channel exerts no pressure on the direction of axonal growth (indicated by the dashed horizontal line), whereas values >1 mean a directional pressure in a wanted direction, and values <1 mean a directional pressure in an unwanted direction. P values generated from post hoc t-tests.

While the effect of cell type on the directionality ratio was insignificant (ANOVA 3,24, F=0.55, p=0.65), the effect of channel width on directionality ratio was extremely significant (ANOVA 2,24, F=28.49, p<0.0001). Multiple comparisons also show that there were significant differences between 15 µm vs 25 µm and 15 µm vs 50 µm, but not between 25 µm vs 50 µm. These data and analysis showed that 15 µm channels present the best directionality ratio, with anything over 1 exerting directional pressure in the desirable direction. Despite the ability of larger channels to contain more axons and therefore potentially direct a greater number of cells into contact with adjacent ports, larger width channels exerted less directional pressure on the cells, when compared to 5-15 µm channels.

3.3 Discussion

3.3.1 Chemical coating

Cells seeded onto PEI/PDL coated surfaces exhibit decreased migration on both coverslips and 5PDs when compared to PDL/LAM coated surfaces, making PEI/PDL a preferable surface coating, with PEI used widely in the literature (Ruegg and Hefti. 1984, Bledi *et al.* 2000, Vancha *et al.* 2004, B. Liu *et al.* 2008, Takayama *et al.* 2012, Kanagasabapathi *et al.* 2013). Cell bodies that migrated fully down channels into adjacent ports caused contamination between neuronal subtypes, such as CTX cells entering the STR port. By coating cell growth surfaces with chemicals with high density positive charges that physically restrict cells from migrating allowed for a more accurate model, in which cells stayed where they were seeded and extended axons into adjacent ports as intended. PEI is a synthetic polymer, designed to have a much greater density of positively charged branches than PDL or laminin, and as such it is far more attractive to the primary cells, which exhibit a negative charge on their cell surface membrane (Jeong *et al.* 2001). PEI was more suitable to restricting cell migration, with PEI/PDL coated surfaces significantly reducing cell migration when compared to PDL/LAM coated surfaces (**Fig.3.12 and 3.13**).

Despite these properties, cells seeded into the centre port of PEI/PDL coated 5PDs were still found in adjacent ports (approx. 25% of cells were determined as being migratory in 5PDs, as seen in **Fig.3.13)**. Upon further inspection, these cells did not migrate into adjacent ports after attaching to the surface but were sucked into channels by capillary action immediately after seeding into ports, when the cell bodies were still in solution. PEI/PDL surface coating only functioned as a means to inhibit migration once the cell bodies came into physical contact with the surface, if the cells moved in suspension above the coated growth surface without encountering it, no feasible coating was able to further restrict cells travelling to adjacent ports, especially STR cells, which were seeded into the centre port and had double the number channels to be drawn into via flow. The only way to fully contain all cell bodies in the port they were seeded into would be a form of gated channel, where the channel ends are blocked during seeding until the cells are all attached to a surface, upon which time the channels are opened to allow axonal outgrowth. This kind of channel design is possible with PDMS, seen in the development of “lifting gate” microvalves combined with pumps in order to have a channel that can be opened and closed with pressure (J. Kim *et al.* 2012), along with numerous other applications of pumps in PDMS devices (Kartalov *et al.* 2006). Despite these limitations, PEI/PDL coating still served as the best means to restrict migration, in comparison to PDL/LAM.

In addition to these migration-restricting qualities, PEI/PDL coated surfaces also resulted in neurons producing a greater number of axonal processes compared to PDL/LAM coated surfaces (see **Fig.3.15**), an effect also observed in retinal explants (Vancha *et al.* 2004). This factor was also related

to axonal length: an axonal process was only counted and recorded once it had fully travelled the length of a channel and emerged into an adjacent port. There may be a situation where there were equal numbers of axonal processes per channel between PEI/PDL and PDL/LAM coated surfaces, but if the axons on PDL/LAM were shorter, they may have entered the channel but never traveled the full length and not emerged on the other side, and thus not be recorded. With this in mind, it was more accurate to say that PEI/PDL coated surfaces resulted in a greater number of axonal processes per neuron, and/or axonal processes of a greater length overall (Ruardij *et al.* 2000, Sun *et al.* 2012). As these were both positives when constructing a neural circuit *in vitro*, PEI/PDL coated surfaces were superior compared to PDL/LAM regardless of the specific effect the surface had on neurons. With these results in mind, PEI/PDL was used as the preferential surface chemical coating for the rest of the project.

3.3.2 Characterising specific neural subtypes

The fact that every cell type stained for the proteins they should have specifically stained for indicated that the dissection protocol was robust and could be relied upon for the length of the project. As the CTX and SNc were the only sources of excitatory glutamatergic and modulatory dopaminergic nuclei respectively in this experiment, they were the only ones to stain positive for the glutamatergic neuron marker VGLUT2 and dopaminergic neuron marker TH respectively. It should be noted that on occasion dopaminergic neurons have co-expressed GABAergic or glutamatergic markers, but as these cells are such a rarity (< 1%) and are found mostly in other areas of the midbrain than the VM, this was not a concern (Nair-Roberts *et al.* 2008).

Characterising STR and GP neurons was more challenging, as they are both inhibitory GABAergic nuclei, and indeed even CTX and SN contain populations of GABAergic neurons (as seen in the GABA staining in **Fig.3.8B** and **Fig.3.9**), as does most of the brain (Mallet *et al.* 2006, Wonders *et al.* 2008, Ellens and Leventhal. 2013). Staining for GABA resulted in similar intensities between STR and GP (as seen in GABAergic proportions **Fig.3.8B**), and a more specific marker was necessary. The phosphorylated form of the amino acid tyrosine (phosphotyrosine) has been shown to be present in the GP (Moss *et al.* 1990, Nagao *et al.* 1998), and this was used as a marker to differentiate GP from STR.

The decreased number of DA neurons with increasing developmental age (**Fig.3.11B**) may not have been a significant reduction, but the difference was still present due to the fact that peak neurogenesis of SNc dopaminergic neurons is closer to E12 than E14 (Gates *et al.* 2006), despite earlier studies suggesting that E14 represents the peak. By E14, dopaminergic neurons in the SNc were projecting axons (> 1 mm at this time point) and innervating the ventral forebrain, consequently by dissecting at this age (or later) these axonal outgrowths and early input-output connections were severed, resulting in a damaged cell population and reduced viability. By dissecting earlier at E12, DA

neurons and neural precursors are still isolated to the SN, resulting in a cleaner dissection, a more viable culture, and a greater number of dopamine neurons *in vitro* (Gates *et al.* 2006, Hegarty *et al.* 2013), with Gates *et al* noting that up to 80% of SNc DA neurons are generated on E12 in Sprague-Dawley rats.

As the neurons in these cultures do not typically proliferate while glial cells do (Anda *et al.* 2016), each culture carried a chance of being overtaken by glial cells as they proliferated while neuron numbers remained relatively static. While the initial SNc neuron:astrocyte ratio was approx. 25:75 after 1 DIV, it had changed to 40:50 after 4 DIV, showing how rapidly astrocytes could proliferate (see **Fig.3.11A**). After 4 DIV, CTX, STR, GP and SNc all exhibited a neuron:astrocyte ratio of approx. 40:50 (see **Fig.3.10**), consistent with the literature (S. H. Chen *et al.* 2013, Y. Huang and Wang. 2016), with the remainder consisting of cells with only DAPI staining (most likely microglia or oligodendrocytes). A visual representation of the neuron:astrocyte ratio at a later date (8 DIV) shows that the ratio is reasonably static, with healthy neurons extending on top of the layer of astrocytes (see **Fig.3.16**).

3.3.3 Channel directionality assessment

The ability to direct axonal outgrowth in one main direction was vital for producing this *in vitro* BG model, and as such having an optimised channel width allowed for more efficient communication between ports.

Axonal growth in channels was directed mostly by the walls of the channels, with cell bodies remaining in ports and extending axons into empty space until they came into contact with neuron cell bodies, glial cells, other axons, or a PDMS wall/channel. Axons rarely extended straight from a neuron into a channel, with the majority of axons following the PDMS wall into the channel until the channel exit (see **Fig.3.17F**). This affinity of axons to grow along PDMS walls may have been due to PDMS being a softer material than glass, with neural cells showing a preference for softer substrates (Balgude *et al.* 2001, Lantoine *et al.* 2016).

Axons that grew and encountered other axons used them as guidance cues. In this process, (termed fasciculation), axons arrange themselves into large bundles. Due to the confining nature of the channels, fasciculation appeared to occur often within the channels, the axons adopting this behaviour when forced into a smaller space containing many other axons (Francisco *et al.* 2007, Honegger *et al.* 2016, Renault *et al.* 2016). This sudden reduction in size of the immediate cell physical microenvironment was mostly encountered when an axon extended from a port into a channel, where the channels were many magnitudes smaller than the ports. However, this decrease in size also occurred when axons were growing into the wider entrance of tapered channels, where the gradually decreasing size of the channel from 50 µm, 25 µm or 15 µm to 5 µm encouraged the axons to fasciculate into a bundle, and thus when exiting the channel the axonal bundle unraveled (see

Fig.3.17A-E). This unravelling of axonal bundles at channel exits resulted in a high density of axons proximate to the channel exits (see **Fig.3.19B**) and consequently a high likelihood of these axons encountering adjacent cell populations, which were also proximate to channel exits (see **Fig.3.19A**). This combination of fasciculation and softer PDMS lead to the presence of many axons within channels of any size.

Each channel could accommodate many axons, and wider channels contained greater number of axons due to increased physical space (see **Figs.3.15, 3.19 and 3.20**). However, the ability to contain a greater number of processes did not appear to guarantee a directional pressure, with a greater number of axons growing in an unwanted direction in 5-50 μm channels (see **Figs.3.20 and 3.21**). Wider 5-25 μm and 5-50 μm channels provided poor directionality ratios, with 5-25 μm appearing to have little influence on directionality and 5-50 μm selecting for the unwanted direction for CTX and GP neurons (see **Fig.3.21**), unacceptable factors when designing a model that aims to reproduce unidirectional BG circuitry. It is unclear exactly why these wider channels had lower directionality ratios, as the 5 μm entrance was identical between each channel size (as assessed with SEM, see **Fig.3.6**) and the width simply increased at a different rate once past the entrance. One theory is that the axons may have been able to sense the channel dimensions before entering the channel, maybe due to an increase in the concentration of certain biochemical factors or the differing capillary action between devices with different channel widths. Another consideration is the wall to channel ratio: because all three model designs have the same number of channels that are the same distance apart (from channel centre to channel centre) but differing channel widths, there is a greater length of PDMS wall between 15 μm channel openings than between 50 μm channel openings. This differing wall to channel ratio is important for axonal guidance, as axons that come into contact with a wall will extend along the wall and into the channel entrance, whereas axons that enter directly into a channel have less contact guidance cues. In this manner 15 μm channel openings present axons with more walls and therefore more guidance into channels, potentially leading to a greater directional pressure. Regardless, the data indicated that only the 5-15 μm channel exerted positive directional pressure on the cells.

It should be noted that as all cell types were taken at E15/16, SNc cells naturally grew at a decreased rate when compared CTX, GP and STR cells, due to the best developmental age to take SN cells being E12-14 (Gates *et al.* 2006). In subsequent experimentation cells were dissected at their optimum developmental stage, as the end goal was to culture all the cell types together in a single device, creating an *in vitro* BG mimic.

The microfluidic device supported culture of different sub-types primary neuronal cells, as well as exerting control over the orientation of axons through micro grooves. The aims of this chapter were achieved, with the optimal chemical coating for circuit formation being PEI/PDL, and the optimal

channel widths to control the directionality of axonal outgrowth were 15-5 µm channels. Primary neural cultures obtained from rat were successfully characterised. This optimisation work was carried through the rest of the project, with all subsequent dissections following the same protocol, seeded onto PEI/PDL-coated surfaces, and when 5PDs were used they had 15-5 µm channels.

3.4 Conclusions

In summary, there were many factors to optimise when designing a microfluidic *in vitro* model of the BG. After the experiments laid out in this chapter, the following can be concluded: The current fabrication protocol for the 5PDs was sufficient to create reproducible features down to 5 µm in size; all future 5PD and cell experimentation should involve a PEI/PDL coating as it inhibits cell migration while promoting axonal outgrowth; current dissection protocols were sufficient to extract the relevant neural sub-types in physiologically relevant proportions; and all future 5PDs should feature 5 µm to 15 µm channel dimensions, as these best exerted directional pressure on axonal outgrowth and allowed for the formation of a unidirectional circuit. By using these optimised and tested factors, the model functioned more efficiently when mimicking the *in vivo* BG.

Recreating the compartmentalisation and connections of the BG nuclei *in vitro* would result in a powerful pre-clinical research platform. This study set out to assess the design and fabrication of a novel compartmentalized microfluidic device intended to serve as such a model. This study also demonstrated the benefits of microfluidic devices compared to other cell culture systems, e.g. conventional well plates and flasks. Microfluidic devices offer design flexibility, due to their template design via AutoCAD, to address specific challenges. The microfluidic model presented here provides a foundation, and first steps towards developing complex circuitry that can potentially be used to model neurodegenerative diseases such as Huntington and Parkinson's diseases *in vitro*.

Chapter Four: Long term study of separate neural culture functionality

4.0 Introduction

In order to determine if this *in vitro* model of the basal ganglia (BG) was functional, it was vital to record the spontaneous electrophysiological activity of the cells in culture, at every stage of their growth and maturation. Only if it can be determined that the neurons were in communication with each other as they are *in vivo*, then the model could be characterised as functional.

Continuing from the outline of electrophysiology in **Chapter One**, this Chapter provides further detail on the spontaneous electrophysiological activity of each of the relevant neural cell types from the nuclei of the BG: the cortex (**CTX**), striatum (**STR**), globus pallidus (**GP**) and substantia nigra (**SN**). This activity compared *in vivo* to *in vitro* findings and to extracellular recordings, as the recording method of choice for these experiments was a multi-electrode array (MEA), which recorded the spontaneous extracellular electrophysiological activity from an entire culture across the long term.

4.0.1 Typical electrophysiology of basal ganglia nuclei

It should be noted that neurons of the GPe, GPi, STN and SNr are autonomous pacemakers, allowing for control of BG activity via the output nuclei, GPi and SNr (Gerfen and Surmeier. 2011). All of the cell types within the BG feature differences in spiking frequency, bursting and duration of activity.

4.0.1.1 Cortex (CTX)

Corticostriatal glutamatergic projection neurons can be intratelencephalic (IT, projecting within the telencephalon) or pyramidal tract-like (PT); form all across the CTX (conveying information from somatosensory (Sippy *et al.* 2015), auditory (Znamenskiy and Zador. 2013) and visual (Reig and Silberberg. 2014) cortical regions); and project to all parts of the STR (the STR being unique as the only subcortical area to receive both IT and PT input projections), making a summary of CTX electrophysiological activity difficult due to the scope (Shepherd. 2013).

Briefly, IT and PT neurons have several different electrophysiological properties: PT neurons have more hyperpolarisation-activated currents compared to IT neurons, PT neurons have faster spiking compared to IT neurons, and PT neurons feature a sustained/accelerating repetitive spiking pattern while IT neurons feature a phasic/adapting repetitive spiking pattern (Shepherd. 2013). These excitatory neurons also differ from the GABAergic interneurons they share the CTX with, with studies showing that the GABAergic interneurons feature short-duration spikes compared to longer-duration

in CTX glutamatergic neurons. These differences can be detected with either intra- or extracellular recording methods by observing the different waveforms and have been used to differentiate between fast-spiking interneurons and PT neurons in the CTX when measured extracellularly (Mitchell *et al.* 2007).

4.0.1.2 Striatum (STR)

The GABAergic medium spiny projection neurons (MSNs) that make up 90% of the STR fire sparsely, requiring coordinated excitatory synaptic input from the CTX to initiate spiking. Both the D1 and D2 type MSNs display largely similar electrophysiological properties with no significant difference in cell capacitance, baseline, input resistance or action potential (AP) amplitudes (Cepeda *et al.* 2008). The only significant difference is that D2 neurons are more excitable, being less depolarised than D1 neurons and having a lower threshold for firing. In addition, both D1 and D2 neurons react with strikingly different electrical patterns upon both dopamine treatment, with dopamine binding to D1 or D2 receptors resulting in stimulation or inhibition of the post-synaptic neuron respectively (Crittenden and Graybiel. 2011). These differing patterns are also observed during dopamine depletion (Orr *et al.* 1987). It should be noted that these MSNs are the only output system of the STR, the remaining 10% of fast-spiking interneurons do not project to other BG nuclei (Ellens and Leventhal. 2013).

In vitro, STR neurons have displayed both regular, irregular and burst firing, a burst being a group of spikes that register ≥10 Hz and cannot be measured as individual spikes but instead as a cluster, with MSNs shown to have an important role in bursting and correlating burst firing for information processing in the BG (B. R. Miller *et al.* 2008). Notably, the cholinergic interneurons of the STR are endogenously active and will spontaneously generate spiking activity without synaptic input, indistinguishable to their activity *in vivo*, suggesting that irregular spontaneous spiking in the STR may be responsible for endogenous activity (Bennett and Wilson. 1999). This activity is likely linked to spontaneous and driven activity from CTX inputs, resulting in STR interneurons and MSNs having temporal signatures *in vivo*, dependent on CTX activity. Indeed, *in vitro* MSNs show exaggerated glutamate-dependent responses (the main glutamatergic inputs to the STR being the subthalamic nucleus (STN) and CTX), more depolarized resting membrane potentials, reductions in potassium (K^+) currents and increased intracellular Ca^{2+} levels, when compared to MSNs *in vivo* (Ariano *et al.* 2005, B. R. Miller *et al.* 2008).

MSNs grown in organotypic cultures show similar morphological and electrophysiological characteristics similar to those seen *in vivo* (Plenz and Kitai. 1998, Sharott *et al.* 2012), this similarity between *in vivo* and *in vitro* electrophysiological properties is reassuring for the development of the *in vitro* BG model. With this consideration, MSN and interneurons *in vitro* likely generate similar firing rates to *in vivo* MSNs and interneurons, with the *in vivo* rates being approx. 0.01-2.0 Hz for MSNs

(B. R. Miller *et al.* 2008) and 10-20 Hz for interneurons (also termed fast-spiking neurons or FSNs) (Gage *et al.* 2010) *in vivo*, with the STR as a whole recorded at 0.7 Hz (Walters *et al.* 2007). This range has been corroborated by *in vitro* extracellular recordings of STR neuronal cultures, which identified two separate modes of electrophysiological activity: phasically activated neurons (PANs) with broad APs and low spike frequency (0.5-1 Hz) and tonically active neurons (TANs) with higher spike frequencies (5-15 Hz). The majority of TANs were found to be cholinergic interneurons which fire in a synchronised pattern without oscillation, these interneurons make up 5-20% of the STR, meaning that the source of PAN activity are MSNs, which consist of the majority of the STR (Boraud *et al.* 2002). With these results in mind, STR neural cultures on MEAs should achieve approx. 0.5-2 Hz spike frequency on average if MSNs are in contact with electrodes, with higher frequencies generated by cholinergic interneurons.

4.0.1.3 Globus Pallidus (GP)

While the internal (GPi) and external (GPe) sections of the GP are near structurally identical, both composing of a majority of GABAergic neurons, they are functionally distinct with different firing properties *in vivo*.

GPi neurons exhibit high frequency spontaneous activity without pauses and can burst at very high rates, features that are enhanced by dopamine depletion (Bergman *et al.* 1994, Kliem *et al.* 2007, Nambu. 2007). BG output neurons (GPi and SNr) both exhibit high levels of spontaneous activity even in anesthetised rats, with GP and SNr firing at 26 Hz and 24 Hz respectively (Walters *et al.* 2007).

GPe neurons tend to synchronise to local field potentials (LFPs), namely the sum of electric activity of multiple neurons within a proximate area (Flandin *et al.* 2010, Mallet *et al.* 2012). In addition, two electrophysiologically heterogenous populations of GABAergic cells exist within the GPe *in vivo*, namely the GPe-TI and GPe-TA, named for firing during the inactive (TI) and active (TA) components of CTX slow wave activity oscillations respectively. GPe-TI neurons make up ~75% of spontaneously active GPe neurons, express parvalbumin and project downstream to the SNr, GPi and STN, firing in antiphase with the latter. GPe-TA neurons make up ~20% of spontaneously active GPe neurons, express preproenkephalin, project upstream to STR MSNs and interneurons, and fire in phase with STN neurons. Thus, the GPe consists of two interacting systems that work together to co-ordinate activity across the BG in a cell-type-specific manner (Mallet *et al.* 2012, Nevado-Holgado *et al.* 2014). However, in our *in vitro* model, GP cells will be first studied in isolation, and then with a connection to STR cells, meaning that this response to CTX activity oscillations will be unobservable as the two cell populations were not connected, although a response to the LFP should still be seen.

In vivo recordings note that single GP neurons can typically fire at high frequencies (15-45 Hz) in a tonic manner and oscillate with other GP neurons at similar (20 Hz) frequencies, but populations of

GP neurons can also generate slow wave activity, which ranged from 0.4-1.6 Hz (Mallet *et al.* 2006, Mallet *et al.* 2008, Mallet *et al.* 2012). However, these values were dependent on input and output signals from the *in vivo* brain and by taking extracellular recordings from GP in isolation *in vitro* the results are likely to differ.

Extracellular recording identifies GPi neurons with random yet high frequency spiking with little oscillation or synchronisation. GPe neurons display regular and irregular spiking alongside bursting and discharging activity (Boraud *et al.* 2002). These GPe neurons show a lower frequency of spiking than GPi neurons, but more bursting and more pauses, occasionally pausing for up to 500 ms between bursts (signifying inactivity or a quiescent period).

Due to our dissection protocol taking the GP as a whole (by dissecting the medial ganglionic eminence at E16 in the rat), in our MEA experiments there will likely be a mix of high-frequency firing from GPi neurons and lower-frequency firing from GPe neurons (both GPe-TI and GPe-TA functional types), lower than their *in vivo* firing frequencies of approx. 15-45 Hz and also featuring 0.4-1.6 Hz slow wave activity.

4.0.1.4 Substantia nigra (SN)

In a conscious rodent *in vivo*, SNr GABAergic neurons feature spontaneous high frequency, short duration firing (~1 ms and 25-30 Hz) enhanced by dopamine depletion (Bergman *et al.* 1994, Maurice *et al.* 2003, Kliem *et al.* 2007). Conversely, SNc DA neurons *in vivo* show low frequency, pacemaker long-duration firing (~2.5 ms and 1-4 Hz) (Boraud *et al.* 2002, F. M. Zhou and Lee. 2011). The SNc DA neurons also feature frequent bursting, both spontaneous and reward-related, even in anesthetised animals *in vivo.* These bursts are followed by a slow after-hyperpolarisation and a pause in spontaneous firing, but it should be noted that these subsequent activities have been found to be due to different mechanisms (Morikawa and Paladini. 2011).

In *in vitro* preparations, firing frequencies are lower, with GABAergic SNr neurons at 10-15 Hz and DA SNc neurons at ~2 Hz (S. Ding *et al.* 2011, Lee *et al.* 2011). GABAergic SNr neurons also have a more negative threshold and a larger spike amplitude (F. M. Zhou and Lee. 2011). The regular firing at low frequencies allows for maintenance of dopamine levels in the STR, and consequently this firing is heavily regulated by upstream processes outside the BG (S. Hong *et al.* 2011, Beeler *et al.* 2012). The low-frequency oscillations of SNc DA neurons identify them as robust autonomous pacemakers, as they maintain this activity even in the absence of spiking, leading to the rhythmic background of firing necessary for sustained release of dopamine in the BG (Guzman *et al.* 2009).

Extracellular recordings of SNr neurons show a similarity to GPi, displaying random yet high frequency spiking with little oscillation or synchronisation. Extracellular recording of SNc DA neurons have identified triphasic spikes, where the spike waveform oscillates from positive-negative-positive

voltage, forming three phases in the waveform. These spikes have a long duration (2-5 ms) and slow spiking frequency (0.5-10 Hz) (Boraud *et al.* 2002). As our GP preparations, in our MEA experiments the SN will be taken as a whole (by dissecting the ventral midbrain from E14 rats), resulting in SN MEAs recording high-frequency SNr activity along with lower-frequency SNc firing. As these firing frequencies are lower *in vitro* compared to *in vivo*, we should expect approx. 10-15 Hz from SNr neurons and ~2 Hz from SNc neurons.

4.0.2 Extracellular recording

While neural electrophysiology was classically performed with patch-clamping and inserting electrodes into cells for precise intracellular measurements, these techniques are unsuitable for recording across a whole cell culture or co-culture over the long term. An alternative comes in the form of extracellular recording, markedly different to intracellular recordings with the latter being monophasic and usually displaying a higher amplitude by several orders of magnitude, as seen in **Fig.4.1**. Extracellular recording allows recording from neurons without impaling them with microelectrodes, resulting in the ability to record from vast numbers of cells over the long term, where neurons can be characterised based on their activity in isolation and connectivity, as well as during maturation. This allows for data with high spatial and temporal resolution as many electrodes can be deployed at once, such as with the multi-electrode array (MEA).

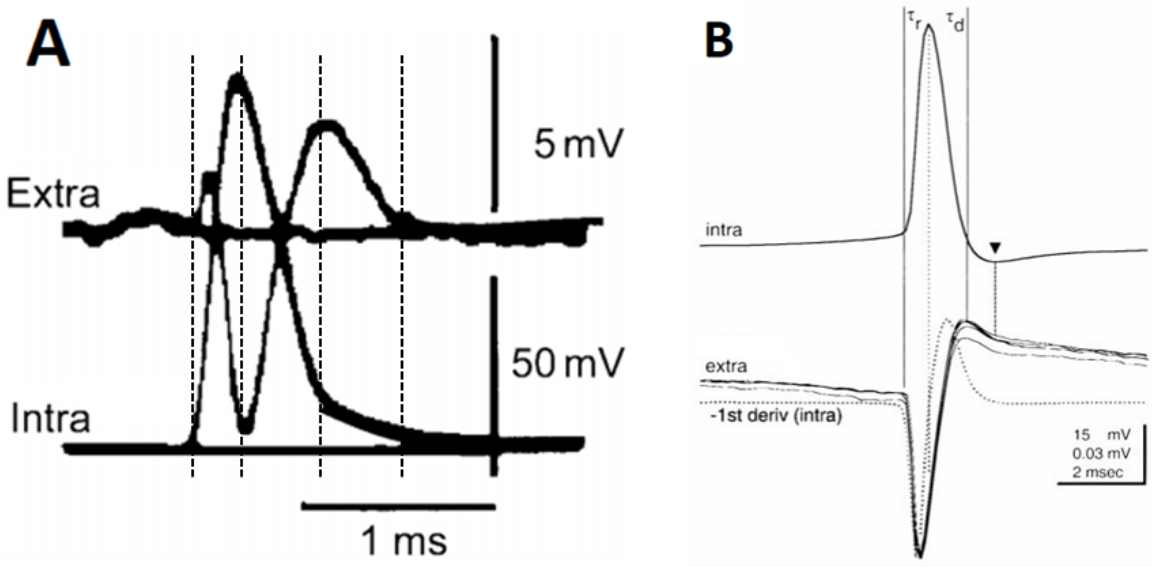

Figure 4.1: Simultaneous intra- and extracellular recording of an action potential. A) The four dashed vertical lines show synchronisation of intra- and extracellular signals at four points: onset, peak, phase change and return to baseline, recorded from a cat ventral horn motoneuron. Image adapted from (Terzuolo and Araki. 1961). B) Average of 849 intra- and extracellularly recorded spikes. τ_r and τ_d indicate rise and decline phases of intra signal which closely align to extra signal, along with the peaks of both signals. The extra signal is also compared to the 1st derivative of the intra signal (dotted trace), which matches closely on the initial negative phase and mismatches at later phases, but rematches at the point of late phase change, indicated by the black triangle. 15 mV scale corresponds to intra, 0.03 mV scale corresponds to extra, time corresponds to both. Recorded from CA1 pyramidal neurons in anaesthetised Sprague-Dawley rats. Image adapted from (Henze *et al.* 2000)**.**

However, much data is lost by recording from outside of the cell membrane rather than within the cell. At the membrane level, any activity below the threshold necessary for the firing of an action potential (AP) is not recorded, as only spiking and firing activity is loud enough to be recorded above the general electric noise of the extracellular environment. Therefore, only APs are recorded by extracellular methods.

But are these recorded APs the same as APs recorded by intracellular methods? The extracellular electrode can only record currents/voltages that are induced to flow in the extracellular space around an active neuron, namely an extracellular medium with low resistance. When the neuron is inactive, the membrane potential across the entire membrane in contact with the electrode is uniform at the resting potential and no current is flowing inside or outside of the cell. When the neuron is activated, the axon is depolarised at some point along its membrane and there is a potential difference between the depolarised region and the resting region, causing current to flow. The current flows from the resting regions to the depolarised region, also termed the 'source' (the resting membrane regions that are the source of the resulting current) and the 'sink' (the depolarised regions where the current flow sinks in towards the membrane) respectively. This flow of current acts outward from the source into the extracellular space and can be recorded extracellularly (Israel *et al.* 2011). This concept of current sinks and sources is outlined in **Fig.4.2**.

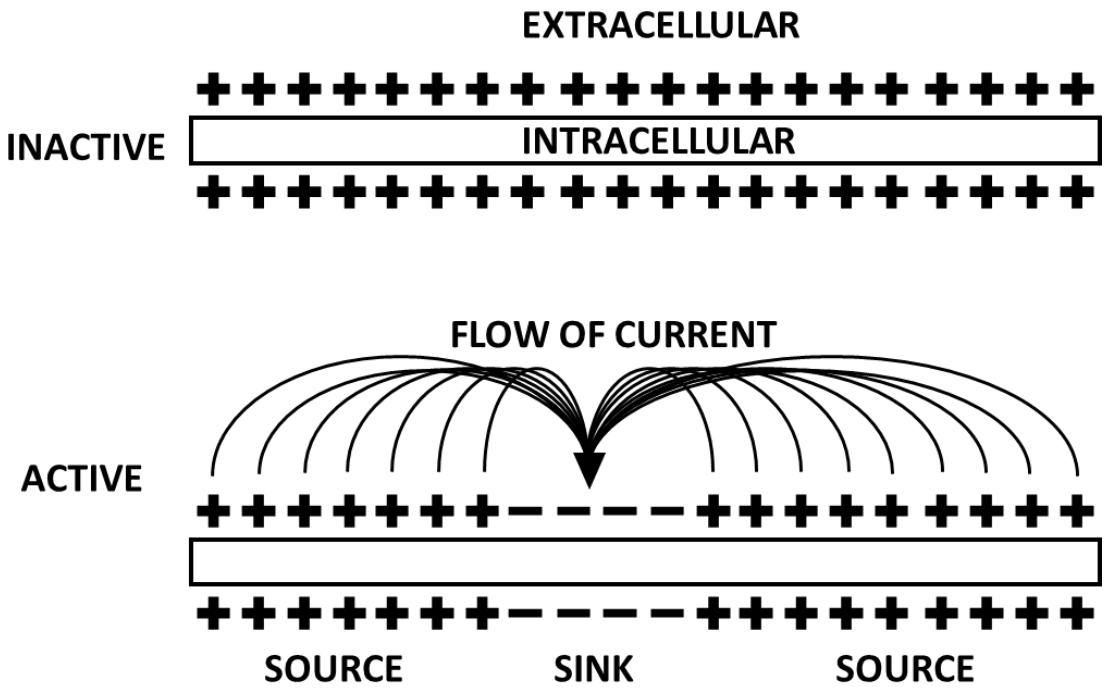

Figure 4.2: Extracellular current sinks and sources. Both rectangles represent axons, + represents membrane at a resting potential, - represents a region of depolarised membrane in response to activity. The INACTIVE axon has a uniform charge as the membrane is at the resting potential, no current is flowing in the extracellular space, and nothing is recorded. The ACTIVE axon has a section of depolarised membrane. Current flows from the resting areas to the depolarised area, (from the source to the sink). This flow of extracellular current can be recorded by extracellular electrodes. Based on images from (Israel *et al.* 2011)**.**

When recording from a section of membrane that is acting as a source, the signal is positive (as current is flowing outwards from the source it is read as more positive than surrounding resting membrane, creating a signal) and when recording from a sink, the signal is negative. The portion of depolarised membrane that acts as a sink moves along the axon until it reaches a synapse. Depending on where the extracellular electrode is recording from, this can result in two different kinds of signal: triphasic signals (recording from axon) and biphasic signals (recording from cell body).

When an extracellular electrode is recording from a length of axon, the signal changes from initially positive (the section just before a sink), negative (the sink), and back to positive (as the sink moves past the electrode), resulting in a positive-negative-positive triphasic signal. When the electrode is recording from a cell body, the cell body is the initial sink when receiving APs from other neurons, so the signal changes from initially negative (the cell body acting as a sink upon depolarisation from another neuron) to positive (as the sink moves down the axon). This concept is outlined in **Fig.4.3.**

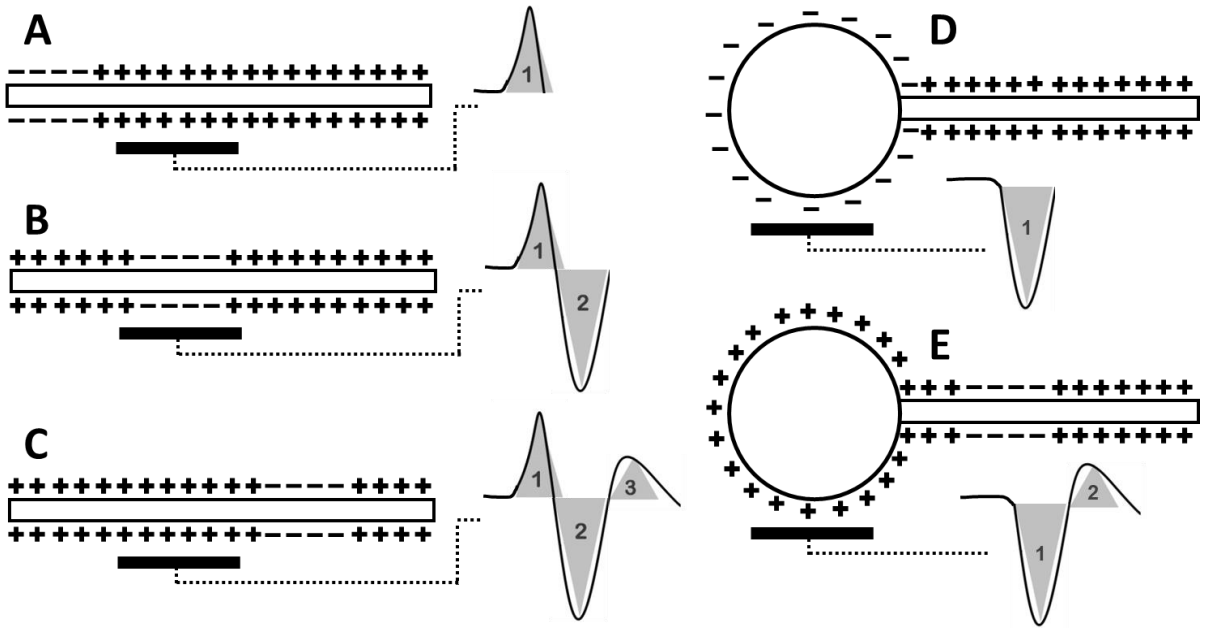

Figure 4.3: Diagram showing how different types of extracellular signals are generated, A-C shows generation of a triphasic signal from an axon, D-E shows generation of a biphasic signal from a cell body. A) sink moves towards the electrode, B) sink is at the electrode, resulting in a negative reading, C) sink moves past electrode, completing the triphasic signal, the membrane then repolarises to the resting membrane potential baseline. D) Sink generated at the cell body by another neuron via a synapse, E) sink moves past electrode, completing the biphasic signal, the membrane then repolarises to the resting membrane potential. Based on images from (Israel *et al.* 2011)**.**

The extracellular triphasic waveform corresponds to an intracellular monophasic waveform, as seen in **Fig.4.1A**. Due to the fact that each single neuron features only one cell body (roughly 10 µm in diameter) and a long axon (up to millimetre scale) with many branches, it is more likely that an extracellular electrode is in contact with an axon than with a cell body.

Recording from a neural culture *in vitro* will result in both triphasic and biphasic AP signal waveforms depending on the position, size and number of the cells, axons and electrodes. A real neuron is far

more complex than suggested in **Figs.4.2 and 4.3**, and each electrode can be in contact with more than one cell/axon at once, resulting in a dynamic and intricate system in which a wide variety of signal waveforms can be obtained, differing widely in frequency, amplitude and positive/negative phase. To outline this point, **Fig.4.4** shows the differences in extracellular signal waveforms received depending on their position in relation to the neuron cell body.

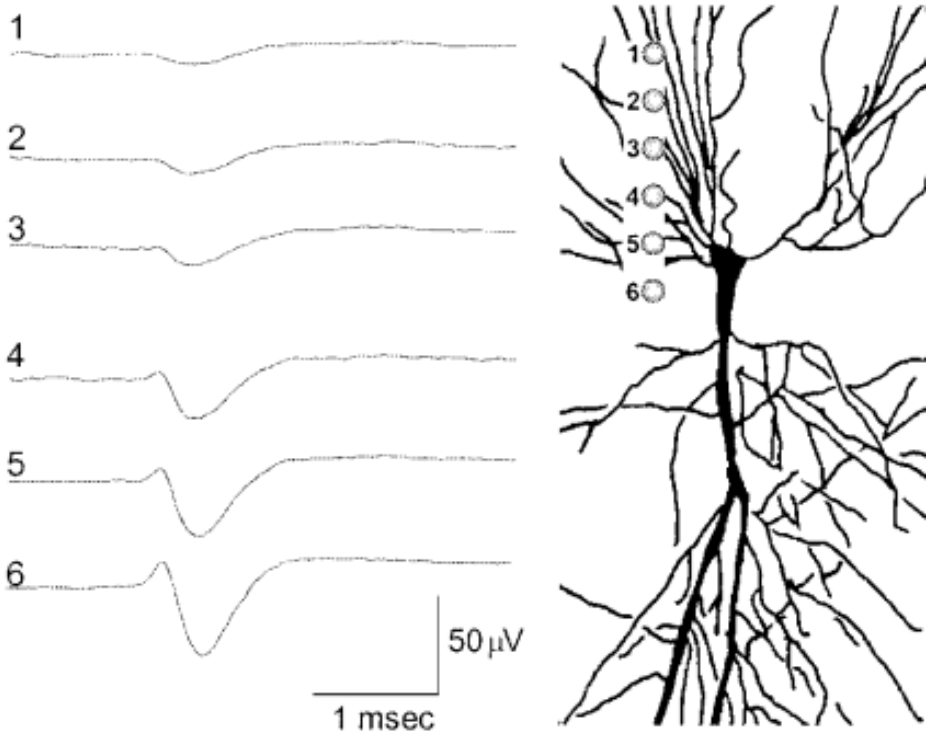

Figure 4.4: Simultaneous recording from six extracellular electrodes of a CA1 pyramidal neuron. The left shows the six averaged waveforms received from each corresponding electrode on the right, which shows their location in relation to the cell body. Electrode 6 is closest to the cell body, as seen by the amplitudes on the right. The distance from electrode 1 to electrode 6 is 25 µm. Scales shown at bottom of image, which is adapted from (Henze *et al.* 2000).

The overall amplitude decreases as the electrode moves away from the cell body, along with the increase and decrease slopes of the extracellular AP, resulting in a drastic change in signal depending on the location of the electrode. This response has also been observed after theoretical modelling (Gold *et al.* 2006). However, these electrodes had very small spacing, six electrodes within 25 µm. By spacing electrodes further apart they can come into contact with more cell bodies, not to mention in a complex *in vitro* culture each electrode is likely to be recording from more than one neuron. With this complex system in mind, the extracellular electrode must be of a quality where it can produce data with a high signal to noise ratio, high selectivity for certain signals, and high stability over long term *in vitro* culture.

4.0.3 MEAs

The fundamentals and uses of multi-electrode arrays (MEAs) were previously outlined **Chapter One (Section 1.2.3 Multi-electrode arrays (MEAs))**. In summation, an MEA is an interface between a cell culture and electronic circuitry, through which an entire cultured network can be functionally assessed over time.

Many types of MEA exist, but for these experiments the MEA used features an ordered 8 x 8 grid of square electrodes, each electrode being 50 x 50 µm with 400 µm spacing between electrodes, a similar example of which can be seen in **Chapter Two (Fig.2.8)** and example data from **Chapter One (Fig.1.11).**

Some of the largest commercially available electrodes are 50 μm^2 square electrodes, larger electrodes being better for extracellular recording of entire neural cultures as physically larger electrodes have a better chance of being near neurons and signalling cells. By using larger electrodes, we can record from more neurons simultaneously. As noted by Obien *et al.*, using electrodes larger than 50 μm^2 square has a tendency to average out peak APs with nearby smaller amplitude signals and reduce the signal received, affect the impedance and increase the noise levels (Obien *et al.* 2015). By using 50 μm^2 square electrodes with 400 µm spacing, we can effectively record from an entire culture while still receiving single-cell resolution in the instance that the electrode is in the correct location.

MEAs detect any changes in the extracellular field caused by current flow (typically from sources to sinks) from the nearest cell/s with ionic processes, usually neurons. The detected potential depends on the magnitude, phase and distance (within 100 µm (Henze *et al.* 2000)) from the recording electrode/s. Data recorded from these electrodes requires amplification, as extracellular electrophysiological signals are several orders of magnitude below intracellular data in amplitude, thus intracellular APs are measured using millivolts whilst extracellular signals are measured in microvolts (Pettersen and Einevoll. 2008). This amplified signal is then band-pass filtered, rejecting any data below 100 Hz or above 10,000 Hz. The former involves noise generated by extracellular local field potentials (LFPs) as extracellular signals often lend noise to the LFP, and whilst relationships exist between spiking and the LFP (particularly with cortical neurons (Einevoll *et al.* 2013)), only spiking activity is recorded in these experiments. The amplified and filtered spiking activity is then digitised and output as a digital signal within MEA software.

When signals received from active cells by MEAs is amplified, all aspects of the recording are amplified, including the noise. This makes the signal to noise ratio (SNR) a vital facet of extracellular recording, as too much noise will drown out the signal when amplified or noise could be mistaken for signal itself. An extensive review concerning MEAs from Obien *et al.* outlines three main forms of

noise that MEAs are subject to, at each stage of the cell-interface-MEA system: biological noise, electrode-electrolyte interface noise and device noise (Obien *et al.* 2015).

Biological noise broadly consists of electrical activity from other cells around the recording electrodes, (also referred to as 'background noise'). This type of noise varies with cell type, size, morphology (such as density of dendritic trees), firing rates, the LFP and general biological chaos. Some of this noise, such as low frequency LFP noise, can be filtered out with band pass filtering.

Electrode-electrolyte interface noise involves the interface that exists between the cell media (liquid) and the surface of the electrode (metal), general electrical vibrations from nearby equipment or power/mains lines and signal travelling to the amplifier. As most of this noise is low frequency it can be filtered out, or otherwise reduced by having a minimal distance between electrode and amplifier, electrical grounding and/or shielding of MEA equipment. In addition, any noise generated by the liquid-metal interface is reduced by the inclusion of reference electrodes. These reference electrodes are large electrodes that are located distant from the central electrode array and are not in contact with any signalling cells, which serve only to detect any noise within the liquid and liquid-metal mediums and subtract that noise from the signal.

Device noise involves noise being added by the amplifier or MEA equipment itself and is affected by the size and density of the electrode array, size of electrodes and the transmission of data if there are bandwidth or other software constraints. Overall, while most forms of noise can be removed by utilising proper MEA equipment with appropriate levels of software filtering and hardware shielding, the only form of noise that cannot be altogether removed is the biological noise caused by the cells. However, there are further software solutions employed by MEA software that can reduce biological noise and the SNR, until only signal remains.

Due to high levels of noise in an *in vitro* MEA experiment, filtration and spike detection software is utilised to determine what is signal and what is noise. The spike detection method involves establishing a threshold and only accepting data as a 'spike' if it can pass this threshold. The threshold can be established in a number of ways, such as X times the standard deviation (STD) or root mean square (RMS) of the background noise. All data beyond this threshold is assumed to be spontaneous extracellular spiking activity, which is subject to further filtration and analysis. The usual method of analysis is spike sorting, where received spikes are sorted into groups based on waveform shape in order to further reduce the SNR and also eliminate any false positives that may exist in the spiking signals. For these experiments these groups of similar shaped spikes are termed 'centroids'. By analysing the raw spiking data and the centroid data from individual electrodes and across the entire array, a complex and comprehensive view of electrical activity across the culture can be built.

Common output data from these recordings include spike frequency, spike amplitude, duration of spiking, inter-spike interval, spike patterns and specific spike waveforms. This assumes that these spikes are single APs fired in relative isolation or randomly, but neurons can also fire **bursts,** namely periods of rapid (>10 Hz) AP spiking followed by quiescent periods. These bursts can be assessed in the same way as spikes, analysing their frequency, amplitude, duration, inter-burst interval, pattern and waveforms. Bursts can be generated by single neurons or by the culture as a whole, defined as network bursting. In this manner, the extracellular activity of an entire neural culture can be assessed over the long term, producing large quantities of dense data that can be filtered and analysed to determine the cell activity, functionality, connectivity, and any similarities to *in vivo* activity.

4.0.4 *In vitro* models with extracellular recording

Numerous *in vitro* neural models include many powerful features and an elegant design, but can lack forms of functional assessment, especially the extracellular recording of spontaneous activity from cells cultured within the model, and particularly over the long term (long term being more than a few weeks, in order to allow embryonic cells to functionally mature *in vitro* and draw more accurate comparisons to adults *in vivo*). As such, recent microfluidic *in vitro* models are often paired with MEAs in order to ensure the cells are functional, forming synapses and connecting in a similar way to *in vivo*.

Goyal *et al.* present a relevant example, where they express the need for several improvements to *in vitro* neural model design. Using the classic example from Taylor *et al*, namely a two-port microfluidic device with each port linked by microchannels (Taylor *et al.* 2005), previously discussed and displayed in **Chapter One**, Goyal *et al.* discuss improvements. These include: more knowledge about the effect of microchannel geometry on the cellular microenvironment and their influence on neuronal cultures; maintaining neurons within the models for long periods of time so that the data can be used along with longitudinal neuronal studies and other neuronal analysis *in vitro* (normally only possible with conventional culture systems); and tracking the electrophysiological properties of the neurons within the model, also over the long term (Goyal and Nam. 2011). These three factors are indeed some of the most-needed improvements to classic and current *in vitro* microfluidic neural devices.

To this end, Goyal *et al.* used soft-lithography to fabricate two-port PDMS devices with 50, 100 or 200 µm uniform width channels (50 µm in height) between the ports, and cultured E18 rat hippocampal neurons in these PDL-coated devices for five weeks, recording the spontaneous extracellular electrophysiological activity from the channels with MEAs. Cells were seeded into the devices in order to achieve 250-300 cells/mm^2 within the channels, as seen below in **Fig.4.5**.

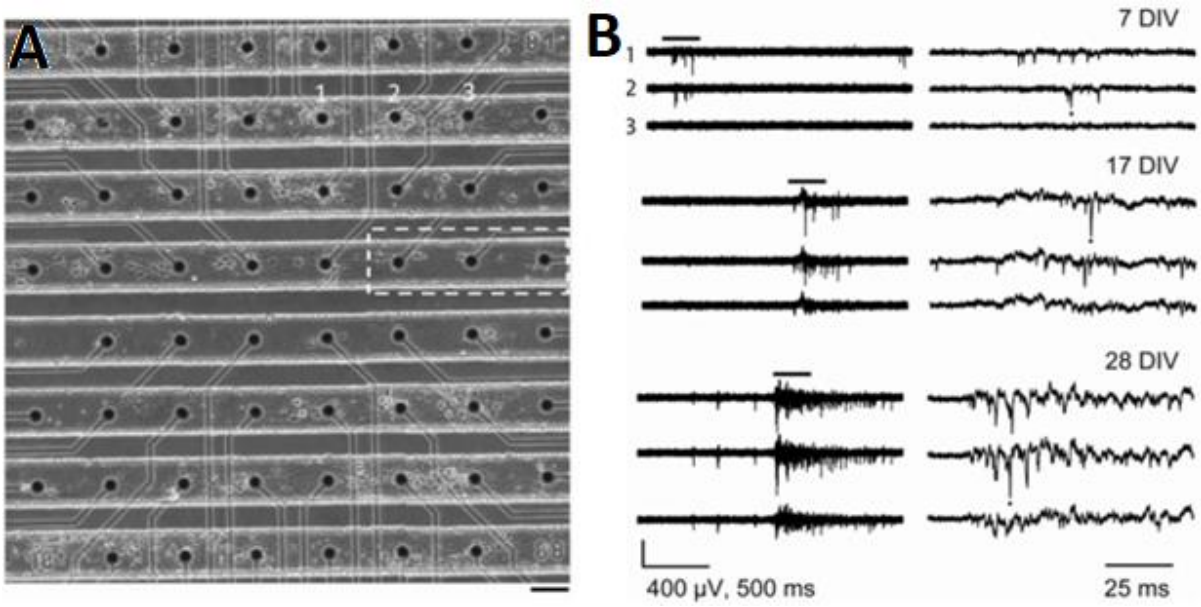

Figure 4.5: A compartmentalised microfluidic *in vitro* neural model with extracellular recording capabilities within microchannels. A) MEA electrodes aligned to 100 µm wide non-tapered channels containing neurons after 17 DIV, scale bar 100 µm. Electrodes marked 1, 2 and 3 correspond to the raw electrical activity in B. B) raw electrical activity at 7, 17 and 28 DIV. The black bar on the left hand traces (which show 2 secs of activity) indicates the location of zoomed in traces (shows 100 ms activity), seen to the right.

However, despite the modifications made to the model and experimental design, there is still room for improvement. Goyal *et al.* only made eight devices, two of which did not show activity and two of which were only recorded from for 3-4 weeks, meaning only four were recorded from for the full five weeks. In addition, only electrical data from 7, 17 and 28 DIV was shown, from only three electrodes, and only the spike rate in spikes per second, burst rate in bursts per minute and raw data (Goyal and Nam. 2011). These protocols are insufficient to determine the activity across an entire culture over the long term but are certainly a step in the right direction. Further analysis of other studies involving compartmentalised *in vitro* neural models with extracellular recording methods can be seen in **Table 4.1**, where they are also compared to the work set out in this chapter.

Table 4.1: Assessing *in vitro* neural devices with integrated extracellular recording methods. STD: standard deviation, RMS: root mean square. Spacing determined as distance from electrode centre to centre.

Model description	Cell type used	Electrophysiological assessment method	Culture time (days *in vitro*)	Reference
Model composed of an ITO-MEA with a glass ring and cells seeded directly onto MEA, no microfluidics.	E18 rat cortical neurons	MEA, 8x8, 30 µm diameter with 180 µm spacing. Analysed at 5x STD.	49 DIV, recorded at 5, 11, 49 DIV. Cultured up to two months (not shown)	(Jimbo. 2007)
Cells patterned directly on top of electrodes for single-cell resolution.	Primary (no age stated) rat hippocampal neurons ($2x10^4$ cells per mL)	MEA, 4x4. Dimensions not mentioned, fabricated in-house.	Not mentioned	(Jing *et al.* 2009)
Two-port microfluidic device, 100 µm width microchannels between ports, integrated PDL-coated MEA	E19 rat hippocampal neurons (250-300 cells/mm^2)	MEA, dimensions not noted. Data shown from only three electrodes. Analysed data at 5x STD.	35 DIV (only half devices went to full time), recorded at 7, 17, 28 DIV.	(Goyal and Nam. 2011)
'Neurofluidic' two-port device, 10 µm width microchannels between ports, integrated PEI-coated MEA	E19 rat cortical neurons (200 cells/mm^2)	MEA, 8x8, 30 µm diameter with 200 µm spacing, 30 electrodes per device port. 10 minute recording sessions, analysed at 8x RMS.	35 DIV, recorded twice a week.	(Kanagasabapathi *et al.* 2011)
PEI-coated MEA, set up for immunostaining of neurons within.	E17 cortical neural culture, 2500 cells/mm^2	MEA, 8x8, 50 µm diameter with 150 µm spacing	35 DIV, recorded twice a week from 7-35 DIV.	(Ito *et al.* 2013)
Two-port microfluidic device, 50 µm width microchannels between ports, integrated PEI-coated MEA	E16 mouse cortical neurons and P19 cell line (100-200 cells per mm^2)	MEA, two 4x8 arrays (one in each port), 30 µm diameter 180 µm spacing, analysed at 6x STD.	18 DIV, recorded at 11 and 18 DIV. Cultured up to a month (not shown).	(Takayama *et al.* 2012)
Two-port microfluidic device, 10 µm width channels, integrated PDL-coated MEA	P4 rat hippocampal neural cultures (up to 1000 cells/mm^2	MEA, 8x8, 30 µm diameter 200 µm spacing, 3 minute recording analysed at 9x RMS.	Up to 21 DIV	(Brewer et al. 2013)
Two-port microfluidic device, 10 µm width channels, integrated PEI-coated MEA	E18 rat cortical and thalamic neural cultures (200 cells per mm^2)	MEA, 8x8, 30 µm diameter 200 µm spacing, 30 electrodes per port., analysed at 8x RMS.	Up to 35 DIV, only recorded from 14 DIV	(Kanagasabapathi et al. 2013)
Microbead structure placed onto standard MEA to make 3D culture, with 2D MEA controls.	E18 rat hippocampal neurons	2D MEA: 8x8, 30 µm diameter 200 µm spacing. Analysed at 8x STD, not spike sorted.	Up to 35 DIV.	(Frega et al. 2014b)
Five-port microfluidic device, 5-15 µm tapered channels and integrated PEI/PDL-coated MEA.	**E16 rat cortical, striatal, pallidal and E14 nigral neuronal/glial cultures.**	**MEA, 8x8, 50 µm diameter with 400 µm spacing. 3x 4 minute recording sessions, analysed at 5x RMS.**	**70 DIV, recording over 12 sessions between 0-70, across all devices.**	**Work described here.**

For this experimentation to best be effective, cells should be cultured and recorded over the long term, with long term being longer than five weeks, the current most popular end point. Recording for double the length of time (ten weeks or 70 DIV) would allow for a better perspective as to how the cells react to longer time frames *in vitro*, how they mature and how the culture changes. Analysis of MEA data should be more robust, with most studies showing raw data and the change of basic variables over time (such as spike frequency), not showing the spatial localisation of activity, spike sorting methods, or relationships between spikes and bursts and inter-activity intervals.

The model should show the presence of any plasticity or long-term potentiation amongst the cells cultured within, in order to indicate if this model is a good model of cells maturing as they do *in vivo*.

Whilst this model is a five-port device (5PD), it is necessary to first establish a baseline of activity from each cell type in isolation before recording from a connected network of two or five cell types at once. Namely, what kind of extracellular activity does each cell type (CTX, STR, GP and SN) produce when cultured in isolation over the long term? This chapter consists of these separate recordings, followed up by dual cultures in **Chapter Five**.

Primary cells from the cortex or BG were assessed on MEAs in isolation for a period of 70 days to determine their baseline of activity when cultured as a single population (in other words, just CTX, STR, GP or SN on each MEA), and the MEA data analysed. These data are discussed below.

4.0.5 Chapter Four aims and objectives

The aim of this chapter was to establish an electrophysiological activity baseline for CTX, STR, GP and SNc cells over the long term (up to 70 days). The spontaneous extracellular activity of these cultures was measured individually with MEAs over ten weeks, to compare against co-culture activity in **Chapter Five** and Parksinsonian co-culture activity in **Chapter Six**, to determine the effects of connectivity and loss of striatonigral dopaminergic neurons respectively, on the spontaneous extracellular electrophysiological activity of these cells over the long term.

4.1 Experimental Methods

The methods involved in this chapter were previously outlined in **Chapter Two**. A brief summary of the key methods is outlined here.

4.1.1 MEA surface preparation

As seen in **section 2.1.1 device preparation: chemical coating,** MEAs were sterilised with 70% IMS for 15 minutes, air dried and coated first with 0.05% PEI for 1 hour at room temperature, then 0.1 mM PDL overnight at 37°C, washing between each stage. MEAs were then air dried and ready for cell culture.

4.1.2 Primary cell culture

As seen in **section 2.2 Primary cell culture,** tissue was dissected from Sprague-Dawley rat embryos: E16 for CTX, lateral and medial ganglionic eminences (LGE and MGE), corresponding to the CTX, STR and GP respectively; and E14 for the ventral midbrain (VM), corresponding to the SN. These tissues were dissociated and 100,000 cells were seeded directly onto the electrode array at the centre of the MEA, within a glass or PDMS ring. The ring was then flooded with growth media and the cells incubated at 37°C, 5% CO_2.

4.1.3 Electrical activity measurement with MEA

Recordings of cell electrophysiological activity (**section 2.5.2 MEA: Recordings**) were taken once a week from 0 DIV to 70 DIV, before a media change. MEAs were moved to a heated bracket (at 37°C) attached to amplifiers and digitisers. Activity was recorded for four minutes in triplicate, totalling 12 minutes of recording.

4.1.4 MEA data management and analysis

Spontaneous electrophysiological data obtained from neural cultures was analysed using Mobius software (**section 2.5.2 MEA: Analysis**). Data was band-pass filtered below 100 Hz and above 10 kHz, and the spike detection threshold was set at 500% of the root mean square. These spikes were further filtered into centroids (discrete filtered groups of spikes), each centroid consisting of >50 spikes that are >80% in similarity. These centroids were assessed to determine the number, frequency, amplitude and waveform of both spikes and bursts.

4.2 Results

4.2.1 Primary cell culture

100,000 CTX, STR, GP or SN cells were seeded onto 8 x 8 MEAs and attached to the surface and electrodes. An example of cell density after 6 DIV is displayed in **Fig.4.6**.

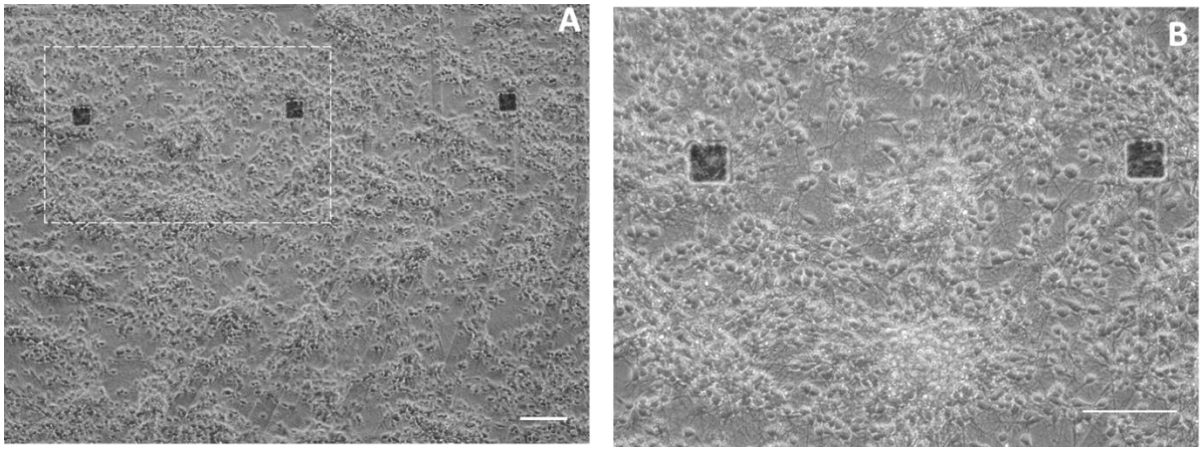

Figure 4.6: 100,000 STR cells after 6 DIV on an MEA. The area shown in B is indicated by the white dashed square in A. Black squares are individual electrodes of the MEA. Scale bars 100 µm.

As seen previously in **Chapter Three (section 3.2.3.2, Fig.3.14)**, cells seeded onto PEI/PDL coated surfaces proliferated in an even monolayer, coating the MEA. The high density of cells ensured that all electrodes were at least in contact with axons, if not in contact with one or more cells. This density increased slowly over the 70-day culture, with most cells being post-mitotic and not displaying much proliferation. The state of the MEA at a very late stage, taken at 120 DIV with CTX cells, can be seen in **Figs.4.7 and 4.8** below and acts as a comparison.

After 120 DIV every surface of the MEA was covered in neurons and astrocytes, with the latter in clear majority. All electrodes were covered in many cells and the neurons had long processes, some extended from one electrode to another. These neurons remained towards the centre of the culture, on the electrodes. The far edges of the culture consisted mostly of large astrocytes, as seen in **Fig.4.7E**, where astrocytes extended into the space next to the culture and no neurons were seen. Essentially, while astrocytes proliferated and spread across the whole MEA, neurons remained where they were seeded on the electrode array in the centre of the MEA. This means that across the whole 70 DIV of recording, electrodes were in contact with neurons and their activity was recorded.

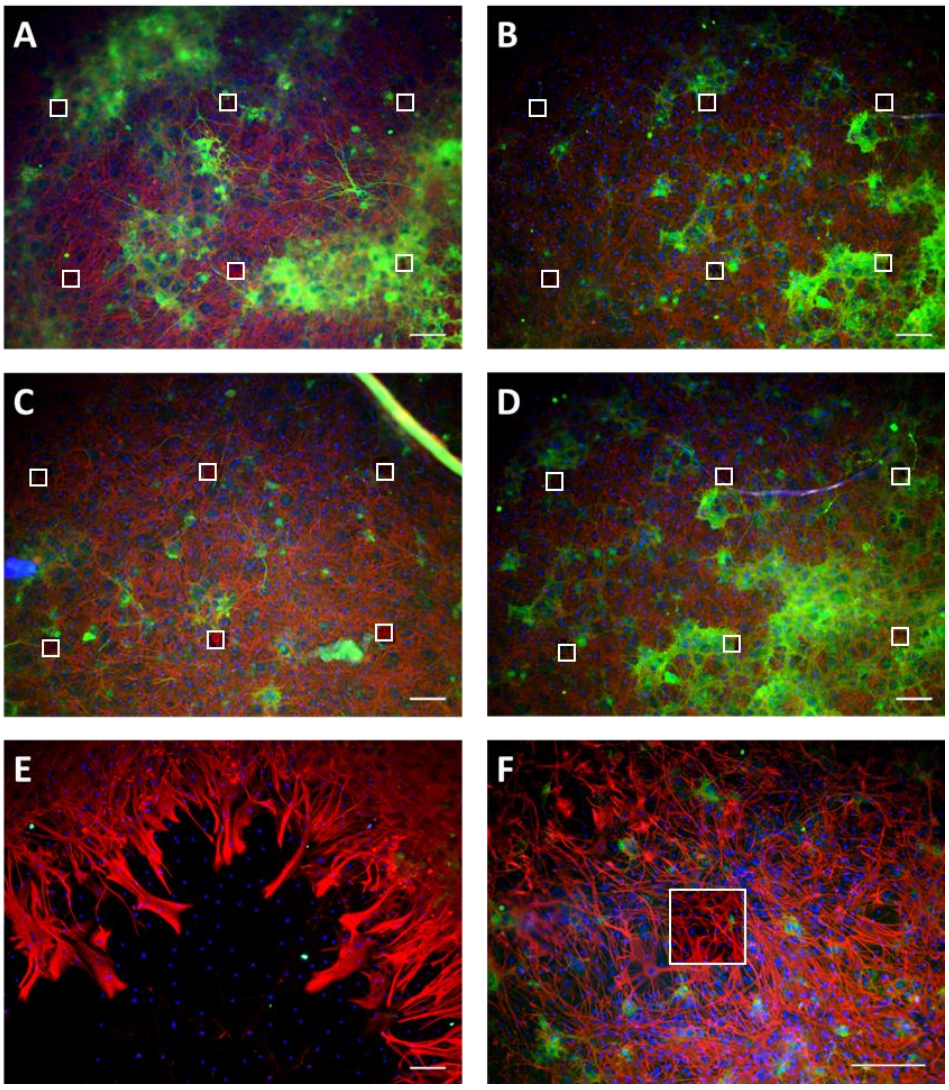

Figure 4.7: 100,000 CTX cells after 120 DIV on an MEA, stained with GFAP (red, shows astrocytes), β-tubulin (green, shows neurons) and DAPI (blue, shows cell nuclei), with electrodes indicated by white squares. A-E show different sets of 6 electrodes across the the MEA. F shows a reference electrode. Scale bars 100 µm.

To measure the viability of these cells after 120 DIV on an MEA, live/dead staining was performed to determine the percentage viability of cells across the MEA, and cell viability across the MEA was analysed (seen in **Fig.4.8**).

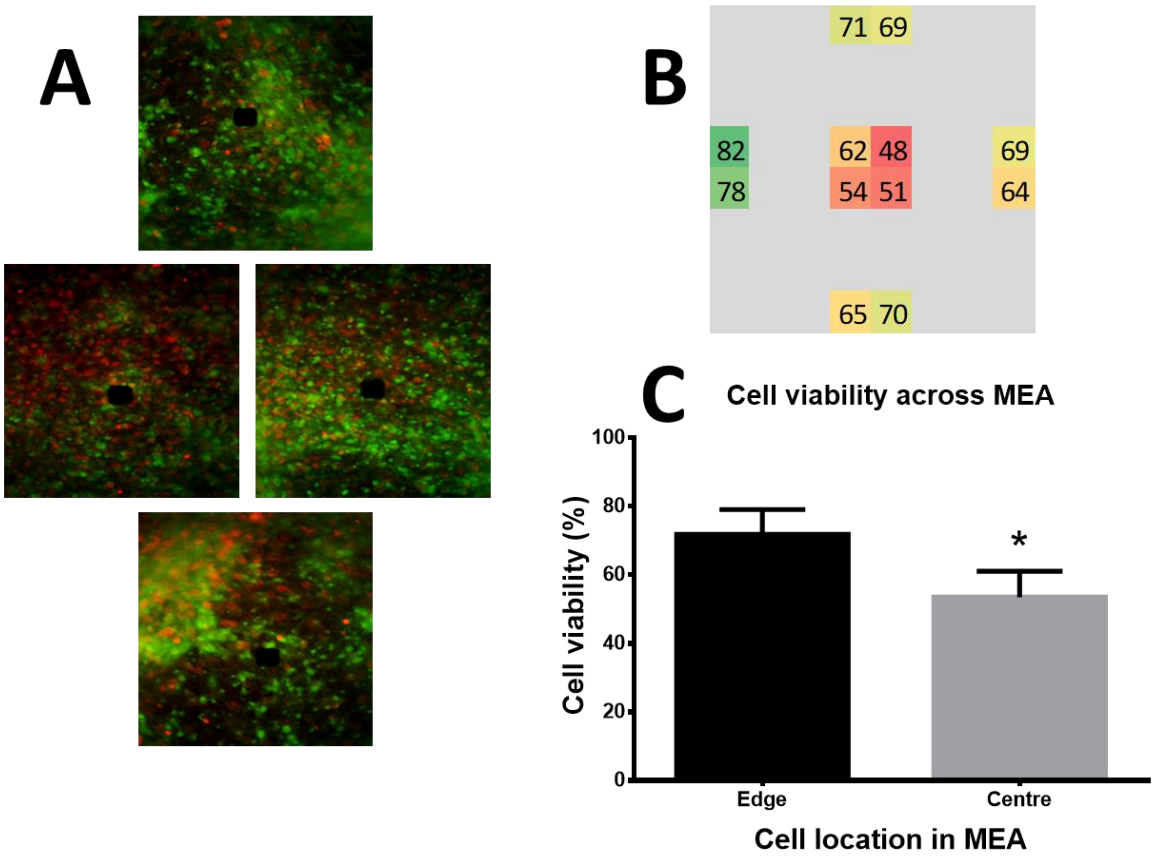

Figure 4.8: Live/dead data for 100,000 CTX cells after 120 DIV. A) Live/dead images with live and dead cells in green and red respectively, and electrodes as black squares. The pictures are arranged as they were taken, with the top image from the top edge of the MEA, the two centre images from the centre and the bottom image from the bottom edge of the MEA. B) Percentage viability of cells depending on their location within the MEA, from four centre images and two images from each edge, with more viable areas shown in green and less viable areas in red. C) Taking the four centre images as 'centre' and the eight edge images as 'edge', a comparison in percentage cell viability between edge and centre (*): $p<0.01$. Data from other cell types not shown, image representative of n=4.

Cells were significantly less viable in the centre of the MEA than the edge after 120 DIV, as the culture was denser in the centre of the MEA. Despite this lower viability, data was still recorded from all electrodes across the MEA, and it should be noted that this was a representation of a super-late stage MEA experiment at 120 DIV, with other experiments terminated at 70 DIV where the density was likely lower and the percentage viability higher. In summary, primary neural cells were successfully cultured on PEI/PDL coated MEAs over the long term (70 DIV).

4.2.2 Spatial activity localisation on MEAs

Activity was recorded from each of the 64 electrodes on every MEA, resulting in the ability to trace not only the timing of the onset of activity, but on which electrodes that activity was located, in order to track activity across each MEA over time. Raw activity can be seen in **Appendix**.

4.2.2.1 Heatmaps

Heatmaps were generated by taking the number of spikes recorded by each electrode and applying a traffic light scale, with green, yellow and red representing the highest, average and lowest activity respectively. These heatmaps are displayed from 0-70 DIV for each cell type in **Figs.4.9-4.12.**

CTX cells featured a later onset of activity compared to STR, GP and SN cells, with activity only seen by 21 DIV (as opposed to 11-15 DIV in other cell types) (see **Fig.4.9**). Activity began at 21 DIV, spread to more electrodes on 27 DIV, and then decreased from 27-70 DIV. High activity areas increased from 21-70 DIV, with more high activity areas seen at later days such as 44 and 51 DIV. While experiment B had lost the majority of activity on 65 and 70 DIV, experiments A and C showed consistent activity throughout, in the same regions. Generally, activity was generated on 21 DIV and was widespread, then high levels of activity were generated consistently in a specific region while activity in other regions decreased. While the number of active electrodes fell over time, the spike frequency increased, suggesting that activity is being adopted by certain electrodes.

For STR, onset of activity occurred around 11 DIV (see **Fig.4.10**). Activity continued to spread across the MEA until around 21-27 DIV, after which activity was confined to specific locations consistently until 70 DIV. The peak of activity occurred around 38 DIV. Experiment C had diminished activity from 51-70 DIV, while experiments A and B retained activity throughout.

For GP, activity began by 11 DIV for experiment A and 15 DIV for experiments B and C (**Fig.4.11**). Activity did not spread across the MEA for B and C, but areas of high activity were highly consistent. For A, activity spread from 11-31 DIV, with high activity seen from days 38-44 DIV.

For SN, onset of activity occurred around 11 DIV (**Fig.4.12**). Activity spread across the MEA until around 27 DIV, occupying nearly 100% of electrodes. For A and B, activity continued until 70 DIV, decreasing for 44-58 DIV. Areas of high activity were consistent. For C, activity was high across the whole MEA for 27-51 DIV, data after this point is not available.

Figure 4.9: CTX activity heatmaps. Each square is an 8 x 8 grid representing an MEA. Horizontal values 4-70 represent *days in vitro* (DIV) and A-D represent separate MEAs from repeat experiments. Red->yellow->green formatting indicates min->mean->max levels of spiking activity. Min, mean and max for each repeat as follows: A) 0, 524, 9551. B) 0, 111, 5847. C) 0, 102, 2060. D) 0, 65, 4060.

Figure 4.10: STR activity heatmaps. Each square is an 8 x 8 grid representing an MEA. Horizontal values 4-70 represent *days in vitro* (DIV) and A-D represent separate MEAs from repeat experiments. Red->yellow->green formatting indicates min->mean->max levels of spiking activity. Min, mean and max for each repeat as follows: A) 0, 137, 6002. B) 0, 661, 12064. C) 0, 126, 8610. D) 0, 199, 8705.

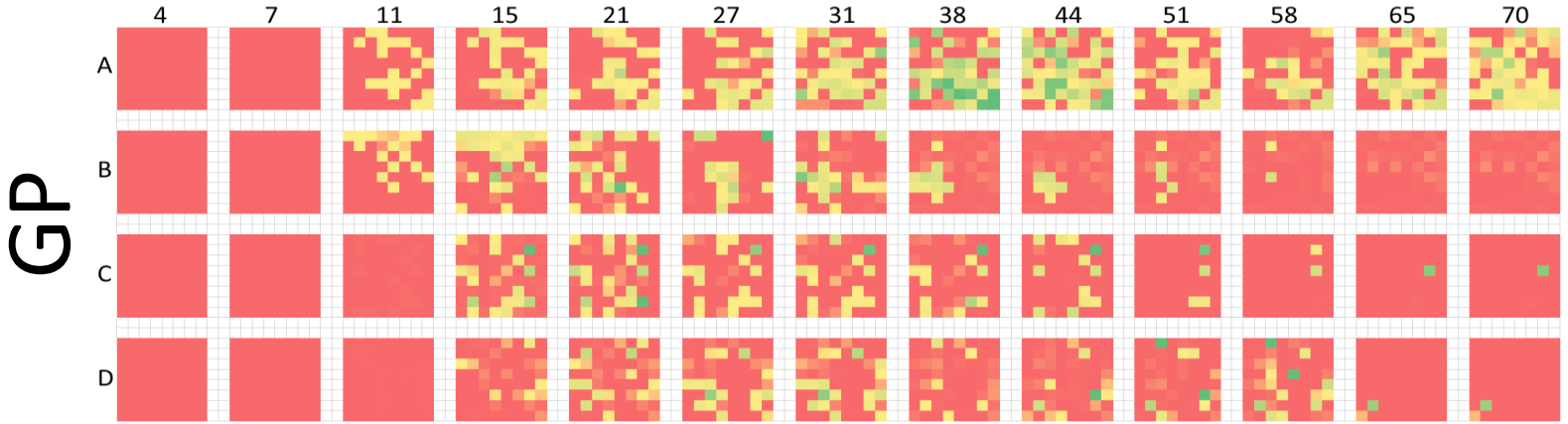

Figure 4.11: GP activity heatmaps. Each square is an 8 x 8 grid representing an MEA. Horizontal values 4-70 represent *days in vitro* (DIV) and A-D represent separate MEAs from repeat experiments. Red->yellow->green formatting indicates min->mean->max levels of spiking activity. Min, mean and max for each repeat as follows: A) 0, 975, 18924. B) 0, 213, 8238. C) 0, 123, 6995. D) 0, 35, 2666.

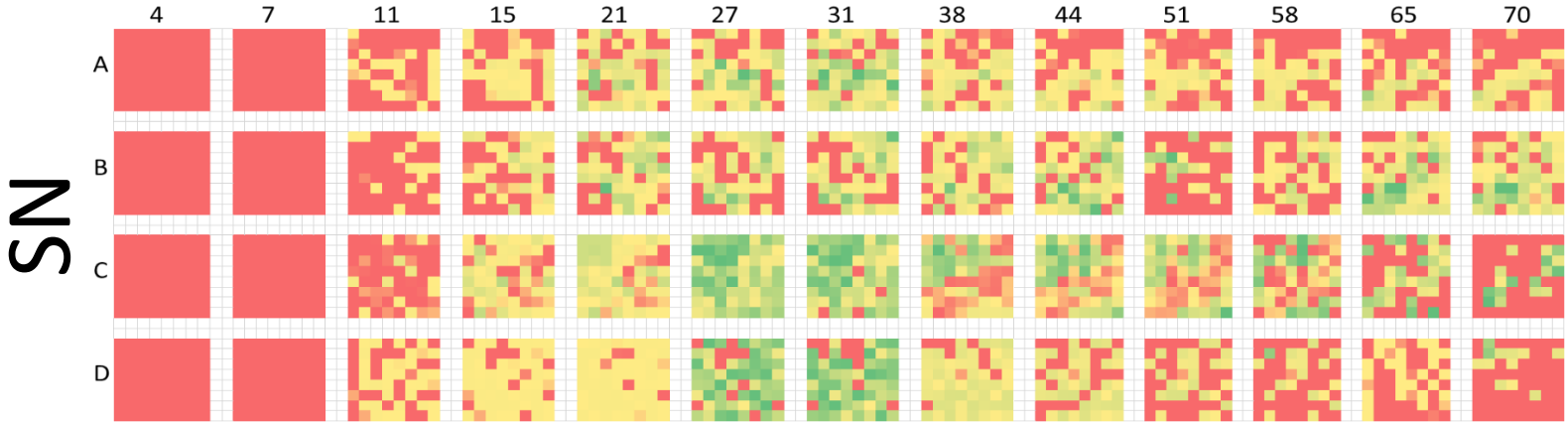

Figure 4.12: SN activity heatmaps. Each square is an 8 x 8 grid representing an MEA. Horizontal values 4-70 represent *days in vitro* (DIV) and A-D represent separate MEAs from repeat experiments. Red->yellow->green formatting indicates min->mean->max levels of spiking activity. Min, mean and max for each repeat as follows: A) 0, 1146, 30450. B) 0, 1041, 14355. C) 0, 6685, 37967. D) 0, 2120, 19983.

4.2.2.2 Percentage activity across the MEA

Spatial activity data could also be presented as percentage activity across the MEA, as seen in **Fig.4.13**. This represents the proportion of electrodes across the MEA that were recording spontaneous activity above a threshold over the 70 DIV (as such it does not take into account the amplitude or frequency of this activity, only the presence or absence of activity).

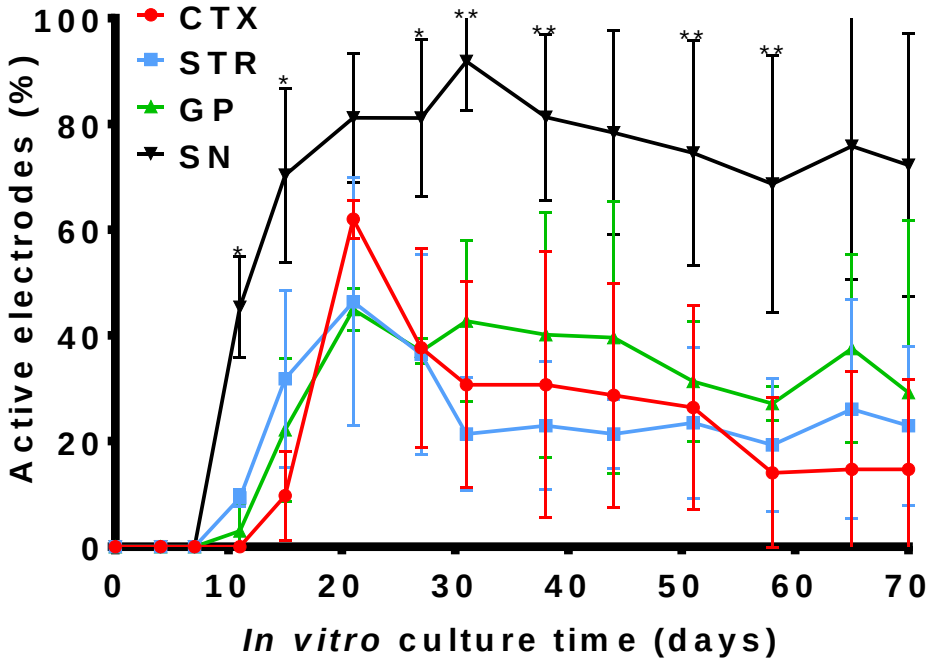

Figure 4.13: Average percentage of MEA electrodes that recorded spontaneous activity over time, for each cell type (n=4). Asterisks represent post-hoc t-tests and in this case, compare SN to the other three cell types (*): p<0.01, (**): p<0.001.

The cell type had a significant effect on the percentage of active electrodes over time (ANOVA (3,8), F=8.908, p=0.0063). There were significant differences between CTX/STR/GP and SNc, the largest difference being between CTX and SNc. SNc had a greater number of active electrodes at all time points when compared to CTX, STR and GP, with the latter cell types having similar trends of onset, peak and slow decline.

CTX neurons had a later onset and peak of activity at 21 DIV. While CTX peaked above STR and GP levels on 21 DIV (60% of MEA active), it persistently decreased from 21 DIV until 70 DIV, finishing with the lowest number of active electrodes overall (10% of MEA active). STR neurons had an earlier onset than CTX and GP (11 DIV) but again peaked at 21 DIV (45% of MEA active). After a sharp decline at 33 DIV levels remained consistent until 70 DIV (20% of MEA active). GP neurons were very similar to STR in the early phase, with onset at 15 DIV and the usual peak at 21 DIV (45% of MEA active). After this point levels remained consistent until 51 DIV where a decline begins, only to rise again at

65 DIV (30% of MEA active). SNc neurons differed to CTX, STR and GP and had the highest percentage of active electrodes across all four cell types at every time point after onset (significant differences marked by asterisks on **Fig.4.13**). SNc onset was earlier than CTX and GP (11 DIV) with the highest initial reading of 45%, rising and peaking later than other cell types at 33 DIV (90% of MEA active), and declining at a far slower rate from 33-70 DIV (finished at 75% of MEA active).

4.2.3 Average spike frequency

Each electrode recorded a set number of spikes per recording. By taking an average of the spikes across all 64 electrodes of the MEA, the level of spiking across the whole MEA was quantified. Knowing the length of the recording session time (740 seconds) the average spike frequency (spikes per second) was calculated. These averaged spikes over time can be seen in **Fig.4.14**.

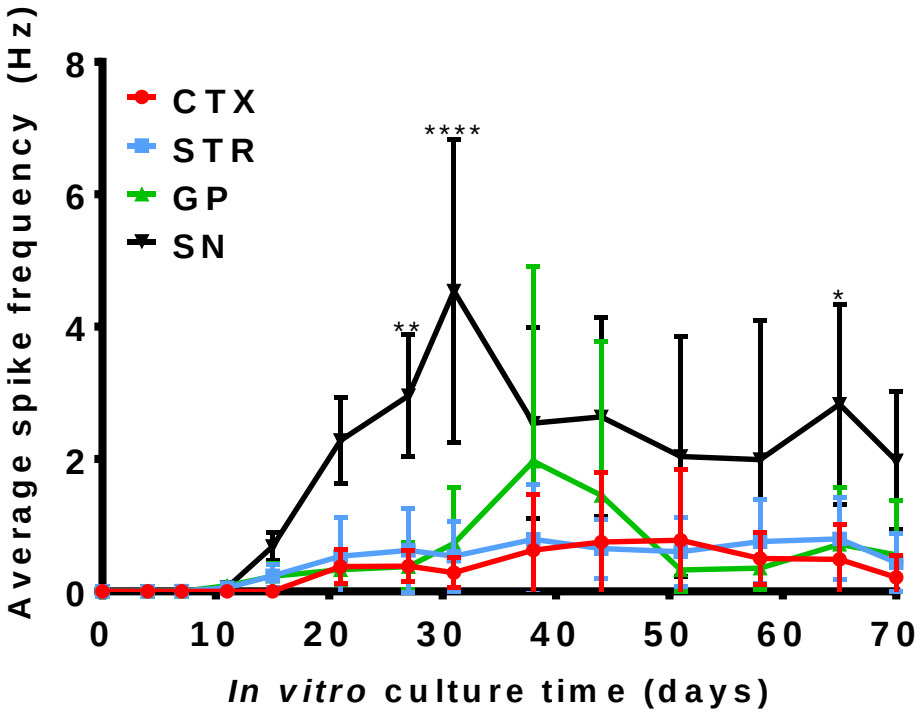

Figure 4.14: Average spike frequency across MEAs over time for CTX, STR, GP and SN (n=4). Asterisks represent post-hoc t-tests and in this case, compare SN to the other three cell types (*): p<0.05, (**): p<0.01, (****): p<0.0001.

The effect of the cell type on the average spike frequency (Hz) was significant (ANOVA (3,8) F=5.028, p=0.0302), with significance differences between SNc and other cell types on 29, 32 and 65 DIV (indicated by asterisks).

CTX spike frequency was the lowest of all cell types from onset (21 DIV) until end (70 DIV), except for a peak (0.77 Hz) at 51 DIV. After onset, CTX neuron firing increased in frequency until 51 DIV and then decreased until 70 DIV (finished at 0.2 Hz).

STR firing was more frequent than CTX from onset (15 DIV) until 38 DIV, where firing peaked at 0.78 Hz. The average frequency remained consistent from this peak until a decrease at 70 DIV (finished at 0.43 Hz). On the whole STR neurons appeared to fire at a higher frequency than CTX neurons, but lower than GP and SN.

GP neuron activity had the lowest frequency of all cell types from onset (15 DIV) until 28 DIV, until GP increased to a high peak at 38 DIV (peaked at 2 Hz), greater than CTX and STR levels of firing. Spike frequency then decreased sharply until 51 DIV, where levels remained consistently low until end (finished at 0.55 Hz). Except for the large peak in firing from 28-51 DIV, GP culture firing frequency was similar to CTX cultures.

SN cells had the highest spike frequencies of all four cell types, with greater spike frequencies at every time point after onset (15 DIV). After onset spiking frequency increased sharply to a peak at 28 DIV (peaked at 4.54 Hz), many times higher than CTX, STR or GP. Spiking then decreased to 2.5 Hz on 38 DIV and remained at this level consistently until end (finished at 1.97 Hz). This high level of spiking shows that SN cells were more active than CTX, STR and GP cells.

Spike frequency measurements consisted of taking an average across all 64 electrodes of an MEA. Due to the fact that not all electrodes registered activity, many zero values were present, which decreased the average. In order to display the activity in an alternate way, the maximum activity per day is also displayed, showing only the electrode that had the maximum number of spikes for each recording session.

4.2.4 Maximum spike frequency

In order to give an alternate display of the spike frequency without taking a non-zero average, the maximum recorded spike frequency each day was recorded, as seen below in **Fig.4.15**.

The effect of the cell type on the maximum spike frequency over time was not significant (ANOVA (3,8) F=1.812, p=0.2230). Despite this, there was still a trend towards SN neurons having a greater maximum spiking frequencies than each other cell type, especially on 29-32 DIV.

CTX maximum spike frequency was the lowest of all cell types from onset (21 DIV) until a peak at 51 DIV (peaked at 8 Hz), and increased steadily from onset to peak. The level of firing then decreased from 51-70 DIV (finished at 4.5 Hz).

STR maximum spike frequency was greater than CTX from onset (15 DIV), increased from onset until a plateau from 28-44 DIV (peaked at 9.78 Hz), then slowly decreased from 44-70 DIV (finished at 7 Hz). STR showed the most consistent maximum spike frequency over time, remaining level after the initial increase from onset.

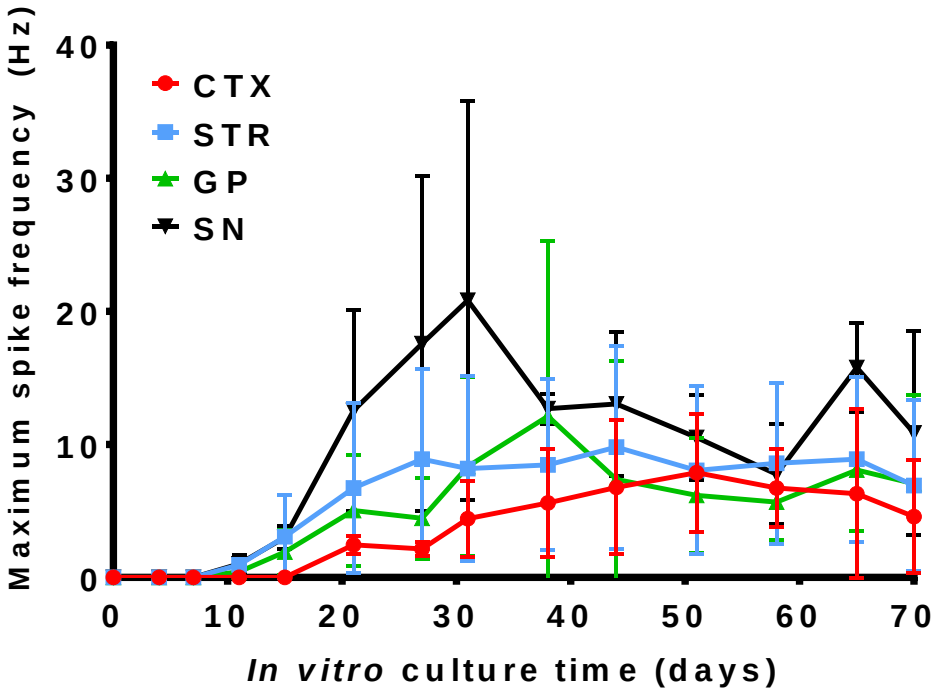

Figure 4.15: Maximum spike frequency across MEA over time for CTX, STR, GP and SNc (n=4). No significance indicated.

While GP maximum spike frequency was lower than STR from onset (15 DIV), it increased above STR during an increase between 28-38 DIV, peaking at 38 DIV (peaked at 12 Hz). The trace then decreased on 44 DIV and remained at a consistent level until end (finished at 7 Hz). The peak of GP maximum spiking on 38 DIV was equivalent to SN maximum spiking at this time.

As with the average spiking, SN maximum spiking was consistently higher than other cells at all time points, except on 58 DIV onwards where it fell below STR. SN onset was 15 DIV (same frequency as STR) and increased until a peak at 33 DIV (peaked at 20.8 Hz). After this peak the level of maximum spiking decreased until 58 DIV and then experienced a small late peak (finished at 10.85 Hz). This data shows that one electrode recorded over 20 spikes a second for a full 12 minutes, demonstrating the high levels of activity that can be achieved even by a single cell type in isolation, *in vitro*.

As well as analysing the activity of neural cultures across the MEA over the long term, it is also important to understand connectivity and potential plasticity in this dynamic system. The location of the maximum activity was not fixed and changed electrode location over time, displayed in **Fig.4.16**. For each cell type, the maximum activity did not remain in the same location for more than three or four consecutive recordings. However, there are clusters of maxima, such as the bottom left corner of CTX, where the maximum activity consistently is recorded.

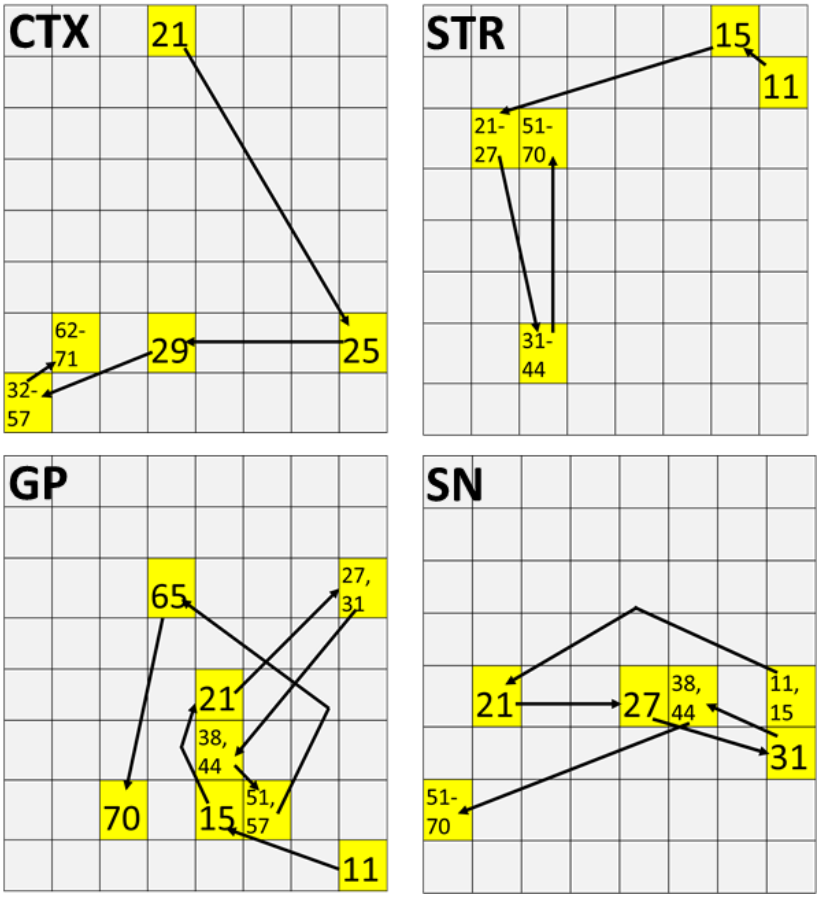

Figure 4.16: Locations of maximum activity for each day of recording, on each cell type, across the MEA. Each 8x8 grid represents an MEA, with the highlighted squares indicating electrodes that registered maximum activity, the number showing the day the activity was recorded on. The arrows show how the maximum changed locations, from the earliest day (21 for CTX, 11 for others) to the latest day (70).

In the early stages of activity (11-21 DIV) the location of the electrode that recorded the highest level of activity continuously changes, but in the mid and late stages of activity the location is more conserved, in some cases remaining on the same electrode for 3-4 recordings in a row. However, this may only be due to neurons dying or glial cells proliferating/moving around over time.

4.2.5 MEA bursting activity

As well as firing random spontaneous spikes, each cell type could also 'burst', where a burst is a bundle of spikes too close to measure separately. In this experiment a burst was defined as a bundle of more than 10 spikes in a second, namely a spike frequency of 10 Hz or above. The electrical activity recorded from each cell type contained numerous bursts, which were averaged and counted in order to calculate the average number of bursts for each cell type over time (**Fig.4.17**).

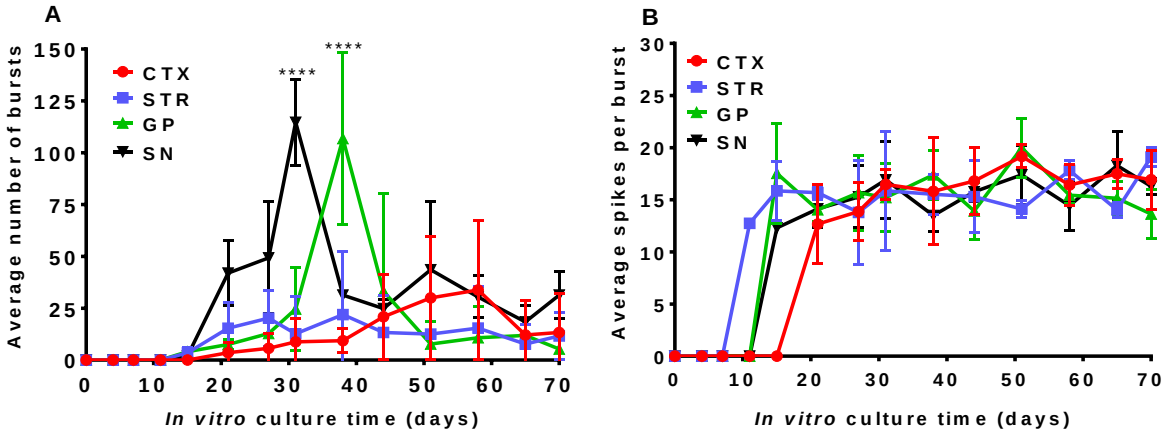

Figure 4.17: Bursting activity across the MEA over time. A) Average number of bursts over time for each cell type, B) average number of spikes per burst for each cell type. Asterisks represent post-hoc t-tests and compare each cell type to the other three cell types (****): p<0.0001. (n=4).

While the effect of cell type on the average number of bursts over time was not significant (ANOVA (3,4) F=1.5, p=0.34), the interaction between cell type over time on the average number of bursts was extremely significant (ANOVA (39,52) F=4.38, p<0.0001). The two significant differences between all four cell types were the peaks from SN (31 DIV, 115 bursts) and GP (38 DIV, 107 bursts), significance marked on **Fig.4.17A**. This demonstrated that while SN had significantly greater spike frequencies and early burst numbers (see **Fig.4.14 and 4.15**), all four cultures otherwise fired bursts at similar rates as the experiments progressed.

As with spike frequency (from **Figs.4.14** and **4.15**), the burst number has an onset, a peak and a decline as the cell activity matured. CTX bursting steadily increased from onset (21 DIV) until a late peak at 58 DIV (peaked at 30 bursts), then decreased from 58-70 (final result of 13 bursts). STR bursting also steadily increased from onset (15 DIV) to a peak on 38 DIV (peaked at 22 bursts), followed by a decrease and plateau from 44-70 DIV (final result of 12 bursts). GP bursting increased sharply from onset (15 DIV) to a high peak at 38 DIV (peaked at 107 bursts), then decreased sharply to 51 DIV and remained at a low level until end (final result of 5 bursts). SN cells had the greatest numbers of bursts from 21-27 DIV, and the greatest peak at 31 DIV (114 bursts), then decreased to a plateau from 44-70 (final result 31 bursts).

The number of spikes per burst was notably similar, with all four cell types plateauing after onset and remaining at a steady level until end, showing that there was a near constant number of spikes contained within each burst, between 15-20 spikes on average. The effect of cell type on the average number of spikes per burst over time was not significant (ANOVA (3,4) F=0.5678, p=0.66).

4.2.6 Centroid number

As part of the processing of the spike signals, spikes were sorted into groups of similar spikes termed centroids (a centroid was formed when there were >50 spikes with >80% similarity), as seen in

Fig.4.18. The maximum number of centroids that could be produced by each electrode was 20, and by tracking the number of centroids over time across the experiment, the variation in signalling could be determined (with less centroids meaning less signal variation). As the cells matured over time the signal variation changes could be assessed. The average number of centroids over time for each cell type is displayed in **Fig.4.19**.

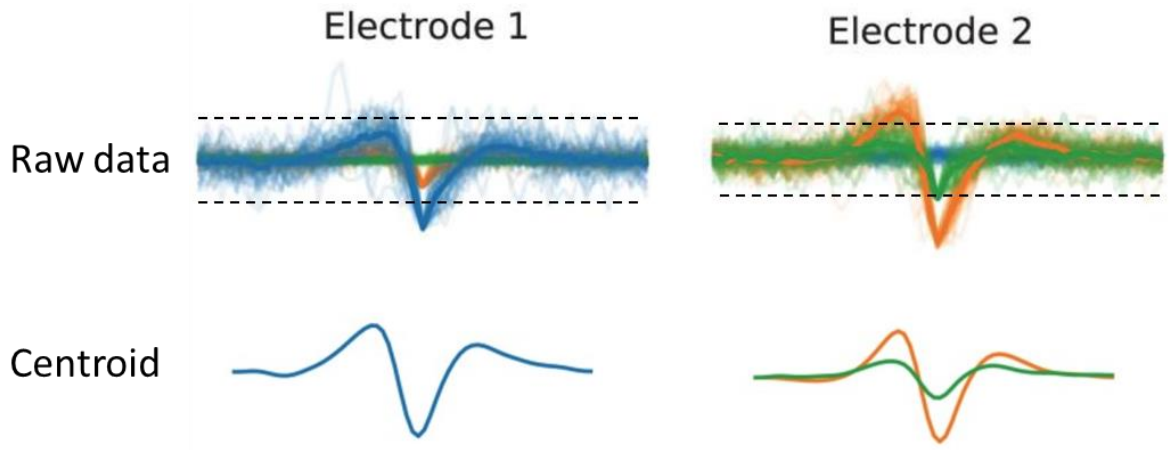

Figure 4.18: How a centroid is generated. Raw data that exceeds a threshold (indicated by dashed black lines) is counted as a spike, and these spikes are grouped into groups of similar spikes, or centroids. This spike sorting method cuts down on noise and allows for streamlined analysis of extracellular electrophysiological data.

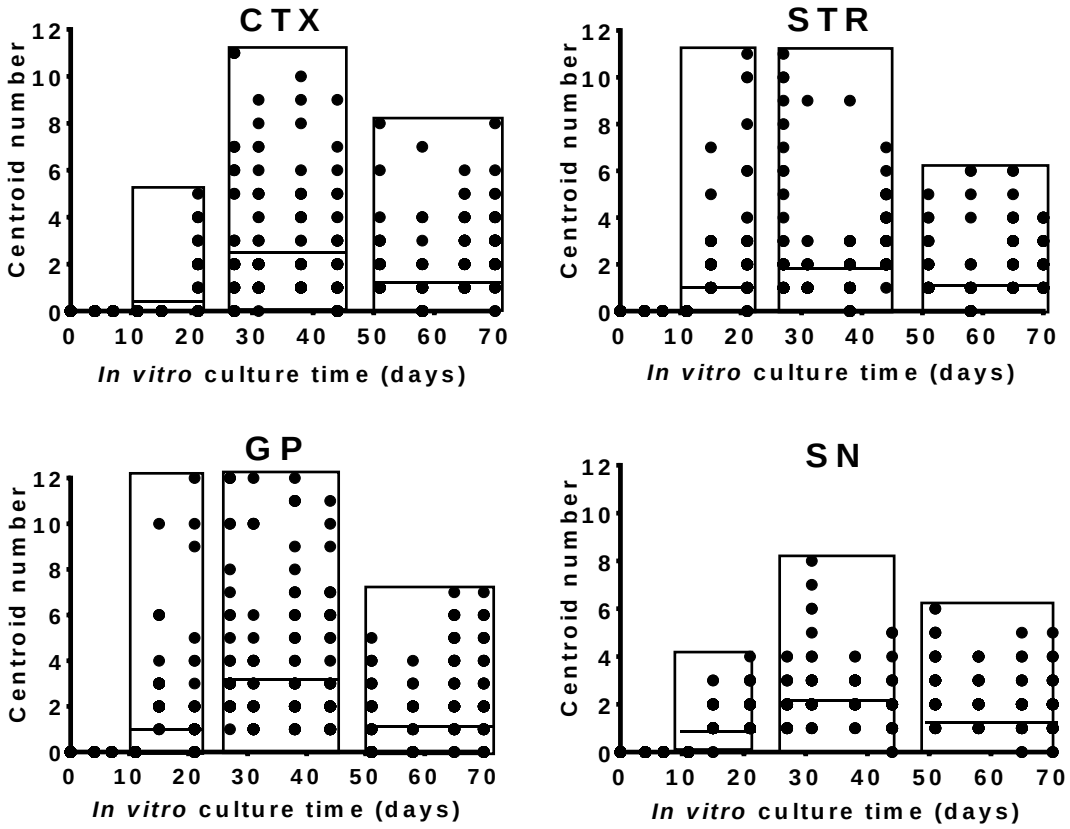

	CTX	STR	GP	SN
Early	0.32	1.05	1.02	0.81
Mid	2.14	1.99	3.20	2.14
Late	1.80	1.58	1.66	2.19

Figure 4.19: Number of centroids formed from spike sorting of the spontaneous activity of all four cell types over time. Each time point has 64 data points stacked into a vertical column depending on the number of centroids generated by each electrode. In order to more clearly indicate the differences between each stage, the early (11-21 DIV), mid (25-44 DIV) and late (50-70) stages are indicated by the rectangular column drawn around each stage. The horizontal black line within each box indicates the mean number of centroids for this period (n=3), with these means summarised in the table.

Early CTX had a low mean number of centroids as onset of activity was 21 DIV rather than 15 DIV from other cell types. All cell types started with a low number of centroids during the early phase, with an increase to the mid phase, and a decrease to the late phase. As a greater number of centroids indicates more signal variety (spikes are sorted into more groups), these results suggest that there was less signal variation in the late stage compared to the mid stage.

4.2.7 Centroid shapes

As well as tracking the number of centroids over time, the waveform (or shape/profile) of major centroids was also tracked over time. Centroids were observed to assume a total of six different shapes, determined by phase and sign. If a centroid waveform crossed the x-axis and exceeded 10 µV

in either direction, it was determined to have begun a new phase. Based on this categorisation there were six possible types of centroid, namely positive/negative monophasic, positive-first/negative-first biphasic and positive-first/negative-first triphasic (see **Fig.4.25**). In this section, examples of centroid waveform change over time are displayed, along with the categorisation of these waveforms into one of the six categories. The top four centroids for each cell type at days 15, 21, 44 and 70 are displayed below (from an active electrode), with mono-, bi- and triphasic centroids represented by red, green and blue respectively.

4.2.7.1 Centroid shape over time

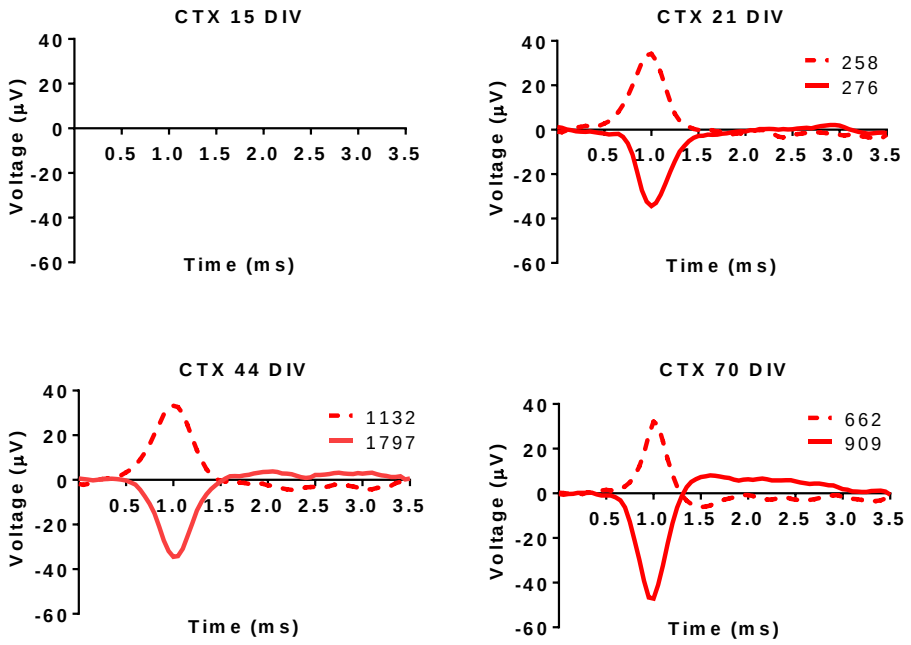

Figure 4.20: CTX centroid waveforms over time from an active electrode, E50. All centroids analysed were monophasic and are in red, dashed lines indicate a positive spike, legend indicates how many spikes made up the centroid.

As with other experiments, there was no activity at 15 DIV due to CTX onset being 21 DIV. There were only two monophasic centroids for electrode 50 on days 21, 44 and 70, and in each case the negative monophasic centroid contained the most spikes. 21 and 44 DIV are very similar in waveform and amplitude, but the negative monophasic centroid had a greater amplitude and recovery at 70 DIV.

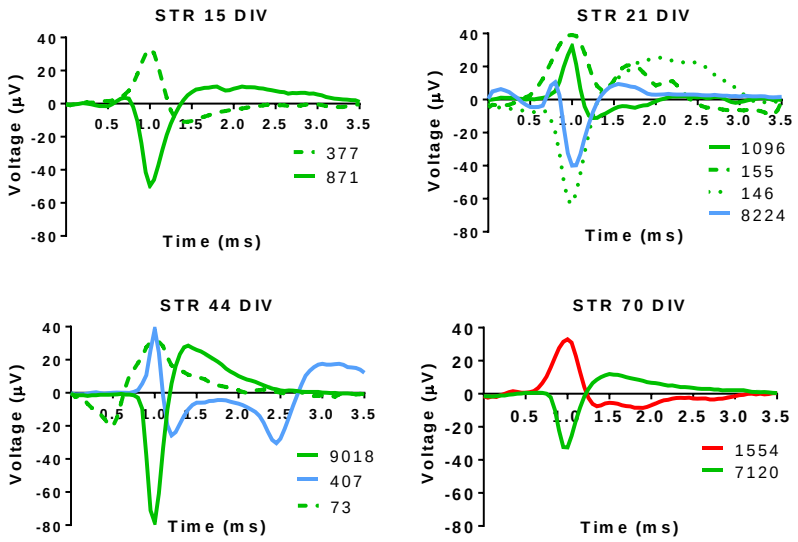

Figure 4.21: STR centroid waveforms over time from an active electrode, E19. Red, green and blue centroids were monophasic, biphasic and triphasic respectively, values in the legend showing how many spikes were sorted into each centroid.

STR displayed activity on all days, also following the trend of negative centroids containing more spikes than positive centroids. There were more centroids on 21 and 44 DIV compared to the two seen at 15 and 70 DIV. 21 DIV showed four centroids of similar shapes while 44 DIV showed two positive centroids with spikes at a similar time but had very different waveforms from 1.5-3.5 ms, showing how centroids can differ post initial spike.

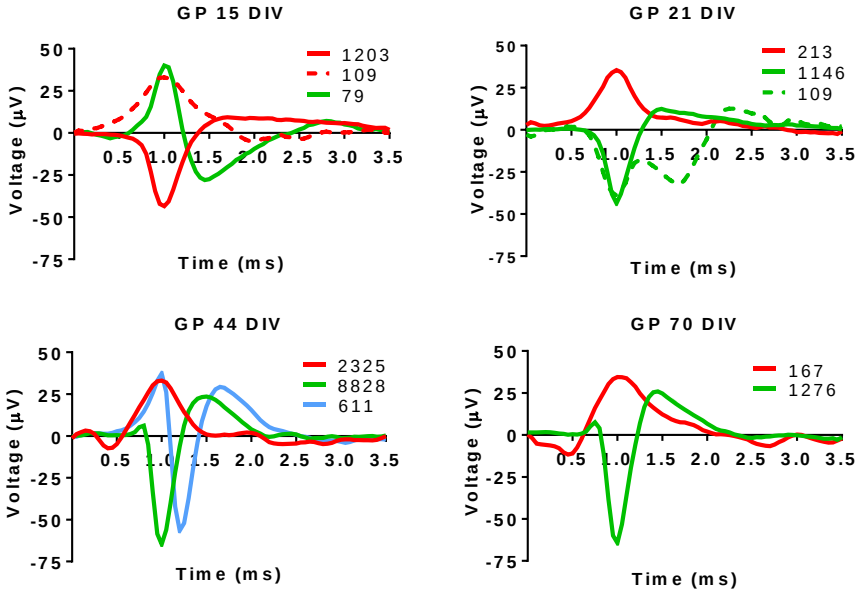

Figure 4.22: GP centroid waveforms over time from an active electrode, E64. Red, green and blue indicate mono-, bi- and tri-phasic centroids respectively, with values in the legend showing how many spikes were sorted into each centroid.

GP displayed activity on all days, and the negative centroids contained a greater number of spikes than the positive centroids. The amplitude of the negative centroids increased from DIV 21 to 44,

whilst the main positive centroid remained unchanged. Of interest are the multiple waveforms on display, with DIV 44 showing mono-, bi- and tri-phasic spikes.

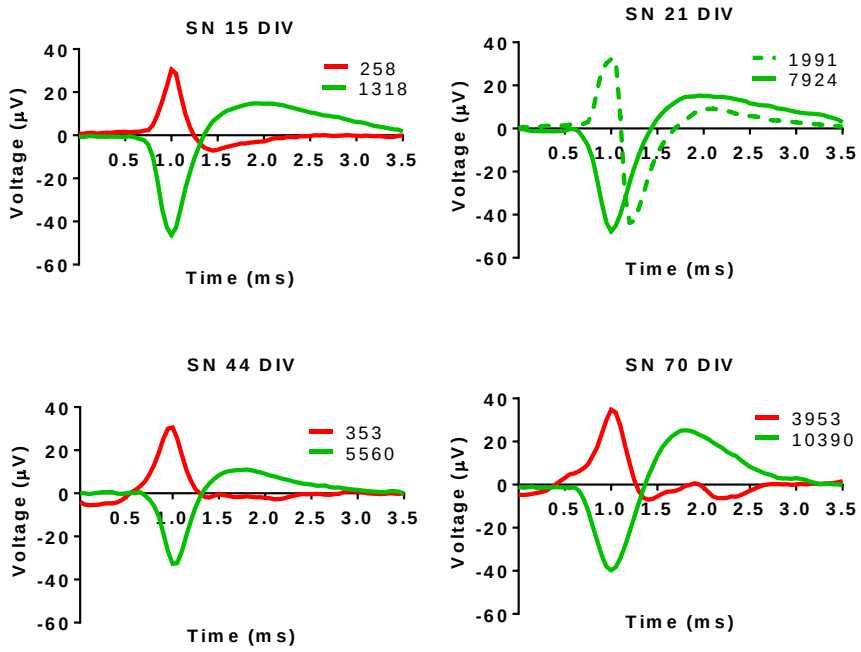

Figure 4.23: SN centroids over time from an active electrode, E44. Red, green and blue indicate mono-, bi- and tri-phasic centroids respectively (with green dashed used to differentiate between similar), with values in the legend showing how many spikes have been sorted into each centroid.

SN only showed one positive and one negative centroid on each day, following the trend of negative centroids having more spikes than positive centroids. The negative centroid waveform remained unchanged over time with only the amplitude and number of spikes changing, while the positive centroid underwent a change at 21 DIV.

4.2.7.2 Whole-MEA centroid shape assessment

Whilst much can be elucidated by assessing centroid waveforms from individual active electrodes, a clearer picture could be gathered by looking at the centroid waveforms across the whole MEA. This was a time-consuming process, as such only one example is provided, namely from CTX DIV 44. This whole MEA centroid waveform analysis is displayed in **Fig.4.24**. As before, only the top four centroids are displayed for each electrode, superimposed onto the relevant electrode location along with the heatmap for DIV 44.

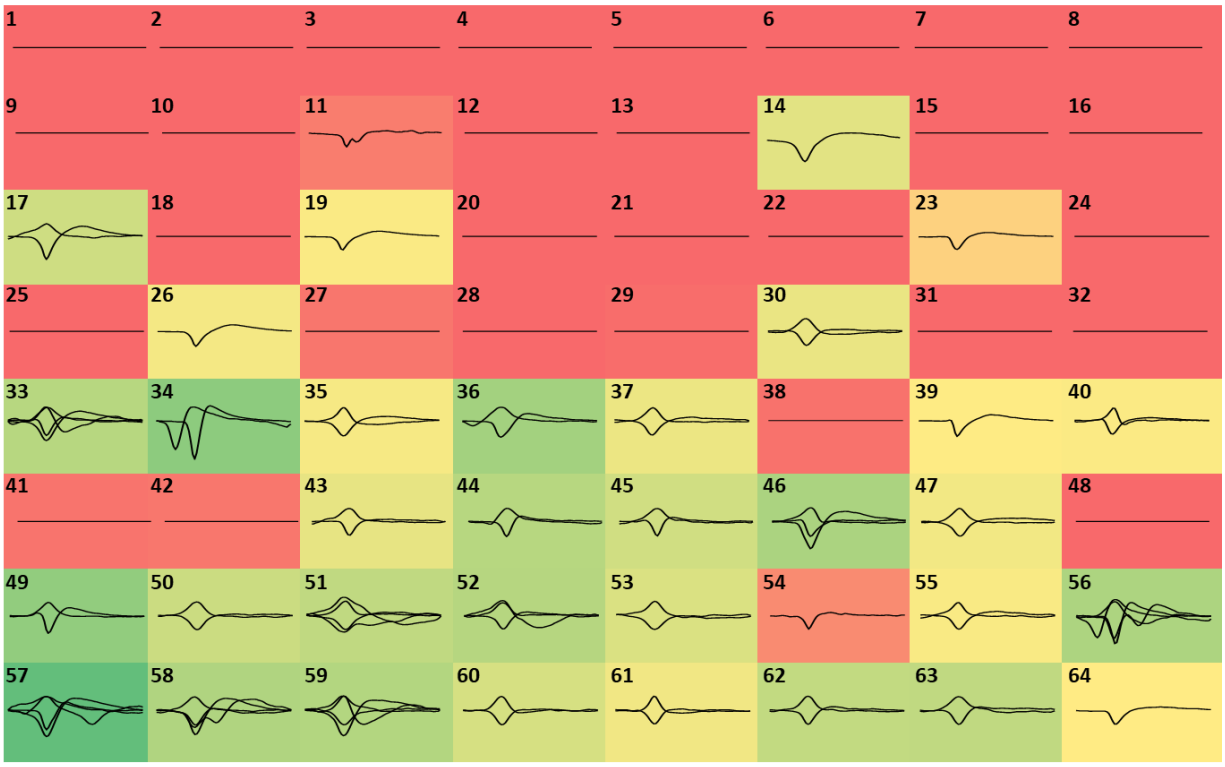

Figure 4.24: Centroid waveforms across a whole MEA, from CTX DIV 44, n=1. Each electrode was labelled from 1-64 and display the centroid(s) produced by that electrode. The same heatmap used in Fig.4.13 (CTX A DIV 44) was used as the background, with red-> yellow-> green indicating min (0), mean (524) and max (9551).

4.2.7.3 Centroid shape categorisation

The sum of all centroids generated by different cell types on MEAs throughout all 70 days of recording were sorted into six types of centroid (positive/negative monophasic, positive-first/negative-first biphasic and positive-first/negative-first triphasic) via Python (code for sorting written by Dr Dimitra Blana, acknowledged), resulting in an overall view of the proportions of different centroids generated by different cell types. The different centroid types are first outlined in **Fig.4.25**, with the categorisation data seen in **Fig.4.26**.

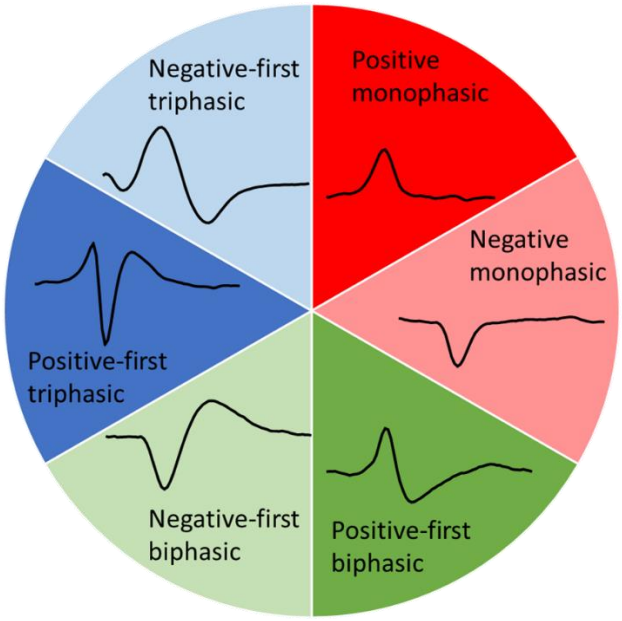

Figure 4.25: The six centroid types generated by cells on MEAs throughout this experiment. Monophasic centroids are red, biphasic centroids are green and triphasic centroids are blue. Centroids were sorted into these three categories based on shape.

There are several notable differences between the centroids generated by each cell type:

- All four cell types had greater proportions of centroids with negative spikes (negative monophasic, negative-first biphasic and positive-first triphasic) compared to their positive counterparts
- There were mainly monophasic and biphasic centroids with a small proportion of triphasic centroids
- CTX cultures generated a larger proportion of monophasic centroids compared to other cell types
- SN cultures generated a larger proportion of biphasic centroids compared to other cell types (potentially due to a lack of negative-first triphasic centroids)
- Proportions of monophasic centroids generated by STR, GP and SN were very similar
- GP cultures generated the most centroids, more than double STR

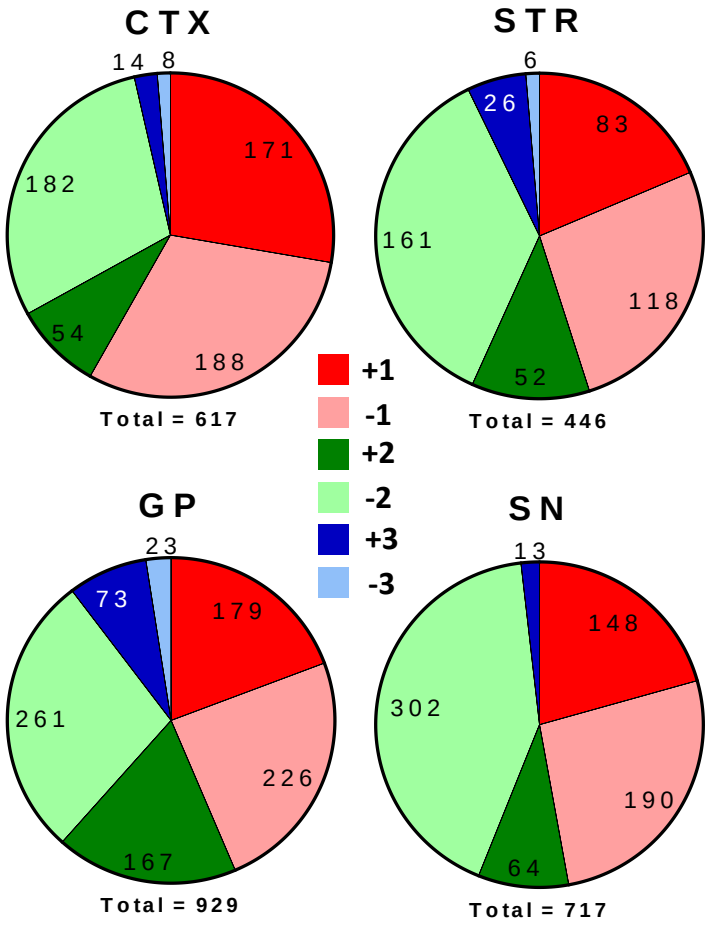

Figure 4.26: Centroid shape categorisation. All centroids from 70 days of recording were sorted into six types, the numbers on pie segments indicating the number of centroids in each category (with total number of centroids below each pie) (n=4).

4.2.7.4 Centroid full duration at half maximum

Centroid spike amplitude and duration (duration of spike, also seen as 'width' on graphs with x-axis of time) can change over time, and the final centroid analysis is to measure the full duration at half maximum (FDHM) of centroid spikes. The FDHM is a standard measure for pulse waveforms where the independent variable is time and is obtained by taking a point at half the maximum spike amplitude and measuring the duration at this point. This measure therefore determines the duration of the spike (whether the spike is 'thin' or 'wide'), and processing centroid FDHM over time determines any changes in centroid shape independent of phase or sign (data displayed in **Fig.4.27**).

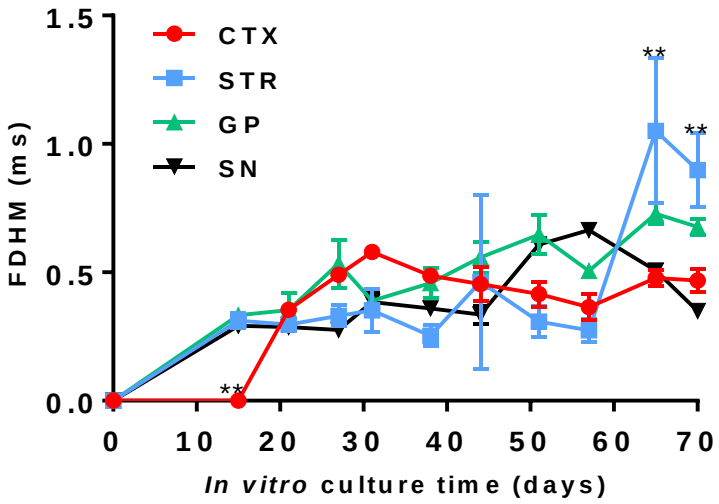

Figure 4.27: Centroid full duration half maximum (FDHM) over time for each cell type, significance generated from post-hoc t-tests comparing one cell type to all others, (**): p<0.01, (n=3).

The majority of centroids for all four cell types appeared to have a FDHM of approximately 0.5 ms, with the interaction between cell types over time having a significant effect on the FDHM of generated centroids (ANOVA (30,40) F=7.34, p<0.0001). CTX was significantly lower on day 15 as no activity had yet been generated, whereas STR had significantly higher FDHM from 65-70 DIV, indicating some change in the culture resulting in 'wider' spikes.

4.3 Discussion

4.3.1 Primary cell culture

Primary CTX, STR, GP and SNc cells all grew well on PEI-coated MEAs. The main difference between culturing on MEAs and glass coverslips was that it was essential to seed cells right into the centre of the MEA, so that the electrodes were in contact with the cells. Unless the electrodes were in physical contact with the cell bodies or axons, they would not be able to measure the cell spontaneous activity. In order to best record from the cells, they were seeded into the exact centre of the MEA. PEI/PDL chemical coating meant that there was no migration, with only glial cells growing outside of the initial seeding area (see **Fig.4.7E-F**). The use of a micro-drop culture eliminated the migration in suspension seen in **Chapter Three (section 3.2.3.1 Cell body migration, Fig.3.13**), as the liquid medium was only a small 50 µL drop that did not extend beyond the edges of the central electrode array.

Initially, cells were far from the reference electrodes, but after over 100 days in culture, astrocytes had spread to the reference electrodes (as seen in **Fig.4.7F**). Astrocytes in contact with the reference electrode may interfere with the noise cancellation role of these reference electrodes, which ideally have a fixed composition for the whole experiment, or it may mean that the reference electrodes are

also subtracting any biological noise generated by the astrocytes from the other electrodes, resulting in only neuronal signals being recorded. It is uncertain at what specific DIV the astrocytes spread to the reference electrode but as the images were taken after 120 DIV (see **Fig.4.7F**) it is possible that for the 0-70 DIV recording period the reference electrodes were entirely free of any cell interference. Regardless, all four cell types were successfully cultured for over 70 days on MEAs at the same density, allowing for long-term observation of a developing neural network.

4.3.2 Electrophysiological assessment

There was a total of 14 recording sessions for all MEAs, recording at least once a week over the 70-day culture period. Recording days were 0, 4, 7, 11, 15, 21, 27, 31, 38, 44, 51, 58, 65 and 70. Days 0-7 showed no activity from any cell type, with electrical activity starting at 11-15 DIV for STR, GP and SN, and 21 DIV for CTX. Please refer to **Appendix One** for the raw data from single electrodes from separate cultures and **Appendix Three** for the whole MEA at each of the same time points.

4.3.2.1 Differences in onset of activity

CTX cells consistently produced electrical signals on or after 21 DIV, unlike STR/GP/SN, which were active as soon as 11 DIV in some cases, 15 DIV in all cases. CTX onset was later because *in vitro* and *in vivo* CTX cells take longer to mature, often taken around E18-19 for experimentation with solely cortical cells (Hatanaka and Murakami. 2002, Chiappalone *et al.* 2006, Anda *et al.* 2016). For experiments in this thesis CTX cells were taken at E16 due to logistics of tissue collection. Thus, the CTX cells may have required a longer time scale in order for CTX cells to functionally mature and start signalling, resulting in the onset being between days 15 and 21, rather than 11-15 in other cell types, which mature quicker than CTX *in vitro* and *in vivo*. Once past 21 DIV, CTX cells were signalling and could be assessed with all the other cell types.

4.3.3 Localisation of activity

The heatmaps seen in **Figs.4.9-4.12** demonstrate how the activity changed in every electrode over time. This is a vital perspective to view data from as each of the 64 electrodes were receiving a wealth of information and while it was not possible to display data in detail from each electrode, it was possible to give a general overview of how the network communication on the MEA changed over time.

As before, the heatmaps first showed that CTX onset was later (21 DIV) as discussed above, while STR, GP and SN displayed onset from 11-15 DIV. Trends observed in detail from just one electrode were observed across the whole MEA. Due to biological variation at every level from the original maternal rat to the way cells dispersed onto the MEA after seeding, there were clear differences in the MEA repeats with the same cell type, as a neuronal network was unlikely to form the same way

twice. Taking this inherent difference between repeats into account, there were several larger-scale differences or trends that could be observed, both over time and between the different cell types.

Each cell type followed a similar trend over time:

1. Initial early onset of low-frequency activity in few locations
2. Spread of activity across the MEA
3. Increase in spike frequency in certain locations
4. 'Concentration' of activity towards these certain locations (as less electrodes continue to remain active)
5. Stable state as certain locations produced the majority of activity

In essence, activity spread across the MEA and then focused onto a certain point while activity elsewhere decreased. When activity was focused to a certain point, the spike frequency of those points increased. This peak and decline of the number of active electrodes can be observed in other *in vitro* studies utilising MEA technology (Biffi *et al.* 2013) and appears to be partly dependent on cell density, a vital factor when forming a functional network. Another reason for this activity format was that neural circuits could be formed by first producing a rough activity-independent wiring map characterised by synaptic connections, followed by activity-dependent elimination (often termed 'pruning') of inappropriate or inefficient connections and reinforcing of efficient and maintained synapses (Tessier and Broadie. 2009), where this pruning stage may be responsible for the decrease in the number of active electrodes and the reinforcing may be responsible for the increase in spiking in certain MEA regions.

This activity suggested that a form of plasticity (neurons that fire together, wire together) or long-term potentiation (LTP) developed within the network. At first most electrodes were firing at an average frequency and producing a number of different activity patterns across the MEA depending on which neurons were functionally synapsed and networked to which other neurons. Some of these patterns of activity were spontaneously strengthened from synapse to synapse persistently over time, and resulted in one particular, more efficient pattern producing far more spikes than other patterns. This may have further resulted in other patterns potentially being suppressed/depressed (long-term depression (LTD) being the opposite of LTP) or re-routing their activity pattern through the strengthened pattern. The end result was several high-activity electrodes surrounded by lesser activity, and with less electrodes receiving activity than the initial spread at the start. Whilst less electrodes were active, electrodes recording activity recorded far more activity than the others. This kind of LTP or plasticity can be invoked *in vitro* with brain slices via stimulation (W. Chen *et al.* 1994, Abrahamsson *et al.* 2016) or recorded spontaneously (Teyler *et al.* 1977, Lalanne *et al.* 2016).

An alternative explanation for the localisation of activity across the MEA over time was that there was a decrease in the number of neurons over time, while their metabolism and functionality remained constant, which resulted in hotspots of activity where neurons are not lost spontaneously to aging, and dark spots where populations of neurons were lost to aging. As a result, the network re-adapted and only surviving neurons were firing, potentially at a higher frequency than before due to a greater load (Lesuisse and Martin. 2002, Chiappalone *et al.* 2006).

For CTX, STR and GP, these trends of peaking and decreasing in percentage activity were seen both in their heatmaps (**Figs 4.9-4.12**) and the graph showing the percentage of active electrodes over time (**Figs.4.13**). There was an initial period where no electrodes were active, followed by a sharp increase and early peak (around 20-30 DIV, indicating the *spread* phase). The number of active electrodes then fell persistently over time (indicating the time frame where LTP/plasticity/cell death may be taking place) until 70 DIV where far fewer electrodes were active. When the percentage of active electrodes was compared to the overall average spike frequency across the MEA over time, there is a clear trend showing that while the spread of activity is decreasing, the overall frequency was increasing: i.e. there is a *focusing* of activity of certain locations on the MEA.

As with the raw spiking, SN neurons on MEAs displayed unique activity compared to CTX, STR and GP neurons on MEAs. While SN cultures on MEAs did show a period of no active electrodes (0-7 DIV) followed by a sharp increase at 11 DIV, the number of active electrodes continued to rise and peaked at nearly 100% active electrodes, i.e. full MEA coverage. This trend was significantly different to the other cell types, with SN neurons on MEAs displaying ~ 70% active electrodes after 70 DIV (compared to 20-30% for CTX, STR, GP). It is unknown if this lack of SN activity spread decrease has been replicated by other groups. While this may suggest a lack of LTP or 'focusing' of activity onto specific locations, the spiking frequency rose in proportion with the spread of activity, the opposite trend compared to CTX, STR and GP. Heatmaps showed that there were indeed certain locations with higher activity, these were simply not accompanied by a decrease in the spread of activity across the MEA, as both the spread of activity and spike frequency increased over time. This suggests that SN cells may have experienced LTP but no LTD, neuron spiking only increased in spike frequency. However, a proportion of the SN neurons are GABAergic and may have been able to inhibit the activity of the other neuronal types (e.g. DA neurons) within SN cultures in some fashion (Ellens and Leventhal. 2013).

4.3.4 Spiking and bursting frequencies

For all cell types the average spike frequency increased over time from onset (15-21 DIV) to peak (30-50 DIV) (**Fig.4.14**). This was potentially due to the fact that cells were functionally maturing *in vitro* (Chiappalone *et al.* 2006), as the activity was from the same location each time and neurons unlikely to migrate due to the PEI/PDL coating. The main variables that changed over time were most

likely the number of glial cells, the size/number/density of axons and dendrites, and the number/density/maturity of synapses formed between neurons. This more highly connected network would have formed between 20-40 DIV and resulted in an increase in detectable extracellular action potentials (EAPs). However, from 40-70 DIV the frequency did not increase, remaining static or decreasing, even though it is unlikely that the network formed at 20-40 DIV underwent large structural changes between 40-70 DIV. *In vitro* studies on primary rat CTX neuron cultures have demonstrated that neuronal cell density, connectivity and number of synapses per neuron have all been shown to increase over the first four weeks in culture, but then decrease after this time as part of the maturation process (Muramoto *et al.* 1993, Ichikawa *et al.* 1993, Chiappalone *et al.* 2006), demonstrated by a lower firing rate and related to activity-dependent processes and homeostatic plasticity (Marom and Shahaf. 2002, Turrigiano and Nelson. 2004), with experiments observing these effects up to 35 DIV. These studies present a timeline where there is a very low density of immature synapses on 7 DIV, followed by increases in the number and maturity of synapses after each week *in vitro*, further followed by decreases in the number of synapses after 5 weeks *in vitro*. This closely follows the trend of activity seen here, where there is an onset of activity within the first two weeks, a peak in activity within the 3rd-4th weeks and a gradual decrease until the 10th week and the end of recording. Chiappalone *et al.* (2006) states that, without any external sensory stimulus, an *in vitro* network matures firstly with modulation and shaping of synaptic connectivity (weeks 1-2, early development) and then with maturation of synaptic connectivity (weeks 4-5, 'late' development) (Chiappalone *et al.* 2006).

Unfortunately, weeks 6-10 of *in vitro* primary neural electrophysiological assessment are mostly unaccounted for in the literature, where studies rarely exceed 35 DIV. One study cultured E16 mouse CTX neurons for 60 DIV, and demonstrated that levels of GAPDH (used as a metabolic marker), synaptophysin (a synapse marker) and glutamate receptors (necessary for CTX glutamatergic neuron functionality) peaked around 25 DIV and remained unchanged through to 60 DIV, indicating that the *in vitro* neural culture system matured, established synapses and were viable across the long term, i.e. up to 60 DIV (Lesuisse and Martin. 2002). Notably, this study also showed that only approx. 40-50% of the original cells (from 5 DIV) survived until 60 DIV, levels of β-tubulin and GFAP (neuron and astrocyte markers respectively) were constant from 5-60 DIV, and levels of NeuN declined from 40-60 DIV, suggesting the loss of a subset of neurons. Lesuisse *et al.* (2002) conclude that older cultures (up to 60 DIV) have fewer neurons than younger cultures (20-25 DIV) due to spontaneous age-related loss of neurons, but the remaining neurons are metabolically and structurally robust. It should be noted this study was performed with immunostaining only and features no functional assessment components. As a result it is important to take into account that by 70 DIV in our models, cells are very likely to be dying in a spontaneous age-related manner and future experiments should

characterise network at each time point. A look at 120 DIV (**Fig.4.8**) shows that there are many dead cells by this time point, particularly towards the centre of the MEA where viability was only 50-60%.

Of particular interest was the activity of SN, which had significantly greater average levels of spike frequency than CTX, STR or GP from onset to the final recording. The main differences between the cell types that may explain these functional differences are that SN cells were taken at E14 (peak SN neurogenesis) rather than E16; neurons in the SN do not originate from the cerebral hemispheres or medial or lateral ganglionic eminences (MGE or LGE) like CTX, STR and GP neurons, instead originating from the ventral midbrain (VM); and SN neurons contain the only source of dopaminergic neurons out of all four cell types (Ellens and Leventhal. 2013). Whilst STR, GP and SN all contain GABAergic neurons, there are clear differences in activity for each cell type when cultured separately *in vitro*. The difference in activity presented by SN neural cultures will be discussed further in **section 4.3.5.1**.

In summary, both the average and maximum spike frequency increased over time from approx. 15-30 DIV and plateaued/decreased from 50-70 DIV. As outlined in the introduction (**section 4.0.1 Typical electrophysiology of basal ganglia nuclei**), predicted values for *in vitro* extracellular recording of basal ganglia nuclei were gleaned from the literature. Our experimental values match all these predictions, showing the robust nature of our spike frequency data (outlined in **Table 4.2**).

Table 4.2: Predicted vs actual spike frequencies. Predicted values from the literature (from *in vitro* extracellular studies where possible) compared to the average (MEAN, Fig.4.14) and maximum (MAX, Fig.4.15) spike frequencies from peak to final result from our MEA experiments.

Basal ganglia nuclei	Predicted spike frequency (Hz)	Actual spike frequency (Hz)
Striatum	~**0.5-2** for MSNs (Miller *et al.* 2008), **10-20** for cholinergic interneurons (Walters *et al.* 2007, Gage *et al.* 2010).	MEAN: **0.43-0.78** MAX: **7.00-9.78**
Globus pallidus (GPe and GPi)	**26** for GPi (*in vivo*), less for GPe (Walters *et al.* 2007). Also show slow **0.4-1.6** firing (Mallet *et al.* 2006, Mallet *et al.* 2008, Mallet *et al.* 2012).	MEAN: **0.55-2.00** MAX: **7.00-12.00**
Substantia nigra (SNr and SNc)	**10-15** for SNr GABAergic (Boraud *et al.* 2002), ~**1-4** for SNc dopaminergic (Ding *et al.* 2011, Lee *et al.* 2011).	MEAN: **1.97-4.54** MAX: **10.85-20.80**

The STR, GP and SN all contain populations of low and high frequency firing neurons: STR contains slow-firing MSNs and fast-firing cholinergic interneurons, GP contains slow-firing GPe GABAergic neurons and fast-firing GPi GABAergic neurons, and SN contains slow-firing SNc dopaminergic neurons and fast-firing SNr GABAergic neurons. For the STR, the slow-firing population is in clear majority (90% of the STR consists of MSNs), while the GP and SN are more likely equally split between the GPe/GPi and SNc/SNr respectively.

One way to interpret the data from **Table 4.2** is that by taking an average of the frequencies across the MEA, the slower-firing population is represented, while by taking the maximum spike frequency the faster-firing population is represented. Our STR MEA results line up closely to *in vitro* and *in vivo* data from the literature (summarised in **section 4.0.1.2 Striatum (STR)**) with this interpretation, the average spike frequency generated by MSNs (~0.7 Hz predicted vs ~0.6 Hz experimental) and the maximum frequency generated by interneurons (~15 Hz predicted vs ~8.4 Hz experimental). By selecting only the maximum spike frequency received each day from a single electrode, it was possible that this is selecting for electrodes that were receiving signals from the STR interneurons, which fired at a much faster rate than STR MSNs (Gage *et al.* 2010). Indeed, the location of the maximum spike frequency on STR MEAs was one of the most consistent (**Fig.4.16**), suggesting that these maximum activity locations were in fact electrodes in contact with populations of STR interneurons, rather than MSNs that were firing at more than ten times the average rate.

SN experimental data from our SN MEAs also closely aligned to the literature, if average spike frequencies were selecting for SNc dopaminergic neurons (~2.5 Hz predicted vs ~3.3 Hz experimental) and maximum frequencies were selecting for SNr GABAergic neurons (~12.5 Hz predicted vs 15.8 Hz experimental). SN MEAs displayed significantly higher spike frequencies over time compared to CTX, STR and GP.

There was less data available for *in vitro* extracellular activity from GP, especially from GPi and GPe subunits, as such the data on **Table 4.2** is not as accurate as STR and SN data. Mean frequencies of firing on GP MEAs were much lower than GPi firing *in vivo*, but as STR and SN have both been shown to fire less in *in vitro* preparations than *in vivo* animal models (S. Ding *et al.* 2011), it is reasonable to assume that GP firing was also attenuated *in vitro*. The large differences between the mean and max values from GP MEAs may have been selecting for GPe (1 Hz predicted vs 1.3 Hz experimental if slow wave activity) and GPi neuron populations (26 Hz predicted from *in vivo* vs 9.5 Hz experimental) respectively. This maximum activity was more mobile across GP MEAs over time, suggesting that there may have been widespread populations of GPi neurons on the MEA.

4.3.4.1 Greater nigral spiking frequencies

SN cultures exhibited greater average and maximum spike frequencies at virtually every time point compared to cultures from the CTX, STR and GP. One possible explanation is the presence of dopaminergic (DA) neurons in SN cultures. There exist multiple firing schemes for midbrain DA neurons, which can either exhibit regular pacemaker-like firing activity (1-5 Hz) (Berretta *et al.* 2010) or irregular clusters of high-frequency spikes, referred to as 'bursts' (10-20 Hz) (Blythe *et al.* 2009, Marinelli and McCutcheon. 2014). These bursts temporarily increase DA levels in the midbrain and can activate certain post-synaptic DA receptors, counteract re-uptake mechanisms and are generally vital for DA neuron function (Grace and Bunney. 1983, Dreyer *et al.* 2010, Marinelli and McCutcheon.

2014). Interestingly, genetically modified DA neurons that cannot produce dopamine lose the ability to fire bursts, showing only pacemaker activity and a significantly lower spike frequency and inter-spike time (Paladini *et al.* 2003, Marinelli and McCutcheon. 2014). In addition, the SN contains GABAergic interneurons that have a firing rate of approx. 10 Hz, although these interneurons should also account for some level of activity in the STR, GP and even CTX cultures as STR and GP are predominantly GABAergic nuclei and CTX contains small populations of GABAergic interneurons (Berretta *et al.* 2010, Ellens and Leventhal. 2013). This combination of fast random firing and frequent bursting from two different cell populations, the presence of dopamine, the different developmental age (E14 vs E16) and the different developmental region (mesencephalon vs telencephalon) may have been responsible for SN neurons having significantly greater average and maximum spiking frequencies when compared to CTX, STR and GP neurons, which all have very different roles in basal ganglia circuitry. Generally, the reason for a significantly increased spiking frequency in SN cultures is challenging to determine, considering that midbrain DA neuron activity is distinctly heterogeneous, with variations in activity across individuals, physiological states, development and time (Marinelli and McCutcheon. 2014).

4.3.4.2 Bursting activity

The number of bursts fired and the number of spikes per burst in each recording session was not significantly different between all four cell types. As bursting activity was the same yet there were significant differences in overall spiking frequencies, (SN and GP had higher spike frequencies overall compared to CTX and STR), SN and GP must have featured significantly more random spikes and sub-burst clusters of spikes (<10 Hz) compared to CTX and STR (Ellens and Leventhal. 2013).

4.3.5 Centroid assessment

For convenience, spikes were grouped into groups of similar spikes, or 'centroids' (see **Fig.4.18**). For this experiment the parameters to create a centroid were a group of more than 50 spikes that were more than 80% similar to each other. Various levels of similarity were tested, showing that the number of spikes necessary to create a centroid did not largely affect the number of centroids (as similar spikes often numbered in the 100s to 1000s), but altering the percentage similarity had a large effect on the number of centroids formed. The software in use [Mobius, AlphaMED] only calculated up to a maximum of 20 centroids, and when using 50% similarity nearly every electrode from every experiment resulted in the full 20 centroids. When using 90-100% similarity, there were rarely more than 1-2 centroids and large amounts of data were filtered out. The current value of 80% represented a compromise between having too much data and too little after processing.

As centroids were representative of the waveforms/profiles/shapes of spikes being produced by neural cells in culture, the greater the number of centroids the greater the variation in spiking

activity. As outlined in the introduction (see **Figs.4.2 and 4.3**), EAPs can be monophasic/biphasic (from cell bodies and/or synapses, see **Fig.4.3** right hand side) or triphasic (from axons, see **Fig.4.3** left hand side), and with a negative or positive voltage. This resulted in six different main spike waveforms, mostly depending on the location of the electrode in relation to the neuron cell body (see **Fig.4.4**). As the neurons were cultured on a PEI-coated surface, they did not migrate and subsequently were always the same distance from the electrodes from day 0 to day 70 (Lelong *et al.* 1992, Vancha *et al.* 2004, B. F. Liu *et al.* 2006). As the neuron cell bodies did not move, any variation in spike waveforms was most likely due to functional maturation or glial proliferation, with cells making more synapses that became more mature over time. If two neurons synapsed over an electrode, or a neuron extended an axon over an electrode, the received signals may have changed. As such, changes in the number and waveform shapes of centroids created from spiking activity presented a new perspective to assess the neural culture functional activity from.

For every cell type, the number of centroids decreased from early (11-21 DIV) to mid (25-44 DIV) to late (50-70 DIV) phases (**Fig.4.19**). This effectively meant that the variation in spikes produced by the cells was decreasing. This may mean that the cells were producing less spikes, but the spike and burst frequency data (**Figs.4.14, 4.15 and 4.17**) clearly showed that the cultures were generally producing more spikes over time as they functionally matured *in vitro*. As the spike variability was decreasing and the spike frequency was increasing over time, this may be another piece of evidence that the cells were experiencing a form of plasticity or LTP/LTD, with certain waveforms and patterns of activity being 'selected' over time and strengthened until they were the only centroids remaining, with other centroids being supressed/depressed (Teyler *et al.* 1977, Lalanne *et al.* 2016). This occurred across every cell type, with the late stages producing significantly less spikes than the early stages, indicating that each cell type was maturing functionally *in vitro*.

The shapes of certain centroids also changed over time (**Fig.4.20-4.24**), but as this data was assessed for one electrode across only four different time points for each cell type (due to the time-consuming nature of MEA data processing and the sheer volume of data produced), there was a compromise between experiments taking too long to complete, and data not being fully representative of the MEA as a whole. Centroid shapes were consistent but also changed gradually over time, such as CTX (see **Fig.4.20**), where from 21-70 DIV there were consistently two monophasic centroids, the negative one containing more spikes than the positive one, and the positive spike peaking at approx. 30 µV. The changes occurred in the negative centroid, which increased in amplitude from approx. -30 µV to -50 µV from 44-70 DIV, had a sharper peak, and hyperpolarised to ~8 µV rather than returning to the baseline as before. In this manner, certain aspects of centroid shape remained unchanged throughout the experiment, whereas other aspects changed. Lewandowksa *et al.* refer to this change of shape over time *in vitro* as spike 'evolution', observing the change in spike shapes recorded from E18 rat CTX cultures in channels until 28 DIV (Lewandowska *et al.* 2015). They also noted that spike

amplitude increased over time from 18-37 DIV, spikes had distinct reproducible shapes depending on whether they were recording from cell bodies or axons, and complex spike shapes can originate from a single cell or from a linear superposition of multiple axonal signals. These findings agree with our study, where centroid shapes from CTX, STR, GP and SN MEAs increased in amplitude from 21-44 or 21-70 DIV (**Figs.4.20-4.24,** mostly increased in the negative phase), had consistent shapes depending on the location of the electrodes, and featured complex spike shapes from STR and GP MEAs (**Figs.4.21-4.22**). This 'evolution' of spike shape over time and the dependence of spike shape on soma/axon proximity is also consistent with data gathered from other PDMS microchannel devices with MEA recording capabilities (Bakkum *et al.* 2013, Habibey *et al.* 2015, L. Pan, Alagapan, Franca, Leondopulos, DeMarse, Brewer and Wheeler. 2015a, N. Hong *et al.* 2017b).

The number of phases of each centroid also differed between cell types, with CTX cells displaying positive and negative monophasic centroids, SN cells displaying positive monophasic and negative-first biphasic centroids while STR and GP displayed all three types, typically with positive monophasic, negative-first biphasic and positive-first triphasic centroids. Theoretically, any triphasic centroids were generated from axons while mono/biphasic centroids were generated from cell bodies and/or synapses. The distinction between 'what part of a neuron generated what signal' in these *in vitro* cultures is very difficult to determine as every electrode was in contact with a mix of axons, cell bodies and synapses (see **Figs.4.6 and 4.7**), but in **Chapter Five** we show that by isolating the cell bodies and the axons in separate compartments we can indeed see triphasic centroids from axons and mono/biphasic centroids from cell bodies. These generated spikes have also been identified by *in vitro* MEA work from other devices (Lewandowska *et al.* 2015, Deligkaris *et al.* 2016) as well as through *in vivo* recordings (Robbins *et al.* 2013, Dipalo *et al.* 2017). Interestingly the *in vivo* recordings from Robbins *et al.* identified monophasic spikes as from pyramidal cells and biphasic spikes as from interneurons, suggesting that centroid shape can identify where the signal originated as well as what type of cell it originated from.

Typically, monophasic centroids had a negative peak, biphasic centroids were negative-first with a smaller positive recovery and triphasic centroids were 'positive-first' followed by a main negative spike, the majority of each centroid type being negative. However, positive mirrors of mono- and biphasic centroids were also observed (positive monophasic centroids in all four cell types **Fig.4.20-4.23**, positive-first biphasic centroids in STR, GP and SNc **Fig.4.21-4.23**), albeit containing less spikes than negatively-spiking centroids. Most recorded centroids had negative spikes because EAPs and extracellular activity were generated by sinks and sources (see **Figs.4.2 and 4.3**), with spikes being negative due to an influx of current from a source to a sink resulting in a negative change in the membrane potential (Nam and Wheeler. 2011). Positive EAPs may have been partially generated by repolarising potassium (K^+) currents, with potassium blockers slightly reducing the amplitude of positive EAP peaks, but EAP peaks were also eliminated by sodium (Na^+) channel blockers, indicating

that there is a strong sodium component to positive EAPs (Sitnikov *et al.* 2016). The biophysical origin of these positive centroids remains to be determined due to the complex extracellular membrane ion currents.

4.3.5.1 Amplitude differences: intracellular vs extracellular

An AP is defined as an event that occurs once a neuron's transmembrane potential reaches a threshold, either due to stimuli or other inputs such as synapses or gap junctions (Obien *et al.* 2015). Intracellular action potentials (IAPs) and EAPs occur across similar time-frames but differ in amplitude (see **Fig.4.1**).

As opposed to taking a measurement from the interior of a single neuron, an EAP is affected by the morphology and type of the neuron as well as distance from electrode and presence of other neurons and glial cells, all potentially on the same electrode (see **Fig.4.4**) (Pettersen and Einevoll. 2008). EAPs also feature a low-pass filtering effect where spike-width increases the further the signal is measured from the cell body (again, see **Fig.4.4**), and EAP amplitude is proportional to the cross-sectional area of all dendrites connected to the cell body, with neurons featuring many, thicker dendrites having larger amplitude spikes and vice versa. EAPs and IAPs are recorded by very different methods, and this results in a very different spike profile and amplitude.

Over time on the MEA, *in vitro* neural cultures may develop spatially localised plasticity with low variability waveform specific and higher frequency firing within certain tight regions of 4-5 electrodes, while the rest of MEA has higher variability and lower activity. This activity comes in the form of mono-, bi- or triphasic EAPs, with more complex activities producing more complex waveforms.

4.4 Conclusions

By recording from CTX, STR, GP and SN cultures in isolation for up to 70 DIV, a robust baseline of activity to compare data from subsequent experiments to was established. A vast amount of data was generated (recording from 64 electrodes for 14 recording sessions for 4 different cell types over >4 repeats each), which is presented in a raw format and also after several different kinds of processing, namely spike sorting into centroids, extracting spike frequencies, burst numbers, generating heatmaps of whole MEAs over time, as well as determining centroid phase, type and duration.

These extracellular recording experiments were able to confirm the neuronal subtypes within each population using a functional method (see **Table 4.2**) which was also reproducible despite the presence of inherent biological noise. This *in vitro* model therefore represents a powerful platform for study and through development can effectively translate to other studies.

By studying the spontaneous extracellular electrophysiological activity generated by each of these basal ganglia nuclei in isolation *in vitro* over the long term (up to ten weeks), we are now better able to produce a model of basal ganglia circuitry. Each of the metrics outlined in the results will be compared to the same metrics generated from co-culture work in **Chapter Five** and Parkinsonian work in **Chapter Six**.

Chapter Five: Long-term study of connected neural co-culture functionality

5.0 Introduction

The basal ganglia (BG) consists of specific nuclei connected in signal pathways, so that input from the cortex can be filtered and integrated in order to output to the brainstem and spinal cord. These pathways also need to be modelled over the long term in order to better mimic the BG.

After analysing CTX, STR, GP and SN in isolation as separate cultures the next step was to combine two cell types together on an MEA, using the five-port device (5PD), in order to measure the spontaneous electrophysiological activity of a co-culture. This was then compared to the seperate culture work (**Chapter Four**) to determine the electrophysiological effects of connecting these basal ganglia using the 5PD.

The relevant *in vivo* pathways being modelled by these co-cultures are the corticostriatal pathway (CTX-STR), striatopallidal pathway (STR-GP) and the nigrostriatal/striatonigral pathways (SNc-STR and STR-SNr), all major connections and signal pathways within the basal ganglia (BG) that have vital roles *in vivo*. This aims of this chapter were to re-create these BG pathways using our 5PD and model their electrophysiological activity *in vitro*.

5.0.1 Corticostriatal (CTX-STR) signal pathway

5.0.1.1 Corticostriatal structure

The BG and frontal CTX operate together to execute planned motor activity and other goal-directed behaviour *in vivo*, as such the connection between the CTX and the STR (where the CTX inputs information to the BG) is a vital and complex pathway. The corticostriatal pathway involves pyramidal glutamatergic neurons of the CTX projecting to and synapsing with the GABAergic medium spiny neurons (MSNs) of the STR (which make up 90% of STR neurons, the other 10% being GABAergic and cholinergic interneurons) (Yager *et al.* 2015). These CTX projections originate from numerous areas of the CTX and form synapses with MSNs across the entire STR, forming dense dendritic trees and topographically complex yet organised connections within the STR (Haber. 2016). Notably, the STR also receives a nearly equal number of projections from the glutamatergic neurons of the thalamus (namely the thalamostriatal pathway) with cortico- and thalamostriatal connections intermixing on MSN dendritic trees (Smith *et al.* 2004).

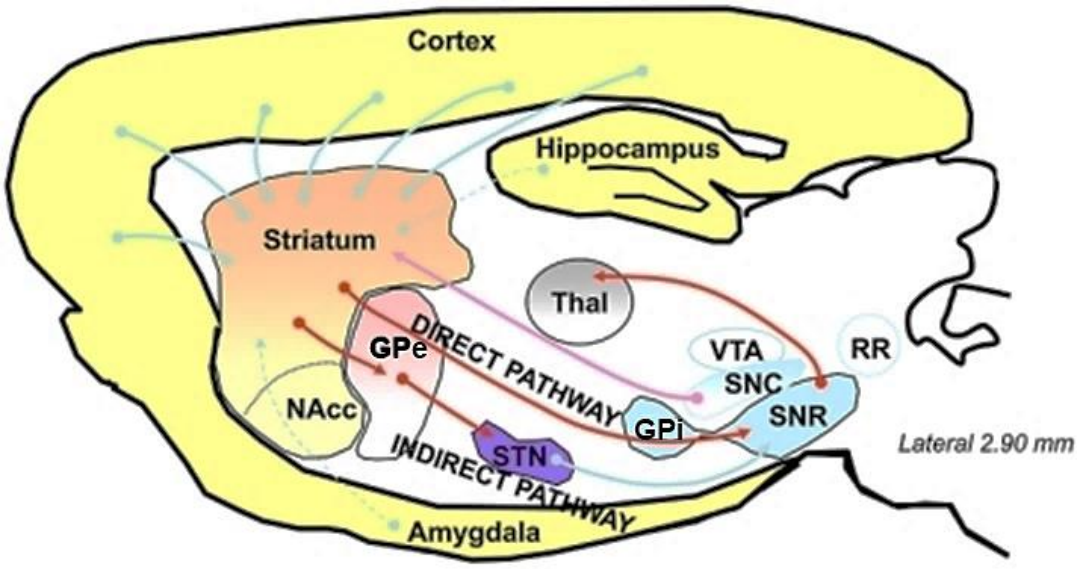

Figure 5.1: Example pathways within the BG. Note the numerous projections from locations across the CTX to areas across the STR. STN: subthalamic nucleus, GPi/e: globus pallidus internal/external segment, SNr/c: substantia nigra pars compacta/reticulata NAcc: nucleus accumbens, VTA: ventral tegmental area, RR: retrorubral nucleus. Direct pathway involves STR projecting to GPi/SNr, which project to the thalamus. Indirect pathway involves STR projecting to GPe and STN, which then project to the GPi/SNr. Light blue arrows are glutamatergic, red is GABAergic and pink is dopaminergic. Image adapted from (David. 2009).

Each of the many excitatory projections from the CTX contain a massive number of neurons, with a CTX projection estimated to consist of 5000 CTX neurons, which converge on a single STR neuron. Despite these projections consisting of huge bundles of CTX neurons, each CTX neuron within the bundle only forms a single synapse on the receiving STR neuron, each projection has the potential to activate only that single STR neuron, and there is only a 10% chance of these projections overlapping with adjacent STR neurons (Randall *et al.* 2011). Thus, CTX projections to STR are huge and dense but highly organised and structured.

The STR is unique in that it is the only subcortical area where two types of CTX pyramidal glutamatergic neuron projections converge: the STR receives projections from both pyramidal tract (PT) neurons and intra-telencephalic (IT) neurons. PT neurons are found in lower layer 5 of the CTX that project ipsilaterally to the STR and IT neurons are found in upper layer 5 of the CTX that project bilaterally to the STR (Khibnik *et al.* 2014). In addition to receiving both PT and IT neurons, STR MSNs consist of two morphologically identical yet functionally distinct types, namely *direct*-pathway MSNs (dMSNs or D1 MSNs), which project directly to the output nuclei of the basal ganglia (GPi and SNr) and express D1-type dopamine (DA) receptors; and *indirect*-pathway MSNs (iMSNs or D2 MSNs), which project to the GPe (which then projects to the STN, which then projects to the GPi and SNr) and express D2-type DA receptors (Shepherd. 2013), both seen above in **Fig.5.1**. This results in potentially complex sets of interactions between input glutamatergic PTs and ITs of the CTX and GABAergic dMSNs and iMSNs of the STR, across many dense functional territories of the STR. This complexity is further increased by the uncertain nature of IT and PT neuron preference for

connectivity with either dMSNs and/or iMSNs (Lei *et al.* 2004, Ballion *et al.* 2008, Rangel-Barajas and Rebec. 2016).

Regardless, the CTX inputs to the STR from numerous different functional and spatial zones and with different glutamatergic neuron subtypes, while the STR receives these inputs across different functional (direct and indirect pathways) and spatial zones and with different GABAergic MSN subtypes. These structurally dense yet organised corticostriatal synapses make up the main input to the BG.

5.0.1.2 Corticostriatal function

Functionally speaking, CTX excitatory inputs shape STR activity and subsequently activity of the BG as a whole. Studies show that corticostriatal plasticity is necessary for abstract skill learning and planning of movement (Koralek *et al.* 2012), including control of motor decisions in response to activity in the somatosensory, auditory, motor and visual cortices (Znamenskiy and Zador. 2013, Khibnik *et al.* 2014).

5.0.1.3 Corticostriatal electrophysiology

The massive and organised excitatory inputs from the CTX are vital for MSN electrophysiological activity patterns and therefore for STR activity itself. MSNs have a high potassium (K^+) conductance at rest and as such are usually in a hyperpolarised state. In order to shift to a depolarised state and fire action potentials (APs), MSNs require excitatory glutamatergic input from the CTX. Initial glutamate input shifts MSNs to their depolarised state and additional glutamate results in firing, albeit at a lower frequency than other BG nuclei such as GPi/GPe and SNc/SNr, MSNs averaging around 15 Hz *in vivo* (Rangel-Barajas and Rebec. 2016). In order to avoid excessive excitation and chronically hyperactive MSNs, high-frequency GABAergic interneuron firing as well as the GABAergic MSNs themselves modulate their own activity via inhibitory GABA. Due to MSNs requiring excitation to fire, STR activity is entrained by CTX activity, with CTX oscillations resulting in depolarised or hyperpolarised STR MSNs and continued CTX activity resulting in extended periods of STR activity. At corticostriatal synapses, a single volley of activity from the CTX increases the glutamate released by the next volley, leading to enhanced post-synaptic depolarization with repetitive stimulation (J. Ding *et al.* 2008).

Studies estimating the number of CTX neurons needed to drive activity in a single STR neuron range from 85-1000 synapses, and approximately 15-30 simultaneous inputs to reach a depolarisation threshold that allow the STR neuron to fire (Randall *et al.* 2011). More work is necessary to determine the effect and strength of the excitatory connection between CTX and STR neurons. Work from this project intend is intended to contribute to the understanding of CTX-STR connectivity, via CTX-STR co-culture with the compartmentalised 5-port device (5PD). *In vitro* work has shown that both mixed

(Randall *et al.* 2011) and compartmentalised-yet-connected (Virlogeux *et al.* 2018) CTX and STR co-cultures have a similar resting activity to the *in vivo* system, as well as demonstrating excitatory firing from CTX neurons to STR neurons in a unidirectional capacity *in vitro*.

Recent models have adopted compartmentalised microfluidic devices in order to study CTX-STR co-cultures in order to study Huntington's disease (HD), a condition caused by degeneration of STR MSNs and specific CTX neurons (Virlogeux *et al.* 2018). Defects in the corticostriatal pathway causing debilitating and progressive neurodegenerative disease is a clear sign of the importance of this pathway and what we stand to gain and learn from modelling it in our functional *in vitro* model.

5.0.2 Striatopallidal (STR-GPe/i) signal pathway

5.0.2.1 Striatopallidal structure

Receiving signals from the CTX and STN, the STR is the main input nuclei to the BG. Information is transferred and filtered through the BG from input (STR) to output (GPi/SNr) by two major signal pathways: the direct and the indirect pathways. Both pathways consist of GABAergic projection MSNs from the STR to GP nuclei and are therefore both inhibitory.

The *indirect* pathway is where iMSNs (or D2 MSNs) project from the STR to the GPe (then to the STN and then GPi/SNr, as seen in **Fig.5.2**) (Sano *et al.* 2013). These projecting iMSNs inhibit GPe activity, reducing GPe inhibition of STN activity (the STN normally acting to excite GPi/SNr activity) resulting in increased GPi/SNr activity output to the thalamus and suppressed movement. Studies show ablating iMSNs of the STR results in motor hyperactivity.

The *direct* pathway is where dMSNs (or D1 MSNs) project from the STR directly to the GPi/SNr. This pathway involves directly inhibiting the activity of the GPi/SNr output nuclei, resulting in decreased GPi/SNr activity and increased movement, namely the opposite effect of the indirect pathway (Ellens and Leventhal. 2013). As a result, the direct and indirect pathways are also referred to as the '*go*' and '*no-go*' pathways respectively. However, these dMSNs also innervate the GPe in passing.

Data on rodent striatopallidal projections is limited but suggests a tripartite organisation of STR projections to GPe, where MSN neurons from the medial, lateral and ventral regions of the STR project to neurons from the same regions on the GPe (Gittis *et al.* 2014).

5.0.2.2 Striatopallidal function

The direct and indirect pathways are functionally distinct and work in concert, carefully regulating the planning and execution of movement by careful inhibition of select nuclei within the BG. However, while the pathways have long been considered functionally separate, they have been shown to not be anatomically separate. Some anatomical studies on mice suggest that most (and

maybe all) MSNs of the STR project to the GPe, with some being part of the indirect pathway that projects directly to the GPe, and others being part of the direct pathway and sending collaterals to the GPe on their way to the GPi/SNr (Kupchik *et al.* 2015), suggesting a degree of overlap between indirect and direct pathways (Bertran-Gonzalez *et al.* 2010). Labelling of 120 STR MSN projection neurons in mice showed that 37% projected exclusively to the GPe (indirect) and 3% projected exclusively to the GPi/SNr (direct). The remaining 60% projected to the GPi/SNr and collaterally to the GPe, bridging both the direct and indirect pathways (Cazorla *et al.* 2014). These relationships are outlined in a simpler BG diagram on **Fig.5.2**.

By culturing STR in one port and GP in another, using our 5PD, we could assess these direct and indirect pathways in isolation.

5.0.3 Striatonigral (STR-SNr)

While the two sections of the GP (GPi and GPe) are largely similar in cellular composition and can represent each other in this model, the SN represents a larger issue. *In vivo* the SN consists of one mostly GABAergic nuclei (SNr) and one mostly dopaminergic nuclei (SNc) (Ellens and Leventhal. 2013). By dissecting the SN as a whole the result is a mix of SNr GABAergic and SNc dopaminergic neurons. This mixture has been used in previous chapters to represent the SNc, as this model is fundamentally aiming to model Parkinson's disease (caused by the loss of dopaminergic neurons projecting from the SNc to the STR and modelled by the nigrostriatal SNc-STR co-culture). The mixture cannot be used to represent the SNr, which does not include any dopaminergic neurons and would be inaccurate, while the SNc is a mixture of dopaminergic and GABAergic. As such, modelling the STR-SNr striatonigral pathway is rather difficult, especially when the direct and indirect pathways are already modelled by the STR-GP striatopallidal co-culture where the GPi performs the same role as the SNr, namely a GABAergic output of the BG. While it is possible to selectively remove the dopaminergic neurons with 6-hydroxydopamine (6-OHDA), this experimental technique was largely confined to **Chapter Six** on SNc seperate cultures and SNc-STR co-cultures in order to mimic Parkinson's disease. As a consequence, modelling the STR-SNr pathway was outside the scope of this project due to time constraints and lack of experimental value.

5.0.4 Nigrostriatal (SNc-STR)

The nigrostriatal pathway consists of dopaminergic neurons from the SNc projecting to and synapsing with the GABAergic MSNs of the STR, with these projecting neurons transporting dopamine (DA) to the STR. The presence of numerous postsynaptic DA receptors in the STR mean that SNc activity results in DA release and downstream modulation of STR activity. There are multiple types of DA receptor in the STR, major receptor sub-types being D1 (forms the direct pathway) and D2 (forms the indirect pathway) but neurons of the STR can also express D3 (Booze and Wallace. 1995), D4 (Rivera,

Cuellar *et al.* 2002) and D5 (Rivera, Alberti *et al.* 2002) DA receptor subtypes, resulting in DA release to the STR having a multitude of effects and being necessary for a functioning BG and consistent motor behaviours (Rice and Cragg. 2008). A summary of the distribution of these five DA receptors can be found in (Tritsch and Sabatini. 2012).

A single nigrostriatal projection influences many STR neurons simultaneously of both D1 and D2 types, with nigrostriatal neurons having dense dendritic trees allowing for many connections with the STR. Studies have shown this dendritic arbour to be approximately 1.12 mm^3 in volume, allowing one SNc neuron to access ~75,000 STR neurons of both D1 and D2 types, due to their dense intermixing (Korchounov *et al.* 2010). This presents a different method of connectivity to corticostriatal projections, which contain many neurons but only one synapse each, whereas SNc projections can contain fewer axons but many more synapses.

With DA having numerous effects on the STR and single SNc neurons synapsing with tens of thousands of STR neurons, DA release from the SNc has a marked effect on STR activity. At rest, there are nanomolar (nM) concentrations of DA in the STR (a concentration which best interacts with D1 receptors and the direct pathway) and upon movement activity there are micromolar (µM) concentrations of DA in the STR (a concentration preferred by D2 receptors and the indirect pathway) (Korchounov *et al.* 2010). The nigrostriatal pathway is therefore vital for the BG to process motor function and planning of movement, with degradation of this pathway resulting in reduced movements observed in Parkinson's disease. Therefore this pathway has been subject to intense research over the decades, and by culturing an SN-STR model within the 5PD, we can potentially accelerate this research.

A summary outlining these pathways is presented schematically in **Fig.5.2**.

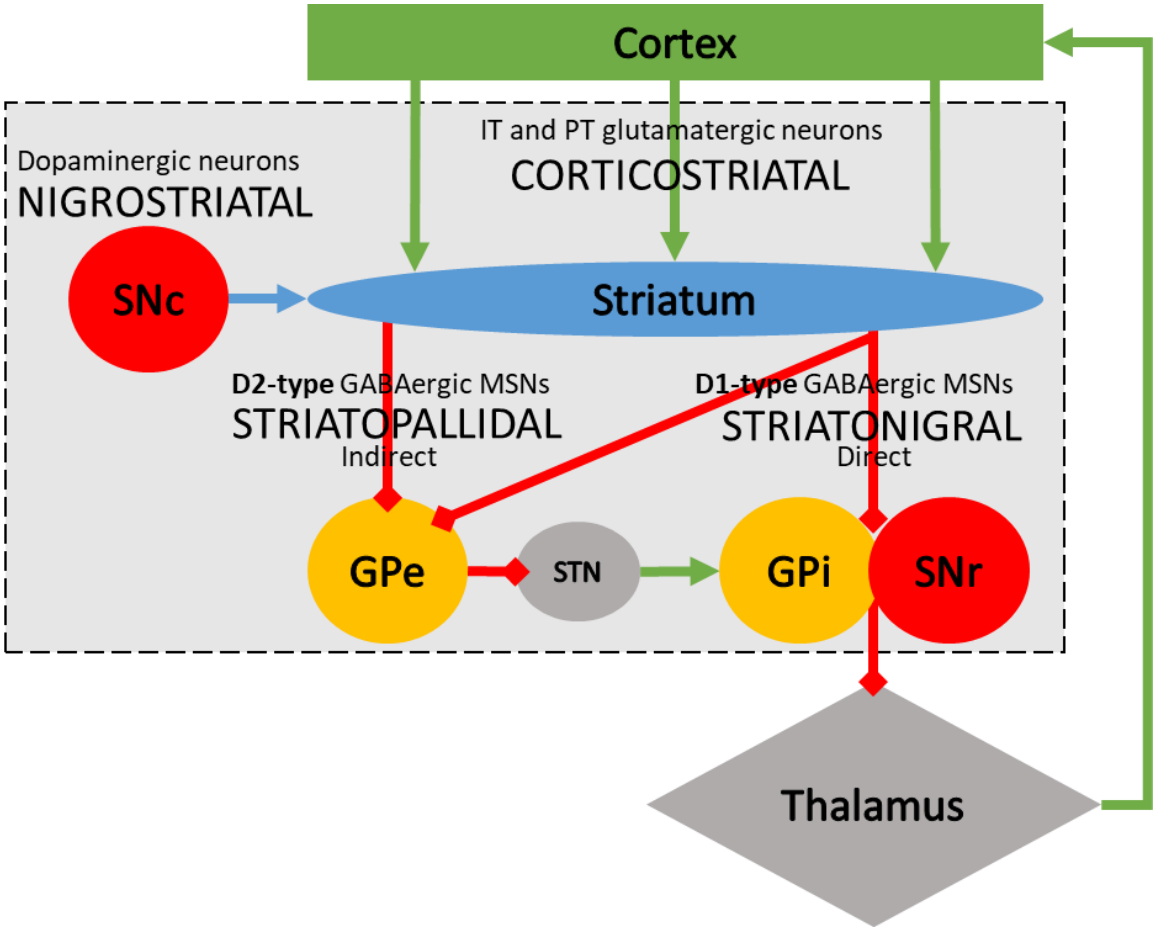

Figure 5.2: Diagram of connectivity within BG. Green arrows are glutamatergic and excitatory, red arrows are GABAergic and inhibitory (also indicated by diamond-head arrows), the blue arrow is dopaminergic and modulatory. Coloured areas indicate those regions of the BG used in the 5PD, namely CTX, STR, GP and SNc/r.

5.0.5 Designing connected co-cultures

Taking into account BG connectivity and the nuclei being modelled throughout this experiment, the three most useful signal pathways to model are the corticostriatal (CTX-STR), nigrostriatal (SNc-STR), and striatopallidal (STR-GP) pathways, allowing for the modelling of two input pathways and one output pathway. In order to best model these pathways, both relevant cell types should be seeded into the five port device (5PD), with the '*input*' port presented with larger channel widths and the '*output*' port presented with smaller channel widths. Corticostriatal and nigrostriatal should be CTX-STR and SNc-STR respectively, while striatopallidal should STR-GP. Design of these co-cultures can be seen in **Fig.5.3**.

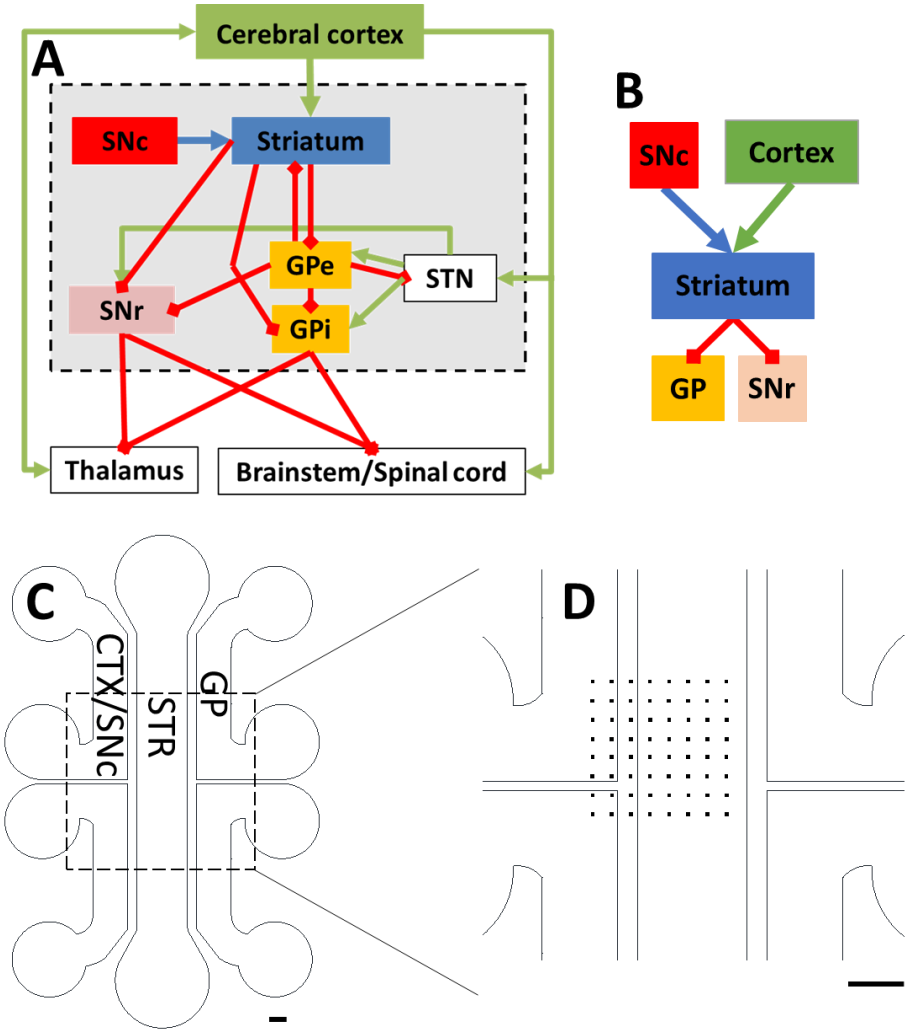

Figure 5.3: Layout of co-cultures on MEA. A) Basal ganglia circuitry within the brain *in vivo*, green, red and blue connections are inhibitory, excitatory and dopaminergic respectively, the coloured rectangles represent the five nuclei being modelled, namely the CTX, STR, GP, SNc and SNr. The grey dashed square represents the boundaries of the basal ganglia. B) the two input, central and two output nuclei being modelled by our five port device, same labelling used in A. C) The five port device, ports labelled with the relevant cell type, namely CTX or SNc into the input port (left hand side), STR into the central port and GP into the output port (right hand side), in order to make CTX-STR, SNc-STR or STR-GP co-cultures. The dashed square represents the magnified area in D. D) The location of the MEA within the five-port device, to scale. The 64 electrodes occupied both a side port and the central port, but the location is suboptimal due to MEA bracket limitations, ideally both the side and centre port would share an equal amount of electrodes. This issue with MEA alignment is discussed in Chapter 7 and is due to MEA hardware. Scale bar for C and D is 1 mm.

5.0.6 Chapter Five Aims and Objectives

Building on the previous work presented in **Chapter Four** on CTX, STR, GP and SNc in isolation, this chapter aimed to study the spontaneous extracellular electrophysiological activity of CTX-STR, STR-GP and SNc-STR co-cultures in 5PDs over the long term in culture (up to 70 DIV).

5.1 Experimental Methods

The methods involved in this chapter were previously outlined in **Chapter Two**.

5.1.1 Device surface preparation

As seen in **section 2.1.1 device preparation: chemical coating**, MEAs were sterilised with 70% IMS for 15 minutes, then dried and coated first with 0.05% PEI for 1 hour (at rtp), then 0.1 mM PDL overnight at 37 °C, washing between each stage. MEAs were then dried and ready for cell culture. 5PDs were cast from PDMS and attached to the centre of the MEA, then flushed with sterile water and incubated to remove any air or bubbles.

5.1.2 Primary cell culture

As seen in **section 2.2 Primary cell culture**, tissue was dissected from E16/14 Sprague-Dawley rat embryos: E16 for CTX, lateral and medial ganglionic eminences (LGE and MGE), corresponding to the CTX, STR and GP respectively; and E14 for the ventral midbrain (VM), corresponding to the SN. These tissues were dissociated and 100,000 cells were seeded directly into the relevant port on the 5PD, namely an input port for CTX/SNc, central port for STR and output port for GP. This made three co-cultures, namely CTX-STR, SNc-STR and STR-GP. After seeding the ports were flooded with growth media and the cells incubated at 37° C, 5% CO_2.

5.1.3 Electrical activity measurement with MEA

Recordings of cell electrophysiological activity (**section 2.5.2 MEA: Recordings**) were taken once a week from 0 DIV to 70 DIV, before a weekly media change. MEAs were moved to a heated bracket (at 37 °C) attached to amplifiers and digitisers. Activity was recorded for four minutes in triplicate, totalling 12 minutes of recording, using MED64 hardware with Mobius software. These data were stored on the MEA PC for analysis.

5.1.4 MEA data management and analysis

Spontaneous electrophysiological data obtained from neural cultures was analysed using Mobius software (**section 2.5.2 MEA: Analysis**). Data was band-pass filtered to remove data below 100 Hz and above 10 kHz, and the spike detection threshold was 500% of the root mean square. These spikes were further filtered into centroids (discrete filtered groups of spikes), each centroid consisting of >50 spikes that are >80% in similarity. These centroids were assessed to determine the number, frequency, amplitude and waveform of both spikes and bursts.

5.2 Results

5.2.1 Primary cell culture

CTX, STR, GP and SNc neural cells were successfully cultured within five-port devices (5PDs) sealed to MEAs in co-culture, namely CTX-STR, STR-GP and SNc-STR. Images of E16 CTX cells on MEA electrodes were used to demonstrate the relationship between cells, channels and electrodes (**Fig.5.4**).

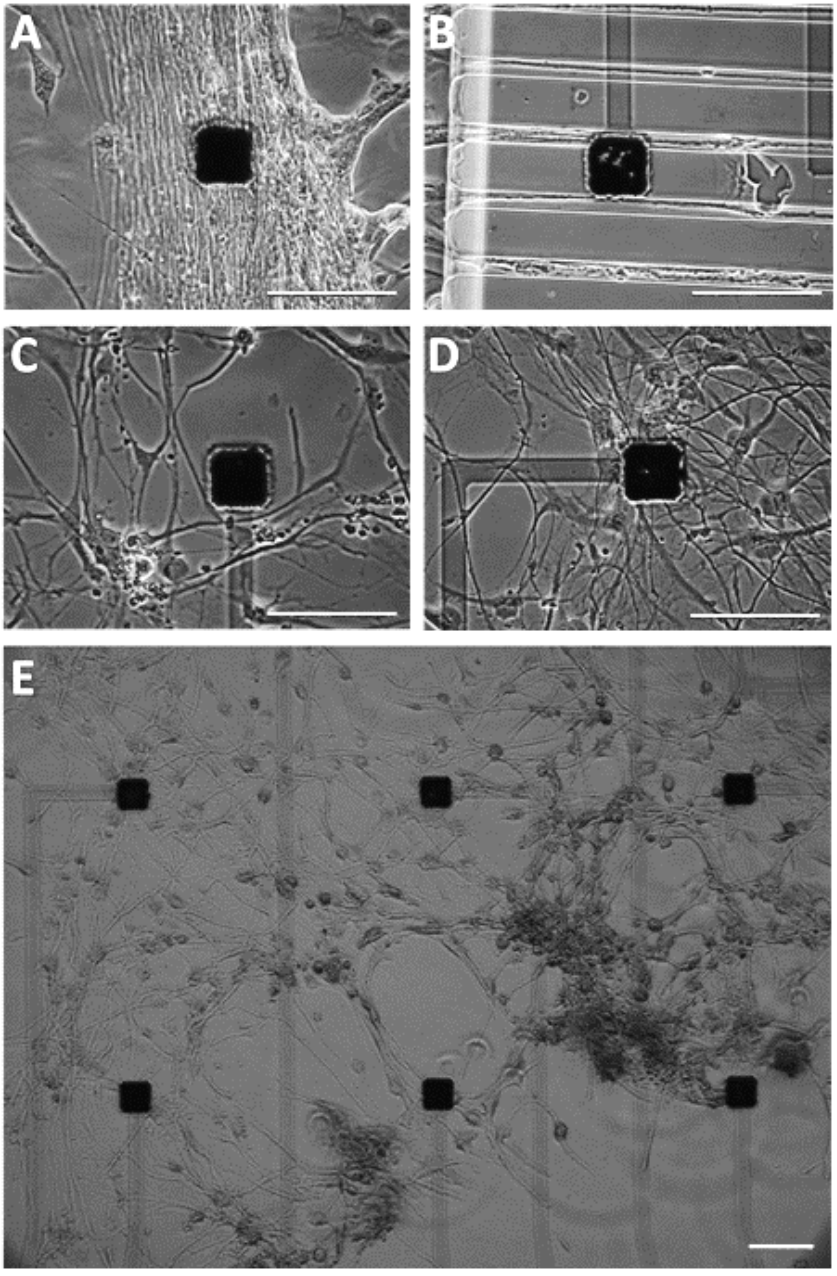

Figure 5.4: 100,000 E16 CTX cells cultured on MEAs, imaged with brightfield after 8 DIV. A) Electrode in contact with cell bodies and axons at high density, B) electrode within channel in contact with just axons, C) electrode not in contact with cell body or axon but both are in close proximity, D) electrode in contact with network of axons and few cell bodies, E) six electrodes all in contact with cell bodies and axons. Scale bars 100 µm.

Most electrodes were in contact with cells, but on occasion cells would grow in a way that meant they avoided contact with the electrodes as seen in **Fig.5.4C**. Electrodes were in position on both sides of the micro-channels as displayed by **Fig.5.5**, which shows the layout of electrodes in relation to the channels, in a device where CTX cells were seeded onto the left-hand side and STR cells onto the right-hand side.

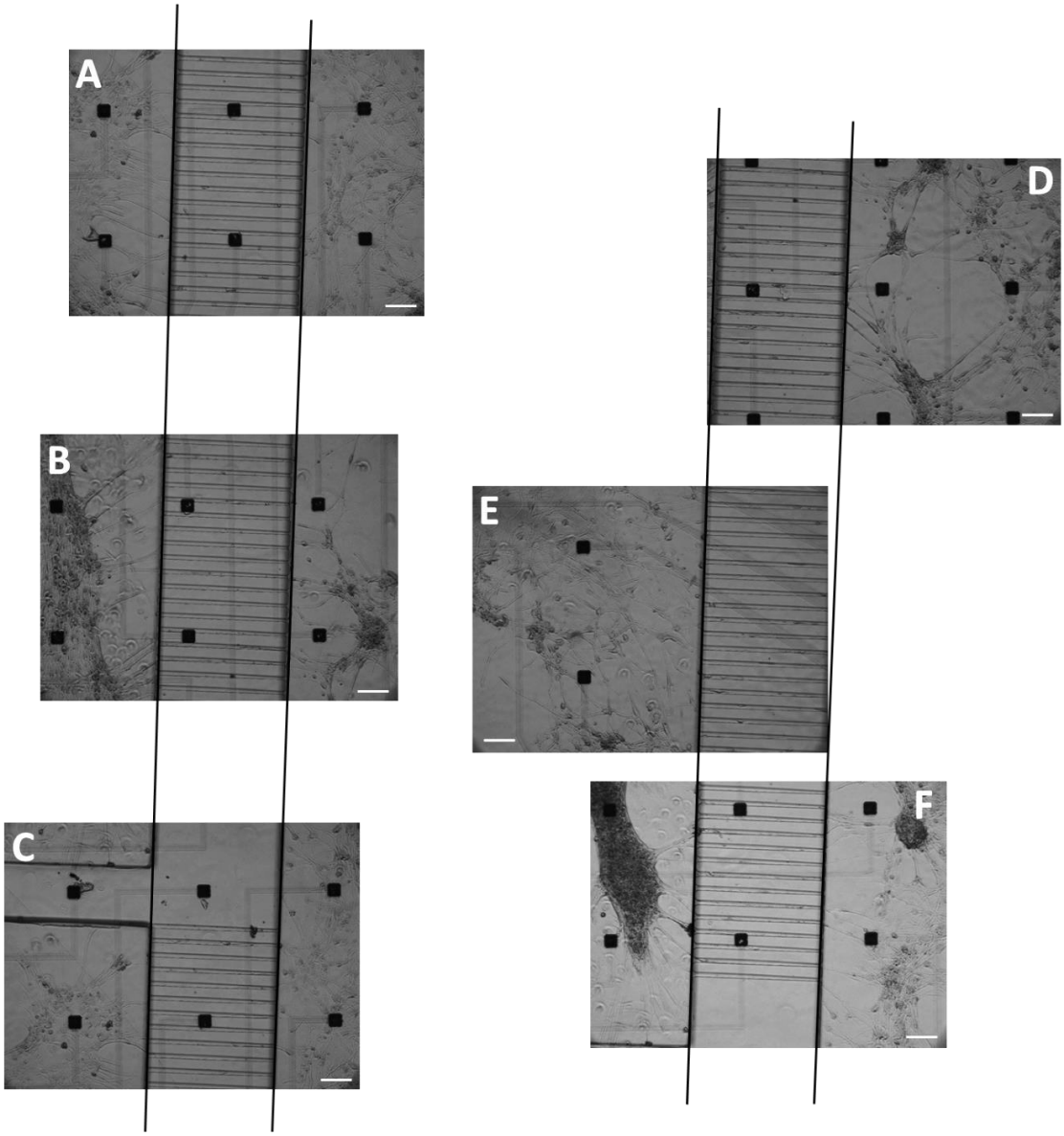

Figure 5.5: 100,000 E16 CTX and STR cells cultured on MEAs (CTX seeded to left of channels STR to right) and imaged with brightfield after 8 DIV, images aligned to channels. A-C and D-F represent the channels of two separate devices (with C showing the boundary between the upper and lower side ports). Images are aligned in relation to their position on the MEA. All scales 100 µm.

5.2.2 Heatmaps

Each co-culture consisted of two cell ports linked by channels, with one port consisting of STR neural cells and one of either CTX, GP or SNc neural cells. As well as noting how the activity varies across the whole MEA, with co-cultures the pattern of activity was also be analysed across each port and the channel section, resulting in multi-sectioned heatmaps and spiking data from each side of the

channels and within the channels themselves. Heatmaps from CTX-STR, STR-GP and SNc-STR devices can be seen in **Fig.5.6**, with each port and the channels outlined in black to indicate the sections of the 5PD. Electrodes not within cell-seeded ports or channels are ignored. Raw data in **Appendix.**

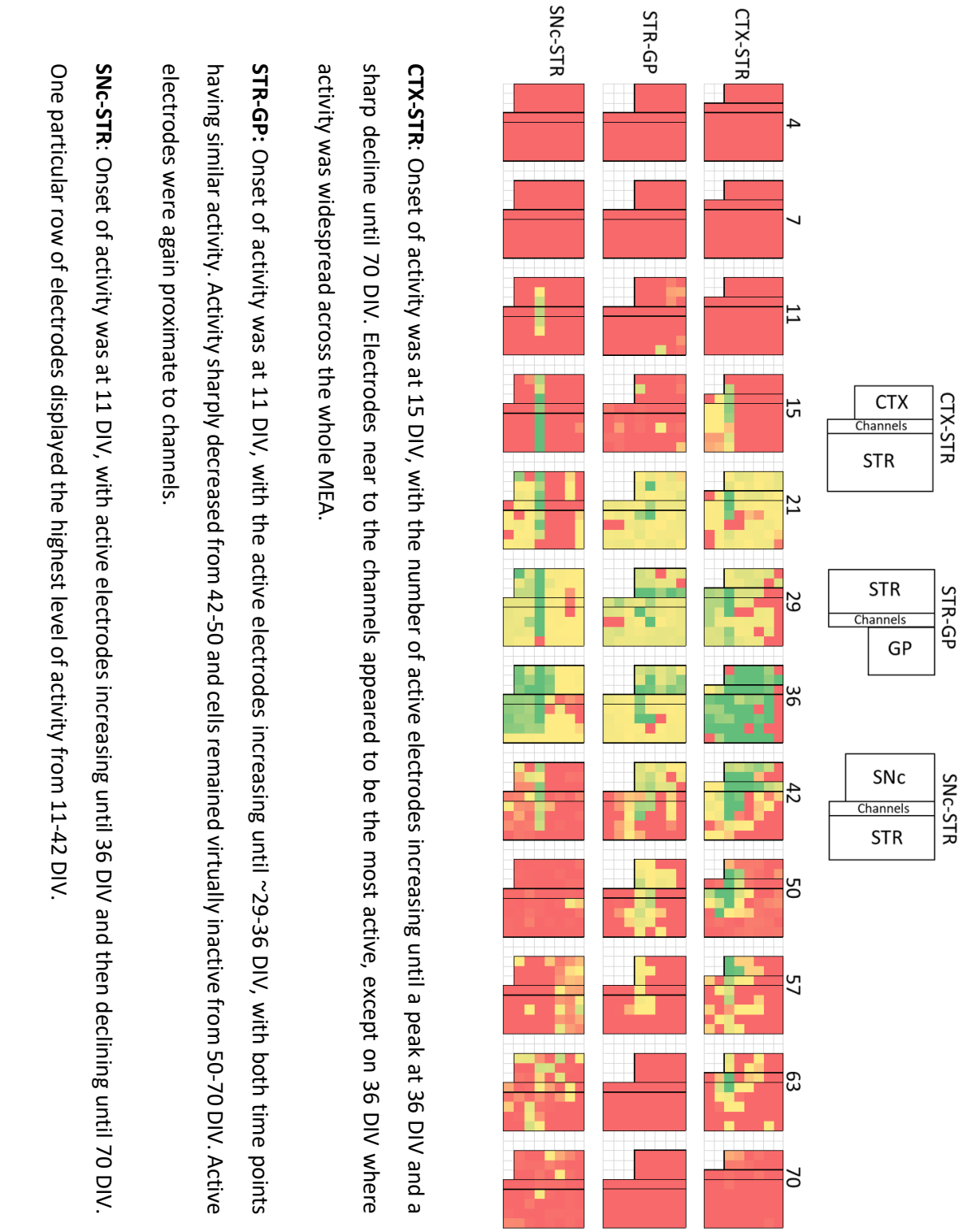

CTX-STR: Onset of activity was at 15 DIV, with the number of active electrodes increasing until a peak at 36 DIV and a sharp decline until 70 DIV. Electrodes near to the channels appeared to be the most active, except on 36 DIV where activity was widespread across the whole MEA.

STR-GP: Onset of activity was at 11 DIV, with the active electrodes increasing until ~29-36 DIV, with both time points having similar activity. Activity sharply decreased from 42-50 and cells remained virtually inactive from 50-70 DIV. Active electrodes were again proximate to channels.

SNc-STR: Onset of activity was at 11 DIV, with active electrodes increasing until 36 DIV and then declining until 70 DIV. One particular row of electrodes displayed the highest level of activity from 11-42 DIV.

Figure 5.6: Averaged representative heatmaps (n=4) from CTX-STR, STR-GP and SNc-STR from 4-70 DIV. Traffic light scale indicates where activity ranged between high (green), average (yellow) or low (red). The three schematics above indicate the orientation and cell types contained within the 5PD on the MEA.

5.2.3 Percentage activity, average and maximum spiking frequency

The percentage activity across the MEA was calculated from the heatmap data by establishing a threshold for activity. This data is combined with the average and maximum spike frequencies over time across each port and the channels of the MEA, and correltion analysis to determine similarities between areas and which area drives activity, as seen in **Fig.5.7.**

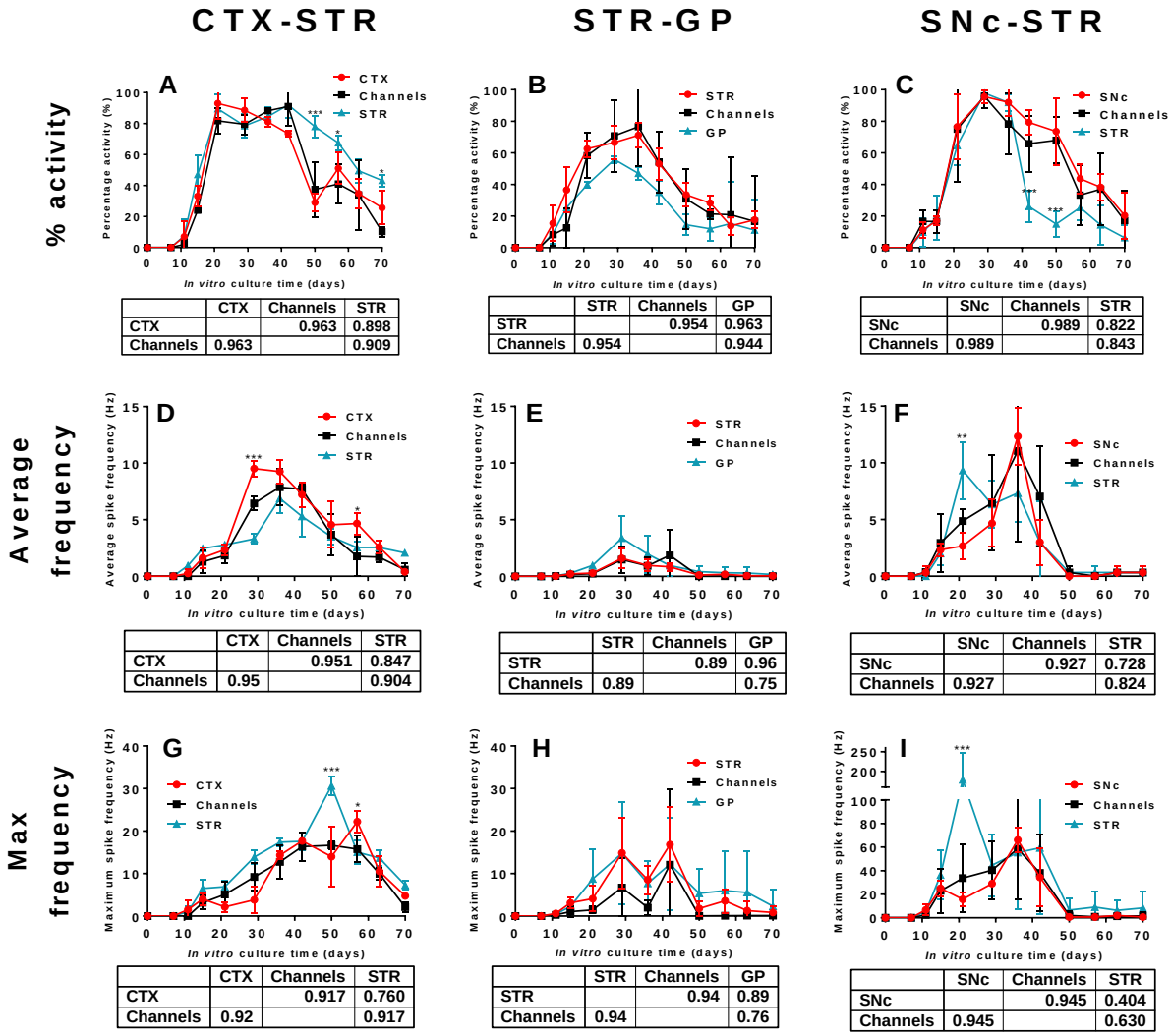

Figure 5.7: Percentage activity, average spike frequency and maximum spike frequency over time for CTX-STR, STR-GP and SNc-STR co-cultures on MEAs. Data was taken from each port and channels between ports, each graph is combined with a table of correlation coefficients (the greater the value, the greater the level of correlation, max value 1). A) CTX-STR percentage activity, B) STR-GP percentage activity, C) SNc-STR percentage activity, D) CTX-STR average spike frequency, E) STR-GP average spike frequency, F) SNc-STR average spike frequency, G) CTX-STR max spike frequency, H) STR-GP max spike frequency, I) SNc-STR max spike frequency. Asterisks represent results of multiple post-hoc t-tests, (*): p<0.01, (**): p<0.001, (***): p<0.0001, compared to other conditons at the same time point. (n=4).

5.2.3.1 Percentage activity

Percentage activity was assessed for both cell ports to determine any differences. All co-cultures displayed a clear onset, peak and decrease in the percentage of MEA electrodes recording activity (**Figs.5.7A-C**) For CTX-STR co-cultures (**Fig.5.7A** graph) the cell type had a significant effect on the percentage activity (ANOVA (2,3) F=10.68, p=0.0432), with the STR port having significantly more activity from 50-57 DIV. The correlation between the cortical port and the channels (CTX-channels) was higher than both the channels and the STR port (channels-STR), and the CTX port and the STR port (**Fig.5.7A** table). For STR-GP cultures (**Fig.5.7B** graph) there was no significant effect of cell type, all correlations were high (**Fig.5.7B** table), but the peak of percentage activity was lower than CTX-STR or SNc-STR cultures (76.7% vs 93% and 95.7% respectively). Lastly, in SNc-STR co-cultures (**Fig.5.7C** graph) the cell type also had a significant effect on the percentage activity (ANOVA (2,6) F=7.927, p=0.02) with the STR port having significantly lower activity from 42-50 DIV, and the correlation between SNc-channels was greater than SNc-STR or STR-channels (**Fig.5.7C** table).

5.2.3.2 Average spiking frequency

Average spiking frequency was calculated by taking the average number of spikes across each area and determining the number of spikes per second over a 12 minute (720 second) recording session. All co-cultures displayed an onset of activity after 11 DIV (**Figs.5.7D-F**), rose to a peak after 20-40 DIV and then fell to negligible spiking levels from 50-70 DIV. For CTX-STR and SNc-STR co-cultures, the interaction between the cell type and time was significant (CTX-STR ANOVA (22,33) F=4.42, p<00001) (with CTX spiking being significantly greater after 30 DIV (**Fig.5.7D**)), (SNc-STR ANOVA (22,66) F=1.723, p=0.0469) (with STR spiking being significantly greater after 20 DIV (**Fig.5.7F**)), but there was no significant effect on STR-GP co-cultures (**Fig.5.7E**). CTX-STR and SNc-STR co-cultures also had the highest correlation between input-channels (as opposed to channels-output) and similar levels/timings of peak activity (9.51 Hz at 29 DIV vs 12.3 Hz at 36 DIV respectively). STR-GP co-cultures had the lowest level of average spike frequency, only peaking at 3.38 Hz.

5.2.3.2 Maximum spiking frequency

As average spiking also included all the electrodes that recorded no activity (zero spikes), the maximum spike frequency from each recording session was also analysed to see how the activity changed over time (**Figs.5.7G-I**). Similarly to average spike frequencies, CTX-STR (**Fig.5.7G**) and SNc-STR (**Fig.5.7I**), co-cultures had a significant interaction between cell type and time (CTX-STR ANOVA (22,33) F=5.56, p<00001) (with STR and CTX spiking being significantly greater after 50 DIV and 57 DIV respectively (**Fig.5.7G**)), (SNc-STR ANOVA (22,66) F=5.162, p<0.0001) (with STR spiking being significantly greater after 21 DIV (**Fig.5.7I**)), but there was no significant effect on STR-GP co-cultures (**Fig.5.7H**). Notably in SNc-STR devices, STR spiking was extremely high after 21 DIV,

reaching 179±60 Hz compared to STR peaks of 30.6±3 Hz in CTX-STR devices and 15±10 Hz in STR-GP devices.

5.2.4 Bursting activity

Bursts were defined as periods of activity of over 10 Hz (a bundle of more than ten spikes produced within a second) and the number of bursts over time for each co-culture was assessed, along with the number of spikes per burst over time. These graphs can be seen in **Fig.5.8**.

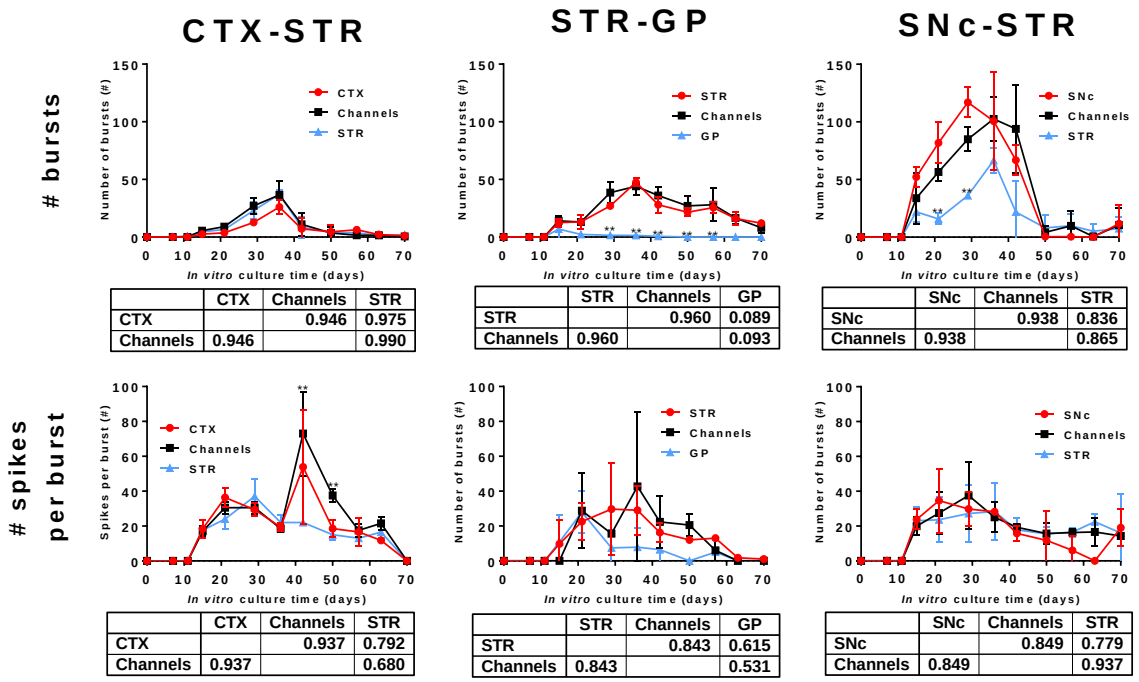

	CTX	Channels	STR
CTX		0.946	0.975
Channels	0.946		0.990

	STR	Channels	GP
STR		0.960	0.089
Channels	0.960		0.093

	SNc	Channels	STR
SNc		0.938	0.836
Channels	0.938		0.865

	CTX	Channels	STR
CTX		0.937	0.792
Channels	0.937		0.680

	STR	Channels	GP
STR		0.843	0.615
Channels	0.843		0.531

	SNc	Channels	STR
SNc		0.849	0.779
Channels	0.849		0.937

Figure 5.8: Bursting activity (split into number of bursts fired and number of spikes per burst) over time for CTX-STR, STR-GP and SNc-STR co-cultures on MEAs. Data was taken from each port and channels between ports, each graph is combined with a table of correlation coefficients (the greater the value, the greater the level of correlation, max value 1). A) number of bursts fired by CTX-STR, B) number of bursts fired by STR-GP, C) number of bursts fired by SNc-STR, D) spikes per burst from CTX-STR, E) spikes per burst from STR-GP, F) spikes per burst from SNc-STR. Asterisks represent results of multiple post-hoc t-tests, (*): p<0.01, (**): p<0.001, (***): p<0.0001, compared to other conditons at the same time point (n=4).

Similarly to spike frequencies, the numbers of bursts had an onset (after 11-15 DIV), peak (from 30-40 DIV) and decline (50-70 DIV). Unlike spike frequencies CTX-STR co-cultures had no significant differences in the number of bursts fired over time, but there was a significant interaction between cell type and time for STR-GP (ANOVA (22,33) F=9.74, p<0.0001) and SNc-STR co-cultures (ANOVA (22,33) F=3.23, p=0.0012). The GP port of STR-GP devices had extremely low bursting activity, negligible from 21-70 DIV, and the STR port of SNc-STR devices had significantly lower bursting from 21-29 DIV. Peak numbers of bursts were 37 bursts (36 DIV) for CTX-STR, 44 bursts (36 DIV) for STR-GP and 116 bursts (29 DIV) for SNc-STR, with the latter having a far greater level of bursting over time of the three co-cultures.

The number or spikes per burst was consistent over time for STR-GP and SNc-STR co-cultures, averaging at 30 spikes per burst over time from onset until 70 DIV. However, the number of spikes per burst changed significantly in the channels and CTX areas of CTX-STR devices from 44-50 DIV, where the average number of spikes per burst increased to 73.

5.2.5 Centroid number

Spikes were sorted into centroids and analysed to determine how the number of centroids changes over time. The number of centroids over time across each of the co-cultures can be seen on **Fig.5.9.**

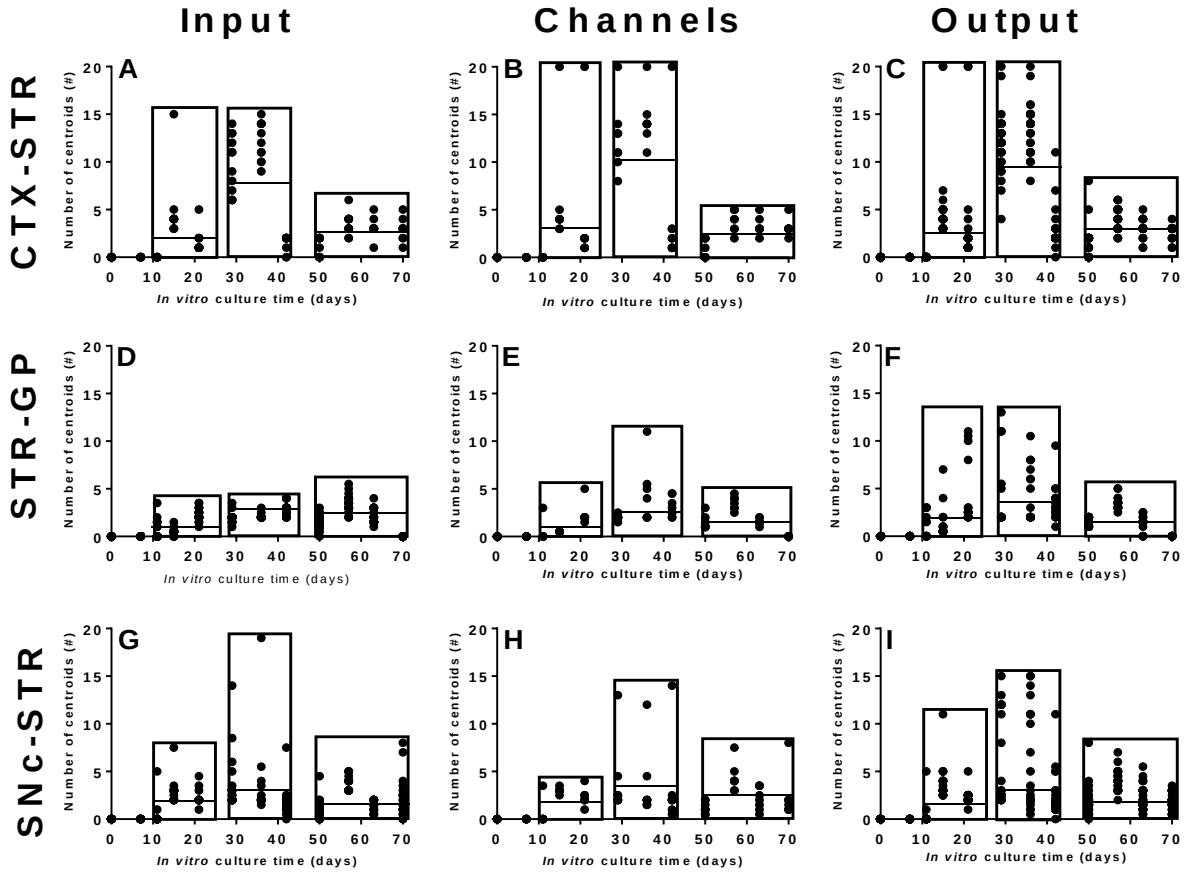

Figure 5.9: Number of centroids for CTX-STR (A-C), STR-GP (D-F) and SNc-STR (G-I) co-cultures, for the left-hand input port (A, D, G), channels (B, E, H) and right-hand output port (C, F, I). Each time point shows how many centroids were registered by each electrode. The early (15-29 DIV), mid (36-51 DIV) and late (58-70) stages are indicated by the rectangular outlines, with the horizontal black line indicating the averaged number of centroids for each section. (n=4), representative average images.

In the majority of cases, the number of centroids at the late stage (50-70 DIV) was significantly lower than the number of centroids at the early (11-25 DIV) and/or mid (29-44 DIV) stage, except for the channels of SNc-STR devices where there was no significant change but otherwise a clear trend. This shows that for every co-culture, spike shape variability was decreasing in all three parts of the co-culture (left port, channels, right port) over time. STR neurons in STR-GP devices displayed a low number of centroids throughout experimentation, suggesting that there was little activity in this port but the variability still fell at the end stage.

5.2.6 Centroid shape categorisation

As with the previous chapter, centroids were sorted into six categories (positive/negative monophasic, positive-first/negative-first biphasic and positive-first/negative-first triphasic), depending on their number of phases and sign (see **Fig.4.25** for more information). Centroid proportions for the left-hand port, channels and right-hand port for CTX-STR, STR-GP and SNc-STR are displayed in **Fig.5.10**.

Centroids generated in channels were mostly triphasic centroids, indicating that channels contained many axons. Channels should contain a much higher concentration of axons than other areas as they are the link between two ports and designed for axonal outgrowth, and axons generate triphasic waveforms (refer to **Fig.4.3**).

In addition, the proportion of centroid shapes produced by STR neurons changed depending on STR connectivity to CTX, SNc or GP, where in CTX-STR and SNc-STR devices STR has similar centroid proportions to CTX and SN respectively, and in STR-GP devices STR has less centroids overall.

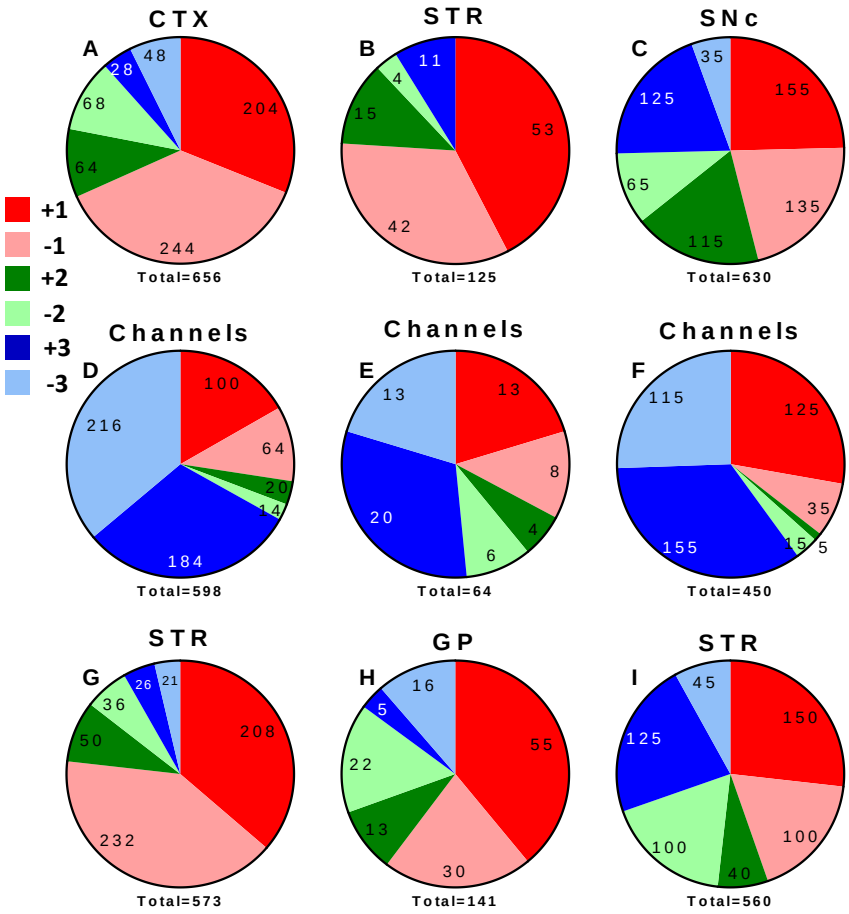

Figure 5.10: Centroid shape categorisation. All centroids from 70 days of recording from each part of each co-culture were sorted into six types. Numbers on pie segments indicating the numbers of centroids in that category (with the total number of centroids below each chart), (n=4).

5.2.7 Centroid full duration at half maximum

The full duration at half maximum (FDHM) is a means of measuring the width of the peaks that make up centroids (as the x-axis is time, the width is also the duration). In this manner, any changes in the width of centroid peaks can be assessed. The FDHM was extracted and processed to determine if centroid shape changes over time, and if there are differences between both ports and the channels, with data displayed in **Fig.5.11**.

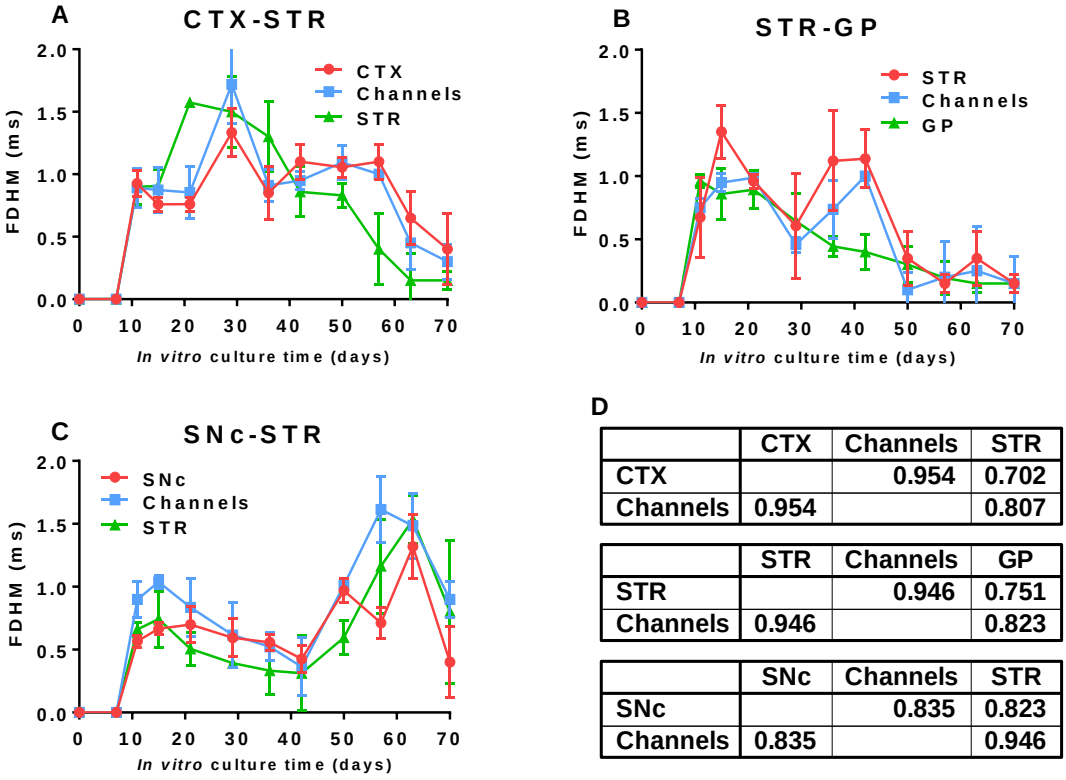

	CTX	Channels	STR
CTX		0.954	0.702
Channels	0.954		0.807

	STR	Channels	GP
STR		0.946	0.751
Channels	0.946		0.823

	SNc	Channels	STR
SNc		0.835	0.823
Channels	0.835		0.946

Figure 5.11: Centroid full duration at half maximum (FDHM) over time for each area (input, channels, and output) of each co-culture, (A-C). D shows a table of correlation coefficients comparing input-channels, channels-output and input-output, with a value of 1 being perfect correlation.

There were no significant differences in the FDHM of centroids generated from the ports and channels of each co-culture. Centroids mostly ranged from 0.5-1.0 ms (**Fig.5.11A-C**) and were closely correlated between input-channels and channels-output (**Fig.5.11D**).

5.3 Comparisons of separate cultures and connected co-cultures

In this section, MEA electrophysiological data from separate cell populations (reported in **Chapter Four**) are compared to data from connected cell populations, namely CTX vs CTX-STR, GP vs STR-GP, SNc vs SNc-STR and STR vs STR in each co-culture. This comparison is to determine how each aspect of activity has altered by connectivity to other BG neural cell types, using the **Chapter Four** separate culture MEA data as a baseline.

5.3.1 Percentage activity

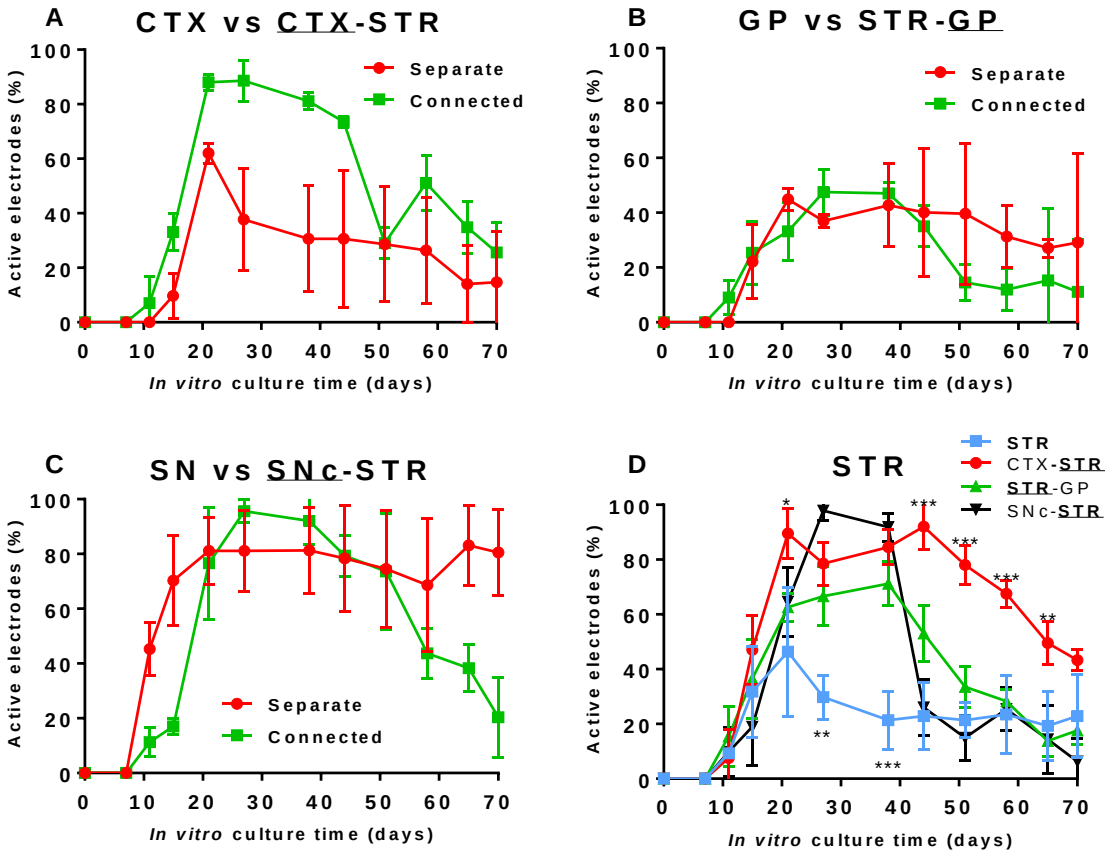

Figure 5.12: A comparison between the percentages of active electrodes over time for separate (CTX, STR, GP or SN) and connected (co-cultures of CTX-STR, STR-GP, and SNc-STR) cultures on MEAs. Each separate culture is compared with the relevant port of the corresponding co-culture, with separate STR compared to the STR port within each co-culture (n=4). Asterisks are generated from post-hoc t-tests (*): p<0.01, (**): p<0.001, (***): p<0.001.

CTX within CTX-STR co-cultures had an earlier onset of activity than separate CTX cultures (**Fig.5.12A**), and while the effect of connectivity on the number of active electrodes was not significant (ANOVA (1,3) F=7.35, p=0.07), there was a trend for connected CTX to have greater activity across the MEA. Both cultures peaked on 21 DIV (separate 62 ± 5% vs connected 88 ± 3%) then decreased from peak to final recording. GP within STR-GP co-cultures and separate GP cultures had similar onset and activity throughout (**Fig.5.12B**), with connectivity not significantly changing the percentage of active

MEA electrodes over time (ANOVA (1,4) F=0.67, p=0.46). For SN within SNc-STR co-cultures and separate SN cultures (**Fig.5.12C**), the effect of connectivity was not significant (ANOVA (1,4) F=3.60, p=0.13). Both SN cultures displayed an onset of activity by 11 DIV, but separate SN cultures had greater activity across the MEA at early (11-15 DIV) and late (50-70 DIV) phases. Comparing separate STR cultures with connected STR co-cultures (**Fig.5.12D**), the effect of connectivity had a significant effect on the percentage of active electrodes across the MEA (ANOVA (3,7) F=18.21, p=0.001). Separate STR cultures had significantly lower activity than connected STR from 27-38 DIV, while STR in CTX-STR co-cultures had significantly greater activity than separate STR on 21 DIV, and then 44-65 DIV.

5.3.2 Average spike frequency

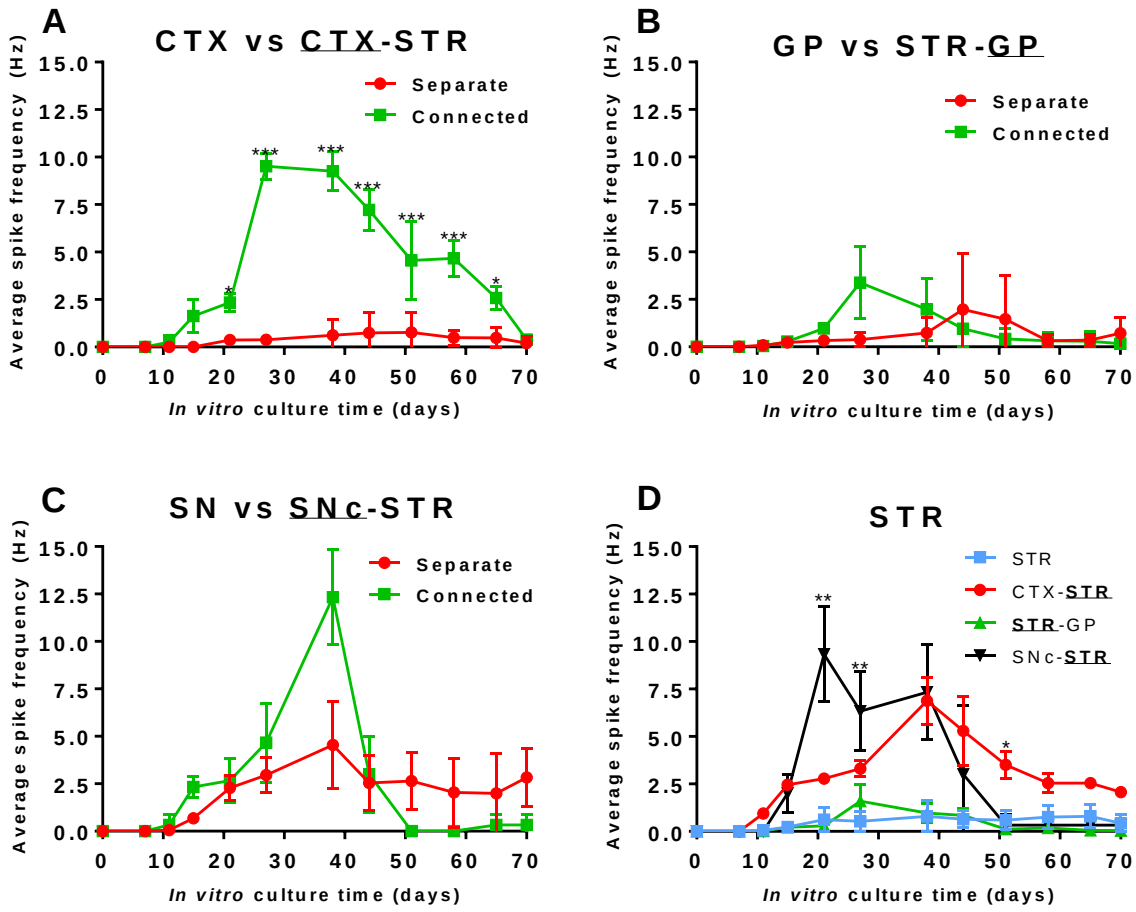

Figure 5.13: A comparison between the average spike frequencies over time for separate (CTX, STR, GP or SN) and connected (co-cultures of CTX-STR, STR-GP, and SNc-STR) cultures on MEAs. Each separate culture is compared with the relevant port of the corresponding co-culture, with separate STR compared to the STR port within each co-culture (n=4). Asterisks are generated from post-hoc t-tests (n=4). (*): p<0.01, (**): p<0.001, (***): p<0.0001.

Compared to separate CTX culutres, CTX average spike frequency was significantly increased through connectivity to STR cultures in CTX-STR devices (ANOVA (1,3) F=99.08, p=0.002). This significant increase is clearly seen from 21-65 DIV (**Fig.5.13A**), with separate CTX cultures peaking at 0.77 ± 2 Hz (51 DIV) while CTX cultures in CTX-STR co-cultures peaked at 9.51 ± 0.5 Hz (27 DIV). This significant

effect of connectivity was not seen between separate GP and connected STR-GP co-cultures (**Fig.5.13B**), but connected GP cultures did have a marginally higher (3.4 ± 2 Hz vs 1.9 ± 3 Hz) and far earlier (27 vs 44 DIV) peak of firing. For separate SN and connected SNc-STR cultures, despite the extremely high peak in spike frequency on 38 DIV (12.3 ± 1.5 Hz), there was not a significant effect of connectivity. However, there was a significant effect of connectivity on the average spike frequency for STR cultures (ANOVA (3,7) F=31.71 p=0.0002), with STR innervated by SNc or CTX cultures firing at a significantly higher frequency from 21-27 DIV or 50-70 DIV respectively. STR in STR-GP co-cultures was not significantly different to separate STR, indicating that innervation by CTX and/or SN neurons had a significant effect on spiking activity.

5.3.3 Maximum spike frequency

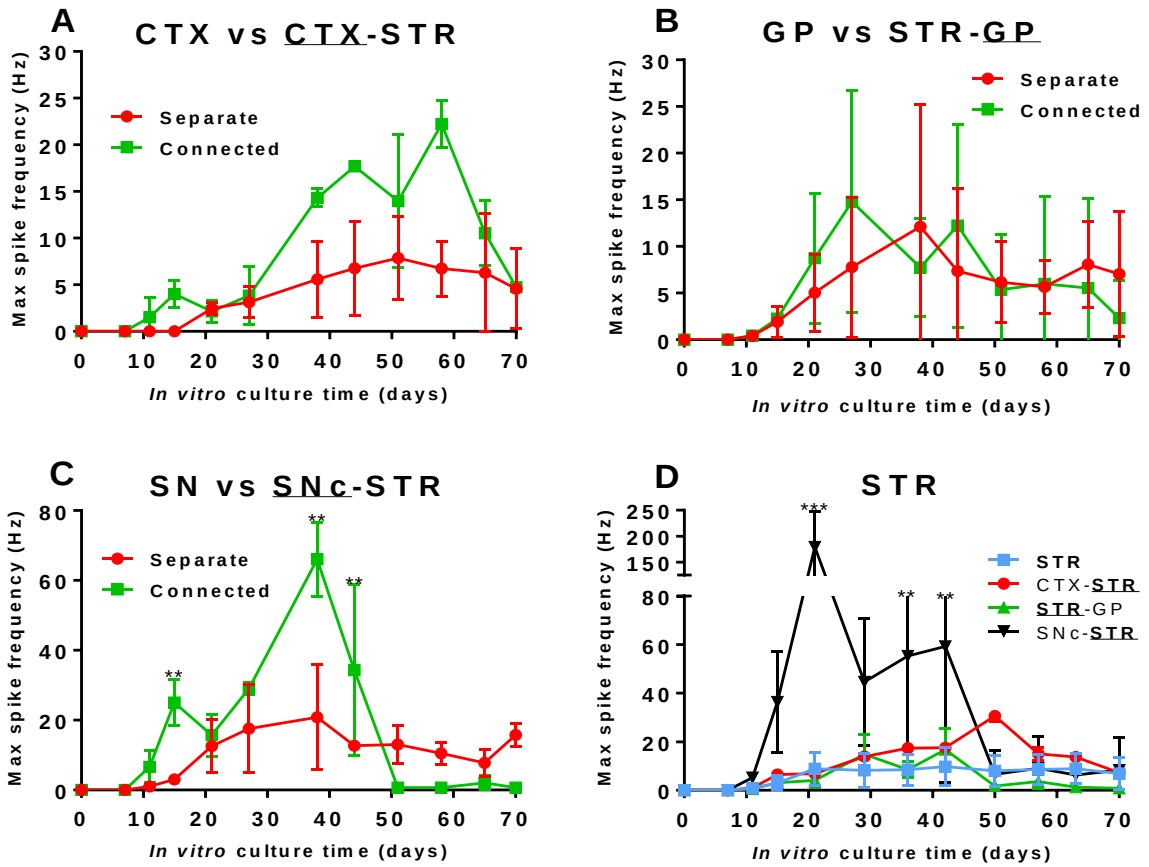

Figure 5.14: A comparison between the maxium spike frequencies over time for separate (CTX, STR, GP or SN) and connected (co-cultures of CTX-STR, STR-GP, and SNc-STR) cultures on MEAs. Each separate culture is compared with the relevant port of the corresponding co-culture, with separate STR compared to the STR port within each co-culture (n=4). Asterisks are generated from post-hoc t-tests (n=4). (*): p<0.01, (**): p<0.001, (***): p<0.0001.

Despite the increased maximum spike frequency of CTX in CTX-STR co-cultures from 39-60 DIV (peaking at 22.5 ± 2.5 Hz vs 7.3 ± 4.2 Hz), the effect of connectivity on CTX maximum spike frequency was not significant. This was also the case for GP cultures, where connectivity did not have a significant effect on maximum spike frequency, both were at similar levels throughout. However, for SN cultures, connectivity did have a significant effect on maximum spike frequency (ANOVA (1,4)

F=11.45, p=0.03). For SNc connected to STR in co-cultures, spike frequency was significantly increased at both early (25 ± 6 Hz at 15 DIV) and late timepoints (peak at 68 ± 6.6 Hz on 39 DIV) but fell to negligible levels from 50-70 DIV, compared to the relatively consistent spiking activity of separate SN cultures. STR connectivity also had a significant effect on maximum spike frequency (ANOVA (3,7) F=6.7, p=0.02), with SNc-STR having the highest levels of max spike frequency. Maximum spiking from SNc-STR co-cultures were significantly greater from 35-44 DIV (57 ± 35 Hz then 61 ± 50 Hz respectively), and with an extremely high peak on 21 DIV (177 ± 70 Hz). STR maximum spiking was also increased through connectivity to CTX, but decreased through connectivity to GP.

5.3.4 Bursting

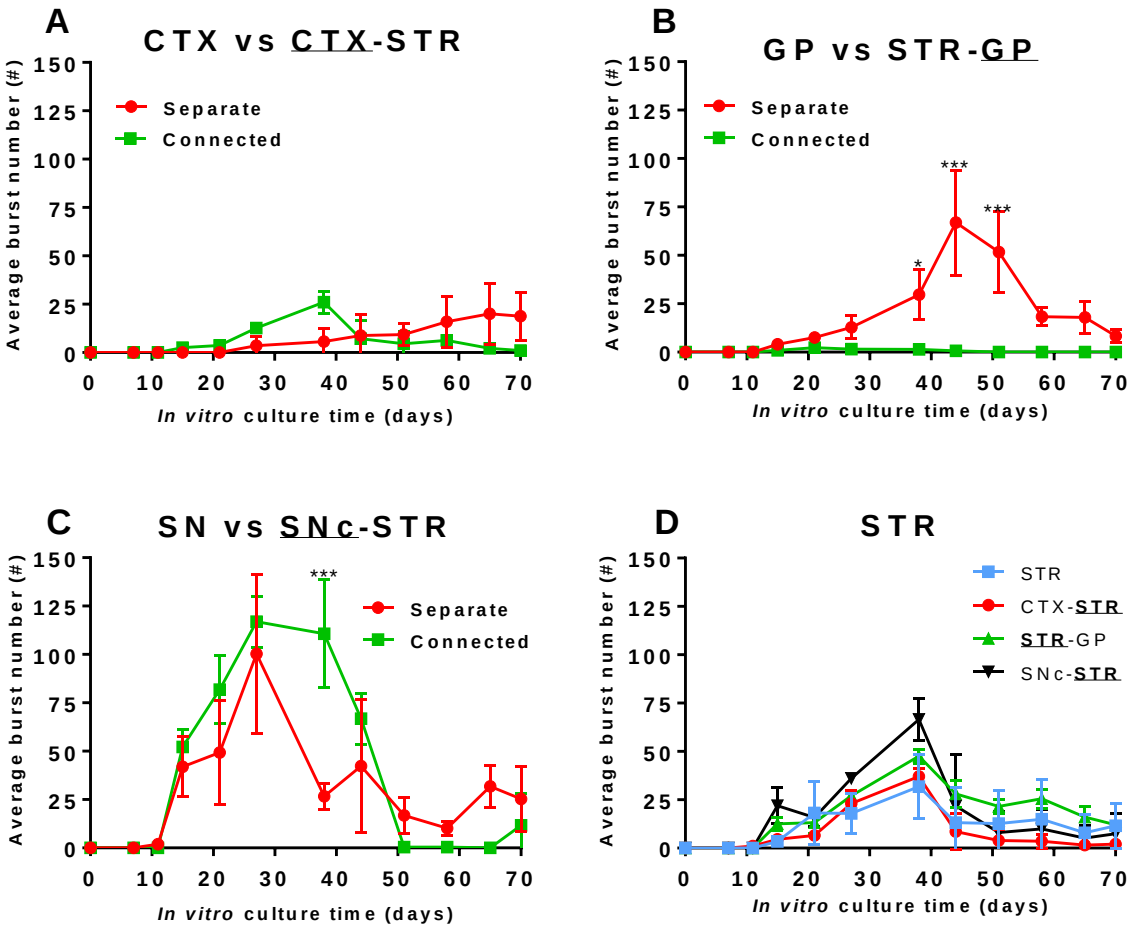

Figure 5.15: A comparison between the average numbers of bursts fired over time for separate (CTX, STR, GP or SN) and connected (co-cultures of CTX-STR, STR-GP, SNc-STR) cultures on MEAs. Each separate culture is compared with the relevant port of the corresponding co-culture, with separate STR compared to the STR port within each co-culture (n=4). Asterisks are generated from post-hoc t-tests (n=4). (*): p<0.01, (***): p<0.0001.

CTX separate cultures and CTX-STR connected co-cultures had similar levels of bursting (**Fig.5.15A**), with connectivity not having a significant effect on the average numbers of burst fired. CTX-STR bursting did peak earlier than separate CTX bursting (39 vs 65 DIV) but otherwise bursting was similar between conditons. For GP, connectivity had a significant effect on burst firing (ANOVA (1,2) F=11.88,

p=0.04), with bursting reduced to negligible levels in STR-GP co-cultures (**Fig.5.15B**). Separate GP culture bursting was significantly greater from 39-50 DIV, peaking at 70 bursts (44 DIV). Connectivity also had a significant effect on SN bursting (ANOVA (1,2) F=35.39, p=0.02), the difference being that connected SNc-STR cultures had significantly greater bursting than separate SN cultures, with 112 bursts on 39 DIV. Overall SN cultures had more bursting than other cell types (**Fig.5.15C**). Interestingly, there was a trend amongst STR cultures for peak bursting on 39 DIV, but connectivity did not have a significant effect on bursting in STR cultures.

As well as comparing the average number of bursts fired over time, the average number of spikes per burst over time was also compared between separate cultures and connected co-cultures, as seen in **Fig.5.16**. This measure determines the length of the 'spike trains' contained within bursts, which can differ between different areas of the basal ganglia (van Pelt *et al.* 2005, Blythe *et al.* 2009, Ellens and Leventhal. 2013, Abrahamsson *et al.* 2016).

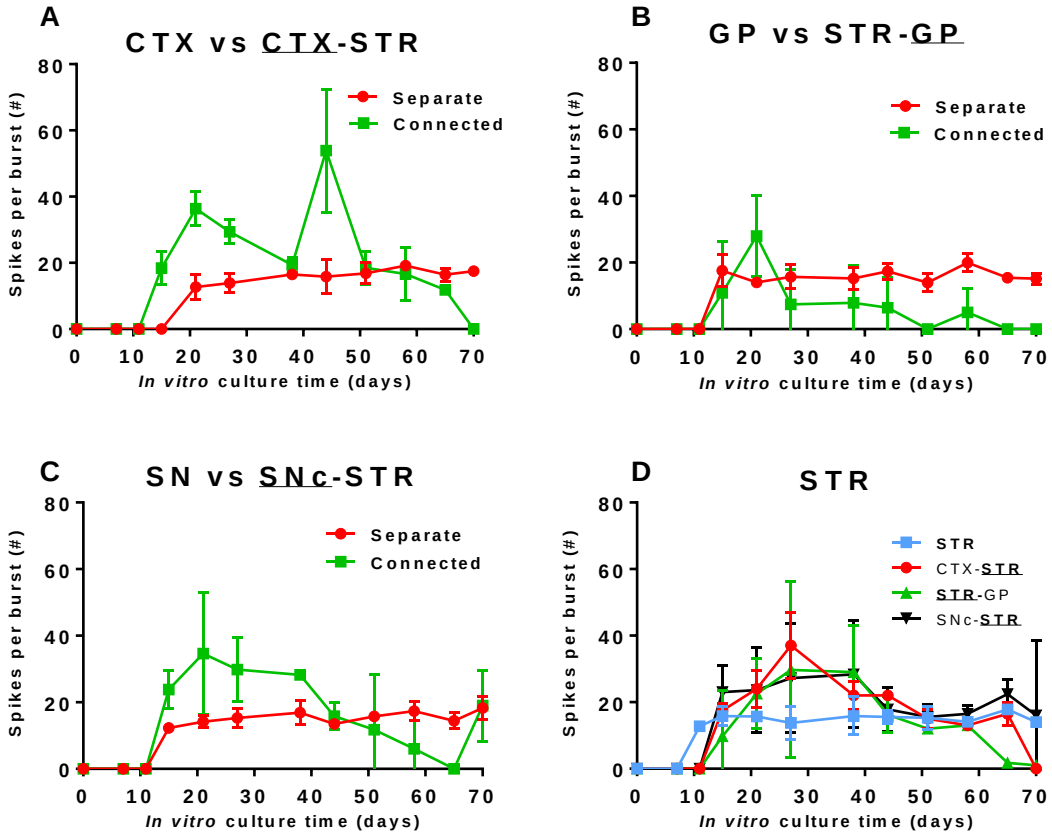

Figure 5.16: A comparison between the numbers of spikes per burst (always ≥10) over time for separate (CTX, STR, GP or SN) and connected (co-cultures of CTX-STR, STR-GP, SNc-STR) cultures on MEAs. Each separate culture is compared with the relevant port of the corresponding co-culture, with separate STR compared to the STR port within each co-culture (n=4).

All comparisons did not feature a significant difference of the number of spikes per burst due to connectivity. Most separate cultures featured bursts with a consistent ~20 spikes per burst, whilst connected cultures had a greater variation, with CTX connected to STR peaking at 55 ± 10 spikes per burst (**Fig.5.16A**), and SNc connected to STR peaking at 38 ± 20 spikes per burst (**Fig.5.16C**).

5.3.5 Centroid shape categorisation

The effect of connectivity was also observed on the number of phases of activity centroids and the proportion of these phases, as seen in **Fig.5.17**.

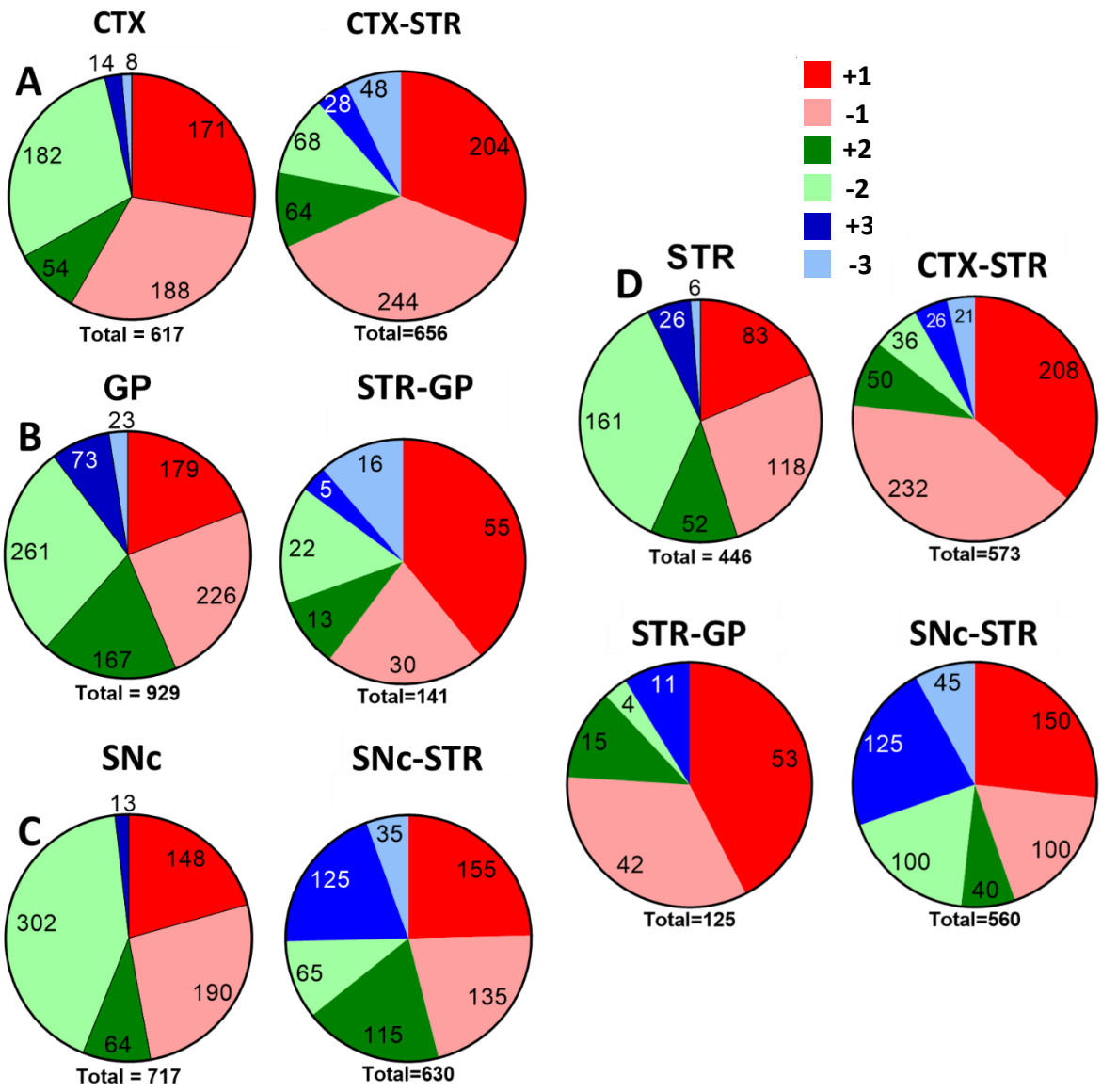

Figure 5.17: Centroid shape categorisation. All centroids from all 70 days of recording from each part of each culture/co-culture was sorted into six types. A) CTX vs CTX in CTX-STR devices, B) GP vs GP in STR-GP devices, C) SNc vs SNc in SNc-STR devices, D) STR vs STR in each co-culture. Numbers on pie segments indicating the numbers of centroids in that category (with the total number of centroids below each pie), (n=4).

Fig.5.17A: Similar overall level of centroids, **CTX**-STR has larger proportion of triphasic centroids but lower proportion of biphasic centroids compared to **CTX**. **Fig.5.17B: GP** in STR-**GP** has much fewer centroids and more monophasic centroids than **GP. Fig.5.17C:** Similar overall level of centroids, **SNc**-STR has larger proportion of triphasic centroids and lower proportion of biphasic centroids compared to **SNc**. **Fig.5.17D: STR** in **STR**-GP devices has less centroids overall and similar proportions to **STR** in CTX-**STR** devices. **STR** in SNc-**STR** devices has a higher proportion of triphasic and biphasic

centroids compared to CTX-**STR** and **STR**-GP, but less biphasic centroids than **STR** alone. Overall, it appears that connectivity increased the number of triphasic centroids and did not change the overall number of centroids, apart from in STR-GP devices.

5.3.6 Centroid full duration at half maximum

The centroid peak duration (FDHM) was also compared between separate and connected cultures to determine any changes (**Fig.5.18**).

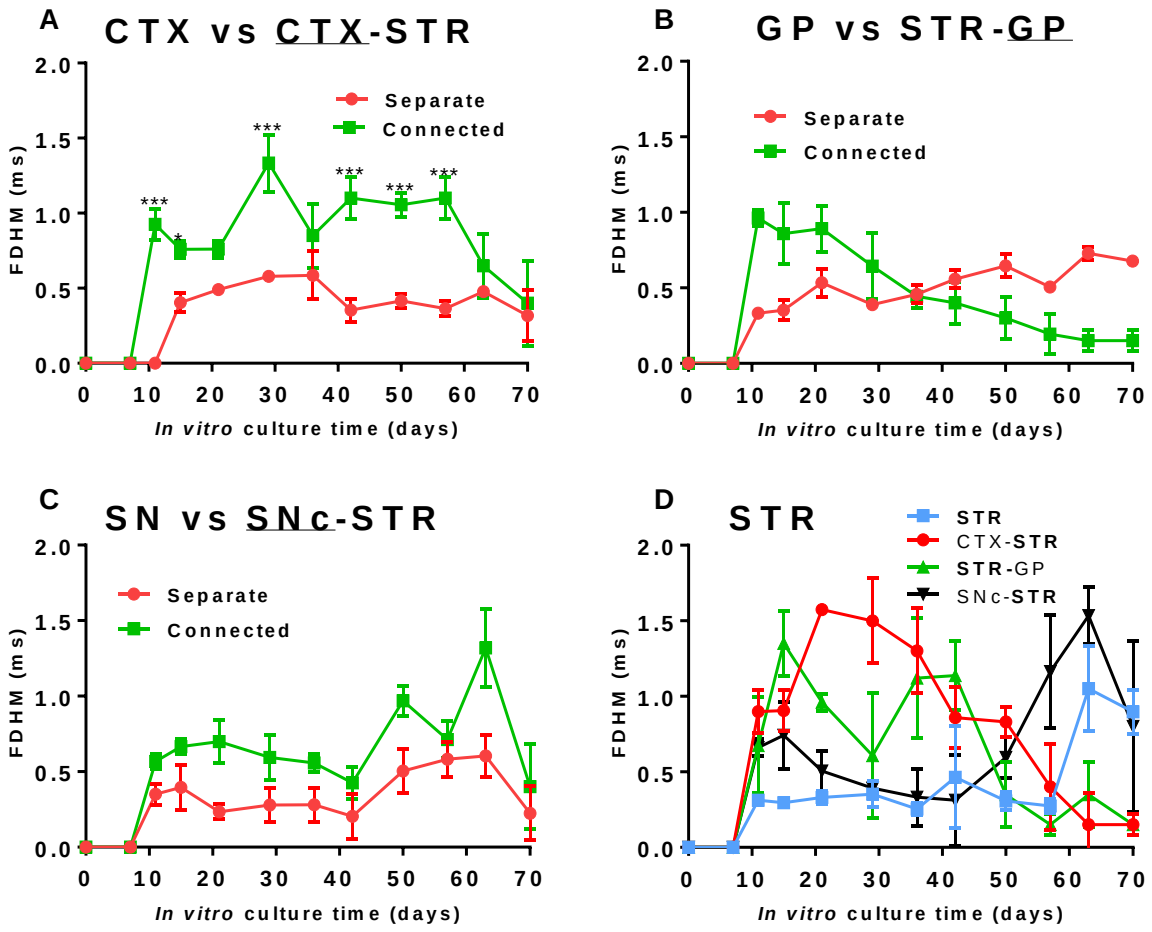

Figure 5.18: A comparison between the average full duration at half maximum (FDHM) of centroids over time for separate (CTX, STR, GP or SN) and connected (co-cultures of CTX-STR, STR-GP, and SNc-STR) cultures on MEAs. Each separate culture is compared with the relevant port of the corresponding co-culture, with separate STR compared to the STR port within each co-culture. Asterisks are generated from post-hoc t-tests (n=4). (*): p<0.01, (***): p<0.0001.

Connectivity had a significant effect on the FDHM of CTX cultures (ANOVA (1,2) F=830.5, p=0.001), with CTX connected to STR in CTX-STR co-cultures having significantly greater FDHM from all recordings bar the latest (65-70) and 21 DIV. This indicates that centroids generated from connected CTX have a significantly longer duration at their peak. GP, SN and STR did not feature a significant

changes in FDHM from connectivity, indicating that centroids were largely similar in duration whether generated by separate cultures or connected co-cultures.

5.4 Discussion

The *in vivo* brain relies on complex 3D connectivity between specific structural and functional zones, areas and territories. Neural cells have long been shown to thrive when they can synapse and connect with other neural cells, as a consequence cell density is very important when working *in vitro* (Biffi *et al.* 2013). With this in mind, culturing a single neural cell type in isolation (in **Chapter Four**) is a far cry from the complex constellation of activity in the brain, but an important first step. Recent *in vitro* neural models also involve culturing multiple cell types, such as neurons, astrocytes and microglia (J. Park *et al.* 2018). By connecting two different neural cell types together in our 5PD on an MEA we have taken the first step to increase the complexity of our model, with neural cells now able to communicate with different types of cells rather than just themselves, bringing the model closer to the *in vivo* situation.

Each nuclei of the basal ganglia receives thousands of afferent axons projecting from upstream nuclei, and in turn sends thousands of efferent axons to their downstream nuclei (Ellens and Leventhal. 2013). Reducing this system to two neural cell types connected by 400 channels is still far from the complexity in the basal ganglia, but in turn is far more complex than the initial basic work in **Chapter Four** and work produced by other groups (Goyal and Nam. 2011, Kanagasabapathi *et al.* 2011). By manageably increasing the complexity in this manner, we could identify the changes that occur in the spontaneous electrophysiological activity of the neural cells, now that they were connected to their appropriate target nuclei and closer to their *in vivo* environment.

5.4.1 Co-culturing

Two different neural cell types were cultured into each 5PD, on a PEI/PDl-coated MEA as the growth surface. This work represents a development of both earlier results chapters: with these primary cells previously cultured successfully within 5PDs, extending through channels into adjacent ports (**Chapter Three,** see **Figs. 3.17-3.18**); and primary cells successfully cultured successfully on PEI/PDL-coated MEAs over the long term (**Chapter Four,** see **Fig.4.6-4.8**). Cells were cultured for up to 70 DIV and extended axons through the microchannels to communicate with adjacent cell populations (see **Figs.5.4B and 5.5**) while their extracellular spontaneous activity was recorded. The main issue presented by these models was the location of the electrodes.

5.4.2 MEA electrode location

As an unfortunate consequence of the MEA bracket hardware design, the location of the 5PD on the MEA was limited to a 30 mm diameter circle, with the centre of the circle being the location of the 64-electrode array itself. As there are 64 (8 x 8) electrodes and two ports containing cells, the ideal situation would be 28 (8 x 3) electrodes in each port and a single 8 x 1 column within the channels between these ports. However, it was necessary to place the 5PD over the centre of the MEA (as placing it too far in any direction would result in the bracket not fitting over the MEA and recording unable to take place), so most of the electrodes were located in the centre port, with a few columns in the upper side port and a few electrodes not in contact with any cells, being covered by PDMS or being in the lower side port (as seen in **Fig.5.19**).

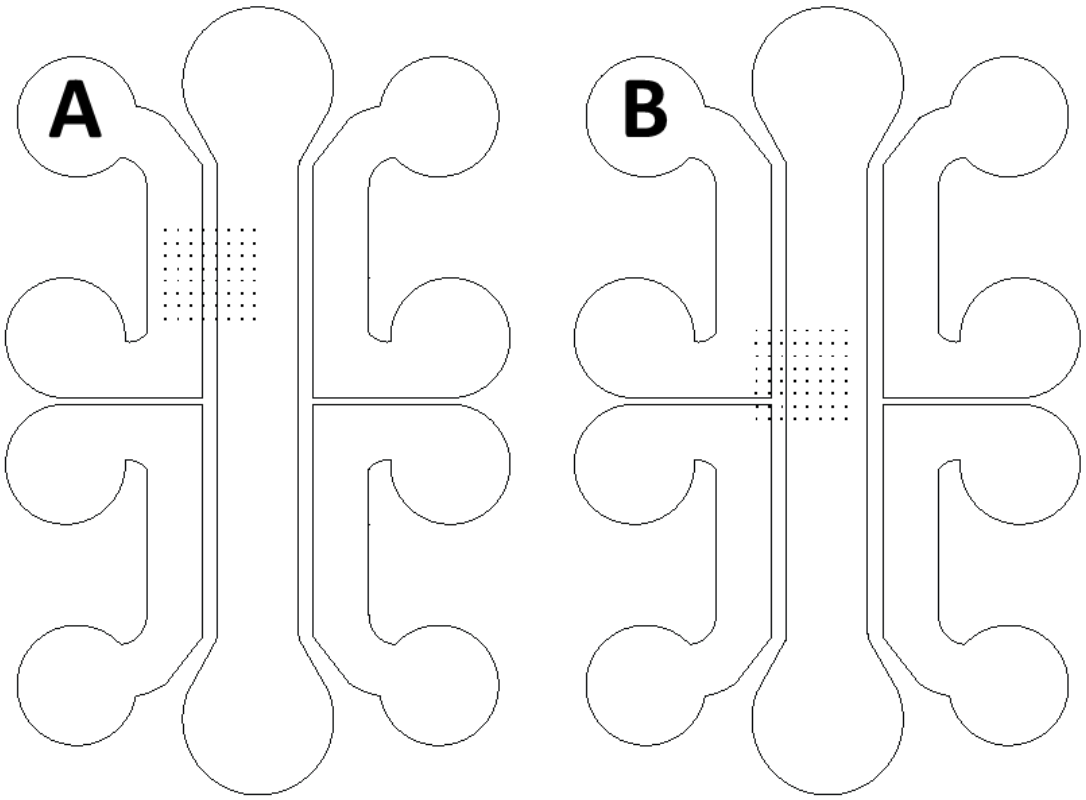

Figure 5.19: Location of the MEA within the 5PD. A) desired location, in the centre of the side port and with roughly half the electrodes on each side with some in the channels. B) actual location, with most electrodes in the centre port and 2-3 columns in the side port, along with 4-10 electrodes of the lower right-hand corner encroaching into the lower right-hand port and therefore not recording from anything. This actual position is due to hardware restrictions and represents the location of the MEA throughout recording of each co-culture.

With the current MEA design this restriction is unavoidable, the only option for future work being to re-design the MEA so that there are equal numbers of electrodes within all five ports, mentioned in more detail in **Chapter Seven**.

5.4.3 Activity localisation

Heatmaps and analysis of percentage activity allowed for tracking of activity across the MEA. This tracking held more significance than in the previous chapter as there were now three different zones located across each MEA, namely CTX/GP/SNc neurons, channels, and STR neurons. The heatmaps for CTX-STR, STR-GP and SNc-STR co-cultures showed onset and high activity in a row directly across the MEA from port to port (see **Fig.5.6**). The highest levels of activity were in and near the channels, most likely due to the fact that the majority of synapses between the two neural cell types formed as projection neurons exited the channels and met with the adjacent cell population (Lu *et al.* 2009).

Activity was greatest proximate to channels, likely due to this being the area where STR cells are encountering the most CTX synapses and subsequently highest concentrations of glutamate (J. Ding *et al.* 2008). After these close connections were established, activity spread across the STR port. This spread of activity is also indicated by the percentage activity, where ~90% activity in the STR port is maintained from 21-51 DIV, unlike CTX and channels which decrease by 36 DIV. This is likely because the STR is the only port receiving excitation via glutamate release, as the channels consisted of CTX axons. Despite this excitation, levels still fell in STR ports from 51-70 DIV, perhaps due to an aging culture, glial cell proliferation, more active GABAergic inhibitory activity or less active glutamatergic stimulus.

STR-GP co-cultures showed onset by 11 DIV, but activity had not spread across the MEA until 29 DIV, was only maintained until 42 DIV before disappearing as soon as 50 DIV, with few active electrodes from 50-70 DIV. This may be a sign of inhibition, with the spread of activity decreasing rapidly after being established due to synapses and GABA inhibitory action maturing. Areas of high activity were in a row and adjacent to channel entrances/exits, suggesting that this is where synapse formation was most dense.

SNc-STR co-cultures showed pronounced high-frequency activity in a row across the MEA, with one row of electrodes producing the most activity from onset until 42 DIV. As this is a central row with the channels in the middle, this may have been initial formation of a SNc cell network projecting through the channels to the STR neurons. As cells were seeded from the wells into the ports, the aim was to ensure that the densest areas of the culture were those in the bottom of the port as this is where the electrodes were (**Fig.5.19B**). This density may have resulted in a network stretching across a row of electrodes and through the channels, while there was little activity or network formation elsewhere until 29 DIV. To my knowledge this has not been reproduced elsewhere.

5.4.4 Spiking activity

With spontaneous electrophysiological activity of each cell type in isolation outlined in **Chapter Four**, this data presents an opportunity to observe any changes in this activity when cell types were

connected together using our 5PD and compare data from the same cell type when in isolation and when connected to STR neural cultures. These comparisons of spiking activity are discussed in the following sections.

*5.4.4.1 CTX **vs** CTX-**STR***

Every aspect of CTX spontaneous extracellular electrophysiological activity was increased by connecting CTX neurons to a population of STR neurons via our 5PD, indicating the effect of connectivity within neural networks on the strength and maturation of synapses between neurons and their subsequent activation, as also described by (Fauth and Tetzlaff. 2016). However, while synapse formation regulated activity between neuronal populations, the opposite is also true, with activity able to regulate synapse formation, in some cases even before the synapses themselves are formed (Tessier and Broadie. 2009, Andreae and Burrone. 2014). In addition, synapses do not form easily after a first encounter between different neuronal subtypes, synapse formation is an extended process of numerous meetings until synapses form and functionally mature (Lu *et al.* 2009). 5PDs consisted of a smaller surface area than the ring used for separated culture, but the cell density was kept constant between the two experiments. As the use of the 5PD and microchannels were unlikely to increase CTX activity, the increased activity is most likely to be due to connectivity to STR neural cultures, with CTX activity shown to increase with connectivity to relevant brain areas (M. N. Miller *et al.* 2008).

Recordings from electrodes within 5PD channels were similar to CTX data as the channels mostly contained CTX axons (**Fig.5.4B**), due to the unidirectional nature of the channel width and the fact that CTX cultures have been shown to produce far more axons than other cell types (**Chapter Three, Fig.3.19**). After seeding, CTX axons fasciculated and bundles entered into channels before exiting the channels, unravelling and synapsing with STR neural cells. As such, data recorded from the channels was similar to data recorded from the CTX port as the channels were full of CTX axons. This process of bundling in microchannels has also been observed in other neural *in vitro* models with channels of similar widths (J. Park, Koito, Li and Han. 2009a, J. Park, Koito, Li and Han. 2009b, J. Park *et al.* 2012).

*5.4.4.2 GP **vs STR-**GP*

When comparing separate GP neural cultures and connected STR-GP co-culture devices, connectivity initially increased GP neuron activity, and this initial increase was likely due to the act of physical connection to another cell type, as seen in the increase in activity present in CTX-STR co-cultures (Fauth and Tetzlaff. 2016). But after ~3-4 weeks GP activity decreased, with lower frequencies and less burst firing, to our knowledge this is the first time this has been observed *in vitro*. Compared to other co-cultures, STR-GP consistently displayed the lowest levels of average and maximum spike frequency, burst number and spikes per burst. The subsequent decrease in activity may be a

consequence of STR neuron activity. STR neurons consisted of inhibitory GABAergic MSNs (Ellens and Leventhal. 2013), therefore GP activity may have been inhibited by the action of STR neuron inputs. This inhibitory action of GABAergic neurons has been shown *in vitro* (Dubinsky. 1989). With these MSNs projecting to GP GABAergic neurons, spontaneous STR firing could have decreased GP bursting and spike frequency over time. The initial higher activity that the GP co-cultures demonstrated may have been due to STR MSN synapses not yet being sufficiently mature to transmit GABA across the synapse, or GABA not yet being a true inhibitory neurotransmitter, as GABA is initially excitatory in development (Maric *et al.* 2001, Ben-Ari. 2002). Overall, it appears that connectivity initially increased GP firing activity, but once functional synapses were formed the STR MSN firing inhibited GP activity and resulted in decreased spike frequencies and burst firing.

5.4.4.3 *SNc* ***vs*** *SNc-****STR***

SNc-STR had the highest peak levels of activity of all co-cultures, with greater average and maximum spike frequencies and more bursting. SNc connectivity to STR was facilitated by the potentially chemoattractive effect that the STR has been shown to have on SN neurons in nigrostriatal circuit formation (Gates *et al.* 2004). After the peak in firing activity, SNc-STR co-culture activity levels fell below separate SNc activity levels, with virtually no spiking or bursting from SNc-STR co-cultures from 50-70 DIV while there was activity observed from separate SNc during the same timeframe. SNc had shown more activity than other cell types before (**Chapter Four Figs.4.12-4.15**), and with connectivity to STR neurons the SNc neurons showed greater initial activity, similarly to GP and CTX neurons when in a co-culture. However, the drop in SNc activity during the late phase (50-70 DIV), was similar to GP neurons. One possibility is that SNc neurons may also have been subject to inhibition from STR MSNs as was seen with GP neurons, but as SNc is in the input port in this co-culture (SNc-STR as opposed to STR-GP), it should be less likely that STR MSNs traversed the tapered channels in the opposite to intended direction. Separate SNc neurons also decreased in spiking frequency during 50-70 DIV, but at a slower rate. Another possibility is that some aspect of SNc-STR connectivity may be enhancing this natural decrease in firing for SNc neurons when connected to STR neurons, the precise mechanism for this remains to be explored, potentially the decrease in STR neuron firing lessened DA release and therefore SNc neuron firing. One explanation for this stark change in spiking activity over time is the nature of dopamine release *in vitro*, with studies showing that *in vitro* nigrostriatal cultures display increased DA release at and after 24 DIV compared to 9 DIV due to more mature functional dopaminergic synapses forming (Struzyna *et al.* 2018).

5.4.4.4 *STR* ***vs CTX-****STR* ***vs*** *STR-****GP vs SNc-****STR*

The STR ports of each co-culture were also compared to determine how CTX, GP and SNc neural cultures affect STR neuron activity once connected. Overall, in comparison to separate STR, all

aspects of STR activity were decreased in STR-GP co-cultures and increased in CTX-STR and SNc-STR co-cultures.

STR neurons within CTX-STR devices featured much greater average and maximum spike frequency when compared to seperate STR neurons and STR-GP cultures, as well as SNc-STR (from 29 DIV onwards). This was most likely due to CTX containing excitatory glutamatergic neurons, which had projected through the channels into the STR port and released glutamate, depolarising STR neurons and reducing the threshold necessary to fire, resulting in more firing (Meldrum. 2000, Rangel-Barajas and Rebec. 2016). This increase in firing also increased over time, with STR eventually having greater maximum spiking than CTX, with a late peak on 51 DIV. STR neurons from STR-GP devices had the lowest average and maximum spiking activity of all three co-cultures, potentially inhibited by the GP GABAergic neurons in a negative feedback loop (Ellens and Leventhal. 2013).

STR within SNc-STR devices had the most spiking in early time-points, these early peaks contained by far the highest rate of firing of all co-cultures, having an average of ~12 Hz and a maximum of over 200 Hz. It was unclear why STR activity was so high when connected to SNc neural cultures, one potential explanation is that dopamine is only acting on the D1 receptors of a subset of STR neurons associated with the direct motor pathway and promoting their activity. This suggests that there was more complex activity in this co-culture rather than just excitation or just inhibition. The average level of spiking was highest at the channels. Average activity of STR and SNc neurons displayed different peaks, with STR activity peaking early on 21 DIV and SN activity peaking at 36 DIV. This suggests that STR neurons were initially excited by SN neurons and later inhibited as SNc activity increased, a concept reinforced by the initial formation of excitatory nigrostriatal connections *in vivo* (during the second postnatal week of mice) (Kozorovitskiy *et al.* 2015), the complex modulatory effect DA has on STR MSNs (Tritsch and Sabatini. 2012) and the fact that nigrostriatal connections made in development can be pared back based on the level of synapse reinforcement (Money and Stanwood. 2013). This can either mark a shift from dopamine affecting D1-type MSNs to D2-type subset of MSNs, or the point at which GABA generated by STR MSNs shifted from excitatory to inhibitory.

A particularly notable feature of SNc-STR co-cultures is the maximum spiking. While SNc and channels achieved a peak of ~70 Hz (36 DIV), already double that of CTX-STR and STR-GP co-cultures, activity from the STR port of SN-STR co-cultures peaked earlier and far higher at 212 Hz (21 DIV). The rat brain *in vivo* can fire up to several hundred times a second (Boudewijns *et al.* 2013), so this is within acceptable bounds.

5.4.5 Centroid assessment

The shape of each electrophysiological spike recording can be useful in defining the activity of the neural cultures, as such the many spikes were categorised into centroids which give further information into the activity of the devices. Centroid number, phase, sign and shape were all assessed over time for each device. The number of centroids were lower in mid and late stages compared to early stages of culture (**Fig.5.9**), showing that the spike variation decreases as the spike frequency increases and the network matures *in vitro* (Chiappalone *et al.* 2006)*,* the same trend seen in separate MEA work (**Chapter Four, section 4.2.6 Centroid number, Fig.4.19**), now observed across two ports and the channels linking them.

Centroid shape categorisation (**Fig.5.10**) indicated that the channels contained a majority of triphasic centroids, which agreed with the theory set out in **Chapter Four (section 4.0.2 Extracellular recording, Fig.4.3),** that axons resulted in triphasic extracellular waveforms and cell bodies and/or synapses resulted in monophasic and/or biphasic centroids. The channels housed axons from the input port, as indicated by the triphasic centroids. Centroid proportions in ports differed, most notably CTX and SN input resulted in changes in STR, with STR having similar proportions of centroids to CTX cultures when functionally linked to CTX cultures, and similar to SN when linked to SN. This indicates that STR activity is changed by innervation from CTX/SN axons, further demonstrating functional connectivity. In STR-GP co-cultures this functional connection is less clear as there were less centroids overall when compared to CTX-STR and SN-STR co-cultures, but STR and GP still feature similar proportions of centroids. These co-cultures are functionally connected. Centroid full duration at half maximum (FDHM) was not significantly changed by functional connectivity, indicating that the centroids were similar in spike duration, even if there were changes in centroid phase and sign.

5.5 Conclusions

Overall, by increasing the complexity of our model from a single cell type to two, it is clear that this resulted in the production of more complex electrical activity when compared to culturing one separate cell type in isolation. Work in this chapter built on previous MEA work (**Chapter Four**) by connecting two neighbouring basal ganglia nuclei in order to create a rudimentary basal ganglia circuit. In this chapter we have advanced from a single separate cultured cell type to two cell types connected by our microfluidic 5PD, with all activity recorded by MEAs. These devices have appropriately re-created relevant circuits for the basal ganglia, namely the corticostriatal, nigrostriatal and striatopallidal pathways of the basal ganglia.

Comparing to the separate cultures form the previous chapter, connectivity resulted in increased amplitude and frequency of spiking and bursting activity from CTX and SN cultures, as well as in STR

cultures when connected to CTX or SN. Conversely, connectivity resulted in decreased spiking overall for GP cultures and STR when connected to GP. These changes were likely due to the natures of each of these cell types, and the rise and fall of activity over time reflected the maturation of synapses and the formation of functional connectivity.

The extracellular recordings could clearly identify the specific neuronal types in appropriate connection with each other, and as with **Chapter Four** these recordings were reproducible. In this manner, these connected co-cultures better represent the activity of the basal ganglia *in vivo* than the separate cultures, by including two physiologically relevant connected neural cell types rather than one. This resulted in more complex MEA activity and interaction between the two populations (inhibition, excitation etc) over the long term, which more accurately models activity from the basal ganglia as s rudimentary neural circuit, marking a vital step towards mimicking basal ganglia activity *in vitro*.

Chapter Six: Mimicking Parkinson's disease

6.0 Introduction

After successfully modelling numerous basal ganglia (BG) pathways, namely the corticostriatal (cortex-striatum or CTX-STR), striatopallidal (striatum-globus pallidus or STR-GP) and nigrostriatal (substantia nigra pars compacta-striatum or SNc-STR) pathways in the previous chapter (**Chapter Five**), the next step was to focus on the nigrostriatal pathway and enable study of Parkinson's disease (PD) by creating a pathological nigrostriatal model. This pathological PD-mimicking device involved damaging/destroying the SNc dopaminergic neurons projecting to the STR, which *in vivo* is known as the cause of PD symptoms (Jackson-Lewis *et al.* 2012, Blesa and Przedborski. 2014, Van Kampen and Robertson. 2017).

To summarise the information from the previous chapter concerning the nigrostriatal pathway (**Chapter Five section 5.0.4 Nigrostriatal (SNc-STR)**), the nigrostriatal dopamine (DA) pathway involves DA neuron projections from the SNc to the STR, with DA release in the STR necessary for BG-mediated motor behaviour (Rice and Cragg. 2008). Within the BG, DA transporters (DATs) are expressed exclusively by the DA neurons of the SNc, with the STR containing many DA receptors (DARs) both synaptically and extrasynaptically (Rice and Cragg. 2008), with examples of DA synapses shown in **Fig.6.1**. When this nigrostriatal DA delivery system breaks down, the result is progressive and functional damage that can result in the numerous symptoms seen in Parkinson's disease (see **Chapter One** for more details).

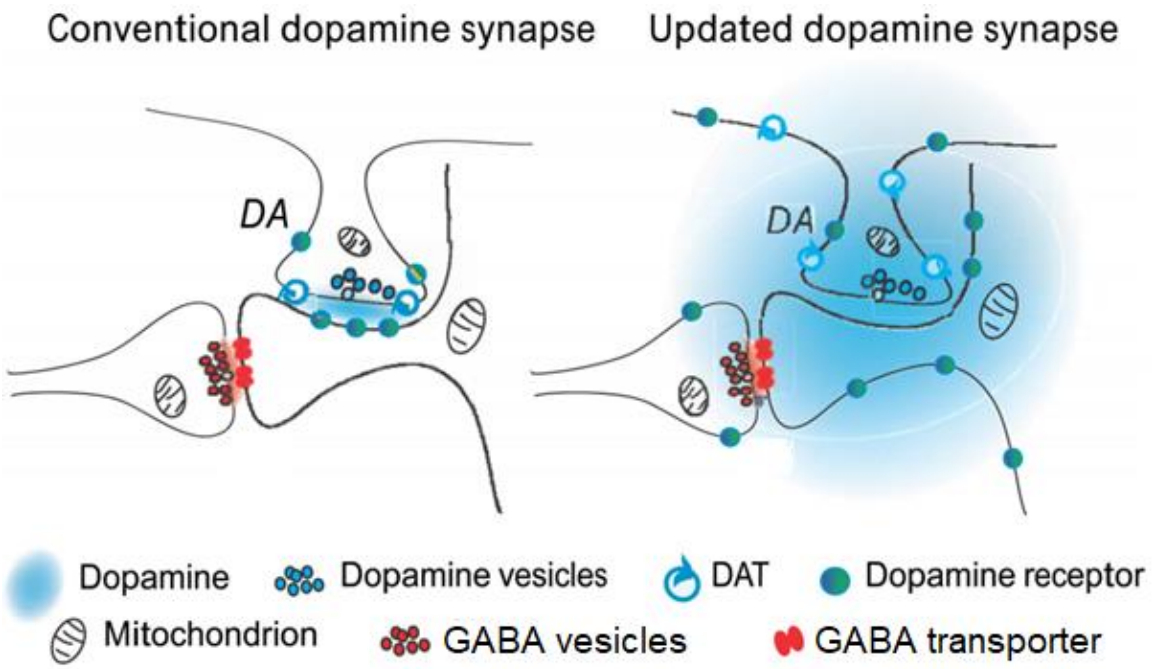

Figure 6.1: Illustrations of DA synapses on the spine of a STR MSN. The conventional model has controlled DA release limited to the synaptic area, with DATs and DARs also limited to this area. However, studies have shown that DATs and DARs are located extrasynaptically and DA release can '*leak*' across a wide area, resulting in the updated view of the dopamine synapse on the right, with a 3D cloud of DA reaching to distal DATs and DARs on the DA neuron itself and surrounding neurons. This DA is only taken up by DATs on the DA neuron itself, and at quite a slow rate, allowing DA release to affect neurons both synaptically and extrasynaptically over time. Figure adapted from (Rice and Cragg. 2008).

6.0.1 Electrophysiology of Parkinson's disease

Damaging nigrostriatal cells and depleting DA within the BG have serious electrophysiological consequences, which can be measured in our model via the MEA. The extreme activity changes upon DA depletion are also covered in numerous reviews (Boraud *et al.* 2002, Ellens and Leventhal. 2013, Lindahl and Hellgren Kotaleski. 2017).

In the BG, DA from the SNc chiefly acts on the STR to increase D1-type (direct pathway) MSN firing and decrease D2-type (indirect pathway) MSN firing, being doubly pro-movement by exciting the 'go' pathway and inhibiting the 'no-go' pathway, by suppressing the SNr/GPi inhibitory outputs of the BG. This concept was covered in further detail in **Chapter One** (section **1.5.1.2 Striatum**) and **Chapter Five** (sections **5.0.2.1 Striatopallidal structure** and **5.0.4 Nigrostriatal**).

DA depletion therefore leads to **decreased** activity from D2-type MSNs, GPe, thalamus and the CTX, and **increased** activity from D1-type MSNs, SNr/GPi and the STN. This 'rate change' model of PD in the BG can be seen in **Fig.6.2**. These changes have been shown both in MPTP- and 6-OHDA-treated models (Mallet *et al.* 2006, Pasquereau and Turner. 2011, Ellens and Leventhal. 2013).

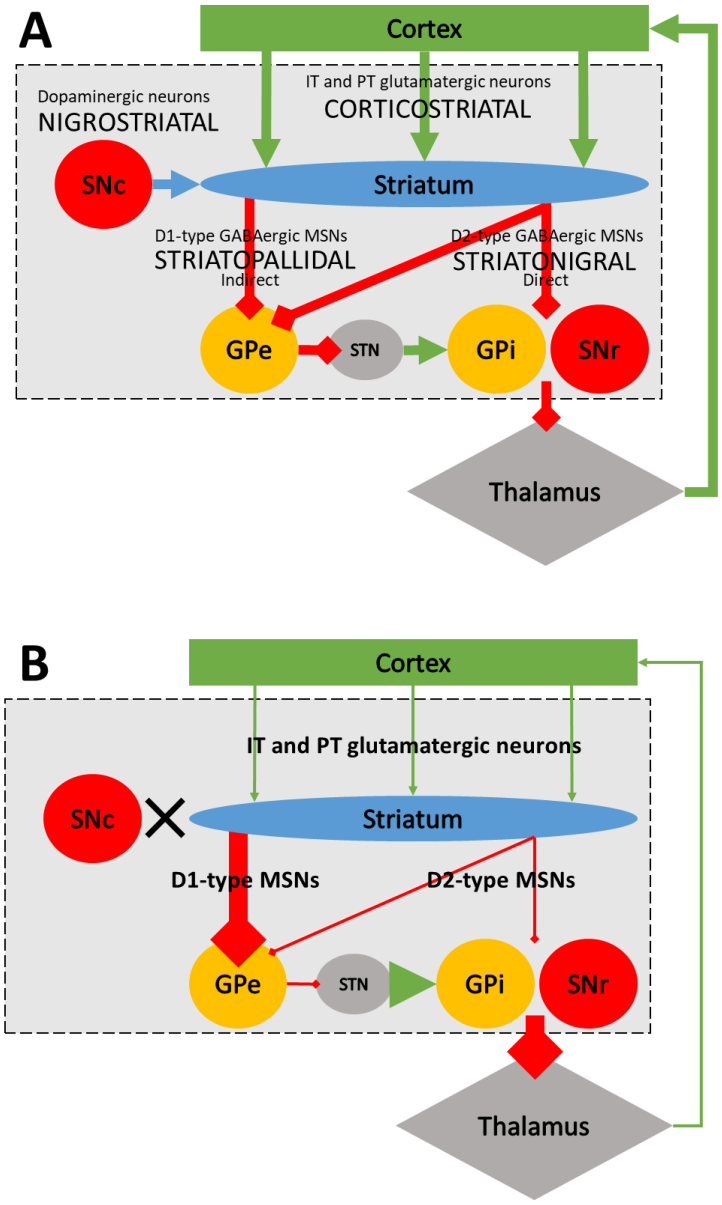

Figure 6.2: Changes in BG circuitry during PD. A) The normal signal pathways in the BG, with CTX and SNc projecting to the STR, and the indirect/direct pathways filtering through to the GPi/SNr output nuclei, which signal the thalamus (to activate the brainstem/spinal cord). Red arrows are GABAergic (inhibitory), green arrows are glutamatergic (excitatory) and the sole blue arrow is dopaminergic, the connection lost in PD. Uniform arrow thickness indicates that these signals are all tonically active. B) Electrical activity in pathways in the BG after a loss of nigrostriatal neurons (indicated by the black cross) and depletion of dopamine in the STR. D1-type indirect pathway MSNs and D2-type direct pathway MSNs have increased and decreased firing rates respectively. As a consequence, the GPe is more inhibited and the STN is less inhibited therefore more excitatory. The GPi/SNr are less inhibited by the STR and more excited by the STN, resulting in the thalamus being more inhibited and the CTX less excited, leading to decreased movement. All electrical activity changes are indicated by arrow thickness.

Studies also show changes in bursting behaviour. In a connected circuit, bursts are brief high-frequency (>10 Hz) bundles of spikes often followed by a pause or quiescent period. These bursts are mostly measured extracellularly across the BG as intracellular methods are too limited. DA depletion leads to enhanced bursting in the GPe, STN and SNr/GPi, namely across the entire indirect pathway of the BG. (Wichmann and Soares. 2006, Tachibana *et al.* 2011, Ellens and Leventhal. 2013). Excessive bursting after dopamine depletion is also found in the thalamus (Vitek *et al.* 2012) and

consequently CTX pyramidal tract (PT) neurons (Pasquereau and Turner. 2011) (driven by the thalamus). This bursting activity in highly organised BG circuitry results in damaging positive-feedback cycles, where GPe (indirect pathway) and CTX excessively stimulate the STN due to bursting, resulting in STN hyperactivity and increased inhibition of the thalamus and brainstem/spinal cord by the GPi/SNr.

DA-depleted BG activity also includes oscillations, namely periodical repeats of activity (often confused with bursts due to similar frequencies) occuring at numerous frequencies (including frequencies comparable to tremor) in both the single unit and local field potential (LFP) activity of GPi and STN neurons, associated with bradykinesia and rigidity (Jenkinson and Brown. 2011). This oscillatory activity is linked to increased bursting, with the GPe-STN bursting also oscillating.

Both these bursting and oscillatory activities can also be synchronous in PD, where spiking or LFPs occur simultaneously/synchronously. This kind of behaviour is rare in the healthy brain *in vivo*, with normal behaviour involving inputs and outputs in order for electrical activity, with this activity occurring in rapid succession but not simultaneously (Bar-Gad *et al.* 2003). After DA depletion in BG models, activity in the GPi, GPe and STN can become highly synchronised (Pessiglione *et al.* 2005, Ellens and Leventhal. 2013), theorised to relate to motor deficits, due to loss of BG nuclei specificity.

Broadly speaking, there are several vital components to model when studying the electrophysiology of PD. It is vital to remove/damage dopaminergic nigrostriatal neurons in order to deprive the STR of DA without damaging the STR itself; to record the spontaneous electrophysiological activity from both the SNc and the STR while the two populations are linked and after the nigrostriatal connections are damaged; and to identify changes in the spontaneous electrophysiological activity between physiological and pathological states. In the model described in this thesis, this equates to a normal SNc-STR model and a SNc-STR model where the SNc port has been treated with 6-OHDA in order to remove the DA neurons and subsequent nigrostriatal connections. This chapter analyses the data received from such a co-culture, where acute PD was mimicked with the use of 6-OHDA on our 5PD containing two connected cultures of SNc and STR neurons respectively, combined with an MEA.

6.0.2 Chapter Six Aims and Objectives

In previous chapters, a baseline of BG nuclei activity in separation was established (**Chapter Four**), followed by creating a rudimentary BG circuit by linking two adjacent BG nuclei through our 5PD (**Chapter Five**). In this chapter, the aim was to use SNc-STR co-cultures to mimic Parkinson's disease through 6-OHDA treatment of the SNc port, where the 6-OHDA neurotoxin was intended to damage or destroy nigrostriatal SNc projections, mimicking acute PD, and using the resultant model to determine any electrophysiological changes that occurred.

6.1 Experimental Methods

The methods involved in this chapter were previously outlined in **Chapter Two**.

6.1.1 Device surface preparation

As seen in **section 2.1.1 device preparation: chemical coating,** MEAs were first sterilised with 70% IMS for 15 minutes, dried and coated first with 0.05% PEI for 1 hour (at rtp), then 0.1 mM PDL overnight at 37 °C, washing between each stage. MEAs were then dried and ready for cell culture. 5PDs were cast from PDMS and attached to the centre of the MEA, then flushed with sterile water and incubated to remove any air or bubbles.

6.1.2 Primary cell culture

As seen in **section 2.2 Primary cell culture**, tissue was dissected from E16/14 Sprague-Dawley rat embryos: E16 lateral ganglionic eminences (LGE) for STR and E14 ventral midbrain (VM), for SN. These tissues were dissociated and 100,000 cells were seeded directly into the relevant port on the 5PD, namely input port for SN and central port for STR. After seeding the ports were flooded with growth media and the cells incubated at 37° C, 5% CO_2.

6.1.3 Electrical activity measurement with MEA

Recordings of cell electrophysiological activity (**section 2.5.2 MEA: Recordings**) were taken once a week from 0 DIV to 70 DIV, before a media change. MEAs were moved to a heated bracket (at 37 °C) attached to amplifiers and digitisers. Activity was recorded for four minutes in triplicate, totalling 12 minutes of recording, using MED64 hardware with Mobius software. These data were stored on the MEA PC for analysis.

6.1.4 6-OHDA treatment

As seen in **section 2.2.4 6-OHDA treatment**, 6-OHDA was dissolved in 0.15% ascorbic acid and diluted to 100 µM in serum-free media before being added to the SN port and incubated. After incubation 6-OHDA was removed and cells washed with culture media. MEA readings were taken immediately before, after and 24h, 48h after treatment, alongside usual 0-70 DIV readings. Immunocytochemistry and fluorescent imaging used to identify GABAergic neurons (using anti-GABA) and DAergic neurons (using anti-TH) (for more information see **section 2.3 Immunocytochemistry**).

6.2 Results

6.2.1 Primary cell culture

E16 STR and E14 SNc neural cells were successfully cultured in ports of 5PDs, with SNc in an input port and STR in the central port. SNc neurons extended processes through channels and into the STR port, making up the nigrostriatal pathway. Cells were in contact with electrodes in both the SNc, STR and channels in between, as seen in **Fig.6.3**, which shows viable SNc and STR cells cultured with MEA electrodes.

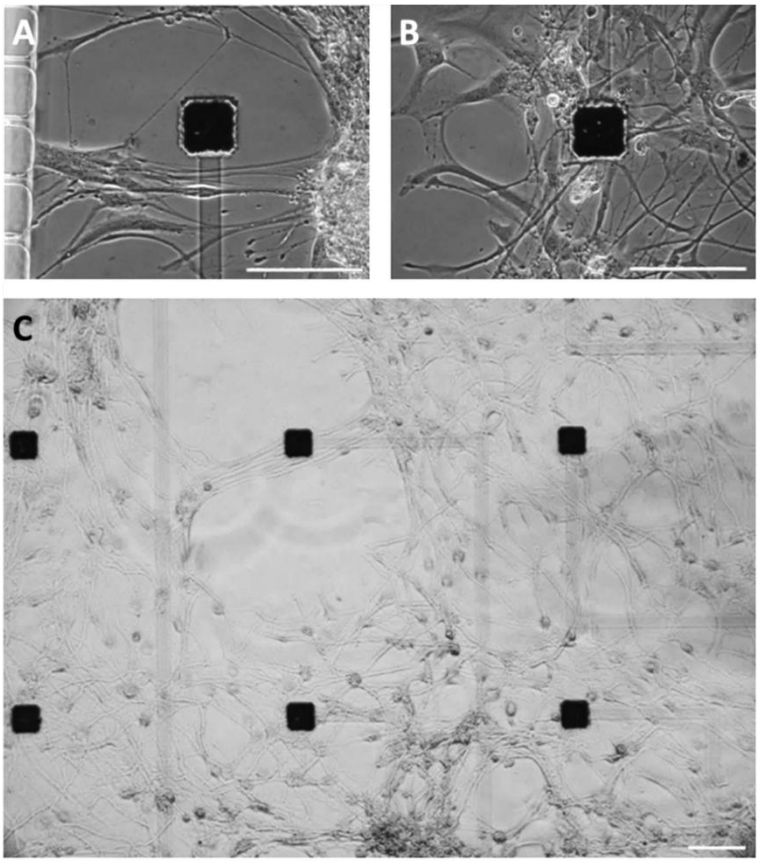

Figure 6.3: 100,000 primary STR and SNc cells seeded onto 5PD MEAs, and brightfield imaged after 8 DIV. A) STR neurons and an electrode for scale near channels, B) SNc neurons and an electrode, C) SNc neurons and electrodes at a lower magnification. All scale bars at 100 µm.

As GABAergic neurons should not be affected by optimised 6-OHDA treatment, it was vital to track the levels of GABAergic neurons within the model, to ensure that damage from 6-OHDA was specific to DAergic neurons. GABAergic and DAergic neurons in SNc cultures were identified with antibody immunostaining, shown in **Fig.6.4,** indicating the different neuronal subtypes. Cultures included a mix of GABAergic and DAergic neurons, quantities stated in the graph included in **Fig.6.4**.

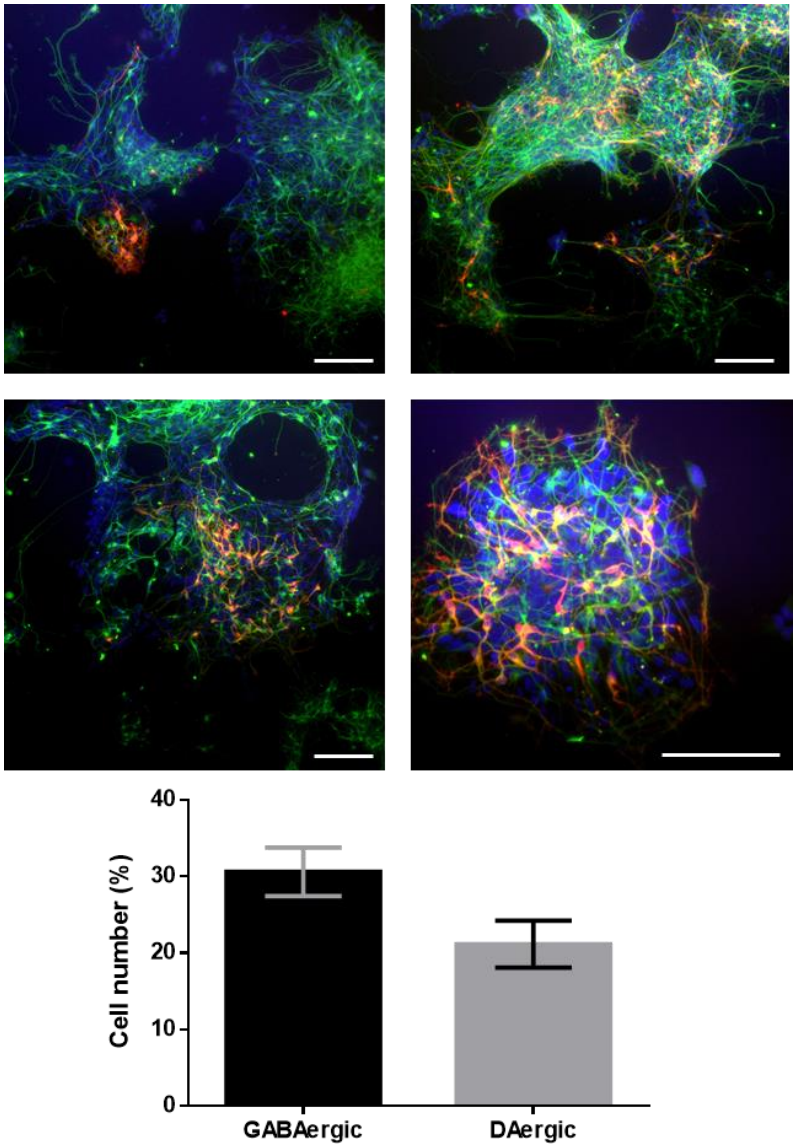

Figure 6.4: Fluorescent imaging of primary SN cultures to identify GABAergic and DAergic neurons. Each image represents 100,000 SN neural cells after 4 DIV, stained with DAPI (blue), GABA (green, GABAergic neurons) and TH (red, DAergic neurons). Each culture presents a mixture of GABAergic and DAergic neurons. Scale bar 100 µm.

6.2.2 6-OHDA optimisation

The SNc port was treated with 6-OHDA in order to selectively remove DA neurons. However, use of 6-OHDA *in vitro* required several optimisation steps, where 6-OHDA was tested on early (6 DIV) SNc cultures to determine the optimum antioxidant vehicle, dosage concentration and exposure time. For each experiment, the levels of GABAergic neurons and DA neurons were assessed, with any significant loss of GABAergic neurons signifying non-selective damage, while loss of DA neurons but unaffected GABAergic neuron levels signifying selective damage. Image data from these experiments can be seen in **Fig.6.5**.

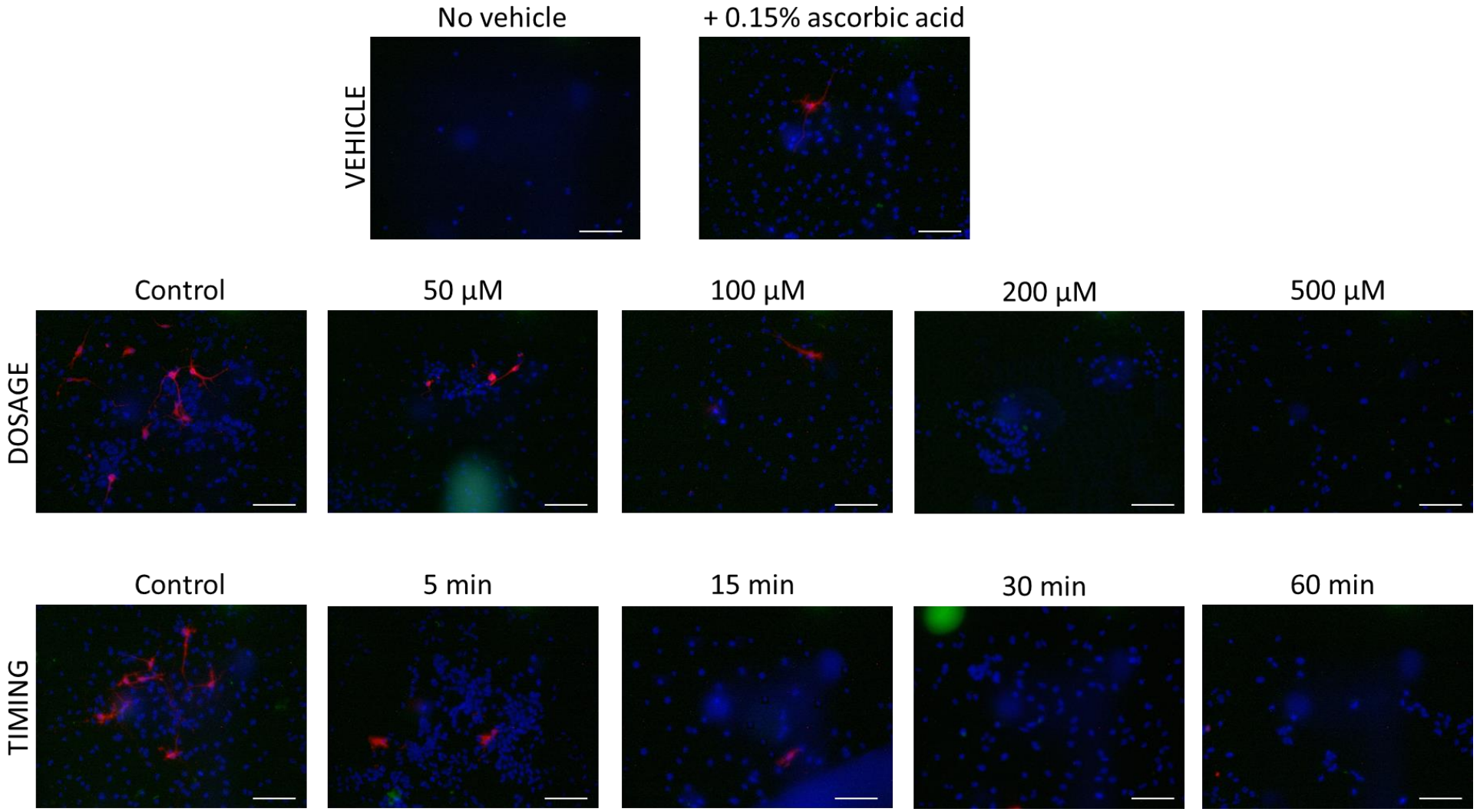

Figure 6.5: Fluorescent images of the 6-OHDA optimisation process. Each image is representative of n=4, shows 100,000 primary SN cells imaged after 6 DIV, after specific treatment with 6-OHDA neurotoxin. Blue: DAPI, Red: TH (DAergic neurons), scale bar 100 µm. GABAergic data not shown.

6.2.2.1 Vehicle

The chosen antioxidant was based on a paper from Ding and colleagues (Y. M. Ding *et al.* 2004), where their successful *in vitro* methodology involved use of 0.15% ascorbic acid as a vehicle for 6-OHDA. SNc cells were exposed to 6-OHDA with and without the vehicle to determine its efficacy, as seen in **Fig.6.6**.

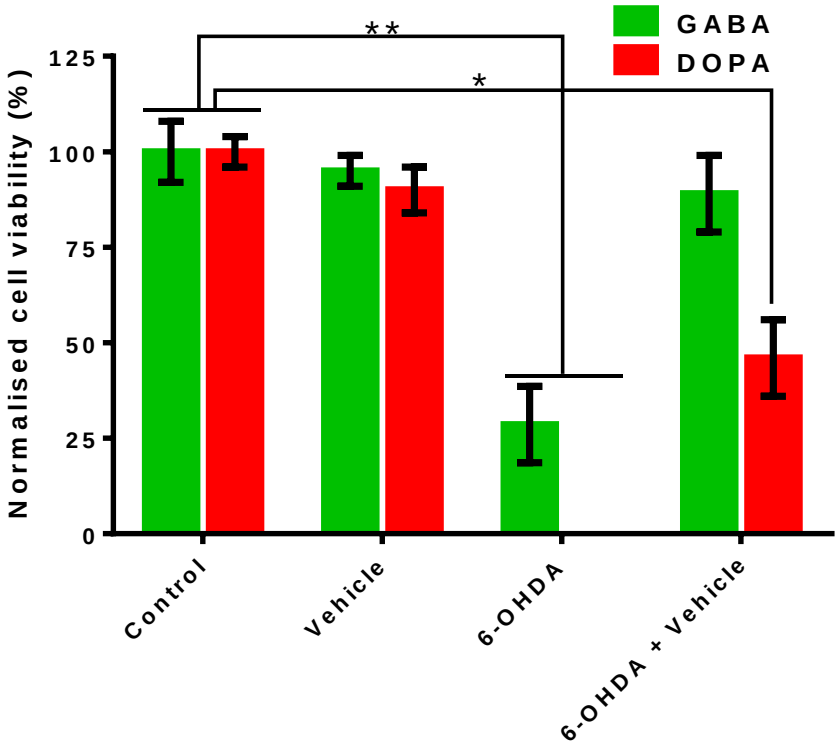

Figure 6.6: Efficacy of 0.15% ascorbic acid as an antioxidant vehicle for 6-OHDA. E14 SNc cells were treated with cell media (control), ascorbic acid (vehicle control), 6-OHDA (to determine the effects without a vehicle) or 6-OHDA dissolved in ascorbic acid vehicle (to determine vehicle efficacy). For 6-OHDA and 6-OHDA+vehicle treatments, cells were exposed to 100 µM 6-OHDA for 20 minutes with and without vehicle respectively as outlined by (Y. M. Ding *et al.* 2004). Two-factor ANOVA (treatment and neuron type) indicated statistical significance, posthoc t-tests indicated by (*): p <0.01, (**): p <0.001, (n=4). GABA: GABAergic neurons, DOPA: dopaminergic neurons.

The presence of the vehicle alone had no significant effect on the viability of GABAergic and DAergic neurons. Exposing the cells to just 6-OHDA without a vehicle resulted in widespread cell death, removing all DAergic neurons but also a significant proportion of GABAergic neurons (27±7 % surviving). A combination of 6-OHDA dissolved within the vehicle resulted in only DAergic neurons being significantly affected, reducing DA neuron numbers to 45±8 % and allowing for selective damage as intended. Based on these results, 0.15% ascorbic acid was used throughout this chapter as a vehicle for 6-OHDA from this point onwards, in order to selectively damage only SNc DA neurons.

6.2.2.2 Dosage concentration

SNc cultures (6 DIV) were then treated with different concentrations of 6-OHDA for the same length of time (20 minutes) in order to determine the optimal concentration for 6-OHDA usage (**Fig.6.7)**.

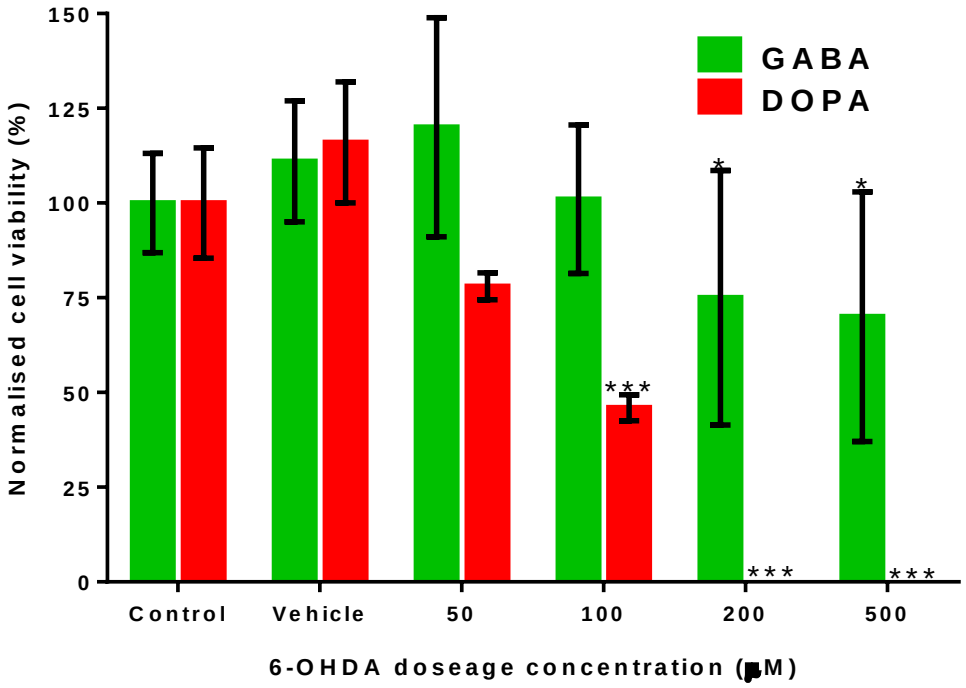

Figure 6.7: 6-OHDA dosage concentration optimisation. E14 SNc cells were treated with cell media (control), ascorbic acid (vehicle control) and 6-OHDA in vehicle (20 minute incubation time) at different concentrations, from 50-500 µM. Two-factor ANOVA (concentration and neuron type) indicated statistical significance, posthoc t-tests used vs control, (*): p<0.01, (***): p <0.0001, (n=4).

The interaction between the different neuron types and the concentration of 6-OHDA had an extremely significant effect on percentage cell viability (ANOVA (5,68) F=11.6, p<0.0001), as did the concentration of 6-OHDA alone (ANOVA (5,68) F=40.8, p<0.0001). Compared to the control, DA neuron levels were significantly reduced by concentrations of 6-OHDA above 50 µM, and GABAergic neurons were also significantly reduced at concentrations of 6-OHDA above 100 µM. This means that 6-OHDA concentrations above 100 µM exhibited a trend of non-specific damage. The concentration that resulted in specific damage to DA neurons while avoiding damage to other cell types was 100 µM, with lower concentrations not damaging DA neurons sufficiently and higher concentrations damaging all cell types. Thus, the optimal concentration of 6-OHDA for specific DA neuron damage in these experiments was 100 µM.

6.2.2.3 Exposure time

As the antioxidant action of ascorbic acid as a vehicle for 6-OHDA was theorised to only be effective for 15-20 minutes in solution before degeneration (Y. M. Ding *et al.* 2004), the exposure time for the two previous 6-OHDA experiments (**Figs.6.6 and 6.7**) was 20 minutes. This exposure time was varied

from 5 to 60 minutes in order to determine the optimum exposure time (while keeping concentration at 100 µM), seen in **Fig.6.8**.

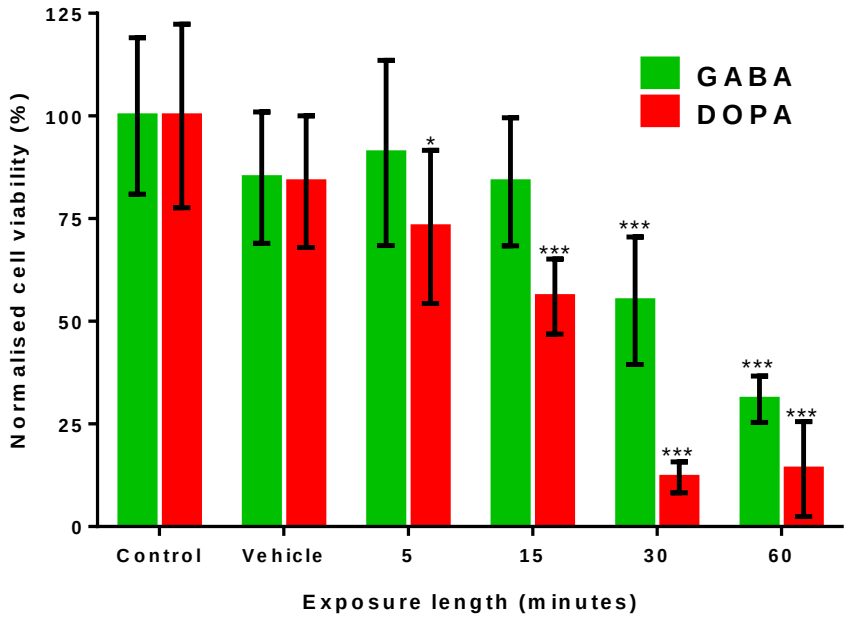

Figure 6.8: 6-OHDA exposure length optimisation. E14 SNc cells were treated with cell media (control), ascorbic acid (vehicle control) and 100 µM 6-OHDA in vehicle with different incubation times, from 5-60 minutes. Two-factor ANOVA (exposure time and neuron type) indicated statistical significance, posthoc t-tests used vs control, (*): p<0.01, (***): p<0.0001, (n=4).

The interaction between neuron types and different 6-OHDA exposure timings showed a significant effect on the percentage cell viability (ANOVA (5,66) F=2.48, p=0.04) and the effect of 6-OHDA exposure timing alone was extremely significant (ANOVA (5,66) F=34.92, p<0.0001). DAergic neuron levels were significantly affected at all 6-OHDA exposure lengths. GABAergic neuron levels were significantly affected at 30-60 minutes exposure, indicating that there was non-specific damage occurring beyond 15-20 minutes exposure. Only 30% of GABAergic neurons survived after 60 minutes of exposure. Despite this loss, only exposure times above 15 minutes resulted in a loss of DA neurons greater than 50%, with 15 minutes exposure only resulting in 33% of DA neurons lost. Due to this, the optimal exposure timing to 6-OHDA required to destroy a sufficient number of DA neurons to mimic PD is likely between 15-30 minutes.

6.2.2.4 Exposure length with 0-70 DIV MEA cultures

The previous three 6-OHDA experiments optimised 6-OHDA usage *in vitro* on 6 DIV cultures, based on experiments performed in the literature. However, later experiments performed on MEAs required cultures to be significantly older than 6 DIV in order to mature and develop spontaneous electrophysiological activity, with any treatment with 6-OHDA before 21 days of culture having no merit, as the effect on the electrical activity would not be seen as there would be little activity to effect. However, when performing 6-OHDA experiments on live cells on MEAs it can be challenging

to directly assess cell viability and cell number. Cells on MEAs could not be fixed or immunostained during the experiment due to a need to record live activity from cells both before and after exposure to 6-OHDA, and cell cultures were too dense for numbers to be determined with brightfield imaging. Due to denser, more functionally mature and networked cultures being exposed to 6-OHDA for up to 48 hours in the literature, both 20 minute and 24 hour exposures were tested to determine if 6 DIV-optimised variables (especially exposure time) would still allow for a similar 6-OHDA action on older MEA cultures, in this case 25 DIV. These experiments can be seen in **Fig.6.9A-D**, which shows representative images, and **Fig.6.9E**, which quantifies these results.

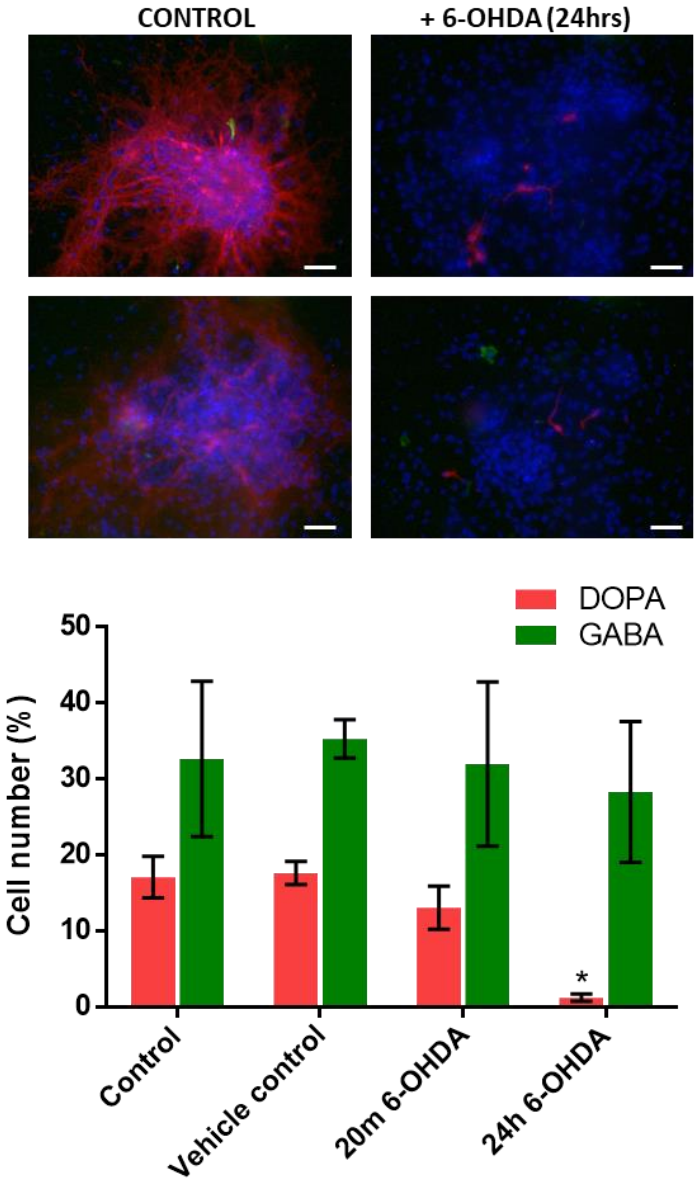

Figure 6.9: Effect of 6-OHDA on more mature cultures, namely after 25 DIV. 100,000 SN cells were cultured on MEAs and imaged after 25 DIV. Cells were either untreated (control) or exposed to 100 µm 6-OHDA for 24 hours (+6-OHDA 24 hrs). Blue: DAPI and Red: TH (DAergic neurons). Images are representative of n=4. Graph shows quantified data from images (GABA and 20 min images not shown). Asterisk indicates post-hoc t-test compared to the control (*): p<0.05

The effect of the different 6-OHDA conditions on DAergic neurons was significant (ANOVA (3,16) F=3.878, p=0.03), while having no significant effect on GABAergic neurons. With 24-hour 6-OHDA exposure determined to be effective whilst avoiding excessive non-specific damage to GABAergic neurons, the experiment was repeated on SNc-STR MEAs. For cells on MEAs any effect of 6-OHDA was determined via any changes in electrophysiological activity recorded via the MEA. As this was an indirect approach to determining the effect of 6-OHDA, death of DAergic neurons was assumed based on the previous experiment (seen in **Fig.6.9**) and not confirmed for each MEA experiment. SNc cultures connected to STR cultures in 5PDs on MEAs were exposed to 100 µM 6-OHDA for 20 minutes or 24 hours at 21 DIV to determine the effect of 6-OHDA on a matured and denser networked culture on MEAs, seen in **Fig.6.10**.

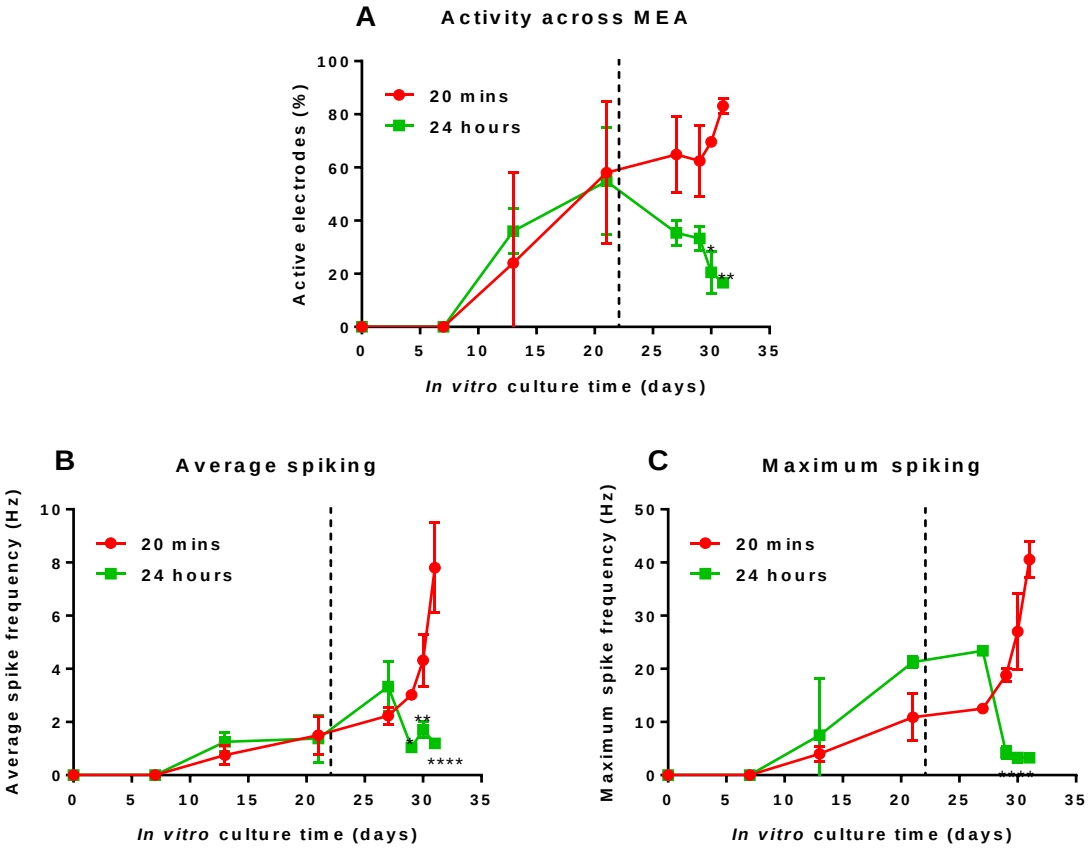

Figure 6.10: SNc cultures treated with 100 µM 6-OHDA for 20 minutes or 24 hours on day 25 in culture. A) Percentage of electrodes recording activity over time, B) average spike frequency over time, C) maximum spike frequency over time. Dotted line at day 21 indicates time of 6-OHDA exposure. Statistical significance was measured in comparison between 24h and 20m conditions, (*): p<0.05, (**): p<0.01, (****): p<0.0001.

The interaction between 6-OHDA incubation length and culture time *in vitro* indicated that there was a significant effect on the percentage activity of SNc neural cultures (ANOVA (7,14) F=4.72, p=0.007), with significantly less activity from 30-31 DIV in cultures that received 6-OHDA exposure for 24 hours on day 25. There was also a significant effect on average SNc neuron spiking over time after treatment (ANOVA (7,14) F=18.24, p<0.0001), with significantly less spiking from 29-31 DIV; and a

significant effect on maximum SNc neuron spiking (ANOVA (7,14) F=23.99, p<0.0001), with significantly less maximum spiking across the same time period (29-31 DIV).

The 24-hour exposure time to 6-OHDA resulted in decreased percentage activity of electrodes (from 60% to 20% activity) and decreased spike frequencies (average from 3 Hz to 1 Hz, max from 20 Hz to 5 Hz), indicating that active neurons within the culture had been damaged sufficiently to not produce spontaneous activity, therefore a good model to mimic PD. From this MEA data alone it is clear that increased exposure times were necessary when working with mature functional MEA cultures rather than the 0-10 DIV cultures that were used for optimisation. From this point on, all 6-OHDA work on functionally mature MEA cultures involved an exposure time of 24 hours.

6.2.2.5 Serum-free assessment

It was important to note that during 6-OHDA exposure serum-free media is used to minimize any interference from serum proteins and allow 6-OHDA access to DA neurons. In order to determine if SNc cell cultures were adversely affected by 24 hours serum-free, 21 DIV SNc cultures on MEAs were placed in serum-free conditions for 24 hours. Activity, average spiking and maximum spiking were measured, as shown in **Fig.6.11**.

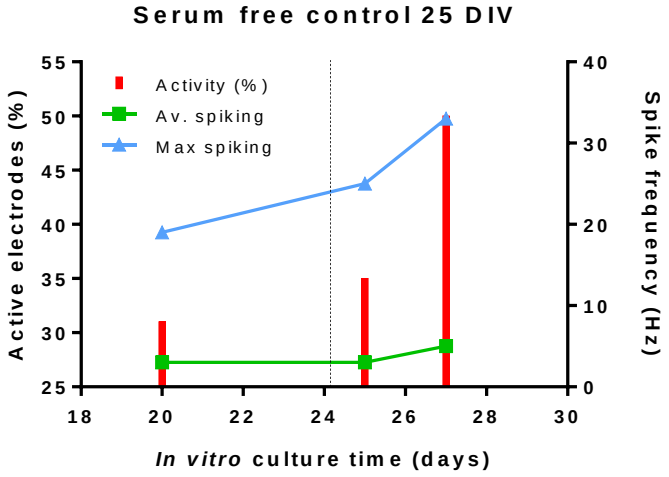

Figure 6.11: 24 hour serum-free assessment. Dotted line indicates 24 hour exposure to serum free culture conditions. Activity (%) columns are drawn against the left y-axis scale, average and maximum spike frequency lines are drawn against the right y-axis scale.

24 hours without serum did not significantly affect the percentage activity or spike frequency of SNc cultures on MEAs, therefore any effect from 6-OHDA incubation is likely to be due to the toxin rather than the serum-free environment.

6.2.3 Activity heatmaps

Heatmaps from 6-OHDA-treated SNc-STR co-cultures were compared to control SNc-STR co-cultures in **Fig.6.12.** After 25 DIV, the SNc port was exposed to 6-OHDA for 24 hours (26 DIV) with the next recording taken 48 hours after exposure (29 DIV). The 6-OHDA-treated heatmaps displayed onset of activity at 11 DIV and increased in activity until 21 DIV, same as the control. After 6-OHDA treatment the number of active electrodes in the SNc port decreased (21-29 DIV), with more inactive electrodes seen by 36 DIV. This low activity in the SNc port did not recover from 36-70 DIV. Channel activity decreased in the same manner, but activity in the STR port was unaffected on 36 DIV and did not decrease until by 50 DIV. This activity of the STR port was similar to control SNc-STR devices, suggesting that cells in the STR port were largely unaffected by 6-OHDA while the SNc port and channels were heavily affected.

Figure 6.12: SNc-STR co-culture activity heatmaps. Each square is an 8 x 8 grid representing an MEA. Horizontal values 4-70 represent *days in vitro* (DIV) and A-C represent separate MEAs from repeat experiments, either control MEAs (from Chapter 5 co-cultures) and 6-OHDA treated MEAs (with 6-OHDA treatment at 25 DIV, indicated by the dashed line). Red->yellow->green formatting indicates min->mean->max levels of spiking activity. Min, mean and max for each repeat as follows: CONTROL: A) 0, 781, 57204. B) 0, 1167, 43403. C) 0, 2747, 257161. 6-OHDA A) 0, 285, 21636. B) 0, 394, 96545. C) 0, 1097, 20561.

6.2.4 Percentage activity across MEA

The percentage of active electrodes per recording was determined from the heatmaps, producing the graphs seen in **Fig.6.13**, comparing each of the sections of the device to control devices.

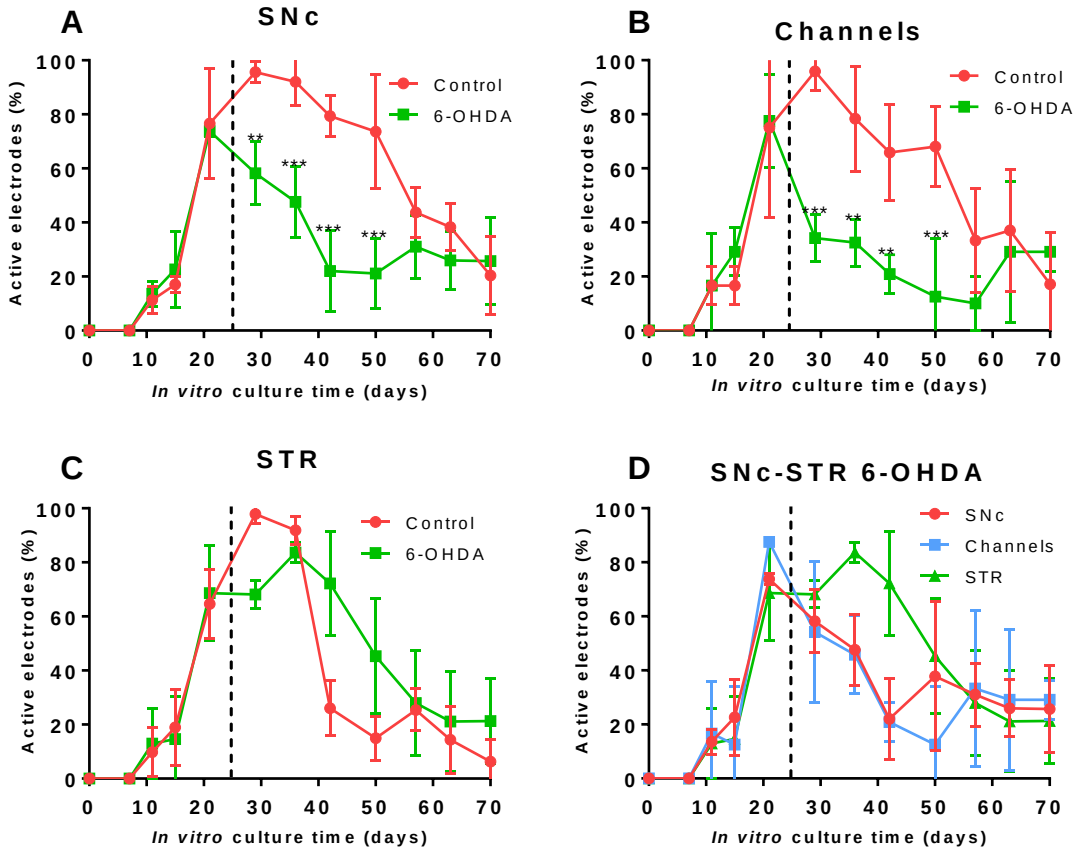

	SNc	Channels	STR
SNc		0.927	0.798
Channels	0.927		0.704

Figure 6.13: Percentage activity of SNc-STR MEAs treated with 6-OHDA on day 25 over time, compared to untreated control devices. A) % activity for SNc port vs control, B) % activity for channels vs control, C) % activity for STR port vs control, D) comparison between 6-OHDA-treated SNc-STR devices with correlation analysis, shown in below table. 6-OHDA treatment time is indicated by the dashed line, 6-OHDA was always applied only to the SNc port. Asterisks indicate post-hoc t-tests comparing each timepoint to the control (*): p<0.05, (**): p<0.01, (***): p<0.001 (n=3).

The use of 6-OHDA had a significant effect on the percentage of active electrodes in the SNc port (**Fig.6.13A**) (ANOVA (1,4) F=16.49, p=0.015) and the channels (**Fig.6.13B**) (ANOVA (1,4) F=24.87, p=0.008) compared to control devices. After 6-OHDA application on 25 DIV, activity was significant lower from 29-50 DIV for both SNc and channels, indicating a loss of activity. After 50 DIV, control activity decreased to similarly low levels. For the STR port (**Fig.6.13C**), there was no significant effect of 6-OHDA treatment, with activity being similar to the control in of onset, peak and decrease. Looking at the correlation within 6-OHDA-treated SNc-STR co-cultures (**Fig.6.13D**), SNc and channel activity was closely correlated, but activity in the STR port did not follow this trend.

6.2.5 Average spike frequency

As with percentage activity, both average and maximum spike frequency were measured across both the SN and STR ports across two time points, seen in **Fig.6.14**.

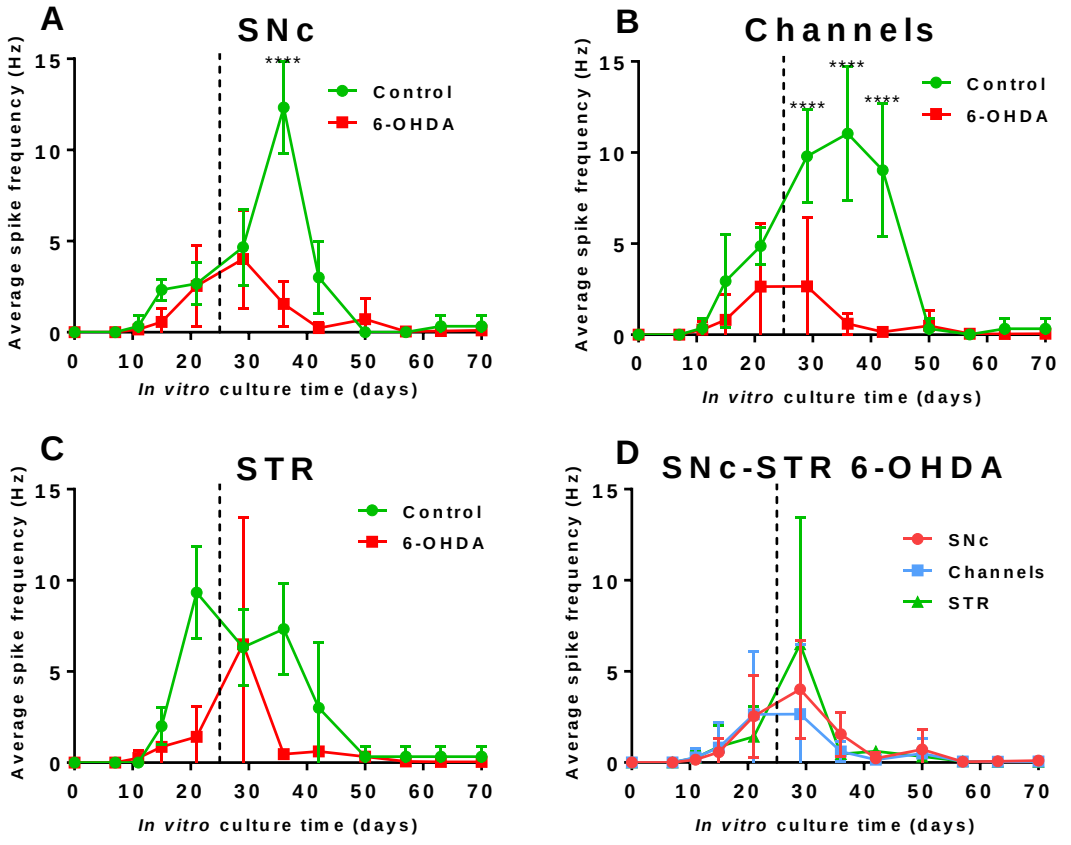

	SNc	Channels	STR
SNc		0.942	0.890
Channels	0.942		0.796

Figure 6.14: Average spiking activity of SNc-STR MEAs treated with 6-OHDA on day 25 over time, compared to untreated control devices. A) Average spike frequency for SNc port vs control, B) Average spike frequency for channels vs control, C) Average spike frequency for STR port vs control, D) comparison between 6-OHDA-treated SNc-STR devices with correlation analysis, shown in below table. 6-OHDA treatment time is indicated by the dashed line, 6-OHDA was always applied only to the SNc port. Asterisks indicate post-hoc t-tests comparing each timepoint to the control (****): p<0.0001 (n=3).

6-OHDA treatment significantly reduced the average spiking frequency in the SNc (**Fig.6.14A**) (ANOVA (1,4) F=11.3, p=0.02) and channels (**Fig.6.14B**) (ANOVA (1,4) F=19.62, p=0.01) sections of SNc-STR devices. Control SNc average spiking peaked at 12.3 ±2 Hz, whereas the peak of activity for 6-OHDA treated devices was only 4 ±3 Hz. However, there was no significant effect of 6-OHDA on STR average spike frequency from the STR port (**Fig.6.14C**). When looking at the SNc-STR device as a whole, there was a peak in all areas on 29 DIV after 6-OHDA treatment, and correlation was highest between SNc port and channels (**Fig.6.14D**).

6.2.6 Maximum spike frequency

In order to determine high levels of activity beyond the average, the maximum spike frequency obtained per day was also analysed, seen in **Fig.6.15**.

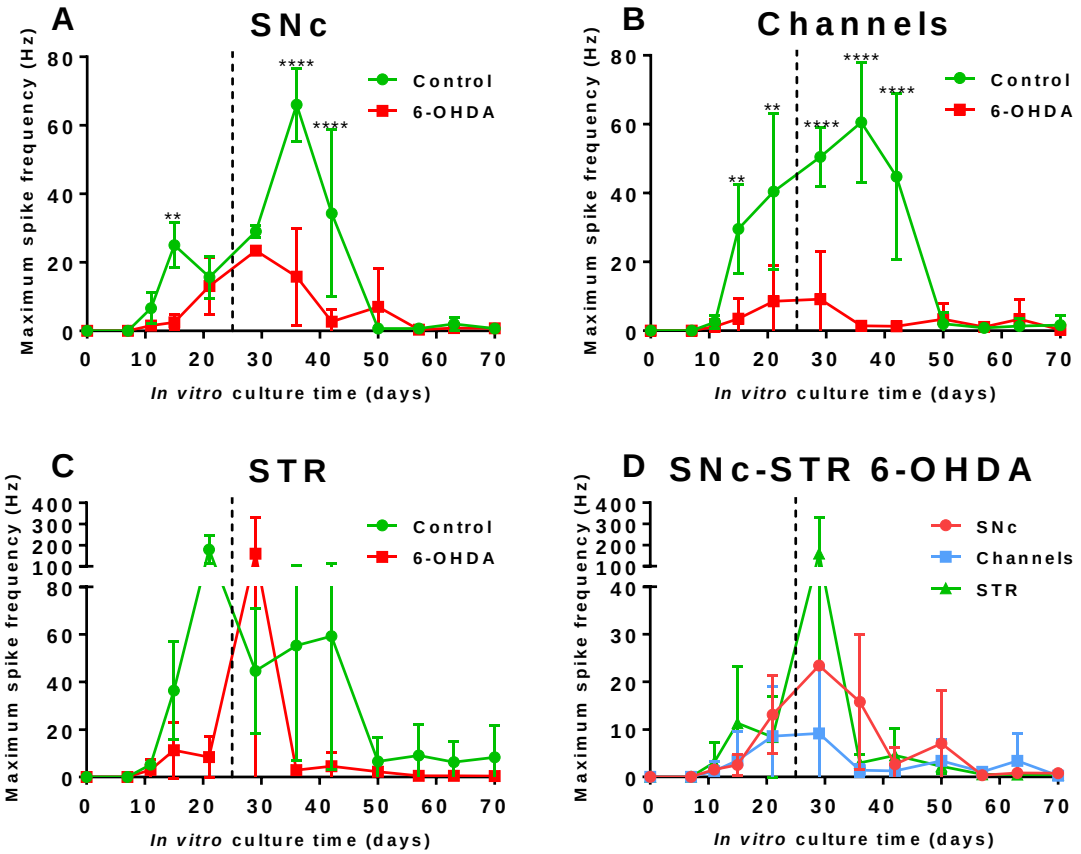

	SNc	Channels	STR
SNc		0.766	0.746
Channels	0.766		0.683

Figure 6.15 Maximum spiking activity of SNc-STR MEAs treated with 6-OHDA on day 25 over time, compared to untreated control devices. A) Max spike frequency for SNc port vs control, B) Max spike frequency for channels vs control, C) Max spike frequency for STR port vs control, D) comparison between 6-OHDA-treated SNc-STR devices with correlation analysis, shown in below table. 6-OHDA treatment time is indicated by the dashed line, 6-OHDA was always applied only to the SNc port. Asterisks indicate post-hoc t-tests comparing each timepoint to the control (****): p<0.0001 (n=3).

6-OHDA had a significant effect on maximum spike frequency in the SNc port (**Fig.6.15A**) (ANOVA (1,4) F=79.8, p=0.001) and channels (**Fig.6.15B**) (ANOVA (1,4) F=21.7, p=0.009). While the SNc port of control devices peaked at 66 ±12 Hz, 6-OHDA treated condition peaked at 23.4 ±5 Hz. Despite this significant effect on SNc and channels, STR ports were unaffected, both peaking at similarly extremely high levels (179 ±33 vs 160 ± 103 Hz for control vs 6-OHDA).

6.2.7 Bursting activity

Defining bursting activity as any portion of activity that exceeded a bundle of 10 spikes per second (10 Hz), both the number of bursts and number of spikes per burst were assessed for the SNc-STR MEAs treated with 6-OHDA on day 25, seen in **Fig.6.16**.

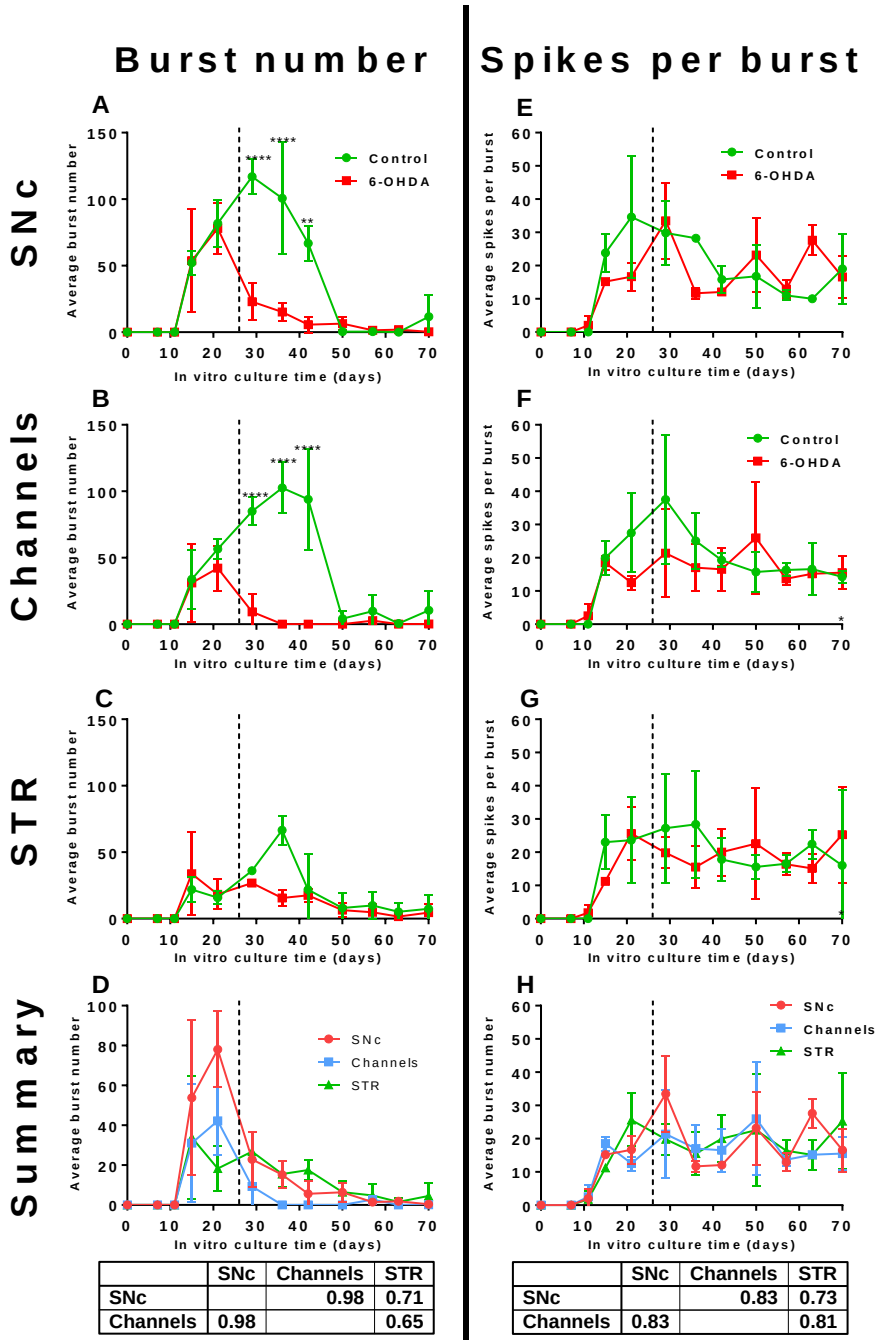

	SNc	Channels	STR
SNc		0.98	0.71
Channels	0.98		0.65

	SNc	Channels	STR
SNc		0.83	0.73
Channels	0.83		0.81

Figure 6.16: Bursting activity activity of SNc-STR MEAs treated with 6-OHDA on day 25 over time, compared to untreated control devices. A-D indicate the average burst number over time, while E-H indicate the average number of spikes per burst over time. A+E) SNc port vs control, B+F) channels vs control, C+G) STR port vs control, D+H) comparison between 6-OHDA-treated SNc-STR devices with correlation analysis, shown in below table. 6-OHDA treatment time is indicated by the dashed line, 6-OHDA was always applied only to the SNc port. Asterisks indicate post-hoc t-tests comparing each timepoint to the control, (**): p<0.01 (****): p<0.0001 (n=3).

6-OHDA had a significant effect on the average number of bursts for the SNc port (**Fig.6.16A**) (ANOVA (1,4) F=40.65, p=0.02)and the channels section (**Fig.6.16B**) (ANOVA (1,4) F=23, p=0.04), effectively reducing bursting to negligible levels after 6-OHDA treatment on 25 DIV. This trend was even seen in the STR port (**Fig.6.16C**), but was not significantly different to control devices. As seen in the correlation analysis (**Fig.6.16D**), the SNc port and channels were highly correlated, unlike channels and STR port (0.98 vs 0.65 respectively).

6-OHDA did not have any significant effect on the number of spiokes per burst, bursts appeared to contain between 10-30 spikes throughout the experiment after onset, regardless of treatment. Because the number of spikes per burst from SNc did not change significantly, the decrease seen in spike frequency appeared to be due to the decrease in the number of bursts fired from SNc cells. The corresponding lack of change in STR spike frequency was also likely due to the lack of change in bursting activity upon 6-OHDA treatment to the adjacent SNc port.

6.2.8 Centroid number

The number of centroids over time was recorded for the SNc, channels and STR ports of SNc-STR devices, both for an untreated control and a 6-OHDA-treated device, as seen in **Fig.6.17**.

Compared to the control, 6-OHDA treatment resulted in a significant change in the number of centroids produced by the cells in the SNc port from 29-50 DIV and channels from 29 DIV, with no change in the STR port. 6-OHDA treatment to the SNc port appeared to perturb the number of centroids produced by SNc neurons, and this number remained significnatly different until 70 DIV, whereas a similar effect in the channels was recovered by 50 DIV. The unchanged STR neuron activity in response to 6-OHDA is consistent with previous findings.

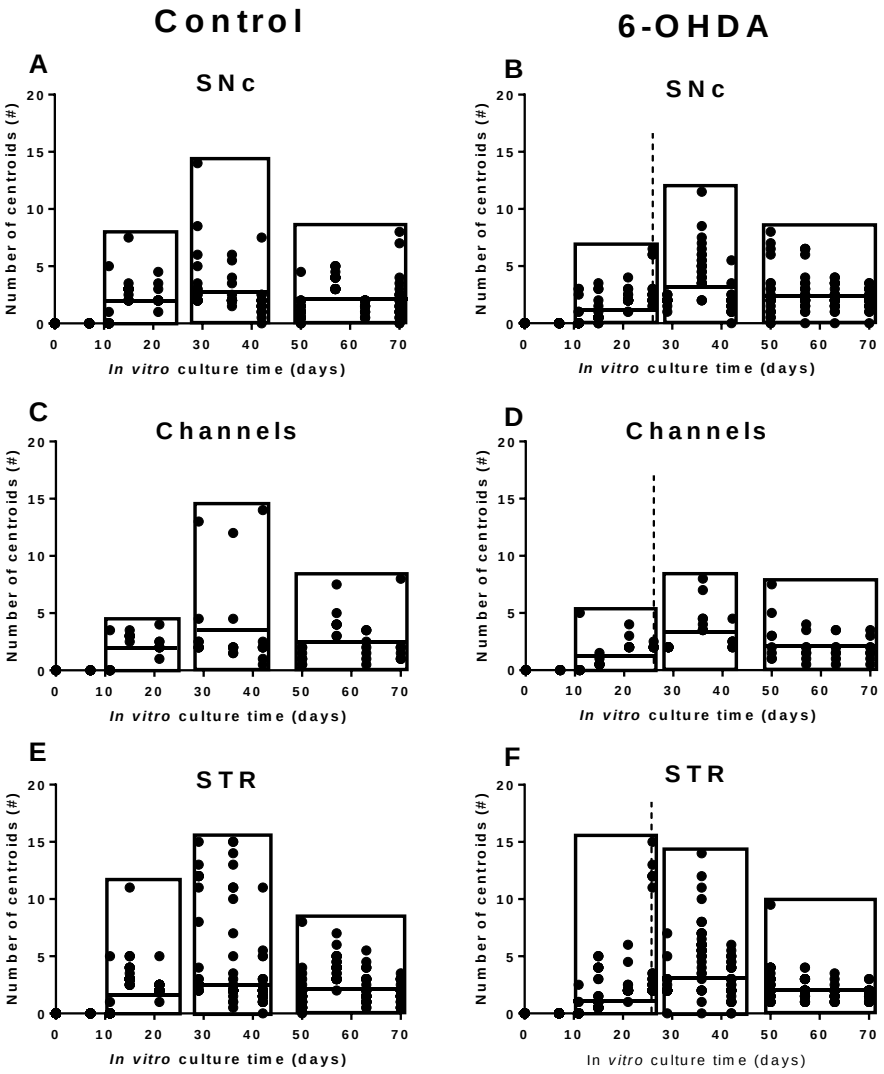

Figure 6.17: Number of centroids for SNc-STR centroids, both 6-OHDA-treated (B,D,F) and control (A,C,E). A+B) Number of centroids from SNc port, C+D) number of centroids from channels, E+F) number of centroids from STR port. Rectangles indicate early (15-25), mid (28-42) and late (50-70) stages, horizontal lines within rectangles indicate the mean of each stage (summaried in Table 6.1), dashed vertical lines indicate day 25, when 6-OHDA was applied to SNc port.

Table 6.1: Average centroid number comparison between control and 6-OHDA-treated SNc-STR MEA devices. Significant differences between control and treated were calculated with ANOVA.

SNc	Treatment			
DIV	Control	6-OHDA	p-value	Significance
21	2.2	2.1	0.65	ns
29	3.8	2	<0.0001	****
50	1.2	2.9	0.0022	**
70	2.4	2.2	0.78	ns

CH	Treatment			
DIV	Control	6-OHDA	p-value	Significance
21	2.3	2.4	0.64	ns
29	4.4	2	0.014	*
50	1.2	3	0.15	ns
70	2.3	1.9	0.67	ns

STR	Treatment			
DIV	Control	6-OHDA	p-value	Significance
21	2.2	2.14	0.68	ns
29	2.6	2.4	0.131	ns
50	2.41	2.3	0.144	ns
70	1.5	1.8	0.193	ns

6.2.9 Centroid shape categorisation

Centroids were sorted into six categories (positive/negative monophasic, positive-first/negative-first biphasic and positive-first/negative-first triphasic) depending on their number of phases and sign (see **Fig.4.25** for more information). Centroid proportions for the SNc port, channels and STR port for control SNc-STR and 6-OHDA-treated SNc-STR devices are displayed in **Fig.6.18**.

For the SNc port, 6-OHDA decreased the number of centroids from 630 (from control SNc) to 214, with 81% of these being monophasic and the remainder being bi- or tri-phasic (compared to 46% monophasic for the control). A similar effect was seen in the channels, where the total number of centroids was reduced by 6-OHDA treatment (442 vs 74) and the proportion of monophasic centroids was greater (35% vs 65%). As channels should mostly contain axons and produce a majority of triphasic signals, this reduction is indicative of axonal death or loss of signals along axons. STR also saw a loss of centroids (563 vs 336) and more monophasic centroids (45% vs 64%) but this effect was less than the effects seen in SNc or channels, for example the number of SNc, channel and STR centroids compared to control were 34%, 16% and 60%, indicating a greater loss in SNc/channels.

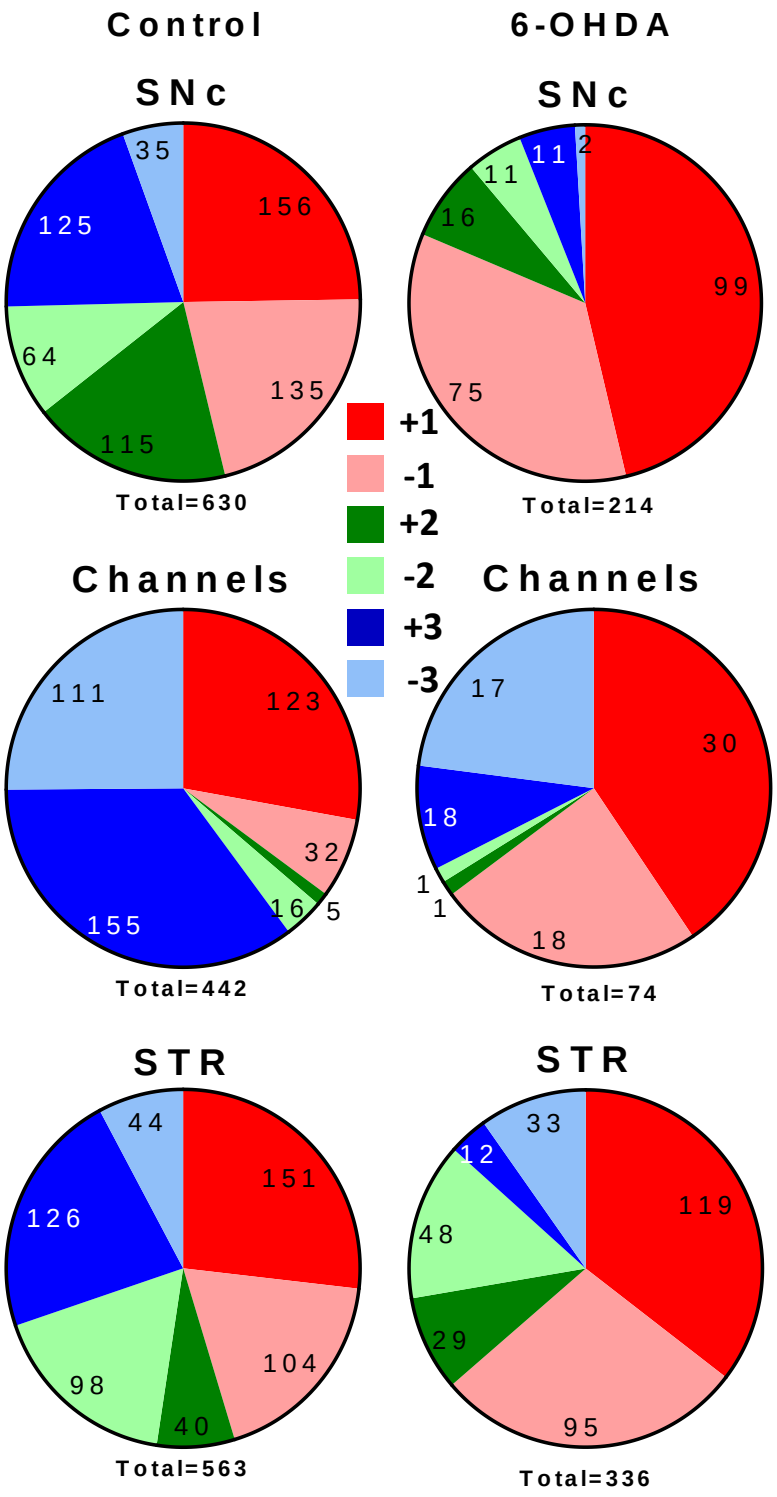

Figure 6.18: Centroid shape categorisation. All centroids from 70 days of recording were sorted into six types, number on chart segments indicating the number of centroids in each category (total centroid number below chart), (n=4).

6.2.9.2 Centroid full duration at half maximum

The centroid full duration at half maximum (FDHM) was analysed for SNc-STR co-cultures to determine the effect of 6-OHDA treatment on the 'width' of centroid spikes, data in **Fig.6.19**.

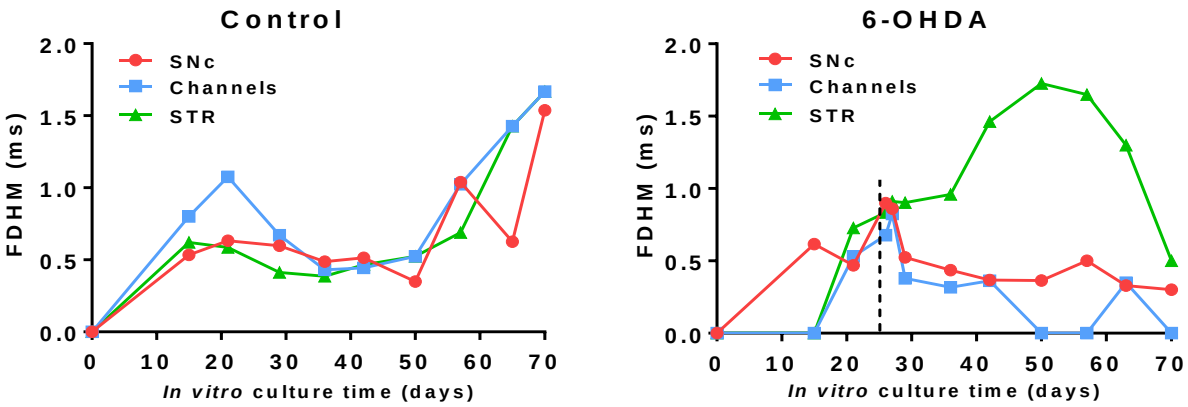

Figure 6.19: Centroid full duration at half maximum (FDHM) over time, for each area of control and 6-OHDA-treated SNc-STR co-cultures (day of treatment indicated by dashed line).

The FDHM for control SNc-STR devices showed a trend of increasing over time, and this trend was perturbed by 6-OHDA treatment. In 6-OHDA devices the FDHM decreased and plateaued at approximately 0.5 ms for SNc ports and channels, but increased for STR neurons from 25-50 DIV until decreasing from 50-70 DIV. The reason for this effect is unclear, but 6-OHDA treatment appeared to shorten SNc and channel centroids while lengthening STR centroids.

6.2.10 Late 6-OHDA exposure

Further experiments were performed to determine the effects of 6-OHDA at a much later time point, in this case after 65 days of culture (results on **Fig.6.20**). This experiment treated cultures with 6-OHDA after 65 DIV to determine if more mature cultures resisted the effect of 6-OHDA compared to 25 DIV cultures.

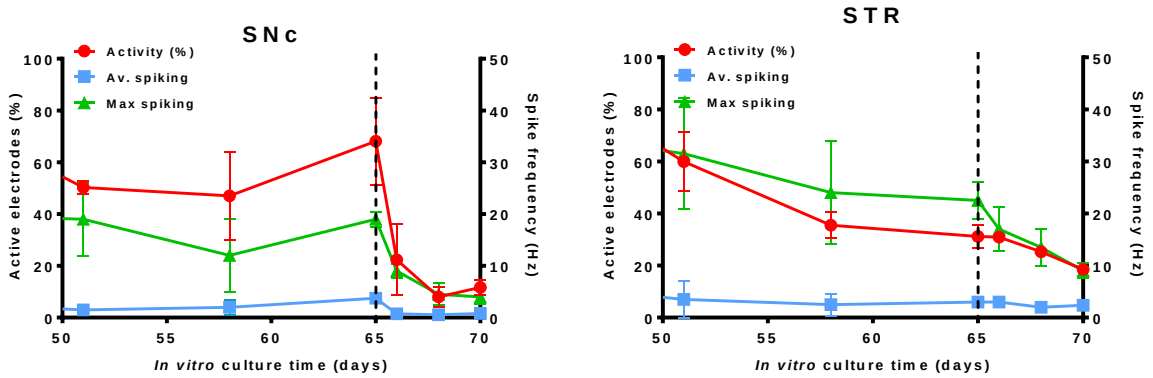

Figure 6.20: Effect of 6-OHDA treatment on day 65. Each graph shows the percentage activity (plotted on left y-axis) and the average and maximum spike frequencies (plotted on right y-axis) over time, with the dotted line indicating the 6-OHDA treatment. The left and right graphs show the effects in the SNc and STR ports respectively. Images not shown.

6-OHDA appeared to have as much of an effect on SNc cultures after 65 DIV as after 25 DIV, with SNc activity decreasing sharply while STR activity was unaffected.

6.3 Discussion

By attempting to selectively remove the DA neurons of the SNc port in a SNc-STR co-culture device, a limited acute model of Parkinson's disease (PD) could be created. The main limitation was that this model only featured the nigrostriatal pathway, and as a consequence any downstream effects to the GPe, STN and GPi/SNr could not be observed. In addition, due to the use of 6-OHDA this was an acute model of PD, destroying/damaging SNc cells within a few hours as opposed to over the course of many years as seen in PD *in vivo*. Most devices were assumed to feature DAergic cell death based on the optimisation (**Fig.6.9**), in the future experiments should be run in tandem so that the DAergic neurons can be characterised at each time point. Nonetheless, this SNc-STR co-culture in a five-port device (5PD) on a MEA and treated with 6-OHDA proved an effective model in highlighting the changes in functionality to the STR and SNc after 6-OHDA treatment.

6.3.1 6-OHDA optimisation

While 6-OHDA has been used in many animal models by direct injection into the SNc or STR, 6-OHDA use *in vitro* is less explored and required numerous steps of optimisation for use in this model and other *in vitro* studies (Y. M. Ding *et al.* 2004).

The first issue was with the tendency of 6-OHDA to rapidly oxidise when made into a solution (even as a powder 6-OHDA is sensitive to light and has a short storage life), producing peroxides, oxygen radicals and other reactive oxygen species (ROS). While these products would certainly be sufficient to damage the DA neurons of our *in vitro* cultures, these products would be in the media and would therefore damage every cell type in the culture, including GABAergic SNc and STR interneurons, STR

MSNs of both types and glial cells. Therefore, to ensure specificity of the toxin, it was necessary to delay 6-OHDA oxidation until the dopamine transporters (DATs) of DA neurons have taken up 6-OHDA and oxidation could occur within these neurons, resulting in specific DAergic neuronal damage (**Fig.6.6**). Ding *et al.* indicated that antioxidants such as ascorbic acid/ascorbate could delay this oxidation for up to 20 minutes, (Y. M. Ding *et al.* 2004). They show that when dissolved in standard media 6-OHDA breaks down almost completely within 5 minutes, but with 0.15% ascorbic acid 82% of 6-OHDA remained after 20 minutes. Our own optimisation process came to a similar conclusion, with exposure to 100 µM of 6-OHDA (within a 0.15% ascorbic acid vehicle) for 15-30 minutes being the optimal conditions to selectively eliminate the DA neurons in a 6 DIV SNc culture (**Figs.6.7 and 6.8**). This resulted in a selective effect of 6-OHDA where GABAergic neuron levels were not significantly changed while DA neuron levels decreased significantly to 25-50% of the control.

This optimisation process was necessary as the literature has opposing pieces of evidence concerning the optimum exposure time and concentration that 6-OHDA should be used when working *in vitro*. Where one study observed total loss of cells after a 6-hour exposure to 100 µM 6-OHDA (H. G. Kim *et al.* 2010), another observed only a 40% loss under the same conditions (D. Chen *et al.* 2015). One study observed no effect of 6-OHDA at 10 µM and significant effects at 40 µM (24-hour exposure time on 6 DIV culture) (Rodriguez-Pallares *et al.* 2007) whereas other studies observed a significant loss of DA neurons after 24 hour exposure to 10 µM 6-OHDA (D. Chen *et al.* 2015) or 200 µM 6-OHDA for a similar exposure time (Chan *et al.* 2009).

In vitro 6-OHDA work is limited in that the treated *in vitro* cultures are typically only a week old, ranging from 2-7 DIV. Ding *et al.* summarises 14 studies of 6-OHDA application and subsequent cytotoxicity *in vitro*, and including the authors work themselves, no study advanced beyond 21 DIV before 6-OHDA treatment with the vast majority applying 6-OHDA between 2-7 DIV (Y. M. Ding *et al.* 2004). While this is ideal to demonstrate the power of 6-OHDA's selectivity *in vitro*, our functional *in vitro* model of the BG operated over a longer timeframe, up to ten weeks. 6-OHDA could be used on the SNc port of the SNc-STR model at an early stage (before 21 DIV), but as functional activity had not matured until after 21 DIV, it would be uncertain what electrophysiological effect the 6-OHDA was having and if the model could be labelled as '*functional*' after treatment. In order to use 6-OHDA to destroy the nigrostriatal connections and determine the electrophysiological effects, it was necessary to use 6-OHDA *in vitro* on cultures beyond 21 DIV.

Using the previously optimised variables, SNc cells were exposed to 100 µM 6-OHDA in a 0.15% ascorbic acid vehicle for 20 minutes, but there was no significant decrease in the levels of DAergic neurons (**Fig.6.9**). This may have been due to insufficient 6-OHDA levels in solution, but as there was little effect over several repeats it was necessary to re-optimise. A 20 minute exposure time may have been ineffective due to a far higher number and density of cells after 25 days of culture, with

intricately networked neurons and unexposed DATs, or a larger protective '*buffer zone*' of astrocytes and other glia between 6-OHDA and the relevant DA neurons. This presence of glial cells in our model makes it a better mimic of the *in vivo* brain, as opposed to the majority of neuron-only work done *in vitro*. Glial cells play an important protective role *in vivo*, with astrocytes shown to have specific reactions to neurotoxins like 6-OHDA, such as 'activation' (determined by upregulation of astrocytic marker GFAP) upon 6-OHDA-induced neurodegeneration *in vivo* (Henning *et al.* 2008), and with astrocyte dysfunction *in vivo* accelerating DAergic degeneration upon 6-OHDA exposure (Kuter *et al.* 2018). As such, tracking the intensity of GFAP expression over 6-OHDA treatment in our model would be a useful experiment to run in the future, keeping in mind the complex astrocyte-microglia-neuron relationship at play *in vivo* and in our model. *In vitro*, 6-OHDA has been shown to significantly reduce the viability of rat primary astrocytes (the same type used in this work), as well as astrocytoma cell lines C6 (rat) and U251 (human) (Raicevic, Mladenovic, Perovic, Harhaji *et al.* 2005, Raicevic, Mladenovic, Perovic, Miljkovic *et al.* 2005, Rodriguez-Pallares *et al.* 2007). Primary astrocytes underwent cell death via apoptosis due to 6-OHDA-induced oxidative stress, in turn because of 6-OHDA autooxidation products hydrogen peroxide (H_2O_2), superoxide anion (O_2^{*-}) and hydroxyl radical (OH^*) (Saito *et al.* 2007). However, in our model the use of an antioxidant vehicle results in less autooxidation products free in the cell media, potentially protecting astrocytes from non-specific action of 6-OHDA (Ding *et al.* 2004). Whilst astrocytes are negatively affected by 6-OHDA, they exert a protective effect on DAergic neurons via the secretion of protective biochemical factors. Seeding primary astrocytes with primary midbrain neurons *in vitro* resulted in increased cell survival upon 6-OHDA exposure (Datta *et al.* 2018), something that should also be occurring in our model. Interestingly, while astrocytes from fore, mid and hindbrain regions all exerted an overall protective effect on midbrain neurons, when repeated with SNc DAergic (TH^+) neurons, astrocytes from the midbrain exerted a significantly greater protective effect due to increased BDNF secretion in response to 6-OHDA exposure. As our SNc port contains both neurons and glia from the midbrain region, it is reasonable to assume that the astrocytes are exerting a similar protective effect. Astrocytes have also been shown to secrete GDNF in the presence of 6-OHDA, with GDNF having a similar neuroprotective effect (Sandhu *et al.* 2009).

Despite the effects of the increased number of glial cells in the more mature cultures, 6-OHDA was not having a significant effect (**Fig.6.9**) and variables had to be changed. As vehicle concentration was matched to the 6-OHDA concentration, the only variable that could be changed easily was the exposure time. Some *in vitro* studies in the literature had up to 48 hours of exposure time (Ding *et al.* 2004), but as this project was limited by time contraints there was no time to attempt to optimise several longer 6-OHDA exposure times 20 minutes and 48 hours. As such, 24 hours was used as a compromise. As this exposure time significantly exceeded 20 minutes, the vehicle may have been ineffective and 6-OHDA may have oxidised in solution and caused widespread damage. However, as

seen in **Fig.6.9**, increasing the exposure time significantly reduced the levels of DAergic neurons, while not significantly affecting the levels of GABAergic neurons. This new exposure time of 24 hours was used throughout the rest of the experimentation, due to its specificity and effect on SNc DAergic neurons. In addition, despite 6-OHDA incubation for 24 hours in the SNc port of SNc-STR co-cultures, spiking activity of the STR port was unaffected. There are a number of potential explanations for this: 1) 6-OHDA may have been entirely taken up by DATs in the initial stages of exposure in the SNc port, meaning that no 6-OHDA ever travelled down channels into the STR port; 2) 6-OHDA may have fully oxidised within the SNc port and the free ROS did not travel down the channels into the STR port due to insufficient capillary action and/or SNc axons plugging the channels; 3) 6-OHDA may have spread to all ports within 24 hours but not at concentrations sufficient to cause damage STR neurons after travelling through the channels. This 24 hour exposure time also significantly affected 65 DIV cultures (see **Fig.6.20**), one that must be far more networked and robust than an early-stage co-culture.

6.3.2 Effects of 6-OHDA on functionality

6-OHDA treatment (on day 25, 24 hour exposure) had numerous effects on the electrophysiological activity of SNc-STR co-culture devices as recorded by MEAs, compared to control SNc-STR devices that were untreated (but still left serum-free for 24 hours).

6.3.2.1 Localisation

As seen from heatmaps (**Fig.6.12**) and percentage activity graphs (**Fig.6.13**), changes were seen in SNc and channel activity by 29-35 DIV, with significantly less active electrodes in the SNc port and channels. This loss of activity may have been due to the loss of DA neurons in the SNc port. As seen in **Fig.6.13**, channel activity was closely correlated to SNc activity compared to STR activity (0.93 vs 0.70) suggesting that these unidirectional channels mostly contained DA projection neurons from the SNc rather than GABAergic projection MSNs from the STR, and damage to the cell bodies in the SNc port may have resulted in the extended axons '*dying back*' and retracting from the channels. All areas had a general decline in activity from peak (30-40 DIV) to 70 DIV, as seen in previous SNc-STR co-culture work (**Chapter Five, section 5.2.3.1 Heatmaps, Fig.5.6**). The decrease in activity from mid to late stages normally seen in SNc-STR cultures was accelerated by 6-OHDA from 29-50 DIV, with control activity levels naturally falling to similar levels from 60-70 DIV.

6.3.2.2 Spiking/bursting

6-OHDA treatment resulted in a significant decrease in both average and maximum spike frequencies from the SNc port, with average spiking not exceeding 1 Hz after treatment despite firing at over 5 Hz beforehand. The STR port was unaffected, with activity even increasing after 25 DIV. This decrease in SNc and channel activity is most likely due to the death of DAergic neurons in the SNc port, suggesting that a large portion of spiking activity from the SNc port is due to either DA neurons

activity or DA release influencing spiking frequency. It is more challenging to determine the effect of 6-OHDA on SNc spiking activity when treating the SNc port after 65 DIV, as by this late stage spiking has already naturally decayed (Marom and Shahaf. 2002, Turrigiano and Nelson. 2004, Chiappalone *et al.* 2006). Despite this, there is still a decrease in average and maximum spiking after 6-OHDA treatment at 65 DIV.

These average and maximum spiking frequencies were a sum of all spiking, such as spontaneous random spikes, oscillations, or regular bursts. While challenging to assess single random spikes, burst data can be extracted and processed (assuming that each bundle of spikes where more than ten spikes occur within a second (≥10 Hz) is a burst) so that the effect of 6-OHDA on bursting can indicate if the decreases in spike frequency are due to decreases in burst number. After 6-OHDA treatment the average number of bursts fell while the number of spikes per burst remained constant, resulting in a reduction of the overall average and the maximum spike frequency.

6.3.2.3 Centroid assessment

In both separate and connected cell populations, centroids and variability in spiking decreased over time from early/mid to late (seen in **Fig.4.19, Fig.5.9** and **Fig.6.17A**). This trend was mostly conserved in centroids from 6-OHDA-treated SNc cultures (**Fig.6.17B**), but there were significant differences in the centroid number on day 29 (48 hours after 6-OHDA treatment) for the SNc port and channels when compared to control. This indicates that while the centroid number was initially perturbed by 6-OHDA treatment in the short term, the centroid number was decreasing over time naturally for the control (as seen in low frequencies from 50-70 DIV), resulting in low centroid numbers regardless of 6-OHDA treatment in the late stage. The impact of 6-OHDA treatment was seen most clearly immediately after treatment, similarly to the effect of 6-OHDA on spiking and bursting, where levels dropped to similar activity seen on 50-70 DIV in the control. STR centroid numbers were unaffected by 6-OHDA treatment. The most significant effects on centroid number can be seen in **Table 6.1**, which outlines that 6-OHDA had a significant effect on the mean number of centroids from the SNc port on 29 DIV ($p<0.0001$) until 50 DIV ($p=0.002$), indicating that there was a long-lasting effect on the average number of centroids.

The proportion of mono/bi/triphasic centroids also changed after 6-OHDA treatment (**Fig.6.18**). While the SNc port from control SNc-STR devices produced a variety of centroid types, after 6-OHDA treatment the vast majority of centroids were positive/negative monophasic centroids (46.2% vs 81.2%), and the number of centroids overall decreased (630 vs 214). This is the same for channels, where centroids change from 60.2% triphasic (the typical signal received from axons) to only 32.4% triphasic, indicating that there may be less SNc DAergic neuron axons within the channels. While the proportions of centroids for the STR port is similar to the SNc port for the SNc-STR control device (also observed in **Chapter Five 5.4.5 Centroid Assessment**), changes in SNc port centroid proportions

after 6-OHDA treatment may have influenced STR activity (as there were more monophasic centroids, (45.2% vs 63.6%) similarly to SNc) or may have no influence (as STR has more biphasic and triphasic centroids than SNc (33% vs 25%). 6-OHDA also had an effect on centroid FDHM (**Fig.6.19**), with 6-OHDA treatment reducing the FDHM of centroids from the SNc port and channels (shorter centroids), while increasing the FDHM of centroids from the STR port (longer centroids). It is unknown why this occurred, and further experimentation is required.

6.3.2.4 Summary

6-OHDA had a significant effect on spiking and bursting immediately after exposure, but these aspects of electrophysiological activity were lowered to levels that the cultures naturally decreased to over the long term (by 50 DIV) without any treatment.

As this model only featured SNc and STR it represents an incomplete model of PD, there are many inputs and outputs missing (e.g. CTX input to STR) which can heavily influence firing of SNc and STR in the absence of DA or nigrostriatal DA neurons. This focused nigrostriatal model needs further development in order to see the effects of DA loss across all five ports of the 5PD. However, 6-OHDA had further long-term effects on SNc-STR devices that were not seen in control devices, such as the centroid number, shape and phase. This indicates that as well as decreasing the number of spikes and bursts, the type of spike and burst produced by SNc-STR co-cultures also changed, both in shape and number of phases, most likely due to destruction of the maturing functional network of neurons. It is uncertain if these unexpected changes mimic changes to the *in vivo* BG, and this data is an interesting effect of 6-OHDA that should be further explored.

6.4 Conclusion

By making use of the 6-OHDA neurotoxin, the SNc-STR nigrostriatal co-culture device could attempt to mimic PD. By treating our SNc-STR devices with 6-OHDA, destroying the DA neurons, and tracking the changes in the electrophysiological activity over ten weeks in culture, we have generated a long-term acute *in vitro* model of PD, potentially for use as a platform of study towards PD. This marks the first step of this device towards a pre-clinical model of PD, with further work the model will be able to accelerate PD research.

Chapter 7: General discussion and conclusions

7.0 General discussion

The aim of this thesis was to use *in vitro* modelling to create an experimental platform to accelerate pre-clinical study of neurodegenerative disease, particularly Parkinson's disease (PD). We developed a five-port device (5PD) capable of isolating and connecting different neural cell populations via micro-channels, all of which could be recorded from via integrated electrodes in the form of an MEA. This enabled not only a morphological assessment of network connectivity, but importantly interrogation of the living neural network functionality (and dysfunction).

The work covered in this thesis involved the design of the 5PD (**Chapter Three**), functional assessment of separate cell populations (**Chapter Four)** to serve as a comparative baseline for the next chapters, functional assessment of connected co-cultures within 5PDs (**Chapter Five**) and functional assessment of a specific chemically-treated connected co-culture designed to mimic the loss of nigrostriatal neurons in PD (**Chapter Six**).

7.0.1 Chapter Three: Device design and optimisation

This chapter presented the re-design and optimisation of a 5PD following on from previous work (Kamudzandu. 2015) in order to more accurately and efficiently mimic basal ganglia (BG) circuitry. While such compartmentalised microfluidic devices have been in use for more than ten years (Taylor *et al.* 2003, Taylor *et al.* 2005, J. W. Park *et al.* 2006), featuring numerous ports (Y. H. Kim *et al.* 2011) and tapered microchannels (Peyrin *et al.* 2011), to my knowledge this is the first example of a five-port device where the side ports connect to a centre port via tapered microchannels. These novel devices can also house from 1-5 separate sets of cells and have an integrated MEA for continuous functionality analysis. These devices required optimising from both an engineering and biological perspective before they would be suitable to act as mimics of BG circuitry.

7.0.1.1 Engineering the five-port device

The compartmentalised microfluidic device represents an alternative to the collection of randomly connected neurons and glia found in standard dissociated neural cultures, by providing a 3D substrate that physically confines neural cells to pre-designed locations. In the case of tapered microchannels, the device also connects cell populations in a controlled manner while confining them, but there are better options for internal channel structure for unidirectional neurite growth, as discussed later. By culturing cells in a device there is far more control of connectivity as opposed to a standard dissociated culture, and it is this control that will allow for better pre-clinical research as more effective and efficient experiments can be designed.

This method of physically trapping neural cultures in a 3D substrate cage is not new, and the vast majority of modern neural devices (Hasan and Berdichevsky. 2016) are fabricated in the same way as the proto-device developed by Taylor and colleagues in 2003: by soft lithography, resulting in a polydimethylsiloxane (PDMS) stamp/shape that can contain cell/tissue cultures (J. Park, Koito, Li and Han. 2009b, Brewer *et al.* 2013, Habibey *et al.* 2015, L. Pan, Alagapan, Franca, Leondopulos, DeMarse, Brewer and Wheeler. 2015a). Our 5PDs used the same fabrication techniques, as this technique resulted in sub-micron resolution, reproducible, non-toxic, transparent, cheap and disposable devices that were quick and easy to fabricate while retaining complex patterns and could be sealed to glass or an MEA.

Most of the compartmentalised devices from the literature remain similar to the original design from Taylor and colleagues, namely two ports linked by microchannels, (Kanagasabapathi *et al.* 2011, Deleglise *et al.* 2014, Tang-Schomer *et al.* 2014, Renault *et al.* 2015). Our device pushed the number of ports up to five, with two side ports linked by channels to the centre, which is also linked to the opposing set of two side ports. To my knowledge this combination of five ports linked by four sets of channels is a novel design and increases the ability of the model to mimic entire networks or circuits, rather than just two cell populations.

As well as the ports, we presented tapered channels ranging from 15, 25 and 50 µm wide at one end to 5 µm wide at the other end. This design was based on work done by Peyrin and colleagues (Peyrin *et al.* 2011) who designed one of the first sets of unidirectional/tapered/diode/asymmetrical channels (15 µm to 3 µm) that had 97% selectivity for one direction. While re-creating channels with the same dimensions would have been desirable, the lowest width we could reliably fabricate was 5 µm, and thus after optimisation our optimal unidirectional channel dimensions were 15-5 µm, which still only resulted in a selectivity of ~76% (25-5 µm and 50-5 µm resulting in 59% and 50% respectively) for axons. This decreased selectivity compared to Peyrin and colleagues might be due to the inability to decrease the smaller width to as low as 3 µm, but as axons are approximately 0.5 µm in diameter (Pesaresi *et al.* 2015) it is difficult to determine how much difference the extra 2 µm would make. From the results presented in this thesis, the method of influencing the directionality of axonal outgrowth needs further work, possibly by adopting one of the many other more recent channel shape paradigms, including barbed (le Feber *et al.* 2015), closed-loop (Renault *et al.* 2016), reverse-fishbone (E *et al.* 2015) and 'new' diode (Na *et al.* 2016) designs. For this 5PD, unidirectionality is only vital for the centre and right-hand ports, as cells in the left hand ports can only extend axons in the correct direction (Pamies *et al.* 2014).

7.0.1.2 Biology of neurons cultured within devices

Despite the walls of the device being fabricated from PDMS, the growth surface for our device was glass, a substance much harder than the *in vivo* brain and not one that delicate primary neural

cultures adapted well to without prior coating (Lantoine *et al.* 2016). Poly-D-lysine (PDL) and laminin (LAM) were both available, previously used by our group, represented a gold standard and were supported in the literature as promoting adhesion and axon generation (Sun *et al.* 2012). As such, initial experiments were performed with PDL/LAM, until migration became an issue. Neural cultures on PDL/LAM would migrate, rendering the idea of a compartmentalised and isolated culture pointless. A comparison between PDL/LAM and polyethylenimine (PEI)/PDL indicated that the latter was superior, both massively inhibiting migration while promoting neurite outgrowth, and established in the literature (Ruegg and Hefti. 1984, Bledi *et al.* 2000, T. Zhou *et al.* 2012). However, cells still migrated in solution and were unaffected by PEI/PDL surfaces until they came into contact with the surface. The best way to confine cells to their ports would be with gated channels, where channels are blocked until cells have settled and attached to the surface, and channels are then unblocked, as seen in the lifting-gate micro-valve design (J. Kim *et al.* 2012).

CTX, STR, GP and SN cells were successfully dissected from primary rat embryos, characterised and seeded into 5PDs where they attached, extended axons and were maintained over the long term (up to 10 weeks). With the majority of other studies halting after 5 weeks *in vitro* (Goyal and Nam. 2011, Ito *et al.* 2013, Kanagasabapathi *et al.* 2013) (see **Table 4.2** for more details), the experiments outlined in this thesis better analyse the condition and function of connected neural cultures over the long term, vital when studying PD due to its progressive nature. Each cell type reacted differently in culture, with CTX cultures extending significantly more axons through channels, SN dopaminergic neurons not expressing marker enzyme tyrosine hydroxylase (TH) until 3-4 days *in vitro* (DIV), and an initial astrocyte:neuron ratio of 50:40.

As other devices featured less than five ports they also featured less than five cell types, meaning that not only is the 5PD design novel it marks the first time, to my knowledge, that CTX, STR, GP and SN cells have all been cultured together within the same device *in vitro.* Most BG studies took place with *in vivo* rat models (Moustafa *et al.* 2014) as opposed to designing complex cell models. By culturing CTX, STR, GP and SN neural cell types together, more control can be exerted over the construction of BG circuitry *in vitro*, and experiments are less limited in scope due to accessibility.

7.0.2 Chapter Four: Long-term study of separate neural culture functionality

It was necessary to establish an electrophysiological baseline of separate CTX, STR, GP and SN neural culture functional activity over the long term, in order to determine how their activity evolved over time as the synapses and network formed, matured and aged. This baseline for separate cells could then be compared to data from the same cell types when connected with the 5PD, and when treated with neurotoxins in order to mimic PD. To establish this baseline, dissociated neural cultures were grown separately on MEAs and their spontaneous extracellular electrical activity was recorded over the long term.

MEAs allow for easy culture-wide extracellular recordings to be taken over the long term and are a widely-used tool that interfaces between cultured cells and recording circuitry (Fejtl *et al.* 2006, Obien *et al.* 2015). Dissociated neural rat cultures on MEAs *in vitro* have shown selective adaption (Eytan *et al.* 2003), network plasticity in response to stimulation (Chiappalone *et al.* 2006, Chiappalone *et al.* 2008), spontaneous plasticity (Madhavan *et al.* 2007) and even short-term memory (Dranias *et al.* 2013). With these studies showing similar results to similar experiments *in vivo*, it indicates that *in vitro* extracellular recordings are comparable to some aspects of the *in vivo* situation, and that our *in vitro* model of BG circuitry can be a robust model that mimics components of BG activity *in vivo*.

Our CTX, STR, GP and SN separate neural cultures on MEAs displayed spontaneous activity ranging from random spiking to regular bursting and whole network bursts, with each facet of activity changing over time through the long term (up to 70 DIV). With the majority of 'long-term' *in vitro* neural culture extracellular recordings stopping after 35 DIV (Jimbo. 2007, Ito *et al.* 2013, Frega *et al.* 2014a), and the longest found in the literature to be up to 60 DIV (Lesuisse and Martin. 2002), our 70 day cultures represent the longest that *in vitro* neural cultures have been cultured for, with integrated MEA recording. This adds to the novelty of our device and shows that it is possible to access the BG circuitry for longer *in vitro*, a useful factor when dealing with progressive neural diseases that worsen over the long-term.

All cell types began to fire spontaneously from 11-15 DIV, except CTX where onset of activity was around 21 DIV due to CTX maturing later *in vivo* compared to STR, GP and SN (Anda *et al.* 2016). CTX had this delay in maturity as CTX, STR and GP were taken at embryonic age (E) 16, when peak neurogenesis for CTX is E18 (Hatanaka and Murakami. 2002, Anda *et al.* 2016), and CTX cultures consequently had this delay in onset of activity as they matured *in vitro*. Spontaneous activity from all cell types increased and then decreased in frequency and amplitude, in line with recorded *in vitro* changes to the number, density and maturation of synapses over time (Chiappalone *et al.* 2006). However, there is less information available concerning the onset of spontaneous activity from the STR, GP and SN, as many studies involve stimulation rather than passive recording of spontaneous activity. Studies with E18 hippocampal cells show activity as early as 9 DIV, but do indicate similar trends, with an early peak in the percentage of active electrodes followed by a plateau and a decrease (N. Hong *et al.* 2017a).

Spontaneous electrophysiological data obtained from MEAs also potentially revealed that the *in vitro* cultures were exhibiting plasticity, where certain spontaneous activity patterns were strengthened over time and electrodes recorded more spikes in certain locations. This localisation and focusing of activity to certain locations highlights an advantage of MEAs as recording both temporal and spatial changes in spontaneous activity, and has been observed in other studies on cell models (Lesuisse and

Martin. 2002, Chiappalone *et al.* 2006) and brain slices (Abrahamsson *et al.* 2016, Lalanne *et al.* 2016), some claiming it to be dependent on cell density (Biffi *et al.* 2013).

Spiking and bursting activity from the STR, GP and SN were consistent with previously recorded *in vitro* and *in vivo* recordings (Boraud *et al.* 2002, Walters *et al.* 2007), all three cell types showing different frequencies of firing most likely due to the dual populations of functionally distinct cells in each culture: STR cultures consist of slower firing medium spiny neurons (MSNs) (B. R. Miller *et al.* 2008) and faster firing cholinergic interneurons (Gage *et al.* 2010), GP cultures consist of slower GPe and faster firing GPi neurons (both GABAergic neurons) (Mallet *et al.* 2012, Mallet *et al.* 2006) and SN cultures consist of slower SNc dopaminergic neurons and faster SNr GABAergic neurons (Lee *et al.* 2011, S. Ding *et al.* 2011, F. M. Zhou and Lee. 2011).

SN cultures showed increased spontaneous activity when compared to CTX, STR and GP, with SN culture spiking and bursting frequencies being consistently higher than CTX, STR and GP, corroborated by the literature (Blythe *et al.* 2009, Berretta *et al.* 2010, Marinelli and McCutcheon. 2014). In addition, SN activity was more widespread across the MEA for longer, and it is unclear why activity did not follow the same '*focusing'* trend seen in other cell types.

Another finding was that centroid shapes (i.e. groups of similar spike patterns) changed over time, also seen by Lewandowska and colleagues who recognised the process of spike '*evolution'* where spike shapes changed over 28 DIV. There is little published information concerning changes in any form of spontaneous activity from 35 DIV onwards, meaning that long-term changes were challenging to corroborate in our experiments from 35-70 DIV or reinforce with data from other studies, which did show a process of evolution over the first 5 weeks (Chiappalone *et al.* 2006, Lewandowska *et al.* 2015)

7.0.3 Chapter Five: Long-term study of connected neural co-culture functionality

Having obtained valuable baseline electrical data for separate cells, reported in **Chapter Four**, the simultaneous measure of co-cultures and structurally connected populations were carried out using the 5PD. Devices were combined with MEAs to determine any changes in activity over the long term for connected dual co-cultures, namely CTX-STR, STR-GP and SNc-STR. As the basics of long term electrophysiology were discussed in the previous section, this section will mainly focus on the effect(s) of connectivity between two neural cell types and what changes did or did not occur to the spontaneous electrophysiological activity.

Broadly, connectivity resulted in the following changes in activity:

- CTX: earlier onset, greater amplitude and more frequent spiking and bursting activity throughout
- GP: greater amplitude and more frequent spiking and bursting for initial 3 weeks followed by reduced activity in all areas afterwards
- SN: greater amplitude, more frequent spiking and bursting activity by 5 weeks (~35 DIV) but decreased activity afterwards
- STR: all aspects of activity increased when innervated by CTX and SN cultures, all aspects of activity decreased when connected to GP cultures.

While CTX-STR and SNc-STR devices resulted in increased activity for both ports, with CTX exciting STR via glutamatergic input and SNc modifying STR activity via dopaminergic input, STR-GP resulted in inhibition for both ports likely due to GABAergic activity which has been demonstrated *in vitro* as inhibitory (Dubinsky. 1989, Sims *et al.* 2008). While there was increased activity for the first 5 weeks, activity generally decreased over the next 5 weeks, an effect to my knowledge not displayed in the literature.

Studies using PDMS devices with channels on MEAs had similar findings, Goyal and colleagues noting that as the confined neurons matured the spike and burst rates increased, attributing it to increased synapse maturation and density over the first few weeks in culture (Goyal and Nam. 2011). However, Goyal and colleagues only measured from 8 devices containing one cell type, while the work reported in this thesis looked at much longer term cultures with multiple cell types. Dworak and colleagues noted spike frequencies from 3-22 Hz, amplitudes of 100-200 µV and synchronous bursting from 10-14 DIV (from 21 devices) all of which align with our findings (Dworak and Wheeler. 2009). Most significantly, Takayama and colleagues demonstrated that connecting neural cell populations together increases periodic synchronized bursting after forming functional networks within 2 weeks and maintaining this activity for up to 4 weeks (Takayama *et al.* 2012). These works reinforce the data generated from our connected co-cultures, with display similar activity trends.

Devices using cells from basal ganglia circuitry, connecting cortex and thalamus, showed that bursting from the CTX region propagated to thalamic cells (Kanagasabapathi *et al.* 2013). This study also showed that even CTX-CTX devices had an input-output relationship, with one port acting as input and controlling the activity, despite both ports containing identical cells. The identity of the input port was dependent on neurite arborisation and strength of synaptic connections. This thesis also demonstrated such input-output modulation of activity, with activity from STR cultures changing depending on the cell type that was the input (CTX or SN), as seen in **Chapter Five** (**section 5.2.8.2 Centroid shape categorisation** and **section 5.3 Comparisons of separate cultures and connected co-cultures**, where the effects of connectivity on STR cultures are highlighted).

Hong and colleagues reported a decrease in activity from microchannel electrodes between 3-4 weeks, stated to be potentially due to the small number of channels in their device resulting in neuronal cultures forming stronger networks within ports rather than between ports (N. Hong *et al.* 2017b). This phenomenon was also shown by Pan *et al.* who noted that the greater the number of channels the stronger the connectivity, the greater the probability of bursting propagating between wells, shorter delays between spikes and faster onset in connected wells (L. Pan, Alagapan, Franca, Leondopulos, DeMarse, Brewer and Wheeler. 2015b), all features noted in this chapter, indicating that our device has sufficient channels to connect two cell populations functionally. The maximum number of channels used by Pan and Hong in their devices were ~50, and as our device features four sets of 200 channels the neural cultures were better connected and able to network across multiple distinct cell populations.

In summary, as the 5PD features more electrodes, more channels and more cell types, it represents an advancement for *in vitro* neural models based on the current work in the field. This will be useful for the development of more state-of-the-art advanced *in vitro* neural models in order to study neurodegenerative disease at a preclinical level and accelerate the research into such conditions as Parkinson's disease (Ellens and Leventhal. 2013, Bahmad *et al.* 2017, Lazaro *et al.* 2017)

7.0.4 Chapter Six: Modelling Parkinson's disease

With many expensive and time-consuming clinical trials focused on Parkinson's disease (PD) and not sufficiently achieving or generating new therapies, treatments or preventative measures, it is time to develop better preclinical platforms for study, enabling PD research to better filter out useful treatments, stem cell therapies, neuroprotective factors etc. before the clinical stage. The 5PD described in this thesis presents a powerful option for a preclinical platform of study, once chemically modified to better suit the study of PD. With separate culture and connected co-culture baselines of activity as reference, the final step was to mimic PD. With the use of 6-OHDA well established both in literature and effectively optimised in our experiments, it was a simple matter to attempt to destroy the dopaminergic (DA) neurons of nigrostriatal SNc-STR co-cultures and record any effects on the spontaneous extracellular electrophysiological activity, having created an acute model of PD *in vitro*. The effects of 6-OHDA treatment on SNc-STR co-culture activity are displayed on **Table.7.1**.

Table 7.1: The electrophysiological effects of 6-OHDA treatment to the SNc port of SNc-STR devices

Effects of 6-OHDA treatment	Suggested reasoning	Implications	Seen in literature?
Decreased number of active SNc and channel electrodes	Less DA neurons, which exist in SNc port and extended axons into channels	Killing of DA neurons results in 'dying back' of DA projection axons	No, too few studies look at percentage activity
Decreased SNc spike frequency	Less DA neurons firing, less bursts (see below)	DA neurons contribute to SNc overall spike frequency	Low SN firing seen *in vivo* (Aristieta *et al.* 2016)
Decreased SNc burst firing but similar numbers of spikes per burst	Insufficient networking to produce bursts with same frequency after DA neuron death	Bursting is a major component of spike frequency, removing neurons halts bursting ability	Decrease in bursting seen *in vivo* (Lobb and Jaeger. 2015)
Increased SNc centroid number immediately after treatment, lower numbers overall	DA neuron death perturbing signal variability as network potentially has to reform, then recover to normal function.	Networks degenerate over the long term whether treated or not	Increase in variability seen *in vivo* (Lobb and Jaeger. 2015)
Decreased proportions of biphasic and triphasic centroids in SNc port and channels	Less cell bodies and axons result in less detectable centroids as there was also lower spike frequency.	Biphasic and triphasic centroids generated by cell bodies and axons respectively	No, few studies classify data with centroid phase
Decreased SNc FDHM ('thinner' spikes)	Unknown, potentially due to network reformation after DA neuron loss	DA neuron loss can affect spike duration	Few studies measure FDHM (Panigrahi *et al.* 2015).
Effects seen with both 25 DIV and 65 DIV treatment	More mature networks still vulnerable to 6-OHDA	Acute models can be developed at any age	Few studies are long-term enough (Lesuisse and Martin. 2002)
Only effect to STR activity was increased FDHM and less triphasic centroids	6-OHDA has very specific action. Larger FDHM potentially in response to smaller FDHM of SNc. Less triphasic centroids due to less SNc axons in STR port	Model mimics the effect of PD with specific action, STR loses dopaminergic input.	Specificity of 6-OHDA well documented.

Decreased spontaneous activity (specifically, decreased spike and burst frequencies) of SNc cultures when treated with a neurotoxin is a natural consequence of destroying DA neurons and thus decreasing the number of neurons that can fire. This decreased firing is displayed on theoretical firing rate and dynamic activity models of PD (Nambu *et al.* 2015), animal models (Branch *et al.* 2016) and human models (Woodard *et al.* 2014), which all display differences in spontaneous bursting and spiking after DA neuron loss.

While there are numerous examples of *in vitro* compartmentalised models coupled to MEAs, there are very few studies that treat such models with 6-OHDA in an effort to model PD. The main use of MEAs in PD study appears to be for the stimulation aspect of MEAs, usually implanted *in vivo* for deep brain stimulation (DBS) on rodents or primate models (Zhang *et al.* 2018). As such there is little *in vitro* literature to compare the results of this chapter to, but insight can be generated from *in vivo* models. Most of these studies involve stereotactic injection of 6-OHDA into the SN or STR (in order to bypass the blood brain barrier and target specific neurons), with large differences. When injected into the SN there is complete and rapid lesion of the nigrostriatal pathway within 12 hours, and loss of DA terminals on the STR 2-3 days later. When injected into the STR there is slow, progressive damage to the nigrostriatal pathway, making injection of 6-OHDA into the STR a more relevant model of PD as it is more progressive and also induces PD symptoms (Cannon and Greenamyre. 2010, Tieu. 2011). These models show decreased SNc firing and bursting but increased SNr firing and bursting (Ellens and Leventhal. 2013). As our model does not separate SNc and SNr but treats SN as a whole with 6-OHDA, it appears there was either a non-specific effect of 6-OHDA and SNr GABAergic neurons were lost, or only SNc DA neurons were lost and this had a large effect on the spiking and bursting *in vitro*.

7.1 Limitations of the model

While the work presented here represents a robust and reproducible model of basal ganglia circuitry and a method of preclinical research into PD, the model was still limited by a number of factors:

- Our basal ganglia circuitry model did not take into account the subthalamic nucleus
- The lowest channel width possible to reliably fabricate was limited to 5 µm, would preferably be <5 µm as seen in other publications (Peyrin *et al.* 2011)
- Tapered channels potentially not as effective as other channel designs for exerting directional pressure and making a unidirectional circuit
- Cells in the right-hand ports of the 5PD could only extend axons in the unwanted direction
- 10-20% of cells migrated between ports while in solution and before contacting with the attractive PEI/PDL-coated growth surface
- Cells on MEA could only be imaged while live by brightfield and could not be fixed (and killed) for fluorescent imaging without halting the spontaneous activity, experiments with recording and imaging would be run separately but in tandem
- MEA was not located in a desirable location within 5PDs due to hardware constraints (discussed in **7.2 Future Work**)
- Not possible to directly determine if dopaminergic cells were damaged/destroyed by 6-OHDA within each device while recording, as any fixing and staining would halt activity

- Only two cell types were seeded as opposed to a maximum of five

7.2 Future work

The work in this thesis represents only a portion of the work done to develop a novel, functional *in vitro* Parkinsonian model. The original aim was to fill the model with CTX, STR, GP, SNc and SNr cell types (to more completely represent the physiological BG), then to damage/destroy the dopamine neurons of the SNc via 6-OHDA treatment (to model the effects of nigrostriatal dopamine neuron loss on further downstream and upstream nuclei, modelling the pathological BG), and finally to attempt to recover function in the model, returning the functionality from damaged pathological to healthy physiological BG. In this manner our device would become a platform for study of Parkinson's disease, where designer drugs and pharmaceuticals, new therapies, stem cell treatments and neuroprotective factors could all be tested at a pre-clinical level in order to accelerate research into Parkinson's and have more efficient clinical trials. As this original aim was altered due to experimental and time constraints, the immediate future work would be to achieve this original aim, developing the full BG, a Parkinsonian BG model and attempt to restore this disease model to normal function.

For a specific piece of future work, the issue of MEA electrode location when paired with the 5PD (as outlined in **Chapter Five** (**section 5.4.2 MEA electrode location, Fig.5.19**) would require a re-design of the electrode array to better suit the shape of the 5PD. This re-design process was started and completed during this project, but the greater noise level of these custom MEAs meant that the experiments in this thesis took place with the MEA layout displayed in **Fig.5.19B**. For future work filling the entire device with all five cell types (CTX, STR, GP, SNc and SN with dopamine neurons removed to represent SNr), these new custom MEAs will be necessary to reach the full potential of this 5PD model. The custom MEA design for the future is outlined in **Fig.7.1.**

In addition, our device allows for any five neuronal cell populations to be connected in a specific unidirectional manner via channels while isolating cell bodies within ports. As the device was designed with the BG in mind, a natural next step would be to further model the corticostriatal (CTX-STR) connections in a full BG model, and then damage this connection (along with STR and CTX neurons) in order to mimic Huntington's disease. Thus, our device can be used as a pre-clinical platform for study for multiple progressive neurological diseases, in an effort to push towards more effective treatment strategies.

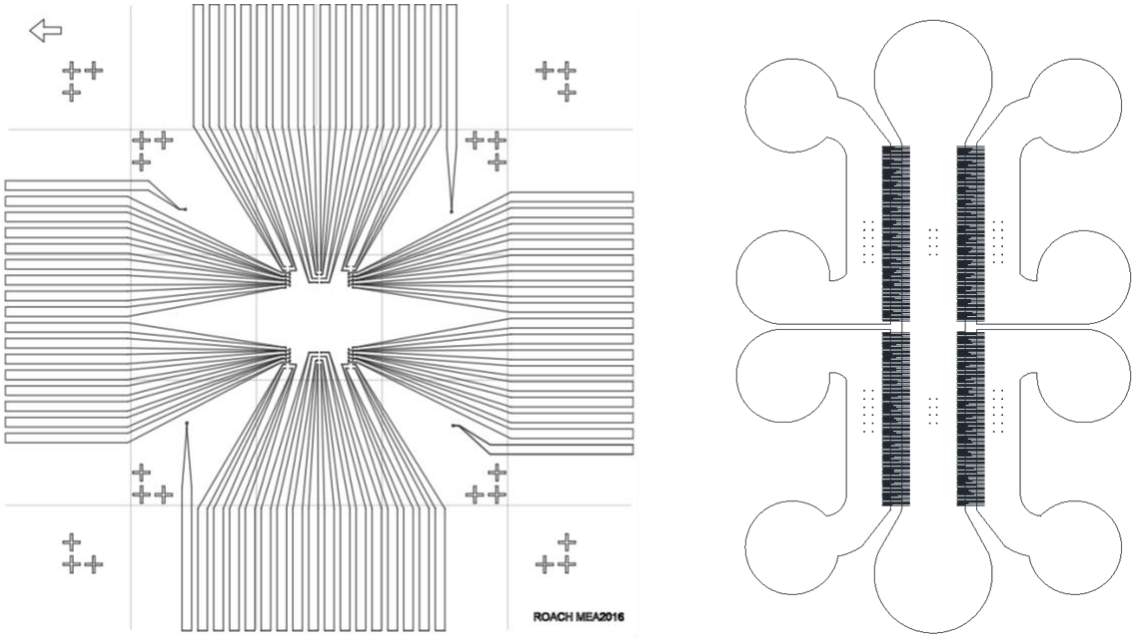

Figure 7.1: MEA redesign for future experimentation. This new custom MEA involved splitting the 64 electrodes split into four groups of 12 (6 x 2, one for each side port) and two groups of 8 (4x2, both for the centre port). The photolithographic mask design for these electrodes is on the left-hand side, and the final placement of these electrodes within the 5PD is on the right-hand side. These groups of electrodes were aligned with the channels entrances and exits, but no electrodes within channels. Electrode diameter and grouped electrode spacing is the same as the original 8x8 grid, 50x50 µm per electrode and 200 µm spacing.

As discussed in the introduction, there are many potential modelling systems available for PD research, including (but not limited to) neurotoxin-based animal models, gene-based animal models, cell line models, primary cell models, stem cell models, reprogrammed cell (iPSC) models, organotypic tissue slice models and organoid models. Good examples of these are summaried by (Ghatak *et al.* 2018).

Despite this wide range of available models, none of them can comprehensively represent all aspects of the human disease. This is due to PD being a very complex and multifactorial human disease, and while the approach of cell modelling provides a powerful tool for PD research, without the use of human nigrostriatal DAergic neurons these models cannot fully reflect the pathogenesis in PD. The most reliable way to generate such human DAergic neuron models would be through iPSCs, which can be generated directly from PD patient cells (from non-invasive manners such as finger prick, hair, urine or mouth swab) (Xiao *et al.* 2016). iPSC-derived neurons have been used *in vitro* to model PD and have produced some interesting results, some concerning the role of mitophagy in PD (Xiao *et al.* 2016), and some through artificial ageing via long-term culture and progerin expression (Miller *et al.* 2013), similarly to the long-term culture used in this thesis. As well as modelling, iPSC-derived human neurons have also been used to discover and screen potential PD therapeutics. By testing experimental therapies on patient-derived iPSC DAergic neurons before their use on the patient themselves, the efficacy of certain treatments can be ensured before they are administered.

However, due to the expensive and time-consuming process of generating iPSCs for each individual PD patient, this kind of screening is unlikely until iPSC technology improves. A combination of this iPSC screening with compartmentalised microfluidic *in vitro* models would allow for a more powerful platform, combining the individualised specificity of iPSCs with the *in vivo* basal ganglia structural mimicry of the microfluidic device, allowing for the formation of a nigrostriatal circuit as opposed to an isolated culture of iPSC-derived human neurons, which mimics the genotypic but not the structural interactions. Another option for screening consists of sequencing patient-derived iPSCs to determine if a PD patient can be categorised in certain genotypic subgroups and given more effective treatments (Xiao *et al.* 2016).

One of the aims with our model was to damage the SNc-STR circuitry with 6-OHDA in order to mimic PD, but another unachieved aim was to restore the function of these damaged models using cell replacement, therapies or neuroprotective factors. iPSCs have enjoyed successful usage in cellular replacement therapies for PD, partly due to the unlimited supply of patient-specific neurons offered. Grafted iPSCs differentiated into DA neurons and rescued motor deficits in rat PD models (Wernig *et al.* 2008), similarly iPSC-derived NSCs also differentiated into DA neurons and survived for 6 months in primate models, albeit with no significant improvement in behaviour (Kikuchi *et al.* 2011), indicating that iPSCs can potentially integrate and restore function in some damaged systems, but a stringent clinical study paradigm is necessary. By testing these iPSC replacement therapies at a pre-clinical level in our device, iPSC replacement can be accelerated.

In addition, the use of iPSCs allow for patient-specific human models to be generated. These human models still have the limitations that other *in vitro* models have when compared to rodent *in vivo* studies, but offer a novel alternative approach and increased relevance to PD, a human disease. Other ways to better humanise PD models would be to make PD models less acute and more progressive to better mimic the human condition *in vivo*. Models with subacute/chronic symptoms are developed by applying low doses of neurotoxin over a long period of time (Iravani *et al.* 2005, Barraud *et al.* 2010, Vezoli *et al.* 2011, Blesa *et al.* 2012), often with non-human primates.

These diseases are modelled in animals first, despite being a human disease. Simply put, animal model systems are the closest to humans that we are able to study. Many of these models are necessary as it is very unlikely that a single model, be it toxic or genetic, can fully recapitulate the complexity of human PD (Blesa *et al.* 2012, Jackson-Lewis *et al.* 2012, Blesa and Przedborski. 2014). Future models will likely combine different methodologies and include both neurotoxin-induced and genetically induced insults, taking into account aging and environmental insults. Despite the similarity of non-human primates to humans and their ability to develop PD-like symptoms, the rodent model is employed far more often. Aside from the ethical, time and financial benefits, the rodent models are useful to test theories and initially screen potential PD treatments and therapies,

while lacking the behavioural and symptomatic components of PD such as the non-human primates. Monkeys essentially represent the last stage in PD treatment before anything is administered to humans (Bezard and Przedborski. 2011). Naturally, when looking to the future of research it is ideal to consider a large reduction in animal usage in compliance with the 3Rs, and an increase in the number of effective and powerful human models of PD, whether through reprogrammed human patient iPSCs or human-derived cell likes such as SH-SY5Y.

The end goal of our model system is to be used for pre-clinical research into PD and to eventually reduce animal use once humanised. In an effort to address gaps in PD knowledge, more investigators are approaching PD using such interdisciplinary approaches with a variety of models.

7.3 Conclusion

This project has gathered data from more cell types in more combinations over a longer time frame than any other project, to this author's knowledge. The vast body of data generated across this project allows for new insights into the workings of BG nuclei *in vitro* over the long term, including neuronal functionality in separate and connected cultures and the effects of dopaminergic loss on this functionality.

This kind of *in vitro* cell model can become part of a departure from using a large number of animal models for each experiment, now that cell models can attain such levels of complexity and generate relevant data. My hope is that these models can grow in complexity until there are models for specific CNS-related experimentation, and that this kind of pre-clinical work can accelerate research into currently incurable neurological diseases.

7.4 References

Abbott, N.J. (2004) *Evidence for bulk flow of brain interstitial fluid: significance for physiology and pathology,* Neurochem.Int., **45,** 545-552.

Abrahamsson, T., Lalanne, T., Watt, A.J. and Sjostrom, P.J. (2016) *Long-Term Potentiation by Theta-Burst Stimulation Using Extracellular Field Potential Recordings in Acute Hippocampal Slices,* Cold Spring Harb Protoc., **2016,** 10.1101/pdb.prot091298.

Acharya, U.R., Vinitha Sree, S., Swapna, G., Martis, R.J. and Suri, J.S. (2013) *Automated EEG analysis of epilepsy: A review,* Knowledge-Based Syst., **45,** 147-165.

Achim, K., Peltopuro, P., Lahti, L., Li, J., Salminen, M. and Partanen, J. (2012) *Distinct developmental origins and regulatory mechanisms for GABAergic neurons associated with dopaminergic nuclei in the ventral mesodiencephalic region,* Development, **139,** 2360-2370.

Akerboom, J., Carreras Calderon, N., Tian, L., Wabnig, S., Prigge, M., Tolo, J., Gordus, A., Orger, M.B., Severi, K.E., Macklin, J.J., Patel, R., Pulver, S.R., Wardill, T.J., Fischer, E., Schuler, C., Chen, T.W., Sarkisyan, K.S., Marvin, J.S., Bargmann, C.I., Kim, D.S., Kugler, S., Lagnado, L., Hegemann, P., Gottschalk, A., Schreiter, E.R. and Looger, L.L. (2013) *Genetically encoded calcium indicators for multi-color neural activity imaging and combination with optogenetics,* Front.Mol.Neurosci., **6,** 2.

Alberio, T., Lopiano, L. and Fasano, M. (2012) *Cellular models to investigate biochemical pathways in Parkinson's disease,* FEBS J., **279,** 1146-1155.

Almodovar, J., Crouzier, T., Selimovic, S., Boudou, T., Khademhosseini, A. and Picart, C. (2013) *Gradients of physical and biochemical cues on polyelectrolyte multilayer films generated via microfluidics,* Lab.Chip, **13,** 1562-1570.

Amin, N.D. and Pasca, S.P. (2018) *Building Models of Brain Disorders with Three-Dimensional Organoids,* Neuron, **100,** 389-405.

Anda, F.C., Madabhushi, R., Rei, D., Meng, J., Graff, J., Durak, O., Meletis, K., Richter, M., Schwanke, B., Mungenast, A. and Tsai, L.H. (2016) *Cortical neurons gradually attain a post-mitotic state,* Cell Res., **26,** 1033-1047.

Andreae, L.C. and Burrone, J. (2014) *The role of neuronal activity and transmitter release on synapse formation,* Curr.Opin.Neurobiol., **27,** 47-52.

Arbab, M., Baars, S. and Geijsen, N. (2014) *Modeling motor neuron disease: the matter of time,* Trends Neurosci., **37,** 642-652.

Ariano, M.A., Cepeda, C., Calvert, C.R., Flores-Hernandez, J., Hernandez-Echeagaray, E., Klapstein, G.J., Chandler, S.H., Aronin, N., DiFiglia, M. and Levine, M.S. (2005) *Striatal potassium channel dysfunction in Huntington's disease transgenic mice,* J.Neurophysiol., **93,** 2565-2574.

Aristieta, A., Ruiz-Ortega, J.A., Miguelez, C., Morera-Herreras, T. and Ugedo, L. (2016) *Chronic L-DOPA administration increases the firing rate but does not reverse enhanced slow frequency oscillatory activity and synchronization in substantia nigra pars reticulata neurons from 6-hydroxydopamine-lesioned rats,* Neurobiol.Dis., **89,** 88-100.

Aston-Jones, G.S. and Siggins, G.R. (2000) *Electrophysiology,* Neuropsychopharmacology, **5,**

Auluck, P.K., Chan, H.Y., Trojanowski, J.Q., Lee, V.M. and Bonini, N.M. (2002) *Chaperone suppression of alpha-synuclein toxicity in a Drosophila model for Parkinson's disease,* Science, **295,** 865-868.

Avila Akerberg, O. and Chacron, M.J. (2009) *Noise shaping in neural populations,* Phys.Rev.E.Stat.Nonlin Soft Matter Phys., **79,** 011914.

Baccei, M.L. and Fitzgerald, M. (2004) *Development of GABAergic and glycinergic transmission in the neonatal rat dorsal horn,* J.Neurosci., **24,** 4749-4757.

Bahmad, H., Hadadeh, O., Chamaa, F., Cheaito, K., Darwish, B., Makkawi, A.K. and Abou-Kheir, W. (2017) *Modeling Human Neurological and Neurodegenerative Diseases: From Induced Pluripotent Stem Cells to Neuronal Differentiation and Its Applications in Neurotrauma,* Front.Mol.Neurosci., **10,** 50.

Baker, B.M. and Chen, C.S. (2012a) *Deconstructing the third dimension: how 3D culture microenvironments alter cellular cues,* J.Cell.Sci., **125,** 3015-3024.

Baker, B.M. and Chen, C.S. (2012b) *Deconstructing the third dimension: how 3D culture microenvironments alter cellular cues,* J.Cell.Sci., **125,** 3015-3024.

Bakkum, D.J., Frey, U., Radivojevic, M., Russell, T.L., Muller, J., Fiscella, M., Takahashi, H. and Hierlemann, A. (2013) *Tracking axonal action potential propagation on a high-density microelectrode array across hundreds of sites,* Nat.Commun., **4,** 2181.

Balgude, A.P., Yu, X., Szymanski, A. and Bellamkonda, R.V. (2001) *Agarose gel stiffness determines rate of DRG neurite extension in 3D cultures,* Biomaterials, **22,** 1077-1084.

Ballion, B., Mallet, N., Bezard, E., Lanciego, J.L. and Gonon, F. (2008) *Intratelencephalic corticostriatal neurons equally excite striatonigral and striatopallidal neurons and their discharge activity is selectively reduced in experimental parkinsonism,* Eur.J.Neurosci., **27,** 2313-2321.

Bal-Price, A.K., Hogberg, H.T., Buzanska, L., Lenas, P., van Vliet, E. and Hartung, T. (2010) *In vitro developmental neurotoxicity (DNT) testing: relevant models and endpoints,* Neurotoxicology, **31,** 545-554.

Barberi, T., Klivenyi, P., Calingasan, N.Y., Lee, H., Kawamata, H., Loonam, K., Perrier, A.L., Bruses, J., Rubio, M.E., Topf, N., Tabar, V., Harrison, N.L., Beal, M.F., Moore, M.A. and Studer, L. (2003) *Neural subtype specification of fertilization and nuclear transfer embryonic stem cells and application in parkinsonian mice,* Nat.Biotechnol., **21,** 1200-1207.

Bar-Gad, I., Heimer, G., Ritov, Y. and Bergman, H. (2003) *Functional correlations between neighboring neurons in the primate globus pallidus are weak or nonexistent,* J.Neurosci., **23,** 4012-4016.

Barkats, M., Millecamps, S., Bilang-Bleuel, A. and Mallet, J. (2002) *Neuronal transfer of the human Cu/Zn superoxide dismutase gene increases the resistance of dopaminergic neurons to 6-hydroxydopamine,* J.Neurochem., **82,** 101-109.

Barraud, Q., Obeid, I., Aubert, I., Barriere, G., Contamin, H., McGuire, S., Ravenscroft, P., Porras, G., Tison, F., Bezard, E. and Ghorayeb, I. (2010) *Neuroanatomical study of the A11 diencephalospinal pathway in the non-human primate,* PLoS One, **5,** e13306.

Bartsch, H., Baca, M., Fernekorn, U., Muller, J., Schober, A. and Witte, H. (2018) *Functionalized Thick Film Impedance Sensors for Use in In Vitro Cell Culture,* Biosensors (Basel), **8,** 10.3390/bios8020037.

Beeler, J.A., Frank, M.J., McDaid, J., Alexander, E., Turkson, S., Bernardez Sarria, M.S., McGehee, D.S. and Zhuang, X. (2012) *A role for dopamine-mediated learning in the pathophysiology and treatment of Parkinson's disease,* Cell.Rep., **2,** 1747-1761.

Begley, C.G. and Ellis, L.M. (2012) *Drug development: Raise standards for preclinical cancer research,* Nature, **483,** 531-533.

Benam, K.H., Dauth, S., Hassell, B., Herland, A., Jain, A., Jang, K.J., Karalis, K., Kim, H.J., MacQueen, L., Mahmoodian, R., Musah, S., Torisawa, Y.S., van der Meer, A.D., Villenave, R., Yadid, M., Parker, K.K. and Ingber, D.E. (2015) *Engineered in vitro disease models,* Annu.Rev.Pathol., **10,** 195-262.

Ben-Ari, Y. (2002) *Excitatory actions of gaba during development: the nature of the nurture,* Nat.Rev.Neurosci., **3,** 728-739.

Ben-Ari, Y. (2014) *The GABA excitatory/inhibitory developmental sequence: a personal journey,* Neuroscience, **279,** 187-219.

Ben-Ari, Y., Khalilov, I., Kahle, K.T. and Cherubini, E. (2012) *The GABA excitatory/inhibitory shift in brain maturation and neurological disorders,* Neuroscientist, **18,** 467-486.

Bennett, B.D. and Wilson, C.J. (1999) *Spontaneous activity of neostriatal cholinergic interneurons in vitro,* J.Neurosci., **19,** 5586-5596.

Bergh, N., Ekman, M., Ulfhammer, E., Andersson, M., Karlsson, L. and Jern, S. (2005) *A new biomechanical perfusion system for ex vivo study of small biological intact vessels,* Ann.Biomed.Eng., **33,** 1808-1818.

Bergman, H., Wichmann, T., Karmon, B. and DeLong, M.R. (1994) *The primate subthalamic nucleus. II. Neuronal activity in the MPTP model of parkinsonism,* J.Neurophysiol., **72,** 507-520.

Bernardinelli, Y., Muller, D. and Nikonenko, I. (2014) *Astrocyte-Synapse Structural Plasticity Neural Plasticity ,* Neural Plasticity, **2014,** 0-13.

Berretta, N., Bernardi, G. and Mercuri, N.B. (2010) *Firing properties and functional connectivity of substantia nigra pars compacta neurones recorded with a multi-electrode array in vitro,* J.Physiol., **588,** 1719-1735.

Bertran-Gonzalez, J., Herve, D., Girault, J.A. and Valjent, E. (2010) *What is the Degree of Segregation between Striatonigral and Striatopallidal Projections?* Front.Neuroanat., **4,** 10.3389/fnana.2010.00136. eCollection 2010.

Betarbet, R., Sherer, T.B., MacKenzie, G., Garcia-Osuna, M., Panov, A.V. and Greenamyre, J.T. (2000) *Chronic systemic pesticide exposure reproduces features of Parkinson's disease,* Nat.Neurosci., **3,** 1301-1306.

Bezard, E. and Przedborski, S. (2011) *A tale on animal models of Parkinson's disease,* Mov.Disord., **26,** 993-1002.

Bezzi, P. and Volterra, A. (2001) *A neuron-glia signalling network in the active brain,* Curr.Opin.Neurobiol., **11,** 387-394.

Bhatia, S.N. and Ingber, D.E. (2014) *Microfluidic organs-on-chips,* Nat.Biotechnol., **32,** 760-772.

Biffi, E., Regalia, G., Menegon, A., Ferrigno, G. and Pedrocchi, A. (2013) *The influence of neuronal density and maturation on network activity of hippocampal cell cultures: a methodological study,* PLoS One, **8,** e83899.

Bilsland, J., Roy, S., Xanthoudakis, S., Nicholson, D.W., Han, Y., Grimm, E., Hefti, F. and Harper, S.J. (2002) *Caspase inhibitors attenuate 1-methyl-4-phenylpyridinium toxicity in primary cultures of mesencephalic dopaminergic neurons,* J.Neurosci., **22,** 2637-2649.

Bilston, L.E. (2011) *In Vitro Models for Biomechanical Studies of Neural Tissues,* Neural Tissue Biomechanics, **3,**

Blandini, F., Nappi, G., Tassorelli, C. and Martignoni, E. (2000) *Functional changes of the basal ganglia circuitry in Parkinson's disease,* Prog.Neurobiol., **62,** 63-88.

Blau, A., Weinl, C., Mack, J., Kienle, S., Jung, G. and Ziegler, C. (2001) *Promotion of neural cell adhesion by electrochemically generated and functionalized polymer films,* J.Neurosci.Methods, **112,** 65-73.

Bledi, Y., Domb, A.J. and Linial, M. (2000) *Culturing neuronal cells on surfaces coated by a novel polyethyleneimine-based polymer,* Brain Res.Brain Res.Protoc., **5,** 282-289.

Blennow, K., Hardy, J. and Zetterberg, H. (2012) *The neuropathology and neurobiology of traumatic brain injury,* Neuron, **76,** 886-899.

Blesa, J., Phani, S., Jackson-Lewis, V. and Przedborski, S. (2012) *Classic and new animal models of Parkinson's disease,* J.Biomed.Biotechnol., **2012,** 845618.

Blesa, J. and Przedborski, S. (2014) *Parkinson's disease: animal models and dopaminergic cell vulnerability,* Front.Neuroanat., **8,** 155.

Blum, D., Torch, S., Lambeng, N., Nissou, M., Benabid, A.L., Sadoul, R. and Verna, J.M. (2001) *Molecular pathways involved in the neurotoxicity of 6-OHDA, dopamine and MPTP: contribution to the apoptotic theory in Parkinson's disease,* Prog.Neurobiol., **65,** 135-172.

Blythe, S.N., Wokosin, D., Atherton, J.F. and Bevan, M.D. (2009) *Cellular mechanisms underlying burst firing in substantia nigra dopamine neurons,* J.Neurosci., **29,** 15531-15541.

Bonilla, S., Hall, A.C., Pinto, L., Attardo, A., Gotz, M., Huttner, W.B. and Arenas, E. (2008) *Identification of midbrain floor plate radial glia-like cells as dopaminergic progenitors,* Glia, **56,** 809-820.

Booze, R.M. and Wallace, D.R. (1995) *Dopamine D2 and D3 receptors in the rat striatum and nucleus accumbens: use of 7-OH-DPAT and [125I]-iodosulpride,* Synapse, **19,** 1-13.

Boraud, T., Bezard, E., Bioulac, B. and Gross, C.E. (2002) *From single extracellular unit recording in experimental and human Parkinsonism to the development of a functional concept of the role played by the basal ganglia in motor control,* Prog.Neurobiol., **66,** 265-283.

Botella, J.A., Bayersdorfer, F., Gmeiner, F. and Schneuwly, S. (2009) *Modelling Parkinson's disease in Drosophila,* Neuromolecular Med., **11,** 268-280.

Boudewijns, Z.S., Groen, M.R., Lodder, B., McMaster, M.T., Kalogreades, L., de Haan, R., Narayanan, R.T., Meredith, R.M., Mansvelder, H.D. and de Kock, C.P. (2013) *Layer-specific high-frequency action potential spiking in the prefrontal cortex of awake rats,* Front.Cell.Neurosci., **7,** 99.

Bourke, J.L., Quigley, A.F., Duchi, S., O'Connell, C.D., Crook, J.M., Wallace, G.G., Cook, M.J. and Kapsa, R.M.I. (2018) *Three-dimensional neural cultures produce networks that mimic native brain activity,* J.Tissue Eng.Regen.Med., **12,** 490-493.

Bove, J., Prou, D., Perier, C. and Przedborski, S. (2005) *Toxin-induced models of Parkinson's disease,* NeuroRx, **2,** 484-494.

Branch, S.Y., Chen, C., Sharma, R., Lechleiter, J.D., Li, S. and Beckstead, M.J. (2016) *Dopaminergic Neurons Exhibit an Age-Dependent Decline in Electrophysiological Parameters in the MitoPark Mouse Model of Parkinson's Disease,* J.Neurosci., **36,** 4026-4037.

Brannvall, K., Bergman, K., Wallenquist, U., Svahn, S., Bowden, T., Hilborn, J. and Forsberg-Nilsson, K. (2007) *Enhanced neuronal differentiation in a three-dimensional collagen-hyaluronan matrix,* J.Neurosci.Res., **85,** 2138-2146.

Brewer, G.J., Boehler, M.D., Leondopulos, S., Pan, L., Alagapan, S., DeMarse, T.B. and Wheeler, B.C. (2013) *Toward a self-wired active reconstruction of the hippocampal trisynaptic loop: DG-CA3,* Front.Neural Circuits, **7,** 165.

Brooks, A.I., Chadwick, C.A., Gelbard, H.A., Cory-Slechta, D.A. and Federoff, H.J. (1999) *Paraquat elicited neurobehavioral syndrome caused by dopaminergic neuron loss,* Brain Res., **823,** 1-10.

Brunello, C.A., Jokinen, V., Sakha, P., Terazono, H., Nomura, F., Kaneko, T., Lauri, S.E., Franssila, S., Rivera, C., Yasuda, K. and Huttunen, H.J. (2013) *Microtechnologies to fuel neurobiological research with nanometer precision,* J.Nanobiotechnology, **11,** 11-3155-11-11.

Bugnicourt, G., Brocard, J., Nicolas, A. and Villard, C. (2014) *Nanoscale surface topography reshapes neuronal growth in culture,* Langmuir, **30,** 4441-4449.

Campenot, R.B. (1982) *Development of sympathetic neurons in compartmentalized cultures. II. Local control of neurite survival by nerve growth factor,* Dev.Biol., **93,** 13-21.

Cannon, J.R. and Greenamyre, J.T. (2010) *Neurotoxic in vivo models of Parkinson's disease recent advances,* Prog.Brain Res., **184,** 17-33.

Cavaliere, F., Vicente, E.S. and Matute, C. (2010) *An organotypic culture model to study nigro-striatal degeneration,* J.Neurosci.Methods, **188,** 205-212.

Cazorla, M., de Carvalho, F.D., Chohan, M.O., Shegda, M., Chuhma, N., Rayport, S., Ahmari, S.E., Moore, H. and Kellendonk, C. (2014) *Dopamine D2 receptors regulate the anatomical and functional balance of basal ganglia circuitry,* Neuron, **81,** 153-164.

Cepeda, C., Andre, V.M., Yamazaki, I., Wu, N., Kleiman-Weiner, M. and Levine, M.S. (2008) *Differential electrophysiological properties of dopamine D1 and D2 receptor-containing striatal medium-sized spiny neurons,* Eur.J.Neurosci., **27,** 671-682.

Chan, W.S., Durairajan, S.S., Lu, J.H., Wang, Y., Xie, L.X., Kum, W.F., Koo, I., Yung, K.K. and Li, M. (2009) *Neuroprotective effects of Astragaloside IV in 6-hydroxydopamine-treated primary nigral cell culture,* Neurochem.Int., **55,** 414-422.

Chen, D., Kanthasamy, A.G. and Reddy, M.B. (2015) *EGCG Protects against 6-OHDA-Induced Neurotoxicity in a Cell Culture Model,* Parkinsons Dis., **2015,** 843906.

Chen, S.H., Oyarzabal, E.A. and Hong, J.S. (2013) *Preparation of rodent primary cultures for neuron-glia, mixed glia, enriched microglia, and reconstituted cultures with microglia,* Methods Mol.Biol., **1041,** 231-240.

Chen, W., Hu, G.Y., Zhou, Y.D. and Wu, C.P. (1994) *Two mechanisms underlying the induction of long-term potentiation in motor cortex of adult cat in vitro,* Exp.Brain Res., **100,** 149-154.

Chesselet, M.F. (2008) *In vivo alpha-synuclein overexpression in rodents: a useful model of Parkinson's disease?* Exp.Neurol., **209,** 22-27.

Chiappalone, M., Massobrio, P. and Martinoia, S. (2008) *Network plasticity in cortical assemblies,* Eur.J.Neurosci., **28,** 221-237.

Chiappalone, M., Bove, M., Vato, A., Tedesco, M. and Martinoia, S. (2006) *Dissociated cortical networks show spontaneously correlated activity patterns during in vitro development,* Brain Research, **1093,** 41-53.

Chiba, S., Iwasaki, Y., Sekino, H. and Suzuki, N. (2003) *Transplantation of motoneuron-enriched neural cells derived from mouse embryonic stem cells improves motor function of hemiplegic mice,* Cell Transplant., **12,** 457-468.

Choi, Y.,Jung, Chae,Sukyung, Kim, J.,Hun, Barald, K.,F., Park, J.,Yull and Lee,Sang-Hoon (2013a) *Neurotoxic amyloid beta oligomeric assemblies recreated in microfluidic platform with interstitial level of slow flow,* Scientific reports, **3,**

Choi, Y.J., Park, J. and Lee, S.H. (2013b) *Size-controllable networked neurospheres as a 3D neuronal tissue model for Alzheimer's disease studies,* Biomaterials, **34,** 2938-2946.

Chun, H.S., Gibson, G.E., DeGiorgio, L.A., Zhang, H., Kidd, V.J. and Son, J.H. (2001) *Dopaminergic cell death induced by MPP(+), oxidant and specific neurotoxicants shares the common molecular mechanism,* J.Neurochem., **76,** 1010-1021.

Cipriani, S., Bakshi, R. and Schwarzschild, M.A. (2014) *Protection by inosine in a cellular model of Parkinson's disease,* Neuroscience, **274,** 242-249.

Cohen, G. (1984) *Oxy-radical toxicity in catecholamine neurons,* Neurotoxicology, **5,** 77-82.

Cohen, G. (2000) *Oxidative stress, mitochondrial respiration, and Parkinson's disease,* Ann.N.Y.Acad.Sci., **899,** 112-120.

Cooke, M.J., Phillips, S.R., Shah, D.S., Athey, D., Lakey, J.H. and Przyborski, S.A. (2008) *Enhanced cell attachment using a novel cell culture surface presenting functional domains from extracellular matrix proteins,* Cytotechnology, **56,** 71-79.

Cooper, A.A., Gitler, A.D., Cashikar, A., Haynes, C.M., Hill, K.J., Bhullar, B., Liu, K., Xu, K., Strathearn, K.E., Liu, F., Cao, S., Caldwell, K.A., Caldwell, G.A., Marsischky, G., Kolodner, R.D., Labaer, J., Rochet, J.C., Bonini, N.M. and Lindquist, S. (2006) *Alpha-synuclein blocks ER-Golgi traffic and Rab1 rescues neuron loss in Parkinson's models,* Science, **313,** 324-328.

Cordero-Erausquin, M., Coull, J.A., Boudreau, D., Rolland, M. and De Koninck, Y. (2005) *Differential maturation of GABA action and anion reversal potential in spinal lamina I neurons: impact of chloride extrusion capacity,* J.Neurosci., **25,** 9613-9623.

Crittenden, J.R. and Graybiel, A.M. (2011) *Basal Ganglia disorders associated with imbalances in the striatal striosome and matrix compartments,* Front.Neuroanat., **5,** 59.

Crocetti, E., Trama, A., Stiller, C., Caldarella, A., Soffietti, R., Jaal, J., Weber, D.C., Ricardi, U., Slowinski, J., Brandes, A. and RARECARE working group (2012) *Epidemiology of glial and non-glial brain tumours in Europe,* Eur.J.Cancer, **48,** 1532-1542.

Cronin-Furman, E.N., Borland, M.K., Bergquist, K.E., Bennett, J.P.,Jr and Trimmer, P.A. (2013) *Mitochondrial quality, dynamics and functional capacity in Parkinson's disease cybrid cell lines selected for Lewy body expression,* Mol.Neurodegener, **8,** 6-1326-8-6.

Cummings, C.J., Sun, Y., Opal, P., Antalffy, B., Mestril, R., Orr, H.T., Dillmann, W.H. and Zoghbi, H.Y. (2001) *Over-expression of inducible HSP70 chaperone suppresses neuropathology and improves motor function in SCA1 mice,* Hum.Mol.Genet., **10,** 1511-1518.

Curtis, A.S., Casey, B., Gallagher, J.O., Pasqui, D., Wood, M.A. and Wilkinson, C.D. (2001) *Substratum nanotopography and the adhesion of biological cells. Are symmetry or regularity of nanotopography important?* Biophys.Chem., **94,** 275-283.

Datta, I., Ganapathy, K., Razdan, R. and Bhonde, R. (2018) *Location and Number of Astrocytes Determine Dopaminergic Neuron Survival and Function Under 6-OHDA Stress Mediated Through Differential BDNF Release,* Mol.Neurobiol., **55,** 5505-5525.

Dauer, W. and Przedborski, S. (2003) *Parkinson's disease: mechanisms and models,* Neuron, **39,** 889-909.

Daviaud, N., Garbayo, E., Lautram, N., Franconi, F., Lemaire, L., Perez-Pinzon, M. and Montero-Menei, C.N. (2014) *Modeling nigrostriatal degeneration in organotypic cultures, a new ex vivo model of Parkinson's disease,* Neuroscience, **256,** 10-22.

David, H.N. (2009) *Towards a reconceptualization of striatal interactions between glutamatergic and dopaminergic neurotransmission and their contribution to the production of movements,* Curr.Neuropharmacol., **7,** 132-141.

Deleglise, B., Magnifico, S., Duplus, E., Vaur, P., Soubeyre, V., Belle, M., Vignes, M., Viovy, J.L., Jacotot, E., Peyrin, J.M. and Brugg, B. (2014) *Beta-Amyloid Induces a Dying-Back Process and Remote Trans-Synaptic Alterations in a Microfluidic-Based Reconstructed Neuronal Network,* Acta Neuropathol.Commun., **2,** 145-014-0145-3.

Deligkaris, K., Bullmann, T. and Frey, U. (2016) *Extracellularly Recorded Somatic and Neuritic Signal Shapes and Classification Algorithms for High-Density Microelectrode Array Electrophysiology,* Front.Neurosci., **10,** 421.

Ding, J., Peterson, J.D. and Surmeier, D.J. (2008) *Corticostriatal and thalamostriatal synapses have distinctive properties,* J.Neurosci., **28,** 6483-6492.

Ding, S., Matta, S.G. and Zhou, F.M. (2011) *Kv3-like potassium channels are required for sustained high-frequency firing in basal ganglia output neurons,* J.Neurophysiol., **105,** 554-570.

Ding, Y.M., Jaumotte, J.D., Signore, A.P. and Zigmond, M.J. (2004) *Effects of 6-hydroxydopamine on primary cultures of substantia nigra: specific damage to dopamine neurons and the impact of glial cell line-derived neurotrophic factor,* J.Neurochem., **89,** 776-787.

Dipalo, M., Amin, H., Lovato, L., Moia, F., Caprettini, V., Messina, G.C., Tantussi, F., Berdondini, L. and De Angelis, F. (2017) *Intracellular and Extracellular Recording of Spontaneous Action Potentials in Mammalian Neurons and Cardiac Cells with 3D Plasmonic Nanoelectrodes,* Nano Lett., **17,** 3932-3939.

Domogatskaya, A., Rodin, S. and Tryggvason, K. (2012) *Functional diversity of laminins,* Annu.Rev.Cell Dev.Biol., **28,** 523-553.

Double, K.L. (2012) *Neuronal vulnerability in Parkinson's disease,* Parkinsonism Relat.Disord., **18 Suppl 1,** S52-4.

Douville, N.J., Zamankhan, P., Tung, Y.C., Li, R., Vaughan, B.L., Tai, C.F., White, J., Christensen, P.J., Grotberg, J.B. and Takayama, S. (2011) *Combination of fluid and solid mechanical stresses contribute to cell death and detachment in a microfluidic alveolar model,* Lab.Chip, **11,** 609-619.

Drachman, D.A. (2005) *Do we have brain to spare?* Neurology, **64,** 2004-2005.

Dranias, M.R., Ju, H., Rajaram, E. and VanDongen, A.M. (2013) *Short-term memory in networks of dissociated cortical neurons,* J.Neurosci., **33,** 1940-1953.

Dreyer, J.K., Herrik, K.F., Berg, R.W. and Hounsgaard, J.D. (2010) *Influence of phasic and tonic dopamine release on receptor activation,* J.Neurosci., **30,** 14273-14283.

Dubinsky, J.M. (1989) *Development of inhibitory synapses among striatal neurons in vitro,* J.Neurosci., **9,** 3955-3965.

Dunnett, S.B. and Bjorklund, A. (1992) *Neural Transplantation: A Practical Approach,* Practical Approach Series,

Durbeej, M. (2010) *Laminins,* Cell Tissue Res., **339,** 259-268.

Dworak, B.J. and Wheeler, B.C. (2009) *Novel MEA platform with PDMS microtunnels enables the detection of action potential propagation from isolated axons in culture,* Lab.Chip, **9,** 404-410.

Dzyubenko, E., Gottschling, C. and Faissner, A. (2016) *Neuron-Glia Interactions in Neural Plasticity: Contributions of Neural Extracellular Matrix and Perineuronal Nets,* Neural Plast., **2016,** 5214961.

E, M., A, P., A, G., Y, P., A, B., V, K., I, M. and M, D. (2015) *Microfluidic device for unidirectional axon growth,* Journal of physics, **643,**

Einevoll, G.T., Kayser, C., Logothetis, N.K. and Panzeri, S. (2013) *Modelling and analysis of local field potentials for studying the function of cortical circuits,* Nat.Rev.Neurosci., **14,** 770-785.

El Ayadi, A., Afailal, I. and Errami, M. (2001) *Effects of voltage-sensitive calcium channel blockers on extracellular dopamine levels in rat striatum,* Metab.Brain Dis., **16,** 121-131.

Ellens, D.J. and Leventhal, D.K. (2013) *Review: electrophysiology of basal ganglia and cortex in models of Parkinson disease,* J.Parkinsons Dis., **3,** 241-254.

Emborg, M.E. (2004) *Evaluation of animal models of Parkinson's disease for neuroprotective strategies,* J.Neurosci.Methods, **139,** 121-143.

Esch, M.B., King, T.L. and Shuler, M.L. (2011) *The role of body-on-a-chip devices in drug and toxicity studies,* Annu.Rev.Biomed.Eng., **13,** 55-72.

Esch, T., Lemmon, V. and Banker, G. (1999) *Local presentation of substrate molecules directs axon specification by cultured hippocampal neurons,* J.Neurosci., **19,** 6417-6426.

Eytan, D., Brenner, N. and Marom, S. (2003) *Selective adaptation in networks of cortical neurons,* J.Neurosci., **23,** 9349-9356.

Faisal, A.A., Selen, L.P. and Wolpert, D.M. (2008) *Noise in the nervous system,* Nat.Rev.Neurosci., **9,** 292-303.

Falkenburger, B.H., Saridaki, T. and Dinter, E. (2016) *Cellular models for Parkinson's disease,* J.Neurochem., **139 Suppl 1,** 121-130.

Fan, K.Y., Baufreton, J., Surmeier, D.J., Chan, C.S. and Bevan, M.D. (2012) *Proliferation of external globus pallidus-subthalamic nucleus synapses following degeneration of midbrain dopamine neurons,* J.Neurosci., **32,** 13718-13728.

Fauth, M. and Tetzlaff, C. (2016) *Opposing Effects of Neuronal Activity on Structural Plasticity,* Front.Neuroanat., **10,** 75.

Fedoroff, S. and Richardson, A. (2001) *Protocols for Neural Cell Culture,* Humana Press Totowa, **3,**

Fejtl,Michael, Stett,Alfred, Nisch,Wilfried, Boven,Karl-Heinz and Moller,Andreas (2006) *On Micro-Electrode Array Revival: Its Development, Sophistication of Recording, and Stimulation,* Advances in Network Electrophysiology, 24-37.

Filograna, R., Beltramini, M., Bubacco, L. and Bisaglia, M. (2016) *Anti-Oxidants in Parkinson's Disease Therapy: A Critical Point of View,* Curr.Neuropharmacol., **14,** 260-271.

Flandin, P., Kimura, S. and Rubenstein, J.L. (2010) *The progenitor zone of the ventral medial ganglionic eminence requires Nkx2-1 to generate most of the globus pallidus but few neocortical interneurons,* J.Neurosci., **30,** 2812-2823.

Fleming, S.M., Fernagut, P.O. and Chesselet, M.F. (2005) *Genetic mouse models of parkinsonism: strengths and limitations,* NeuroRx, **2,** 495-503.

Fleming, S.M., Salcedo, J., Fernagut, P.O., Rockenstein, E., Masliah, E., Levine, M.S. and Chesselet, M.F. (2004) *Early and progressive sensorimotor anomalies in mice overexpressing wild-type human alpha-synuclein,* J.Neurosci., **24,** 9434-9440.

Ford, C.P., Gantz, S.C., Phillips, P.E. and Williams, J.T. (2010) *Control of extracellular dopamine at dendrite and axon terminals,* J.Neurosci., **30,** 6975-6983.

Francisco, H., Yellen, B.B., Halverson, D.S., Friedman, G. and Gallo, G. (2007) *Regulation of axon guidance and extension by three-dimensional constraints,* Biomaterials, **28,** 3398-3407.

Franz, D., Olsen, H.L., Klink, O. and Gimsa, J. (2017) *Automated and manual patch clamp data of human induced pluripotent stem cell-derived dopaminergic neurons,* Sci.Data, **4,** 170056.

Frega,Monica, Tedesco,Mariateresa, Massobrio,Paolo, Pesce,Mattia and Martinoia,Sergio (2014a) *Network dynamics of 3D engineered neuronal cultures: a new experimental model for in-vitro electrophysiology,* Scientific reports, **4,**

Frega, M., Tedesco, M., Massobrio, P., Pesce, M. and Martinoia, S. (2014b) *Network dynamics of 3D engineered neuronal cultures: a new experimental model for in-vitro electrophysiology,* Sci.Rep., **4,** 5489.

Freire, E., Gomes, F.C., Linden, R., Neto, V.M. and Coelho-Sampaio, T. (2002) *Structure of laminin substrate modulates cellular signaling for neuritogenesis,* J.Cell.Sci., **115,** 4867-4876.

Frischknecht, R. and Gundelfinger, E.D. (2012) *The brain's extracellular matrix and its role in synaptic plasticity,* Adv.Exp.Med.Biol., **970,** 153-171.

Fujiyama, F., Sohn, J., Nakano, T., Furuta, T., Nakamura, K.C., Matsuda, W. and Kaneko, T. (2011) *Exclusive and common targets of neostriatofugal projections of rat striosome neurons: a single neuron-tracing study using a viral vector,* Eur.J.Neurosci., **33,** 668-677.

Gage, G.J., Stoetzner, C.R., Wiltschko, A.B. and Berke, J.D. (2010) *Selective activation of striatal fast-spiking interneurons during choice execution,* Neuron, **67,** 466-479.

Gallo, V., Pende, M., Scherer, S., Molne, M. and Wright, P. (1995) *Expression and regulation of kainate and AMPA receptors in uncommitted and committed neural progenitors,* Neurochem.Res., **20,** 549-560.

Ganguly, K., Schinder, A.F., Wong, S.T. and Poo, M. (2001) *GABA itself promotes the developmental switch of neuronal GABAergic responses from excitation to inhibition,* Cell, **105,** 521-532.

Gao, J., Kim, Y.M., Coe, H., Zern, B., Sheppard, B. and Wang, Y. (2006) *A neuroinductive biomaterial based on dopamine,* Proceedings of the National Academy of Sciences, **103,** 16681-16686.

Gao, Y., Majumdar, D., Jovanovic, B., Shaifer, C., Lin, P.C., Zijlstra, A., Webb, D.J. and Li, D. (2011) *A versatile valve-enabled microfluidic cell co-culture platform and demonstration of its applications to neurobiology and cancer biology,* Biomed.Microdevices, **13,** 539-548.

Garza, J.M., Jessel, N., Ladam, G., Dupray, V., Muller, S., Stoltz, J.F., Schaaf, P., Voegel, J.C. and Lavalle, P. (2005) *Polyelectrolyte multilayers and degradable polymer layers as multicompartment films,* Langmuir, **21,** 12372-12377.

Gates, M.A., Coupe, V.M., Torres, E.M., Fricker-Gates, R.A. and Dunnett, S.B. (2004) *Spatially and temporally restricted chemoattractive and chemorepulsive cues direct the formation of the nigro-striatal circuit,* Eur.J.Neurosci., **19,** 831-844.

Gates, M.A., Torres, E.M., White, A., Fricker-Gates, R.A. and Dunnett, S.B. (2006) *Re-examining the ontogeny of substantia nigra dopamine neurons,* Eur.J.Neurosci., **23,** 1384-1390.

Gelman, D.M. and Marin, O. (2010) *Generation of interneuron diversity in the mouse cerebral cortex,* Eur.J.Neurosci., **31,** 2136-2141.

Gerfen, C.R. and Surmeier, D.J. (2011) *Modulation of striatal projection systems by dopamine,* Annu.Rev.Neurosci., **34,** 441-466.

Gerlach, M., Riederer, P. and Double, K.L. (2008) *Neuromelanin-bound ferric iron as an experimental model of dopaminergic neurodegeneration in Parkinson's disease,* Parkinsonism Relat.Disord., **14 Suppl 2,** S185-8.

Ghatak, S., Trudler, D., Dolatabadi, N. and Ambasudhan, R. (2018) *Parkinson's disease: what the model systems have taught us so far,* J.Genet., **97,** 729-751.

Giasson, B.I., Duda, J.E., Murray, I.V., Chen, Q., Souza, J.M., Hurtig, H.I., Ischiropoulos, H., Trojanowski, J.Q. and Lee, V.M. (2000) *Oxidative damage linked to neurodegeneration by selective alpha-synuclein nitration in synucleinopathy lesions,* Science, **290,** 985-989.

Giasson, B.I., Duda, J.E., Quinn, S.M., Zhang, B., Trojanowski, J.Q. and Lee, V.M. (2002) *Neuronal alpha-synucleinopathy with severe movement disorder in mice expressing A53T human alpha-synuclein,* Neuron, **34,** 521-533.

Gittis, A.H., Berke, J.D., Bevan, M.D., Chan, C.S., Mallet, N., Morrow, M.M. and Schmidt, R. (2014) *New roles for the external globus pallidus in basal ganglia circuits and behavior,* J.Neurosci., **34,** 15178-15183.

Gold, C., Henze, D.A., Koch, C. and Buzsaki, G. (2006) *On the origin of the extracellular action potential waveform: A modeling study,* J.Neurophysiol., **95,** 3113-3128.

Goldenberg, M.M. (2012) *Multiple sclerosis review,* P.T., **37,** 175-184.

Gonzalez-Burgos, G. and Lewis, D.A. (2012) *NMDA receptor hypofunction, parvalbumin-positive neurons, and cortical gamma oscillations in schizophrenia,* Schizophr.Bull., **38,** 950-957.

Gordon, J.K. and McKinlay, J. (2012) *Physiological changes after brain stem death and management of the heart-beating donor,* Continuing Education in Anaesthesia, Critical Care & Pain,

Goyal,Gaurav and Nam,Yoonkey (2011) *Neuronal micro-culture engineering by microchannel devices of cellular scale dimensions,* Biomedical Engineering Letters, **1,** 89-98.

Grace, A.A. and Bunney, B.S. (1983) *Intracellular and extracellular electrophysiology of nigral dopaminergic neurons--2. Action potential generating mechanisms and morphological correlates,* Neuroscience, **10,** 317-331.

Gramowski, A., Jugelt, K., Stuwe, S., Schulze, R., McGregor, G.P., Wartenberg-Demand, A., Loock, J., Schroder, O. and Weiss, D.G. (2006) *Functional screening of traditional antidepressants with primary cortical neuronal networks grown on multielectrode neurochips,* Eur.J.Neurosci., **24,** 455-465.

Gramowski, A., Jugelt, K., Weiss, D.G. and Gross, G.W. (2004) *Substance identification by quantitative characterization of oscillatory activity in murine spinal cord networks on microelectrode arrays,* Eur.J.Neurosci., **19,** 2815-2825.

Griggs, A.M., Agim, Z.S., Mishra, V.R., Tambe, M.A., Director-Myska, A.E., Turteltaub, K.W., McCabe, G.P., Rochet, J.C. and Cannon, J.R. (2014) *2-Amino-1-methyl-6-phenylimidazo[4,5-b]pyridine (PhIP) is selectively toxic to primary dopaminergic neurons in vitro,* Toxicol.Sci., **140,** 179-189.

Gross, G.W., Rieske, E., Kreutzberg, G.W. and Meyer, A. (1977) *A new fixed-array multi-microelectrode system designed for long-term monitoring of extracellular single unit neuronal activity in vitro,* Neurosci.Lett., **6,** 101-105.

Guzman, J.N., Sanchez-Padilla, J., Chan, C.S. and Surmeier, D.J. (2009) *Robust pacemaking in substantia nigra dopaminergic neurons,* J.Neurosci., **29,** 11011-11019.

Guzman, J.N., Sanchez-Padilla, J., Wokosin, D., Kondapalli, J., Ilijic, E., Schumacker, P.T. and Surmeier, D.J. (2010) *Oxidant stress evoked by pacemaking in dopaminergic neurons is attenuated by DJ-1,* Nature, **468,** 696-700.

Haber, S.N. (2016) *Corticostriatal circuitry,* Dialogues Clin.Neurosci., **18,** 7-21.

Habibey, R., Golabchi, A., Latifi, S., Difato, F. and Blau, A. (2015) *A microchannel device tailored to laser axotomy and long-term microelectrode array electrophysiology of functional regeneration,* Lab.Chip, **15,** 4578-4590.

Hague, S.M., Klaffke, S. and Bandmann, O. (2005) *Neurodegenerative disorders: Parkinson's disease and Huntington's disease,* J.Neurol.Neurosurg.Psychiatry., **76,** 1058-1063.

Halassa, M.M., Fellin, T., Takano, H., Dong, J.H. and Haydon, P.G. (2007) *Synaptic islands defined by the territory of a single astrocyte,* J.Neurosci., **27,** 6473-6477.

Hales, C.,M., Rolston, J.,D. and Potter, S.,M. (2010) *How to Culture, Record and Stimulate Neuronal Networks on Micro-electrode Arrays (MEAs),* Journal of visualized experiments : JoVE, **39,**

Hanrott, K., Gudmunsen, L., O'Neill, M.J. and Wonnacott, S. (2006) *6-hydroxydopamine-induced apoptosis is mediated via extracellular auto-oxidation and caspase 3-dependent activation of protein kinase Cdelta,* J.Biol.Chem., **281,** 5373-5382.

Harrington, A.J., Hamamichi, S., Caldwell, G.A. and Caldwell, K.A. (2010) *C. elegans as a model organism to investigate molecular pathways involved with Parkinson's disease,* Dev.Dyn., **239,** 1282-1295.

Harris,Joseph, Lee,Hyuna, Vahidi,Behrad, Tu,Christina, Cribbs,David, Jeon, N.,Li and Cotman,Carl (2007) *Fabrication of a Microfluidic Device for the Compartmentalization of Neuron Soma and Axons,*

Hartfield, E.M., Yamasaki-Mann, M., Ribeiro Fernandes, H.J., Vowles, J., James, W.S., Cowley, S.A. and Wade-Martins, R. (2014) *Physiological characterisation of human iPS-derived dopaminergic neurons,* PLoS One, **9,** e87388.

Hasan, F.,Md. and Berdichevsky, Y. (2016) *Neural Circuits on a Chip,* Micromachines, **7,** 157.

Hatanaka, Y. and Murakami, F. (2002) *In vitro analysis of the origin, migratory behavior, and maturation of cortical pyramidal cells,* J.Comp.Neurol., **454,** 1-14.

Hattori, S., Suzurikawa, J., Kanzaki, R., Jimbo, Y., Hamaguchi, T., Takahashi, H. and Nakao, M. (2010) *Direction control of information transfer between neuronal populations with asymmetric three-dimensional microstructure.* Electon. Comm Jpn., **93,** 17-25.

Hausser, M., Stuart, G., Racca, C. and Sakmann, B. (1995) *Axonal initiation and active dendritic propagation of action potentials in substantia nigra neurons,* Neuron, **15,** 637-647.

Hegarty, S.V., Sullivan, A.M. and O'Keeffe, G.W. (2013) *Midbrain dopaminergic neurons: a review of the molecular circuitry that regulates their development,* Dev.Biol., **379,** 123-138.

Heikkilä, T.J., Ylä-Outinen, L., Tanskanen, J.M.A., Lappalainen, R.S., Skottman, H., Suuronen, R., Mikkonen, J.E., Hyttinen, J.A.K. and Narkilahti, S. (2009) *Human embryonic stem cell-derived neuronal cells form spontaneously active neuronal networks in vitro,* Exp.Neurol., **218,** 109-116.

Henning, J., Strauss, U., Wree, A., Gimsa, J., Rolfs, A., Benecke, R. and Gimsa, U. (2008) *Differential astroglial activation in 6-hydroxydopamine models of Parkinson's disease,* Neurosci.Res., **62,** 246-253.

Henze, D.A., Borhegyi, Z., Csicsvari, J., Mamiya, A., Harris, K.D. and Buzsaki, G. (2000) *Intracellular features predicted by extracellular recordings in the hippocampus in vivo,* J.Neurophysiol., **84,** 390-400.

Herculano-Houzel,Suzana (2009) *The human brain in numbers: a linearly scaled-up primate brain,* Front. Hum. Neurosci.,

Hernan, M.A., Takkouche, B., Caamano-Isorna, F. and Gestal-Otero, J.J. (2002) *A meta-analysis of coffee drinking, cigarette smoking, and the risk of Parkinson's disease,* Ann.Neurol., **52,** 276-284.

Hernandez-Baltazar, D., Zavala-Flores, L.M. and Villanueva-Olivo, A. (2015) *The 6-hydroxydopamine model and parkinsonian pathophysiology: Novel findings in an older model,* Neurologia,

Hernandez-Baltazar, D., Zavala-Flores, L.M. and Villanueva-Olivo, A. (2017) *The 6-hydroxydopamine model and parkinsonian pathophysiology: Novel findings in an older model,* Neurologia, **32,** 533-539.

Hirsch, E.C., Faucheux, B., Damier, P., Mouatt-Prigent, A. and Agid, Y. (1997) *Neuronal vulnerability in Parkinson's disease,* J.Neural Transm.Suppl., **50,** 79-88.

Hodgkin, A.L. and Huxley, A.F. (1939) *Action Potentials Recorded from Inside a Nerve Fibre,* Nature, **144,** 710-711.

Hogberg, H.T., Sobanski, T., Novellino, A., Whelan, M., Weiss, D.G. and Bal-Price, A.K. (2011) *Application of micro-electrode arrays (MEAs) as an emerging technology for developmental neurotoxicity: evaluation of domoic acid-induced effects in primary cultures of rat cortical neurons,* Neurotoxicology, **32,** 158-168.

Holmgren, N. (1925) *Points of view concerning fore-brain morphology in higher vertebrates,* Acta Zoologica, **6,** 413-459.

Honegger, T., Thielen, M.I., Feizi, S., Sanjana, N.E. and Voldman, J. (2016) *Microfluidic neurite guidance to study structure-function relationships in topologically-complex population-based neural networks,* Sci.Rep., **6,** 28384.

Hong, N., Joo, S. and Nam, Y. (2017a) *Characterization of Axonal Spikes in Cultured Neuronal Networks Using Microelectrode Arrays and Microchannel Devices,* IEEE Transactions on Biomedical Engineering, **64,** 492-498.

Hong, S., Jhou, T., Smith, M., Saleem, K. and Hikosaka, O. (2011) *Negative Reward Signals from the Lateral Habenula to Dopamine Neurons Are Mediated by Rostromedial Tegmental Nucleus in Primates,* Journal of Neuroscience, **31,** 11457-11471.

Hong, N., Joo, S. and Nam, Y. (2017b) *Characterization of Axonal Spikes in Cultured Neuronal Networks Using Microelectrode Arrays and Microchannel Devices,* IEEE Trans.Biomed.Eng., **64,** 492-498.

Horn, A., Ostwald, D., Reisert, M. and Blankenburg, F. (2014) *The structural-functional connectome and the default mode network of the human brain,* Neuroimage, **102 Pt 1,** 142-151.

Horner, P.J. and Gage, F.H. (2000) *Regenerating the damaged central nervous system,* Nature, **407,** 963-970.

Hosmane, S., Fournier, A., Wright, R., Rajbhandari, L., Siddique, R., Yang, I.H., Ramesh, K.T., Venkatesan, A. and Thakor, N. (2011) *Valve-based microfluidic compression platform: single axon injury and regrowth,* Lab.Chip, **11,** 3888-3895.

Huang, Y. and Wang, J. (2016) *Primary Neuron-glia Culture from Rat Cortex as a Model to Study Neuroinflammation in CNS Injuries or Diseases,* Bio-protocol, **8,** e1788.

Huang, C.P., Lu, J., Seon, H., Lee, A.P., Flanagan, L.A., Kim, H.Y., Putnam, A.J. and Jeon, N.L. (2009) *Engineering microscale cellular niches for three-dimensional multicellular co-cultures,* Lab.Chip, **9,** 1740-1748.

Huh, D., Hamilton, G.A. and Ingber, D.E. (2011) *From 3D cell culture to organs-on-chips,* Trends Cell Biol., **21,** 745-754.

Hutson, C.B., Lazo, C.R., Mortazavi, F., Giza, C.C., Hovda, D. and Chesselet, M.F. (2011) *Traumatic brain injury in adult rats causes progressive nigrostriatal dopaminergic cell loss and enhanced vulnerability to the pesticide paraquat,* J.Neurotrauma, **28,** 1783-1801.

Hynds, D.L. and Snow, D.M. (1999) *Neurite outgrowth inhibition by chondroitin sulfate proteoglycan: stalling/stopping exceeds turning in human neuroblastoma growth cones,* Exp.Neurol., **160,** 244-255.

Ichikawa, M., Muramoto, K., Kobayashi, K., Kawahara, M. and Kuroda, Y. (1993) *Formation and maturation of synapses in primary cultures of rat cerebral cortical cells: an electron microscopic study,* Neurosci.Res., **16,** 95-103.

Imura, Y., Asano, Y., Sato, K. and Yoshimura, E. (2009) *A microfluidic system to evaluate intestinal absorption,* Anal.Sci., **25,** 1403-1407.

Iravani, M.M., Syed, E., Jackson, M.J., Johnston, L.C., Smith, L.A. and Jenner, P. (2005) *A modified MPTP treatment regime produces reproducible partial nigrostriatal lesions in common marmosets,* Eur.J.Neurosci., **21,** 841-854.

Israel, Z., Burchiel, K.J. and Heinricher, M.M. (2011) *Principles of extracellular single-unit recording,* Microelectrode Recording in Movement Disorder Surgery, **3,** 8-14.

Ito, D., Komatsu, T. and Gohara, K. (2013) *Measurement of saturation processes in glutamatergic and GABAergic synapse densities during long-term development of cultured rat cortical networks,* Brain Res., **1534,** 22-32.

Ivins, K.J., Bui, E.T. and Cotman, C.W. (1998) *Beta-amyloid induces local neurite degeneration in cultured hippocampal neurons: evidence for neuritic apoptosis,* Neurobiol.Dis., **5,** 365-378.

Jackson-Lewis, V., Blesa, J. and Przedborski, S. (2012) *Animal models of Parkinson's disease,* Parkinsonism Relat.Disord., **18 Suppl 1,** S183-5.

Jahanshahi, M., Obeso, I., Baunez, C., Alegre, M. and Krack, P. (2015) *Parkinson's disease, the subthalamic nucleus, inhibition, and impulsivity,* Mov.Disord., **30,** 128-140.

Jang, K.J. and Suh, K.Y. (2010) *A multi-layer microfluidic device for efficient culture and analysis of renal tubular cells,* Lab.Chip, **10,** 36-42.

Jankovic, J. (2008) *Parkinson's disease: clinical features and diagnosis,* J.Neurol.Neurosurg.Psychiatry., **79,** 368-376.

Jellinger, K., Linert, L., Kienzl, E., Herlinger, E. and Youdim, M.B. (1995) *Chemical evidence for 6-hydroxydopamine to be an endogenous toxic factor in the pathogenesis of Parkinson's disease,* J.Neural Transm.Suppl., **46,** 297-314.

Jenkinson, N. and Brown, P. (2011) *New insights into the relationship between dopamine, beta oscillations and motor function,* Trends Neurosci., **34,** 611-618.

Jenner, P., Schapira, A.H. and Marsden, C.D. (1992) *New insights into the cause of Parkinson's disease,* Neurology, **42,** 2241-2250.

Jeong, J.H., Song, S.H., Lim, D.W., Lee, H. and Park, T.G. (2001) *DNA transfection using linear poly(ethylenimine) prepared by controlled acid hydrolysis of poly(2-ethyl-2-oxazoline),* J.Control.Release, **73,** 391-399.

Jimbo, Y. (2007) *MEA-based recording of neuronal activity in vitro,* Arch.Ital.Biol., **145,** 289-297.

Jing, G., Yao, Y., Gnerlich, M., Perry, S. and Tatic-Lucic, S. (2009) *Towards a multi-electrode array (MEA) system for patterned neural networks,* Procedia Chemistry, **1,** 329-332.

Jo, J., Xiao, Y., Sun, A.X., Cukuroglu, E., Tran, H.D., Goke, J., Tan, Z.Y., Saw, T.Y., Tan, C.P., Lokman, H., Lee, Y., Kim, D., Ko, H.S., Kim, S.O., Park, J.H., Cho, N.J., Hyde, T.M., Kleinman, J.E., Shin, J.H., Weinberger, D.R., Tan, E.K., Je, H.S. and Ng, H.H. (2016) *Midbrain-like Organoids from Human Pluripotent Stem Cells Contain Functional Dopaminergic and Neuromelanin-Producing Neurons,* Cell.Stem Cell., **19,** 248-257.

Jokinen, V., Sakha, P., Suvanto, P., Rivera, C., Franssila, S., Lauri, S.E. and Huttunen, H.J. (2013) *A microfluidic chip for axonal isolation and electrophysiological measurements,* J.Neurosci.Methods, **212,** 276-282.

Kadoshima, T., Sakaguchi, H., Nakano, T., Soen, M., Ando, S., Eiraku, M. and Sasai, Y. (2013) *Self-organization of axial polarity, inside-out layer pattern, and species-specific progenitor dynamics in human ES cell-derived neocortex,* Proc.Natl.Acad.Sci.U.S.A., **110,** 20284-20289.

Kahle, P.J., Haass, C., Kretzschmar, H.A. and Neumann, M. (2002) *Structure/function of alpha-synuclein in health and disease: rational development of animal models for Parkinson's and related diseases,* J.Neurochem., **82,** 449-457.

Kam, L., Shain, W., Turner, J.N. and Bizios, R. (2001) *Axonal outgrowth of hippocampal neurons on micro-scale networks of polylysine-conjugated laminin,* Biomaterials, **22,** 1049-1054.

Kamudzandu, M. (2015) *Fabrication of functional basal ganglia circuitry in vitro: from nano- and micro-scale topographies to microfluidic devices,* Keele University, http://eprints.keele.ac.uk/2380/.

Kanagasabapathi, T.,T., Franco,Maria, Barone, R.,Andrea, Martinoia,Sergio, Wadman, W.,J. and DecrÃ©, M.,M.J. (2013) *Selective pharmacological manipulation of cortical–thalamic co-cultures in a dual-compartment device,* Journal of neuroscience methods, **214,**

Kanagasabapathi, T.T., Ciliberti, D., Martinoia, S., Wadman, W.J. and Decre, M.M. (2011) *Dual-compartment neurofluidic system for electrophysiological measurements in physically segregated and functionally connected neuronal cell culture,* Front.Neuroeng, **4,** 13.

Kanagasabapathi, T.T., Massobrio, P., Barone, R.A., Tedesco, M., Martinoia, S., Wadman, W.J. and Decre, M.M. (2012) *Functional connectivity and dynamics of cortical-thalamic networks co-cultured in a dual compartment device,* J.Neural Eng., **9,** 036010-2560/9/3/036010. Epub 2012 May 22.

Kanagasabapathi, T.T., Wang, K., Mellace, M., Ramakers, G.J. and Decre, M.M. (2009) *Dual compartment neurofluidic system for electrophysiological measurements in physically isolated neuronal cell cultures,* Conf.Proc.IEEE Eng.Med.Biol.Soc., **2009,** 1655-1658.

Kandler, K. and Friauf, E. (1995) *Development of glycinergic and glutamatergic synaptic transmission in the auditory brainstem of perinatal rats,* J.Neurosci., **15,** 6890-6904.

Kartalov, E.P., Anderson, W.F. and Scherer, A. (2006) *The analytical approach to polydimethylsiloxane microfluidic technology and its biological applications,* J.Nanosci Nanotechnol, **6,** 2265-2277.

Kearns, S.M., Scheffler, B., Goetz, A.K., Lin, D.D., Baker, H.D., Roper, S.N., Mandel, R.J. and Steindler, D.A. (2006) *A method for a more complete in vitro Parkinson's model: slice culture bioassay for modeling maintenance and repair of the nigrostriatal circuit,* J.Neurosci.Methods, **157,** 1-9.

Keefer, E.W., Gramowski, A. and Gross, G.W. (2001) *NMDA receptor-dependent periodic oscillations in cultured spinal cord networks,* J.Neurophysiol., **86,** 3030-3042.

Kelly, E.J., Wang, Z., Voellinger, J.L., Yeung, C.K., Shen, D.D., Thummel, K.E., Zheng, Y., Ligresti, G., Eaton, D.L., Muczynski, K.A., Duffield, J.S., Neumann, T., Tourovskaia, A., Fauver, M., Kramer, G., Asp, E. and Himmelfarb, J. (2013) *Innovations in preclinical biology: ex vivo engineering of a human kidney tissue microperfusion system,* Stem Cell.Res.Ther., **4 Suppl 1,** S17.

Khalilov, I., Dzhala, V., Ben-Ari, Y. and Khazipov, R. (1999) *Dual role of GABA in the neonatal rat hippocampus,* Dev.Neurosci., **21,** 310-319.

Khazipov, R., Khalilov, I., Tyzio, R., Morozova, E., Ben-Ari, Y. and Holmes, G.L. (2004) *Developmental changes in GABAergic actions and seizure susceptibility in the rat hippocampus,* Eur.J.Neurosci., **19,** 590-600.

Khibnik, L.A., Tritsch, N.X. and Sabatini, B.L. (2014) *A direct projection from mouse primary visual cortex to dorsomedial striatum,* PLoS One, **9,** e104501.

Kikuchi, T., Morizane, A., Doi, D., Onoe, H., Hayashi, T., Kawasaki, T., Saiki, H., Miyamoto, S. and Takahashi, J. (2011) *Survival of human induced pluripotent stem cell-derived midbrain dopaminergic neurons in the brain of a primate model of Parkinson's disease,* J.Parkinsons Dis., **1,** 395-412.

Kim, Y.H., Kim, Y.E., Chung, S., Kim, B., Kim, T.S. and Kang, J.Y. (2011) *Three dimensional co-culture of neuron and astrocyte in microfluidic device,* 15th International Conference on Miniaturized Systems for Chemistry and Life Sciences,

Kim, H.F. and Hikosaka, O. (2015) *Parallel basal ganglia circuits for voluntary and automatic behaviour to reach rewards,* Brain, **138,** 1776-1800.

Kim, H.G., Ju, M.S., Kim, D.H., Hong, J., Cho, S.H., Cho, K.H., Park, W., Lee, E.H., Kim, S.Y. and Oh, M.S. (2010) *Protective effects of Chunghyuldan against ROS-mediated neuronal cell death in models of Parkinson's disease,* Basic Clin.Pharmacol.Toxicol., **107,** 958-964.

Kim, J., Kang, M., Jensen, E.C. and Mathies, R.A. (2012) *Lifting gate polydimethylsiloxane microvalves and pumps for microfluidic control,* Anal.Chem., **84,** 2067-2071.

Kita, H. (2007) *Globus pallidus external segment,* Prog.Brain Res., **160,** 111-133.

Klein, E.A., Yin, L., Kothapalli, D., Castagnino, P., Byfield, F.J., Xu, T., Levental, I., Hawthorne, E., Janmey, P.A. and Assoian, R.K. (2009) *Cell-cycle control by physiological matrix elasticity and in vivo tissue stiffening,* Curr.Biol., **19,** 1511-1518.

Kleinfeld, D., Kahler, K. and Hockberger, P. (1988) *Controlled outgrowth of dissociated neurons on patterned substrates,* The Journal Of Neuroscience, **11,** 4098-4120.

Kliem, M.A., Maidment, N.T., Ackerson, L.C., Chen, S., Smith, Y. and Wichmann, T. (2007) *Activation of nigral and pallidal dopamine D1-like receptors modulates basal ganglia outflow in monkeys,* J.Neurophysiol., **98,** 1489-1500.

Kliem, M.A., Pare, J.F., Khan, Z.U., Wichmann, T. and Smith, Y. (2010) *Ultrastructural localization and function of dopamine D1-like receptors in the substantia nigra pars reticulata and the internal segment of the globus pallidus of parkinsonian monkeys,* Eur.J.Neurosci., **31,** 836-851.

Koralek, A.C., Jin, X., Long, J.D.,2nd, Costa, R.M. and Carmena, J.M. (2012) *Corticostriatal plasticity is necessary for learning intentional neuroprosthetic skills,* Nature, **483,** 331-335.

Korchounov, A., Meyer, M.F. and Krasnianski, M. (2010) *Postsynaptic nigrostriatal dopamine receptors and their role in movement regulation,* J.Neural Transm.(Vienna), **117,** 1359-1369.

Kozorovitskiy, Y., Peixoto, R., Wang, W., Saunders, A. and Sabatini, B.L. (2015) *Neuromodulation of excitatory synaptogenesis in striatal development,* Elife, **4,** 10.7554/eLife.10111.

Kramer, B.C., Goldman, A.D. and Mytilineou, C. (1999) *Glial cell line derived neurotrophic factor promotes the recovery of dopamine neurons damaged by 6-hydroxydopamine in vitro,* Brain Res., **851,** 221-227.

Kunze, A., Lengacher, S., Dirren, E., Aebischer, P., Magistretti, P.J. and Renaud, P. (2013) *Astrocyte-neuron co-culture on microchips based on the model of SOD mutation to mimic ALS,* Integr.Biol.(Camb), **5,** 964-975.

Kupchik, Y.M., Brown, R.M., Heinsbroek, J.A., Lobo, M.K., Schwartz, D.J. and Kalivas, P.W. (2015) *Coding the direct/indirect pathways by D1 and D2 receptors is not valid for accumbens projections,* Nat.Neurosci., **18,** 1230-1232.

Kuter, K., Olech, L. and Glowacka, U. (2018) *Prolonged Dysfunction of Astrocytes and Activation of Microglia Accelerate Degeneration of Dopaminergic Neurons in the Rat Substantia Nigra and Block Compensation of Early Motor Dysfunction Induced by 6-OHDA,* Mol.Neurobiol., **55,** 3049-3066.

Kyrozis, A., Chudomel, O., Moshe, S.L. and Galanopoulou, A.S. (2006) *Sex-dependent maturation of GABAA receptor-mediated synaptic events in rat substantia nigra reticulata,* Neurosci.Lett., **398,** 1-5.

Laight, D. (2013) *Overview of peripheral nervous system pharmacology,* Nurse Prescribing,

Lakard, S., Herlem, G., Propper, A., Kastner, A., Michel, G., Valles-Villarreal, N., Gharbi, T. and Fahys, B. (2004) *Adhesion and proliferation of cells on new polymers modified biomaterials,* Bioelectrochemistry, **62,** 19-27.

Lalanne, T., Abrahamsson, T. and Sjostrom, P.J. (2016) *Using Multiple Whole-Cell Recordings to Study Spike-Timing-Dependent Plasticity in Acute Neocortical Slices,* Cold Spring Harb Protoc., **2016,** 10.1101/pdb.prot091306.

Lancaster, M.A., Renner, M., Martin, C.A., Wenzel, D., Bicknell, L.S., Hurles, M.E., Homfray, T., Penninger, J.M., Jackson, A.P. and Knoblich, J.A. (2013) *Cerebral organoids model human brain development and microcephaly,* Nature, **501,** 373-379.

Langston, J.W., Ballard, P., Tetrud, J.W. and Irwin, I. (1983) *Chronic Parkinsonism in humans due to a product of meperidine-analog synthesis,* Science, **219,** 979-980.

Langston, J.W., Forno, L.S., Tetrud, J., Reeves, A.G., Kaplan, J.A. and Karluk, D. (1999) *Evidence of active nerve cell degeneration in the substantia nigra of humans years after 1-methyl-4-phenyl-1,2,3,6-tetrahydropyridine exposure,* Ann.Neurol., **46,** 598-605.

Lantoine, J., Grevesse, T., Villers, A., Delhaye, G., Mestdagh, C., Versaevel, M., Mohammed, D., Bruyere, C., Alaimo, L., Lacour, S.P., Ris, L. and Gabriele, S. (2016) *Matrix stiffness modulates formation and activity of neuronal networks of controlled architectures,* Biomaterials, **89,** 14-24.

Lauder, J.M. (1993) *Neurotransmitters as growth regulatory signals: role of receptors and second messengers,* Trends Neurosci., **16,** 233-240.

Lavdas, A.A., Grigoriou, M., Pachnis, V. and Parnavelas, J.G. (1999) *The medial ganglionic eminence gives rise to a population of early neurons in the developing cerebral cortex,* J.Neurosci., **19,** 7881-7888.

Lazaro, D.F., Pavlou, M.A.S. and Outeiro, T.F. (2017) *Cellular models as tools for the study of the role of alpha-synuclein in Parkinson's disease,* Exp.Neurol., **298,** 162-171.

le Feber, J., Postma, W., de Weerd, E., Weusthof, M. and Rutten, W.L. (2015) *Barbed channels enhance unidirectional connectivity between neuronal networks cultured on multi electrode arrays,* Front.Neurosci., **9,** 412.

Lee, C.R., Witkovsky, P. and Rice, M.E. (2011) *Regulation of Substantia Nigra Pars Reticulata GABAergic Neuron Activity by H(2)O(2) via Flufenamic Acid-Sensitive Channels and K(ATP) Channels,* Front.Syst.Neurosci., **5,** 14.

Lees, A.J. (2007) *Unresolved issues relating to the shaking palsy on the celebration of James Parkinson's 250th birthday,* Mov.Disord., **22 Suppl 17,** S327-34.

Lei, W., Jiao, Y., Del Mar, N. and Reiner, A. (2004) *Evidence for differential cortical input to direct pathway versus indirect pathway striatal projection neurons in rats,* J.Neurosci., **24,** 8289-8299.

Lelong, I.H., Petegnief, V. and Rebel, G. (1992) *Neuronal cells mature faster on polyethyleneimine coated plates than on polylysine coated plates,* J.Neurosci.Res., **32,** 562-568.

Leonzino, M., Busnelli, M., Antonucci, F., Verderio, C., Mazzanti, M. and Chini, B. (2016) *The Timing of the Excitatory-to-Inhibitory GABA Switch Is Regulated by the Oxytocin Receptor via KCC2,* Cell.Rep., **15,** 96-103.

Lesuisse, C. and Martin, L.J. (2002) *Long-term culture of mouse cortical neurons as a model for neuronal development, aging, and death,* J.Neurobiol., **51,** 9-23.

Lewandowska, M.K., Bakkum, D.J., Rompani, S.B. and Hierlemann, A. (2015) *Recording large extracellular spikes in microchannels along many axonal sites from individual neurons,* PLoS One, **10,** e0118514.

Li, J., Scheller, C., Koutsilieri, E., Griffiths, F., Beart, P.M., Mercer, L.D., Halliday, G., Kettle, E., Rowe, D., Riederer, P., Gerlach, M., Rodriguez, M. and Double, K.L. (2005) *Differential effects of human neuromelanin and synthetic dopamine melanin on neuronal and glial cells,* J.Neurochem., **95,** 599-608.

Li, K. and Xu, E. (2008) *The role and the mechanism of gamma-aminobutyric acid during central nervous system development,* Neurosci.Bull., **24,** 195-200.

Li, N. and Folch, A. (2005) *Integration of topographical and biochemical cues by axons during growth on microfabricated 3-D substrates,* Exp.Cell Res., **311,** 307-316.

Liangliang, X., Yonghui, H., Shunmei, E., Shoufang, G., Wei, Z. and Jiangying, Z. (2010) *Dominant-positive HSF1 decreases alpha-synuclein level and alpha-synuclein-induced toxicity,* Mol.Biol.Rep., **37,** 1875-1881.

Lin, M.Z. and Schnitzer, M.J. (2016) *Genetically encoded indicators of neuronal activity,* Nat.Neurosci., **19,** 1142-1153.

Lindahl, M. and Hellgren Kotaleski, J. (2017) *Untangling Basal Ganglia Network Dynamics and Function: Role of Dopamine Depletion and Inhibition Investigated in a Spiking Network Model,* eNeuro, **3,** 10.1523/ENEURO.0156-16.2016. eCollection 2016 Nov-Dec.

Liu, B., Ma, J., Gao, E., He, Y., Cui, F. and Xu, Q. (2008) *Development of an artificial neuronal network with post-mitotic rat fetal hippocampal cells by polyethylenimine,* Biosens.Bioelectron., **23,** 1221-1228.

Liu, B.F., Ma, J., Xu, Q.Y. and Cui, F.Z. (2006) *Regulation of charged groups and laminin patterns for selective neuronal adhesion,* Colloids Surf.B Biointerfaces, **53,** 175-178.

Lobb, C.J. and Jaeger, D. (2015) *Bursting activity of substantia nigra pars reticulata neurons in mouse parkinsonism in awake and anesthetized states,* Neurobiol.Dis., **75,** 177-185.

Lopes, F.M., Bristot, I.J., da Motta, L.L., Parsons, R.B. and Klamt, F. (2017) *Mimicking Parkinson's Disease in a Dish: Merits and Pitfalls of the Most Commonly used Dopaminergic In Vitro Models,* Neuromolecular Med., **19,** 241-255.

Lu, B., Wang, K.H. and Nose, A. (2009) *Molecular mechanisms underlying neural circuit formation,* Curr.Opin.Neurobiol., **19,** 162-167.

Luchtman, D.W. and Song, C. (2010) *Why SH-SY5Y cells should be differentiated,* Neurotoxicology, **31,** 164-5; author reply 165-6.

Luhmann, H.J. and Prince, D.A. (1991) *Postnatal maturation of the GABAergic system in rat neocortex,* J.Neurophysiol., **65,** 247-263.

Luni, C., Serena, E. and Elvassore, N. (2014) *Human-on-chip for therapy development and fundamental science,* Curr.Opin.Biotechnol., **25,** 45-50.

Lyng, G.D., Snyder-Keller, A. and Seegal, R.F. (2007) *Dopaminergic development of prenatal ventral mesencephalon and striatum in organotypic co-cultures,* Brain Res., **1133,** 1-9.

Ma, J., Liu, B.F., Xu, Q.Y. and Cui, F.Z. (2005) *AFM study of hippocampal cells cultured on silicon wafers with nano-scale surface topograph,* Colloids Surf.B Biointerfaces, **44,** 152-157.

Madhavan, R., Chao, Z.C. and Potter, S.M. (2007) *Plasticity of recurring spatiotemporal activity patterns in cortical networks,* Phys.Biol., **4,** 181-193.

Madrigal, M.P., Moreno-Bravo, J.A., Martinez-Lopez, J.E., Martinez, S. and Puelles, E. (2016) *Mesencephalic origin of the rostral Substantia nigra pars reticulata,* Brain Struct.Funct., **221,** 1403-1412.

Maetzler, W., Liepelt, I. and Berg, D. (2009) *Progression of Parkinson's disease in the clinical phase: potential markers,* Lancet Neurol., **8,** 1158-1171.

Mah, J.K., Korngut, L., Dykeman, J., Day, L., Pringsheim, T. and Jette, N. (2014) *A systematic review and meta-analysis on the epidemiology of Duchenne and Becker muscular dystrophy,* Neuromuscul.Disord., **24,** 482-491.

Majumdar, D., Gao, Y., Li, D. and Webb, D.J. (2011) *Co-culture of neurons and glia in a novel microfluidic platform,* J.Neurosci.Methods, **196,** 38-44.

Makinen, M., Joki, T., Yla-Outinen, L., Skottman, H., Narkilahti, S. and Aanismaa, R. (2013) *Fluorescent probes as a tool for cell population tracking in spontaneously active neural networks derived from human pluripotent stem cells,* J.Neurosci.Methods, **215,** 88-96.

Mallet, N., Ballion, B., Le Moine, C. and Gonon, F. (2006) *Cortical inputs and GABA interneurons imbalance projection neurons in the striatum of parkinsonian rats,* J.Neurosci., **26,** 3875-3884.

Mallet, N., Micklem, B.R., Henny, P., Brown, M.T., Williams, C., Bolam, J.P., Nakamura, K.C. and Magill, P.J. (2012) *Dichotomous organization of the external globus pallidus,* Neuron, **74,** 1075-1086.

Mallet, N., Pogosyan, A., Marton, L.F., Bolam, J.P., Brown, P. and Magill, P.J. (2008) *Parkinsonian beta oscillations in the external globus pallidus and their relationship with subthalamic nucleus activity,* J.Neurosci., **28,** 14245-14258.

Mansour, A.A., Goncalves, J.T., Bloyd, C.W., Li, H., Fernandes, S., Quang, D., Johnston, S., Parylak, S.L., Jin, X. and Gage, F.H. (2018) *An in vivo model of functional and vascularized human brain organoids,* Nat.Biotechnol., **36,** 432-441.

Marchand, R. and Lajoie, L. (1986) *Histogenesis of the striopallidal system in the rat. Neurogenesis of its neurons,* Neuroscience, **17,** 573-590.

Marchetto, M.C., Winner, B. and Gage, F.H. (2010) *Pluripotent stem cells in neurodegenerative and neurodevelopmental diseases,* Hum.Mol.Genet., **19,** R71-6.

Mariani, J., Simonini, M.V., Palejev, D., Tomasini, L., Coppola, G., Szekely, A.M., Horvath, T.L. and Vaccarino, F.M. (2012) *Modeling human cortical development in vitro using induced pluripotent stem cells,* Proc.Natl.Acad.Sci.U.S.A., **109,** 12770-12775.

Maric, D., Liu, Q.Y., Maric, I., Chaudry, S., Chang, Y.H., Smith, S.V., Sieghart, W., Fritschy, J.M. and Barker, J.L. (2001) *GABA expression dominates neuronal lineage progression in the embryonic rat neocortex and facilitates neurite outgrowth via GABA(A) autoreceptor/Cl- channels,* J.Neurosci., **21,** 2343-2360.

Marin, O. and Muller, U. (2014) *Lineage origins of GABAergic versus glutamatergic neurons in the neocortex,* Curr.Opin.Neurobiol., **26,** 132-141.

Marinelli, M. and McCutcheon, J.E. (2014) *Heterogeneity of dopamine neuron activity across traits and states,* Neuroscience, **282,** 176-197.

Marini, A.M., Lipsky, R.H., Schwartz, J.P. and Kopin, I.J. (1992) *Accumulation of 1-methyl-4-phenyl-1,2,3,6-tetrahydropyridine in cultured cerebellar astrocytes,* J.Neurochem., **58,** 1250-1258.

Marom, S. and Shahaf, G. (2002) *Development, learning and memory in large random networks of cortical neurons: lessons beyond anatomy,* Q.Rev.Biophys., **35,** 63-87.

Martinez-Morales, P.L. and Liste, I. (2012) *Stem cells as in vitro model of Parkinson's disease,* Stem Cells Int., **2012,** 980941.

Martínez-Serrano, A. and Liste, I. (2010) *Recent progress and challenges for the use of stem cell derivatives in neuron replacement therapy for Parkinson's disease,* Future Neurology, **5,** 161-165.

Marx, V. (2015) *Tissue engineering: Organs from the lab,* Nature, **522,** 373-377.

Mathai, A. and Smith, Y. (2011) *The corticostriatal and corticosubthalamic pathways: two entries, one target. So what?* Front.Syst.Neurosci., **5,** 64.

Maurice, N., Thierry, A.M., Glowinski, J. and Deniau, J.M. (2003) *Spontaneous and evoked activity of substantia nigra pars reticulata neurons during high-frequency stimulation of the subthalamic nucleus,* J.Neurosci., **23,** 9929-9936.

McBurney, M.W., Reuhl, K.R., Ally, A.I., Nasipuri, S., Bell, J.C. and Craig, J. (1988) *Differentiation and maturation of embryonal carcinoma-derived neurons in cell culture,* J.Neurosci., **8,** 1063-1073.

McMahon, C.P., Rocchitta, G., Kirwan, S.M., Killoran, S.J., Serra, P.A., Lowry, J.P. and O'Neill, R.D. (2007) *Oxygen tolerance of an implantable polymer/enzyme composite glutamate biosensor displaying polycation-enhanced substrate sensitivity,* Biosens.Bioelectron., **22,** 1466-1473.

Medina, L., Abellan, A., Vicario, A. and Desfilis, E. (2014) *Evolutionary and developmental contributions for understanding the organization of the basal ganglia,* Brain Behav.Evol., **83,** 112-125.

Medina, L. and Abellán, A. (2012) *Chapter 7 - Subpallial Structures,* 173-220.

Megias, M., Emri, Z., Freund, T.F. and Gulyas, A.I. (2001) *Total number and distribution of inhibitory and excitatory synapses on hippocampal CA1 pyramidal cells,* Neuroscience, **102,** 527-540.

Meldrum, B.S. (2000) *Glutamate as a neurotransmitter in the brain: review of physiology and pathology,* J.Nutr., **130,** 1007S-15S.

Mercanti, G., Bazzu, G. and Giusti, P. (2012) *A 6-hydroxydopamine in vivo model of Parkinson's disease,* Methods Mol.Biol., **846,** 355-364.

Meredith, G.E. and Rademacher, D.J. (2011) *MPTP mouse models of Parkinson's disease: an update,* J.Parkinsons Dis., **1,** 19-33.

Meyer, H.S., Egger, R., Guest, J.M., Foerster, R., Reissl, S. and Oberlaender, M. (2013) *Cellular organization of cortical barrel columns is whisker-specific,* Proc.Natl.Acad.Sci.U.S.A., **110,** 19113-19118.

Michel, P.P. and Hefti, F. (1990) *Toxicity of 6-hydroxydopamine and dopamine for dopaminergic neurons in culture,* J.Neurosci.Res., **26,** 428-435.

Miller, B.R., Walker, A.G., Shah, A.S., Barton, S.J. and Rebec, G.V. (2008) *Dysregulated information processing by medium spiny neurons in striatum of freely behaving mouse models of Huntington's disease,* J.Neurophysiol., **100,** 2205-2216.

Miller, J.D., Ganat, Y.M., Kishinevsky, S., Bowman, R.L., Liu, B., Tu, E.Y., Mandal, P.K., Vera, E., Shim, J.W., Kriks, S., Taldone, T., Fusaki, N., Tomishima, M.J., Krainc, D., Milner, T.A., Rossi, D.J. and Studer, L. (2013) *Human iPSC-based modeling of late-onset disease via progerin-induced aging,* Cell.Stem Cell., **13,** 691-705.

Miller, M.N., Okaty, B.W. and Nelson, S.B. (2008) *Region-specific spike-frequency acceleration in layer 5 pyramidal neurons mediated by Kv1 subunits,* J.Neurosci., **28,** 13716-13726.

Mitchell, J.F., Sundberg, K.A. and Reynolds, J.H. (2007) *Differential attention-dependent response modulation across cell classes in macaque visual area V4,* Neuron, **55,** 131-141.

Mizuno, N., Varkey, J., Kegulian, N.C., Hegde, B.G., Cheng, N., Langen, R. and Steven, A.C. (2012) *Remodeling of lipid vesicles into cylindrical micelles by alpha-synuclein in an extended alpha-helical conformation,* J.Biol.Chem., **287,** 29301-29311.

Mohajerani, M.H. and Cherubini, E. (2005) *Spontaneous recurrent network activity in organotypic rat hippocampal slices,* Eur.J.Neurosci., **22,** 107-118.

Momiyama, T. (2002) *Dopamine receptors and calcium channels regulating striatal inhibitory synaptic transmission,* Nihon Yakurigaku Zasshi., **120,** 61P-63P.

Money, K.M. and Stanwood, G.D. (2013) *Developmental origins of brain disorders: roles for dopamine,* Front.Cell.Neurosci., **7,** 260.

Montagu, K.A. (1957) *Catechol compounds in rat tissues and in brains of different animals,* Nature, **180,** 244-245.

Morgan, S.J., Elangbam, C.S., Berens, S., Janovitz, E., Vitsky, A., Zabka, T. and Conour, L. (2013) *Use of animal models of human disease for nonclinical safety assessment of novel pharmaceuticals,* Toxicol.Pathol., **41,** 508-518.

Morikawa, H. and Paladini, C.A. (2011) *Dynamic regulation of midbrain dopamine neuron activity: intrinsic, synaptic, and plasticity mechanisms,* Neuroscience, **198,** 95-111.

Morrison, B.,III, Cullen, D.K. and LaPlaca, M. (2011) *In Vitro Models for Biomechanical Studies of Neural Tissues,* Stud. Mechanobiol. Tissue Eng. Biomater., **3,** 247-285.

Moss, A.M., Unger, J.W., Moxley, R.T. and Livingston, J.N. (1990) *Location of phosphotyrosine-containing proteins by immunocytochemistry in the rat forebrain corresponds to the distribution of the insulin receptor,* Proc.Natl.Acad.Sci.U.S.A., **87,** 4453-4457.

Moustafa, A.A., Bar-Gad, I., Korngreen, A. and Bergman, H. (2014) *Basal ganglia: physiological, behavioral, and computational studies,* Front.Syst.Neurosci., **8,** 150.

Muguruma, K., Nishiyama, A., Kawakami, H., Hashimoto, K. and Sasai, Y. (2015) *Self-organization of polarized cerebellar tissue in 3D culture of human pluripotent stem cells,* Cell.Rep., **10,** 537-550.

Muramoto, K., Ichikawa, M., Kawahara, M., Kobayashi, K. and Kuroda, Y. (1993) *Frequency of synchronous oscillations of neuronal activity increases during development and is correlated to the number of synapses in cultured cortical neuron networks,* Neurosci.Lett., **163,** 163-165.

Musick, K., Khatami, D. and Wheeler, B.C. (2009a) *Three-dimensional micro-electrode array for recording dissociated neuronal cultures,* Lab.Chip, **9,** 2036-2042.

Musick, K., Khatami, D. and Wheeler, B.C. (2009b) *Three-dimensional micro-electrode array for recording dissociated neuronal cultures,* Lab.Chip, **9,** 2036-2042.

Na, S., Kang, M., Bang, S., Park, D., Kim, J., Sim, S.,Jun, Chang, S. and Jeon, N.,Li (2016) *Microfluidic neural axon diode,* Technology, **4,** 240.

Nagao, M., Kato, S., Oda, M. and Hirai, S. (1998) *Expression of phosphotyrosine and SNAP-25 immunoreactivity in grumose (foamy) spheroid bodies suggests axonal regeneration,* Acta Neuropathol., **96,** 388-394.

Nagatsu, T. (1997) *Isoquinoline neurotoxins in the brain and Parkinson's disease,* Neurosci.Res., **29,** 99-111.

Nair-Roberts, R.G., Chatelain-Badie, S.D., Benson, E., White-Cooper, H., Bolam, J.P. and Ungless, M.A. (2008) *Stereological estimates of dopaminergic, GABAergic and glutamatergic neurons in the ventral tegmental area, substantia nigra and retrorubral field in the rat,* Neuroscience, **152,** 1024-1031.

Nakano, T., Ando, S., Takata, N., Kawada, M., Muguruma, K., Sekiguchi, K., Saito, K., Yonemura, S., Eiraku, M. and Sasai, Y. (2012) *Self-formation of optic cups and storable stratified neural retina from human ESCs,* Cell.Stem Cell., **10,** 771-785.

Nam, Y. and Wheeler, B.C. (2011) *In vitro microelectrode array technology and neural recordings,* Crit.Rev.Biomed.Eng., **39,** 45-61.

Nambu, A. (2007) *Globus pallidus internal segment,* Prog.Brain Res., **160,** 135-150.

Nambu, A., Tokuno, H. and Takada, M. (2002) *Functional significance of the cortico-subthalamo-pallidal 'hyperdirect' pathway,* Neurosci.Res., **43,** 111-117.

Nambu, A., Tachibana, Y. and Chiken, S. (2015) *Cause of parkinsonian symptoms: Firing rate, firing pattern or dynamic activity changes?* Basal Ganglia, **5,** 1-6.

Nedergaard, M., Ransom, B. and Goldman, S.A. (2003) *New roles for astrocytes: redefining the functional architecture of the brain,* Trends Neurosci., **26,** 523-530.

Nelander, J., Hebsgaard, J.B. and Parmar, M. (2009) *Organization of the human embryonic ventral mesencephalon,* Gene Expr.Patterns, **9,** 555-561.

Nemani, V.M., Lu, W., Berge, V., Nakamura, K., Onoa, B., Lee, M.K., Chaudhry, F.A., Nicoll, R.A. and Edwards, R.H. (2010) *Increased expression of alpha-synuclein reduces neurotransmitter release by inhibiting synaptic vesicle reclustering after endocytosis,* Neuron, **65,** 66-79.

Nevado-Holgado, A.J., Mallet, N., Magill, P.J. and Bogacz, R. (2014) *Effective connectivity of the subthalamic nucleus-globus pallidus network during Parkinsonian oscillations,* J.Physiol., **592,** 1429-1455.

Nguyen, H.N., Byers, B., Cord, B., Shcheglovitov, A., Byrne, J., Gujar, P., Kee, K., Schule, B., Dolmetsch, R.E., Langston, W., Palmer, T.D. and Pera, R.R. (2011) *LRRK2 mutant iPSC-derived DA neurons demonstrate increased susceptibility to oxidative stress,* Cell.Stem Cell., **8,** 267-280.

Nolbrant, S., Heuer, A., Parmar, M. and Kirkeby, A. (2017) *Generation of high-purity human ventral midbrain dopaminergic progenitors for in vitro maturation and intracerebral transplantation,* Nat.Protoc., **12,** doi:10.1038/nprot.2017.078.

Obien, M.E., Deligkaris, K., Bullmann, T., Bakkum, D.J. and Frey, U. (2015) *Revealing neuronal function through microelectrode array recordings,* Front.Neurosci., **8,** 423.

Obrietan, K. and van den Pol, A.N. (1995) *GABA neurotransmission in the hypothalamus: developmental reversal from Ca2+ elevating to depressing,* J.Neurosci., **15,** 5065-5077.

Orr, W.B., Stricker, E.M., Zigmond, M.J. and Berger, T.W. (1987) *Effects of dopamine depletion on the spontaneous activity of type I striatal neurons: relation to local dopamine concentration and motor behavior,* Synapse, **1,** 461-469.

Paladini, C.A., Robinson, S., Morikawa, H., Williams, J.T. and Palmiter, R.D. (2003) *Dopamine controls the firing pattern of dopamine neurons via a network feedback mechanism,* Proc.Natl.Acad.Sci.U.S.A., **100,** 2866-2871.

Palmer, A.E. and Tsien, R.Y. (2006) *Measuring calcium signaling using genetically targetable fluorescent indicators,* Nat.Protoc., **1,** 1057-1065.

Pamies, D., Hartung, T. and Hogberg, H.T. (2014) *Biological and medical applications of a brain-on-a-chip,* Exp.Biol.Med.(Maywood), **239,** 1096-1107.

Pan, L., Alagapan, S., Franca, E., Leondopulos, S.S., DeMarse, T.B., Brewer, G.J. and Wheeler, B.C. (2015a) *An in vitro method to manipulate the direction and functional strength between neural populations,* Front.Neural Circuits, **9,** 32.

Pan, L., Alagapan, S., Franca, E., Leondopulos, S.S., DeMarse, T.B., Brewer, G.J. and Wheeler, B.C. (2015b) *An in vitro method to manipulate the direction and functional strength between neural populations,* Front.Neural Circuits, **9,** 32.

Pan, T. and Wang, W. (2011) *From cleanroom to desktop: emerging micro-nanofabrication technology for biomedical applications,* Ann.Biomed.Eng., **39,** 600-620.

Panigrahi, B., Martin, K.A., Li, Y., Graves, A.R., Vollmer, A., Olson, L., Mensh, B.D., Karpova, A.Y. and Dudman, J.T. (2015) *Dopamine Is Required for the Neural Representation and Control of Movement Vigor,* Cell, **162,** 1418-1430.

Park, J., Koito, H., Li, J. and Han, A. (2009a) *Microfluidic compartmentalized co-culture platform for CNS axon myelination research,* Biomed.Microdevices, **11,** 1145-1153.

Park, J., Koito, H., Li, J. and Han, A. (2009b) *A multi-compartment CNS neuron-glia Co-culture microfluidic platform,* J.Vis.Exp., **(31). pii: 1399. doi,** 10.3791/1399.

Park, J., Koito, H., Li, J. and Han, A. (2012) *Multi-compartment neuron-glia co-culture platform for localized CNS axon-glia interaction study,* Lab.Chip, **12,** 3296-3304.

Park, J., Lee, B.K., Jeong, G.S., Hyun, J.K., Lee, C.J. and Lee, S.H. (2014) *Three-dimensional brain-on-a-chip with an interstitial level of flow and its application as an in vitro model of Alzheimer's disease,* Lab.Chip,

Park, J., Wetzel, I., Marriott, I., Dreau, D., D'Avanzo, C., Kim, D.Y., Tanzi, R.E. and Cho, H. (2018) *A 3D human triculture system modeling neurodegeneration and neuroinflammation in Alzheimer's disease,* Nat.Neurosci., **21,** 941-951.

Park, J.W., Vahidi, B., Taylor, A.M., Rhee, S.W. and Jeon, N.L. (2006) *Microfluidic culture platform for neuroscience research,* Nat.Protoc., **1,** 2128-2136.

Parnas, D. and Linial, M. (1995) *Cholinergic properties of neurons differentiated from an embryonal carcinoma cell-line (P19),* Int.J.Dev.Neurosci., **13,** 767-781.

Parnas, D. and Linial, M. (1997) *Acceleration of neuronal maturation of P19 cells by increasing culture density,* Brain Res.Dev.Brain Res., **101,** 115-124.

Paspala, S.A., Murthy, T.V., Mahaboob, V.S. and Habeeb, M.A. (2011) *Pluripotent stem cells - a review of the current status in neural regeneration,* Neurol.India, **59,** 558-565.

Pasquereau, B. and Turner, R.S. (2011) *Primary motor cortex of the parkinsonian monkey: differential effects on the spontaneous activity of pyramidal tract-type neurons,* Cereb.Cortex, **21,** 1362-1378.

Perea, G., Navarrete, M. and Araque, A. (2009) *Tripartite synapses: astrocytes process and control synaptic information,* Trends Neurosci., **32,** 421-431.

Perez Koldenkova, V. and Nagai, T. (2013) *Genetically encoded Ca(2+) indicators: properties and evaluation,* Biochim.Biophys.Acta, **1833,** 1787-1797.

Perry, J.L., Ramachandran, N.K., Utama, B. and Hyser, J.M. (2015) *Use of genetically-encoded calcium indicators for live cell calcium imaging and localization in virus-infected cells,* Methods, **90,** 28-38.

Pesaresi, M., Soon-Shiong, R., French, L., Kaplan, D.R., Miller, F.D. and Paus, T. (2015) *Axon diameter and axonal transport: In vivo and in vitro effects of androgens,* Neuroimage, **115,** 191-201.

Pessiglione, M., Guehl, D., Rolland, A.S., Francois, C., Hirsch, E.C., Feger, J. and Tremblay, L. (2005) *Thalamic neuronal activity in dopamine-depleted primates: evidence for a loss of functional segregation within basal ganglia circuits,* J.Neurosci., **25,** 1523-1531.

Pettersen, K.H. and Einevoll, G.T. (2008) *Amplitude variability and extracellular low-pass filtering of neuronal spikes,* Biophys.J., **94,** 784-802.

Peyrin, J.M., Deleglise, B., Saias, L., Vignes, M., Gougis, P., Magnifico, S., Betuing, S., Pietri, M., Caboche, J., Vanhoutte, P., Viovy, J.L. and Brugg, B. (2011) *Axon diodes for the reconstruction of oriented neuronal networks in microfluidic chambers,* Lab.Chip, **11,** 3663-3673.

Pietz, K., Odin, P., Funa, K. and Lindvall, O. (1996) *Protective effect of platelet-derived growth factor against 6-hydroxydopamine-induced lesion of rat dopaminergic neurons in culture,* Neurosci.Lett., **204,** 101-104.

Pine, J. (1980) *Recording action potentials from cultured neurons with extracellular microcircuit electrodes,* J.Neurosci.Methods, **2,** 19-31.

Pinel, J.P.J. (2013) *Neuropsychological Disorders: Human Brain Damage and Animal Models,* Neurophychological Disorders, **9,** 6a.

Plenz, D. and Kitai, S.T. (1998) *Up and down states in striatal medium spiny neurons simultaneously recorded with spontaneous activity in fast-spiking interneurons studied in cortex-striatum-substantia nigra organotypic cultures,* J.Neurosci., **18,** 266-283.

Polikov, V., Block, M., Zhang, C., Reichert, W.M. and Hong, J.S. (2008) *In Vitro Models for Neuroelectrodes: A Paradigm for Studying Tissue–Materials Interactions in the Brain,* Indwelling Neural Implants: Strategies for Contending with the In Vivo Environment., **4,** Available from: https://www.ncbi.nlm.nih.gov/books/NBK3934/.

Potashkin, J.A., Blume, S.R. and Runkle, N.K. (2010) *Limitations of animal models of Parkinson's disease,* Parkinsons Dis., **2011,** 658083.

Potter, S.M. and DeMarse, T.B. (2001) *A new approach to neural cell culture for long-term studies,* J.Neurosci.Methods, **110,** 17-24.

Pringsheim, T., Jette, N., Frolkis, A. and Steeves, T.D. (2014) *The prevalence of Parkinson's disease: a systematic review and meta-analysis,* Mov.Disord., **29,** 1583-1590.

Pringsheim, T., Wiltshire, K., Day, L., Dykeman, J., Steeves, T. and Jette, N. (2012) *The incidence and prevalence of Huntington's disease: a systematic review and meta-analysis,* Mov.Disord., **27,** 1083-1091.

Raicevic, N., Mladenovic, A., Perovic, M., Harhaji, L., Miljkovic, D. and Trajkovic, V. (2005) *Iron protects astrocytes from 6-hydroxydopamine toxicity,* Neuropharmacology, **48,** 720-731.

Raicevic, N., Mladenovic, A., Perovic, M., Miljkovic, D. and Trajkovic, V. (2005) *The mechanisms of 6-hydroxydopamine-induced astrocyte death,* Ann.N.Y.Acad.Sci., **1048,** 400-405.

Rajput, A.H., Rozdilsky, B. and Rajput, A. (1993) *Alzheimer's disease and idiopathic Parkinson's disease coexistence,* J.Geriatr.Psychiatry Neurol., **6,** 170-176.

Randall, F.E., Garcia-Munoz, M., Vickers, C., Schock, S.C., Staines, W.A. and Arbuthnott, G.W. (2011) *The corticostriatal system in dissociated cell culture,* Front.Syst.Neurosci., **5,** 52.

Rangel-Barajas, C. and Rebec, G.V. (2016) *Dysregulation of Corticostriatal Connectivity in Huntington's Disease: A Role for Dopamine Modulation,* J.Huntingtons Dis., **5,** 303-331.

Recasens, A., Dehay, B., Bove, J., Carballo-Carbajal, I., Dovero, S., Perez-Villalba, A., Fernagut, P.O., Blesa, J., Parent, A., Perier, C., Farinas, I., Obeso, J.A., Bezard, E. and Vila, M. (2014) *Lewy body extracts from Parkinson disease brains trigger alpha-synuclein pathology and neurodegeneration in mice and monkeys,* Ann.Neurol., **75,** 351-362.

Reig, R. and Silberberg, G. (2014) *Multisensory integration in the mouse striatum,* Neuron, **83,** 1200-1212.

Reitz, C. (2012) *Alzheimer's disease and the amyloid cascade hypothesis: a critical review,* Int.J.Alzheimers Dis., **2012,** 369808.

Renault, R., Durand, J.B., Viovy, J.L. and Villard, C. (2016) *Asymmetric axonal edge guidance: a new paradigm for building oriented neuronal networks,* Lab.Chip, **16,** 2188-2191.

Renault, R., Sukenik, N., Descroix, S., Malaquin, L., Viovy, J.L., Peyrin, J.M., Bottani, S., Monceau, P., Moses, E. and Vignes, M. (2015) *Combining microfluidics, optogenetics and calcium imaging to study neuronal communication in vitro,* PLoS One, **10,** e0120680.

Rice, M.E. and Cragg, S.J. (2008) *Dopamine spillover after quantal release: rethinking dopamine transmission in the nigrostriatal pathway,* Brain Res.Rev., **58,** 303-313.

Richfield, E.K., Thiruchelvam, M.J., Cory-Slechta, D.A., Wuertzer, C., Gainetdinov, R.R., Caron, M.G., Di Monte, D.A. and Federoff, H.J. (2002) *Behavioral and neurochemical effects of wild-type and mutated human alpha-synuclein in transgenic mice,* Exp.Neurol., **175,** 35-48.

Rivera, A., Alberti, I., Martin, A.B., Narvaez, J.A., de la Calle, A. and Moratalla, R. (2002) *Molecular phenotype of rat striatal neurons expressing the dopamine D5 receptor subtype,* Eur.J.Neurosci., **16,** 2049-2058.

Rivera, A., Cuellar, B., Giron, F.J., Grandy, D.K., de la Calle, A. and Moratalla, R. (2002) *Dopamine D4 receptors are heterogeneously distributed in the striosomes/matrix compartments of the striatum,* J.Neurochem., **80,** 219-229.

Roach, P., Parker, T., Gadegaard, N. and Alexander, M.R. (2010) *Surface strategies for control of neuronal cell adhesion: A review,* Surface Science Reports, **65,** 145-173.

Robberecht, W. and Philips, T. (2013) *The changing scene of amyotrophic lateral sclerosis,* Nat.Rev.Neurosci., **14,** 248-264.

Robbins, A.A., Fox, S.E., Holmes, G.L., Scott, R.C. and Barry, J.M. (2013) *Short duration waveforms recorded extracellularly from freely moving rats are representative of axonal activity,* Front.Neural Circuits, **7,** 181.

Robertson, G., Bushell, T.J. and Zagnoni, M. (2014) *Chemically induced synaptic activity between mixed primary hippocampal co-cultures in a microfluidic system,* Integr.Biol.(Camb), **6,** 636-644.

Rodriguez-Pallares, J., Parga, J.A., Munoz, A., Rey, P., Guerra, M.J. and Labandeira-Garcia, J.L. (2007) *Mechanism of 6-hydroxydopamine neurotoxicity: the role of NADPH oxidase and microglial activation in 6-hydroxydopamine-induced degeneration of dopaminergic neurons,* J.Neurochem., **103,** 145-156.

Roeper,Jochen (2013) *Dissecting the diversity of midbrain dopamine neurons,* Trends Neurosci., **36,** 336-342.

Rommelfanger, K.S. and Wichmann, T. (2010) *Extrastriatal dopaminergic circuits of the Basal Ganglia,* Front.Neuroanat., **4,** 139.

Rosen, A.R., Steenland, N.K., Hanfelt, J., Factor, S.A., Lah, J.J. and Levey, A.I. (2007) *Evidence of shared risk for Alzheimer's disease and Parkinson's disease using family history,* Neurogenetics, **8,** 263-270.

Ruardij, T.G., Goedbloed, M.H. and Rutten, W.L. (2000) *Adhesion and patterning of cortical neurons on polyethylenimine- and fluorocarbon-coated surfaces,* IEEE Transactions on Biomedical Engineering, **47,** 1593-1599.

Ruegg, U.T. and Hefti, F. (1984) *Growth of dissociated neurons in culture dishes coated with synthetic polymeric amines,* Neurosci.Lett., **49,** 319-324.

Russell, W.M.S. and Burch, R.L. (1959) *The principles of humane experimental technique,* The University of Michigan, 238.

Sahathevan, R., Brodtmann, A. and Donnan, G.A. (2012) *Dementia, stroke, and vascular risk factors; a review,* Int.J.Stroke, **7,** 61-73.

Saito, Y., Nishio, K., Ogawa, Y., Kinumi, T., Yoshida, Y., Masuo, Y. and Niki, E. (2007) *Molecular mechanisms of 6-hydroxydopamine-induced cytotoxicity in PC12 cells: involvement of hydrogen peroxide-dependent and -independent action,* Free Radic.Biol.Med., **42,** 675-685.

Sandhu, J.K., Gardaneh, M., Iwasiow, R., Lanthier, P., Gangaraju, S., Ribecco-Lutkiewicz, M., Tremblay, R., Kiuchi, K. and Sikorska, M. (2009) *Astrocyte-secreted GDNF and glutathione antioxidant system protect neurons against 6OHDA cytotoxicity,* Neurobiol.Dis., **33,** 405-414.

Sandy, M.S., Armstrong, M., Tanner, C.M., Daly, A.K., Di Monte, D.A., Langston, J.W. and Idle, J.R. (1996) *CYP2D6 allelic frequencies in young-onset Parkinson's disease,* Neurology, **47,** 225-230.

Sanes, D.H., Reh, T.A. and Harris, W.A. (2012) *Development of the Nervous System (Third Edition),* Elsevier, **3,**

Sano, H., Chiken, S., Hikida, T., Kobayashi, K. and Nambu, A. (2013) *Signals through the striatopallidal indirect pathway stop movements by phasic excitation in the substantia nigra,* J.Neurosci., **33,** 7583-7594.

Schmidt, E.R., Morello, F. and Pasterkamp, R.J. (2012) *Dissection and culture of mouse dopaminergic and striatal explants in three-dimensional collagen matrix assays,* J.Vis.Exp., **(61). pii: 3691. doi,** 10.3791/3691.

Schomberg, S.L., Bauer, J., Kintner, D.B., Su, G., Flemmer, A., Forbush, B. and Sun, D. (2003) *Cross talk between the GABA(A) receptor and the Na-K-Cl cotransporter is mediated by intracellular Cl-,* J.Neurophysiol., **89,** 159-167.

Sedelis, M., Hofele, K., Auburger, G.W., Morgan, S., Huston, J.P. and Schwarting, R.K. (2000) *MPTP susceptibility in the mouse: behavioral, neurochemical, and histological analysis of gender and strain differences,* Behav.Genet., **30,** 171-182.

Segura-Aguilar, J. and Kostrzewa, R.M. (2015) *Neurotoxin mechanisms and processes relevant to Parkinson's disease: an update,* Neurotox Res., **27,** 328-354.

Sharma, S., Johnson, R.W. and Desai, T.A. (2004) *XPS and AFM analysis of antifouling PEG interfaces for microfabricated silicon biosensors,* Biosens.Bioelectron., **20,** 227-239.

Sharott, A., Doig, N.M., Mallet, N. and Magill, P.J. (2012) *Relationships between the firing of identified striatal interneurons and spontaneous and driven cortical activities in vivo,* J.Neurosci., **32,** 13221-13236.

Shepherd, G.M. (2013) *Corticostriatal connectivity and its role in disease,* Nat.Rev.Neurosci., **14,** 278-291.

Shi, M., Majumdar, D., Gao, Y., Brewer, B.M., Goodwin, C.R., McLean, J.A., Li, D. and Webb, D.J. (2013) *Glia co-culture with neurons in microfluidic platforms promotes the formation and stabilization of synaptic contacts,* Lab.Chip, **13,** 3008-3021.

Shoham, S., O'Connor, D.H. and Segev, R. (2006) *How silent is the brain: is there a "dark matter" problem in neuroscience?* J.Comp.Physiol.A.Neuroethol Sens.Neural Behav.Physiol., **192,** 777-784.

Shoichet, M., Tate, C., Baumann, M. and Reichert, W. (2008) *Strategies for Regeneration and Repair in the Injured Central Nervous System.* Indwelling Neural Implants: Strategies for Contending with the In Vivo Environment., **8,** http://www.ncbi.nlm.nih.gov/books/NBK3941/.

Silva, N.A., Sousa, N., Reis, R.L. and Salgado, A.J. (2014) *From basics to clinical: a comprehensive review on spinal cord injury,* Prog.Neurobiol., **114,** 25-57.

Simmons, S.B., Pierson, E.R., Lee, S.Y. and Goverman, J.M. (2013) *Modeling the heterogeneity of multiple sclerosis in animals,* Trends Immunol., **34,** 410-422.

Sims, R.E., Woodhall, G.L., Wilson, C.L. and Stanford, I.M. (2008) *Functional characterization of GABAergic pallidopallidal and striatopallidal synapses in the rat globus pallidus in vitro,* Eur.J.Neurosci., **28,** 2401-2408.

Singh, S., Kumar, S. and Dikshit, M. (2010) *Involvement of the mitochondrial apoptotic pathway and nitric oxide synthase in dopaminergic neuronal death induced by 6-hydroxydopamine and lipopolysaccharide,* Redox Rep., **15,** 115-122.

Sippy, T., Lapray, D., Crochet, S. and Petersen, C.C. (2015) *Cell-Type-Specific Sensorimotor Processing in Striatal Projection Neurons during Goal-Directed Behavior,* Neuron, **88,** 298-305.

Sitnikov, S., Jaeckel, D. and Hierlemann, A. (2016) *Studying extracellular action potential waveforms using HD MEAs,* Frontiers in neuroscience, **10th International Meeting on Substrate-Integrated Electrode Arrays,**

Smalley, K.S., Lioni, M. and Herlyn, M. (2006) *Life isn't flat: taking cancer biology to the next dimension,* In Vitro Cell.Dev.Biol.Anim., **42,** 242-247.

Smeets, W.J., Marin, O. and Gonzalez, A. (2000) *Evolution of the basal ganglia: new perspectives through a comparative approach,* J.Anat., **196 (Pt 4),** 501-517.

Smith, Y., Raju, D.V., Pare, J.F. and Sidibe, M. (2004) *The thalamostriatal system: a highly specific network of the basal ganglia circuitry,* Trends Neurosci., **27,** 520-527.

Sofroniew, M.V. and Vinters, H.V. (2010) *Astrocytes: biology and pathology,* Acta Neuropathol., **119,** 7-35.

Sofroniew, N.J., Flickinger, D., King, J. and Svoboda, K. (2016) *A large field of view two-photon mesoscope with subcellular resolution for in vivo imaging,* Elife, **5,** 10.7554/eLife.14472.

Spira, M.,E. and Hai,Aviad (2013) *Multi-electrode array technologies for neuroscience and cardiology,* Nature Nanotechnology, **8,** 83-94.

Stahl, K., Skare, O. and Torp, R. (2009) *Organotypic cultures as a model of Parkinson s disease. A twist to an old model,* ScientificWorldJournal, **9,** 811-821.

Stiles, J. and Jernigan, T.L. (2010) *The basics of brain development,* Neuropsychol.Rev., **20,** 327-348.

St-Pierre, F., Marshall, J.D., Yang, Y., Gong, Y., Schnitzer, M.J. and Lin, M.Z. (2014) *High-fidelity optical reporting of neuronal electrical activity with an ultrafast fluorescent voltage sensor,* Nat.Neurosci., **17,** 884-889.

Strand, D.W., Franco, O.E., Basanta, D., Anderson, A.R. and Hayward, S.W. (2010) *Perspectives on tissue interactions in development and disease,* Curr.Mol.Med., **10,** 95-112.

Struzyna, L.A., Browne, K.D., Brodnik, Z.D., Burrell, J.C., Harris, J.P., Chen, H.I., Wolf, J.A., Panzer, K.V., Lim, J., Duda, J.E., Espana, R.A. and Cullen, D.K. (2018) *Tissue engineered nigrostriatal pathway for treatment of Parkinson's disease,* J.Tissue Eng.Regen.Med., **12,** 1702-1716.

Suga, H., Kadoshima, T., Minaguchi, M., Ohgushi, M., Soen, M., Nakano, T., Takata, N., Wataya, T., Muguruma, K., Miyoshi, H., Yonemura, S., Oiso, Y. and Sasai, Y. (2011) *Self-formation of functional adenohypophysis in three-dimensional culture,* Nature, **480,** 57-62.

Sun, Y., Huang, Z., Liu, W., Yang, K., Sun, K., Xing, S., Wang, D., Zhang, W. and Jiang, X. (2012) *Surface coating as a key parameter in engineering neuronal network structures in vitro,* Biointerphases, **7,** 29-012-0029-7. Epub 2012 Apr 24.

Sur, S., Newcomb, C.J., Webber, M.J. and Stupp, S.I. (2013) *Tuning supramolecular mechanics to guide neuron development,* Biomaterials, **34,** 4749-4757.

Surmeier, D.J., Halliday, G.M. and Simuni, T. (2017) *Calcium, mitochondrial dysfunction and slowing the progression of Parkinson's disease,* Exp.Neurol.,

Szabo, G. (2004) *Physiologic changes after brain death,* J.Heart Lung Transplant., **23,** S223-6.

Tachibana, Y., Iwamuro, H., Kita, H., Takada, M. and Nambu, A. (2011) *Subthalamo-pallidal interactions underlying parkinsonian neuronal oscillations in the primate basal ganglia,* Eur.J.Neurosci., **34,** 1470-1484.

Takahashi, K., Tanabe, K., Ohnuki, M., Narita, M., Ichisaka, T., Tomoda, K. and Yamanaka, S. (2007) *Induction of pluripotent stem cells from adult human fibroblasts by defined factors,* Cell, **131,** 861-872.

Takahashi, K. and Yamanaka, S. (2006) *Induction of pluripotent stem cells from mouse embryonic and adult fibroblast cultures by defined factors,* Cell, **126,** 663-676.

Takayama, Y., Moriguchi, H., Kotani, K., Suzuki, T., Mabuchi, K. and Jimbo, Y. (2012) *Network-wide integration of stem cell-derived neurons and mouse cortical neurons using microfabricated co-culture devices,* BioSystems, **107,** 1-8.

Takehara, H., Nagaoka, A., Noguchi, J., Akagi, T., Kasai, H. and Ichiki, T. (2014) *Lab-on-a-brain: Implantable micro-optical fluidic devices for neural cell analysis in vivo,* Sci.Rep., **4,** 6721.

Tang-Schomer, M.D., Davies, P., Graziano, D., Thurber, A.E. and Kaplan, D.L. (2014) *Neural circuits with long-distance axon tracts for determining functional connectivity,* J.Neurosci.Methods, **222,** 82-90.

Taylor, A.M., Blurton-Jones, M., Rhee, S.W., Cribbs, D.H., Cotman, C.W. and Jeon, N.L. (2005) *A microfluidic culture platform for CNS axonal injury, regeneration and transport,* Nat.Methods, **2,** 599-605.

Taylor, A.M., Dieterich, D.C., Ito, H.T., Kim, S.A. and Schuman, E.M. (2010) *Microfluidic local perfusion chambers for the visualization and manipulation of synapses,* Neuron, **66,** 57-68.

Taylor, A.M., Rhee, S.W., Tu, C.H., Cribbs, D.H., Cotman, C.W. and Jeon, N.L. (2003) *Microfluidic Multicompartment Device for Neuroscience Research,* Langmuir, **19,** 1551-1556.

Tepper, J., Martin, L. and Anderson, D. (1995) *GABAA receptor-mediated inhibition of rat substantia nigra dopaminergic neurons by pars reticulata projection neurons,* J.Neurosci., **15,** 3092-3103.

Terzioglu, M. and Galter, D. (2008) *Parkinson's disease: genetic versus toxin-induced rodent models,* FEBS J., **275,** 1384-1391.

Terzuolo, C.A. and Araki, T. (1961) *An analysis of intra- versus extracellular potential changes associated with activity of single spinal motoneurons,* Ann.N.Y.Acad.Sci., **94,** 547-558.

Tessier, C.R. and Broadie, K. (2009) *Activity-dependent modulation of neural circuit synaptic connectivity,* Front.Mol.Neurosci., **2,** 8.

Teyler, T.J., Alger, B.E., Bergman, T. and Livingston, K. (1977) *A comparison of long-term potentiation in the in vitro and in vivo hippocampal preparations,* Behav.Biol., **19,** 24-34.

Therriault, D., White, S.R. and Lewis, J.A. (2003) *Chaotic mixing in three-dimensional microvascular networks fabricated by direct-write assembly,* Nat.Mater., **2,** 265-271.

Tian, L., Hires, S.A. and Looger, L.L. (2012) *Imaging neuronal activity with genetically encoded calcium indicators,* Cold Spring Harb Protoc., **2012,** 647-656.

Tieu, K. (2011) *A guide to neurotoxic animal models of Parkinson's disease,* Cold Spring Harb Perspect.Med., **1,** a009316.

Tritsch, N.X. and Sabatini, B.L. (2012) *Dopaminergic modulation of synaptic transmission in cortex and striatum,* Neuron, **76,** 33-50.

Tse, J.R. and Engler, A.J. (2011) *Stiffness gradients mimicking in vivo tissue variation regulate mesenchymal stem cell fate,* PLoS One, **6,** e15978.

Tseng, K.Y., Snyder-Keller, A. and O'Donnell, P. (2007) *Dopaminergic modulation of striatal plateau depolarizations in corticostriatal organotypic cocultures,* Psychopharmacology (Berl), **191,** 627-640.

Turrigiano, G.G. and Nelson, S.B. (2004) *Homeostatic plasticity in the developing nervous system,* Nat.Rev.Neurosci., **5,** 97-107.

Tyzio, R., Cossart, R., Khalilov, I., Minlebaev, M., Hubner, C.A., Represa, A., Ben-Ari, Y. and Khazipov, R. (2006) *Maternal oxytocin triggers a transient inhibitory switch in GABA signaling in the fetal brain during delivery,* Science, **314,** 1788-1792.

Tyzio, R., Represa, A., Jorquera, I., Ben-Ari, Y., Gozlan, H. and Aniksztejn, L. (1999) *The establishment of GABAergic and glutamatergic synapses on CA1 pyramidal neurons is sequential and correlates with the development of the apical dendrite,* J.Neurosci., **19,** 10372-10382.

Ulrich, H. and Majumder, P. (2006) *Neurotransmitter receptor expression and activity during neuronal differentiation of embryonal carcinoma and stem cells: from basic research towards clinical applications,* Cell Prolif., **39,** 281-300.

Ungerstedt, U. (1968) *6-Hydroxy-dopamine induced degeneration of central monoamine neurons,* Eur.J.Pharmacol., **5,** 107-110.

Valeeva, G., Valiullina, F. and Khazipov, R. (2013) *Excitatory actions of GABA in the intact neonatal rodent hippocampus in vitro,* Front.Cell.Neurosci., **7,** 20.

van de Beek, D., Brouwer, M.C., Thwaites, G.E. and Tunkel, A.R. (2012) *Advances in treatment of bacterial meningitis,* Lancet, **380,** 1693-1702.

Van Den Eeden, S.K., Tanner, C.M., Bernstein, A.L., Fross, R.D., Leimpeter, A., Bloch, D.A. and Nelson, L.M. (2003) *Incidence of Parkinson's disease: variation by age, gender, and race/ethnicity,* Am.J.Epidemiol., **157,** 1015-1022.

Van Kampen, J.M. and Robertson, H.A. (2017) *The BSSG rat model of Parkinson's disease: progressing towards a valid, predictive model of disease,* EPMA J., **8,** 261-271.

van Pelt, J., Vajda, I., Wolters, P.S., Corner, M.A. and Ramakers, G.J. (2005) *Dynamics and plasticity in developing neuronal networks in vitro,* Prog.Brain Res., **147,** 173-188.

van Vliet, E., Stoppini, L., Balestrino, M., Eskes, C., Griesinger, C., Sobanski, T., Whelan, M., Hartung, T. and Coecke, S. (2007) *Electrophysiological recording of re-aggregating brain cell cultures on multi-electrode arrays to detect acute neurotoxic effects,* Neurotoxicology, **28,** 1136-1146.

Vancha, A.R., Govindaraju, S., Parsa, K.V., Jasti, M., Gonzalez-Garcia, M. and Ballestero, R.P. (2004) *Use of polyethyleneimine polymer in cell culture as attachment factor and lipofection enhancer,* BMC Biotechnol., **4,** 23.

Verstraeten, A., Theuns, J. and Van Broeckhoven, C. (2015) *Progress in unraveling the genetic etiology of Parkinson disease in a genomic era,* Trends Genet., **31,** 140-149.

Vezoli, J., Fifel, K., Leviel, V., Dehay, C., Kennedy, H., Cooper, H.M., Gronfier, C. and Procyk, E. (2011) *Early presymptomatic and long-term changes of rest activity cycles and cognitive behavior in a MPTP-monkey model of Parkinson's disease,* PLoS One, **6,** e23952.

Virlogeux, A., Moutaux, E., Christaller, W., Genoux, A., Bruyere, J., Fino, E., Charlot, B., Cazorla, M. and Saudou, F. (2018) *Reconstituting Corticostriatal Network on-a-Chip Reveals the Contribution of the Presynaptic Compartment to Huntington's Disease,* Cell.Rep., **22,** 110-122.

Vitek, J.L., Zhang, J., Hashimoto, T., Russo, G.S. and Baker, K.B. (2012) *External pallidal stimulation improves parkinsonian motor signs and modulates neuronal activity throughout the basal ganglia thalamic network,* Exp.Neurol., **233,** 581-586.

von Coelln, R., Kugler, S., Bahr, M., Weller, M., Dichgans, J. and Schulz, J.B. (2001) *Rescue from death but not from functional impairment: caspase inhibition protects dopaminergic cells against 6-hydroxydopamine-induced apoptosis but not against the loss of their terminals,* J.Neurochem., **77,** 263-273.

Vroman, L. and Adams, A.L. (1969) *Identification of rapid changes at plasma?solid interfaces,* J.Biomed.Mater.Res., **3,** 43-67.

Walker, F.O. (2007) *Huntington's disease,* Lancet, **369,** 218-228.

Walters, J.R., Hu, D., Itoga, C.A., Parr-Brownlie, L.C. and Bergstrom, D.A. (2007) *Phase relationships support a role for coordinated activity in the indirect pathway in organizing slow oscillations in basal ganglia output after loss of dopamine,* Neuroscience, **144,** 762-776.

Wang, J., Ren, L., Li, L., Liu, W., Zhou, J., Yu, W., Tong, D. and Chen, S. (2009) *Microfluidics: a new cosset for neurobiology,* Lab.Chip, **9,** 644-652.

Wernig, M., Zhao, J.P., Pruszak, J., Hedlund, E., Fu, D., Soldner, F., Broccoli, V., Constantine-Paton, M., Isacson, O. and Jaenisch, R. (2008) *Neurons derived from reprogrammed fibroblasts functionally integrate into the fetal brain and improve symptoms of rats with Parkinson's disease,* Proc.Natl.Acad.Sci.U.S.A., **105,** 5856-5861.

Whitesides, G.M. (2006) *The origins and the future of microfluidics,* Nature, **442,** 368-373.

WHO (World Health Organisation) (2006) *Neurological Disorders: Public Health Challenges,* Geneva: WHO,

Wichmann, T. and Soares, J. (2006) *Neuronal firing before and after burst discharges in the monkey basal ganglia is predictably patterned in the normal state and altered in parkinsonism,* J.Neurophysiol., **95,** 2120-2133.

Wonders, C.P., Taylor, L., Welagen, J., Mbata, I.C., Xiang, J.Z. and Anderson, S.A. (2008) *A spatial bias for the origins of interneuron subgroups within the medial ganglionic eminence,* Dev.Biol., **314,** 127-136.

Woodard, C.M., Campos, B.A., Kuo, S.H., Nirenberg, M.J., Nestor, M.W., Zimmer, M., Mosharov, E.V., Sulzer, D., Zhou, H., Paull, D., Clark, L., Schadt, E.E., Sardi, S.P., Rubin, L., Eggan, K., Brock, M., Lipnick, S., Rao, M., Chang, S., Li, A. and Noggle, S.A. (2014) *iPSC-derived dopamine neurons reveal differences between monozygotic twins discordant for Parkinson's disease,* Cell.Rep., **9,** 1173-1182.

Wu, D.C., Teismann, P., Tieu, K., Vila, M., Jackson-Lewis, V., Ischiropoulos, H. and Przedborski, S. (2003) *NADPH oxidase mediates oxidative stress in the 1-methyl-4-phenyl-1,2,3,6-tetrahydropyridine model of Parkinson's disease,* Proc.Natl.Acad.Sci.U.S.A., **100,** 6145-6150.

Xiao, B., Ng, H.H., Takahashi, R. and Tan, E.K. (2016) *Induced pluripotent stem cells in Parkinson's disease: scientific and clinical challenges,* J.Neurol.Neurosurg.Psychiatry., **87,** 697-702.

Xicoy, H., Wieringa, B. and Martens, G.J. (2017a) *The SH-SY5Y cell line in Parkinson's disease research: a systematic review,* Mol.Neurodegener, **12,** 10-017-0149-0.

Xicoy, H., Wieringa, B. and Martens, G.J. (2017b) *The SH-SY5Y cell line in Parkinson's disease research: a systematic review,* Mol.Neurodegener, **12,** 10-017-0149-0.

Xin, W., Emadi, S., Williams, S., Liu, Q., Schulz, P., He, P., Alam, N.B., Wu, J. and Sierks, M.R. (2015) *Toxic Oligomeric Alpha-Synuclein Variants Present in Human Parkinson's Disease Brains Are Differentially Generated in Mammalian Cell Models,* Biomolecules, **5,** 1634-1651.

Yager, L.M., Garcia, A.F., Wunsch, A.M. and Ferguson, S.M. (2015) *The ins and outs of the striatum: role in drug addiction,* Neuroscience, **301,** 529-541.

Yamada, J., Okabe, A., Toyoda, H., Kilb, W., Luhmann, H.J. and Fukuda, A. (2004) *Cl- uptake promoting depolarizing GABA actions in immature rat neocortical neurones is mediated by NKCC1,* J.Physiol., **557,** 829-841.

Yavin, E. and Yavin, Z. (1974) *Attachment and culture of dissociated cells from rat embryo cerebral hemispheres on polylysine-coated surface,* J.Cell Biol., **62,** 540-546.

Yazdani, U., German, D.C., Liang, C.L., Manzino, L., Sonsalla, P.K. and Zeevalk, G.D. (2006) *Rat model of Parkinson's disease: chronic central delivery of 1-methyl-4-phenylpyridinium (MPP+),* Exp.Neurol., **200,** 172-183.

Yin, X., Mead, B.E., Safaee, H., Langer, R., Karp, J.M. and Levy, O. (2016) *Engineering Stem Cell Organoids,* Cell.Stem Cell., **18,** 25-38.

Yla-Outinen, L., Heikkila, J., Skottman, H., Suuronen, R., Aanismaa, R. and Narkilahti, S. (2010) *Human cell-based micro electrode array platform for studying neurotoxicity,* Front.Neuroeng, **3,** 10.3389/fneng.2010.00111. eCollection 2010.

Yum, K., Hong, S.G., Healy, K.E. and Lee, L.P. (2014) *Physiologically relevant organs on chips,* Biotechnology Journal, **9,** 16-27.

Zairi, S., Reybier, K., Jaffrezic-Renault, N., Martelet, C. and Fahys, B. (2002) *Enhanced ionodetection by using polyethyleneimine as an insulator material,* Materials Science and Engineering: C, **21,** 35-41.

Zhang,Song, Song,Yilin, Wang,Mixia, Xiao,Guihua, Gao,Fei, Li,Ziyue, Tao,Guoxian, Zhuang,Ping, Yue,Feng, Chan,Piu and Cai,Xinxia (2018) *Real-time simultaneous recording of electrophysiological activities and dopamine overflow in the deep brain nuclei of a non-human primate with Parkinsonâ€™s disease using nano-based microelectrode arrays,* Nature Microsystems and Nanoengineering, **4,** 17070.

Zhang, X.M., Yin, M. and Zhang, M.H. (2014) *Cell-based assays for Parkinson's disease using differentiated human LUHMES cells,* Acta Pharmacol.Sin., **35,** 945-956.

Zhou, F.M. and Lee, C.R. (2011) *Intrinsic and integrative properties of substantia nigra pars reticulata neurons,* Neuroscience, **198,** 69-94.

Zhou, T., Benda, C., Dunzinger, S., Huang, Y., Ho, J.C., Yang, J., Wang, Y., Zhang, Y., Zhuang, Q., Li, Y., Bao, X., Tse, H.F., Grillari, J., Grillari-Voglauer, R., Pei, D. and Esteban, M.A. (2012) *Generation of human induced pluripotent stem cells from urine samples,* Nat.Protoc., **7,** 2080-2089.

Znamenskiy, P. and Zador, A.M. (2013) *Corticostriatal neurons in auditory cortex drive decisions during auditory discrimination,* Nature, **497,** 482-485.

Zuo, L., Yu, S., Briggs, C.A., Kantor, S. and Pan, J.Y. (2017) *Design and Fabrication of a Three-Dimensional Multi-Electrode Array for Neuron Electrophysiology,* J.Biomech.Eng., **139,** 10.1115/1.4037948.

Appendices

These appendices consist of images of raw MEA activity.

- Appendix 1: Raw images of MEA activity from separate MEA cultures (linked to Chapter 4), indicating 20 s of activity, 0.5 s and 10 ms, for 15, 21, 44 and 70 DIV
    - 1.1: CTX
    - 1.2: STR
    - 1.3: GP
    - 1.4: SN.
- Appendix 2: Raw images of MEA activity from connected MEA cco-ultures (linked to Chapter 5), indicating 240 s of activity from an electrode of a port for 15, 21, 44 and 70 DIV
    - 2.1: CTX port of CTX-STR device
    - 2.2: GP port of STR-GP device
    - 2.3: SNc port of SNc-STR device
- Appendix 3: Images of centroids from connected co-cultures on MEAs with some discussion of what they show
    - 2.1: CTX port of CTX-STR device
    - 2.2: GP port of STR-GP device
    - 2.3: SNc port of SNc-STR device
- Appendix 4: Images of raw data across an entire MEA generated by Python code, showing 240 seconds of activity for 15, 21, 44 and 70 DIV.
    - Appendix 1: CTX (separate culture) on days 15, 21, 44 and 70
    - Appendix 2: STR (separate culture) on days 15, 21, 44 and 70
    - Appendix 3: GP (separate culture) on days 15, 21, 44 and 70
    - Appendix 4: SN (separate culture) on days 15, 21, 44 and 70
    - Appendix 5: CTX-STR (connected co-culture) on days 15, 21, 42 and 70
    - Appendix 6: STR-GP (connected co-culture) on days 15, 21, 42 and 70
    - Appendix 7: SNc-STR (connected co-culture) on days 15, 21, 42 and 70

Appendix One

CTX

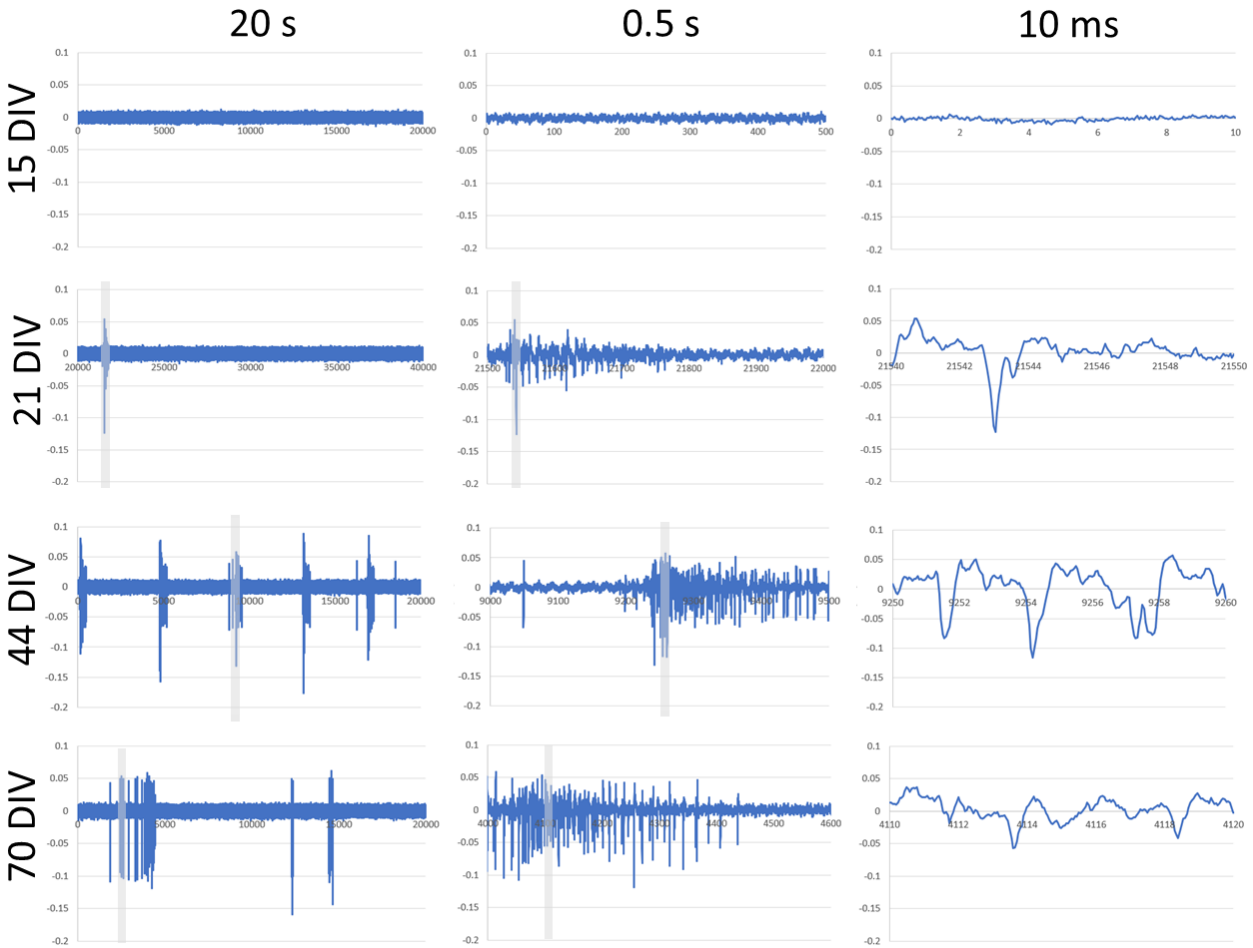

Appendix 1.1: Raw spontaneous spiking extracellular activity recorded from cells isolated from the CTX. Rows indicate culture activity at DIV 15, 21, 44 and 70, while columns indicate the time of each trace, namely 20 s, 0.5 s and 10 ms. X-axis is 0.1 to -0.2 mV. Activity shown is taken from an active electrode and is representative of the average activity each day. Number of active electrodes on each day is as follows: 0, 36, 36 and 17. RAW data for the whole MEA can be seen in Appendix .

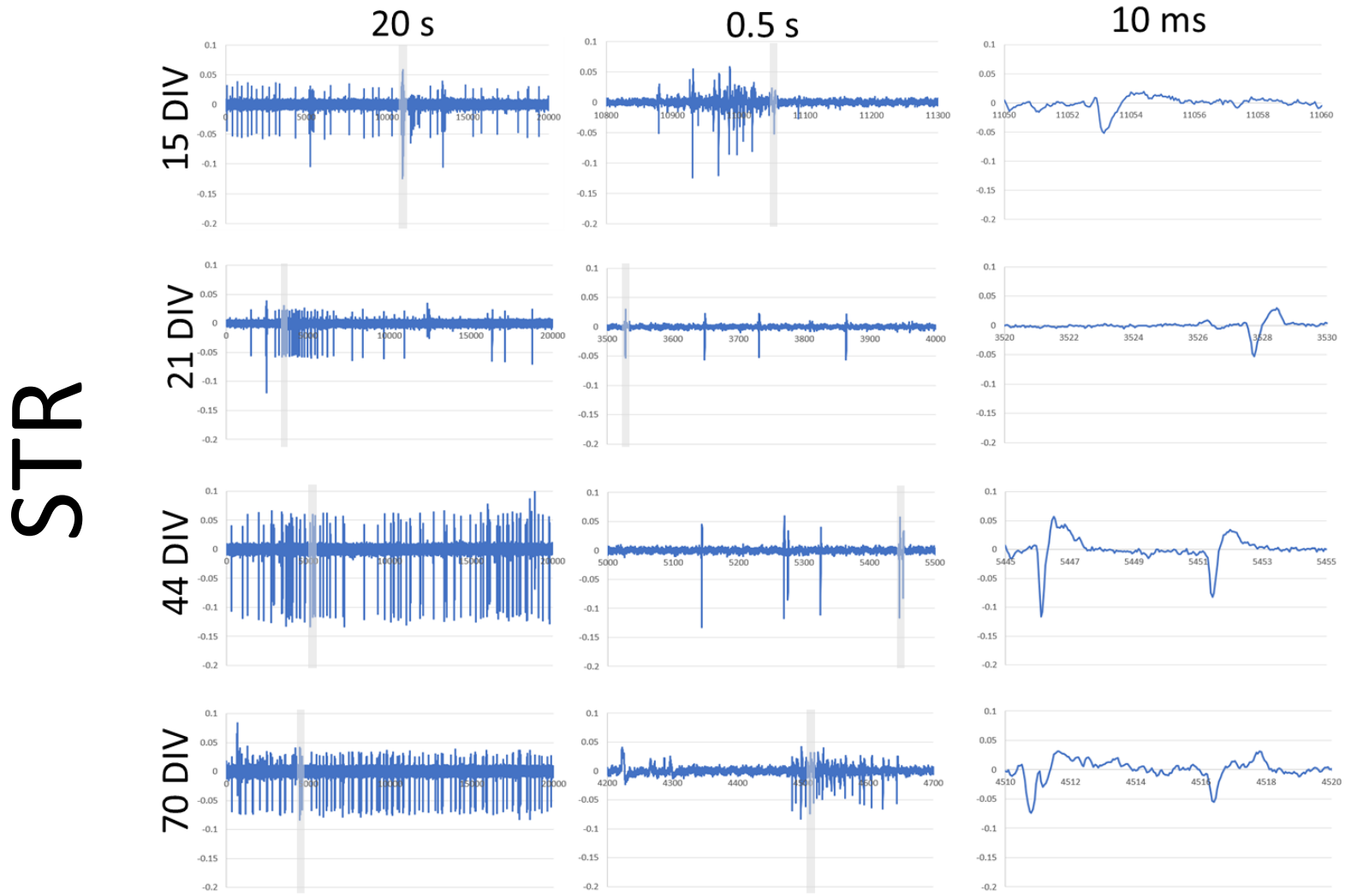

Appendix 1.2: Raw spontaneous spiking extracellular activity recorded from cells isolated from the STR. Rows indicate culture activity at DIV 15, 21, 44 and 70, while columns indicate the time of each trace, namely 20 s, 0.5 s and 10 ms. Each trace ranges from 0.1 to -0.2 mV. Activity shown is taken from an active electrode and is representative of the average activity each day. Number of active electrodes on each day is as follows: 0, 36, 36 and 17. RAW data for the whole electrode can be seen in APPENDIX.

GP

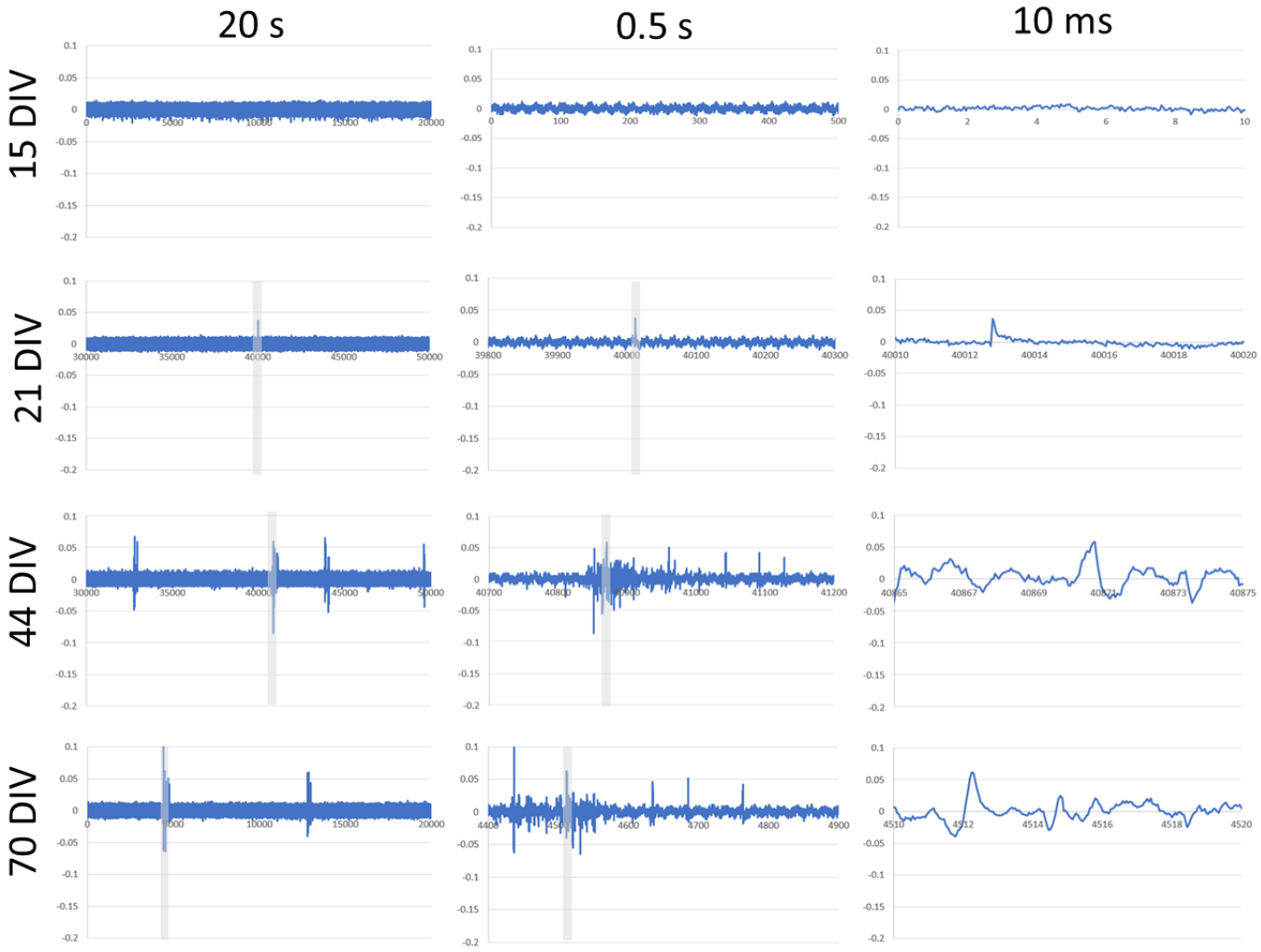

Appendix 1.3: Raw spontaneous spiking extracellular activity recorded from cells isolated from the GP. Rows indicate culture activity at DIV 15, 21, 44 and 70, while columns indicate the time of each trace, namely 20 s, 0.5 s and 10 ms. Each trace ranges from 0.1 to -0.2 mV. Activity shown is taken from an active electrode and is representative of the average activity each day. Number of active electrodes on each day is as follows: 0, 36, 36 and 17. RAW data for the whole electrode can be seen in APPENDIX.

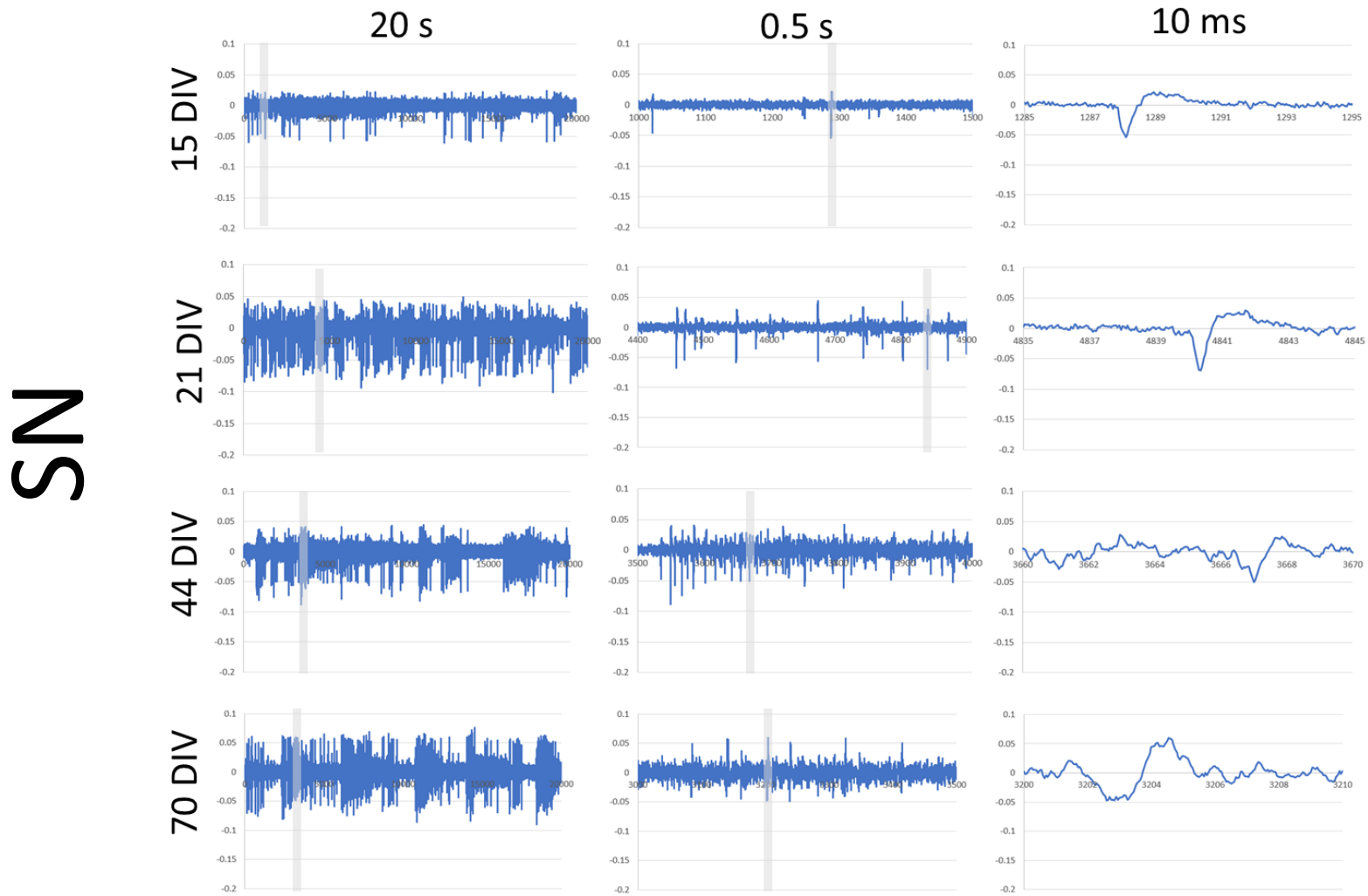

Appendix 1.4: Raw spontaneous spiking extracellular activity recorded from cells isolated from the SN. A-D show the spiking activity at DIV 15, 21, 44 and 70 respectively. Each trace lasted for 240 s (measured in milliseconds in the figure) and ranged from 0.1 to -0.15 mV. Activity shown is representative of the average activity each day. Number of active electrodes on each day is as follows: 47, 52, 44 and 44. RAW data for the whole electrode can be seen in APPENDIX.

Appendix Two

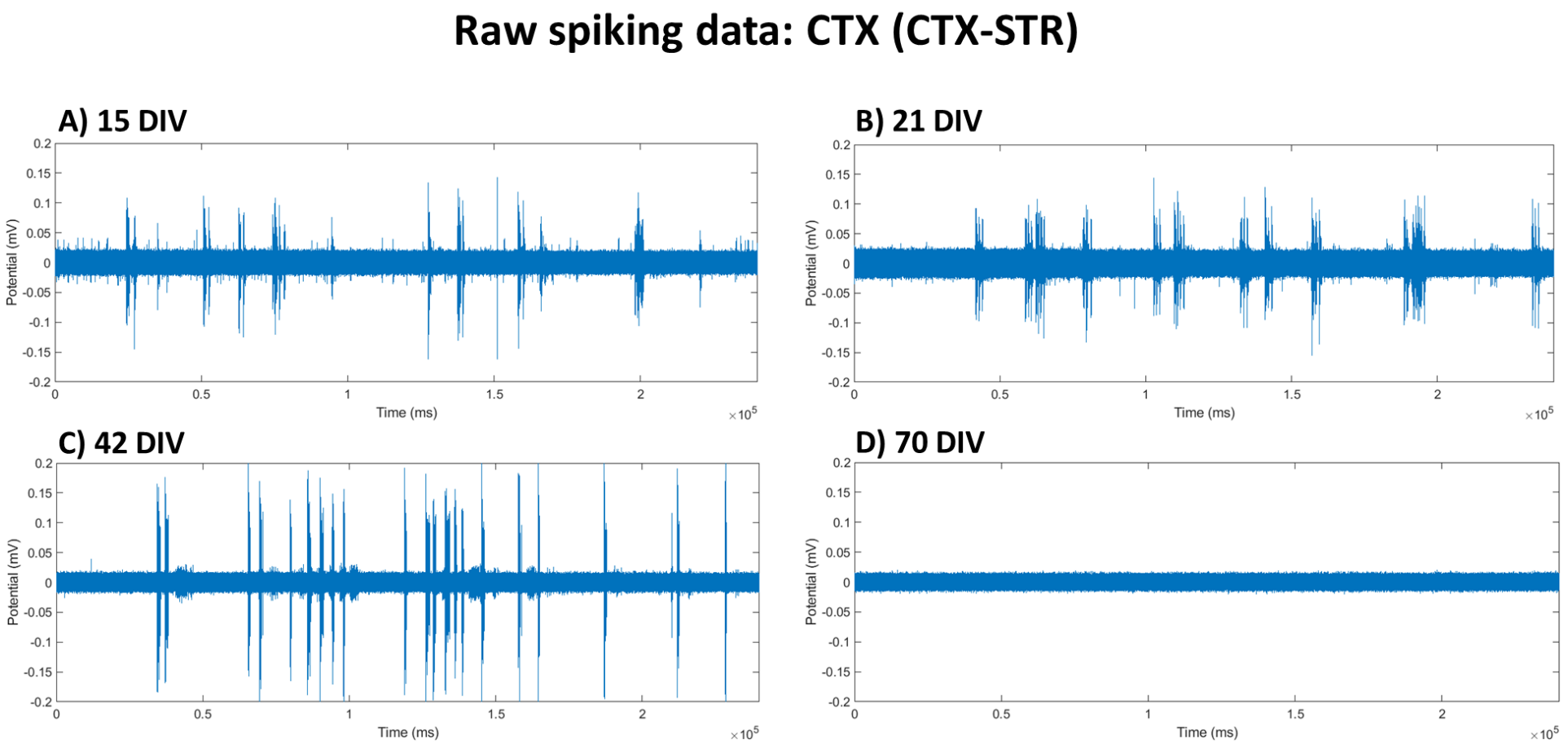

Appendix 2.1: 240 seconds of raw activity from the CTX port of a CTX-STR device. Activity from electrode 42 at 15, 21, 42 and 70 DIV, scaled from -0.2 to 0.2 mV. Images of raw activity across the whole MEA can be see in the APPENDIX.

Raw spiking data: GP (STR-GP)

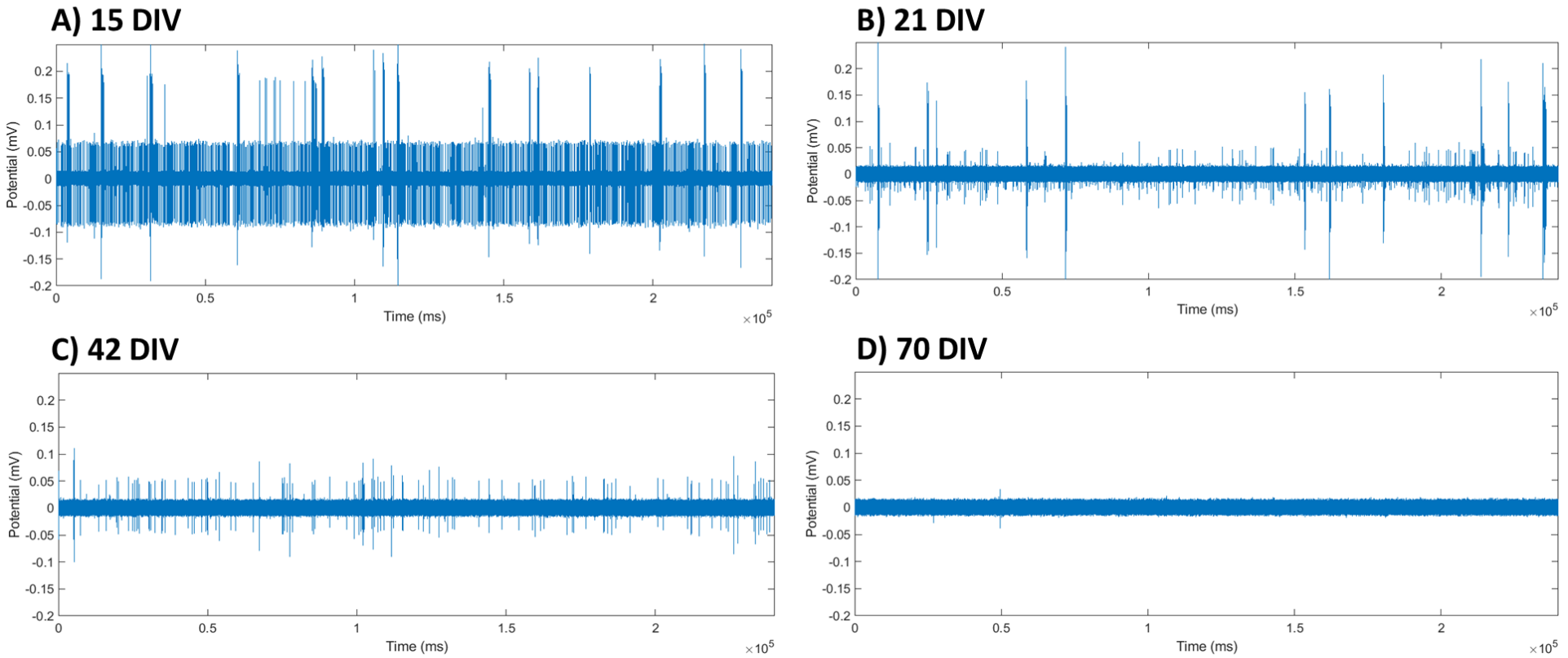

Appendix 2.2: 240 seconds of raw activity from the GP port of a GP-STR device. Activity from electrode 27 at 15, 21, 42 and 70 DIV, scaled from -0.2 to 0.25 mV. Images of raw activity across the whole MEA can be see in the APPENDIX.

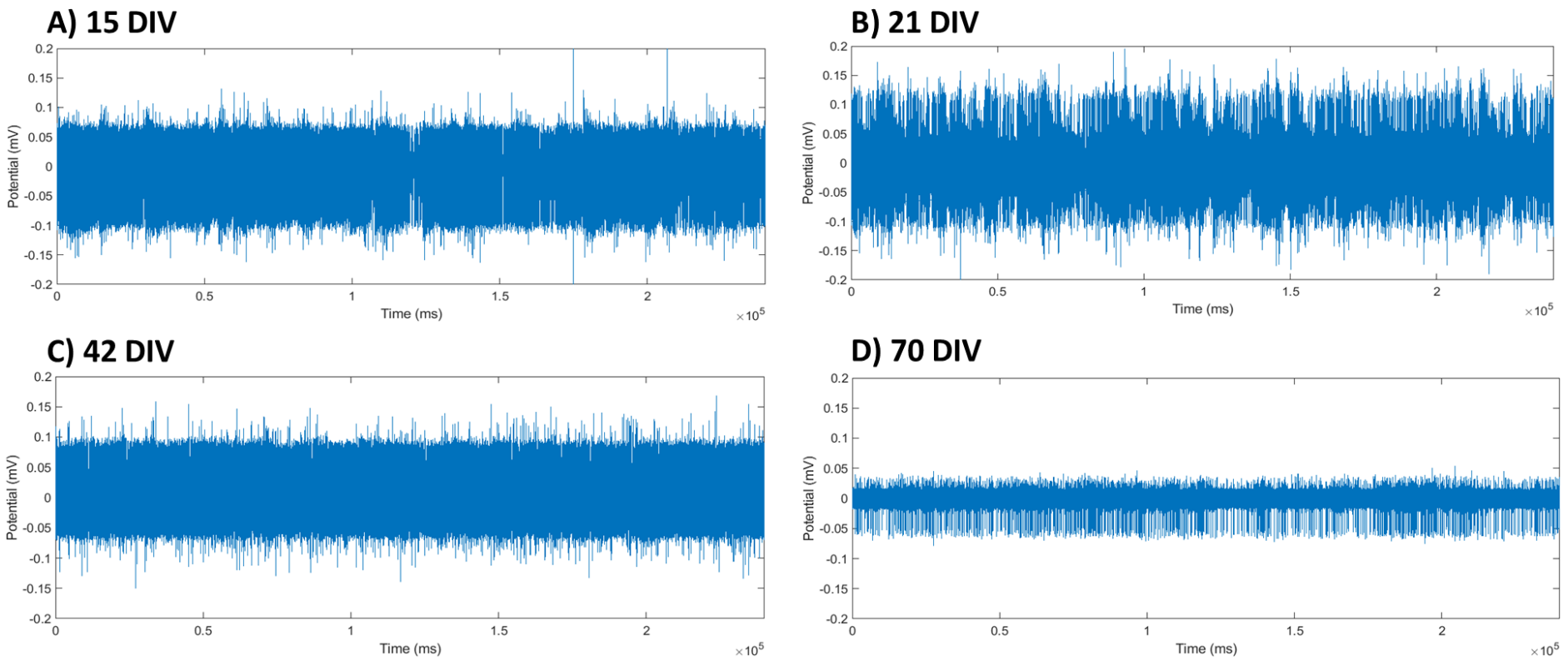

Appendix 2.3: 240 seconds of raw activity from the SN port of a SN-STR device. Activity from electrode 35 at 15, 21, 42 and 70 DIV, scaled from -0.2 to 0.2 mV. Images of raw activity across the whole MEA can be see in the APPENDIX.

Appendix Three

The largest four centroids for each co-culture are displayed for days 15, 21, 42 and 70 (if there were less than four centroids then all centroids were displayed). A new phase was defined by the measured potential crossing the x-axis and exceeding ≥10 µV in either direction.

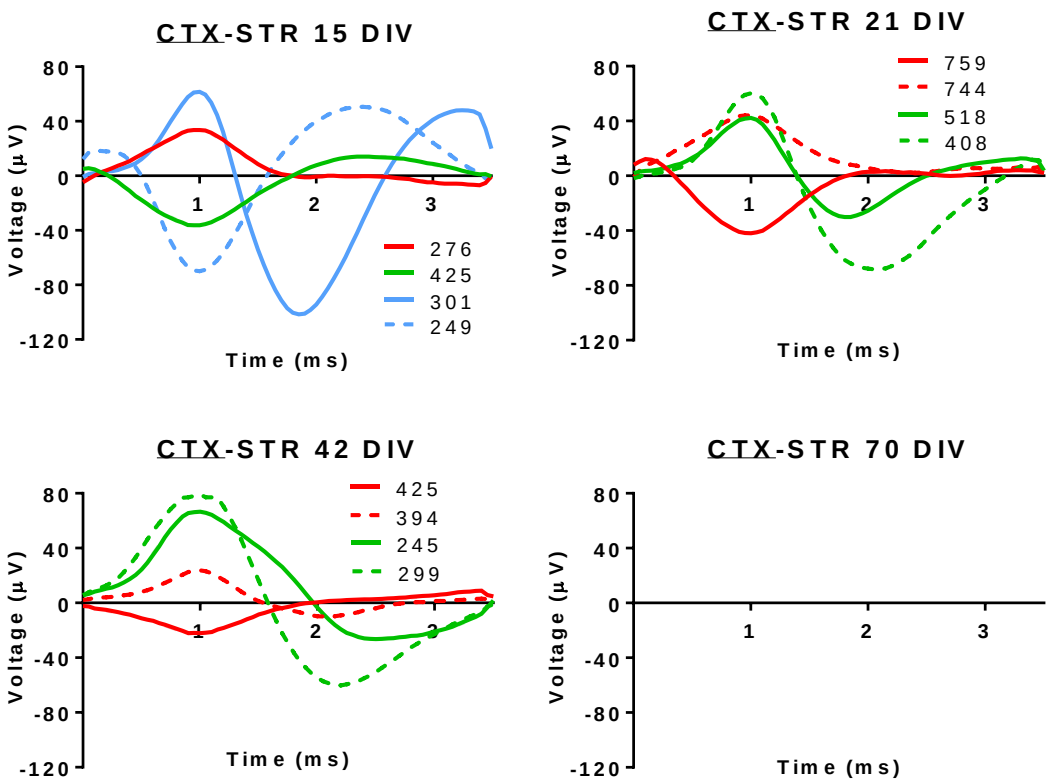

Appendix 3.1: Centroid waveforms for CTX-STR co-culture from electrode 43 across four time points. Red, green and blue signify mono-, bi- and tri-phasic centroids respectively, legend indicates how many spikes make up the centroid.

CTX-STR centroids began with a high level of variability, displaying mono-, bi- and triphasic centroids with both positive and negative spikes. 15 DIV centroids are unaligned and varied, with large negative and positive spikes. By 21 and 42 DIV the centroids are more similar in amplitude and alignment with only mono- and biphasic centroids remaining by 42 DIV. By 70 DIV there was no signal remaining from this electrode.

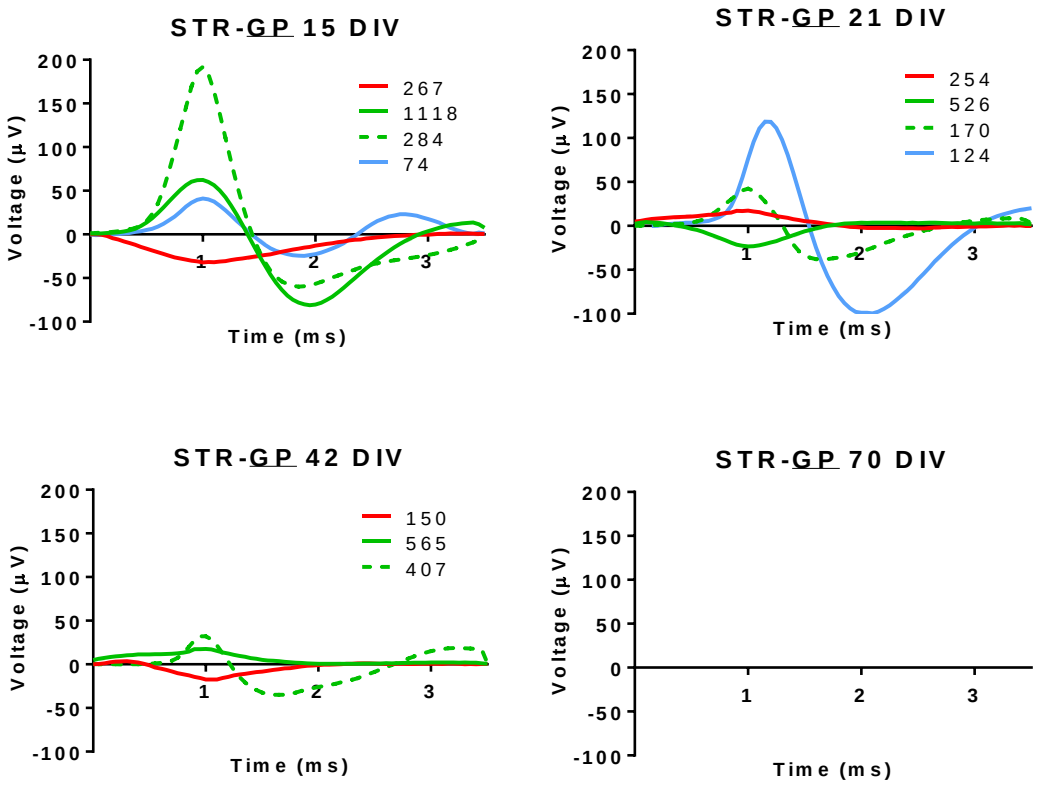

Appendix 3.2 Centroid waveforms for GP-STR co-culture from electrode 43 across four time points. Red, green and blue signify mono-, bi- and tri-phasic centroids respectively, legend indicates how many spikes make up the centroid.

GP-STR centroids decreased in amplitude, variability and number of spikes per centroid over time. 15 DIV centroids featured mono-, bi- and triphasic waveforms, with one biphasic centroid ranging from 200 to -80 µV, a greater amplitude than any other cell type. By 21 DIV this range decreased to 100 to -100 µV with only monophasic and biphasic centroids remaining, and by 42 DIV this range was 30 to -30 µV with mainly monophasic centroids and a triphasic centroid, decreasing further to zero by 70 DIV.

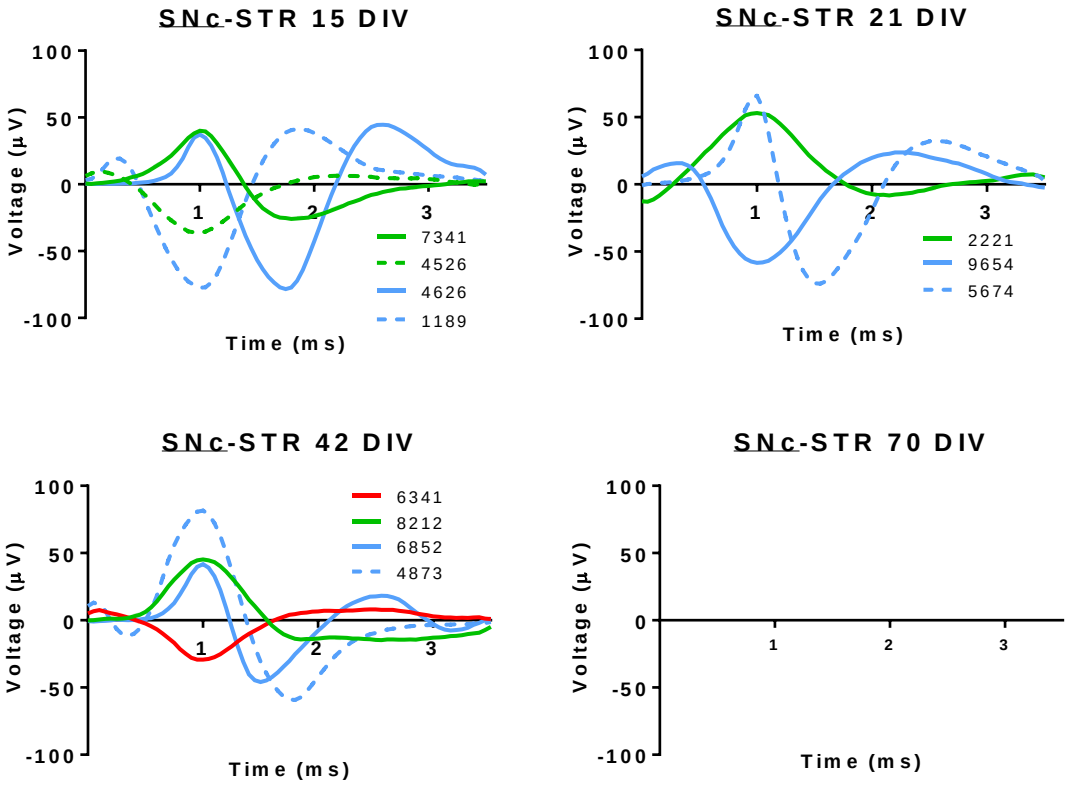

Appendix 3.3: Centroid waveforms for CTX-STR co-culture from electrode 43 across four time points. Red, green and blue signify mono-, bi- and tri-phasic centroids respectively, legend indicates how many spikes make up the centroid.

SNc-STR centroids contained the most spikes out of all cell types (as indicated by the legends), and did not contain any monophasic spikes until 42 DIV, suggesting complex networking. There were few changes from 15-42 DIV except the single monophasic centroid, and all signal was lost at 70 DIV.

Appendix Four

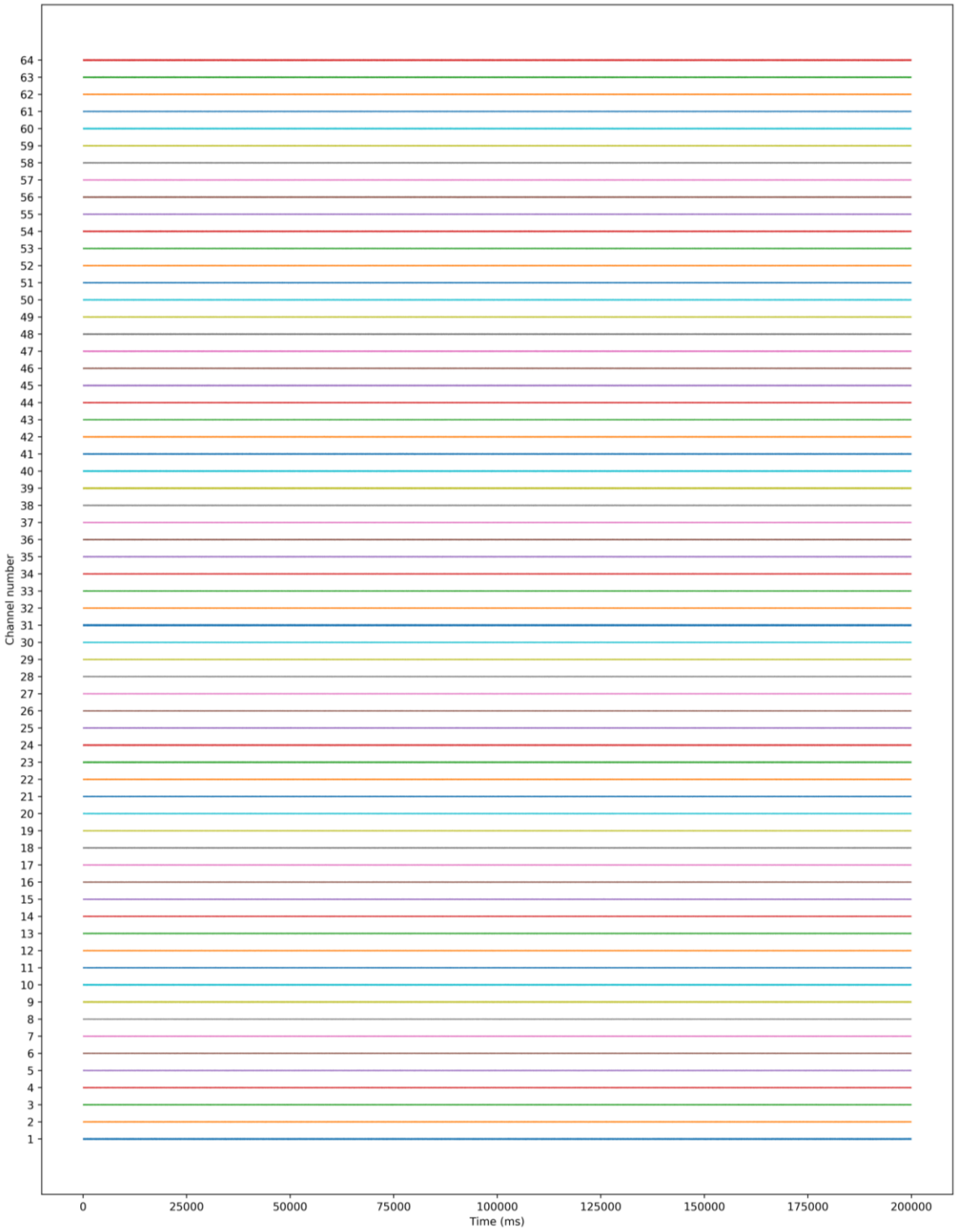

Appendix 1.1: 240 seconds of raw activity from all 64 electrodes of an MEA seeded with a CTX neural culture, after 15 DIV.

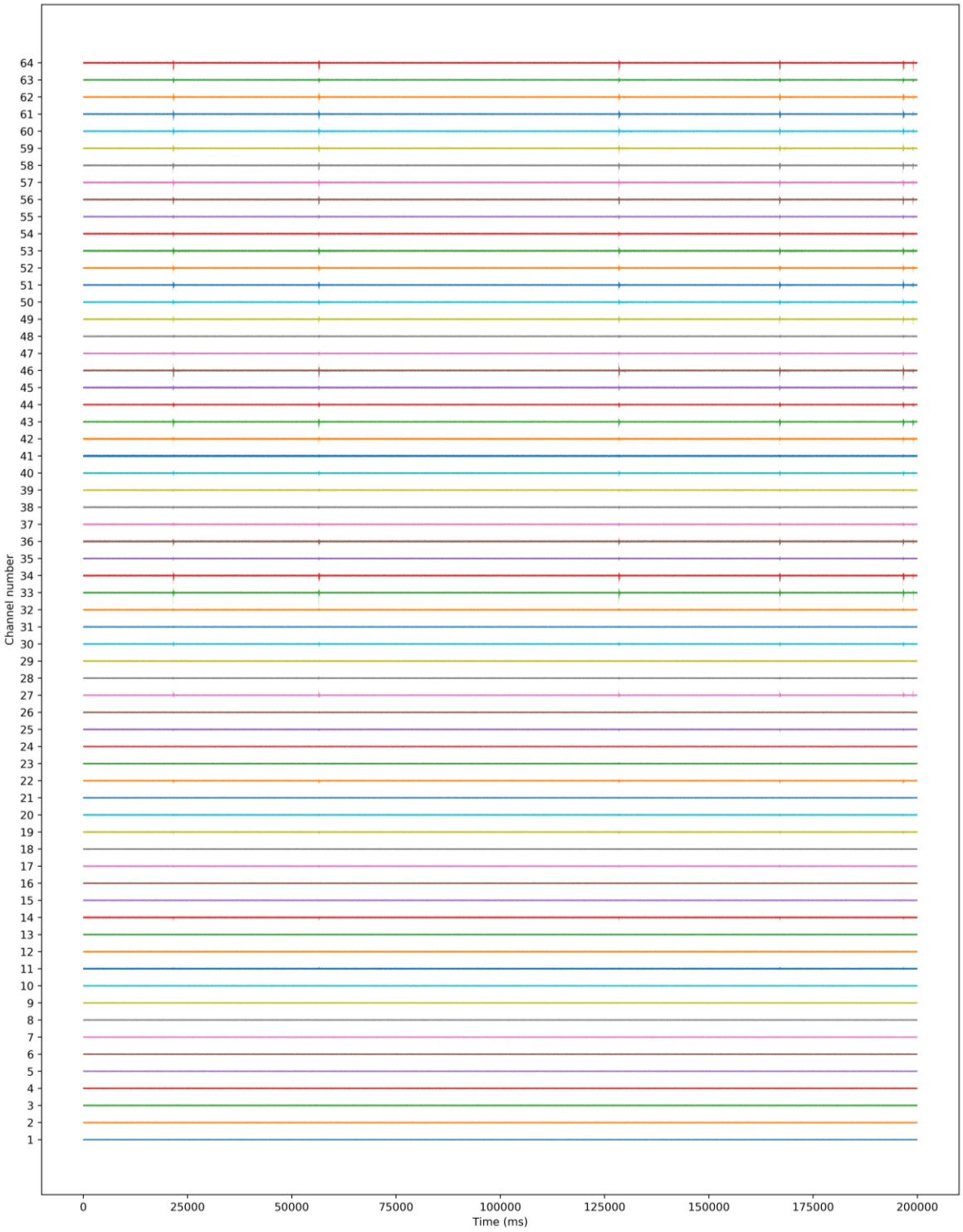

Appendix 1.2: 240 seconds of raw activity from all 64 electrodes of an MEA seeded with a CTX neural culture, after 21 DIV. Note the network activity and alignment of bursts.

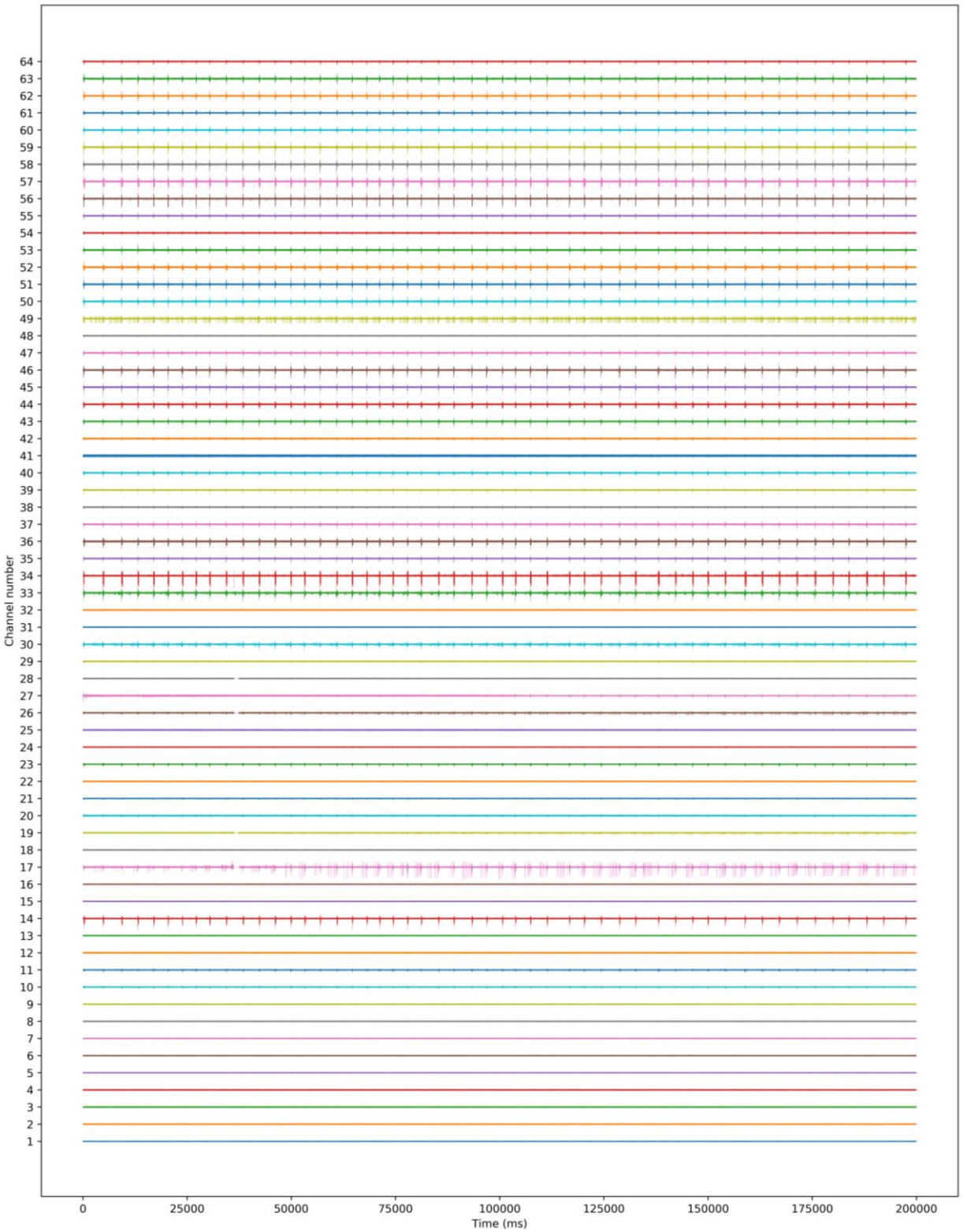

Appendix 1.3: 240 seconds of raw activity from all 64 electrodes of an MEA seeded with a CTX neural culture, after 44 DIV. Note the network activity and alignment of bursts.

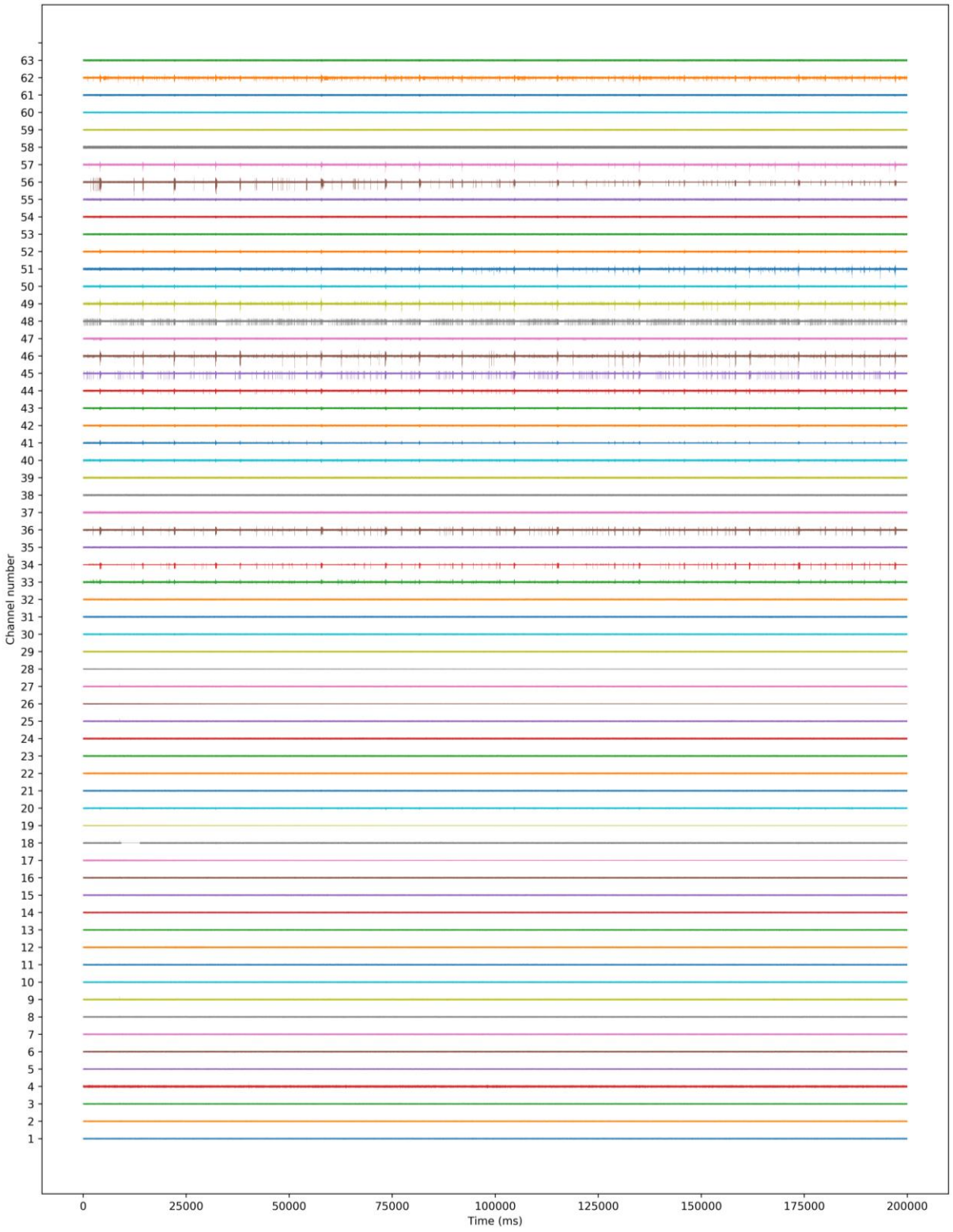

Appendix 1.4: 240 seconds of raw activity from all 64 electrodes of an MEA seeded with a CTX neural culture, after 70 DIV. Note the network activity and alignment of bursts.

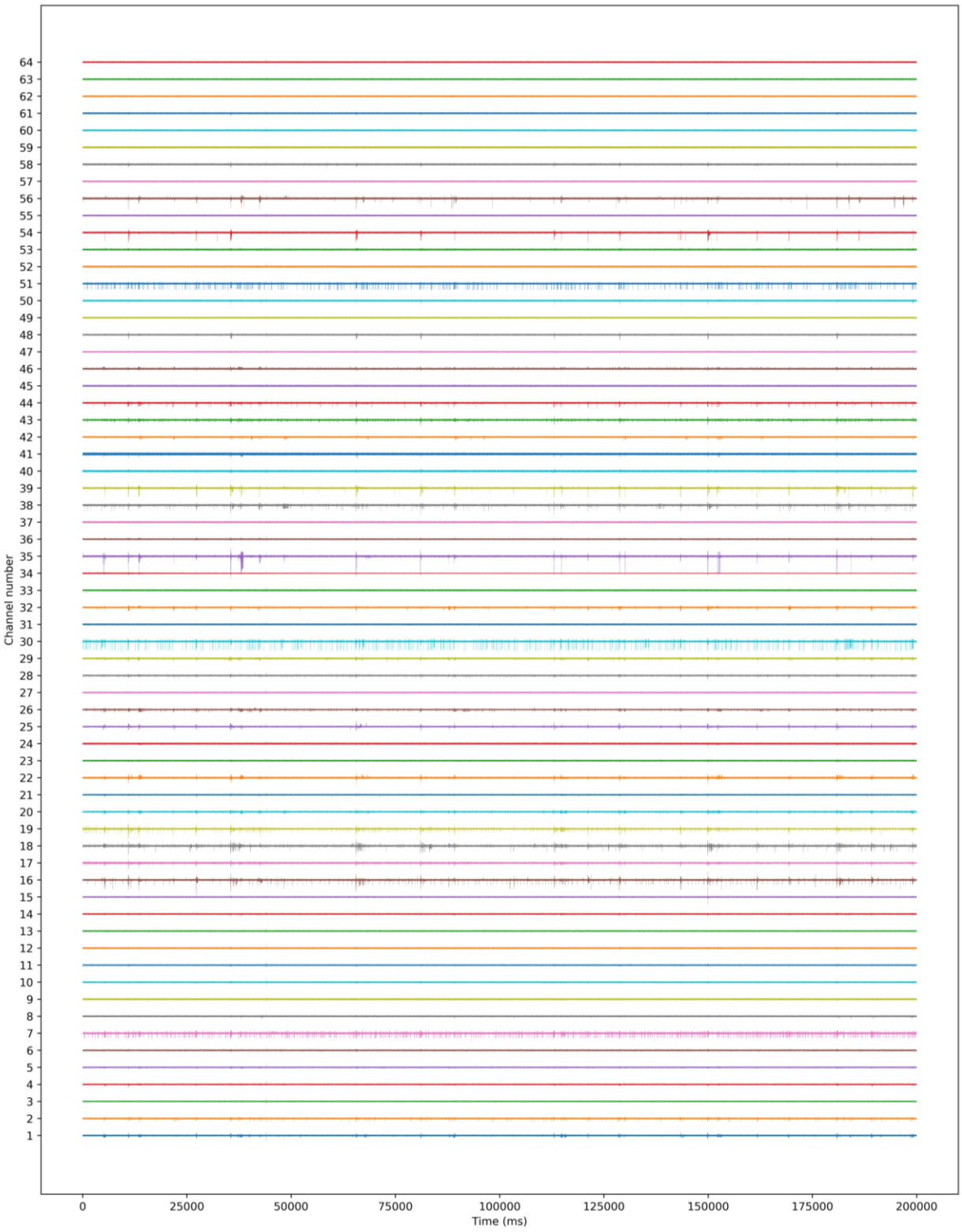

Appendix 2.1: 240 seconds of raw activity from all 64 electrodes of an MEA seeded with a STR neural culture, after 15 DIV.

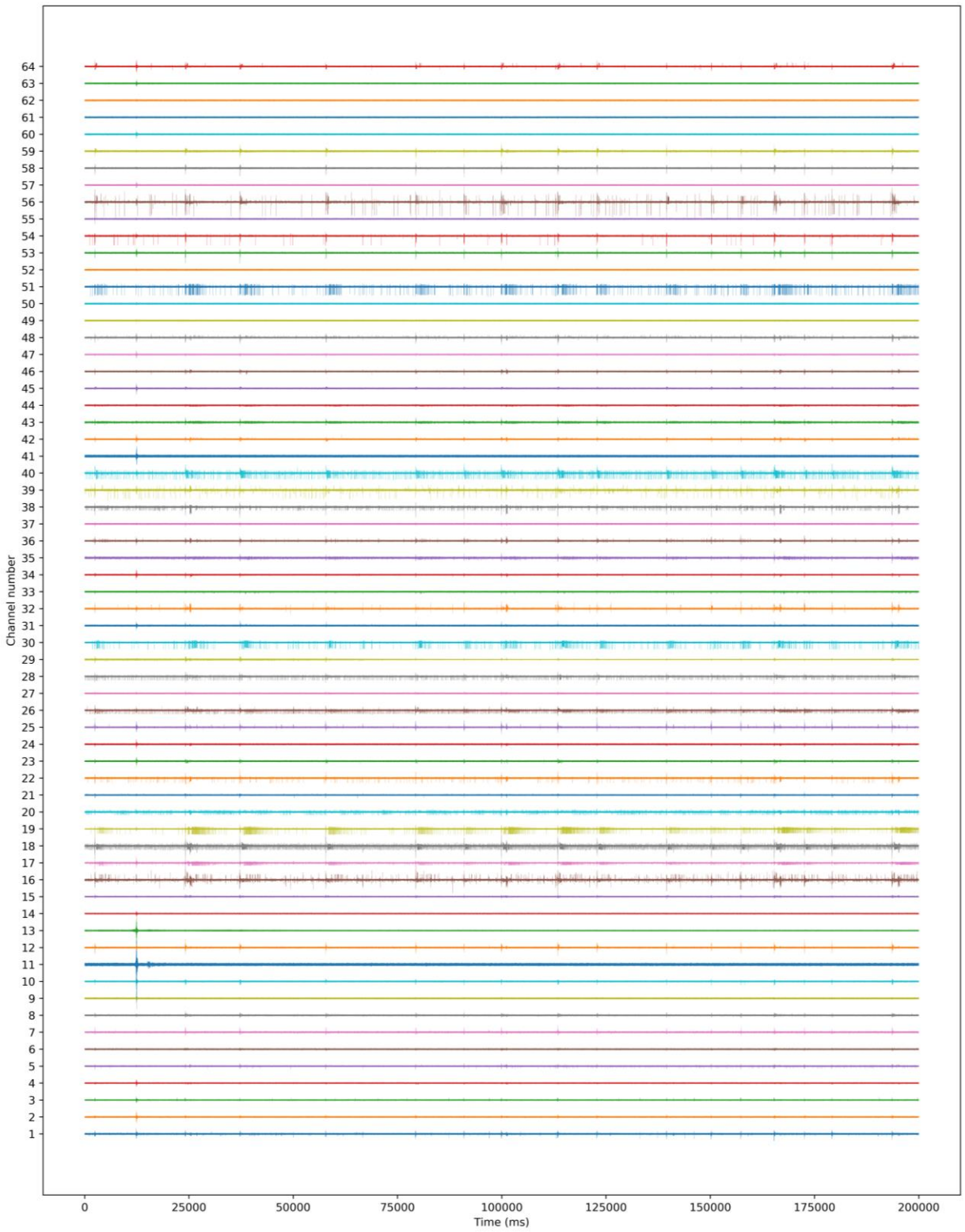

Appendix 2.2: 240 seconds of raw activity from all 64 electrodes of an MEA seeded with a STR neural culture, after 21 DIV.

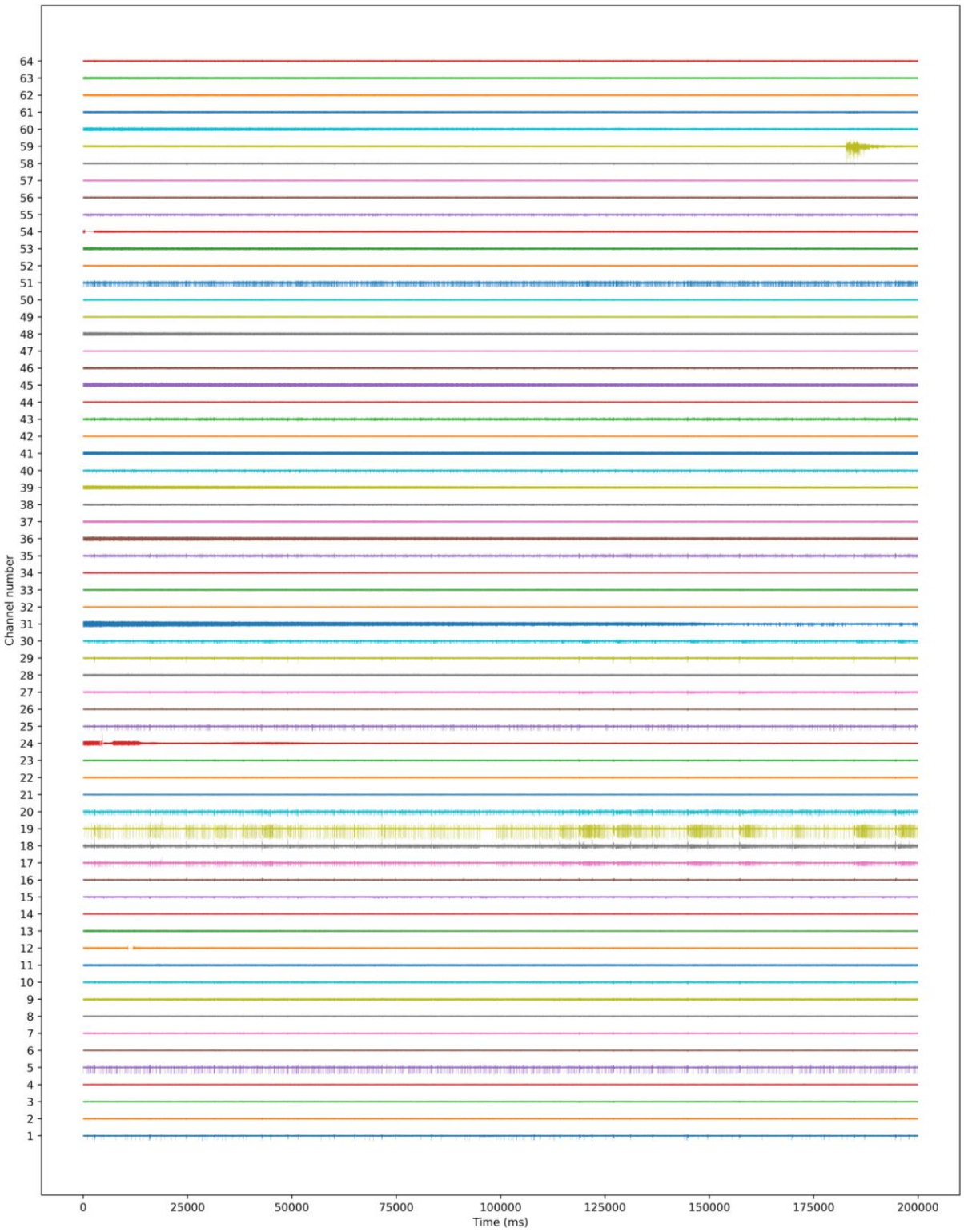

Appendix 2.3: 240 seconds of raw activity from all 64 electrodes of an MEA seeded with a STR neural culture, after 44 DIV.

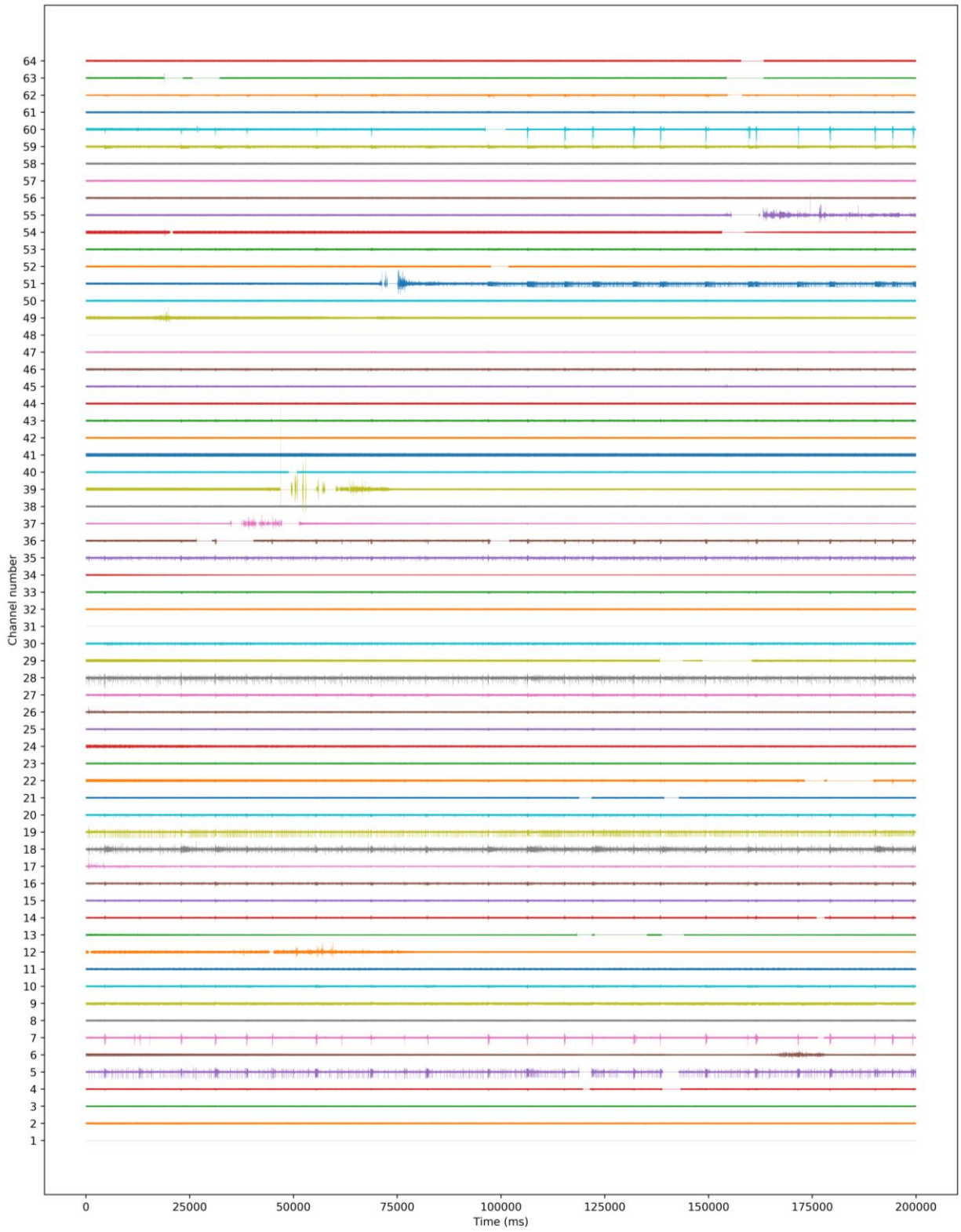

Appendix 2.4: 240 seconds of raw activity from all 64 electrodes of an MEA seeded with a STR neural culture, after 70 DIV.

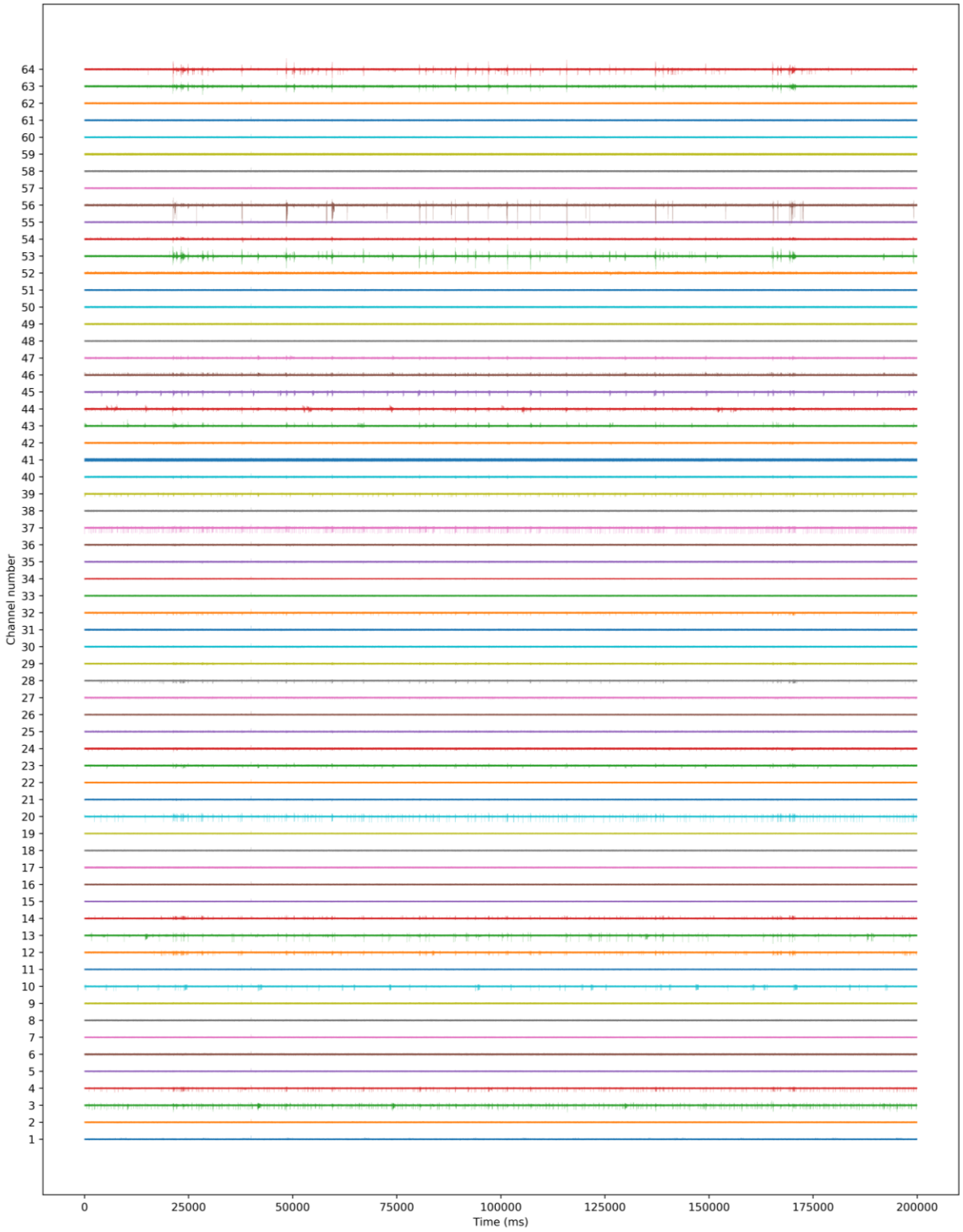

Appendix 3.1: 240 seconds of raw activity from all 64 electrodes of an MEA seeded with a GP neural culture, after 15 DIV.

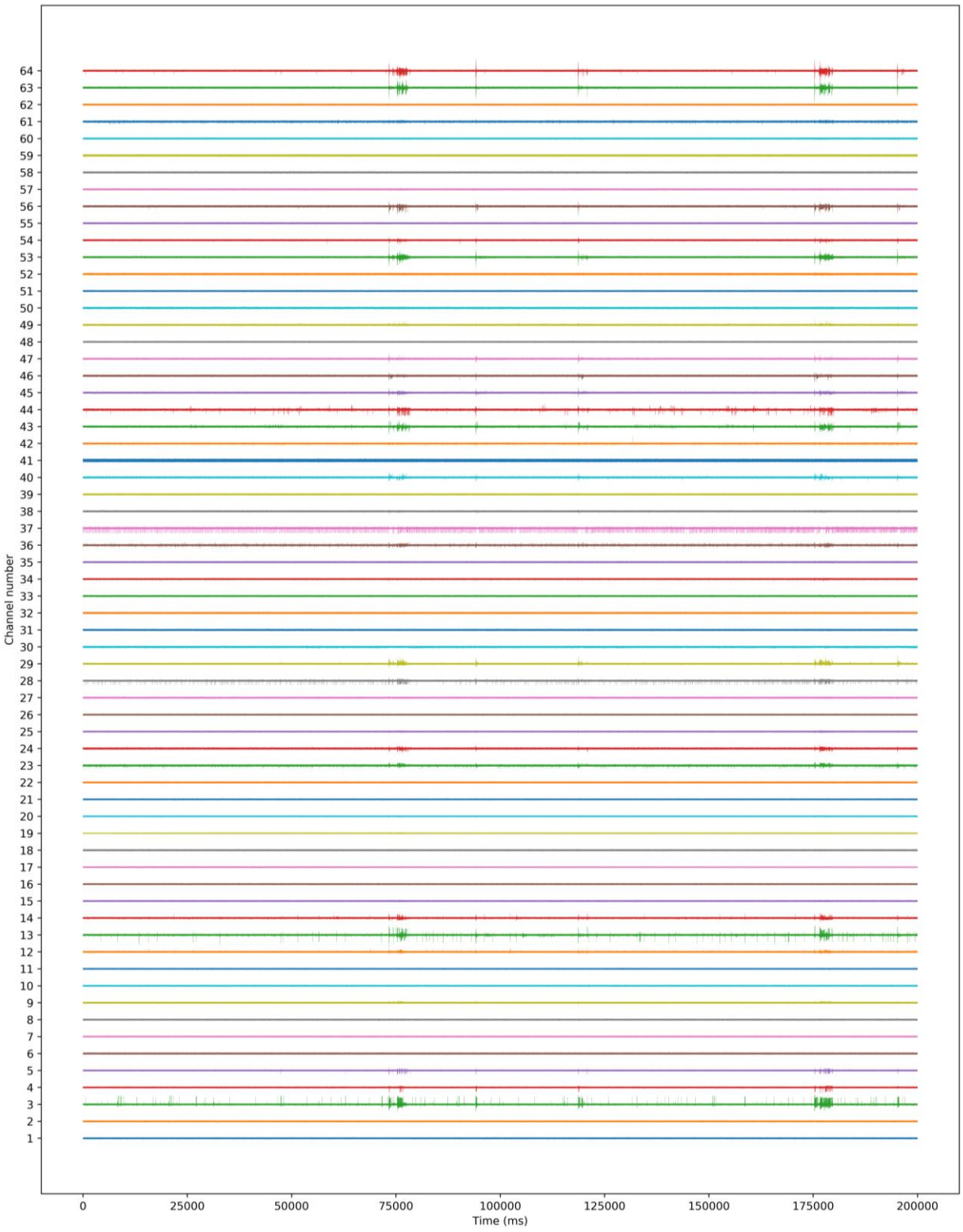

Appendix 3.2: 240 seconds of raw activity from all 64 electrodes of an MEA seeded with a GP neural culture, after 21 DIV.

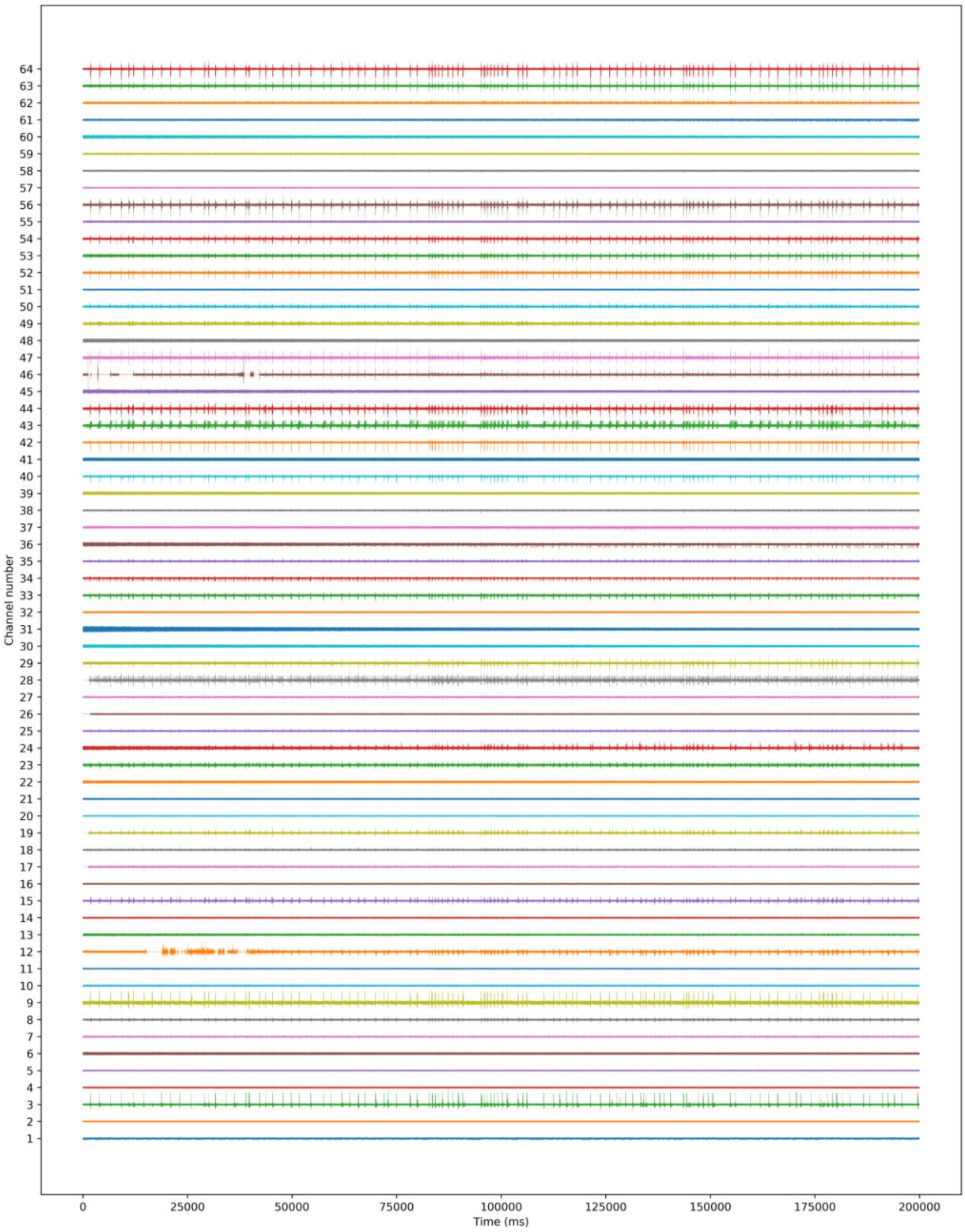

Appendix 3.3: 240 seconds of raw activity from all 64 electrodes of an MEA seeded with a GP neural culture, after 44 DIV.

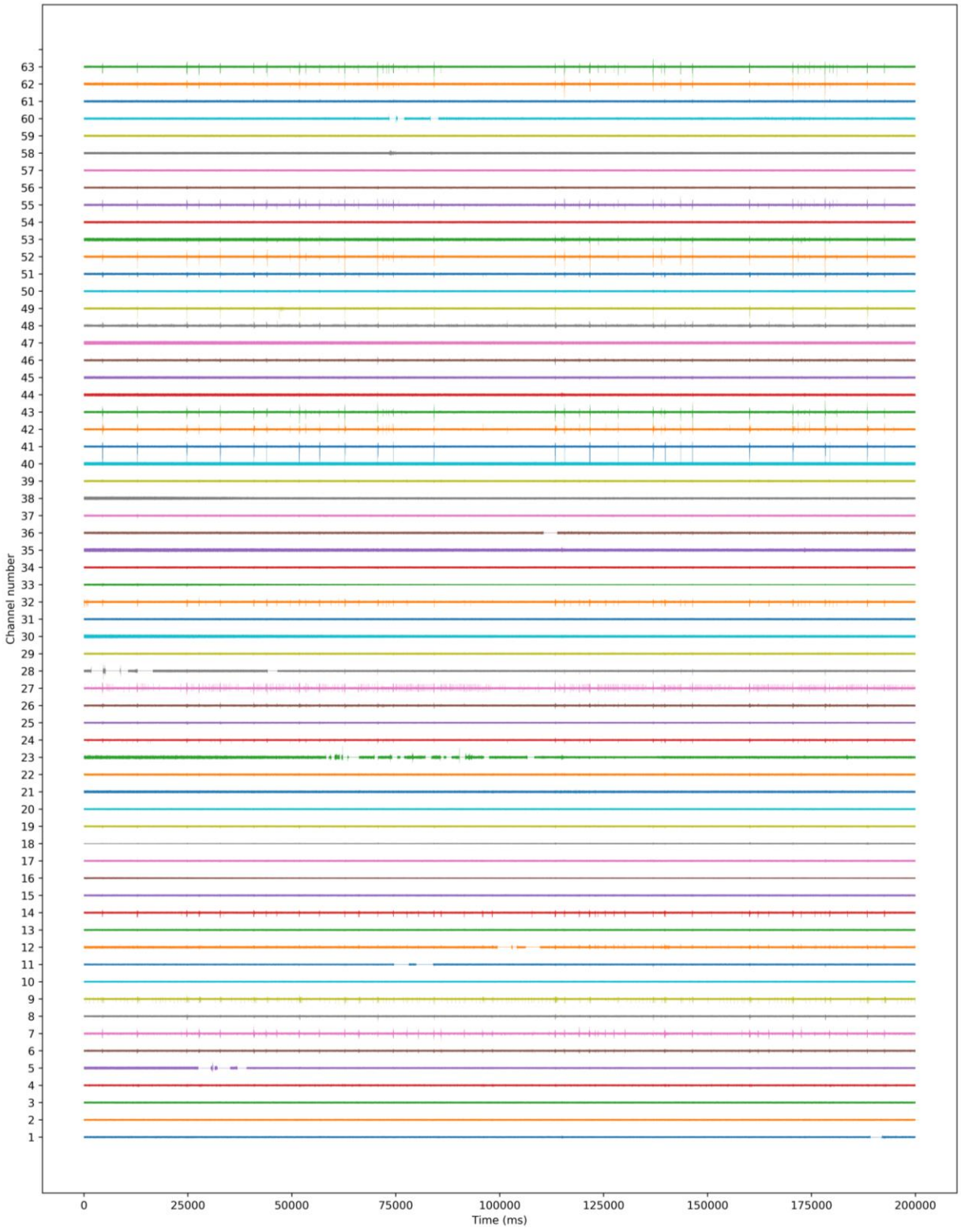

Appendix 3.4: 240 seconds of raw activity from all 64 electrodes of an MEA seeded with a GP neural culture, after 70 DIV.

Appendix 4.1: 240 seconds of raw activity from all 64 electrodes of an MEA seeded with a SN neural culture, after 15 DIV.

Appendix 4.2: 240 seconds of raw activity from all 64 electrodes of an MEA seeded with a SN neural culture, after 21 DIV.

Appendix 4.3: 240 seconds of raw activity from all 64 electrodes of an MEA seeded with a SN neural culture, after 44 DIV.

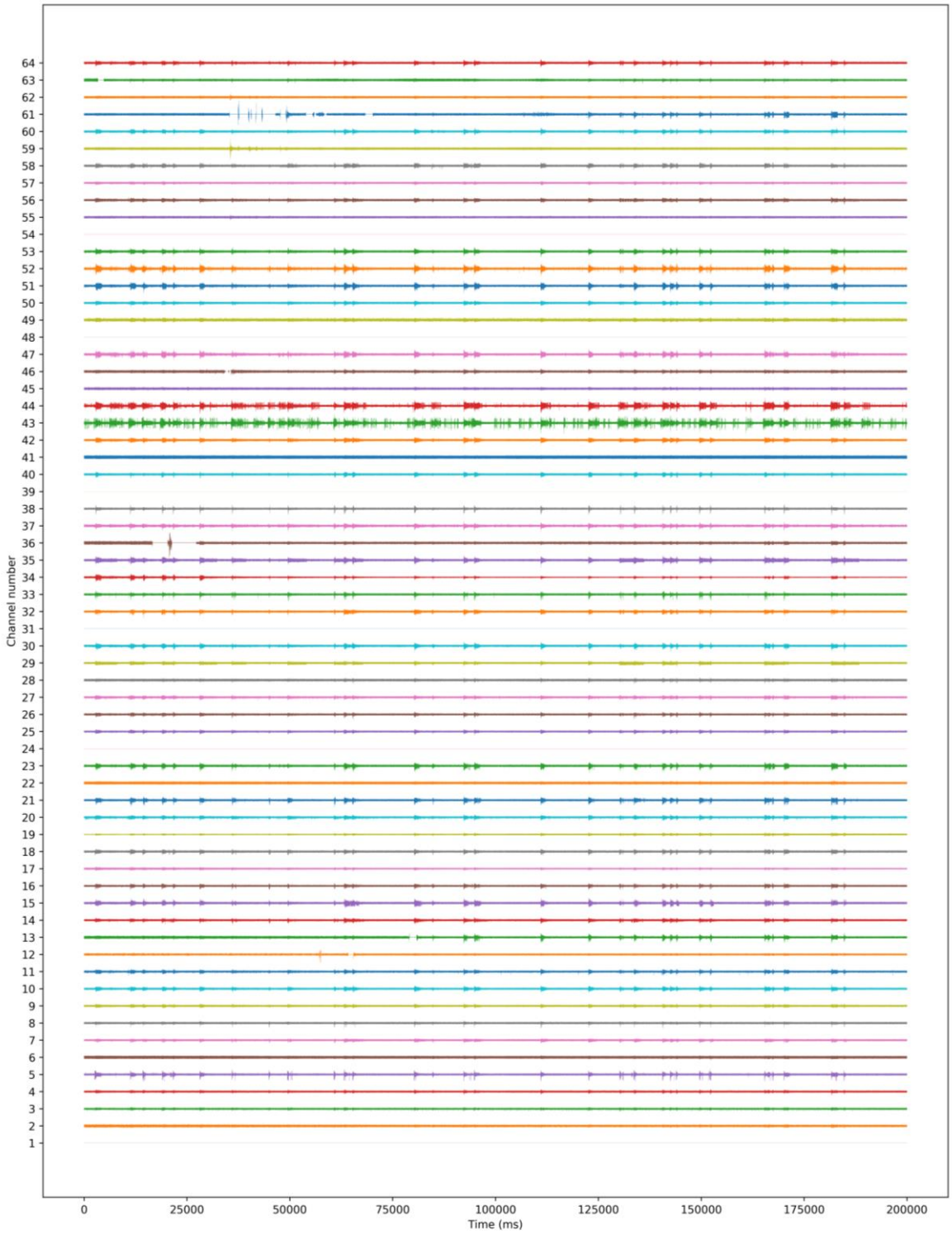

Appendix 4.4: 240 seconds of raw activity from all 64 electrodes of an MEA seeded with a SN neural culture, after 70 DIV.

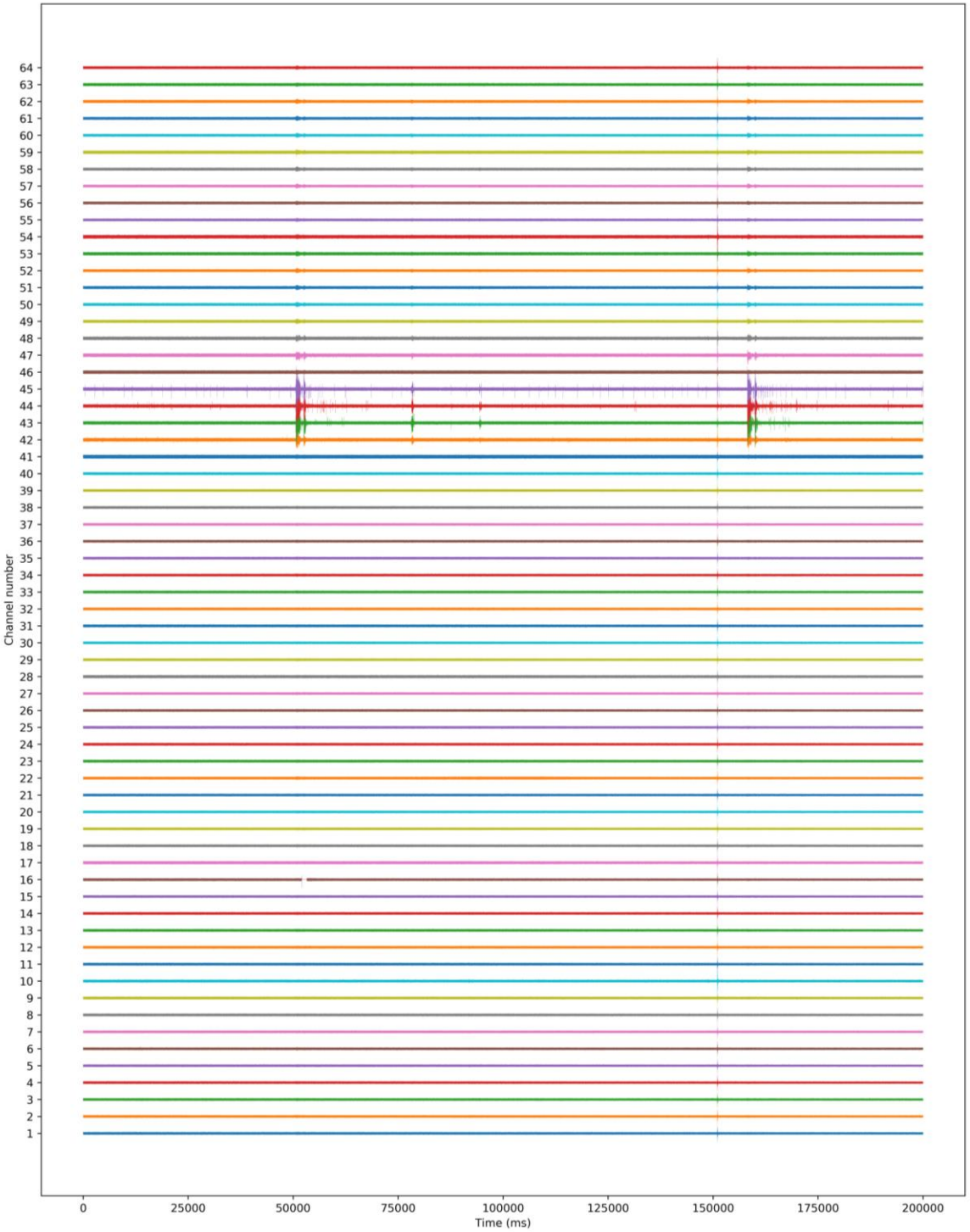

Appendix 5.1: 240 seconds of raw activity from all 64 electrodes of an MEA seeded with a CTX-STR neural co-culture, after 15 DIV.

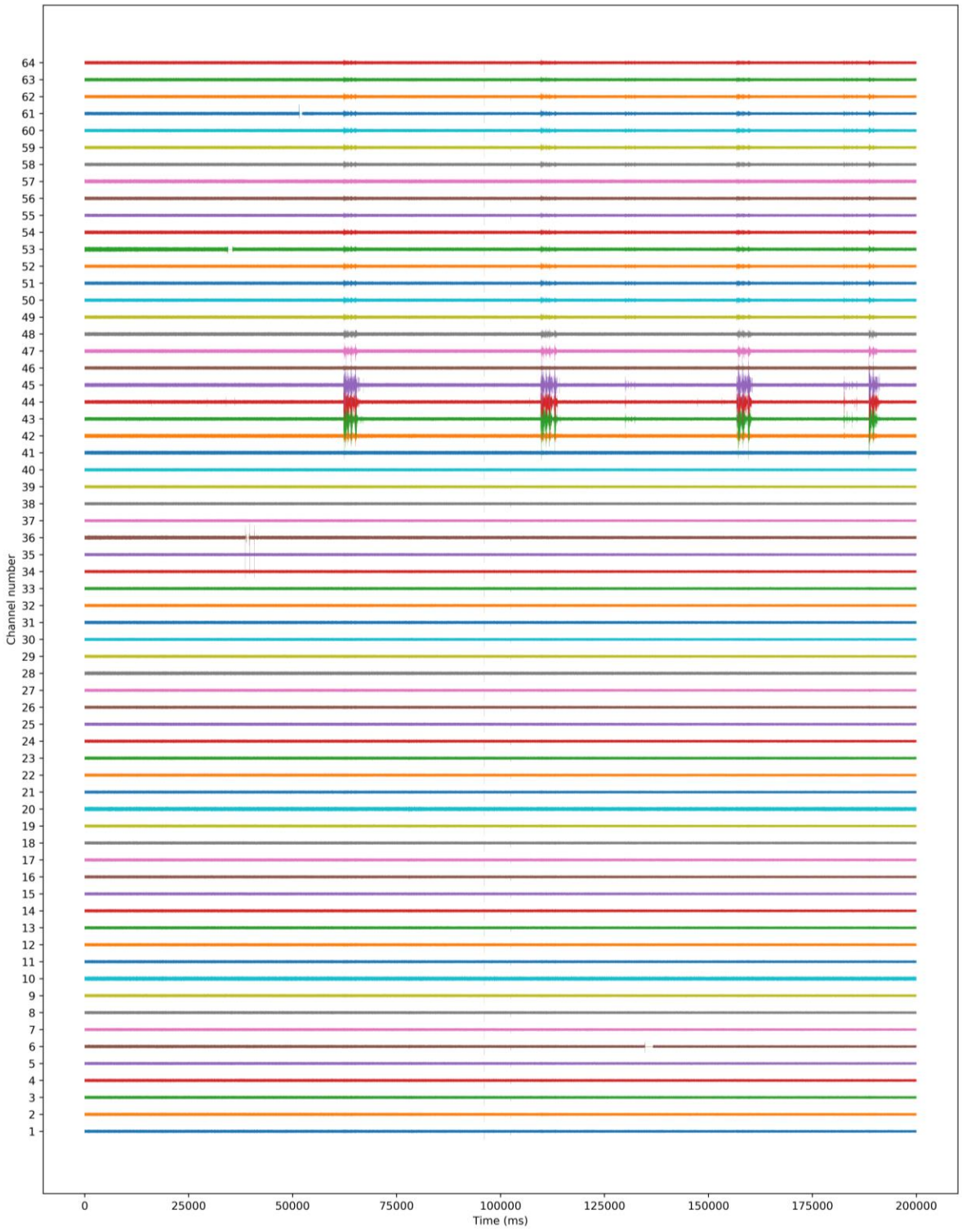

Appendix 5.2: 240 seconds of raw activity from all 64 electrodes of an MEA seeded with a CTX-STR neural co-culture, after 21 DIV.

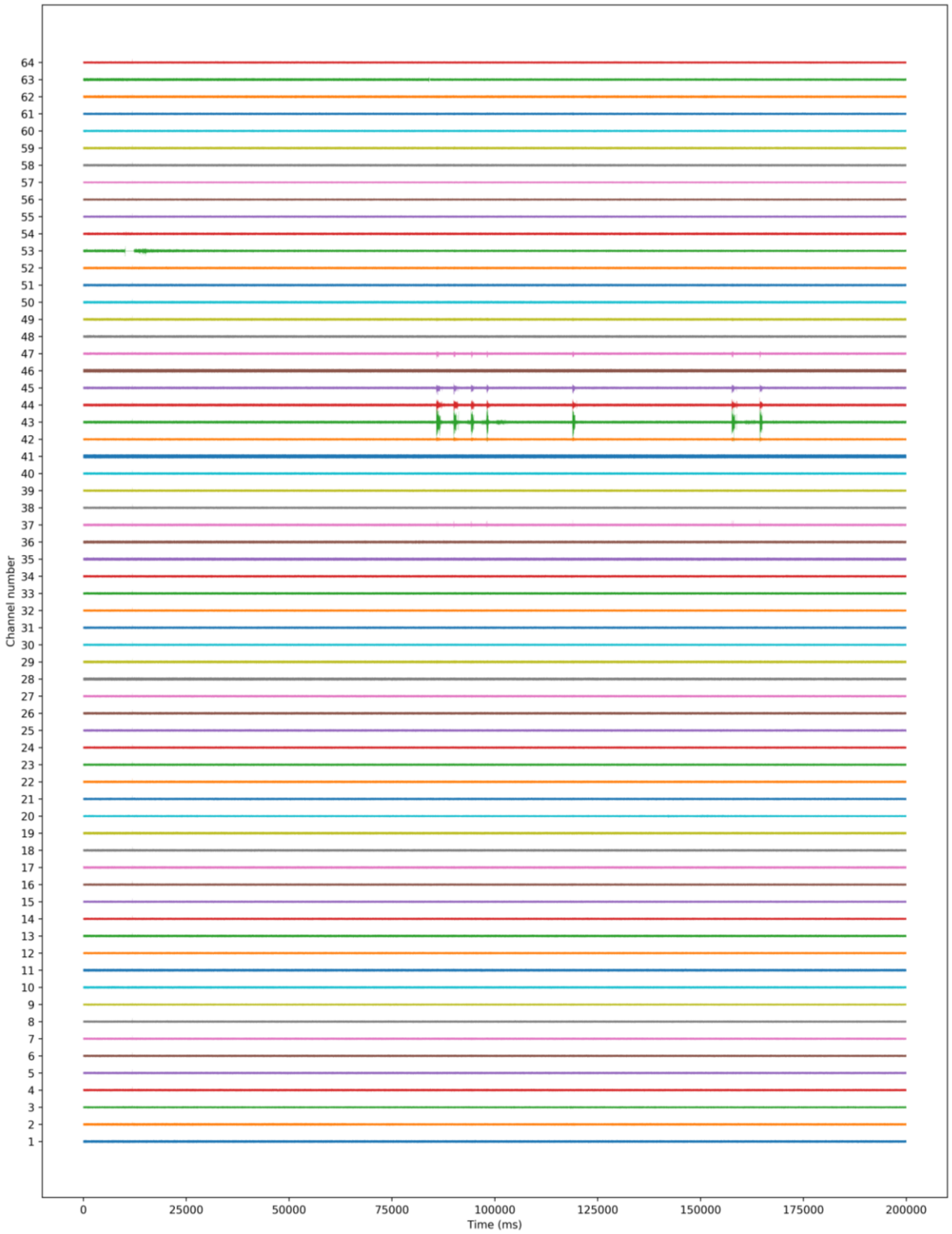

Appendix 5.3: 240 seconds of raw activity from all 64 electrodes of an MEA seeded with a CTX-STR neural co-culture, after 42 DIV.

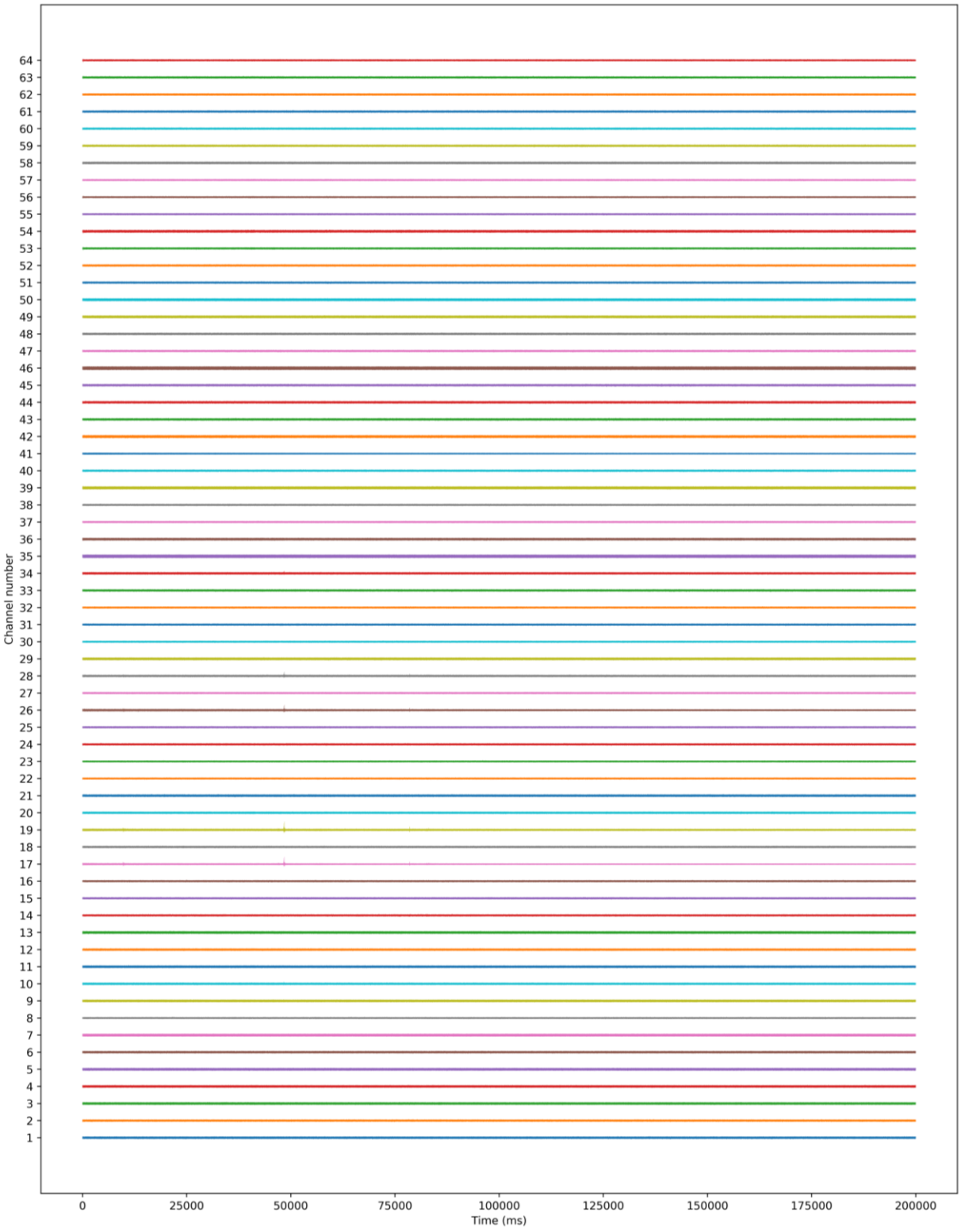

Appendix 5.4: 240 seconds of raw activity from all 64 electrodes of an MEA seeded with a CTX-STR neural co-culture, after 70 DIV.

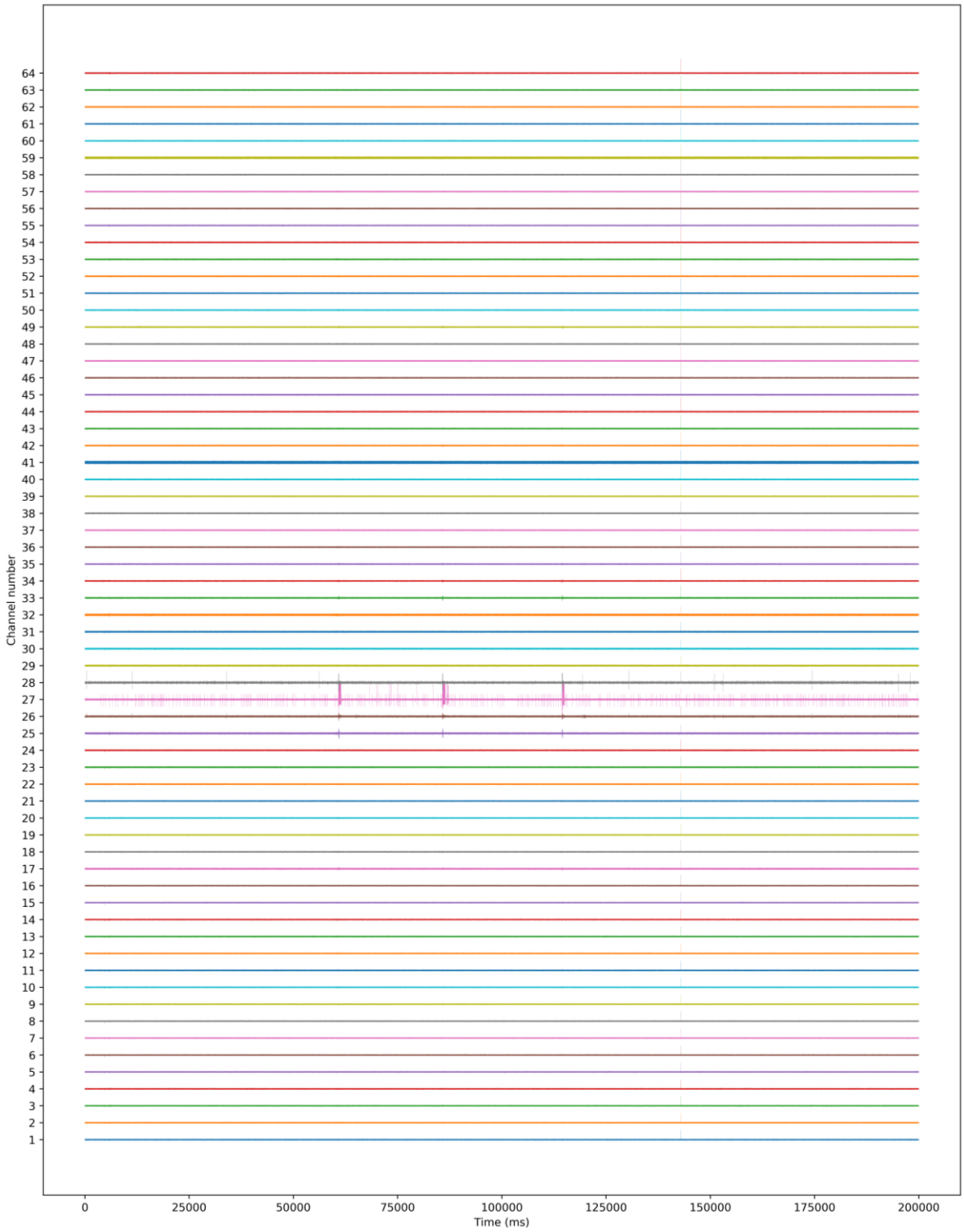

Appendix 6.1: 240 seconds of raw activity from all 64 electrodes of an MEA seeded with a STR-GP neural co-culture, after 15 DIV.

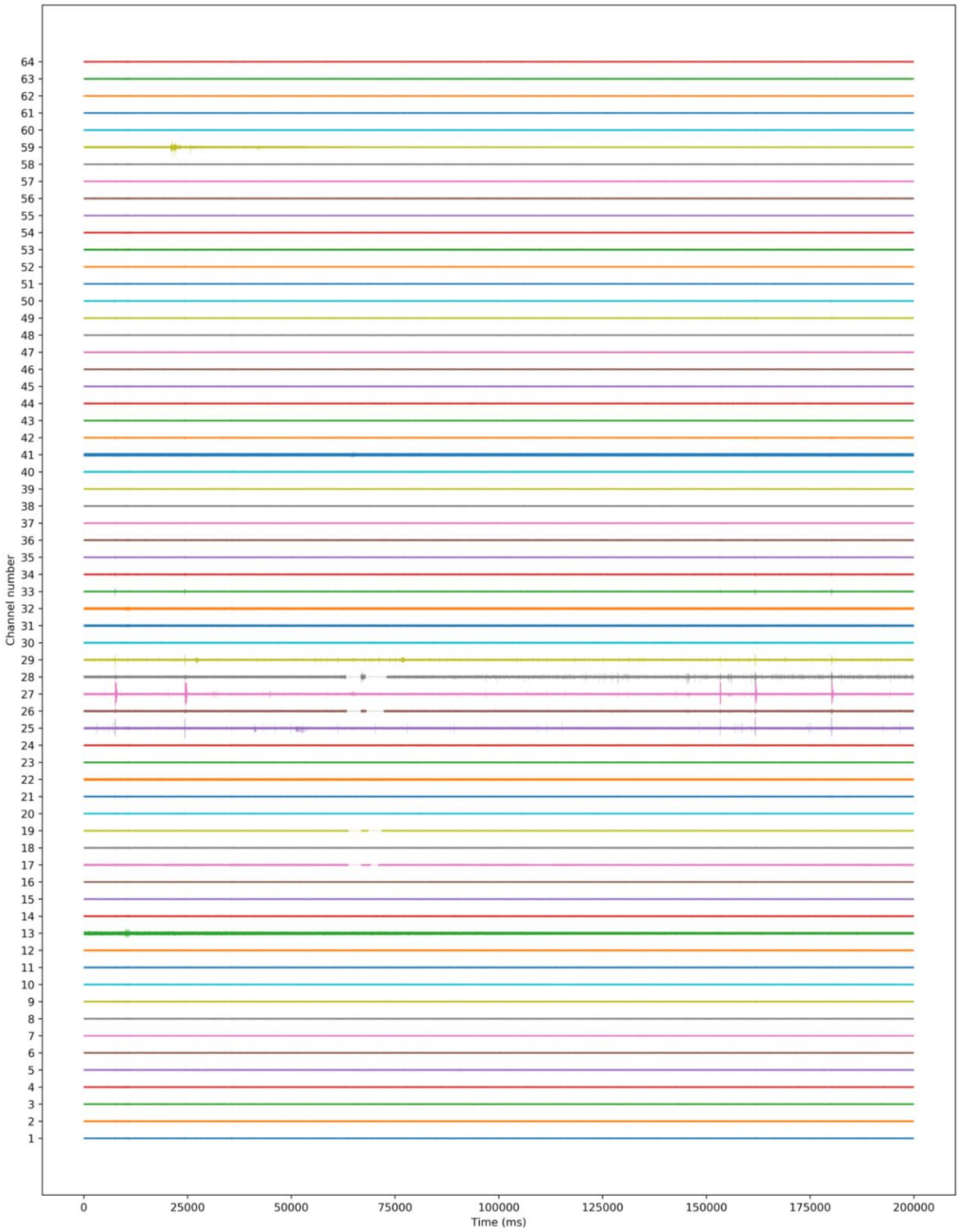

Appendix 6.2: 240 seconds of raw activity from all 64 electrodes of an MEA seeded with a STR-GP neural co-culture, after 21 DIV.

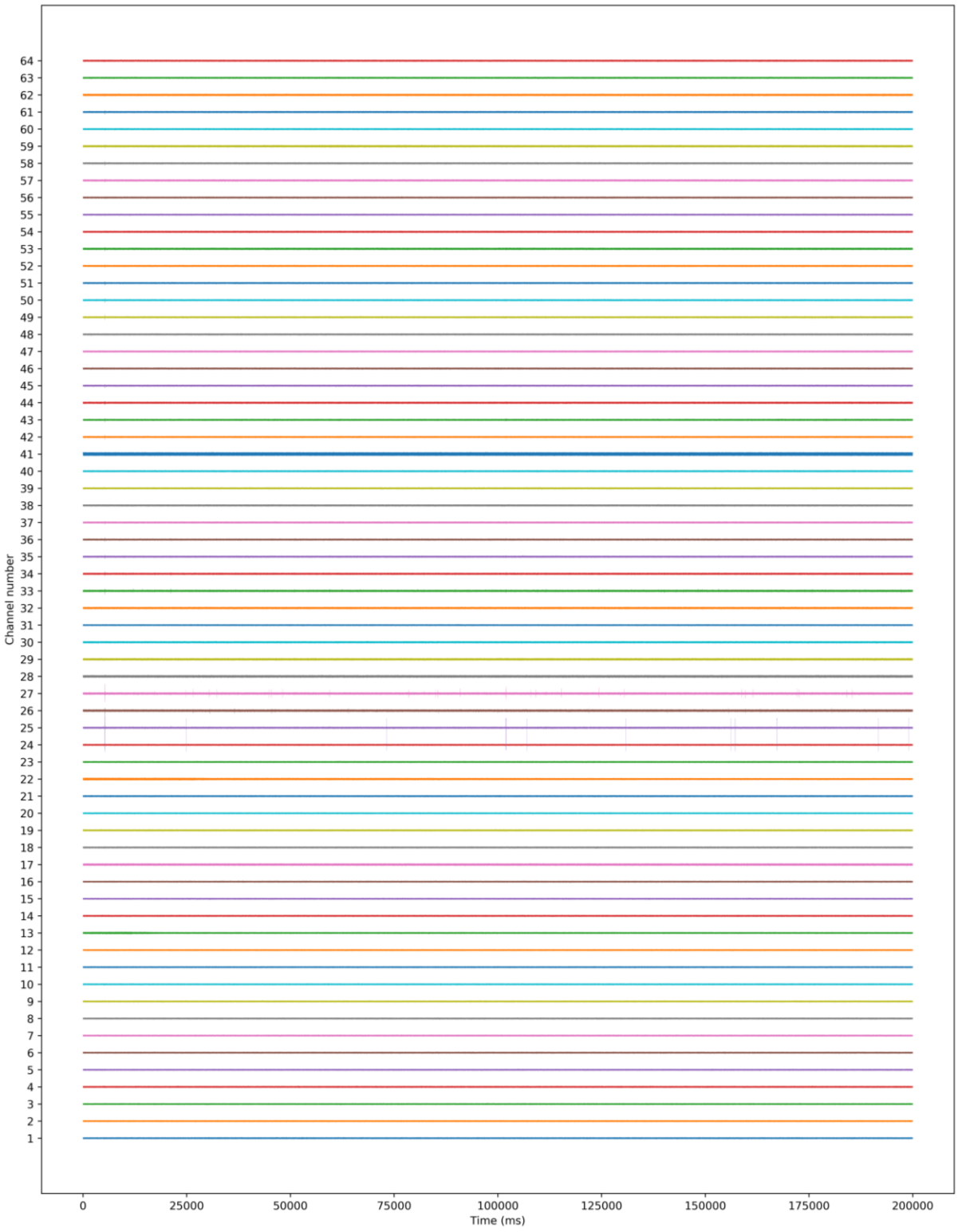

Appendix 6.3: 240 seconds of raw activity from all 64 electrodes of an MEA seeded with a STR-GP neural co-culture, after 42 DIV.

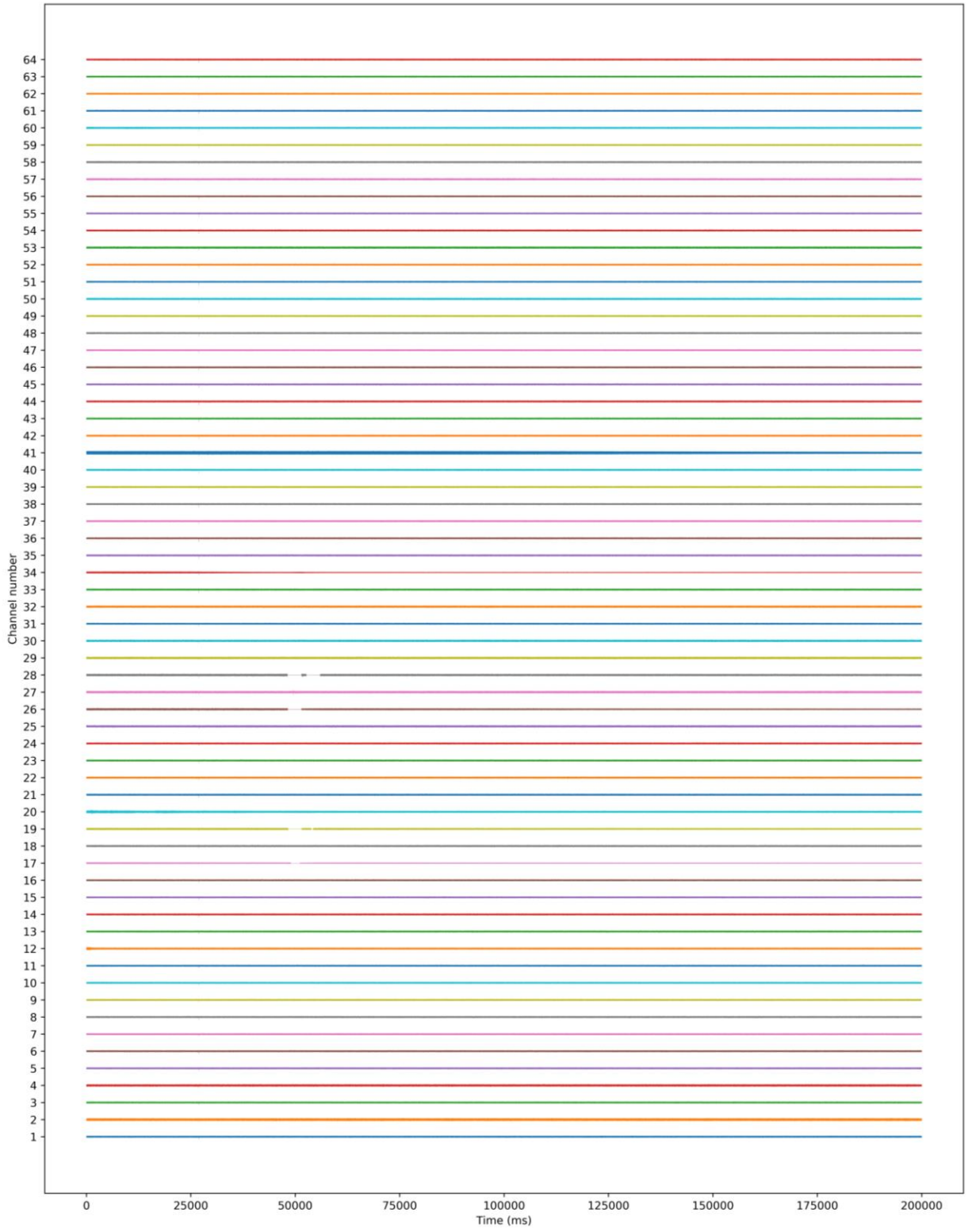

Appendix 6.4: 240 seconds of raw activity from all 64 electrodes of an MEA seeded with a STR-GP neural co-culture, after 70 DIV.

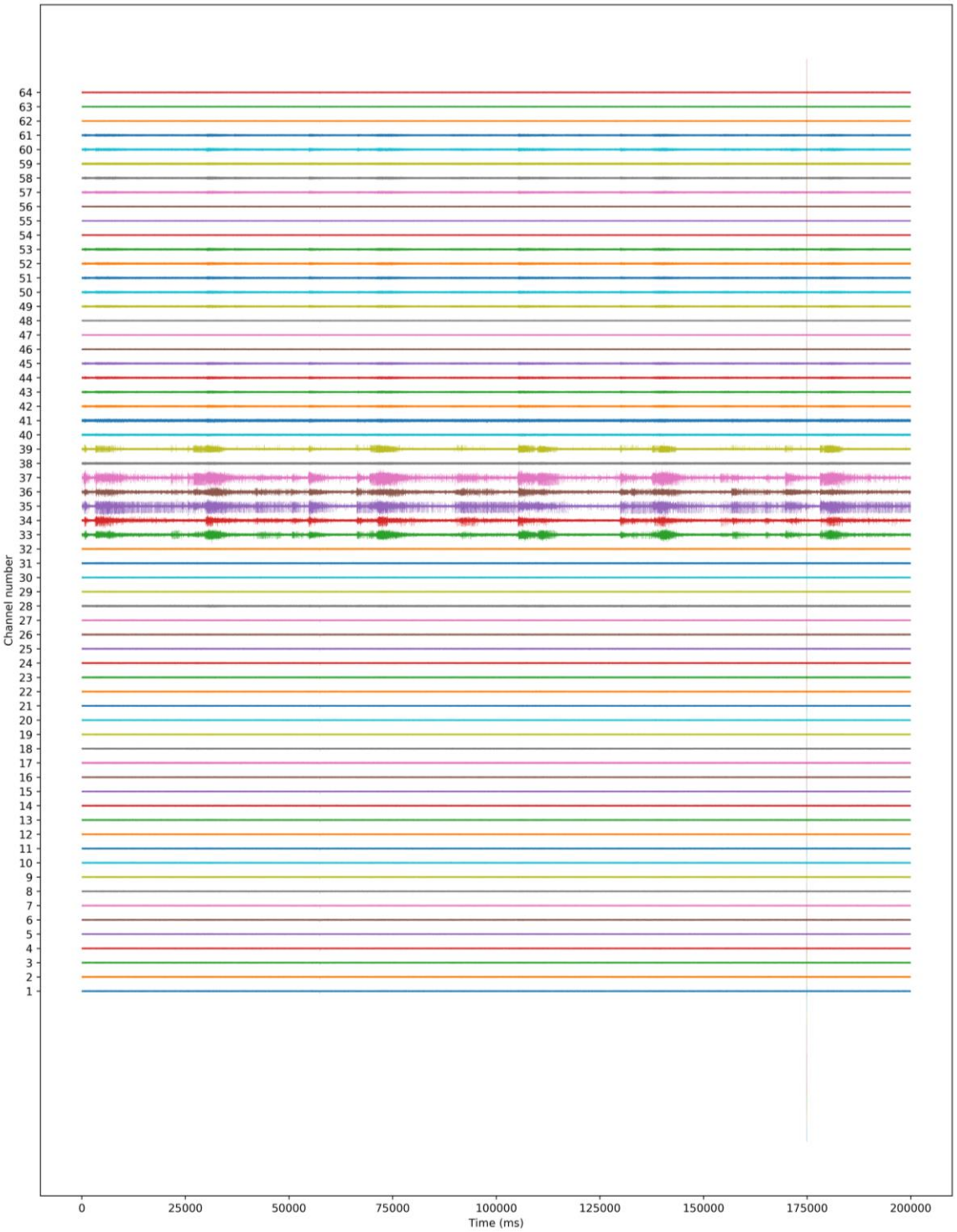

Appendix 7.1: 240 seconds of raw activity from all 64 electrodes of an MEA seeded with a SNc-STR neural co-culture, after 15 DIV.

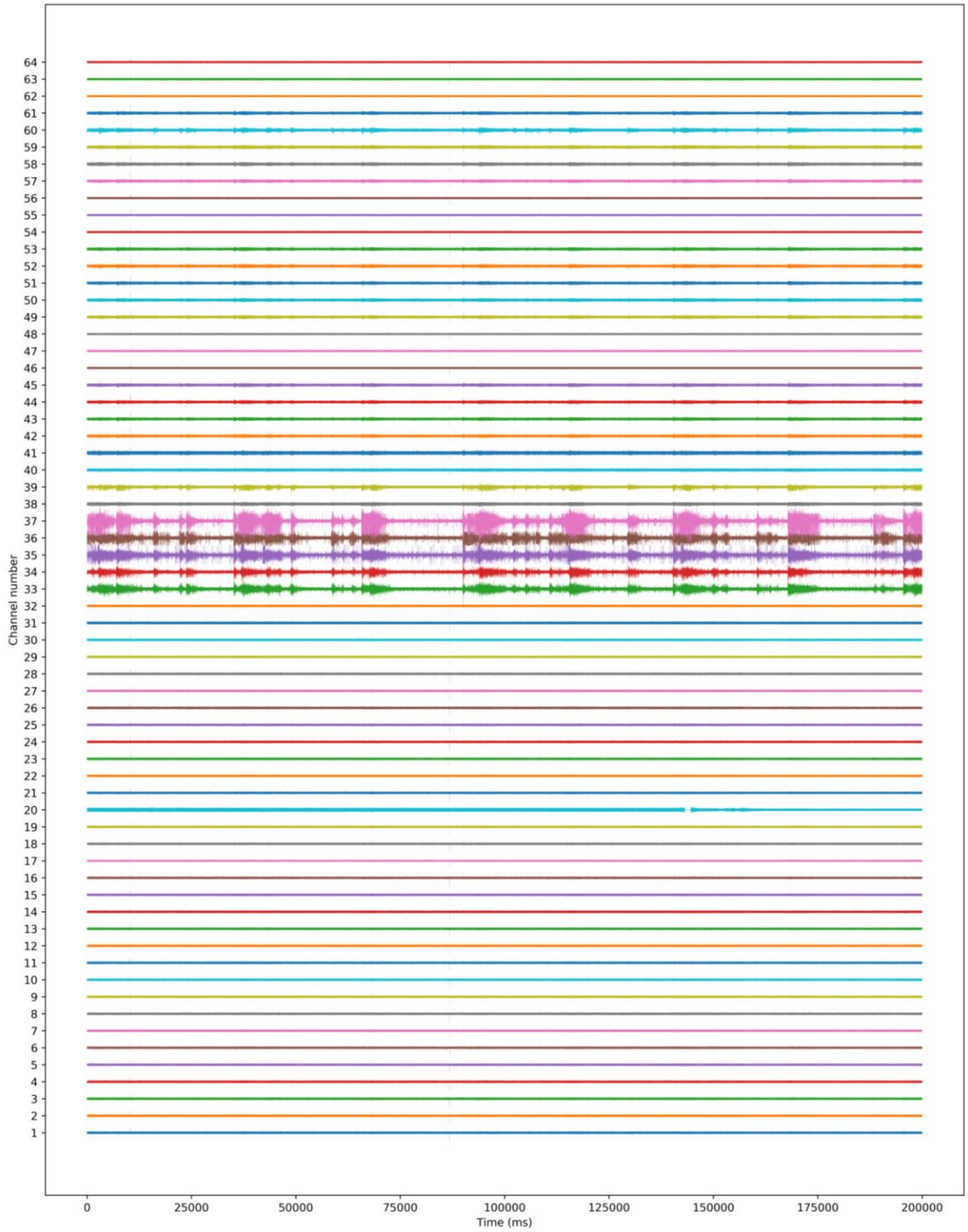

Appendix 7.2: 240 seconds of raw activity from all 64 electrodes of an MEA seeded with a SNc-STR neural co-culture, after 21 DIV.

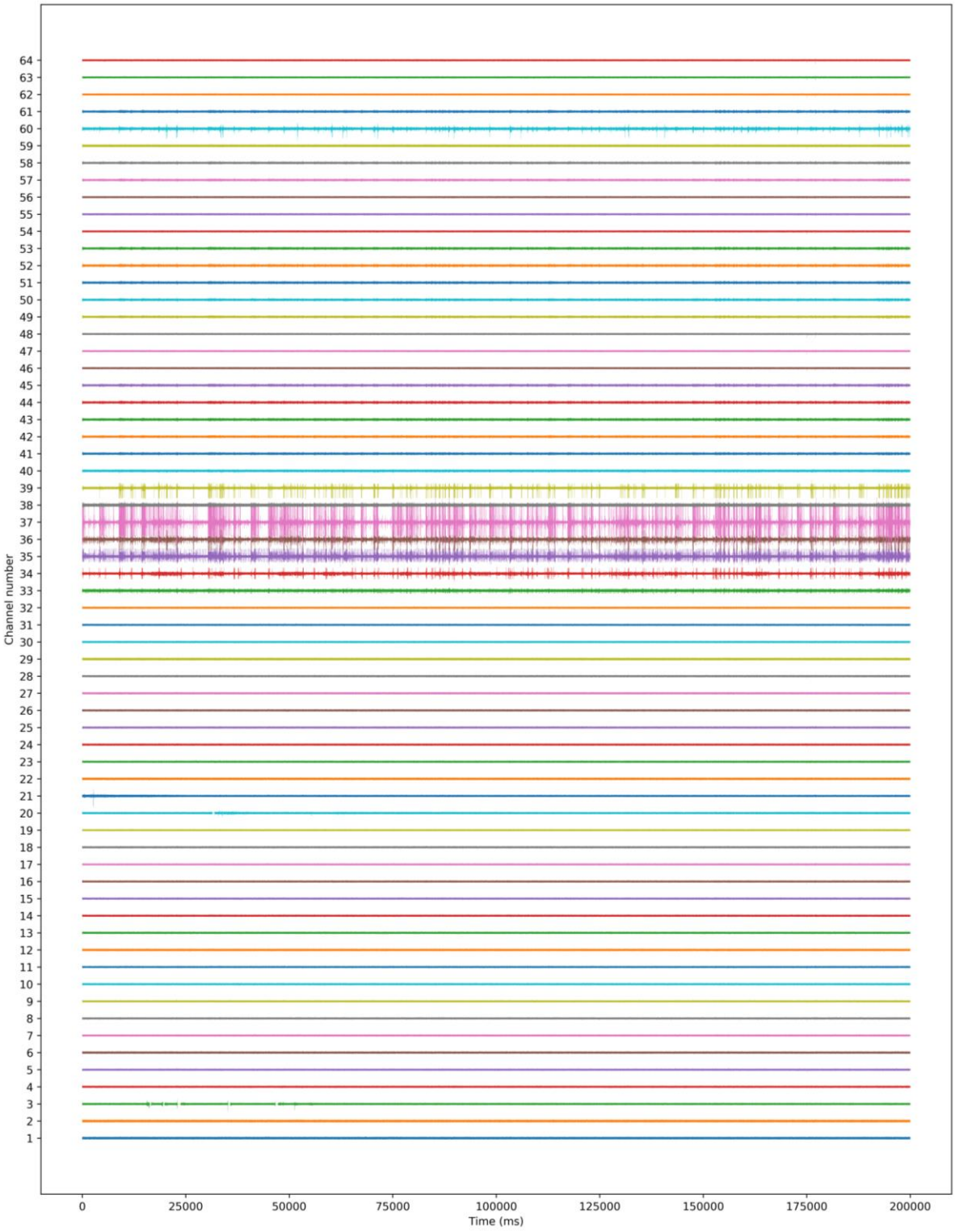

Appendix 7.3: 240 seconds of raw activity from all 64 electrodes of an MEA seeded with a SNc-STR neural co-culture, after 42 DIV.

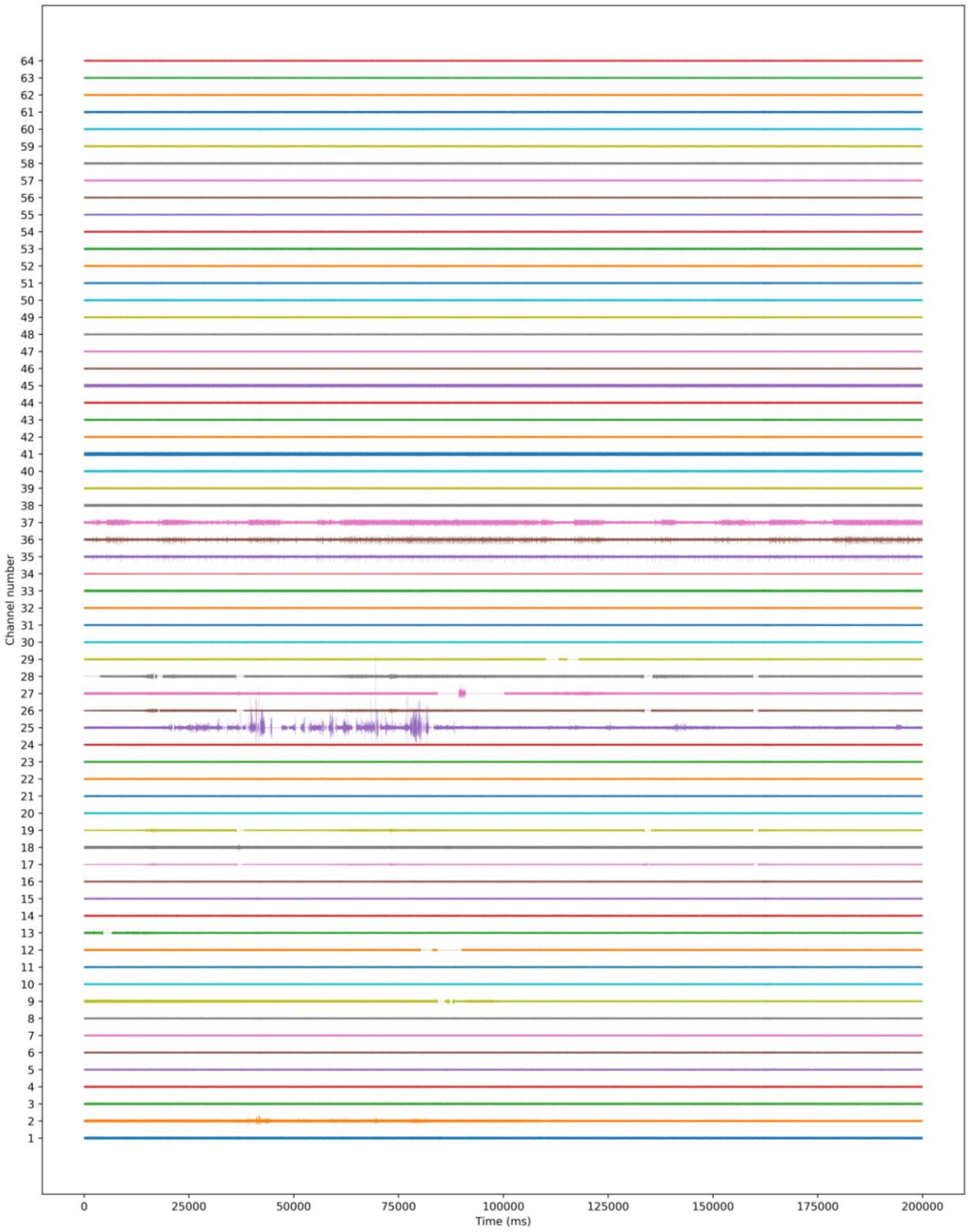

Appendix 7.4: 240 seconds of raw activity from all 64 electrodes of an MEA seeded with a SNc-STR neural co-culture, after 70 DIV.